NASA Conference Publication 2444

R488

Turbine Engine Hot Section Technology 1986

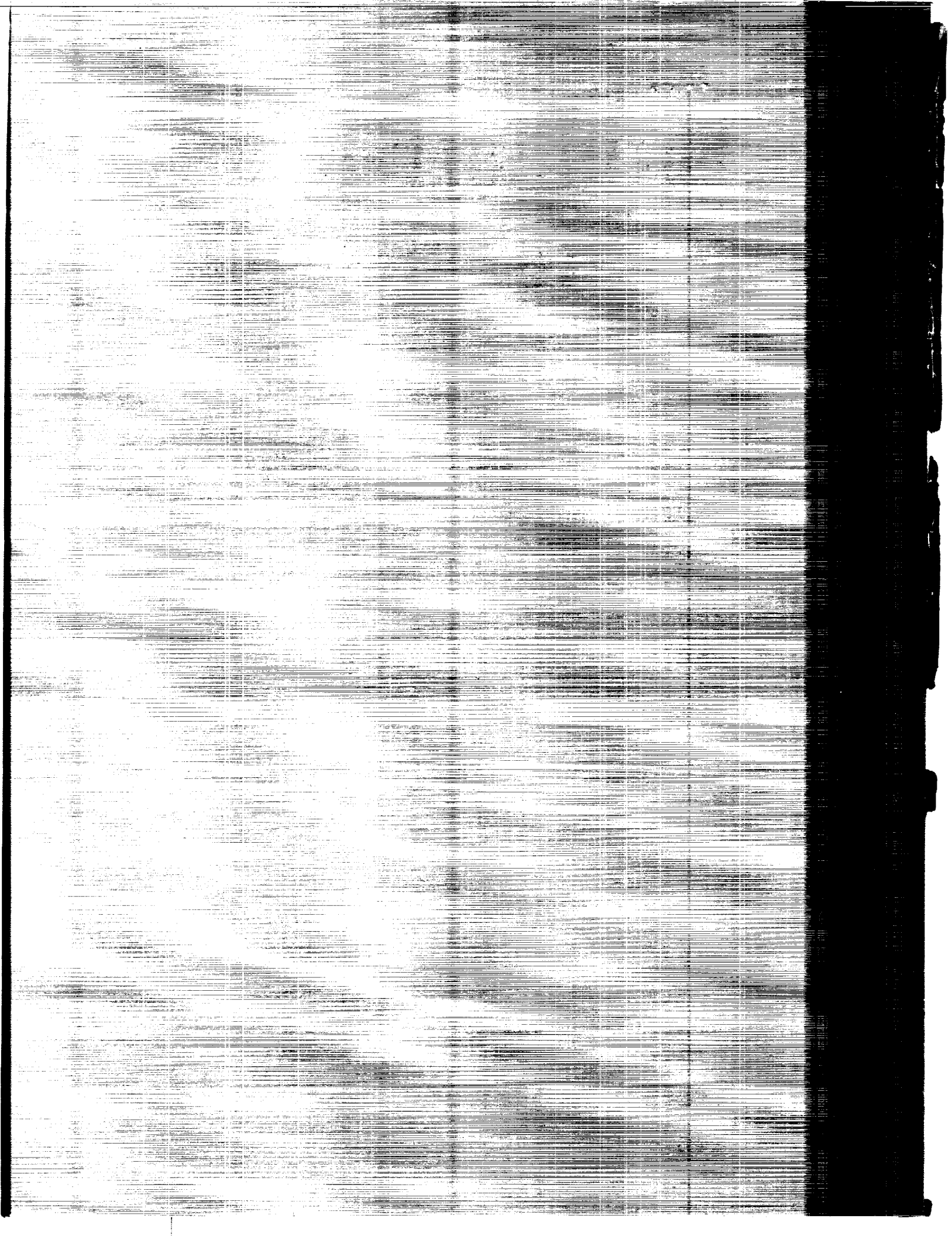

NASA Conference Publication 2444

Turbine Engine Hot Section Technology 1986

Proceedings of a conference
sponsored by NASA Lewis Research Center
Cleveland, Ohio
October 21 and 22, 1986

NASA
National Aeronautics
and Space Administration
Scientific and Technical
Information Branch
1986

FOREWORD

Aircraft gas-turbine engine designs have been pushed to ever higher levels of performance, primarily due to competition and the need for improved fuel efficiency. Such improved performance is possible primarily due to higher operating pressures and temperatures. The effect, however, has been a decrease in engine durability. In hot-section components - the combustor and turbine - the more hostile environments have accelerated damage and wear of parts, with associated dramatically increased maintenance costs. In the past, minimal efforts have been made to ensure required durability - technology advances being directed primarily toward improving performance.

The activities of the NASA Turbine Engine Hot Section Technology (HOST) Project are directed toward durability needs, as defined by industry, and a more balanced approach to engine design. The HOST efforts will improve the understanding and prediction of thermal environments, thermal loads, structural responses, and life by focused experimental and analytical research activities. The overall approach is to assess existing analysis methods for strengths and deficiencies, to conduct supporting analytical and experimental research to rectify these deficiencies, to incorporate state-of-the-art improvements into the analysis methods, and finally to verify the improvements by bench-mark quality experiments. The research is supported by the HOST Project with contracts, grants, and Lewis in-house activities.

To provide representatives from industry, academia, and government with the latest findings and progress toward improved aircraft turbine engine durability, a two-day workshop was held in October 1986. This publication contains the papers presented at the workshop.

Daniel E. Sokolowski
Manager, HOST Project

CONTENTS

OVERVIEWS

INSTRUMENTATION

COMBUSTION

TURBINE HEAT TRANSFER

STRUCTURAL ANALYSIS

FATIGUE AND FRACTURE

SURFACE PROTECTION

CONCLUDING REMARKS

N89-12877

TURBINE ENGINE HOT SECTION TECHNOLOGY (HOST) PROJECT

Daniel E. Sokolowski and C. Robert Ensign
NASA Lewis Research Center
Cleveland, Ohio

The Hot Section Technology (HOST) Project is a NASA-sponsored endeavor to improve the durability of advanced gas-turbine engines for commercial and military aircraft. Through improvements in analytical models and life-prediction systems, designs for future turbine-engine hot section components - the combustor and turbine - will be analyzed more accurately and, thus, will incorporate features required for longer life in the more hostile operating environment of high performance engines.

Started in fiscal year 1981, the HOST Project has activities currently planned through 1989 with an estimated total cost of over $44 million. While the Project's focused research activities are necessarily analytical in nature, significant experimental testing is required for better understanding of problems as well as model verifications. The efforts are being conducted in-house at the NASA Lewis Research Center, under contracts with major domestic turbine-engine manufacturers and under grants to qualified universities. The contract and grant total funding is approximately one-half of the total budget for fiscal year 1987.

At NASA Lewis the HOST Project serves as the focal point for advocacy, funding, technical coordination, and information exchange. This workshop serves as the primary vehicle for this last function; that is, to disseminate information and elicit the exchange of ideas among participants.

Activities of the HOST Project are categorized under six disciplines: (1) instrumentation, (2) combustion, (3) turbine heat transfer, (4) structural analysis, (5) fatigue and fracture, and (6) surface protection. Management of the project uses the matrix approach, as shown in figure 1. A subproject manager is responsible for each discipline and reports to the manager of the HOST Project

All technical activities initiated and supported by the HOST Project are listed in table I. To summarize these activities and their objectives, instrumentation is being developed to obtain high-temperature, benchmark-quality data to develop and verify analysis methods. These include flow sensors (LDV), heat flux sensors (thin film), strain sensors (1800 °F static thin film), a high-frequency-response gas temperature sensor (frequency compensated), and a hot-section optical viewing system. Combustion work includes aerothermal model assessment and development as well as dilution jet modeling. In turbine heat transfer two- and three-dimensional flow and heat transfer are being studied on airfoil external boundaries, emphasizing boundary-layer transition and viscous modeling. Also being investigated is coolant-passage heat transfer, including midchord jet impingement cooling and rotational passage effects. Structural analysis includes research into thermal mechanical load models, component geometry-specific models, three-dimensional inelastic analysis methods development, development of a thermal structural cyclic test facility, and constitutive model development for both isotropic and anisotropic

materials in single-crystal and directionally solidified forms. Fatigue and fracture includes research in life-prediction methods for creep-fatigue interactions and elastoplastic crack propagation. Surface protection research includes studies of corrosion phenomena, and thermal barrier coating analysis method developments.

To further understand the organization of the project and, more importantly, the reasons for its activities, it is useful to consider the critical steps leading to life prediction. The flow diagram in figure 2 shows such critical steps and may be used for any hot section subcomponent; for example, combustor liners, turbine blades, or turbine vanes. The first series of steps in figure 2 defines the engine subcomponent geometry, material, and operating requirements. The remaining steps are those being addressed by the HOST Project: (1) characterizing the hot section environment, (2) characterizing thermomechanical loads, (3) determining material behavior and structural response due to imposed loads, and (4) predicting life for subcomponents exposed to cyclic operation. For these steps the technology needs and notable technical progress to date are shown in figures 3 to 6.

Workshop publications and many contractor final reports carry the label "For Early Domestic Dissemination" (FEDD) to protect national interests and, thus, are available only to qualified U.S. citizens. Although contractor final reports have been published, they often represent initial phases of multiphased work. Thus, this annual workshop report is the primary document for reporting technical results for the entire project.

TABLE I. - HOST Project Activities

	Contract (C), Grant (G), or NASA Organization (N)	Number
Instrumentation		
Hot Section Viewing System	C	NAS3-23156
Dynamic Gas Temperature Measurement System - A	C	NAS3-23154
Dynamic Gas Temperature Measurement System - B	C	NAS3-24228
Turbine Static Strain Gage - A	C	NAS3-23169
Turbine Static Strain Gage - B	C	NAS3-23722
Turbine Heat Flux Sensors	C	NAS3-23529
Laser Speckle Strain Measurement	C	NAS3-26615
High Temperature Strain Gage Materials	G	NAG3-501
Hot Section Sensors	N	2510
Laser Anemometry for Hot Section Applications	N	2520/2530
HOST Instrument Applications	N	2510
Combustion		
Assessment of Combustor Aerothermal Models - I	C	NAS3-23523
Assessment of Combustor Aerothermal Models - II	C	NAS3-23524
Assessment of Combustor Aerothermal Models - III	C	NAS3-23525
Improved Numerical Methods - I	C	NAS3-24351
Improved Numerical Methods - II	C	NAS3-24350
Improved Numerical Methods - III	G	NAG3-596
Flow Interaction Experiment	C	NAS3-24350
Fuel Swirl Characterization - I	C	NAS3-24350
Fuel Swirl Characterization - II	C	NAS3-24352
Mass and Momenta Transfer	C	NAS3-22771
Diffuser/Combustor Interaction	C	F33615-84-C-2427
Dilution Jet Mixing Studies	C	NAS3-22110
Lateral Jet Injection into Typical Combustor Flowfields	G	NAG3-549
Flame Radiation Studies	N	2650
Turbine Heat Transfer		
Mainstream Turbulence Influence on Flow in a Turning Duct - A	C	NAS3-23278
Mainstream Turbulence Influence on Flow in a Turning Duct - B	G	NAG3-617
2-D Heat Transfer without Film Cooling	C	NAS3-22761
2-D Heat Transfer with Leading Edge Film Cooling	C	NAS3-23695
2-D Heat Transfer with Downstream Film Cooling	C	NAS3-24619
Measurement of Blade and Vane Heat Transfer Coefficient in a Turbine Rotor	C	NAS3-23717
Assessment of 3-D Boundary Layer Code	C	NAS3-23716
Coolant Side Heat Transfer with Rotation	C	NAS3-23691
Analytic Flow and Heat Transfer	C	NAS3-24358
Effects of Turbulence on Heat Transfer	G	NAG3-522
Tip Region Heat Transfer	G	NAG3-623
Impingement Cooling	G	NSG3-075
Computation of Turbine Blade Heat Transfer	G	NAG3-579
Advanced Instrumentation Development	N	2640
Warm Turbine Flow Mapping with Laser Anemometry	N	2620
Real Engine-Type Turbine Aerothermal Testing	N	2640
Structural Analysis		
Thermal/Structural Load Transfer Code	C	NAS3-23272
3-D Inelastic Analysis Methods - I	C	NAS3-23697
3-D Inelastic Analysis Methods - II	C	NAS3-23698
Component Specific Modeling	C	NAS3-23687
Liner Cyclic Life Determination	N	5210
Structural Components Response Program	N	5210
High Temperature Structures Research Laboratory	N	5210
Constitutive Model Development	N	5210
Constitutive Modeling for Isotropic Materials - I	C	NAS3-23925
Constitutive Modeling for Isotropic Materials - II	C	NAS3-23927
Theoretical Constitutive Models for Single Crystal Alloys	G	NAG3-511
Biaxial Constitutive Equation Development for Single Crystals and Directionally Solidified Alloys	G	NAG3-512
Fatigue and Fracture		
Creep-Fatigue Life Prediction for Isotropic Materials	C	NAS3-23288
Elevated Temperature Crack Propagation	C	NAS3-23940
Life Prediction and Material Constitutive Behavior for Anisotropic Materials	C	NAS3-23939
Analysis of Fatigue Crack Growth Mechanism	G	NAG3-348
Vitalization of High Temperature Fatigue and Structures Laboratory	N	5220
Surface Protection		
Effects of Surface Chemistry on Hot Corrosion	C	NAS3-23926
Thermal Barrier Coating Life Prediction - I	C	NAS3-23943
Thermal Barrier Coating Life Prediction - II	C	NAS3-23944
Thermal Barrier Coating Life Prediction - III	C	NAS3-23945
Airfoil Deposition Model	G	NAG3-201
Mechanical Behavior of Thermal Barrier Coatings	G	NCC3-27
Coating Oxidation/Diffusion Prediction	N	5160
Deposition Model Verification	N	5160
Dual Cycle Attack	N	5160
Rig/Engine Correlation	N	5160
Burner Rig Modernization	N	5160

Notes: A, B Activities in series
I, II, III Activities in parallel.

ORGANIZATION: HOT SECTION TECHNOLOGY (HOST) PROJECT

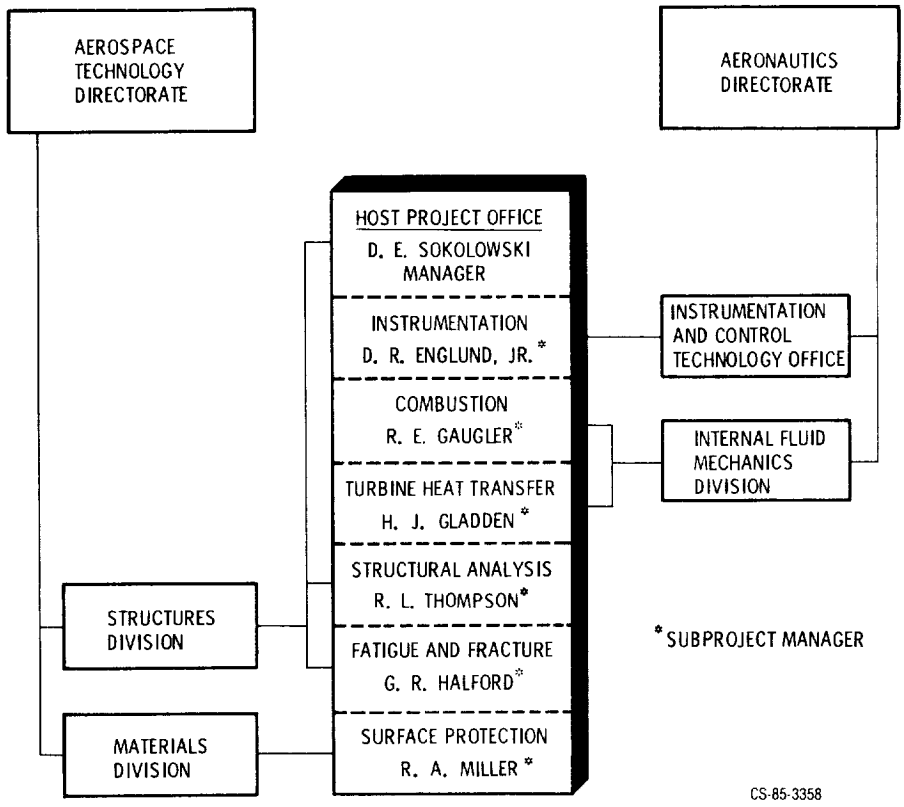

Figure 1

FRAMEWORK FOR THE HOST PROJECT

INTEGRATION OF ANALYSES LEADS TO LIFE PREDICTION

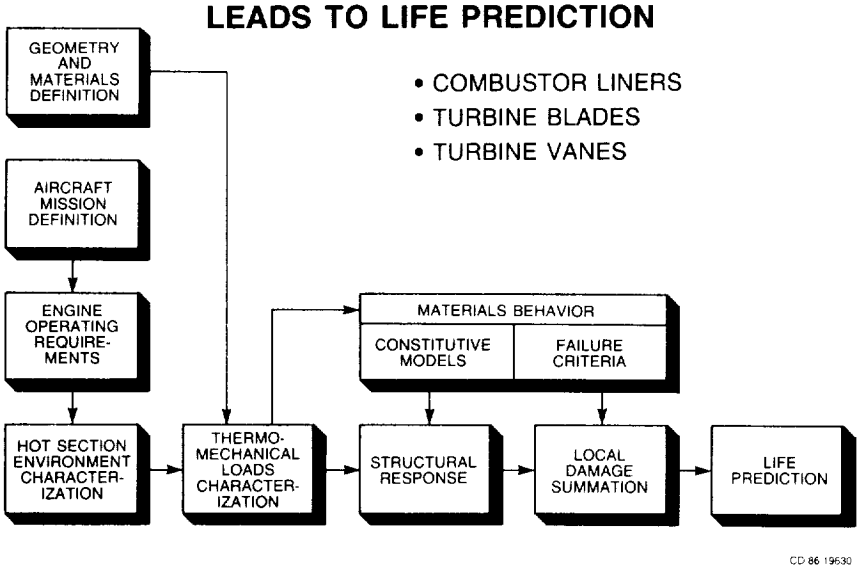

Figure 2

HOT SECTION ENVIRONMENT

NEED

- TO BETTER UNDERSTAND AND PREDICT THE AEROTHERMAL ENVIRONMENT AROUND HOT SECTION PARTS.

HOST PROGRESS

- DEVELOPED VIEWING SYSTEM AND TESTED IN PW 2037 AND HPF; FUEL INJECTOR OPERATION, LINER HOT SPOTS, AND LINER/VANE CRACKING CAN BE OBSERVED.
- DEVELOPED DYNAMIC GAS TEMPERATURE MEASUREMENT SYSTEM AND TESTED IN F-100 AND HPF; GAS TEMPERATURE FLUCTUATIONS CAN BE ACCURATELY DETERMINED UP TO 1-KHz AND 3000 °F PEAKS.
- EVOLVED LASER ANEMOMETRY FOR MEASUREMENTS IN COMBUSTOR EXHAUST STREAM; EFFORTS UNDERWAY FOR MEASUREMENTS WITHIN TURBINE.
- IMPROVING RESOLUTION OF SPATIAL PROPERTY VARIATIONS AND QUANTITATIVE ACCURACY OF AEROTHERMAL CODES, THROUGH 3-D NUMERICAL SCHEMES, IMPROVED TURBULENCE AND CHEMISTRY MODELS, AND RELEVENT BENCHMARK DATA.
- OBTAINED BROAD DATA BASE AND DEVELOPED EMPIRICAL MODEL FOR MIXING DILUTION AIR JETS WITH COMBUSTION GASES; COMBUSTOR EXIT TEMPERATURES PREDICTED ACCURATELY WITHIN RANGE OF DATA BASE; 3-D NUMERICAL CODES BEING IMPROVED IN SPEED AND GEOMETRIC CAPABILITIES.

CD-86-19639

Figure 3

THERMOMECHANICAL LOADS

NEED

- TO BETTER UNDERSTAND AND PREDICT THE THERMAL AND MECHANICAL LOADS ON CRITICAL PARTS LIKE LINERS, BLADES, AND VANES.

HOST PROGRESS

- EVOLVED TOTAL HEAT FLUX SENSORS FROM LINERS TO AIRFOILS; SENSITIVITY TO HEAT FLUX GRADIENTS ALONG AIRFOIL MUST BE MINIMIZED.
- DETERMINED THE EFFECTS OF ROTATION ON COOLANT HEAT TRANSFER IN SMOOTH-WALL PASSAGES AND MODIFIED "TEACH" CODE; SIMILAR EFFORTS UNDERWAY FOR TURBULATED PASSAGES.
- DETERMINATION OF ROTATION ON AIRFOIL HEAT TRANSFER STARTING TO PRODUCE RESULTS.
- ASSESSED 3-D BOUNDARY LAYER CODE; AGREEMENT WITH DATA IS GENERALLY GOOD.
- OBTAINED BROAD DATA BASES AND MODIFIED STAN5 CODE TO ACCURATELY PREDICT HEAT TRANSFER COEFFICIENTS, ESPECIALLY AT THE TRANSITION POINT, FOR FILM AND NON-FILM COOLED AIRFOILS.

CD-86-19637

Figure 4

STRUCTURAL RESPONSE

NEED

- TO IMPROVE PREDICTION ACCURACY AND EFFICIENCY OF STRESSES AND STRAINS ON HOT SECTION METALLIC PARTS DUE TO THERMOMECHANICAL LOADS.

HOST PROGRESS

- DEVELOPED STRAIN MEASUREMENT APPROACH HAVING 1300 °F CAPABILITY; EFFORTS UNDERWAY TOWARD 1800 °F CAPABILITY.
- DEVELOPED INTERFACING CODE WHICH AUTOMATICALLY TRANSFERS 3-D THERMAL INFORMATION FROM A HEAT TRANSFER CODE (COARSE GRID) TO A STRUCTURAL ANALYSIS CODE (FINER GRID).
- DEVELOPED 3-D INELASTIC STRUCTURAL ANALYSIS CODES FOR NONLINEAR BEHAVIOR AT HIGH THERMOMECHANICAL LOADS; THREE CODES COVER DIFFERENT APPROACHES--MOMM, MHOST, BEST3D; PROVIDED TENFOLD INCREASE IN COMPUTATIONAL EFFICIENCY WITH IMPROVED ACCURACY.
- DEVELOPED SEVERAL VISCOPLASTIC CONSTITUTIVE MODELS FOR BOTH ISOTROPIC AND ANISOTROPIC MATERIALS; BROADENED DATA BASE; VERIFIED MODELS FOR RANGE OF TEST CONDITIONS; HIGH TEMPERATURE STRESS/STRAIN PREDICTION CAPABILITY IMPROVED BY 30-PERCENT; LEWIS IS INTERNATIONALLY RECOGNIZED LEADER IN CONSTITUTIVE MODEL DEVELOPMENT.
- DEVELOPED MODULAR CODE FOR NONLINEAR STRUCTURAL ANALYSES OF LINERS, BLADES, AND VANES OVER MISSION CYCLE; AUTOMATIC SOLUTION STRATEGY FOR LINERS--SIMILAR STRATEGY UNDERWAY FOR BLADES AND VANES.

CD-86-19640

Figure 5

LIFE PREDICTION

NEED

- TO ACCURATELY PREDICT THE NUMBER OF CYCLES TO FATIGUE CRACK INITIATION (LIFE) AND CRACK GROWTH FOR COMPONENTS MADE OF ISOTROPIC AND ANISOTROPIC MATERIALS THAT ARE SUBJECTED TO COMPLEX CYCLIC MECHANICAL AND THERMAL LOADS AT HIGH TEMPERATURES.
- TO ACCURATELY PREDICT THE LIFE OF THERMAL BARRIER COATINGS ON LINERS AND AIRFOILS.

HOST PROGRESS

- DEVELOP NEW CONSTITUTIVE EQUATIONS AND LIFE MODELS THAT CAN BE USED TO PREDICT LIFE FOR ADVANCED CONFIGURATIONS AND MATERIALS UNDER COMPLEX LOADING CONDITIONS.
- EXTENDED MODELING CAPABILITIES TO INCLUDE MULTIAXIAL (2-D AND 3-D) STRESS STATES AND THERMOMECHANICAL LOADING CONDITIONS.
- EXTENDED LABORATORY TESTING CAPABILITIES TO PERMIT COMPLEX THERMOMECHANICAL TESTS NEVER BEFORE POSSIBLE.
- SOME PREDICTIONS HAVE SHOWN IMPROVEMENTS IN ACCURACY BY A FACTOR OF TWO.
- SIGNIFICANT PROGRESS TOWARD DEVELOPING LIFE PREDICTION MODELS FOR BLADES MADE WITH ANISOTHOPIC MATERIALS.
- FORMULATED OXIDATION/THERMAL STRAIN MODEL FOR TBC LIFE PREDICTION (LeRC) THAT IS BASIS FOR TWO PRELIMINARY LIFE PREDICTION MODELS DEVELOPED BY P&W AND GTEC.

CD 86 19632

Figure 6

N89-12878

HOST INSTRUMENTATION R&D PROGRAM OVERVIEW

D.R. Englund
NASA Lewis Research Center
Cleveland, Ohio

The HOST Instrumentation R&D program is directed at the development of two categories of instrumentation. One is instrumentation capable of characterizing the environment imposed on turbine engine hot-section components. This category includes instruments for the measurements of gas flow, gas temperature, and heat flux. The second category is instrumentation to measure the effect of the environment on the hot-section components. This category includes strain measuring instruments and an optical system capable of providing interior views of a burner liner during operation. The program was formulated to concentrate on critial measurements that could not be made with available instruments or with instruments under development via other NASA- or DOD-funded programs or via Industrial Research and Development programs.

The HOST instrumentation program for fiscal years 1984 through 1989 is shown in the accompanying figure. There are no additions to the program this year, and two contracts have been completed within this past year. One is the development of the dynamic gas temperature measurement system. This work has included the demonstration of the frequency response of the system and improvements in the data-reduction software that speeds up data reduction and makes the system work on a general-purpose computer. The second completed contract is the demonstration of the laser speckle photogrammetry system on the structural components response rig. Results from this work were limited by the inability of the measurement to account for errors due to out-of-plane distortion and rotation of the test sample. Further use of optical instrumentation on the structural component response rig is anticipated for measurements of test sample surface deflection and, we hope, strain.

Other parts of the HOST instrumentation program have either been completed in previous years or are continuing. The development of the turbine blade and vane static strain gauge is progressing, with the major effort directed at thin-film gauges made from the palladium-base alloy. Development of a wire strain gauge system will also be undertaken when wire becomes available. Work on a process for drawing the palladium-base alloy into suitable wire is underway at Battelle-Columbus. We are also looking at alternative materials that may have potential for high-temperature strain gauge applications through a research grant to Northwestern University. The emphasis here is on the high-temperature resistance properties of materials, including alloys, nitrides and carbides of transition metals, and silicon carbide. Work at Lewis on high-temperature strain gauges has included the establishment of an automated strain gauge test laboratory and work on application techniques. The automated strain gauge laboratory is now operational. Contract work to develop heat flux sensors for combustor liners and blades and vanes was completed in 1985. Additional work on heat flux sensors and the establishment of an in-house heat flux sensor calibrator is continuing under non-HOST funding. The experiment on turbulence measurement in the exhaust stream of an atmospheric burner uses the dynamic gas-temperature measurement system and a laser anemometer to

determine the instantaneous product of density and velocity. Analysis of data from an initial set of measurements is in progress; an additional test is being planned in which heat flux sensors will also be tested. Finally, the work on laser anemometry is continuing with a goal of operating a two-axis anemometer on the warm turbine rig early in 1987.

HOST INSTRUMENTATION R&D PROGRAM

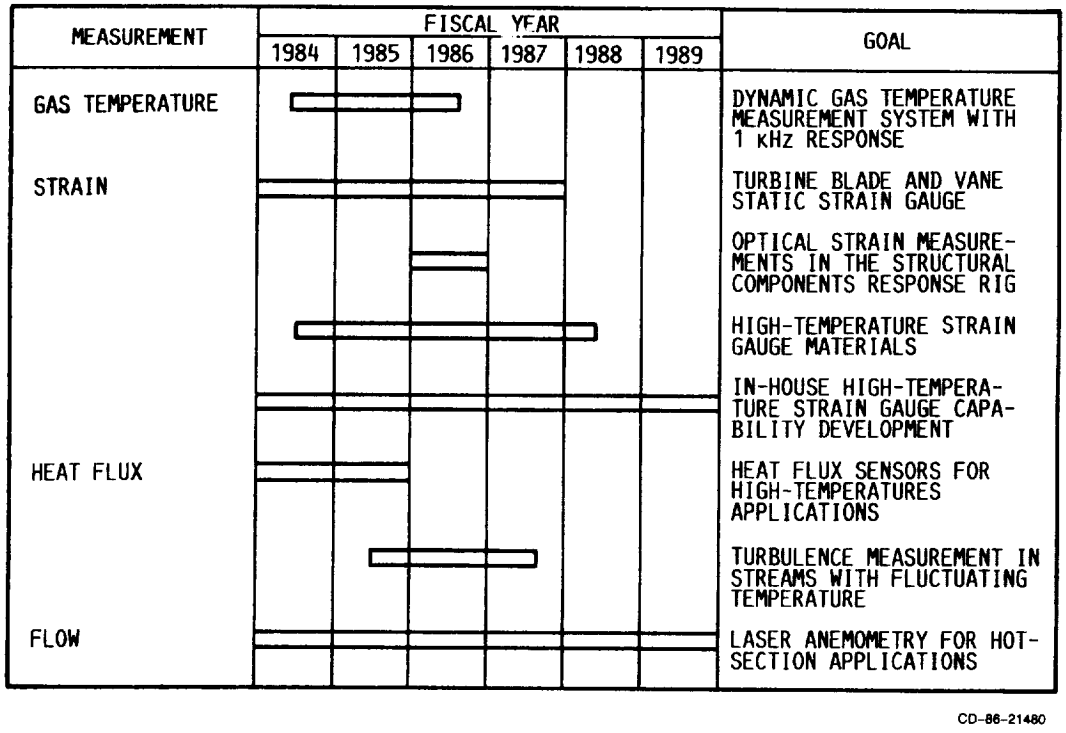

Figure 1

HOST COMBUSTION R&T OVERVIEW

Raymond E. Gaugler
NASA Lewis Research Center
Cleveland, Ohio

The overall objective of the Turbine Engine Hot Section Technology Combustion Project is to develop and verify improved and more accurate numerical analysis methods for increasing the ability to design with confidence combustion systems for advanced aircraft gas turbine engines.

The objective is being approached from two directions: computational and experimental. On the computational side, the approach was to first assess and evaluate existing combustor aerothermal analysis models by means of a contracted effort initiated during fiscal year 1982. This effort has quantified the strengths and deficiencies of existing models. The results of this assessment were summarized at a previous HOST Workshop. Next, phase II contracts were let in fiscal 1984 to develop new/improved numerical methods for the analysis of turbulent viscous recirculating flows, with the prime objectives being improved accuracy and speed of convergence. Progress reports under two contracts and a University Grant will be presented at this workshop. The third part of the computational approach ties very closely to the experiments. It will consist of incorporating improved physical models into the computational codes.

On the experimental side, three types of experiments can be identified; first, fundamental experiments directed toward improved understanding of the flow physics and chemistry; second, experiments run to provide data for the empirical modeing of complex phenomena; and third, benchmark experiments for computer code validation.

Four experimental efforts have been completed and reported on previously, and three are still under way. Progress reports will be presented on those three at this workshop.

The completed experimental programs were aimed primarily at obtaining a basic understanding of the flows and improving empirical models. Two programs that concentrated on the interaction of dilution jets and the main stream flow field have added substantially to the understanding of such flows. A third experimental program examined in detail the mass and momentum transport in swirling and nonswirling coaxial jets. The fourth effort was an investigation of the radiative heat loading in an advanced high pressure gas turbine combustor.

The other three experimental programs are concentrating on the generation of benchmark quality data for use in validating new computer codes and models.

The phase III efforts are planned to get under way this year. Since last year's workshop, discussions have been held with representatives of a number of engine manufacturers, and, based on those meetings and the constraints of the HOST program, it was decided that phase III will concentrate on generating benchmark data for a reacting flow. The data will be used to verify computer codes and physical models.

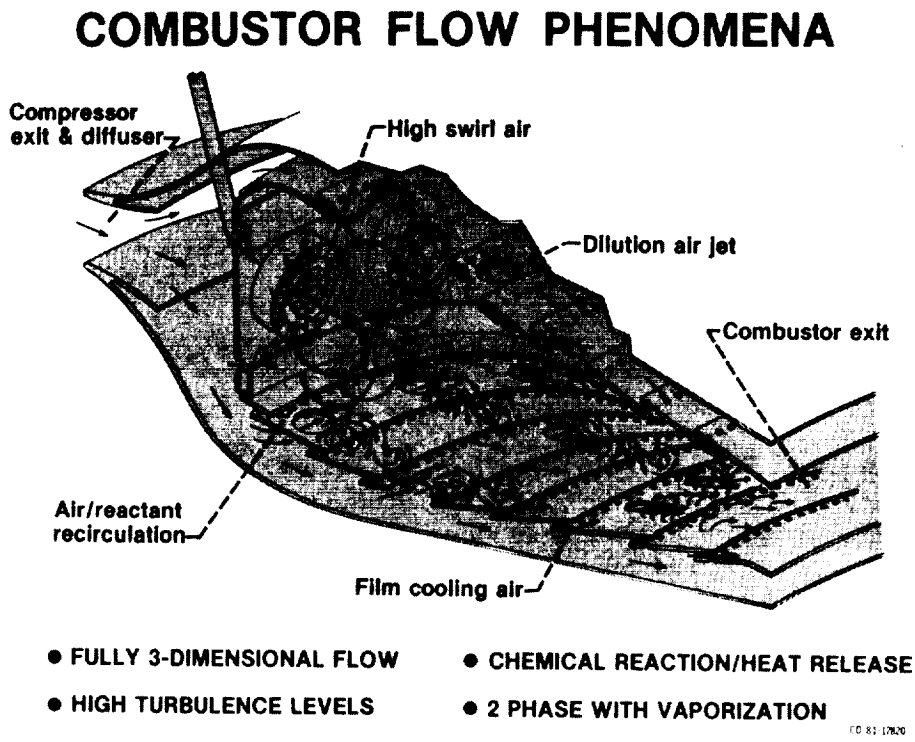

Figure 1

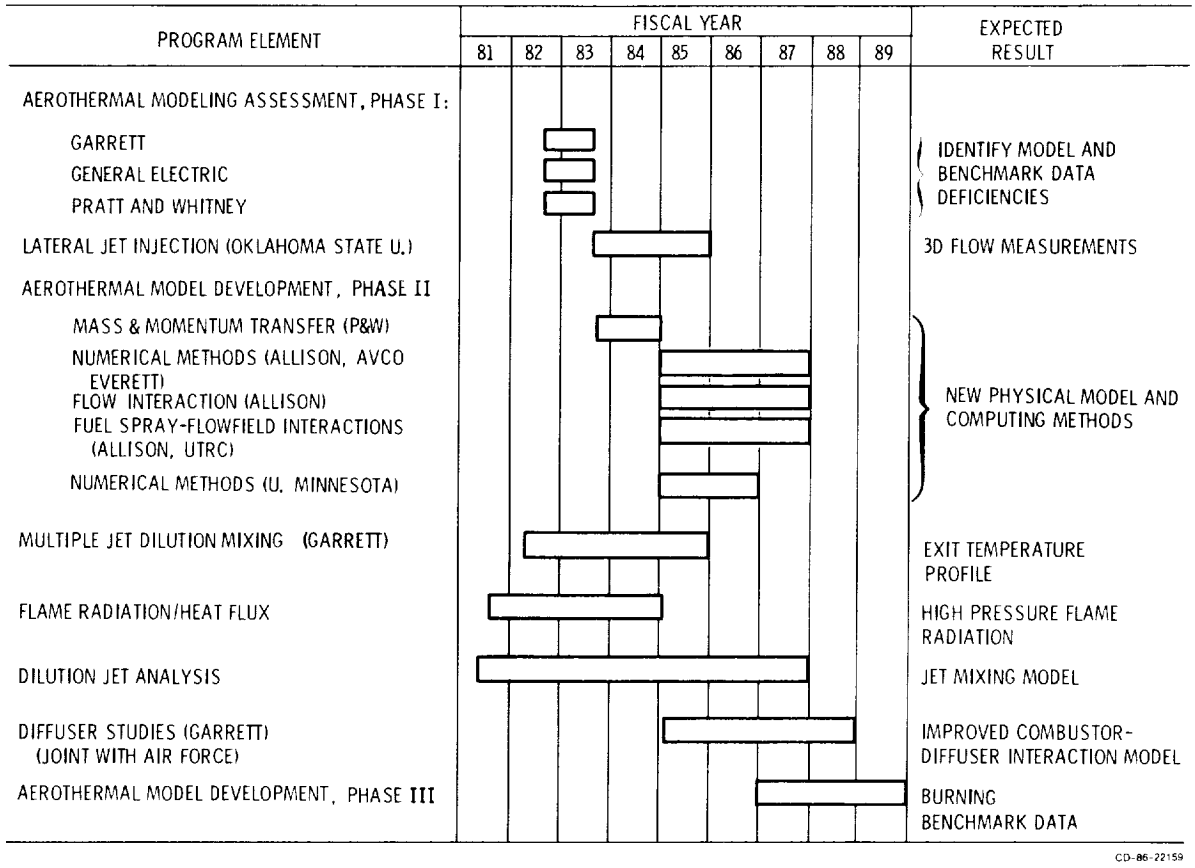

Figure 2

AEROTHERMAL MODEL DEVELOPMENT PHASE-III

- FORMAL ANNOUNCEMENT OF INTENT MADE LAST APRIL.
- DETAILED DISCUSSIONS HELD WITH A NUMBER OF GAS-TURBINE-ENGINE MANUFACTURERS.
- CURRENTLY DEFINING THE SCOPE OF PHASE III, CONSTRAINED BY INDUSTRY NEEDS AND NASA HOST RESOURCES.
- MAJOR EMPHASIS WILL BE ON GENERATION OF BENCHMARK-QUALITY REACTING FLOW DATA.
- THIRD QUARTER FY '87 IS NOW TARGET FOR CONTRACT INITIATION.

CD-86-22158

Figure 3

N89-12880

HOST TURBINE HEAT TRANSFER SUBPROJECT OVERVIEW

Herbert J. Gladden
NASA Lewis Research Center
Cleveland, Ohio

The HOST turbine heat transfer subproject is maturing with all programs in place and many bearing fruit. The accomplishments are interesting, varied, and in abundance as will be seen at this workshop. The experimental data base are leading the analyses slightly, particularly in the nonrotating area of research (figs. 1 and 2). This situation is somewhat by tradition and somewhat by design.

The experimental part of the turbine heat transfer subproject consists of six large experiments, which will be highlighted in this overview, and three of somewhat more modest scope. Three of the large experiments were conducted in the stationary frame of reference and are at or near completion. One of the initial efforts was the stator airfoil heat-transfer program conducted at Allison Gas-Turbine Division. The non-film-cooled and the showerhead-film-cooled data have already been reported. Highlights of the data are shown in figure 3. The gill-region film-cooling effort is currently underway. The investigation of secondary flows in a 90° curved duct, conducted at the University of Tennessee Space Institute, has also been completed. The first phase examined flows with a relatively thin inlet boundary layer and low free-stream turbulence. The second phase studied a thicker inlet boundary layer and higher free-stream turbulence. A comparison of analytical and experimental cross-flow velocity vectors is shown for the 60° plane in figure 4. Two experiments were also conducted at Lewis in the high-pressure facility. One examined full-coverage film-cooled vanes, and the other, advanced instrumentation. Reports on some of these results were published last year.

The other three large experimental efforts were conducted in a rotating reference frame. An experiment to obtain gas-path airfoil heat-transfer coefficients in the large, low-speed turbine at United Technologies Research Center has been completed. Single-stage data with both high- and low-inlet turbulence were taken in phase I. The second phase examined a one and one-half stage turbine and focused on the second vane row. Under phase III aerodynamic quantities such as interrow time-averaged and rms values of velocity, flow angle, inlet turbulence, and surface pressure distribution were measured.

Coolant passage heat-transfer data in a rotating frame are also being obtained at Pratt & Whitney/United Technologies Research Center. Experiments with smooth wall serpentine passages and with skewed turbulators have been completed. Some results of the effect of rotation and heat transfer are shown in figure 5 for the smooth-wall case. An experiment with turbulators normal to the flow will be started this year.

The final large experiment will be conducted at Lewis in the warm-core turbine. This facility, which fully scales a modern turbine stage, is being modified for laser anemonetry access to the vane and blade passages. Research will

begin in 1987. Once intended to be a step on the way to the high-pressure turbine, this rig is now the main verification rig in the turbine heat-transfer subproject.

The three smaller and somewhat more fundamental experiments are directed at important mechanisms. Two are being conducted by Arizona State University. The first, on impingement cooling, is complete; the second, on tip region heat transfer simulation, is providing excellent data. An experiment on the heat-transfer effects of large-scale, high-intensity turbulence, similar to that found at combustor exits, is also underway at Stanford University.

The analytic efforts in the turbine-heat-transfer subproject are characterized by efforts to adapt existing codes and analyses to turbine heat transfer. In general these codes and analyses were well established before HOST became involved; however, the applications were not for turbine heat transfer, and extensive revision has often been required. In some cases the analytic and experimental work were part of the same contract.

The well-known STAN5 boundary-layer code was modified by Allison Gas Turbine Division to define starting points and transition to turbulent flow to accommodate their data, with and without film cooling, as well as data in the literature.

United Technologies Research Center assessed its three-dimensional boundary layer code and modified it to allow for easier application of turbine type inviscid edge conditions. The same code is being modified for use as a two-dimensional unsteady code in order to analyze the rotor-stator interaction data.

The also well-known three-dimensional Navier-Stokes TEACH code has been modified by Pratt & Whitney to incorporate rotational terms. The modified code has been delivered to NASA Lewis and work has begun on it here.

A fully elliptic three-dimensional Navier-Stokes code has been under development at Scientific Research Associates (SRA) for many years. It was primarily directed at inlets and nozzles. SRA, first as a subcontractor to Allison Gas Turbine Division and now as a prime contractor, has been modifying the code for turbine applications. This includes grid work for turbine airfoils, adding an energy equation and turbulence modeling, and improved user friendliness. The code has been installed on the Lewis Cray XMP, and a first report on its use for turbine heat-transfer has been published. A comparison with the Allison nonrotating experimental data is shown in figure 6.

Finally, a fundamental study on numerical turbulence modeling, directed specifically at the airfoil in the turbine environment, is underway at the University of Minnesota.

TURBINE HEAT TRANSFER SUBPROJECT (1)

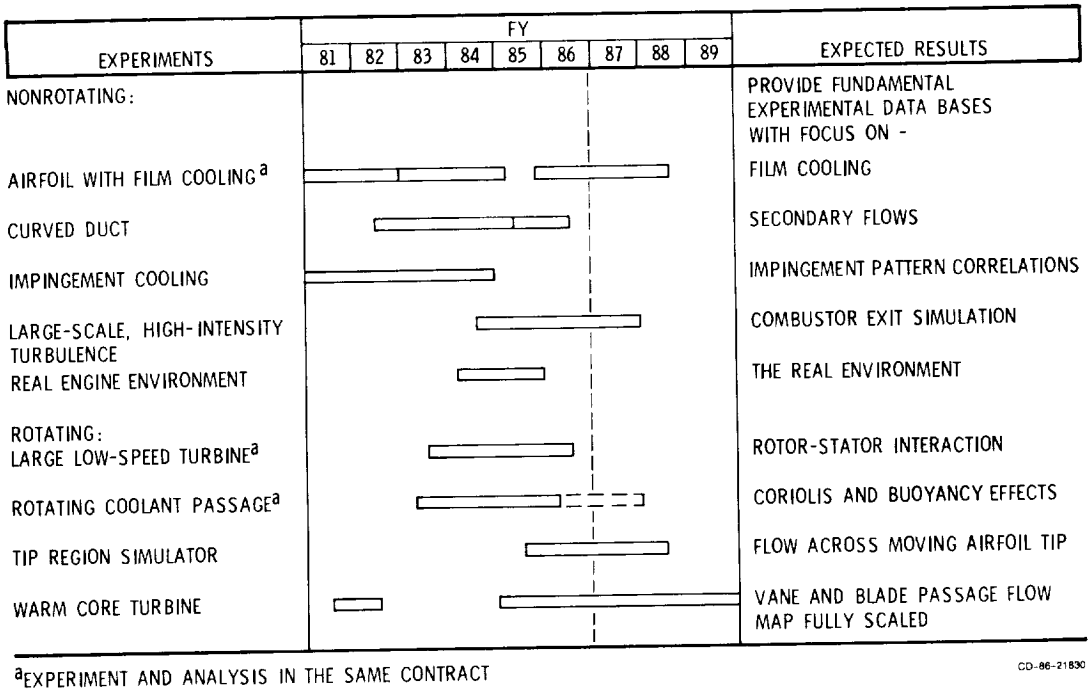

[a]EXPERIMENT AND ANALYSIS IN THE SAME CONTRACT

CD-86-21830

Figure 1

TURBINE HEAT TRANSFER SUBPROJECT (2)

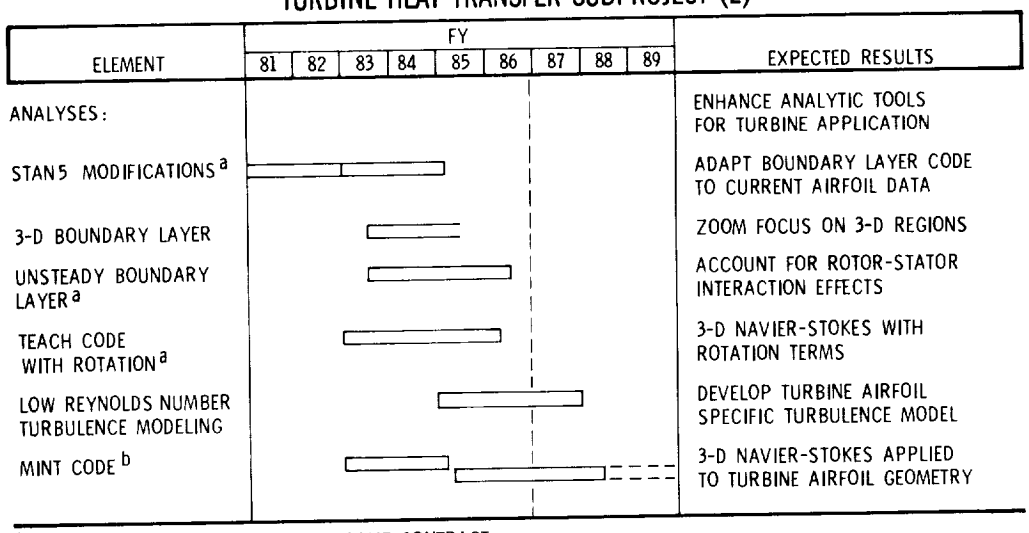

[a]EXPERIMENT AND ANALYSIS IN THE SAME CONTRACT

[b]WORK DONE UNDER TWO SEPARATE CONTRACTS

CD-86-21828

Figure 2

GAS-SIDE HEAT TRANSFER WITH LEADING EDGE FILM COOLING

ORIGINAL PAGE IS OF POOR QUALITY

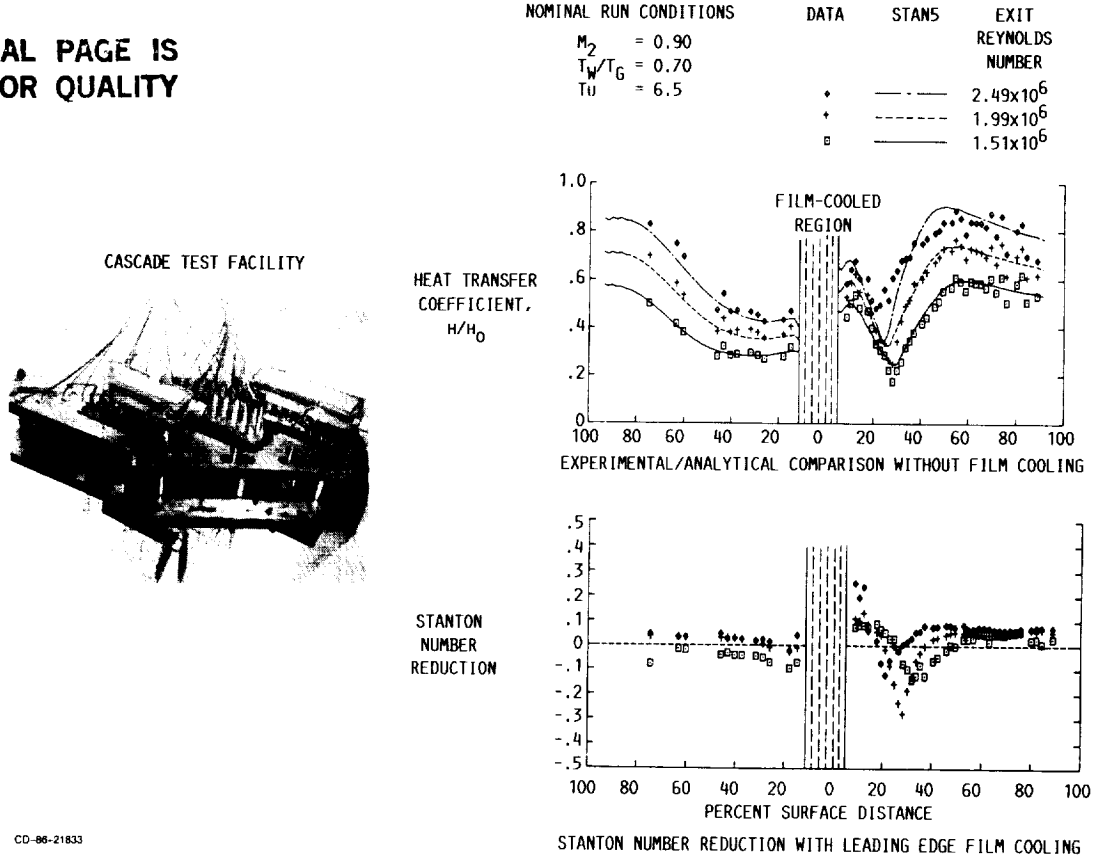

Figure 3

THREE-DIMENSIONAL FLOW FIELD SIMULATING TURBINE PASSAGES

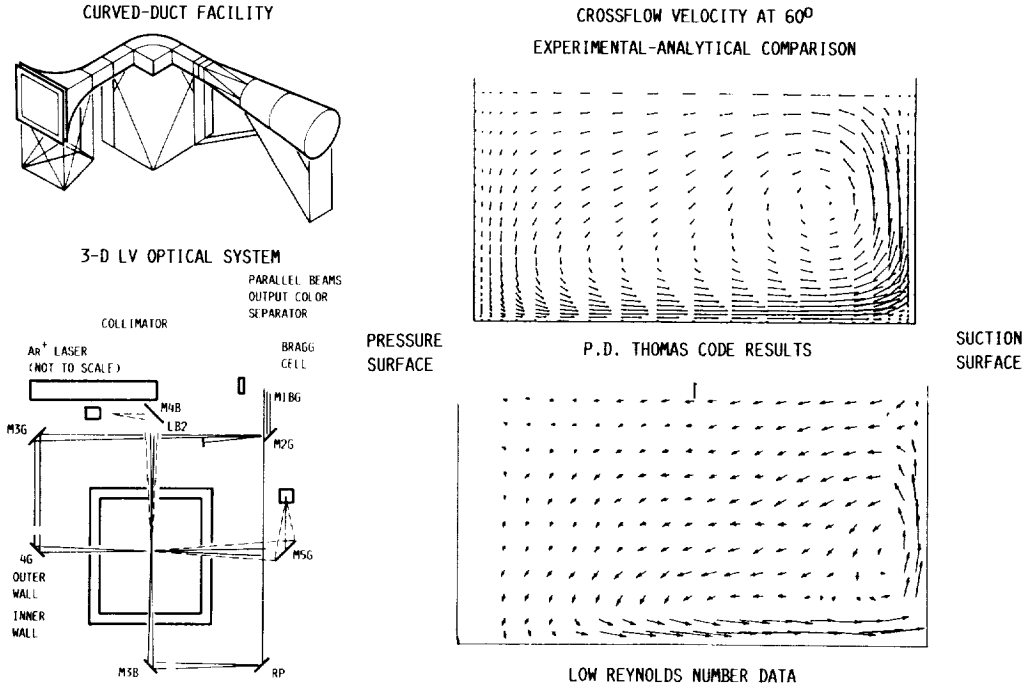

Figure 4

EFFECT OF ROTATION ON COOLANT PASSAGE HEAT TRANSFER

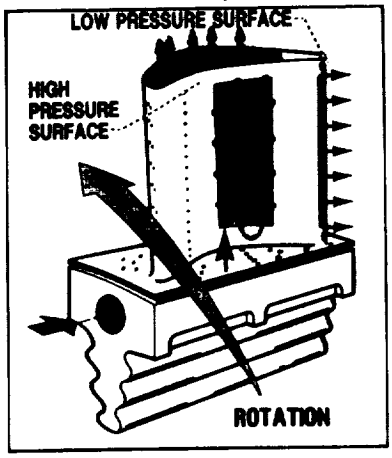

HEAT TRANSFER IN MULTIPASS GEOMETRIES IS ALREADY VERY COMPLEX. ROTATION INTRODUCES ADDITIONAL FIRST-ORDER EFFECTS WHICH MUST BE CORRECTLY UNDERSTOOD AND MODELED

HEAT TRANSFER IN SMOOTH-WALLED TEST MODEL

RADIALLY OUTWARD FLOW, FIRST LEG; Re ≈ 25,000; Δ T = 80°F

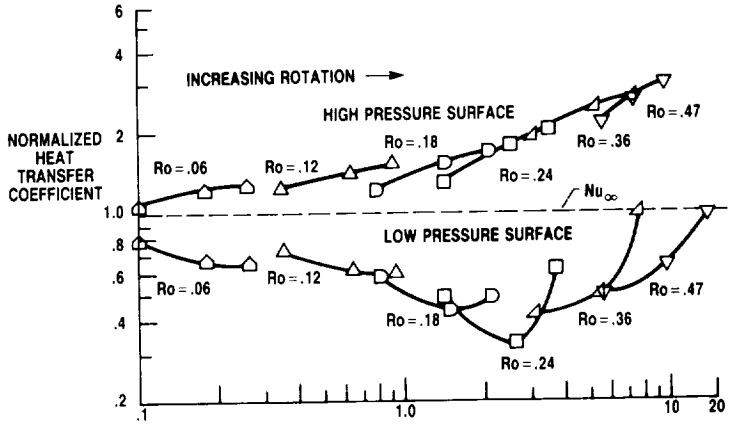

CD-86-21831

GRASHOF No./(REYNOLDS No.)^2 = $\left(\frac{\Omega D}{\nu}\right)\left(\frac{\Omega R}{\nu}\right)\left(\frac{X}{D}\right)\left(\frac{\Delta T}{T}\right)$

Figure 5

CALCULATION OF AIRFOIL HEAT TRANSFER USING A FULL NAVIER-STOKES CODE

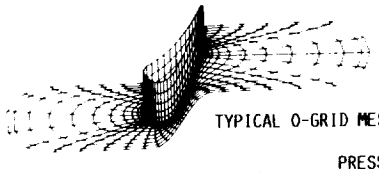

TYPICAL O-GRID MESH

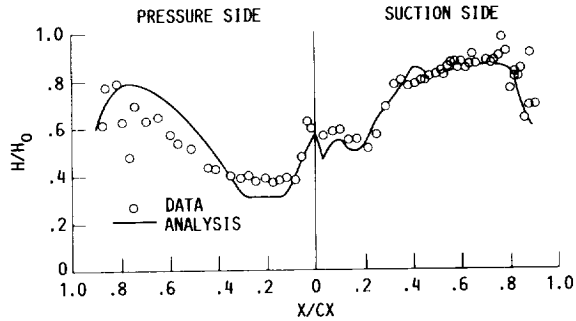

AIRFOIL HEAT TRANSFER

CD-86-21832

Figure 6

HOST STRUCTURAL ANALYSIS PROGRAM OVERVIEW

R.L. Thompson
NASA Lewis Research Center
Cleveland, Ohio

Hot-section components of aircraft gas-turbine engines are subjected to severe thermal-structural loading conditions, especially during the startup and takeoff portions of the engine cycle. The most severe and damaging stresses and strains are those induced by the steep thermal gradients induced during the startup transient. These transient stresses and strains are also the most difficult to predict, in part because the temperature gradients and distributions are not well known or readily predictable and, in part, because the cyclic elastic-viscoplastic behavior of the materials at these extremes of temperature and strain are not well known or readily predictable.

A broad spectrum of structures-related technology programs is underway to address these deficiencies at the basic as well as the applied level, with participation by industry and universities, as well as in-house at NASA Lewis. The three key program elements in the HOST structural analysis program are computations, constitutive modeling, and experiments for each research activity. Also shown are tables summarizing each of the activities. These elements are shown in the accompanying schedule and figures.

The computations element of the structures program focuses on developing improved time-varying thermal-mechanical load models for the entire engine mission cycle from startup to shutdown. The thermal model refinements will be consistent with those required by the structural code, including considerations of mesh-point density, strain concentrations, and thermal gradients. Models will be developed for the engine hot section components namely, the burner liner, turbine vane, and turbine blade. An automated component-specific geometric modeling capability, which will produce three-dimensional finite-element models of the components, is another part of this element. Self-adaptive solution strategies will be developed and included to facilitate the selection of appropriate elements, mesh sizes, etc. The development of new and improved, nonlinear, three-dimensional finite elements and associated structural analysis programs, including the development of temporal elements with time-dependent properties to account for creep effects in the materials and component, is another major part of this element.

The second element of the structures program is the development of constitutive models and their implementations in structural analysis codes. Improved constitutive modeling methods to improve the prediction of cyclic thermomechanical viscoplastic material behavior are being developed for both isotropic and anisotropic materials. The models are being incorporated in nonlinear, finite-element structural analysis computer programs and will be exercised on combustor liners, and turbine blades and vanes.

The third element of the structures program is experimentation. Experimental facilities to aid in developing and verifying theories and models as well as to aid

in evaluating advanced instrumentation have been constructed at Lewis. These include the high temperature structures laboratory for testing tubular specimens and the structural component response test facility for testing plates, cylinders, and combustor liner segments. Large quality data bases have been generated in the test facilities. Advanced strain measurement systems have also been evaluated.

Further explanation and details about the three elements in the structures program mentioned above are given in the Structural Analysis section of this publication.

STRUCTURAL ANALYSIS... IT'S ROLE IN HOST

GOAL:

TO DEVELOP AND VALIDATE INTEGRATED TIME-VARYING THERMAL/MECHANICAL LOAD MODELS, COMPONENT-SPECIFIC AUTOMATED GEOMETRIC MODELING AND SOLUTION STRATEGY CAPABILITIES, AND ADVANCED INELASTIC ANALYSIS METHODS AND CONSTITUTIVE MODELS, INCLUDING PLASTICITY AND CREEP EFFECTS, FOR NONLINEAR, ANISOTROPIC, FINITE ELEMENT STRUCTURAL ANALYSIS AND DESIGN COMPUTER CODES.

PROGRAM INTEGRATION

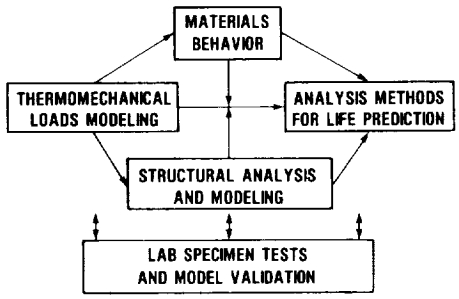

PROGRAM ELEMENTS:

- THERMAL/STRUCTURAL DATA TRANSFER MODULE
- THERMAL/MECHANICAL LOAD/MISSION AND COMPONENT-SPECIFIC STRUCTURAL MODELS
- 3-D INELASTIC ANALYSIS METHODS
- CONSTITUTIVE MODELING
- STRUCTURAL COMPONENT RESPONSE RIG
- HIGH TEMPERATURE STRUCTURES LABORATORY

CS-85-3351

Figure 1

STRUCTURAL ANALYSIS

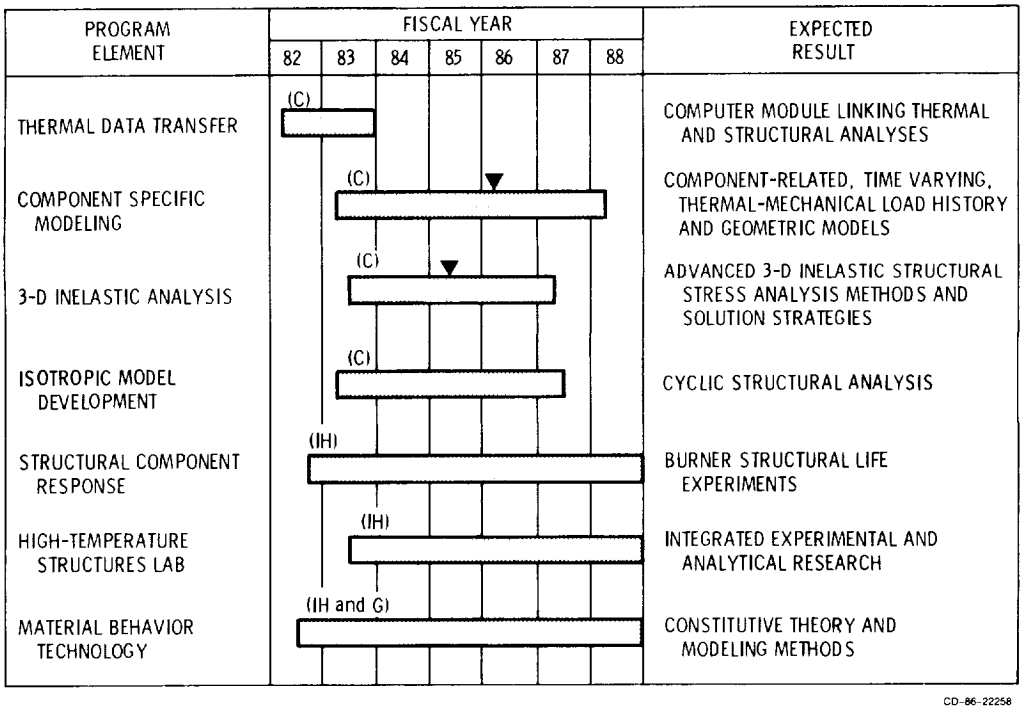

CD-86-22258

Figure 2

HOT SECTION COMPONENTS REQUIRING 3-D INELASTIC ANALYSIS

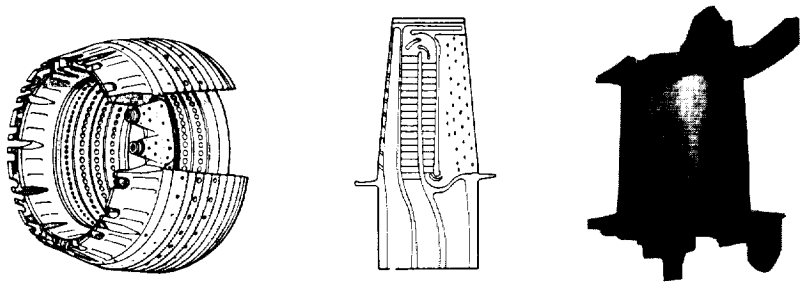

COMBUSTOR LINER | TURBINE BLADE | TURBINE VANE

CS-85-3293

Figure 3

BIAXIAL CONSTITUTIVE EQUATION DEVELOPMENT FOR SINGLE CRYSTALS

OBJECTIVE:

DEVELOP AND VERIFY TWO NEW TYPES OF CONSTITUTIVE MODELS IN MULTIAXIAL FORM FOR A REALISTIC AIRCRAFT ENGINE SINGLE CRYSTAL ALLOY.

GRANT:

UNIVERSITY OF CONNECTICUT (NAG3-512).

APPROACH:

DEVELOPMENT IS DIRECTED TOWARD ANISOTROPICNICKEL BASE SUPERALLOYS FOR TURBINE BLADES AND VANES.

- BIAXIAL CLASSIFICATION EXPERIMENTS, INCLUDING PROPORTIONAL AND NONPORTIONAL LOADS, WILL BE PERFORMED TO DETERMINE QUALIFICATIONS MATERIAL BEHAVIOR FOR PWA 1480.
- MODEL DEVELOPMENT WILL BE BASED ON A CRYSTALLOGRAPHIC SLIPSYSTEM VIEWPOINT AS WELL AS A MACROSCOPIC CONTINUUM APPROACH.
- HIGH TEMPERATURE BIAXIAL EXPERIMENTS WILL BE CONDUCTED TO DETERMINE FUNCTIONAL FORMS AND MATERIAL CONSTANTS.
- COMPLEX MODEL VERIFICATION TESTS, INCLUDING THERMOMECHANICAL TESTS, WILL BE CONDUCTED.
- THE SINGLE CRYSTAL CONSTITUTIVE MODELS WILL BE INCORPORATED IN A FINITE-ELEMENT PROGRAM.

STATUS:

THIRD YEAR OF GRANT.

ACCOMPLISHMENTS:

TWO ANISTROPIC CONSTITUTIVE MODELS FOR PWA 1480 HAVE BEEN DEVELOPED AND INCORPORATED IN A FINITE ELEMENT CODE.

A HIGH-TEMPERATURE BIAXIAL COMPUTER CONTROLLED TEST CAPABILITY EXISTS AT THE UNIVERSITY OF CONNECTICUT.

A DATA BASE ON PWA 1480 IS BEING GENERATED.

COMPLEX BIAXIAL VERIFICATION TESTS HAVE BEEN INITIATED.

CD-86-22331

Figure 4

CONTITUTIVE MODELING OF INELASTIC ANISOTROPIC MATERIAL RESPONSES

OBJECTVE:
DEVELOP A WORKABLE CONSTITUTIVE MODEL THAT PREDICTS THE INELASTIC STRUCTURAL RESPONSES OF SINGLE-CRYSTAL ALLOYS USED IN GAS TURBINE ENGINE BLADES AND VANES.

GRANT:
UNIVERSITY OF CINCINNATI (NAG3-511).

APPROACH:
- DEVELOPMENT DIRECTED TOWARD ANISTROPIC, NICKEL-BASE SUPER ALLOYS FOR TURBINE BLADES AND VANES.
- A DATA BASE OF ISOTHERMAL CYCLES UNIAXIAL BEHAVIOR WILL BE OBTAINED FOR RENE N4.
- AN AUTOMATED PROCEDURE (CODE) FOR OBTAINING MATERIAL CONSTANTS WILL BE DEVELOPED.
- THE MODEL WILL BE INCORPORATED IN A NONLINEAR FINITE ELEMENT CODE AND EXCERCISED ON A TURBINE BLADE PROBLEM.

STATUS:
THIRD YEAR OF GRANT.

ACCOMPLISHMENTS:
- AN ANISTROPIC CONSTITUTIVE MODEL FOR RENE N4 HAS BEEN DEVELOPED AND INCORPORATED IN A FINITE-ELEMENT CODE.
- A CODE TO DETERMINE THE MATERIAL CONSTANTS FROM EXPERIMENTAL DATA HAS BEEN DEVELOPED.
- A HIGH-TEMPERATURE UNIAXIAL COMPUTER CONTROLLED TEST CAPABILITY EXISTS AT THE UNIVERSITY OF CINCINNATI.
- TESTING TO ESTABLISH A LARGE QUALTIY DATA BASE FOR RENE N4 AT TEMPERATURES OF 1400, 1600, AND 1800 °F HAS BEEN INITIATED.

CD-86-22324

Figure 5

MULTIAXIAL TEST PROGRAM TO DETERMINE SURFACES OF CONSTANT CONSTANT INELASTIC STRAIN RATE AT ELEVATED TEMPERATURE

OBJECTIVE:
PROVIDE HIGH-TEMPERATURE BIAXIAL EXPERIMENTAL DATA TO ASSIST IN THE FORMULATION OF NONLINEAR CONSTITUTIVE MODELS FOR STRUCTURAL ALLOYS USED IN TURBINE ENGINE HOT-SECTION COMPONENTS.

INTERAGENCY AGREEMENT:
OAK RIDGE NATIONAL LABORATORY.

APPROACH:
- COMPUTER CONTROLLED BIAXIAL (TENSION TORSION) TESTS AT A TEMPERATURE OF 650 °C ON A REFERENCE HEAT OF TYPE 316 STAINLESS STEEL WILL BE CONDUCTED.
- REFERENCE TESTS ON INCONEL 718 WILL BE CARRIED ON AT 950 °C.
- SURFACES OF CONSTANT INELASTIC STRAIN RATE WILL BE GENERATED AND DATA STORED IN A COMPUTER.
- A HIGH TEMPERATURE BIAXIAL EXTENSOMETER WILL BE EVALUATED.

STATUS:
SECOND YEAR OF AGREEMENT.

ACCOMPLISHMENT:
- EVALUATION OF A HIGH-TEMPERATURE EXTENSOMETER HAS BEEN COMPLETED.
- SURFACES OF CONSTANT INELASTIC STRAIN RATE ARE BEING GENERATED. SOFTWARE FOR STORAGE, TRANSFER, REDUCTION, AND ANALYSIS OF DATA HAS BEEN DEVELOPED.

CD-86-22323

Figure 6

HIGH-TEMPERATURE STRUCTURES LABORATORY

OBJECTIVE:
PROVIDE HIGH-TEMPERATURE UNIAXIAL AND BIAXIAL EXPERIMENTAL DATA ON CYLINDRICAL SPECIMENS TO ASSIST IN THE FORMULATION, DEVELOPMENT, AND VERIFICATION OF NEW AND IMPROVED CONSTITUTIVE MODELS AND TO EVALUATE ADVANCED INSTRUMENTATION ISOTROPIC AND ANISOTROPIC.

IN HOUSE

APPROACH:
- COMPUTER CONTROLLED UNIAXIAL AND BIAXIAL (TENSION/TORSION) TEST MACHINES WILL BE USED TO PROVIDE EXPERIMENTAL DATA.
- RADIOFREQUENCY AND AUDIOFREQUENCY INDUCTION HEATERS WILL BE USED TO HEAT SPECIMENS TO DESIRED TEMPERATURES.
- DATA WILL BE STORED ON COMPUTERS FOR FUTURE DATA REDUCTION, ANALYSIS, AND DISPLAY.
- LARGE QUALITY DATA BASES, BOTH ISOTHERMAL AND NONISOTHERMAL, WILL BE OBTAINED AND HIGH-TEMPERATURE BIAXIAL EXTENSOMETERS WILL BE EVALUATED.

STATUS:
COMPLETED FOURTH YEAR.

ACCOMPLISHMENTS:
- GENERATED LARGE QUALITY UNIAXIAL DATA BASE, BOTH CYCLIC ISOTHERMAL AND NONISOTHERMAL, FOR HASTALLOY-X.
- DEVELOPED SOFTWARE FOR DETAILED ANALYSIS OF DATA.
- DEMONSTRATED THAT COMPUTER CONTROLLED BIAXIAL TEST MACHINES FOR HIGH-TEMPERATURE TESTING ARE OPERATIONAL.
- EVALUATION OF A HIGH-TEMPERATURE BIAXIAL EXTENSOMETER HAS BEEN COMPLETED.
- HIGH-TEMPERATURE TORSIONAL TESTING IN UNDERWAY.

CD-86-22326

HIGH TEMPERATURE FATIGUE & STRUCTURES LABORATORY

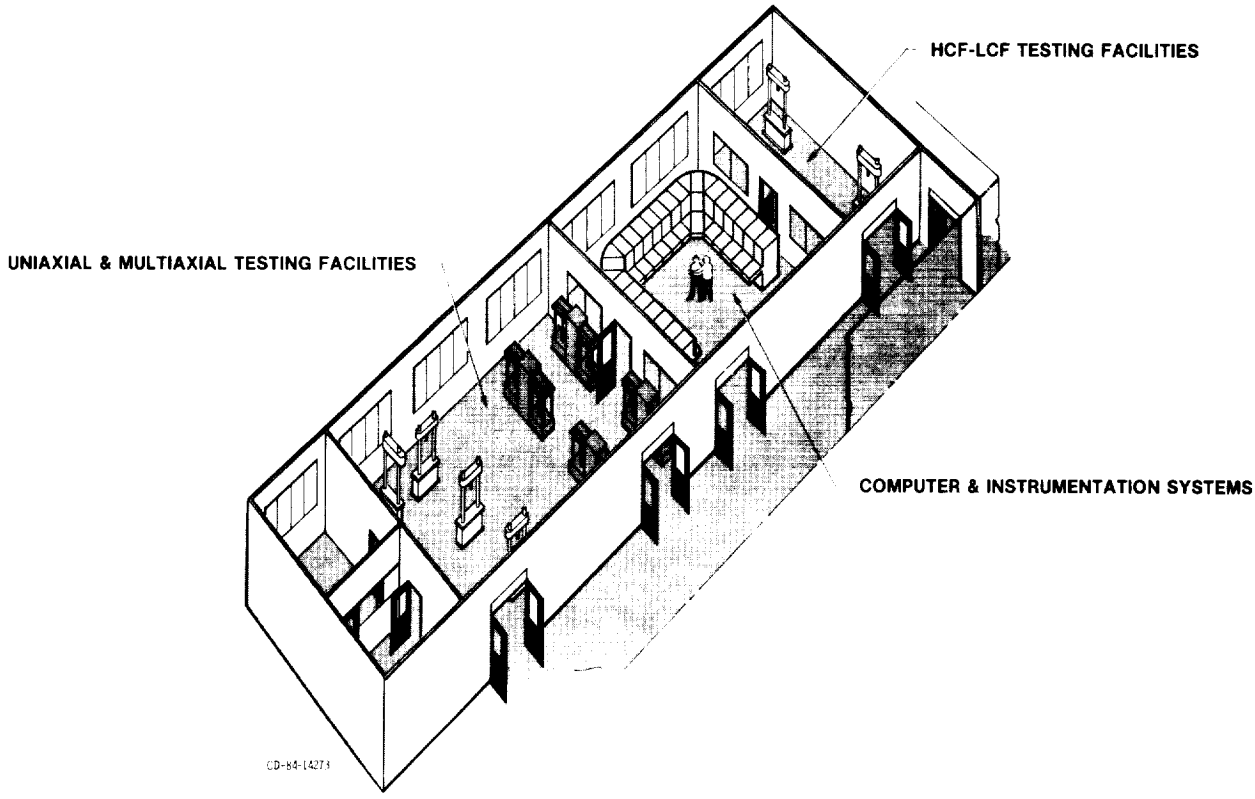

Figure 8

BENCH TOP RIG

OBJECTIVE:
PROVIDE HIGH-TEMPERATURE EXPERIMENTAL DATA ON FLAT PLATES TO ASSIST IN THE DEVELOPMENT AND VERIFICATION OF NEW AND IMPROVED STRUCTURAL ANALYSIS AND LIFE PREDICTION TOOLS AND TO EVALUATE ADVANCED INSTRUMENTATION.

IN HOUSE

APPROACH:
- A QUARTZ LAMP HEATING SYSTEM IS USED TO IMPROVE METAL TEMPERATURES SIMILAR TO AN IN-SERVICE LINER ON 5 BY 8 IN. FLAT PLATES.
- A 2-3 MIN. THERMOANALYSIS SIMULATES A 3-4 HR ENGINE MISSION CYCLE.
- POWER SETTINGS, COOLING AIR FLOW ROLES, AND COOLING TEMPERATURES ARE VARIED TO MATCH A DESIRED TEMPERATURE HISTORY ON A LIST PLATE.
- ADVANCED TEMPERATURE, DEVELOPMENT AND STRAIN MEASUREMENT SYSTEMS ARE EVALUATED.
- AN AUTOMATED DATA ACQUISITION SYSTEM IS USED TO STORE, REDUCE, AND DISPLAY THE DATA.

STATUS:
COMPLETED FOURTH YEAR.

ACCOMPLISHMENTS:
- DEMONSTRATED THAT TEST RIG IS A VIABLE STRUCTURAL COMPONENT EXPERIMENTAL TOOL.
- INFRARED THERMOVISION SYSTEM HAS PROVIDED TEMPERATURE MAPS OF COOL SURFACE OF TEST PLATE.
- EVALUATED A UTRC LASER SPECKLEGRAM SYSTEM TO MEASURE STRAINS.
  EVALUATED A HIGH-RESOLUTION CAMERA SYSTEM TO MEASURE DISPLACEMENTS.
- PLATE TEMPERATUARES WERE REPEATABLE FROM CYCLE TO CYLE.
- THERMAL/STRUCTURAL ANALYSIS OF PLATES HAVE BEEN PERFORMED.

CD-86-22328

Figure 9

BENCH-TOP RIG

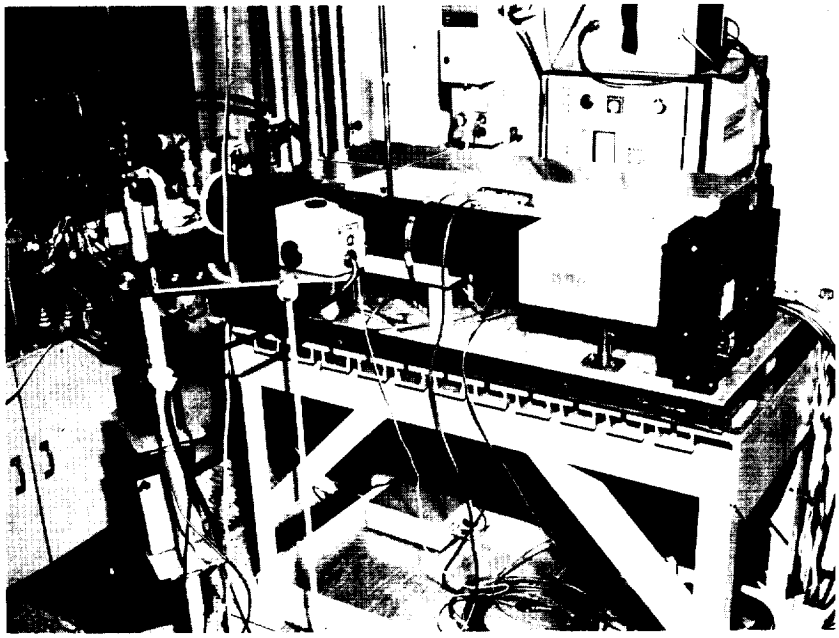

CD-86-22226

Figure 10

STRUCTURAL COMPONENT RESPONSE RIG

OBJECTIVE:
PROVIDE HIGH-TEMPERATURE EXPERIMENTAL DATA ON COMBUSTOR LINER SEGMENTS TO ASSIST IN THE DEVELOPMENT AND VERIFICATION OF NEW AND IMPROVED STRUCTURAL ANALYSIS AND LIFE-PREDICTION TOOLS, AND TO EVALUATE ADVANCED INSTRUMENTATION.

COOPERATIVE NASA LEWIS AND PRATT & WHITNEY EFFORT.

APPROACH:
- A QUARTZ LAMP HEATING SYSTEM IS USED TO IMPOSE METAL TEMPERATURES ON A 20 IN. DIAMETER TEST LINER SIMILAR TO AN IN-SERVICE LINER.
- A 2-3 MIN. THERMAL CYCLE SIMULATES THE TAKEOFF, CRUISE, LANDING, AND TAXI MODES OF A 3-4 HR ENGINE MISSION CYCLE.
- POWER SETTINGS, COOLING AIRFLOW RATES, AND COOLING AIR TEMPERATURES ARE VARIED TO MATCH A DESIRED TEMPERATURE HISTORY OF A POINT ON THE TEST LINER.
- BOTH THERMOCOUPLES AND AN INFRARED CAMERA SYSTEM ARE USED TO MEASURE SURFACE METAL TEMPERATURES.
- DISPLACEMENT MEASUREMENTS AT CRITICAL LOCATIONS ON THE TEST LINER ARE OBTAINED.
- AN AUTOMATED DATA ACQUISITION SYSTEM IS USED TO STORE, REDUCE AND DISPLAY THE DATA.

STATUS:
COMPLETED FOURTH YEAR.

ACCOMPLISHMENTS:
- DEMONSTRATED THAT TEST RIG IS A VIABLE STRUCTURAL COMPONENT EXPERIMENTAL TOOL.
- COMPLETED LISTING OF A CONVENTIONAL COMBUSTOR LINER SEGMENT.
- LINER CRACKING AT THE SEAM WELD WAS OBSERVED AFTER 1600 THERMAL CYCLES.
- TESTING WAS STOPPED AFTER 1800 THERMAL CYCLES DUE TO LARGE LINER DISTORTION.
- RAISING LINER MAXIMUM TEMPERATURE BY 100°F ACCELERATED DAMAGE.
- LINER TEMPERATURES WERE REPEATABLE FROM CYCLE TO CYCLE.
- LARGE QUALITY DATA BASE INCLUDING TEMPERATURE DISPLACEMENT MEASUREMENTS WAS OBTAINED.
- THERMAL STRUCTURAL: ANALYSIS OF THE LINER HAS BEEN PERFORMED.

CD-86-22330

Figure 11

STRUCTURAL COMPONENT RESPONSE RIG

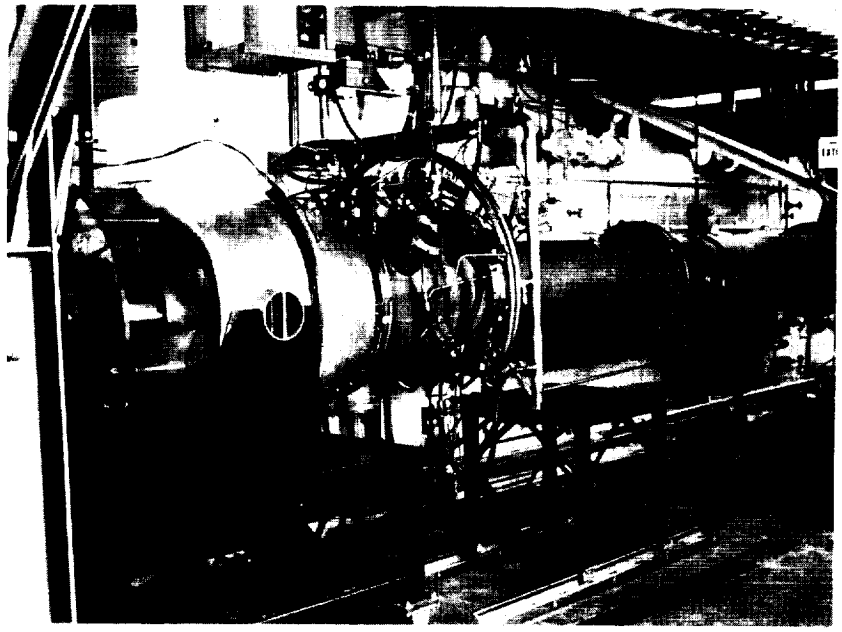

CD-86-22225

Figure 12

COMBUSTOR TEST LINER AFTER 1280 THERMAL CYCLES

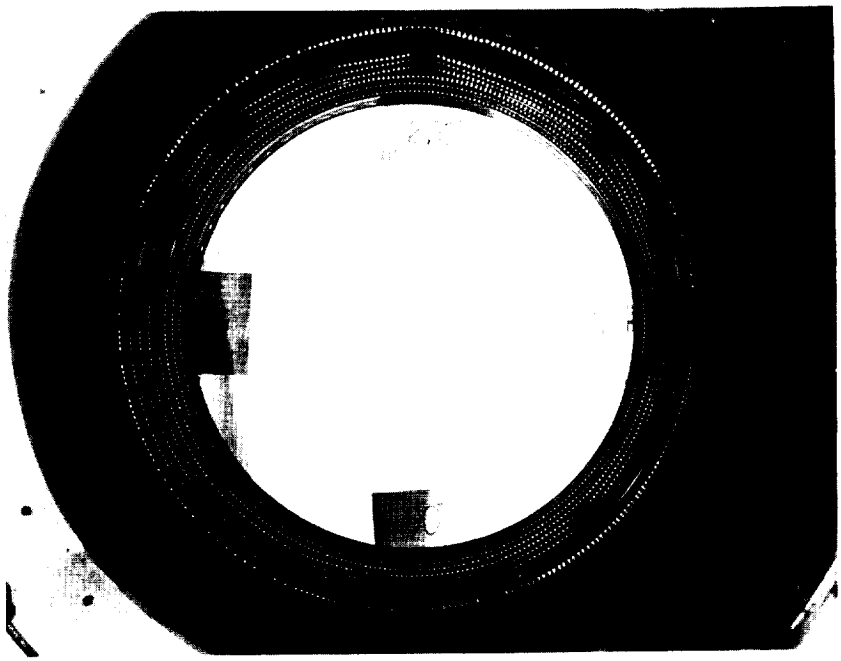

CD-86-22259

Figure 13

THERMAL-TO-STANDARD DATA TRANSFER MODULE

OBJECTIVE:
DEVELOP AN AUTOMATED PROCEDURE FOR EFFICIENT AND ACCURATE TRANSFER OF TEMPERATURES FROM A HEAT TRANSFER CODE TO A STRUCTURAL ANALYSIS CODE.

CONTRACT:
GENERAL ELECTRIC (NAS3-23272).

APPROACH:
DEVELOP A CODE WITH THE FOLLOWING FEATURES AND CAPABILITIES: MODULAR, USER FRIENDLY, DIFFERENT 3D MESH DENSITIES, BOTH FINITE-ELEMENT AND FINITE DIFFERENCE HEAT TRANSFER CODES, EFFICIENT 3D SEARCH AND WEIGHTING ROUTINES, HARD-WIRED THERMAL AND STRUCTURAL CODES, FILES TO EASILY ACCESS OTHER CODES WINDOWING, ALIGNMENT OF HEAT TRANSFER AND STRESS MODES, EXTERIOR STRESS POINT BY AN OUTSIDE HEAT TRANSFER MODEL, AND ABILITY TO SELECT A TIME SLIP FROM A LARGE TRANSIENT THERMAL ANALYSIS.

STATUS:
COMPLETED.

ACCOMPLISHMENTS:
- FINAL REPORTS HAVE BEEN COMPLETED.
- OVER 30 USERS HAVE A COPY OF THE CODE FOR USE AND EVALUATION.
- CODE HAS BEEN SENT TO COSMIC.

CD-86-22322

Figure 14

OVERALL PROGRAM SCHEMATIC FOR
3-DIMENSIONAL TRANCITS (HOST)

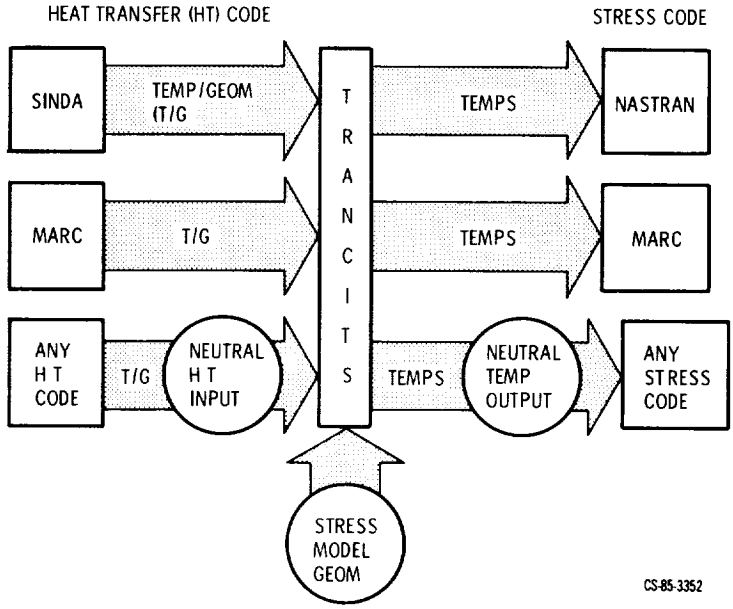

Figure 15

COMPONENT—SPECIFIC MODELING (HOST)

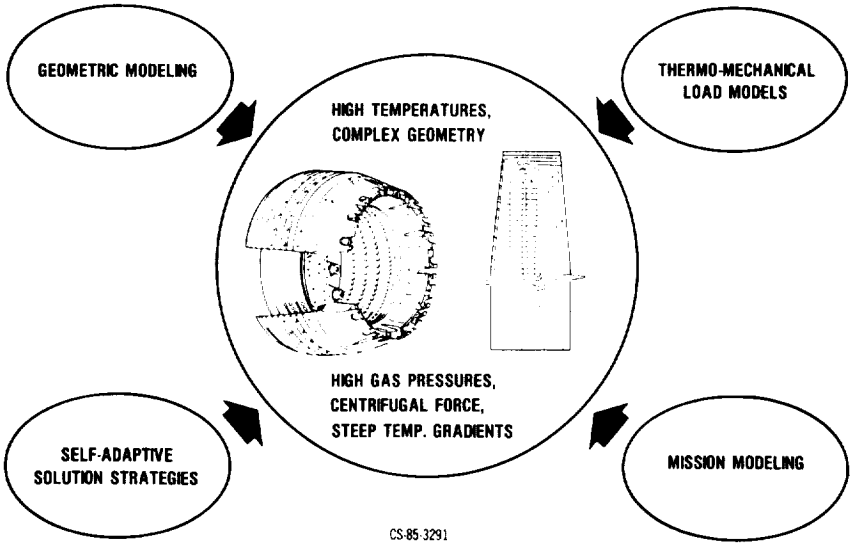

Figure 16

COMPONENT'S SPECIFIC MODELING (COSMO)

OBJECTIVE:
DEVELOP/VERIFY INTERDISCIPLINARY MODELING ANALYSIS METHODS AND REQUISITE COMPUTER CODES STREAMLINED FOR THREE HOT-SECTION COMPONENTS.

CONTRACTOR:
GENERAL ELECTRIC BUSINESS GROUP (NAS3-23687).

APPROACH:
- AVAILABLE METHODS FOR GAS DYNAMICS, HEAT TRANSFER 3D INELASTIC.
- ANALYSES AND MODELING TECHNIQUES REQUIRED TO COMPUTATIONALLY VALIDATE HOT-SECTION COMPONENT DESIGNS WILL BE MODIFIED.
- EXTENDED AND INTEGRATED INTO A MODULAR COMPUTER CODE (COSMO) VIA A TWO-PHASE INCREMENTALLY FUNDED CONTRACT.

STATUS:
THE FIRST PHASE (BASE PROGRAM) OF COSMO IS NEAR COMPLETION.

ACCOMPLISHMENTS:
THE THERMODYNAMIC, THERMOCHEMICAL LOAD TRANSFER, AND EXECUTIVE MODULES ARE OPERATIONAL ON THE LEWIS CRAY COMPUTER.

CO-86-22332

Figure 17

CONSTITUTIVE MODELING FOR ISOTROPIC MATERIALS

OBJECTIVE:
TO DEVELOP UNIFIED CONSTITUTIVE MODEL FOR FINITE-ELEMENT STRUCTURAL ANALYSES OF TURBINE-ENGINE HOT-SECTION COMPONENTS.

CONTRACTOR:
SOUTHWEST RESEARCH INSTITUTE (NAS3-23925.)

APPROACH:
- DEVELOPMENT IS DIRECTED TOWARD ISOTROPIC, CAST NICKEL-BASE ALLOYS FOR AIR-COOLED TURBINE BLADES AND VANES.
- A DATA BASE OF CYCLIC UNIAXIAL AND MULTIAXIAL BEHAVIOR WILL BE OBTAINED FOR A BASE MATERIAL (B1900) AND AN ALTERNATE MATERIAL (MAR M247).
- EFFICIENT METHODS FOR OBTAINING MODEL CONSTANTS WILL BE DEVELOPED.
- MODELS WILL BE INCORPOATED IN FINITE-ELEMENT CODE AND EXERCISED ON A BLADE AIRFOIL PROBLEM.

STATUS:
- THE BASE PROGRAM HAS BEEN COMPLETED.
- AN OPTIONAL PHASE OF THE PROGRAM IS UNDERWAY IN WHICH THE ALTERNATE MATERIAL WILL BE STUDIED AND MODEL DEVELOPMENT WILL BE EXTENDED TO INCLUDE COATING, GRAN SIZE, AND THERMAL HISTORY EFFECTS. IF NECESSARY.

ACCOMPLISHMENTS:
- UPDATED VERSIONS OF THE BODNER AND WALKER MODELS, WITH COMPATIBLE NUMERICAL INTEGRATION SCHEMES WERE INCORPORATED IN THE MARC CODE.
- THESE WERE EXERCISED IN SIMULATIONS OF A LARGE NUMBER OF CYCLIC TESTS WITH GENERALLY GOOD RESULTS.
- FOR THE FIRST TIME UNIFIED CONSTITUTIVE MODELS HAVE BEEN APPLIED TO THE CYCLIC STRUCTURAL ANALYSIS OF AN ENGINE HOT SECTION COMPONENT.

CO-86-22329

Figure 18

3-D INELASTIC ANALYSIS (HOST)

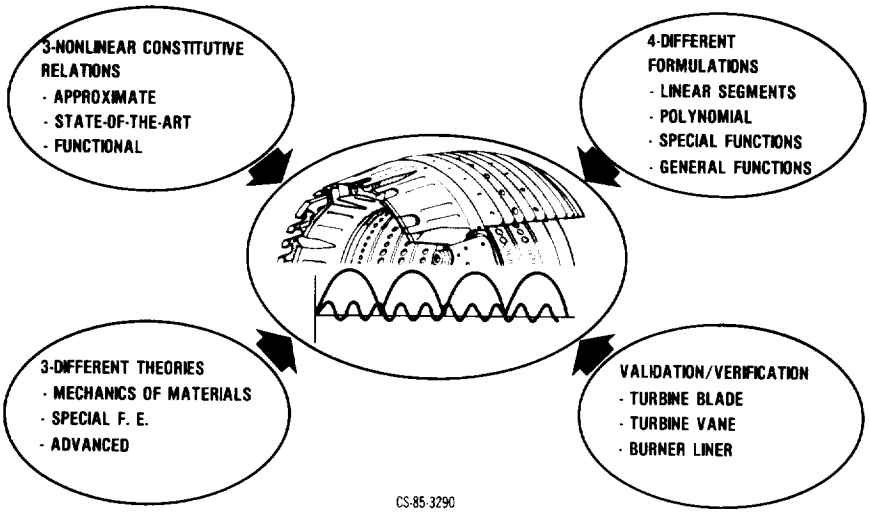

Figure 19

THREE-DIMENSIONAL INELASTIC ANALYSIS METHODS FOR HOT-SECTION COMPONENTS–I

OBJECTIVE:
DEVELOP NEW ANALYTICAL METHODS THAT PERMIT MORE ACCURATE AND EFFICIENT STRUCTURAL ANALYSIS FOR COMBUSTER LINERS, TURBINE BLADES AND VANES.

CONTRACTOR:
PRATT & WHITNEY.

APPROACH:
PROVIDE A SERIES OF NEW COMPUTER CODES THAT EMBODY PROGRESSIVELY MORE SOPHISTICATED ANALYSIS CAPABILITIES BASED ON:

- AN APPROXIMATE MECHANICS OF MATERIALS FORMULATION (MOMM)
- A STATE-OF-THE-ART, SPECIAL FINITE-ELEMENT FORMULATION (MHOST)
- AN ADVANCED TECHNOLOGY BOUNDARY-ELEMENT FORMULATION (BEST3D).

STATUS:
PROGRAM IN FOURTH YEAR.

ACCOMPLISHMENTS:

- COMPUTER CODES GENERATING WIDESPREAD INTEREST IN GOVERNMENT/INDUSTRY/UNIVERSITY SECTORS.
- FIRST USERS WORKSHOP HELD IN JUNE 1985.
- PRELIMINARY VERSIONS DISTRIBUTED FOR EARLY EVALUATION.
- SECOND USERS WORKSHOP ANTICIPATED FOR LATE 1987.

CD-86-22327

Figure 20

THREE-DIMENSIONAL INELASTIC ANALYSIS METHODS FOR HOT SECTION COMPONENTS-II

OBJECTIVE:
DEVELOP IMPROVED ANALYSIS TOOLS THAT ALLOW MORE ACCURATE AND EFFICIENT CHARACTERIZATION OF THE CYCLIC TIME DEPENDENT PLASTICITY OCCURRING IN HOT-SECTION COMPONENTS.

CONTRACTOR:
GENERAL ELECTRIC.

APPROACH:
PROVIDE A MATRIX OF FINITE-ELEMENT-BASED CODES WITH VARYING SOPHISITICATION RELATIVE TO
- ELEMENT TYPE FORMULATION
- MATERIAL CONSTITUTIVE MODEL REPRESENTATION SHARING A COMMON EMPHASIS ON EFFICIENT SOLUTION ALGORITHMS.

STATUS:
PROGRAM COMPLETED.

ACCOMPLISHMENTS:
- CODE EVALUATION UNDERWAY AT LEWIS.
- USERS WORKSHOP ANTICIPATED FOR LATE 1986.
- CODE DISTRIBUTION THROUGH COSMIC ANTICIPATED IN EARLY 1987.

Figure 21

FATIGUE AND FRACTURE OVERVIEW

Gary R. Halford
NASA Lewis Research Center
Cleveland, Ohio

The programs in the fatigue and fracture area of the HOST Project have developed to the point that we can now refer to accomplishments rather than goals. This has necessitated a change from the overview format that I've used in the past couple of years. This year, for each program, I will briefly discuss the major accomplishments, the on-going work, and any that remains for the future. A list of the programs currently supported under fatigue and fracture is shown in table I. There are three contract programs, one grant, and an in-house activity. As I look back over the past few years, it is gratifying to see the advances that have been achieved. Indeed, we now know more about how to design for greater durability, and we are better equipped with analysis tools and hardware for performing durability studies - these advances will be noted as accomplishments. We are also in our prime performance period, during which advances come more easily than before - these advances will be mentioned as on-going work, and greater detail will be provided by the individual presenters. Finally, numerous tasks remain to be accomplished in the future.

Figure 1 summarizes the accomplishments achieved under the isotropic creep-fatigue crack initiation life prediction program. This program was handled by Pratt & Whitney under contract NAS3-23288. Dr. Vito Moreno was the original project manager, and Mr. Richard Nelson took over about 2 years ago. To date, a sizeable creep-fatigue crack initiation data base has been generated on the nickel-base superalloy, B-1900. Companion constitutive modeling programs have also generated extensive data bases on the same heat of material. The crack initiation results have formed the basis of a new approach to creep-fatigue life prediction. The term CDA (Cyclic Damage Accumulation) has been coined for the method, which has been evaluated under isothermal, uniaxial conditions. Stringent laboratory verification experiments have been used to test the accuracy of the method. Considering the quite limited material property data needed to evaluate the constants in the approach, the prediction accuracy is acceptable. At the expense of the larger data base required, the Lewis developed total strain - strainrange partitioning method (TS-SRP) is capable of a higher degree of accuracy. Details of both the CDA and the TS-SRP methods can be found in reference 1.

The current work will be described in greater depth in the Fatigue and Fracture Session by Mr. Nelson. Suffice it to say here that the work is concentrating on the development of modules to account for multiaxial loading, complex loading histories (i.e., cumulative fatigue damage) and thermomechanical loading. Color graphics (fig. 2) of the temperature and stress and strain distributions are quite revealing to the designer in pinpointing hot spots and concentrations of potential damage.

Future activities under the contract call for the development of modules to deal with environmental attack, protective coatings, and mean stress (fig. 3). These modules will be integrated into the master life-prediction model, and

laboratory verification of the completed model will be achieved through use of an alternative alloy. Inco 718 will be used for verification purposes.

The isotropic high-temperature crack growth program at the General Electric Company, under the direction of Dr. J.H. Laflen, has reached a couple of significant milestones. Following a great deal of analysis and experimentation, a satisfactory crack-growth specimen geometry has been selected (fig. 4) that can provide the reliable cyclic growth results needed in the program. Also, numerous so-called path-independent integrals J(x) have been screened to determine their applicability to high-temperature crack propagation problems. Three approaches have been shown to adequately capture the stress intensity around a loaded crack in a thermal gradient field (fig. 5). Greater detail of the path-independent integral approach for high-temperature crack growth will be presented by General Electric in the Fatigue and Fracture Session. Future work will concentrate on finalizing the cyclic crack growth computer code and on verifying the code through use of an alternate material/specimen geometry.

Figure 6 summarizes the major accomplishments under the anisotropic cyclic crack initiation and constitutive modeling program of Pratt & Whitney under the direction of Mr. Gus Swanson. Work has concentrated on developing the cyclic constitutive model applicable to material response before crack initiation. A workable single-crystal constitutive model has been developed and integrated into a computer code. Based on the classical Schmid law for critical resolved shear stress and upon the unified constitutive modeling theory of Dr. Kevin Walker, the anisotropic constitutive model has proven itself to be powerful tool for the analysis of high-temperature components such as turbine blades. Verification of the model has been achieved at the laboratory specimen level. A composite computer-generated plot of a cyclic stress-strain hysteresis loop of single crystal PWA 1480 and of its PWA 286 overlay coating is shown in figure 6. Note the nominally elastic response of the PWA 1480 and the elasto-plastic-creep response of the much weaker, ductile coating.

Currently, the crack initiation data base is being generated upon which the life-prediction method will be built. Both isothermal low-cycle fatigue and thermomechanical fatigue experiments are being conducted. Results are also being collected on the behavior of PWA 273, an aluminide coating. Preliminary evaluations of existing life-prediction methods are being made. Some of the complexities of this task are illustrated by the sketch in figure 7.

The root attachment area of single-crystal turbine blades (fig. 8) poses additional complexities that are to be addressed later in the program. As a final note, the life models for the root attachment area and the higher-temperature airfoil region will have to be integrated into a single life-prediction that can be interfaced with the cyclic constitutive modeling programs for an overall analysis of gas turbine blades.

Figure 8 illustrates the significant accomplishments of the basic research grant with Prof. H.W. Liu at Syracuse University. From a phenomenological viewpoint, he has developed a parameter, based on ΔJ, that accurately describes fatigue crack growth under large-scale plastic yielding. An indication of the predictive capabilities is given in figure 9. Seven different alloys are included, and the normalized growth rates cover four orders of magnitude. Details of this room temperature work are contained in reference 2. In his attempts to gain a better understanding of the micromechanisms of cyclic crack growth at elevated temperatures, he has proposed a model based on the oxidation kinetics at the growing

crack tip. The model provides for a transistion between the time-independent plasticity-induced crack growth and the time-dependent oxidation-governed growth. More detail will be provided by Prof. Liu in his presentation in the Fatigue and Fracture Session. Work is continuing on modeling of the micromechanisms of crystallographic slip at the tip of a growing crack. The effort is directed at the so-called small crack problem, and, to make the problem easier to address experimentally, specimens with extremely large grain sizes have been manufactured. A typical specimen is shown in figure 10 wherein only two or three grain boundaries are encountered as the crack grows across the specimen.

Lewis' in-house effort focused principally on the refurbishment of the high-temperature fatigue and structures laboratory. This facility is now operational and growing daily. To date, we have been able to add seven new closed-loop, servo-controlled cyclic testing machines, each of which is capable of being interfaced with dedicated satellite minicomputers which, in turn, communicate with the master computer in the centralized control room. A view of part of the new control room is shown in figure 11. Experiments are now being performed on a routine basis that just could not have been attempted a couple of years ago. Our computer-aided capabilities are constantly growing as the available software continues to expand. Over the new few years, we expect to be generating valuable theory verification using the multiaxial, thermomechanical, and cumulative damage test equipment that is now coming on-line.

In summary, I would like to emphasize the significant progress that has been achieved in the fatigue and fracture arena through the atmosphere created by the HOST Project. Unquestionably, we are now better prepared than ever before to deal with durability enhancement in the aeronautical propulsion industry through theoretical, analystical, and experimental approaches. Given the opportunity to complete the tasks we have started, we expect to reap even greater rewards over the next year or two.

REFERENCES

1. Moreno, V.; Nissley, D.M.; Halford, G.R.; and Saltsman, J.F.: Application of Two Creep Fatigue Life Models of the Prediction of Elevated Temperature Crack Initiation of a Nickel Base Alloy. Presented at the AIAA/SAE/ASME/ASEE 21st Joint Propulsion Conference, Monterey, Calif., July 8-10, 1985. Preprint No.

2. Minzhong, Z and Liu, H.W.: Crack Tip Field and Fatigue Crack Growth in General Yielding and Low Cycle Fatigue. (Syracuse University, NASA Grant NAG3-348), NASA CR-174686, Sept. 1984.

TABLE I

FATIGUE AND FRACTURE PROGRAMS

- NAS3-23288, PRATT & WHITNEY (R.S. NELSON), LEWIS (G.R. HALFORD)
  CREEP-FATIGUE CRACK INITIATION—ISOTROPIC
- NAS3-23940, GENERAL ELECTRIC (J.H. LAFLEN), LEWIS (T.W. ORANGE)
  ELEVATED TEMPERATURE CRACK GROWTH—ISOTROPIC
- NAS3-23939, PRATT & WHITNEY (G.A. SWANSON), LEWIS (R.C. BILL)
  LIFE PREDICTION/CONSTITUTIVE MODELING—ANISOTROPIC
- NAG3-348, SYRACUSE UNIVERSITY (H.W. LIU), LEWIS (I.J. TELESMAN)
  CRACK GROWTH MECHANISMS—ISOTROPIC
- LEWIS,(M.A. McGAW)
  HIGH-TEMPERATURE FATIGUE AND STRUCTURES LABORATORY

CD-86-21861

CREEP-FATIGUE CRACK INITIATION—ISOTROPIC ACCOMPLISHMENTS

- LARGE DATA BASE
- CDA MODEL-P&W
- TS-SRP MODEL-LEWIS
- MODELS VERIFIED-ISOTHERMAL

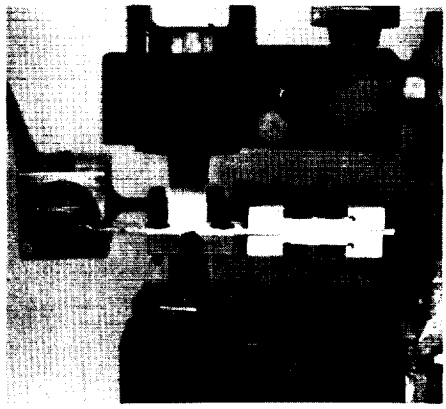

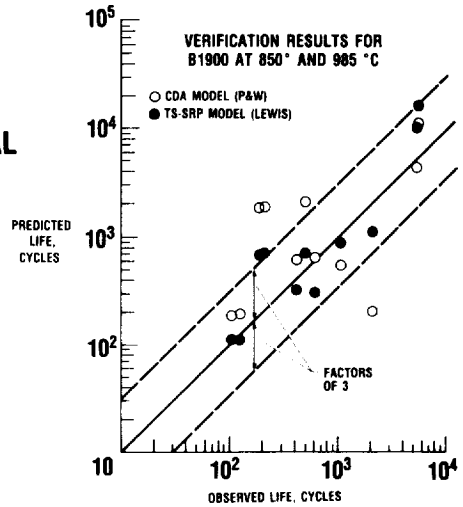

CD-86-21867

Figure 1

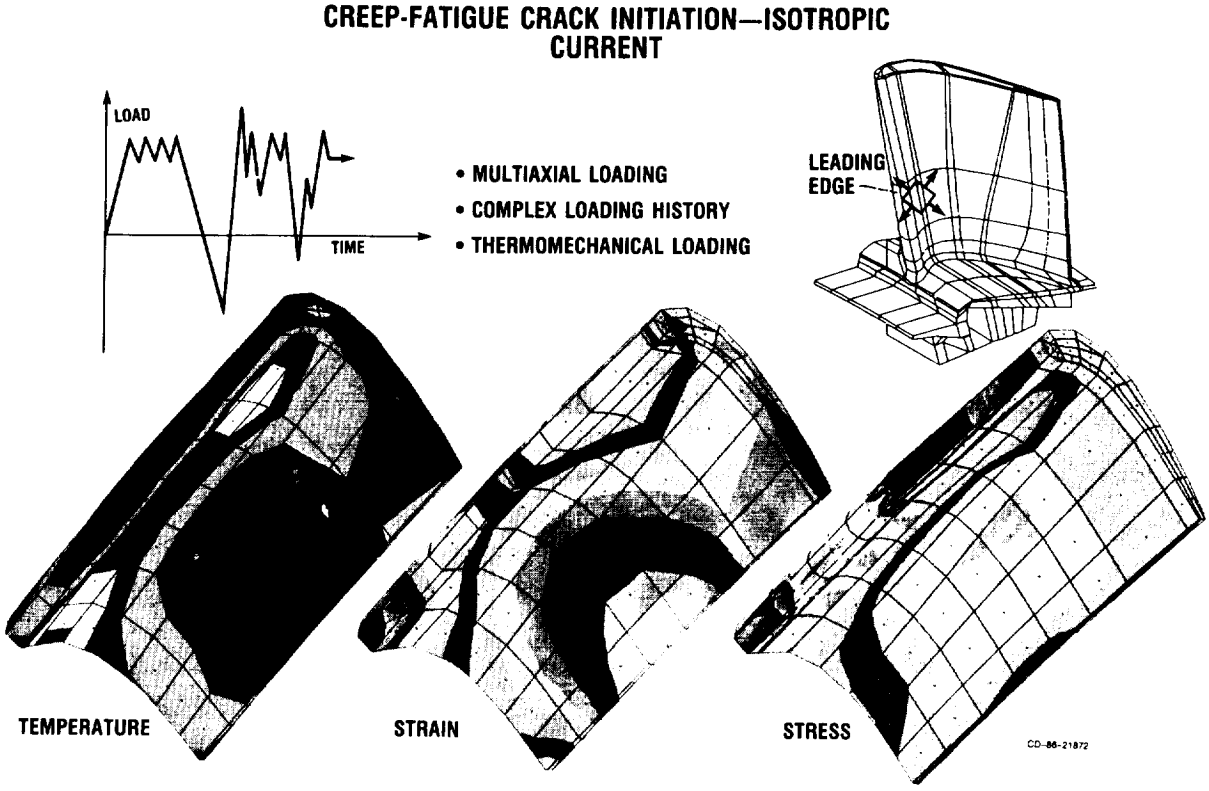

Figure 2

CREEP-FATIGUE CRACK INITIATION—ISOTROPIC FUTURE

- ENVIRONMENTAL MODULE
- COATINGS MODULE
- MEAN STRESS MODULE
- MODULES INTEGRATED INTO MODEL
- ALTERNATIVE ALLOY VERIFICATION

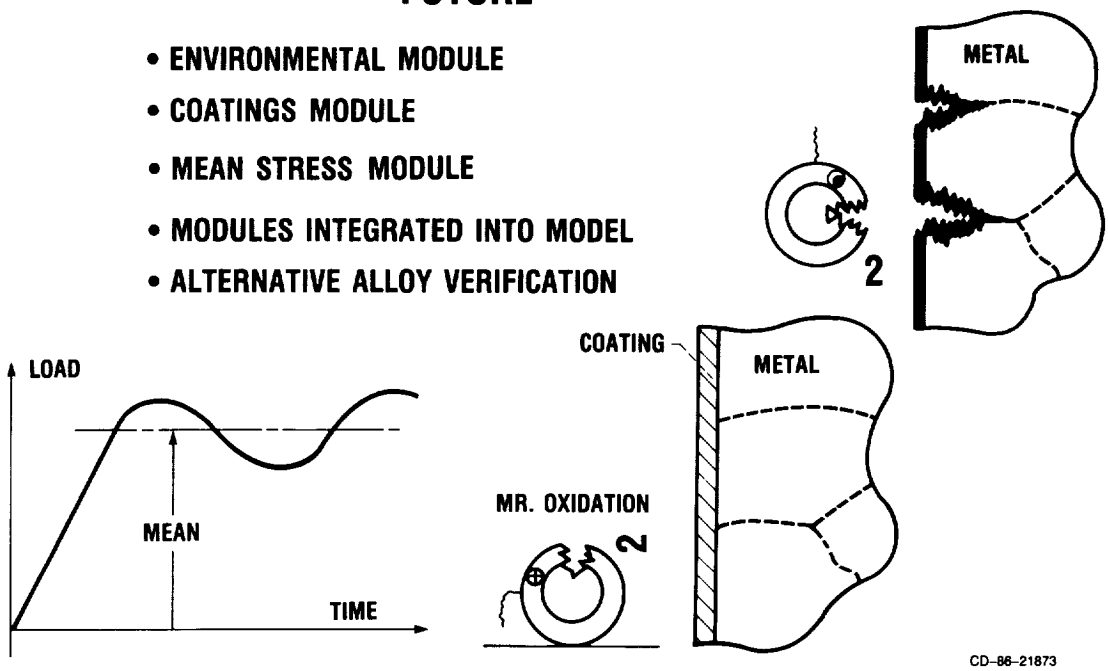

Figure 3

CRACK GROWTH—ISOTROPIC ACCOMPLISHMENTS

- DEVELOPED STANDARDIZED CRACK GROWTH SPECIMEN
- PATH-INDEPENDENT INTEGRALS (J_X) IDENTIFIED

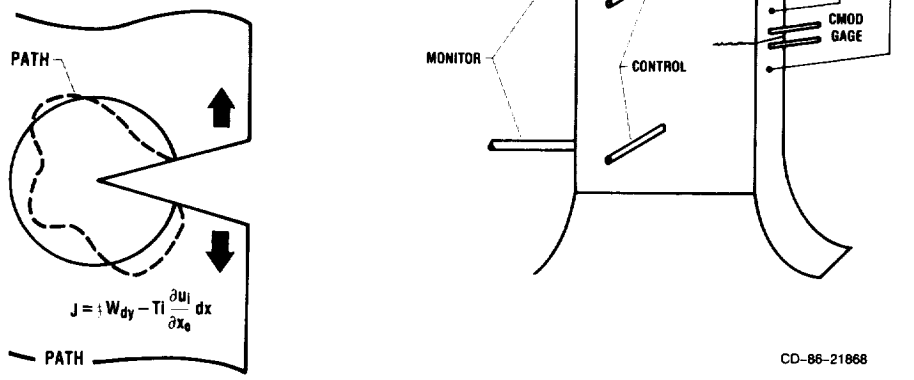

Figure 4

CRACK GROWTH—ISOTROPIC CURRENT

- ISOTHERMAL VERIFICATION
- NONISOTHERMAL VERIFICATION

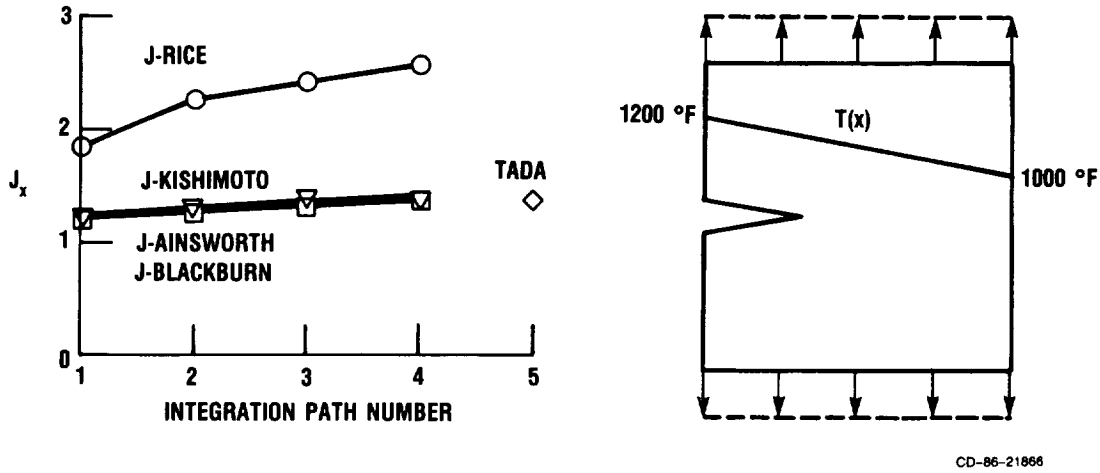

Figure 5

INITIATION AND CONSTITUTIVE MODELING—ANISOTROPIC ACCOMPLISHMENTS

- SINGLE-CRYSTAL CONSTITUTIVE MODEL (PWA 1480)
  - SCHMID LAW
  - WALKER THEORY
- OVERLAY COATING CONSTITUTIVE MODEL (PWA 286)
  - WALKER THEORY

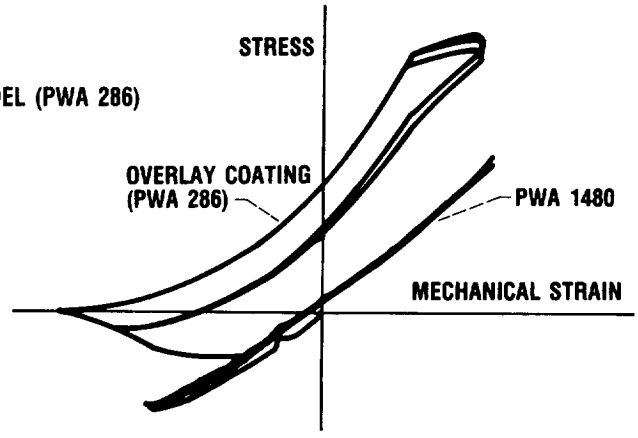

Figure 6

INITIATION AND CONSTITUTIVE MODELING—ANISOTROPIC CURRENT

- LCF/TMF DATA BASE (COATED PWA 1480)
- ALUMINIDE COATING DATA BASE (PWA 273)
- PRELIMINARY LIFE MODELS

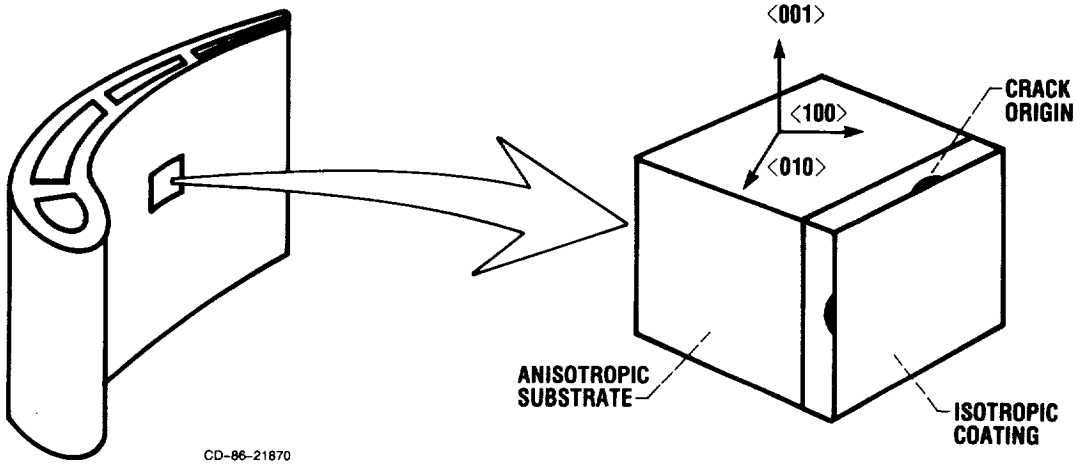

Figure 7

INITIATION AND CONSTITUTIVE MODELING—ANISOTROPIC FUTURE

- BLADE ATTACHMENT
- INTEGRATED LIFE MODELS

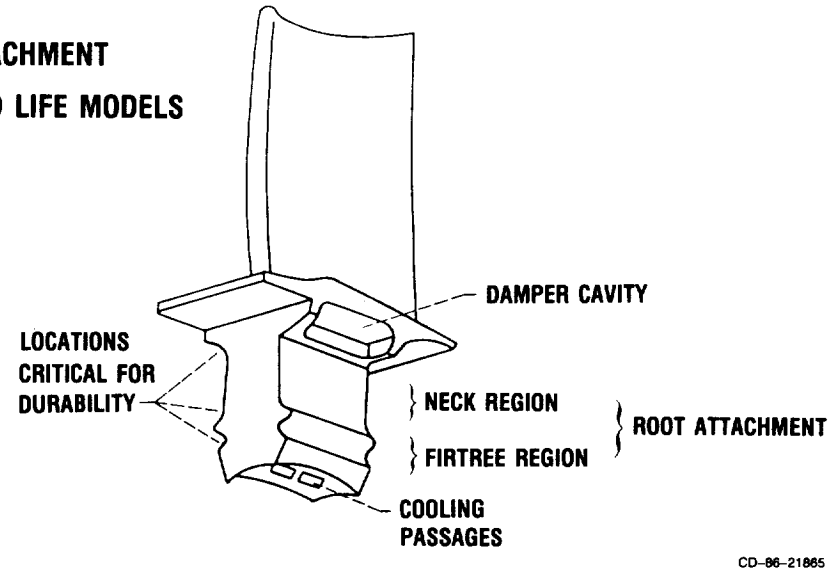

Figure 8

CRACK GROWTH MECHANISMS—ISOTROPIC ACCOMPLISHMENTS

- ΔJ PARAMETER FOR LOW TEMPERATURE da/dN
- OXIDATION MODEL FOR HIGH TEMPERATURE da/dN

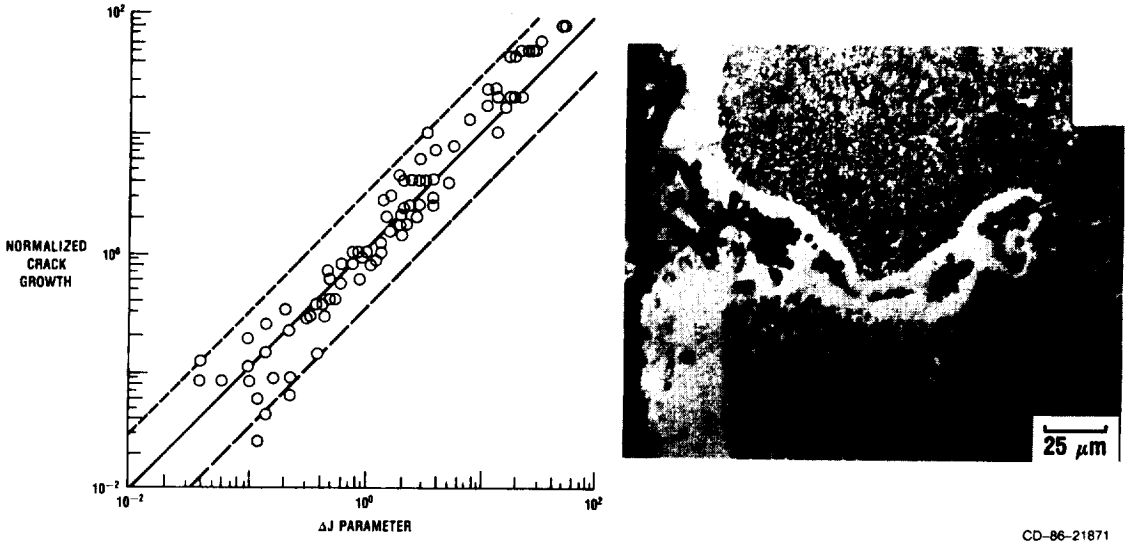

Figure 9

CRACK GROWTH MECHANISMS—ISOTROPIC CURRENT/FUTURE

- CRYSTALLOGRAPHIC MODEL OF da/dN

CD-86-21863

Figure 10

HIGH-TEMPERATURE FATIGUE AND STRUCTURES LABORATORY ACCOMPLISHMENTS

- INTEGRATED/AUTOMATED MATERIALS TESTING CAPABILITY
  - SEVEN NEW CLOSED-LOOP MACHINES
  - ONE HOST COMPUTER
  - 16 SATELLITE MINICOMPUTERS

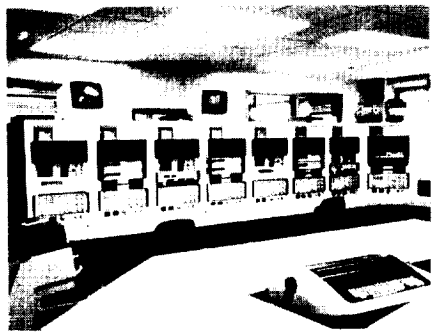

Figure 11

CD-86-21859

HOST SURFACE PROTECTION R&T OVERVIEW

Robert A. Miller
NASA Lewis Research Center
Cleveland, Ohio

Most of the efforts in the HOST Surface Protection Subproject were focused on thermal barrier coating (TBC) life prediction in fiscal year 1986 (fig. 1). Also, small effort - consisting primarily of wrapping up and reporting the work of previous years - remained on the airfoil deposition modeling. The metallic coating life prediction program, which had been an element in the surface protection subprogram in previous years, was not continued into FY 1986.

The TBC life prediction element is divided into contractural, grant, and in-house efforts (fig. 2). The contracts - with Pratt & Whitney Aircraft, General Electric Co., and the Garrett Turbine Engine Co. - were designed to produce "engine-capable" TBC life-prediction models. The grant with Cleveland State University is focused on finite-element modeling of TBC stress states. The in-house work is focused primarily on developing laboratory burner rig tests that can simulate the pressures and heat fluxes of aircraft gas-turbine engines.

AIRFOIL DEPOSITION MODEL

The work performed under the airfoil deposition modeling program element in FY 1986 is outlined in figure 3. This effort was concerned with modeling the deposition of corrodants onto turbine airfoils. Accomplishments included verification of the chemically frozen boundary (CFBL) theory, which had been developed in previous years at Yale University under HOST and other NASA programs. Encouraging results were also received with the recently developed local thermochemical equilibrium (LTCE) theory.

THERMAL-BARRIER-COATING LIFE PREDICTION

Most of the FY 1986 surface protection subprogram was devoted to thermal-barrier-coating life modeling. This modeling is an essential step in the development of TBC's. This is because the full benefits of TBC's can only be achieved when it becomes possible to use them in the "prime-reliant" mode. An uncoated airfoil cannot survive the temperatures that are encountered in this environment. Therefore, a failed TBC would lead directly to a failed component. As noted in figure 4 TBC life prediction models combined with other advances in coatings technology will be required before designers will be willing to use TBC's in the prime reliant mode.

Figure 5 shows that the TBC life modeling contracts are divided into two phases. Currently, each of the three contractors is in the third and final year of phase I. The output of phase I will be a preliminary model. The output of the second phase will be a design-capable model. The modeling strategy is indicated in figure 6. Figure 5 also shows how the mechanical behavior of TBC's program is focused on the modeling of TBC residual stresses. The in-house rig/engine

correlation work is aimed at high pressure burner rig development as is shown in figures 5 and 7.

TBC HOST FY 1986 accomplishments are shown in figure 8. These include the development and initial verification of a preliminary life model by one of the contractors (Pratt & Whitney Aircraft). Coating mechanical and thermal properties have been determined. Failure mechanisms have been ellucidated. Stresses have been modeled by finite element methods. Also, NDE methods have been evaluated, and an engine test has been conducted (by the Garrett Turbine Engine Co.).

SURFACE PROTECTION

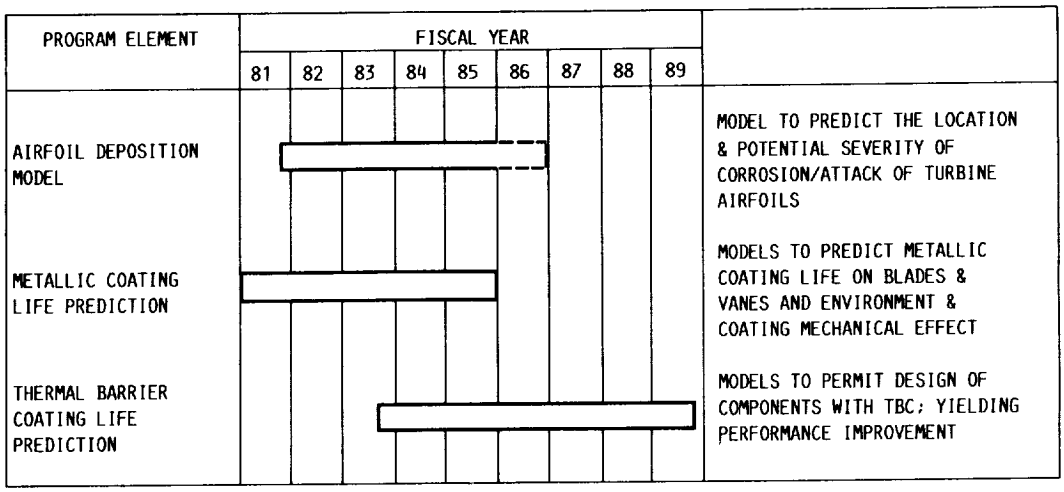

CD-86-21503

Figure 1

SURFACE PROTECTION

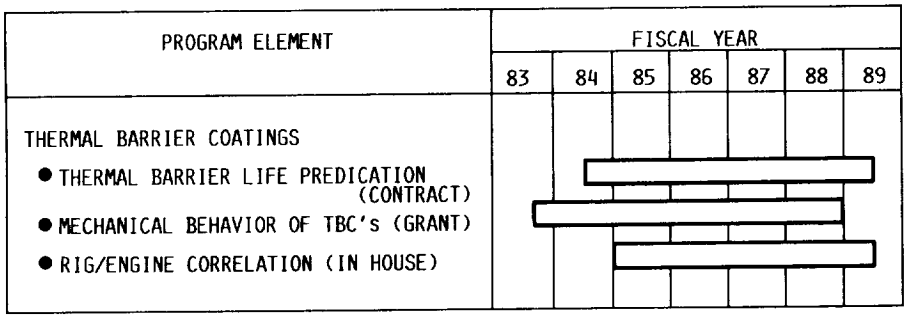

Figure 2

CD-86-21498

AIRFOIL DEPOSITION MODEL

GOAL:
- TO DEVELOP AND VERIFY A MODEL TO PREDICT CORRODANT DEPOSITION QUANTITY AND LOCATION ON TURBINE AIRFOILS

APPROACH:
- AIRFOIL MODEL DEVELOPMENT VIA GRANT WITH DAN ROSNER, YALE
- MODEL VERIFICATION VIA IN HOUSE RESEARCH WITH SUPPORT FROM GOKOGLU
  - MACH 0.3 BURNER RIG
  - HIGH PRESSURE BURNER RIG
- BURNER RIG MODERNIZATION
  - COMPUTER DATA ACQUISITION AND LIMIT MONITORING
  - COMPUTER CONTROL

STATUS:
- CFBL THEORY VERIFIED FOR SEGMENTED COLLECTORS SIMULATING TURBINE NOSE REGION
- LTCE THEORY, RECENTLY DEVELOPED, WHICH ASSUMES LOCAL THERMOCHEMICAL EQUILIBRIUM AS OPPOSED TO FROZEN CHEMISTRY (CFBL THEORY), AGREES TO WITHIN 7% IN PREDICTING DEPOSITION RATES
- PUBLICATIONS IN PROGRESS

CD-86-21496

Figure 3

STRONG HOST SUPPORT VITAL TO TBC PROGRESS

NOW: TBC's USED AS ADD-ONS;
INADEQUATE DESIGN CAPABILITY

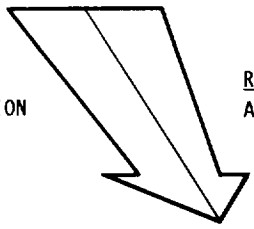

HOST
TBC LIFE PREDICTION

R&T BASE PROGRAMS
ADVANCED COATINGS

FUTURE: PRIME RELIANT TBC's FOR USE ON AIRFOILS FOR BIG PERFORMANCE IMPROVEMENT

Figure 4

CD-86-21501

THERMAL BARRIER COATING LIFE PREDICTION

GOAL:
- TO DEVELOP AND VERIFY LIFE PREDICTION METHODOLOGIES FOR (TBC's)

APPROACH:
- TBC LIFE PREDICTION MODEL DEVELOPMENTS (CONTRACT)
  - PHASE I: FAILURE ANALYSIS AND PRELIMINARY MODEL (MULTIPLE CONTRACTS)
  - PHASE II: DESIGN CAPABLE MODELS (TBD)
- MECHANICAL BEHAVIOR OF TBC (GRANT, CSU)
  - RESIDUAL STRESS MODELING
- RIG AND ENGINE CORRELATION (IN-HOUSE)
  - HIGH-HEAT FLUX TESTS IN HIGH-PRESSURE BURNER RIG TO COMPLEMENT CONTRACT EFFORT
  - FAILURE MECHANISMS
  - MODEL VERIFICATION
  - COMPLEMENTARY PROGRAMS

STATUS:
- PRELIMINARY LIFE MODEL UNDER DEVELOPMENT

CD-86-21497

Figure 5

THERMAL-BARRIER-COATING LIFE PREDICTION

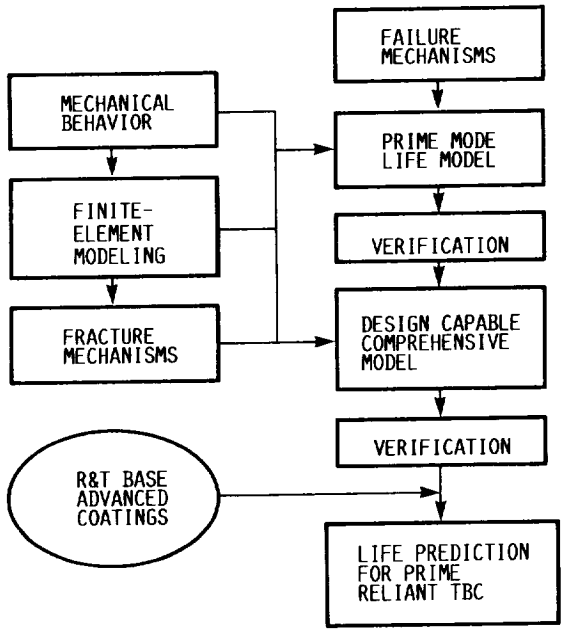

CD-86-21500

Figure 6

RIG/ENGINE CORRELATION

GOAL:
- PROVIDE A UNIQUE AND RELATIVELY INEXPENSIVE LABORATORY TO AID IN THE DEVELOPMENT OF ENVIRONMENT ATTACK LIFE PREDICTION TOOLS FOR HOT SECTION MATERIALS

APPROACH:
- VERIFY ADVANCES MADE IN THE LIFE PREDICTION OF HOT-SECTION MATERIALS AT PRESSURE LEVELS ENCOUNTERED IN GAS-TURBINE ENGINES

STATUS:
- RIG OPERATIONAL
- LIMITED TESTING PLANNED FOR MID 1987

CD-86-21499

Figure 7

HOST FY86 TBC ACCOMPLISHMENTS

- PRELIMINARY LIFE MODEL DEVELOPED (PWA)
- COATING MECHANICAL AND THERMAL PROPERTIES DETERMINED
- FAILURE MECHANISMS ELLUICIDATED
- STRESSES MODELLED BY FINITE ELEMENT ANALYSES
- NDE METHODS EVALUATED (GTEC)
- ENGINE TEST CONDUCTED (GTEC)

CD-86-21502

Figure 8

FURTHER DEVELOPMENT OF THE DYNAMIC GAS TEMPERATURE MEASUREMENT SYSTEM*

D. L. Elmore, W. W. Robinson, W. B. Watkins
Pratt & Whitney Engineering Division

INTRODUCTION

The objective of this effort was to experimentally verify a dynamic gas temperature measurement system in laboratory experiments. In previous work (Ref. 1) a measurement system was developed for gas turbine combustor exhausts, with special emphasis placed on dynamic response to enable determination of fluctuating components. The measurement probe was demonstrated to have greater than one hour life in a jet engine combustor, and very long (>5 hours) life in an atmospheric burner. Under the current program the measurement and compensation methods were verified by comparing the results obtained by the compensated dynamic sensors with those of a fine-wire resistance thermometer of intrinsically high frequency response. Two signal sources were used: 1) a rotating wheel which alternately directed hot and cold gas streams at the sensors and 2) an atmospheric pressure kerosene/air burner. A commercially available optical fiber thermometer was tested for dynamic response in the burner experiment.

The following sections describe the dynamic gas temperature measurement system verification program. A brief description of the sensor geometry and construction is followed by a discussion of the probe heat transfer analysis and subsequent compensation method. The laboratory experiments are described and experimental results are discussed. Finally, directions for further investigation are given.

PROBE DESCRIPTION

The dynamic temperature probe concept is shown in Figure 1. The probe employs two thermocouples of different wire diameters positioned in close proximity. The thermoelements are large enough in diameter that frequency response above a few Hertz is limited by thermal inertia. When the thermocouples are exposed to the same instantaneous temperature and velocity in the gas stream, the difference in thermal responses will be governed by convective effects (proportional to wire diameter) and conductive effects (proportional to specific heat, thermal conductivity and wire length). Many previous studies (Refs. 2 and 3) used thermoelements of sufficiently large ($\approx$100) length-to-diameter ratio that conduction effects may be neglected, and compensations were based on first-order convective time constants. The present sensor, however, is designed for engine hot-section applications, and the

*Work performed under NASA Contract NAS3-24228

smaller length-to-diameter ratios required for structural adequacy necessitates inclusion of transient conduction effects in the compensation method.

A novel feature of each thermocouple is the beadless, butt-welded thermoelement. The beadless construction allows the sensor to be modelled as a cylinder in crossflow, which simplifies the model considerably. ISA type B (Pt/6Rh - Pt/30Rh) thermocouples were used for the burner tests and type K (chromel-alumel) thermocouples were used for the rotating wheel tests.

PROBE THERMAL ANALYSIS AND COMPENSATION METHOD

The energy conservation equation describing convective and conductive heat transfer to the thermocouples is

$$\frac{dTw}{dt} = \frac{4hg}{\rho wCpwd} (Tg - Tw) + \alpha \frac{d^2Tw}{dx^2} \qquad (1)$$

The thermoelement and support wires were modelled with the nodal breakup shown in Figure 2, and equation (1) is implemented in this model in finite difference form to describe the temperature versus time history of the wire. Material properties for the two t/c legs are averaged in these calculations. To determine the thermocouple response to a given gas stream frequency component, a sinusoidal temperature variation a(t) is used as a boundary condition on the nodes exposed to the gas stream, and several cycles of gas stream temperature are iterated. The true dynamic response of the wire is obtained when peak response amplitudes change less than 0.1% from one-half-cycle to the next.

Comparisons between parametric modelling and experimental data are required in the compensation scheme to determine an in situ value of hg and the resulting compensation spectrum. This method is described as follows. Let the calculated thermocouple and gas stream temperature dynamic amplitudes be denoted by θ_i (f) and a(f), respectively, where i = 1 for the smaller thermocouple and i = 2 for the larger thermocouple. Gas stream signal a(t) is used as a boundary condition for nodes 0-9 and wire temperatures θi (t) are calculated at discrete frequencies f_n, over a practical frequency bandwidth (usually 4 to 30 Hz). At each frequency f_n signal amplitude ratio is determined:

$$\theta_i(f_n)/a(f_n) \qquad (2)$$

Note that $\theta_i(f_n)/a(f_n)$ forms a portion of the linear compensation spectrum in the practical bandwidth; this spectrum may be extended to cover the bandwidth of interest. Calculations are repeated for several values of the aerodynamic parameter (Figure 3a)

$$\Gamma = \frac{0.48 Kg Pr^{1/3} ug^{1/2}}{\left(\frac{\mu g}{\rho g}\right)^{\frac{1}{2}} \rho w \; Cpw} \qquad (3)$$

which provides aerodynamic scaling between the two different diameter thermocouples (Ref. 1). Note that Γ is proportional to an Hilpert equation (Ref. 4) form of heat transfer coefficient h_g for a cylinder in crossflow:

$$hg = \frac{\rho_w C_{pw}}{d^{\frac{1}{2}}} \quad \Gamma = \frac{0.48 Kg}{d} Pr^{1/3} Re^{1/2} \tag{4}$$

Variation of Γ, therefore, corresponds to a variation in h_g. At constant values of Γ the ratio of the small and large diameter thermocouple responses at given frequencies yields a calculated transfer function $H_c(f_n)$ (Figure 3b).

$$Hc(f_n) = \theta_2(f_n)/\theta_1(f_n) \tag{5}$$

The experimental portion of the compensation method includes recording of the two-wire probe signals, digitizing and converting to temperature using appropriate calibration curves. Temperature versus time waveforms $\theta_{j,E}(t)$ are Fourier transformed to yield $\theta_{j,E}(f)$ and division of θ_2 by θ_1 yields an experimental transfer function $H_E(f)$. Experimental and theoretical transfer functions are compared; where the two match at the discrete frequencies in the practical frequency bandwidth, experimental Γ's are then averaged, the calculated $\theta_2(f)/\theta_1(f)$ associated with the average Γ is identified, thereby identifying the calculated $\theta_1(f)/a(f)$, the compensation spectrum gain, and $\eta(f)$, the compensation spectrum phase, for the smaller thermocouple. The calculated compensation spectrum is used over the bandwidth of interest (0-1 KHz). The compensated gas stream temperature spectrum is calculated by dividing the experimentally-measured frequency spectrum by the calculated thermocouple compensation spectrum.

$$a(f) = \theta_{j,E}(f)/(\theta_j(f)/a(f))_c \tag{6}$$

These concepts have been reduced to practice in dynamic temperature sensor compensation software. Fortran coding is used and the program is operational on IBM computers with execution time of about 4 minutes per case.

EXPERIMENT

The rotating wheel experiment is shown in Figure 4. A drive assembly consisting of electric motor and shaft was used to rotate a wheel plate which had 8 holes on a 20.32 cm (8 inch) bolt circle diameter. Heated and ambient temperature air was supplied to two tubes mounted close together on one side of the rotating wheel and in-line with the holes' bolt circle diameter. As the wheel rotated the holes passed the two air supply tubes and allowed hot and cold air pulses to flow. A bifurcated manifold was placed on the opposite side of the rotating wheel in-line with the supply tubes to collect the hot (568K(563F)) and cold (289K(60F)) pulses and feed them into a transition section which became a single circular tube. Hot and cold air pulses were thereby delivered to the sensors mounted immediately downstream of the single circular tube. The wheel was rotated to produce a 250 Hz narrowband signal. Chromel-alumel thermocouples were used in the dynamic temperature sensor, and an analog-compensated 6.4μm (.00025 inch) diameter fine wire resistance thermometer was used as reference sensor.

An atmospheric pressure combustor with flowfield containing large amplitude (several hundred degrees) temperature fluctuations was used as source in the second experiment (Figure 5). An 1159K (1626F) mean temperature test point compared dynamic temperature sensors, a fine wire (12.7μm(.0005 in.) diameter) resistance thermometer and compensated optical fiber thermometer responses in the 0-1 KHZ bandwidth. An 1655K (2519F) mean temperature point

compared dynamic temperature sensor and optical fiber thermometer responses in the same bandwidth. ISA type B thermocouples were used in the dynamic temperature sensor.

RESULTS

A 20 Hz rotating wheel test point was used to derive the Γ for the 250 Hz test point compensation. Compensated 6.4μm (.00025 inch) resistance thermometer and 76μm (.003 inch) thermocouple spectra are shown in Figure 6. Compensated time-domain waveshapes are compared in Figure 7. The 76μm thermocouple has been compensated approximately 28db at the fundamental frequency; the resistance thermometer, however, required 0.9db of compensation due to its inherently higher response.

Figure 8 compares compensated 76μm (3 mil) and 127μm (5 mil) thermocouples and 12.7μm (.0005 mil) resistance thermometer spectra for the atmospheric burner 1159K (1626F) test point. The compensated thermocouples differ by 10% or less over the 0-1 KHz bandwidth, whereas the 12.7μm resistance thermometer is between 37 and 56% lower than the 127μm thermocouple. The amplitude spectrum of the resistance thermometer is shown in Figure 9. Note that a difference of 56% at 1 KHz between the compensated 127μm t/c and 12.7μm resistance thermometer represents about 1.5K$\sqrt{\text{Hz}}$.

Figure 10 is the transfer function between the uncompensated optical fiber thermometer and the compensated 76μm thermocouple for the 1159K (1626F) test point. Figure 11 shows the percentage difference of line amplitudes between the compensated optical fiber thermometer and compensated 76μm (3 mil) thermocouple. Qualitatively similar results were obtained in a second burner test at 1655K (2519F) as shown in Figures 12 and 13.

CONCLUDING REMARKS

The dynamic gas temperature measurement system offers measurement capabilities previously unavailable for gas turbine engines. Structural adequacy of the probes demonstrated in previous work is now more meaningful in combination with measurement fidelity verification. The method can potentially be adapted to transient engine acceleration combustor exit temperature measurements, associated blade and vane cooling flow temperature measurements during transients, as well as used for measurement of steady-state engine dynamic gas temperature signals.

Directions for further work in this measurement technique include fine-tuning and optimization of the basic method as well as extending the work to investigate some fundamental aspects of heat transfer.

1. Measurement uncertainty contribution, both precision and bias, should be determined for each source in the experiment and compensation method, including the fine-wire thermometer standard. The need is to optimize thermoelement diameter ratio and frequency range for determining Γ, and to improve the experimental setup and other factors to minimize uncertainty in the compensated gas stream measurement. Such an uncertainty analysis would involve propagation of uncertainties for

time-dependent quantities, and would require combining uncertainties in both time and frequency domains.

2. The finite-difference model should be extended to include material properties for both halves of the thermoelement. Use of average properties simplifies the model with compromise to uncertainty in the compensation method. The average properties versus individual properties change would determine the corresponding measurement uncertainty contribution, and allow cost versus complexity trade-offs to be made for the compensation scheme.

3. The variation of Γ with frequency should be investigated. The Γ values used in this work were averaged over the practical working bandwidth. Investigation of frequency dependent Γ effects were beyond the scope of this work.

4. Values of hg implicit in Γ should be determined explicitly according to equation (4). The measurement technique developed here offers a novel possibility for measuring hg for a cylinder in crossflow in a combustion stream.

LIST OF SYMBOLS

a = gas stream temperature amplitude at frequency f
Cp = heat capacity
d = thermocouple element diameter
D = thermocouple support wire diameter
f = frequency
$H(f)$ = transfer function
h = convective heat transfer coefficient
K = thermal conductivity
M = Mach number
P = gas pressure
Pr = Prandtl number = $\frac{Cp\mu}{K}$
Re = Reynolds number
T = Temperature
t = time
u = velocity
x = wire length coordinate
α = thermal diffusivity = $\frac{K}{\rho Cp}$
Γ = aerodynamic parameter defined in Equation (3)
μ = viscosity
η = phase shift of thermocouple response with respect to gas temperature at frequency f
ρ = density
θ = thermocouple response

Subscripts

C	=	calculated
E	=	experimental
i	=	1, 2 denoting smaller and larger thermocouples, respectively
n	=	frequency index
T	=	theoretical; total gas properties
w	=	wire
g	=	gas

REFERENCES

1. Elmore, D. L., Robinson, W. W., and Watkins, W. B., "Dynamic Gas Temperature Measurement System," NASA CR-168267, Final Report for NASA Contract NAS3-23154. See also ISA Transactions 24, No. 2, pp. 73-82.

2. Dils, R. R., and Follansbee, P. S., "Wide Bandwidth Gas Temperature Measurements in Combustor and Combustor Exhaust Gases," Instrumentation in the Aerospace Industry, Vol. 22, Proceedings of the 22nd International Instrumentation Symposium, San Diego, Calif., 1976, pp. 307-328.

3. Yule, A. J., Taylor, D. S., and Chigier, B. A., "On-line Digital Compensation and Processing of Thermocouple Signals for Temperature Measurement in Turbulent Flames," AIAA 16th Aerospace Sciences Meeting, 16-18 January 1978, Paper No. 78-3.

4. Eckert, E. R. G., and Drake, R. M., Heat and Mass Transfer, 2nd Edition, 1959, McGraw-Hill, New York, p. 242.

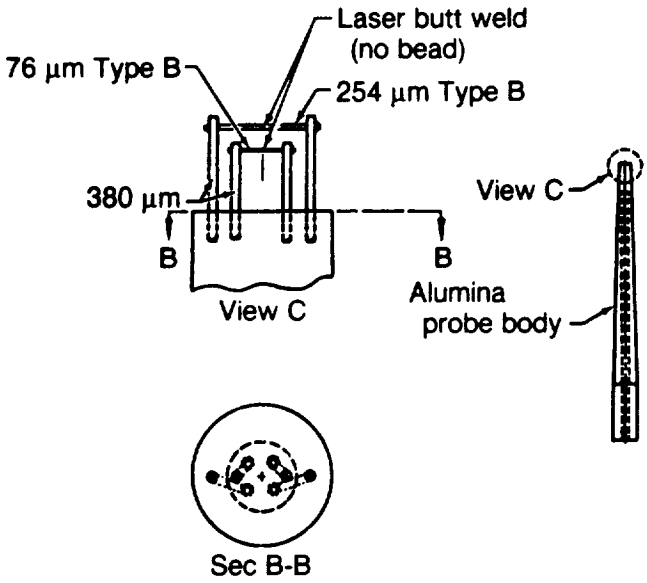

Fig. 1 Dynamic Temperature Sensor Concept

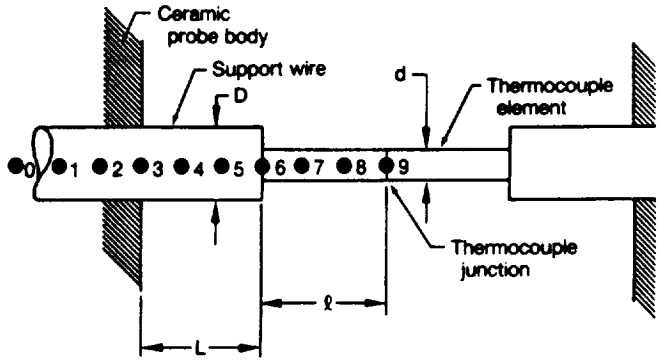

Fig. 2 Nine-Node Finite Difference Model

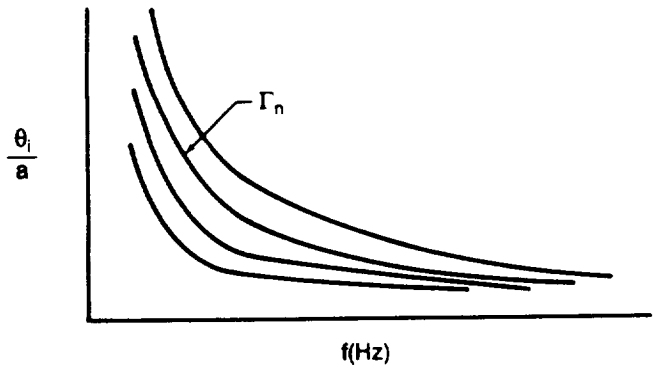

Fig. 3A Parametric Calculation Of θi(f)/a(f)

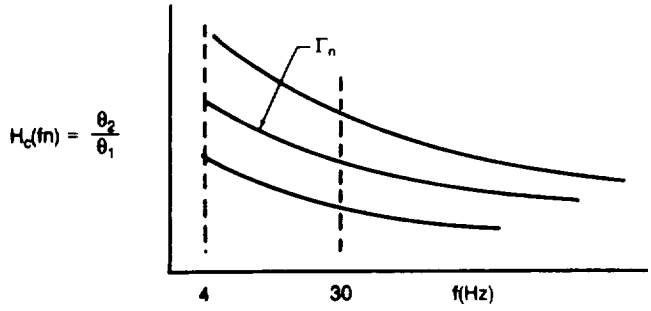

Fig. 3B Ratio θ_2/θ_1 For Several Values Of Γ

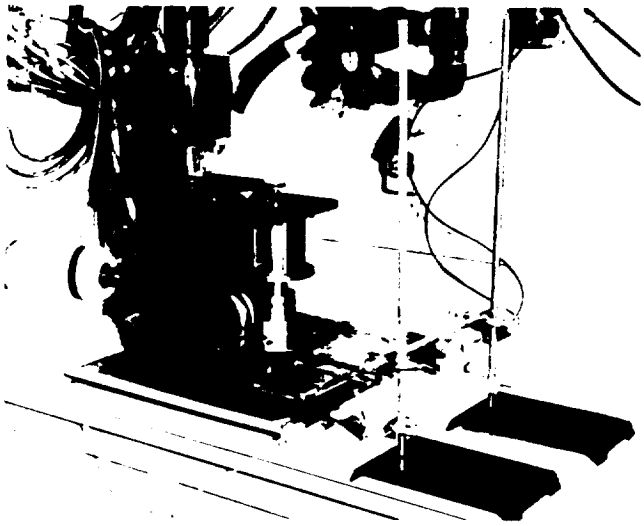

Fig. 4 Rotating Wheel Experiment θ

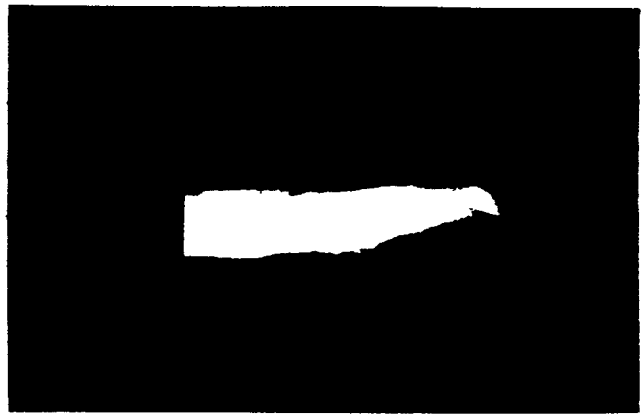

Fig. 5 Atmospheric Pressure Burner Experiment

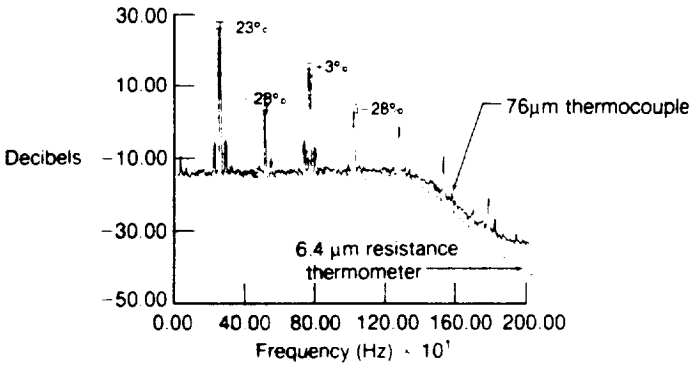

Fig. 6 Rotating Wheel Experiment Compensated 76μm And 6.4μm Sensor Power Spectral Densities

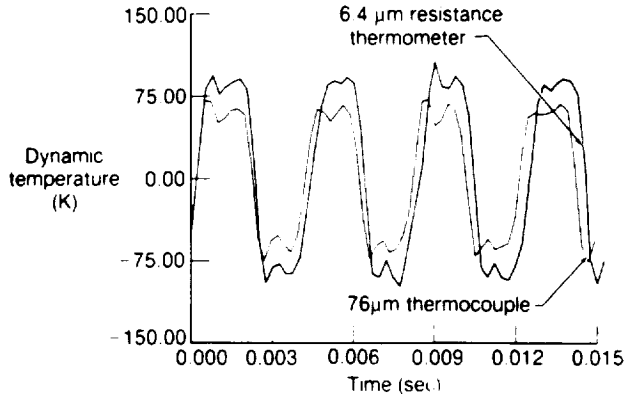

Fig. 7 Rotating Wheel Experiment Compensated 76μm And 6.4μm Sensor Wave-Forms

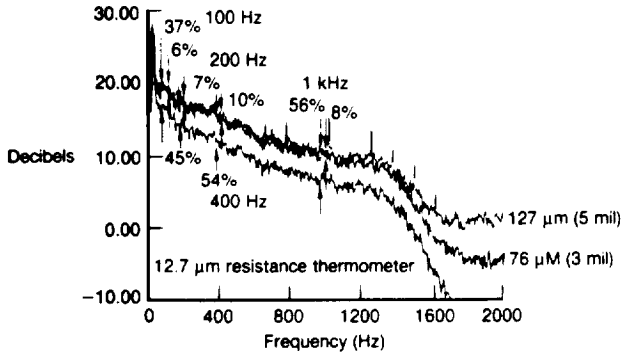

Fig. 8 Atmosphereric Pressure Burner Compensated Thermocouples And Resistance Thermometer Power Spectral Densities

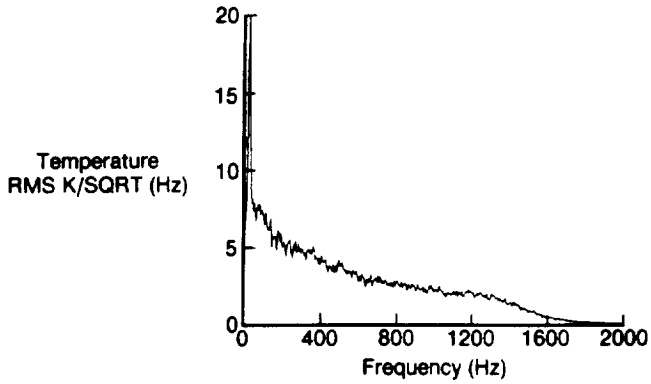

Fig. 9 Resistance Thermometer Linear Spectrum

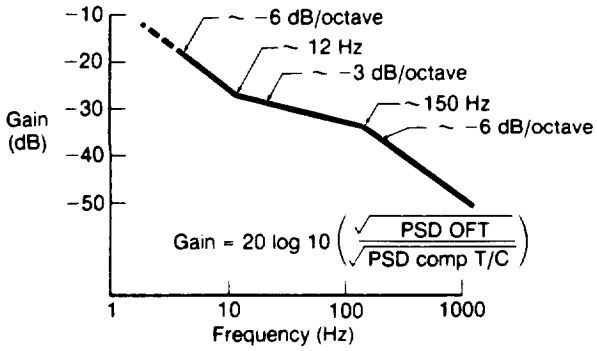

Fig. 10 Transfer Function Between Uncompensated Optical Fiber Thermometer And Compensated 76μm Thermocouple (1159K(1626°F) Test Point)

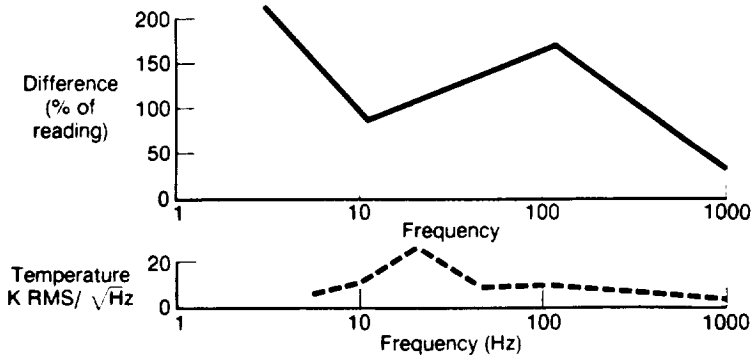

Fig. 11 Differences Between Optical Fiber Thermometer And 76μm Thermocouple Amplitudes (1159K (1626°F) Test Point)

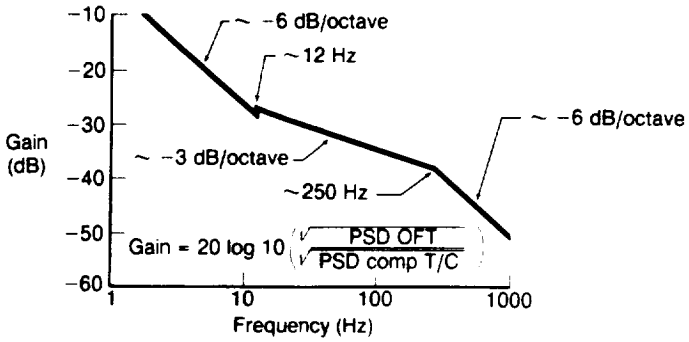

Fig. 12 Transfer Function Between Uncompensated Optical Fiber Thermometer and Compensated 76μm Thermocouple (1655K(2519°F) Test Point)

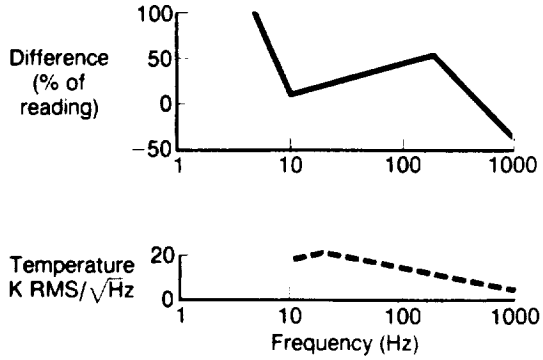

Fig. 13 Differences Between Optical Fiber Thermometer and 76μm Thermocouple Amplitudes (1655K(2519°F) Test Point)

N89-12885

LASER ANEMOMETRY: A STATUS REPORT

Mark P. Wernet, Richard G. Seasholtz, Donald H. Weikle, and Lawrence G. Oberle
NASA Lewis Research Center
Cleveland, Ohio

A laser anemometer system is being developed for the warm turbine facility as part of the HOST program. The system will be built using results obtained from our analytical and experimental research program. A status report of the laser anemometry applications research effort will be presented.

SUMMARY OF LASER ANEMOMETER STATUS FOR WARM TURBINE FACILITY

The designs for the turbine casing, the windows, and the positioning system have been completed. A block diagram of the laser anemometer system, signal processing scheme, and computer system is shown in figure 1. The status of these components is as follows:

Optics. - The optics will use an f/2.5 diffraction-limited final focusing lens. This fast lens was selected to allow the collection of the maximum amount of scattered light. It also will allow measurements close to surfaces by using large aperture masks. The primary optical design will be a single color laser fringe design (LFA). The use of a second color is being considered to provide simultaneous two-component measurements, if required. Both designs will include provision for rotation of the sample volume so that both the axial and circumferential velocity component can be measured. The four-spot time-of-flight anemometer system (TOFA) will be evaluated for use in hot, high-speed flows. If it proves superior to the LFA, the TOFA will be used.

Because of the aberration caused by the curved windows (0.250 and 0.3752 in. thick), it will be necessary to use compensating optics. Without compensation, the two beams will not, in general, cross and no measurements would be possible. The correction scheme consists of using a cylindrical lens and actuator which act as a zoom lens element.

Positioning system. - The optics will be mounted on a custom-designed optical table attached to a three-axis linear positioning system. In addition, the viewing direction will be determined by a mirror mounted on a two-axis goniometer, and the sample volume orientation by an image rotator. These six axes are adjusted by a controller that is interfaced to the system computer.

Seed injection system. - Because of the high-temperature flow environment, a solid seed material will be used. A fluidized-bed seeder generator has been purchased. The seed material will be alumina or another refractory material such as titanium dioxide. An identical seed generator has been successfully used in the NASA Lewis open jet burner. The seed injection will be through an 0.125-in. o.d. diameter tube. The tube position will be determined by an actuator controlled by the system computer. The seed injection mechanism is part of the casing design. One alternative approach that is being investigated is the injection of titanium

tetrachloride vapor into the gas stream. Titanium tetrachloride reacts with water vapor to form small titanium dioxide particles and hydrochloric acid.

Window cleaning. - One anticipated problem is maintaining optically clean windows. It is expected that during operation the windows will be coated with seed material and, perhaps, by combustion products and/or lubricating oil. The following steps have been taken to alleviate this problem: First, provision has been made in the design of the window frame for the injection of purge gas to prevent the accumulation of contaminants on the windows. These purge holes can also be used to inject a cleaning solution during operation. Finally, an access window has been located so that the windows can be cleaned without removing them from the rig.

Data acquisition. - The data acquisition and experiment control will be handled through the system computer, PDP 11/44. The signal processor for the LFA is a counter processor. (The TOFA uses a custom-designed processor.) Each velocity measurement will result in three quantities being sent via a DMA channel to the PDP 11/44: (1) the velocity, (2) the time between the current velocity measurement to the previous measurement, and (3) the rotor position as determined by an electronic shaft angle encoder (ref. 1). A custom signal preprocessor will be used to allow computer control of a number of functions, including the selection of filters, selection of the PMT high voltage, selection of the gain of the signal amplifier, and monitoring of the PMT current.

Software. - The software needed to control the system and to acquire the data is a major part of the project. It will determine both the quality of the data and the efficiency of taking the data. The general goals of the system are

(1) To obtain axial and circumferential components of the velocity and turbulence intensity through the measurement region (which includes both the stator and the rotor)
(2) To determine the accuracy of these data
(3) To obtain a complete survey at one flow condition in a 4-hour test run
(4) To obtain estimates of the turbulence scale
(5) To have operating procedures simple enough so the system can be used by the facility engineers without extensive training.

SEEDING WITH TITANIUM TETRACHLORIDE

The reaction of $TiCl_4$ with water to form TiO_2 is being investigated to form seed particles for hot-section applications. Titanium tetrachloride reacts with water in air as shown:

$$TiCl_4 + 2H_2O \Rightarrow TiO_2 + 4HCl$$

The technique being used for forming particles in the open jet burner uses a dry air carrier for the $TiCl_4$ gas. Moist air is generated by running a separate line of air through a water bubbler. The $TiCl_4$ gas and moist air are then mixed 1 in. from the entrance to the hot section by a concentric injector with the $TiCl_4$ stream in the center. The TiO_2 particles are formed in the gas stream before it enters the burner. The moist air surrounding the $TiCl_4$ gas tube keeps the tube free of accumulated TiO_2 and HCl.

In the initial tests run, data rates of 20 kHz were achieved. Data indicated that the particles were small (≤ 1 μm), but the size was not measured. Current tests are being conducted to obtain samples of the TiO_2 from the burner exit. SEM photographs will be taken to determine of the TiO_2 particle size.

Some advantages of using $TiCl_4$ are (1) large number density of particles, (2) small size, (3) generated where needed, and (4) constant rate of generation.

Some disadvantages are (1) toxic liquid and gas, (2) large amount of HCl to neutralize, and (3) necessary use of special container materials (glass, ceramic, or stainless steel)

FOUR-SPOT TIME-OF-FLIGHT LASER ANEMOMETER

The four-spot time-of-flight laser anemometer system (TOFA) is a hybrid system, designed specifically for use in high-speed, turbulent flows near walls or surfaces. These are the anticipated conditions inside the warm turbine facility. The performance of the TOFA in low-speed flows (< Mach 0.3) was reported in the 1985 HOST Workshop (ref. 3). In early 1986 the new high-speed ECL version of the signal processor, capable of measurements greater than Mach 2, was received from Case Western Reserve University. An interface for the new signal processor to the system computer has been completed and initial tests of the processor have shown good performance up to Mach 1.3. A test was also conducted to determine additional performance characteristics of the system.

The TOFA sample volume contains approximately half the illuminated area of a typical LFA. The higher light flux in the probe volume enables the TOFA to measure smaller particles than an LFA. Detection of smaller particles is desirable because they follow the flow more accurately. A particle velocity lag experiment was conducted to determine range of particle diameters detectable by the TOFA.

In the particle velocity lag experiment, the velocity of particles entrained in the flow are measured downstream of a sonic nozzle. The gas accelerates through the nozzle, reaching Mach 1 at the exit. Particles greater in diameter than approximately 0.3 μm will lag behind the gas velocity at the nozzle exit. The amount of velocity lag is proportional to the particle diameter. The gas velocity can be calculated from the plenum temperature and the pressure drop across the nozzle. Since the laser anemometer can only measure the velocity of the particles entrained in the flow, the particle lag velocity is directly obtained. The measured particle velocity histograms are converted to particle diameter histograms. The mean particle diameter and standard deviation are then determined from the particle diameter histograms.

The seed particles used in the experiment were diagnostic latex spheres of 0.5- and 0.8-μm diameter, with a specific gravity of 1.05. A LFA cannot measure particles less than approximately 0.7 μm in diameter. The results of the particle lag experiment are shown in the table below and the corresponding velocity histograms are shown in figures 2 and 3.

Seed particle diameter, μm	Measured particle diameter, μm	Standard deviation of mean diameter, μm
0.50	0.54	0.20
.80	.82	.14

The spread in the histograms is caused by both error in the measurement and

agglomeration of the seed particles. The estimates of the mean particle diameter are biased to higher values than the true particle diameters because of these effects. The results from the analysis show that the TOFA system can detect particles down to at least 0.5 μm in diameter.

CORRECTION OPTIC FOR CURVED TURBINE WINDOW

The turbine casing for the warm turbine facility has been refabricated with an optical access window. The window, which is curved to match the inner radius of the turbine casing, will minimize disturbance to the flow. The disadvantage of using a curved window is its astigmatic aberration. The curved window acts as a lens with uneven powers in the horizontal and vertical planes. An alternative approach and previously the only approach, is to use planar windows (ref. 5). This minimizes the astigmatic aberrations, but disturbs the flow field.

The laser anemometer system for the warm turbine will initially be a one component system with an image rotator. Rotation of the probe volume through various angles permits the measurement of the axial and circumferential velocity components. Rotating the probe volume through the turbine window causes varying degrees of image distortion. A solution to this problem is to preaberrate the image before it passes through the turbine window. This correction optic must also have continuous compensation throughout the survey range of the probe volume.

A lens design software package was purchased, and a correction optic for the warm turbine window was designed. The correction optic will be zoomed in and out as the three-axis table is moved to position the probe volume (figs. 4 and 5). The corrector has been optimized for normal incidence to the turbine window. The astigmatic errors in the image formation can be reduced through the use of the correction optic.

REFERENCES

1. Powell, J.A.; Strazisar, A.J.; and Seasholtz, R.G.: Efficient Laser Anemometer for Intra-Rotor Flow Mapping in Turbomachinery, Trans. ASME, vol. 103, pp. 424-429, Apr. 1981.
2. Seasholtz, R.G.; Oberle, L.G.; and Weikle, D.H.: Laser Anemometers of Hot-Section Applications. Turbine Engine Hot Section Technology - 1984. NASA CP-2339, pp. 59-69, 1984.
3. Wernet, M.P.: The Four Spot Time-of-Flight Laser Anemometer. Turbine Engine Hot Section Technology - 1985, NASA CP-2405, pp. 67-75, 1985.
4. Wernet, M.P.; and Edwards, R.V.: Implementation of a New Type of Time-of-Flight Laser Anemometer, Appl. Opt., vol. 25, pp. 644-648, Mar. 1986.
5. Schodl, R.: Laser-Two-Focus Velocimetry, AGARD Conference paper no. CPP-399, pp. 7.1-7.30, 1986.

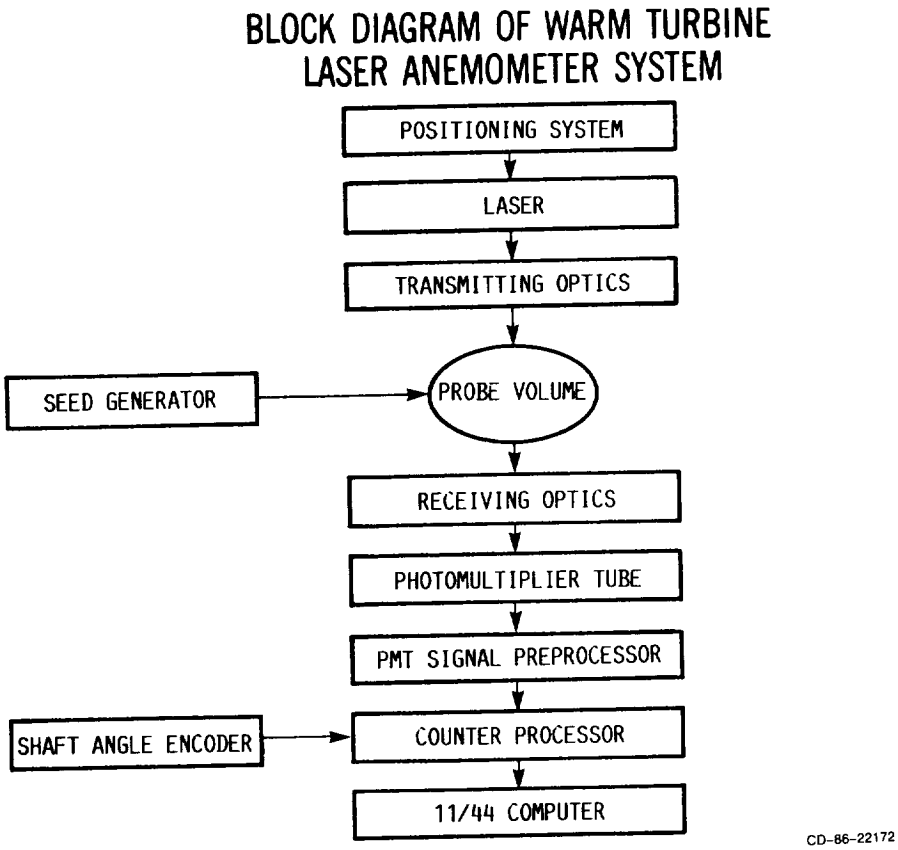
BLOCK DIAGRAM OF WARM TURBINE
LASER ANEMOMETER SYSTEM
POSITIONING SYSTEM
LASER
TRANSMITTING OPTICS
SEED GENERATOR
PROBE VOLUME
RECEIVING OPTICS
PHOTOMULTIPLIER TUBE
PMT SIGNAL PREPROCESSOR
SHAFT ANGLE ENCODER
COUNTER PROCESSOR
11/44 COMPUTER
CD-86-22172

Figure 1

PARTICLE-LAG VELOCITY HISTOGRAM

0.5-μM SEED PARTICLES; TAKEN 200 μM FROM NOZZLE EXIT; CRITICAL VELOCITY, 315 M/SEC

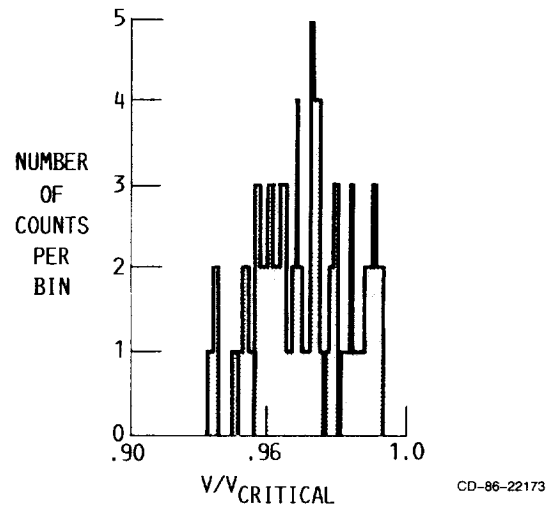

Figure 2

PARTICLE-LAG VELOCITY HISTOGRAM

0.8-μM SEED PARTICLES; TAKEN 200 μM FROM NOZZLE EXIT; CRITICAL VELOCITY, 315 M/SEC

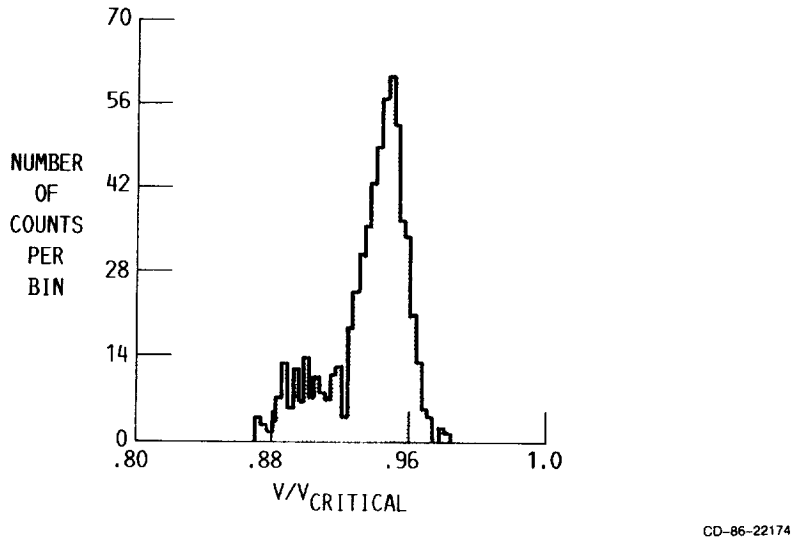

Figure 3

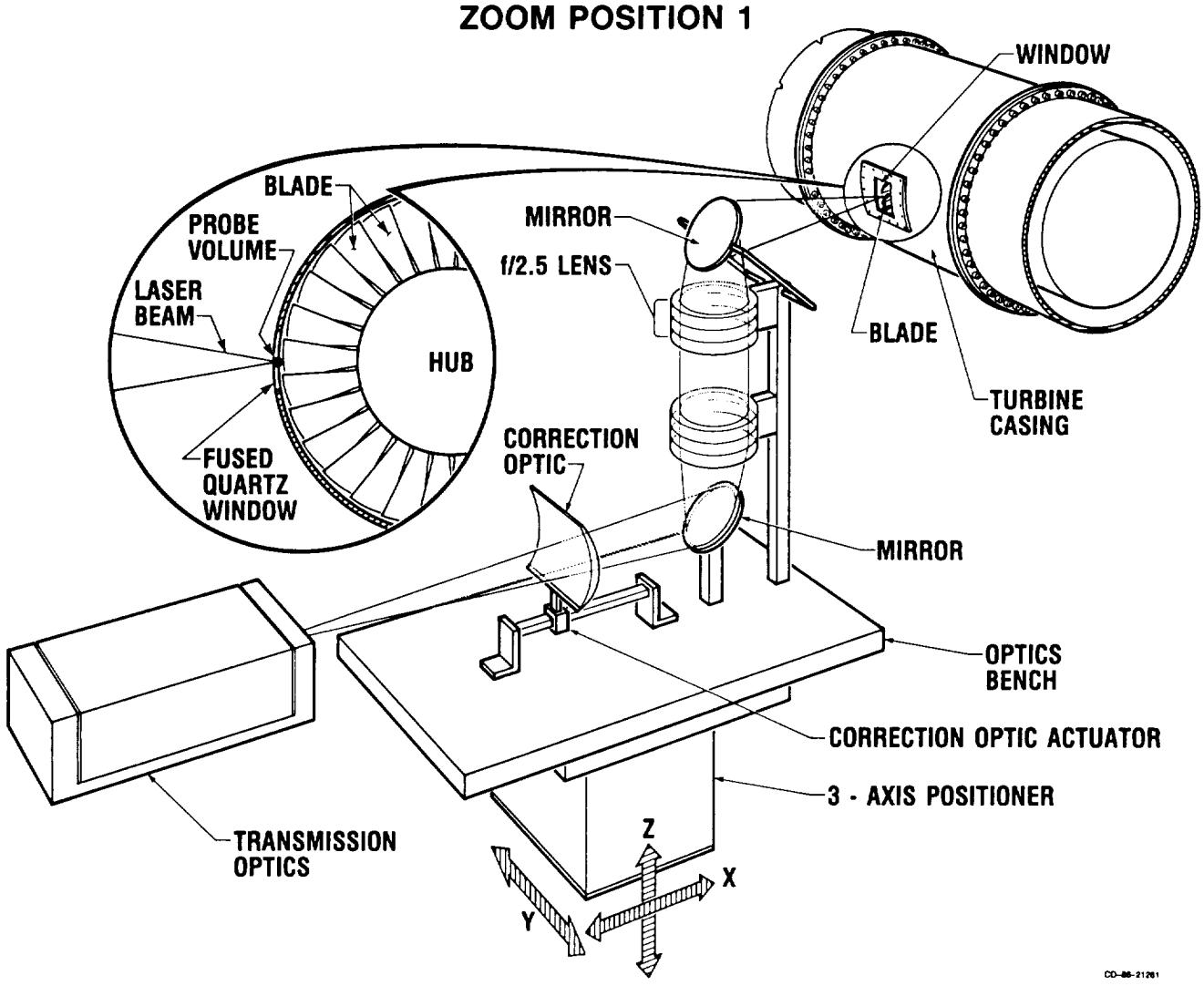
ZOOM POSITION 1
WINDOW
BLADE
PROBE VOLUME
LASER BEAM
HUB
MIRROR
f/2.5 LENS
BLADE
TURBINE CASING
FUSED QUARTZ WINDOW
CORRECTION OPTIC
MIRROR
OPTICS BENCH
CORRECTION OPTIC ACTUATOR
3 - AXIS POSITIONER
TRANSMISSION OPTICS
Z
X
Y

Figure 4

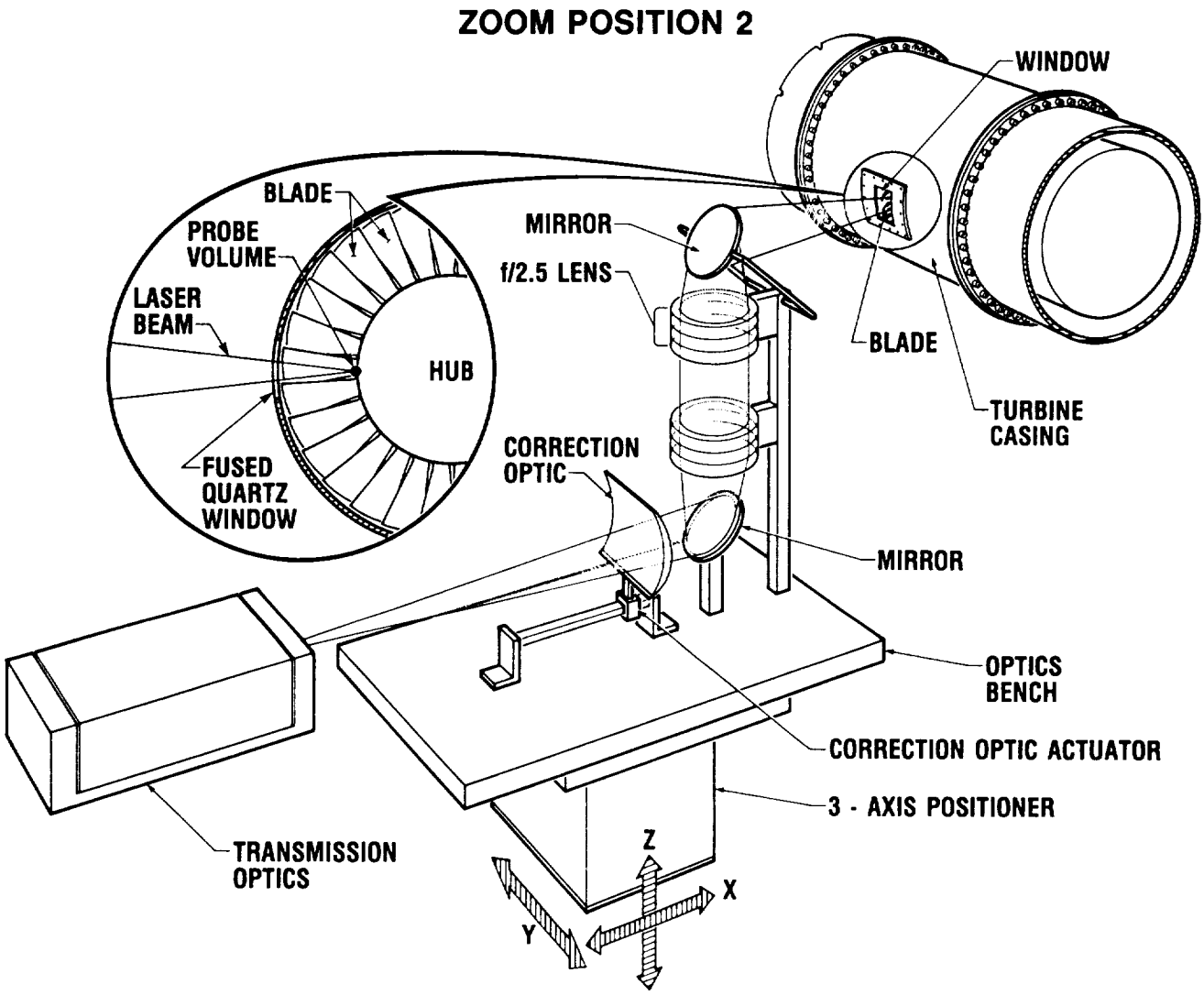
ZOOM POSITION 2
WINDOW
BLADE
PROBE VOLUME
LASER BEAM
HUB
FUSED QUARTZ WINDOW
MIRROR
f/2.5 LENS
BLADE
TURBINE CASING
CORRECTION OPTIC
MIRROR
OPTICS BENCH
CORRECTION OPTIC ACTUATOR
3 - AXIS POSITIONER
TRANSMISSION OPTICS
Z
X
Y

Figure 5

ELEVATED TEMPERATURE STRAIN GAGES*

J. O. Brittain, D. Geslin and J. F. Lei
Northwestern University

One of the goals of the Host Program is the development of electrical resistance strain gages for static strain measurements at temperatures ≥ 1273 K. Strain gage materials must have a reproducible or predictable response to temperature, time and strain. It is the objective of this research to investigate criteria for the selection of materials for such applications through electrical properties studies. The results of the investigation of two groups of materials, refractory compounds and binary alloy solid solutions are presented in this report.

The materials selection criteria are summarized as follows:

(1) The material should not undergo a phase transformation in the temperature range of interest. This was ascertained by studying existing phase diagrams.

(2) The materials should not undergo any order-disorder transitions or the formation of clusters. In order to satisfy this criteria interstitial refractory compounds were selected for a study of their elevated temperature behavior. In the case of binary alloys an effort was made to locate ideal solid solutions, i.e., alloys in which both elements had activity coefficients close to one (1). In the present case based upon a recommendation of one of our colleagues (2) we set a limit on the activity coefficients of within 15% of one. Thermodynamic data (3,4) suggested that the systems Ag-Pd and Al-V have ranges of concentrations that satisfy this criterion. However, because of the shortage of activity coefficients data, alternative qualitative parameters have been used to select alloys that appear to satisfy this second criterion. Based upon the Hume-Rothery's work, elements that have similar electronegativities and molar volume tend to form ideal solutions. The systems Mo-W, Mo-Re, and Nb-V were selected based upon these qualitative parameters.

(3) Chemical and thermal stability of the materials are important in order to reduce the tendency for oxidation and in order to insure mechanical stability. It was deemed useful to have a high melting temperature in order to minimize recrystallization and grain growth. The importance of insuring elastic behavior over the useful or desired strain range could in principle be achieved by selecting materials for which $(\sigma_{E.L.}/E) > \epsilon_{max}$ where $\sigma_{E.L.}$ is the stress at the elastic limit. E is the Young's Modulus, and ϵ_{max} is the maximum strain to be measured. This parameter will have to be evaluated experimentally due to the lack of published data on the materials under investigation.

(4) Finally, several materials have been selected for the experimental phase of this work based upon published electrical resistivity-temperature data. This was true of the Cr-V alloys for which results were presented last year. Table I listed all of the materials evaluated and the basis for their selection for this program.

*Work done under NASA Grant NAG 3-501

MATERIALS PREPARATION, PROCESSING AND EXPERIMENTAL TECHNIQUE

The alloys listed in Table I have been prepared by arc melting in the usual manner under a purified Ar atmosphere. The 5 to 10 gm homogenized ingots were sliced into thin plates via a diamond cut off disc. Specimens for electrical resistance measurements were processed from the plates by electrical discharge machining. An alternative method of preparing longer and thinner specimens by means of drawing the molten alloy into a quartz tube connected to a vacuum was tried. However, some pick up of Si occurred and we have abandoned this technique.

With two exceptions all of the refractory compounds were prepared as thin films on Al_2O_3 substrate by the various methods listed in Table II. The two exceptions, B_4C and α-SiC, were prepared as bulk specimens by hot pressing and subsequently thinned by slicing into electrical resistance specimens. The refractory compounds thin films were obtained from several sources that have had considerable experience in the various techniques utilized.

The electrical resistance (ER) of the specimens were measured via a four probe technique using Pt or W leads and pressure contacts in conjunction with a ceramic specimen holder. The contacts were checked and found to be ohmic at all temperatures. Measurements were conducted in an evacuated quartz tube under a dynamic vacuum of $\sim 10^{-5}$ torr. Thermal Emf were eliminated by alternating the direction of the current. Initially measurements were conducted on individual specimens; currently three specimens are held in the ceramic device and readings on the three specimens are made by rotating the contacts in the circuit.

RESULTS - REFRACTORY COMPOUND

A. Transition Metal Nitrides

(a) TiN

The ER of two TiN films have been measured, one sample had been prepared by HCD method and the other by CVD method. The electrical resistance-temperature (ER-T) curves are shown in Figs. 1 and 2. We can see that their electrical behaviors are different, the resistance of TiN-1 (HCD) was metallic and increased with increasing temperature while the resistance of TiN-2 (CVD) decreased with increasing temperature like a semiconductor. TiN-2 (CVD) was not as stable as TiN-1 (HCD), however, its TCR at the higher temperatures was much smaller ($\sim$ 143 ppm/K) and its reproducibility can probably be improved by thermal cycling. An x-ray analysis indicated that these two TiN films have different lattice parameters and compositions. TiN-1 is TiN with a = 4.174 Å and TiN-2 is $TiN_{0.9}$ with a = 4.167 Å, by using EDAX of SEM, we also found that there are some chlorine (Cl) in the TiN-2 films.

(b) TaN

Two TaN Rf sputtered thin films prepared with different nitrogen (N_2) partial pressures during sputtering (Table I) were tested. The ER-T data of both films displayed metallic behavior, Fig. 3, however, the film with the lower N_2 partial pressure (TaN-1) had a smaller TCR ($\sim$ 260 ppm/K) and the TCR of both specimens decreased with thermal cycling. The drift rates were about 0.5%/hr for both films.

(c) ZrN

Three Rf sputtered ZrN specimens were studied. A comparison of these three samples during the second cycle of heating is shown in Fig. 4. The film with the highest ratio of N_2 during sputtering (i.e., ZrN-1) had the lowest TCR ($\sim$ 290 ppm/K) but it also had the highest drift rate (DR) ($\sim$ 0.54%/hr).

(d) CrN

The ER-T data for the CrN was metallic with a very large TCR ($\sim$ 710 ppm/K). The drift rate of resistance was also very large ($\sim$ 20%/hr). This may have been due to the oxidation of CrN and the formation of a Cr_2O_3 layer that may not have been protective. Figure 5 compares the resistance-temperature data for four different nitrides, clearly TaN has the lowest TCR while CrN has the highest TCR.

B. Transition Metal Carbides

TiC

The results of measurements on Two TiC films are shown in Figs. 6 and 7 respectively. Just like TiN, the film prepared by CVD method (TiC-2) had the higher drift rate at 1275 K ($\sim$ -0.5%/hr) but a lower TRC ($\sim$ 250 ppm/K).

C. Semiconductor

(a) B_4C

Among all the specimens studied, the results obtained for the B_4C specimen are most promising: (1) the smallest TCR ($\sim$ 160 ppm/K) and (2) the smallest drift rate ($\sim$ 0.1%/hr for 17 hours) as shown in Fig. 8. Additional experiments are planned for B_4C.

(b) SiC

Figure 9 shows the ER-T result of a β-SiC film prepared by the EBE method on an Al_2O_3 substrate (SiC-1), its TCR at 1273 K is $\sim$ 330 ppm/K and the drift rate is $\sim$ 0.3%/hr. This high drift rate may be reduced by increasing the thickness of the film in order to minimize the apparent evaporation effect. ER-T measurements in an Argon atmosphere are planned in order to minimize any effects that may be associated with the high vacuum utilized in the present measurements. Future plans will also include measurements in an oxidizing environment with the β-SiC protected by a nonconducting high temperature cement. The hot pressed high purity α-SiC was more stable, with a drift rate of only $\sim$ 0.04%/hr but a larger TCR ($\sim$ 1940 ppm/K), Fig. 10. It may be possible to decrease the TCR in the α-SiC by doping.

SUMMARY - REFRACTORY COMPOUNDS

The results for all the specimens are summarized in Table III. Based upon the target values for TCR of 200 ppm/K and a drift rate of $\sim$ 0.1%/hr (5) only B_4C meets the target values. However, for a total error of 10% (6), even this drift value appears to be too large. However, TaN-1 (Rf sputtered), TiN-2 (CVD), TiC-1 (ARE), TiC-2 (CVD) and β-SiC) (EBE) also warrant further investigation. Since the ratio of the non-metal atoms to the metallic atoms play an important role in the electrical properties of the transition metal compounds (7), future work will involve this

parameter in the search for strain gage materials with low TCR and high electrical resistance stability, i.e., low drift rate at high temperatures.

RESULTS - BINARY ALLOYS

A. Silver-Palladium System

Based upon the ideal-solid solution criteria we anticipated reproducible and stable electrical resistance-temperature data for alloys with Ag content of less than 5 w/o. Experimental confirmation was reported last year but the TCR at 1273 K of that composition was large. An increase of the Ag content from 4.1 to 15.5 w/o reduced the TCR from 774 ppm/K to 260 ppm/K without a loss of reproducibility or stability of the electrical resistance, Figs. 11, 12, Table IV. With a further increase in the Ag content to 35.3 w/o Ag, the composition known to produce an even lower TCR ($<$ 100 ppm/K) a large drift of the resistance at 1273 K occurred, Table IV.

B. Aluminum-Vanadium System

As reported last year an Al-V alloy 79.3 w/o V had a very low but negative TCR (-22 ppm/K) and a low drift (50 ppm/KO at 1273 K. This alloy had been prepared by drawing the molten alloy into a quartz tube. A microprobe analysis indicated the presence of Si. Three additional specimens with higher V contents were prepared by conventional arc melting. The results of the electrical measurements are shown in Figs. 13, 14. The (ER-T) curves were metallic in form and the TCR for the three alloys improved as the V content increased. A ternary alloy of Al-82.1 w/o V-2 Si was prepared to verify the effect of Si additions, the resulting Er-T curves, Fig. 15 was of a different form from the binary alloy, the effect of Si was quite pronounced. This alloy had good TCR and drift characteristics. Further work on the ternary system is planned.

C. Niobium-Vanadium System

The composition 5.2 w/o V was selected for investigation based upon the reported good oxidation resistance (8). While the reproducibility after the first heating cycle and the agreement in the ER-T curves for three specimens were good, Fig. 16 and 17; the TCR was large ($\sim$ 550 ppm/K) and the drift at 1273 K of 500 ppm/K was larger than desired. It may be that similar to the Al-V system a ternary addition might result in a lower TCR and drift rate.

C. Molybdenum-Rhenium

Based upon published data (9) the 71% Mo alloy was selected to provide an acceptable TCR. The Er-T curve was quite reproducible after the first heating cycle and the drift at 1273 K was quite low ($<$ 80 ppm/hr), however, the TCR of (623 ppm/K) was higher than desired (Fig. 18). Here again there is the potential to improve the TCR by a ternary addition.

SUMMARY - BINARY ALLOYS

With the exception of the Al-V-Si system, the alloys investigated thus far behave as predicted in terms of reproducibility between cycles after stabilization if the drift at 1273 K is neglected. In an effort to meet the TCR requirement of

< 300 ppm/K, several of the alloys show promise. These alloys are the 15.6 w/o Ag and 35.5 w/o Ag-Pd alloys and the Al-V alloys. While the 35.5 w/o Ag-Pd alloy does not meet our selection criterion as an ideal solution, the low TCR indicates that further study may be of interest. It is also possible that improvements in the electrical behavior of the Nb-V and Mo-Re alloys can be achieved by the addition of third elements.

In order to improve the oxidation resistance of several of the alloys an effort is underway to prepare alloys via mechanical alloying with the inclusion of Yttrium or Cerium oxide. The oxide additions may also serve to stabilize the structure, especially grain size, and improve the electrical behavior at elevated temperatures.

REFERENCES

1. Kubaschevski, O., Evans, E. L. and Alcock, C. B.: Metalurgical Thermodynamics, Pergamon, N.Y., 1967, p. 76.

2. Whitmore, D.: Private conversation, March, 1985.

3. Hultgren, R., et al., "Selected Values of Thermodynamic Properties of Binary Alloys," ASM, 1973.

4. Raychaudhuri, P. K., Ph.D. Dissertation, Northwestern University, 1971.

5. Pratt & Whitney: Thin film strain gage development program, NASA-21242.

6. Hulse, C. O., Bailey, R. S.: The Development of a High Temperature Static Strain Gage System, NASA Conference Publication 2405, p. 45.

7. Toth, Louis E.: Transition Metal Carbides and Nitrides, Academic Press, 1971.

8. Lazarev, E. M., Eklund, G. S. (Moscos) Izv. Akad. Nauk. SSSR, Met. 1979, (4),

9. Schröder, K.: "Handbook of Electrical Resistivities of Binary Metallic Alloys," CRC Press, 1983.

TABLE I

MATERIALS SELECTED FOR EVALUATION

Material	Basis for Selection
Pd-Ag	1
Al-V	1
Nb-V	2
Cr-V	3
Mo-Re	2, 3
TiN	4
TiC	4
ZrN	4
TaN	4
CrN	4
B_4C	4
SiC	4

1. Ideal solution, thermodynamic data.
2. Qualitative parameters, tendency to form ideal solutions.
3. Resistance-temperature data.
4. Refractory compounds, high melting temperature, structural stability, oxidation resistance.

TABLE II

PREPARATION METHODS FOR REFRACTORY COMPOUNDS

Specimen	Preparation Method	Remarks
TiN-1	HCD, Hollow Cathode Discharge	
-2	CVD, Chemical Vapor Deposition	
TaN-1	RfS Radio Frequency Sputtering	with $N_2/Ar+N_2 \sim 22$ %
-2		with $N_2/Ar+N_2 \sim 25$ %
ZrN-1	RfS, Radio Frequency Sputtering	with $N_2/Ar+N_2 \sim 1.65\%$
-2		$\sim 0.19\%$
-3		$\sim 0.16\%$
CrN	HCD	
TiC-1	ARC, Activated Reactive Evaporation	
-2	CVD	
B_4C	Hot Pressed	Bulk Sample
β-SiC-1	EBE, Electron Beam Evaporation	
α-SiC-2	Hot Pressed	Bulk Sample

TABLE III

SUMMARIZED RESULTS FOR REFRACTORY COMPOUNDS

Specimen	TCR (ppm/K)	Drift Rate (ppm/hr) (DR)	Remarks
TiN-1 (HCD)	588	1400	
TiN-2 (CVD)	143	2200	Reproducibility improved by thermal cycling
TaN-1	260	4900	TCR and DR decreased with thermal cycling
-2	300	5000	
ZrN-1	290	-5400	TCR increased while DR decreased with cycling.
-2	330	-2600	
-3	420	600	
CrN	710	20%	
TiC-1 (ARE)	366	580	
TiC-2 (CVD)	250	-5000	TCR increased while DR decreased with cycling
B_4C	160	940	
β-SiC-1	330	-3000	DR decreased by increasing thickness
α-SiC-2	1940	380	

TABLE IV

SUMMARIZED RESULTS FOR ALLOYS

Sample w/o	TCR (1270 K) ppm/K	Drift (1270 K) ppm/hr
AgPd 4.3 Ag	774	1723
11.7	460	62
15.5	260	140
35.3	30 to 165	7000 to 38,000
AlV 79.3 V	-22	50
86.65	150	1280
88.9	134	6000
82.1 - 2Si	-20	-1800 cycle 1 - 800 cycle 2
NbV 5.2 V	550	800
CrN 67.4 V	556	1130
MoRe 71 Mo	623	60 cycle 1 75 cycle 2

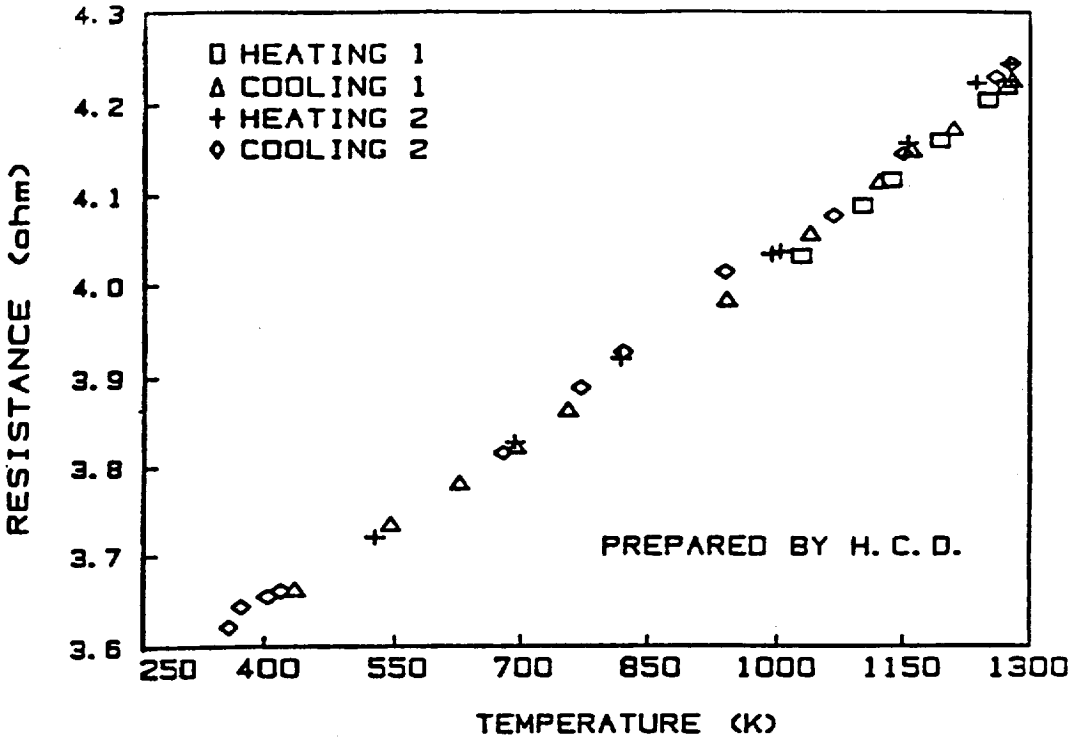

RESISTANCE Vs. TEMPERATURE OF TiN-1

Figure 1

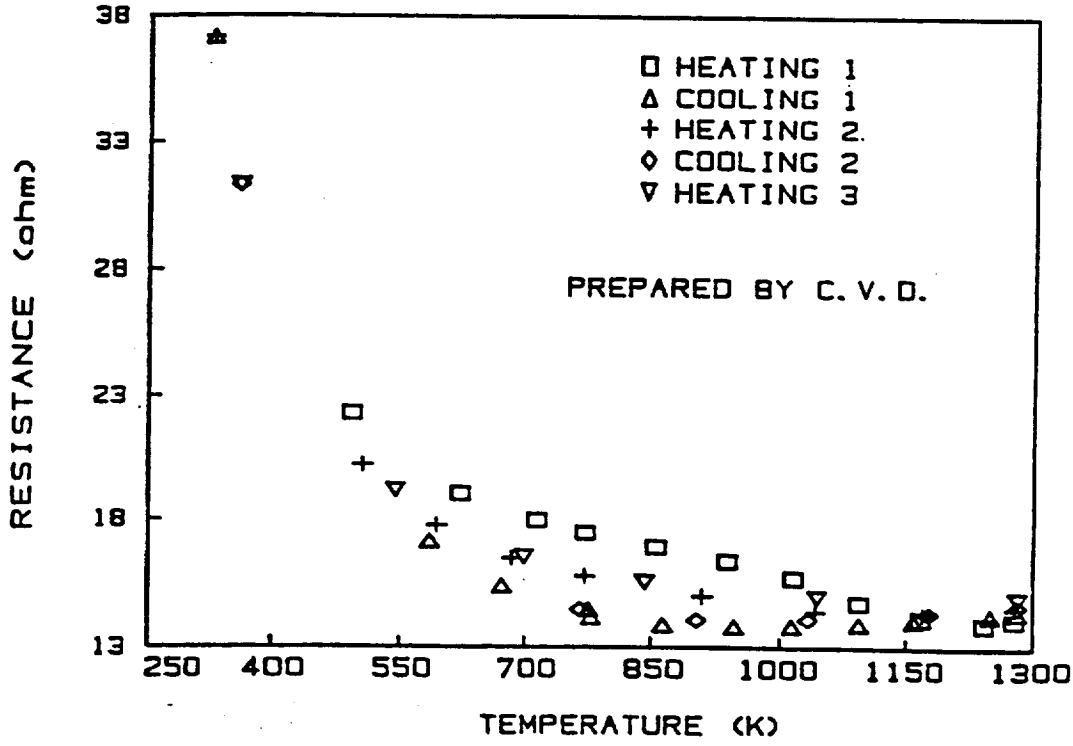

RESISTANCE Vs. TEMPERATURE OF TiN-2

Figure 2

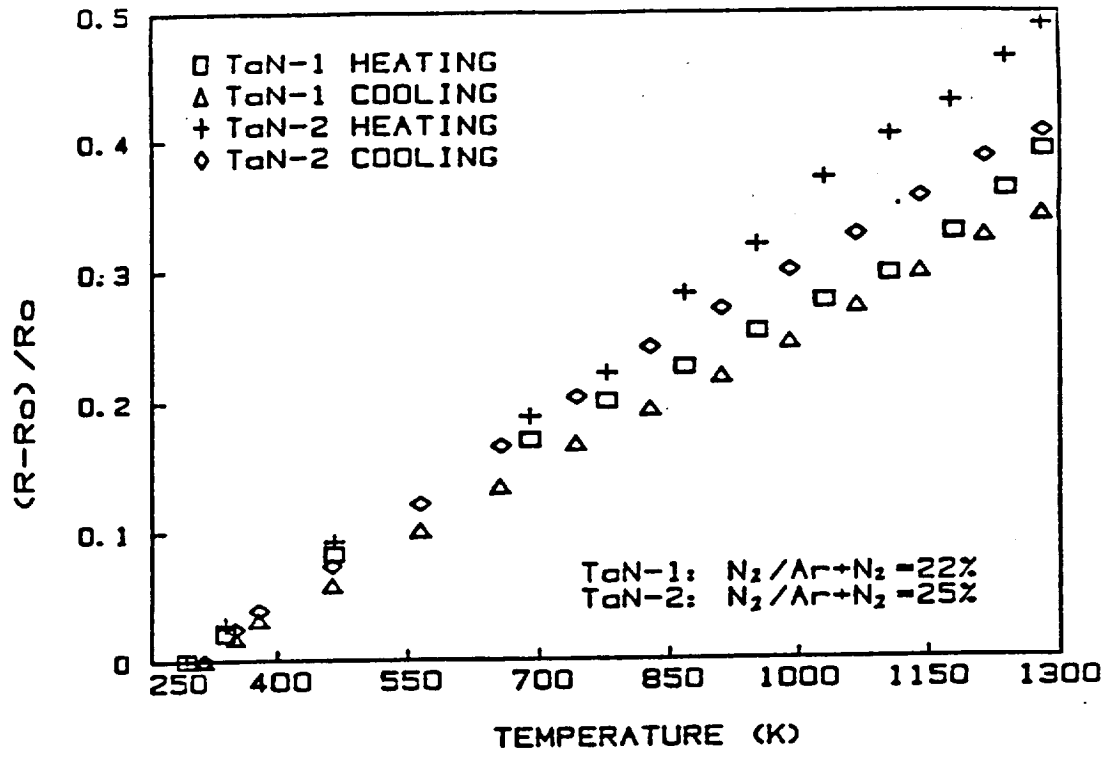

Comparison of Resistance vs. Temperature of two TaN films

Figure 3

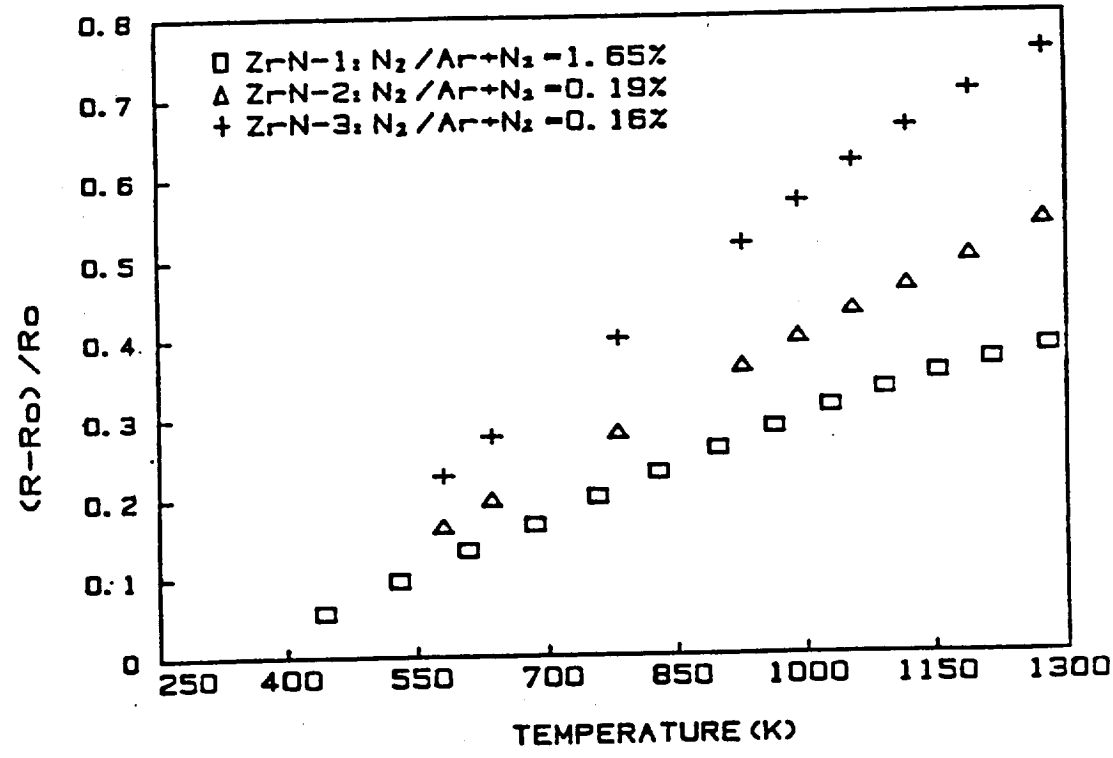

Comparison of Resistance vs. Temperature of three ZrN film

Figure 4

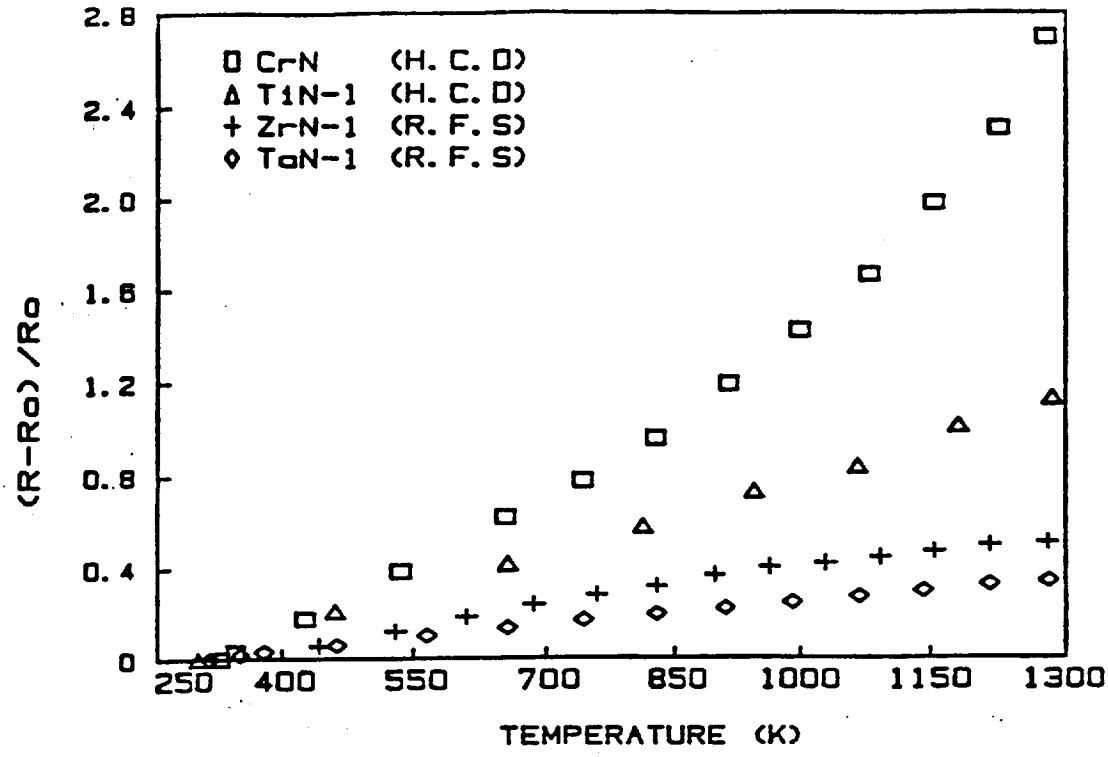

Comparison of Resistance vs. Temperature of four Nitrides

Figure 5

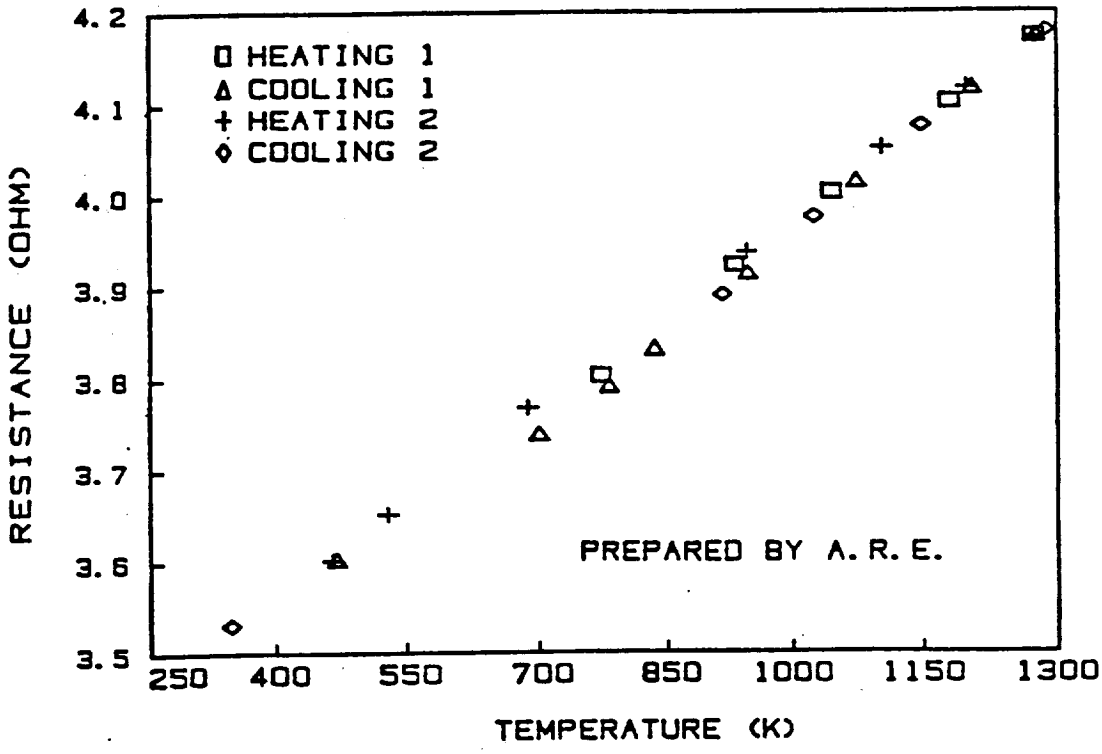

RESISTANCE Vs. TEMPERATURE OF TiC-1

Figure 6

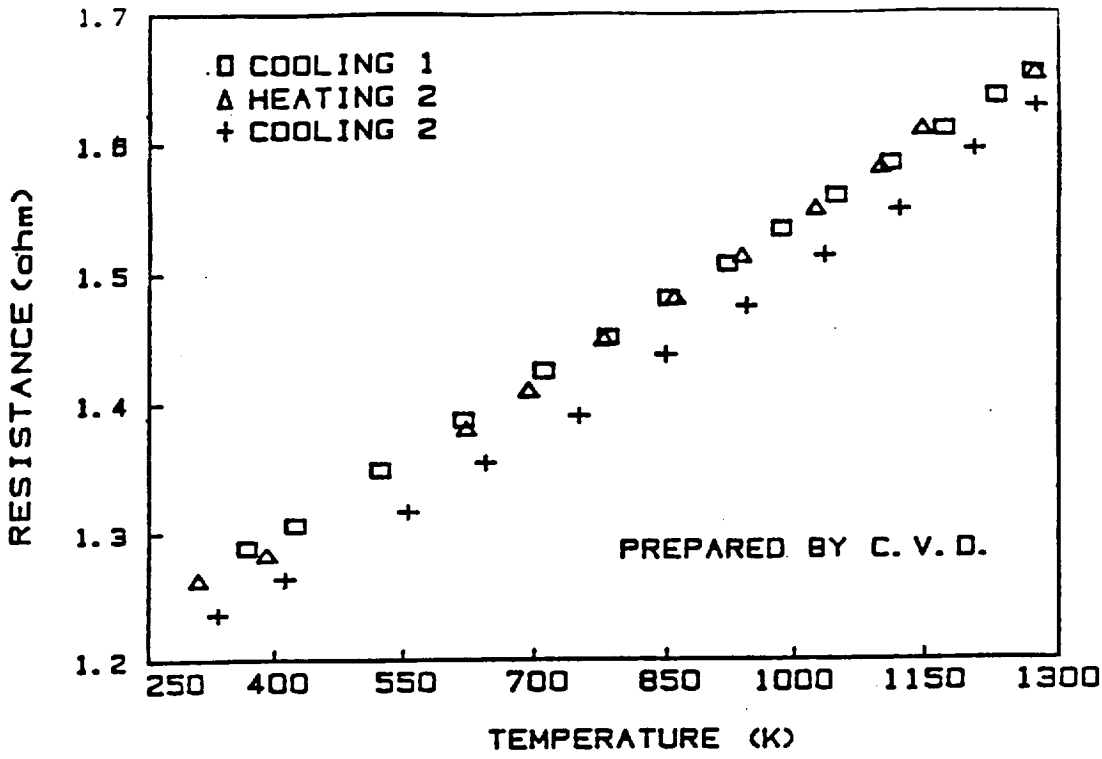

RESISTANCE Vs. TEMPERATURE OF TiC-2

Figure 7

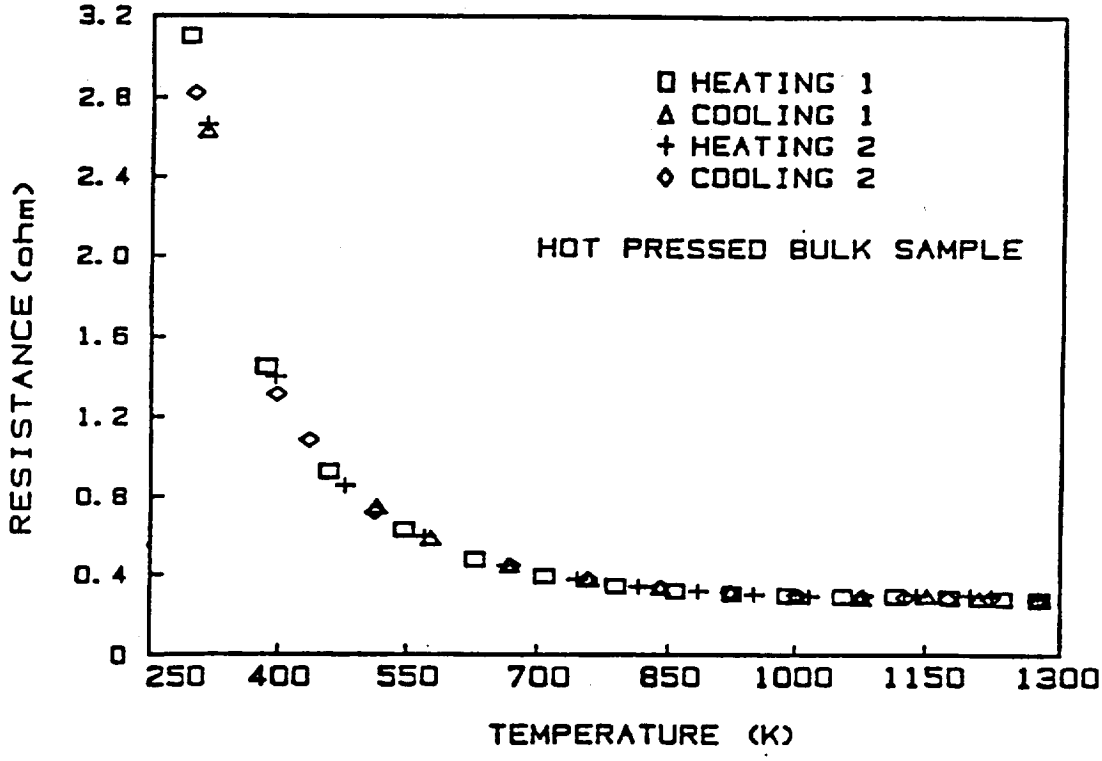

RESISTANCE Vs. TEMPERATURE OF B_4C

Figure 8

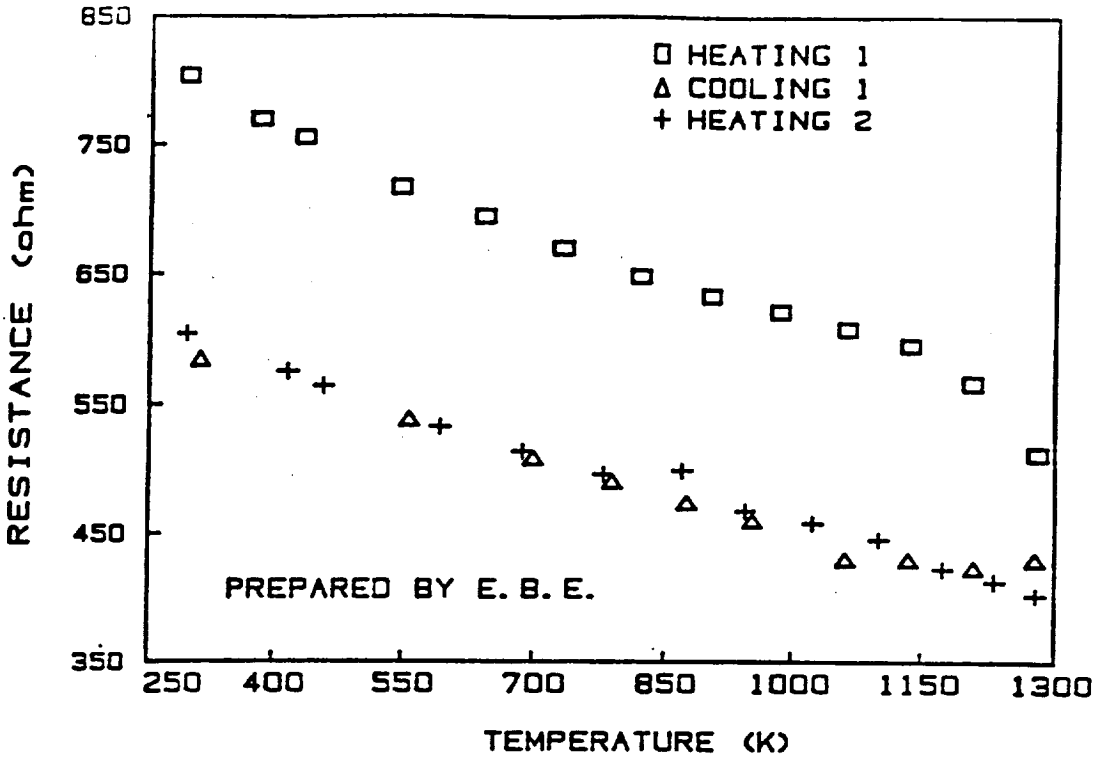

RESISTANCE Vs. TEMPERATURE OF β-SiC-1

Figure 9

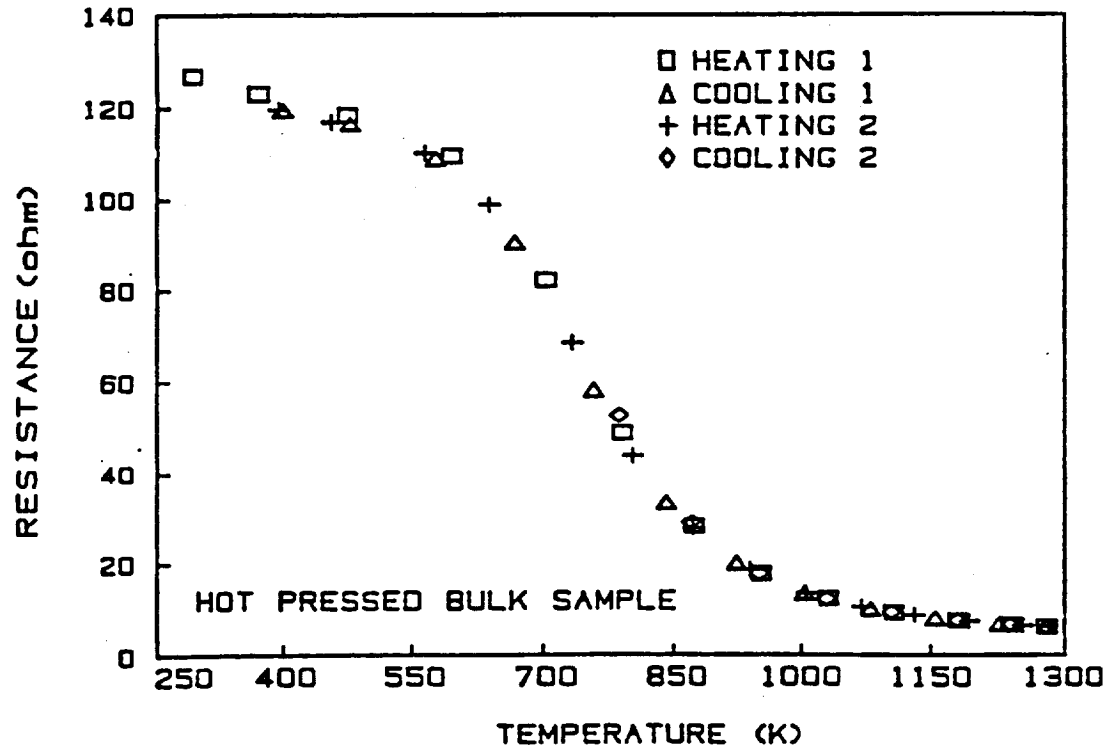

RESISTANCE Vs. TEMPERATURE OF α-SiC-2

Figure 10

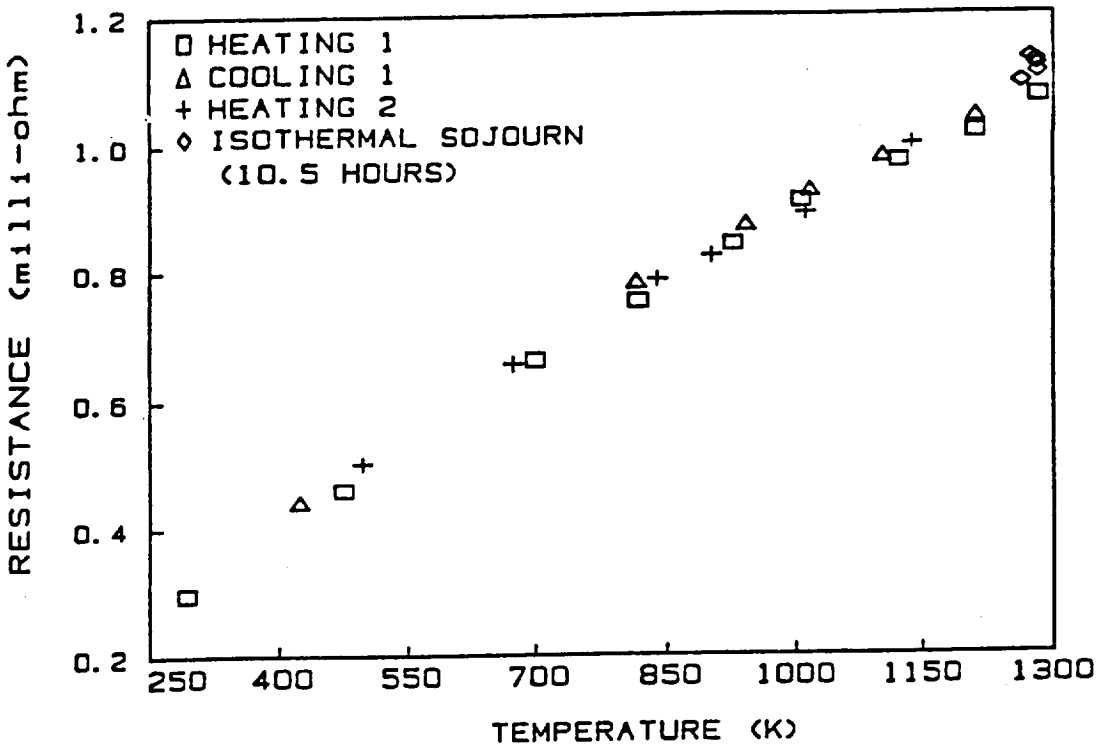

RESISTANCE vs TEMPERATURE of 4.1 w% Ag-Pd

Figure 11

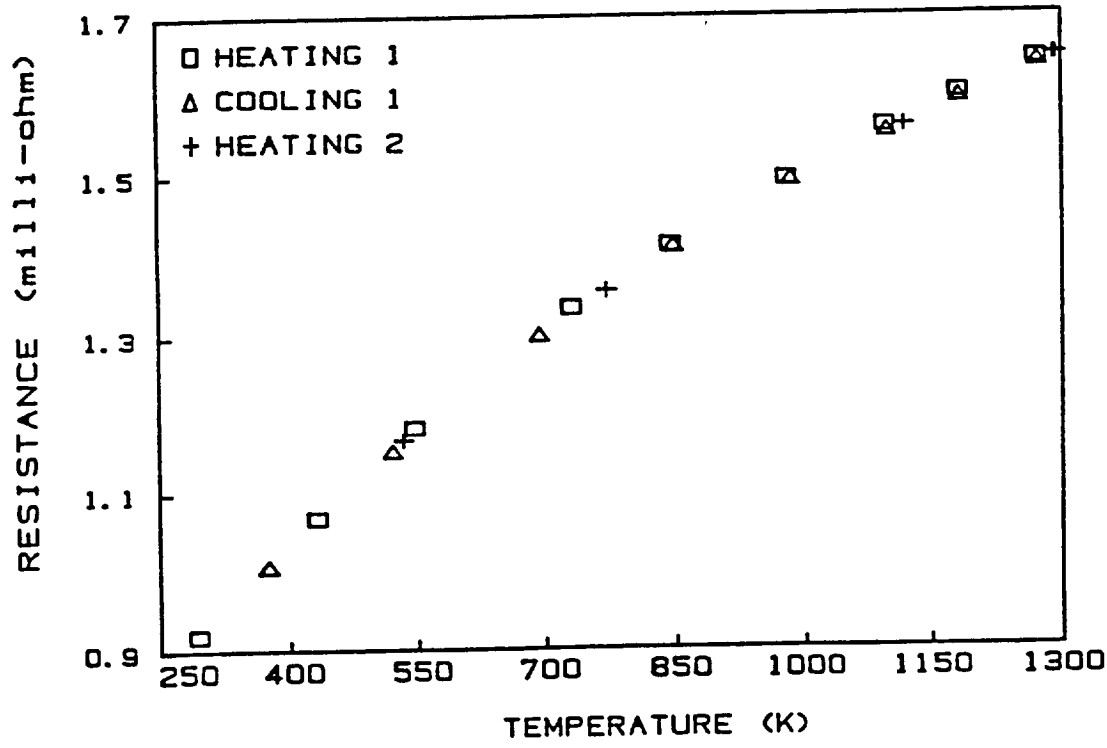

RESISTANCE vs TEMPERATURE of 15.6 w% Ag-Pd

Figure 12

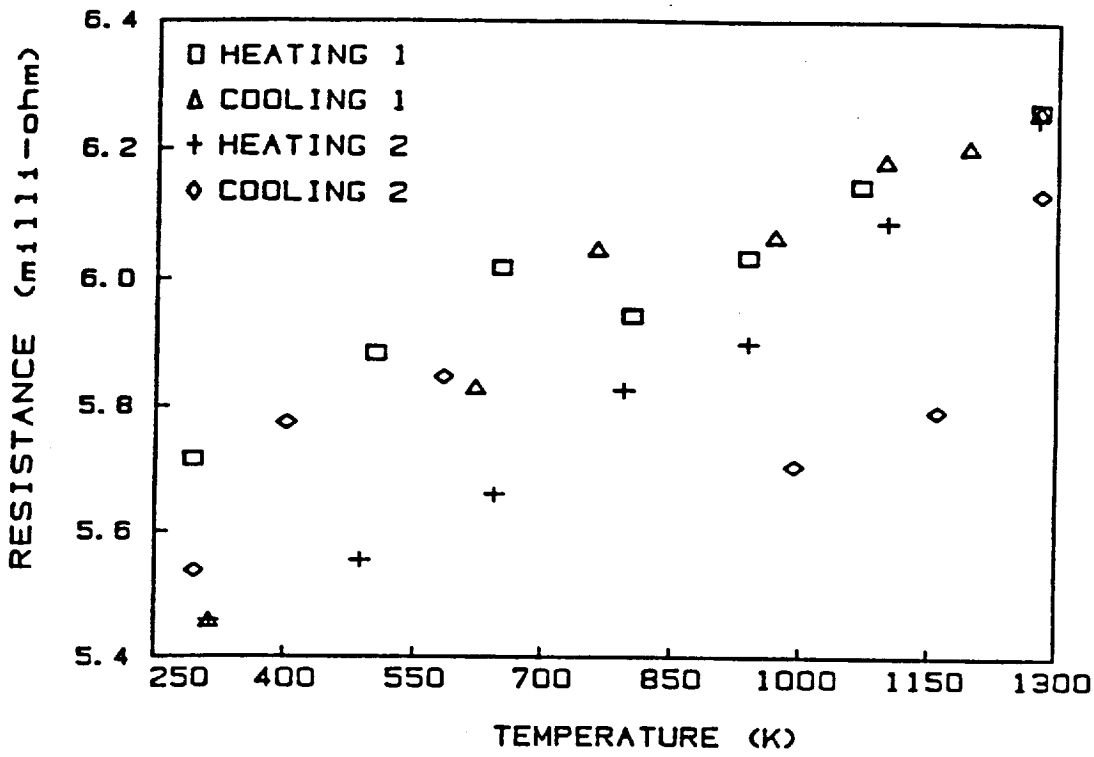

RESISTANCE vs TEMPERATURE of 86.65 w% V-Al

Figure 13

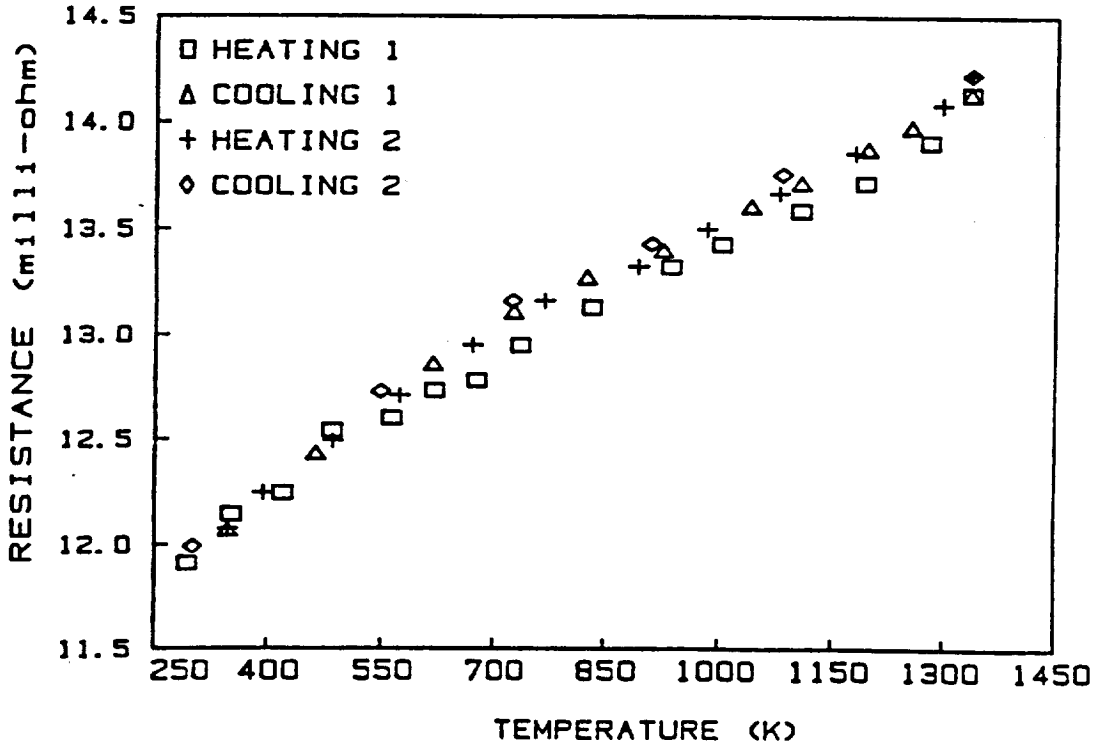

RESISTANCE vs TEMPERATURE of 88.9 w% V-Al

Figure 14

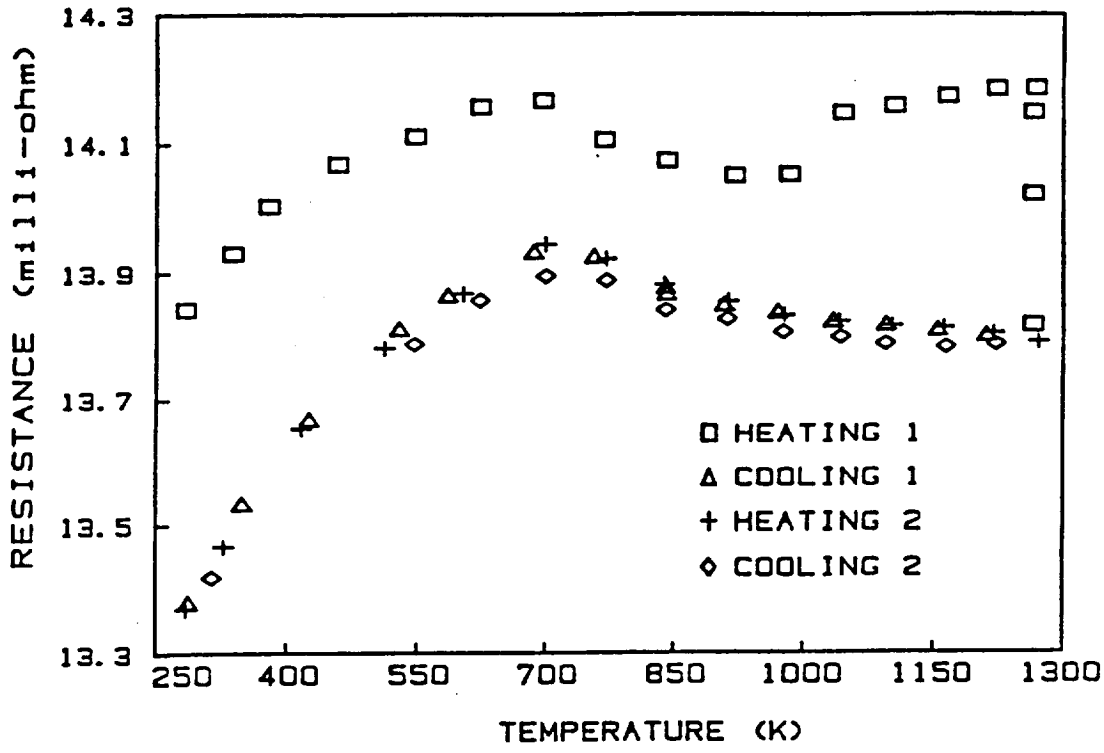

RESISTANCE vs TEMPERATURE of Al- 82.1V- 2Si

Figure 15

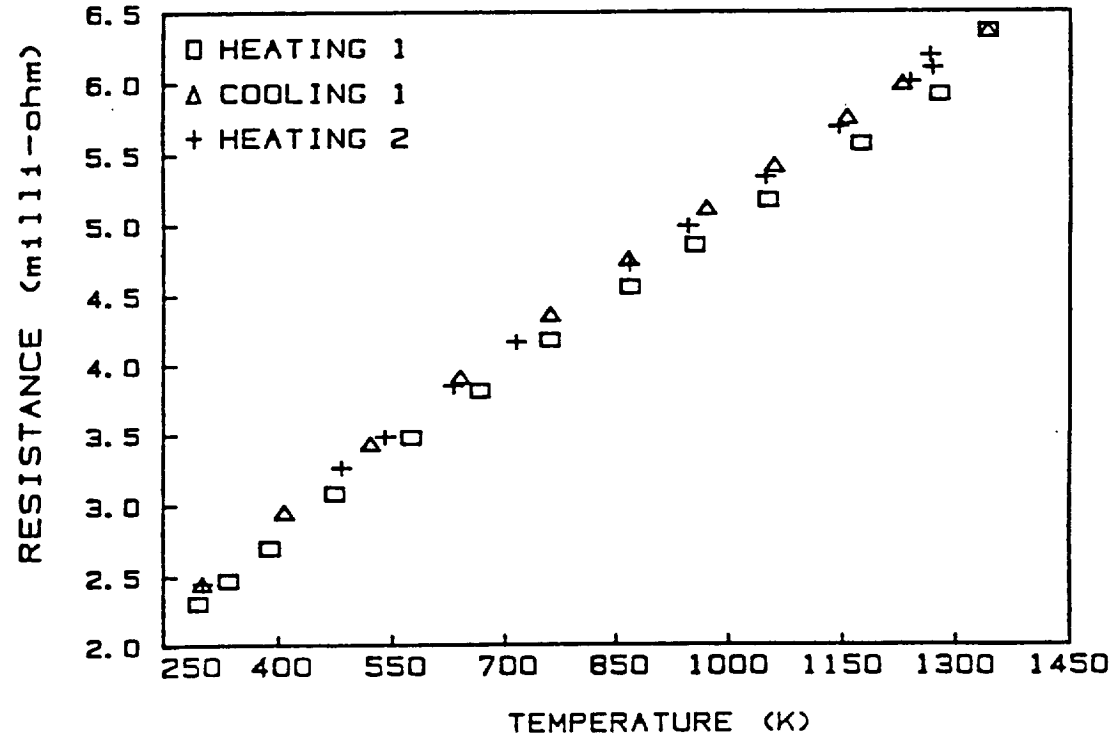

RESISTANCE vs TEMPERATURE of 5.2 w% V-Nb

Figure 16

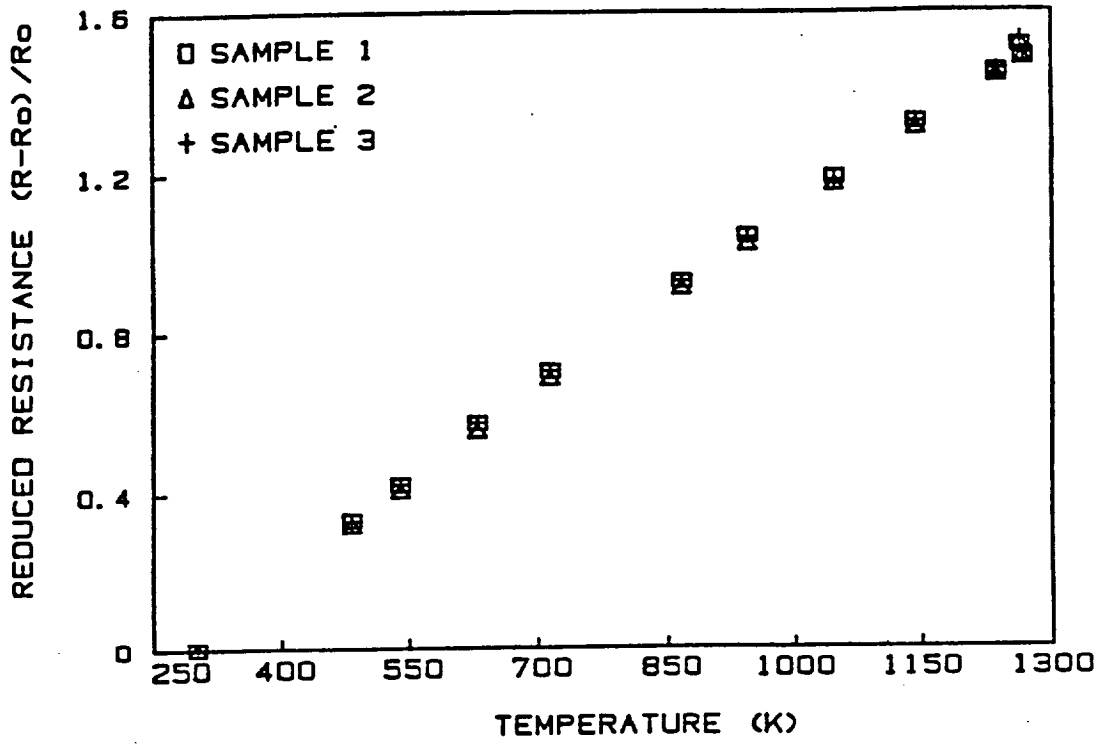

REDUCED RESISTANCE vs TEMPERATURE for 3 5.2 w% V-Nb SAMPLES

Figure 17

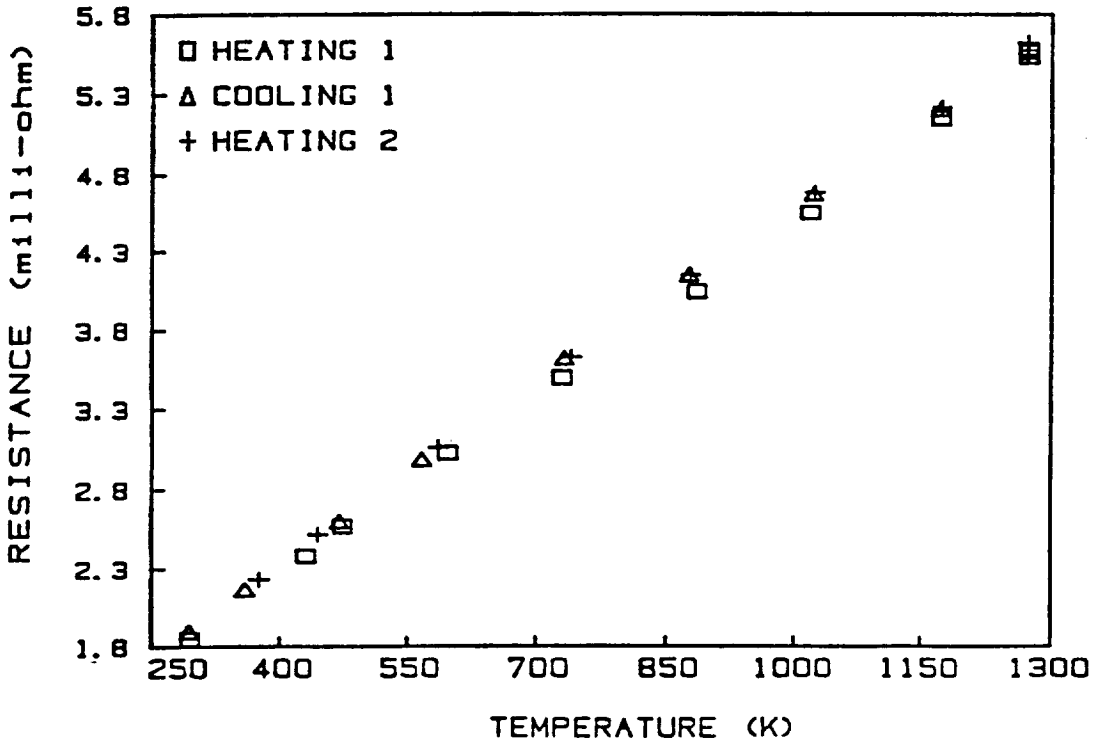

RESISTANCE vs TEMPERATURE of 71 w% Mo-Re

Figure 18

DEVELOPMENT OF A HIGH TEMPERATURE STATIC STRAIN SENSOR*

Charles O. Hulse and Richard S. Bailey
United Technologies Research Center
and
Howard P. Grant
Pratt and Whitney

INTRODUCTION

The goal of this program is to develop an electrical resistance strain gage system which will accurately measure the static strains of superalloy blades and vanes in gas turbine engines running on a test stand. Accurate knowledge of these strains is essential to reaching the goals of the Hast program in the selection and experimental verification of the various theoretical models developed to understand and improve the performance of these engines.

The specific objective of this work is to develop a complete system capable of making strain measurements of up to ±2000 microstrain with a total error of no more than ±10 percent of full scale during a 50 hour period at temperatures as high as 1250 K. In addition to survival and stability, attaining a low temperature coefficient of resistance, of the order of 20 ppm/K or less, was a major goal. This requirement arises from the presently unavoidable uncertainties in measurement of the exact temperatures inside gas turbines for use in making corrections for apparent strain due to temperature.

EXPERIMENTAL FACILITIES

The thermal cycling apparatus shown in figure 1 was used to make resistance measurements up to 1250 K at constant temperatures or at heating and cooling rates as high as 250 K/min. The sample, which is positioned axially in the center of a split metal tube heater, can be either in the form of an end to end strip or as a gage installed on a substrate with both of the electrical connections at the same end. The system also includes an external plenum, not shown in figure 1, to permit cooling gases to be introduced at lower temperatures for better temperature control and, in addition, a computer system with special features to obtain accurate resistivity data at high speeds.

SENSOR PROPERTIES

In previous alloy development work (refs. 1,2) the Pd-13Cr (in weight %) alloys was identified as the best alloy candidate available for use at these temperatures in terms of stability and reproducibility. Regardless of the rates of heating and cooling, this alloy always shows a very linear resistivity versus temperature behavior. This indicates that the Cr is always in complete solid solution and that no ordering or second phases are formed at any temperature in this system. Although the addition of Cr dramatically lowers the

*Work done under NASA Contract NAS3-23722

C-2

thermal coefficient of resistivity compared to that of pure Pd, this coefficient is still too high for this application. In order to reduce the thermal sensitivity to acceptable levels, the thermally compensated design shown in figure 2 was developed. The strain sensitive resistive element in the center of the gage is still 3 mm x 3 mm as defined by the program goals but symmetrical outlying grids have been added to provide thermal compensation. These additional low resistance compensation grids of Pd or Pt have high temperature coefficients of resistance and are relatively strain insensitive. Because all of these resistive elements show linear resistance versus temperature behavior, this compensation should apply over the full temperature range of interest.

An important feature of the PdCr alloy was that it should be inherently self protective with regard to oxidation. At exposed surfaces, the Cr oxidizes to form an adherent scale of Cr_2O_3 to protect the Cr electron scattering centers dissolved in the alloy beneath the oxide from further oxidation. The earlier conclusions about the stability and repeatability of the resistance of the PdCr alloy was based on measurements made using 0.46 mm (460 µm) thick metal strips of the alloy prepared by drop casting followed by grinding and annealing. A primary objective this year was to verify that this good behavior remained when the alloy was prepared as an even thinner film prepared by sputtering. Sputtering is the preferred fabrication technique for actual gages because of good bonding and the ability to form well-bonded undercoats of alumina insulation films using the same process.

One of the problems with sputtering is that the material is deposited as nodules which must be separated by boundaries with significant misorientations which should provide paths for fast diffusion. The concentration of these boundaries and the potential for these boundaries to be unstable during the use of this material as a strain gage can be avoided by annealing. We have determined that these films can be recrystallized by a 12 hour heat treatment in argon (1×10^{-5} ppm O_2) at 1420 K. An unfortunate side effect of this treatment was the observation that the resultant films sometimes contain holes. Figure 3 shows a severe example of this effect. It is believed that these holes are caused by the loss of some of the much larger nodules which always seem to be present in these films. It is believed that the loss of these nodules may be related to differential thermal expansion stresses set up between the substrate and the overlying films during heating and cooling.

Experimental data on the effect of sensor thickness on the stability of resistance at 1250 K in air is presented in figure 4. The material for the 50 µm thickness was prepared by splat quenching while that at the 6.5 µm thickness was prepared by sputtering on top of sputtered alumina on a Hastelloy X substrate. Due to an error by the vendor in preparing the target, the sputtered samples also contained approximately 5 wt percent Al as an impurity replacing some of the Pd. All of these samples were heated for at least 10 hours at 1250 K in air prior to drift testing in order to form stable oxide surface scales.

The rate of drift of the sputtered film, even with only one side exposed to oxidation, is unacceptable for our use. Measurements of the thermal coefficient of resistivity of this film gave results which indicated that most of the Cr and Al in the film had been lost. When the material is this thin, most of the oxide forming elements must apparently be consumed in order to form the protective scale. The reason why the resistance of the intermediate thickness film increased rather than decreased with time is not clearly understood. It may indicate the operation of a fundamentally different oxidation process.

Experience with the fabrication of sputtered resistive grids has shown that it is difficult to make films thicker than 6.5 µm when the spacing between the individual grid resistors is as small as 76 µm. The high strength of the PdCr films makes it difficult to break the unwanted film loose along the lines separating the film sputtered on the photo resist and that on the part. Although recent work has indicated that we may be able to

make thicker deposits by using thicker masks, it also rapidly becomes more difficult to develop the desired level of total grid resistance with this small a grid area if thicker films are used. Avoiding this problem by increasing the voltage across the sensor increases the probability of voltage breakdown across the insulation layer and causing unacceptable levels of self-heating of the gage.

PROTECTIVE OVERCOATS

Attempts have been made to completely or significantly seal the exposed sputtered PdCr surfaces by forming an additional top overcoating of alumina. It is recognized that aluminum oxide would be a superior film to prevent oxidation. The diffusion of Cr is relatively rapid through its oxide and Cr can form volatile oxides ($Cr(OH)_2$ and CrO_3) which do not form in the case of alumina. Attempts to oxidize sputtered aluminum overcoats in place were not particularly successful because the aluminum oxide formed was so impervious to any further oxidation. Figure 5 shows "spurs" of alumina formed along the edges of PdCr resistive grid lines. Apparently the aluminum melted, the volume expansion ruptured the thin oxide surface, and more oxidation occurred until all of the aluminum metal was oxidized or dissolved in the alloy. Curent experimental approaches to identify the optimum top coating configuration are summarized in Table 1. In some of these experiments, the alumina is being sputtered with the substrate heated to reduce the maximum tensile forces that could be generated in these films by the differential thermal expansions between the oxide and the Hast X substrate.

REFERENCES

1. Hulse, C. O.; Bailey, R. S.; and Lemkey, F. D.: High Temperature Static Strain Gage Alloy Development Program, NASA CR-174833, March 1985.

2. Hulse, C. O.; Bailey, R. S.; and Grant, H. P.: The Development of a High Temperature Static Strain Gage System. Turbine Engine Hot Section Technology 1985, NASA CP-2405, pp. 45-49.

HIGH SPEED THERMAL CYCLE-RESISTANCE MEASUREMENT APPARATUS

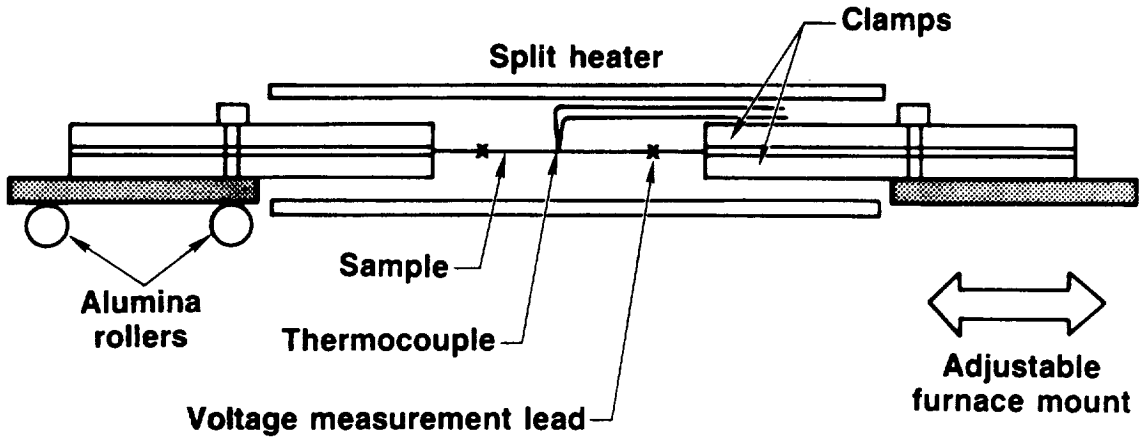

Figure 1

THERMALLY COMPENSATED STRAIN GAGE GRID DESIGN

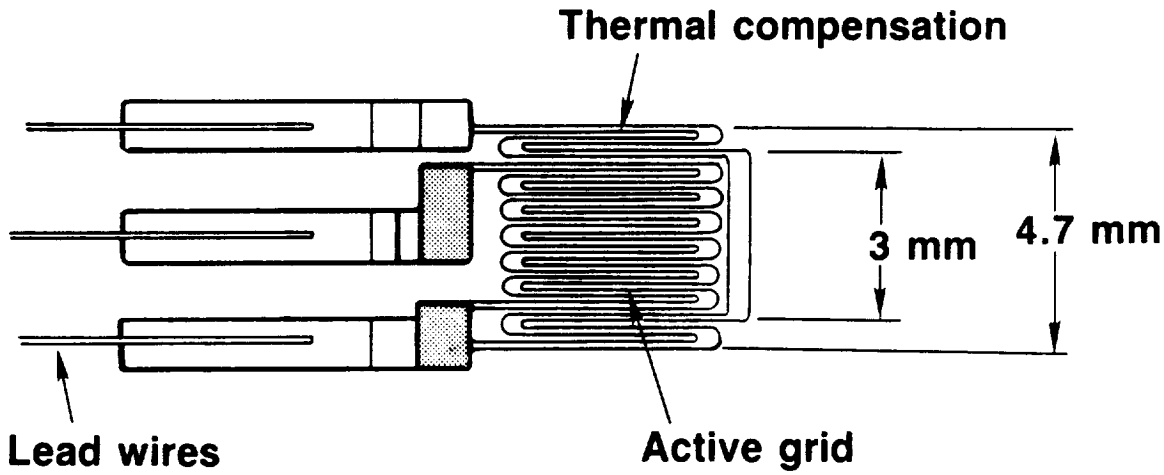

Figure 2

HOLES IN SPUTTERED PdCr FILMS AFTER RECRYSTALLIZATION

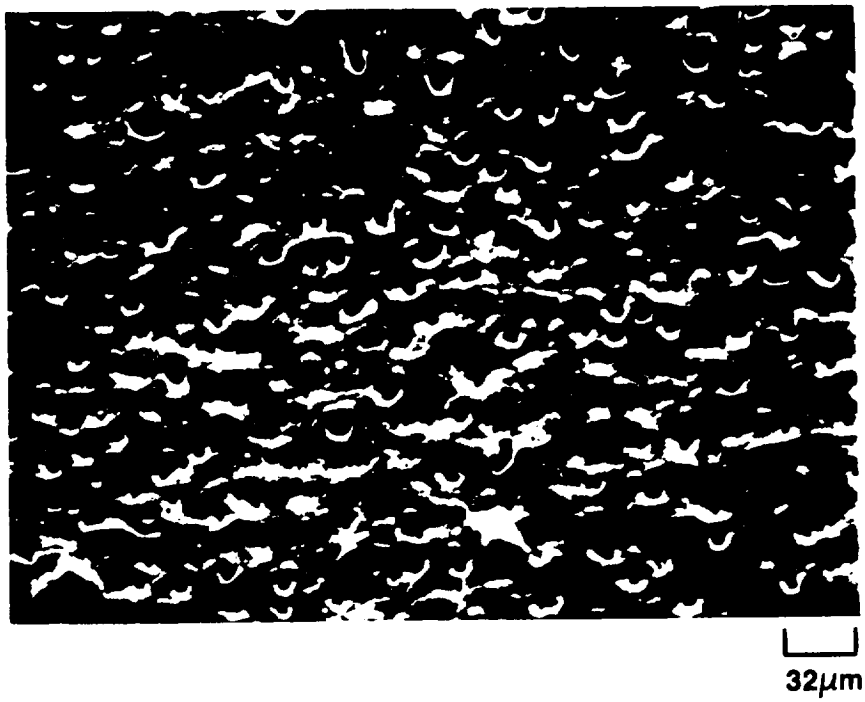

Figure 3

EFFECT OF FILM THICKNESS ON DRIFT IN RESISTANCE OF Pd-13 wt % Cr

(1250 K in air for 50 hours)

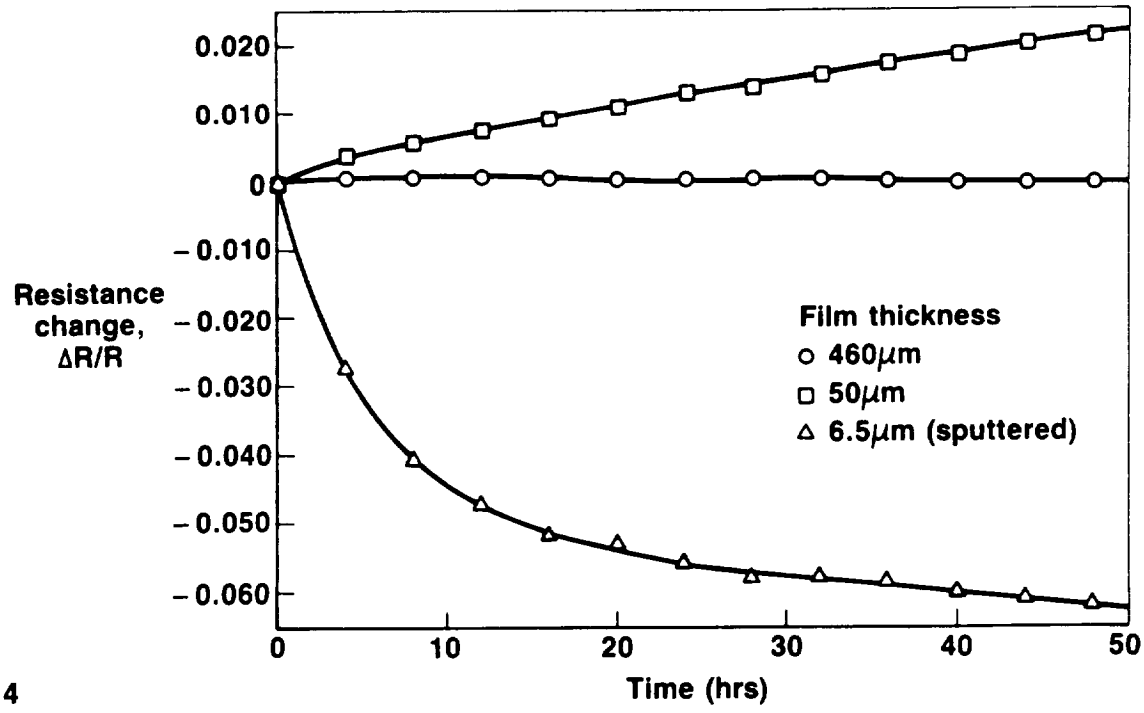

Figure 4

86-9-6-8

EDGE PROTRUSIONS ON PdCr GRID AFTER OXIDATION OF 0.5μm Al OVERCOAT

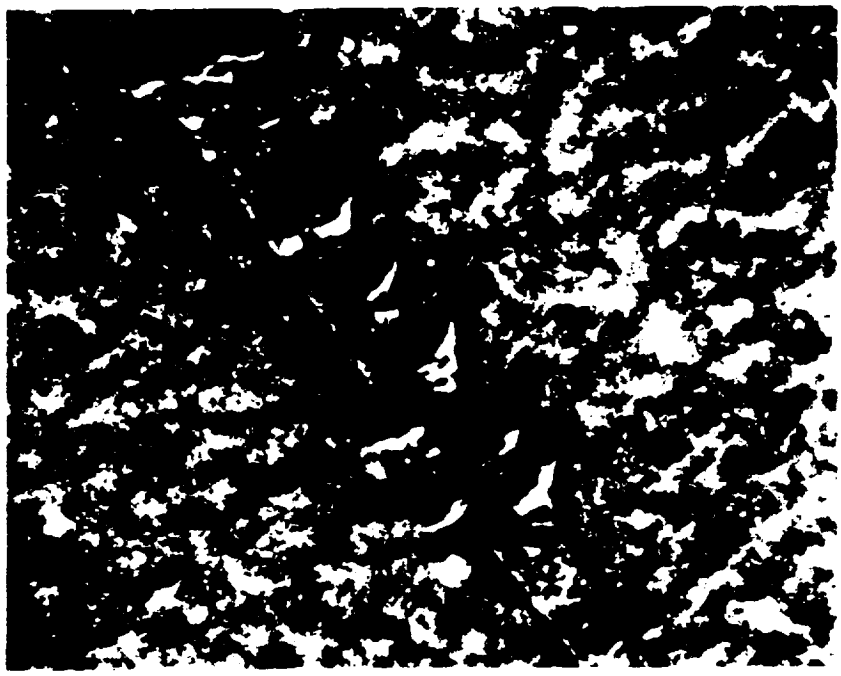

Figure 5

TABLE I

STRAIN GAGE OVERCOAT SYSTEMS

Type	Sensor PdCr	Sputtered Al_2O_3	Sputtered FeCrAl	Sputtered Pt	Sputtered Glass	Sputtered Al	Transfer tape Glass
1	X	X					
2	X	X	X				
3	X	X		X			
4	X	X			X		
5	X	X				X	
6	X	X					X

THE NASA LEWIS STRAIN GAUGE LABORATORY - AN UPDATE

H.F. Hobart
NASA Lewis Research Center
Cleveland, Ohio

At the 1985 HOST conference the status of the Lewis strain gauge laboratory was described. The goals were outlined, a description of the apparatus was presented, and some preliminary data were shown which demonstrated the ability of the laboratory to perform the types of tests required to characterize high temperature static strain gauges. At present the goals are unchanged, that is, to support HOST programs in the area of high-temperature static-strain measurement both in-house and through contract work.

Efforts continue in the development and evaluation of electrical-resistance strain gauges of the thin-film and small-diameter wire type. This paper presents results obtained early in 1986 on some Chinese gauges and Kanthal A-1 gauges mounted on a Hastelloy-X substrate. Also, the status of several activities currently in progress will be presented. These more recent efforts include (1) the determination of the uncertainty in our ability to establish gauge factor, (2) the evaluation of sputtered gauges that were fabricated at Lewis, (3) an investigation of the efficacy of dual-element temperature-compensated gauges when using strain-gauge alloys having large thermal coefficients of resistance, and (4) an evaluation of the practical methods of stabilizing gauges whose apparent strain is dependent on cooling rate (e.g., FeCrAl gauges).

MEASUREMENT CAPABILITY

A major characteristic of interest when using electrical resistance strain gauges is the sensitivity to strain or gauge factor. Because some early data showed excessive hysteresis, repeat tests were run to try to determine our ability to impose a known strain on a test gauge. Gauge factor determination tests use constant-moment beams as shown in figure 1. An Inconel 718 beam with four reference gauges was mounted in the bending fixture and stressed to about ±2000 microstrain (με) using different types of clamps, round and square edged.

Strain in the test beam is calculated from the equation:

$$e = \frac{td}{\ell^2}$$

where e is strain, t is thickness, d is deflection, and ℓ is length.

The beam thickness and deflection can be measured very accurately, but, due to clamping/mounting variations, the length must be determined experimentally. Tests results between the square and round edged clamps show the rounded edge had about 35 percent less data scatter.

Figure 2 shows the variation of the effective, calculated beam length versus deflection in both tension and compression; a deflection of about 1.2 cm is equivalent to 2000 με. Also, a ±1.0 percent of full-scale error band is shown. Repeated cycling to check on zero shift showed a residual ±5 με that is apparently due to hysteresis. Zero shift can be minimized by exercising the beam before taking data. All of these tests tend to show that strain calculations based on beam deflection have an uncertainty that is a small fraction of the total error budget; that is, they have an inaccuracy of less than 1 percent.

SPUTTERED GAUGES

One goal of the Lewis sensor development section has been to develop in-house capability for sputtering thin-film sensors. Eight thin-film strain gauges were recently fabricated. Four were sputtered from a FeCrAl target, the others from a PdCr target. The estimated thickness of the film is 2 μm. Two types of lead wires were used: a 0.76-mm-diameter NiCrSi wire and a 0.025- by 0.25-mm ribbon of Pd. The leads were attached to the film with a parallel-gap welder.

The substrates were 1.1-mm-thick alumina beams similar in shape to that shown in figure 1. Alumina beams were used for several reasons - alumina is a good high-temperature material, it doesn't require an insulating layer before gauge installation, and, because advanced turbine engines will be using components of ceramics, some experience will be gained in learning to instrument nonmetallic material.

These gauges are scheduled to be tested for gauge factor determination and apparent strain tests in the near future. However, before testing, a heat treatment will be required to recrystallize the as-sputtered alloy in order to have good resistance to oxidation. In the case of the PdCr alloy, the self-protective scale of Cr_2O_3 that prevents additional oxidation may not be sufficient for long-term use, and an additional overcoat may have to be sputtered. An investigation for implementing this additional protection is in progress under UTRC contract to develop this gauge system.

TEMPERATURE COMPENSATION

Many strain-gauge alloys exhibit a large apparent strain when heated, partly due to high values of thermal coefficient of resistance (TCR). One well-known technique to minimize this effect is to install a second element of a selected material in an adjacent arm of a Wheatstone bridge. The two elements will compensate for each other over a range of temperatures.

A major effort of HOST funded research in strain measurement has been the search for a strain-gauge alloy usable to 1000 °C. The PdCr alloy developed at UTRC under NASA contract appears to have the desired characteristics of a linear, stable, repeatable resistance versus temperature relationship, but, because of a high TCR, gauges of this alloy will require a compensation element. In anticipation of this need, an experiment to learn how to achieve the compensation was performed. Two Pt8W gauges and two compensating resistors were flame sprayed over an alumina insulating layer on an Inconel 718 test beam. One gauge used a Pt wire compensating resistor, the other a Pd wire. The components were connected as shown in figure 3. Tests are currently underway to measure apparent strain versus temperature of these two gauges.

TEST RESULTS ON FeCrAl GAUGES

Two 13- by 20-cm Hastelloy-X plates were instrumented, each with two Chinese-type gauges and two Kanthal A-1 gauges. The Chinese gauges were bonded with a high-temperature ceramic adhesive. The Kanthal gauges were applied by flame-spraying an insulator onto the substrate. The Kanthal gauge was then cemented down and given another flame-sprayed overcoat. Type K thermocouples measure plate temperature. One plate will be used in an experiment on combustor liner thermal cycling; the other has been thermally cycled at zero stress in an isothermal oven to determine apparent strain.

The FeCrAl alloy used in these gauges undergoes an order-disorder effect between 400 and 600 °C, and the shape of the apparent strain curve during a heating cycle is strongly dependent on the rate of cooling of the gauges during the previous cooling cycle. Figure 4 shows data on all four gauges after a fast cooldown. A fast cooldown is defined as one traversing the critical temperature zone (600 to 400 °C) in less than 20 seconds.

If these gauges are soaked at a temperature of 700 °C for several hours, the gauge resistance will stabilize and have a repeatable value. Figure 5 shows the effect of three cooling rates on the apparent strain curves for both types of gauges. The conclusion to be drawn from figure 5 is that at 700 °C Kanthal A-1 has an apparent strain that is approximately eight times that of the alloy used in the Chinese gauges. Also, the Kanthal A-1 is much more affected by the cooling rate. For each type of gauge, the upper, middle, and lower curves represent cooling rates of 5.5, 1.0, and 0.1 K/s, respectively.

These data clearly show that, in order to use these gauges in an actual high temperature application, the following precautions must be observed: (1) in order to make a correction for apparent strain, the thermal history of the gauge must be known - or preferably controlled, (2) gauges must be soaked at 700 °C for a few hours to define the starting point, and (3) temperature excursions through the critical temperature range should be made as quickly as possible to avoid errors due to excessive drift.

The requirement for heating these gauges to 700 °C for at least 1 hour before use may preclude their use in certain applications. We will attempt to stabilize a gauge after installation by heating it with an electrical current. Test components are now being fabricated so we can explore this approach. Particular attention will be paid to the lead wire selection, attachment method, etc. If the gauges can be heated to 700 °C and held at that temperature for the proper length of time, the chance is good that when the power is shut off, the relatively large mass of the test piece will act as a heat sink to rapidly cool the gauge, resulting in a known, repeatable apparent strain curve.

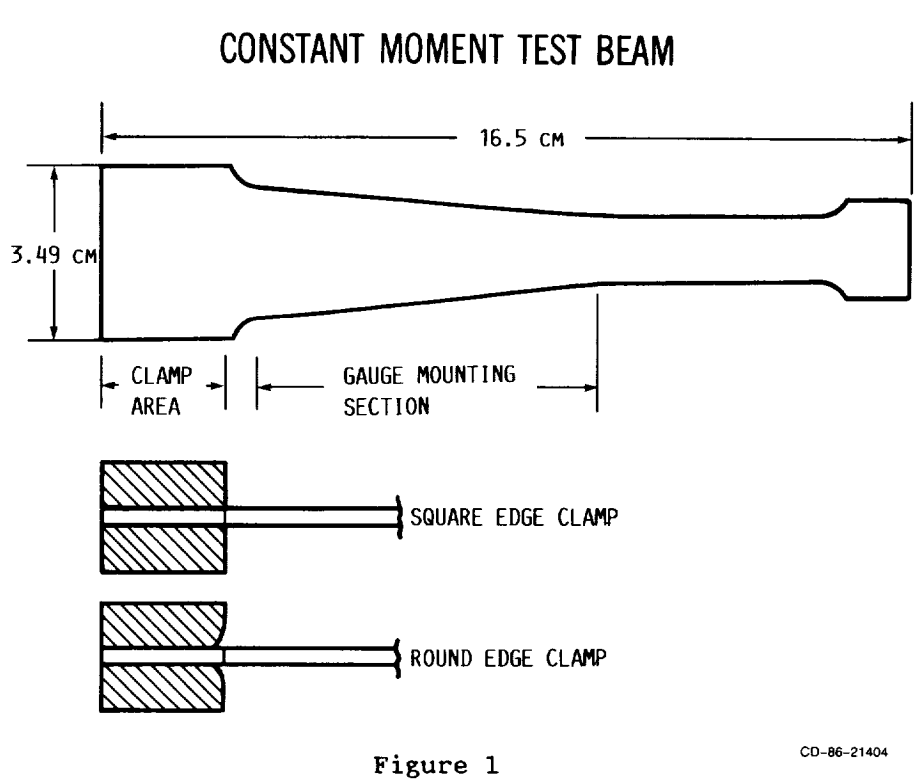

Figure 1

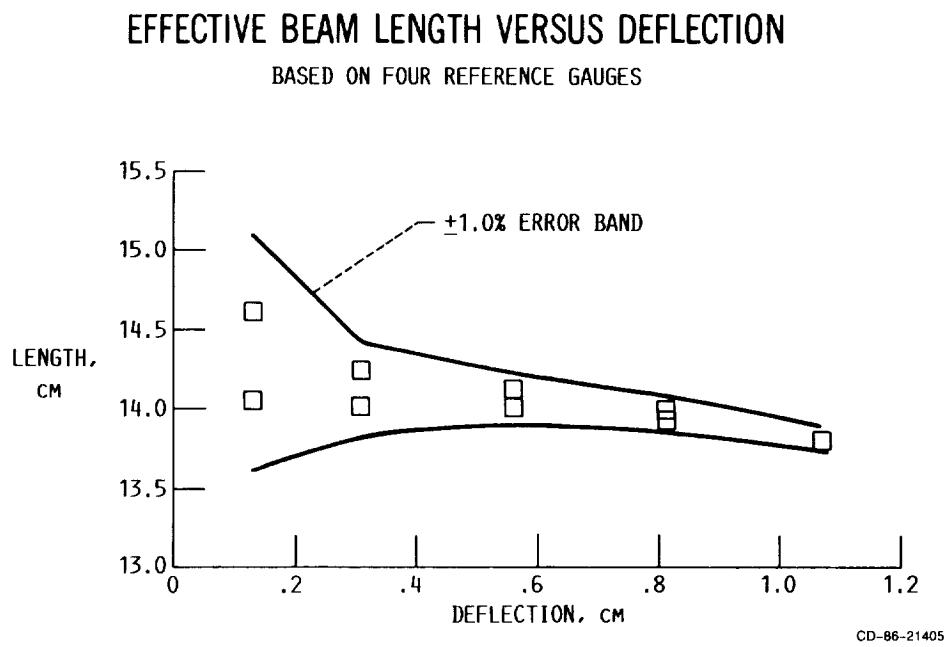

Figure 2

BRIDGE LAYOUT FOR COMPENSATION TEST

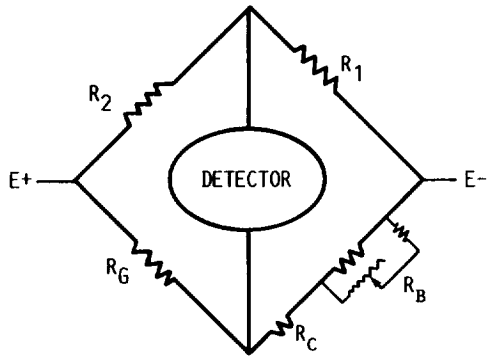

TEMPERATURE, ^{o}C	20	700
STRAIN GAUGE RESISTANCE, R_G, Ω	104.4	144.4
COMPENSATING GAUGE RESISTANCE, R_C, Ω	14.7	37.18
BALLAST RESISTANCE, R_B, Ω	43.97	43.97

R_1 AND R_2 = BRIDGE COMPLETION RESISTORS

$$R_B = \frac{\Delta R_C}{\Delta R_G} R_G - R_C$$

CD-86-21408

Figure 3

APPARENT STRAIN VERSUS TEMPERATURE

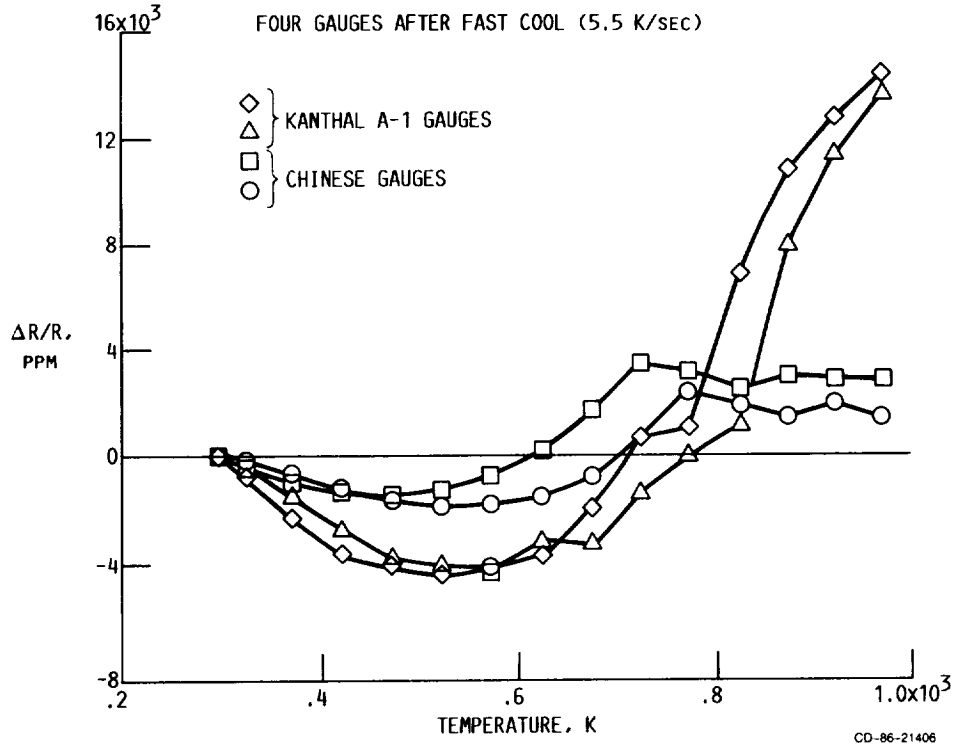

Figure 4

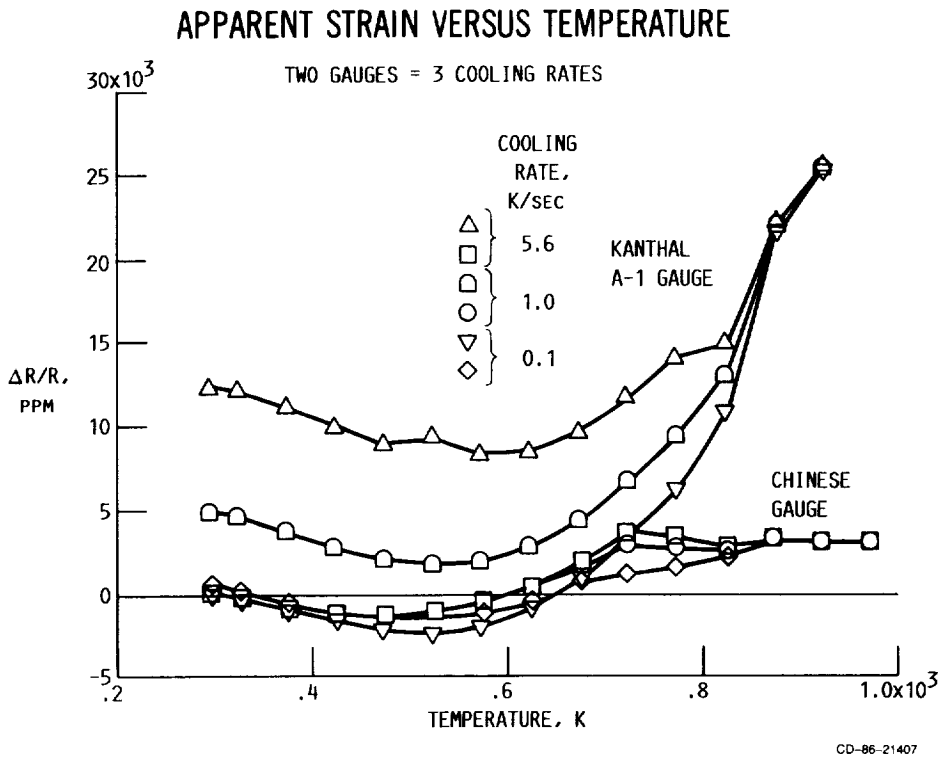
APPARENT STRAIN VERSUS TEMPERATURE
TWO GAUGES = 3 COOLING RATES
30x10^3
25
20
15
10
5
0
-5
ΔR/R, PPM
COOLING RATE, K/SEC
5.6
1.0
0.1
KANTHAL A-1 GAUGE
CHINESE GAUGE
.2
.4
.6
.8
1.0x10^3
TEMPERATURE, K
CD-86-21407

Figure 5

SUMMARY OF LASER SPECKLE PHOTOGRAMMETRY FOR HOST

Frank G. Pollack
NASA Lewis Research Center
Cleveland, Ohio

High-temperature static-strain measurement capability is important for the success of the HOST program. As part of the NASA Lewis effort to develop the technology for improved hot-section durability, the HOST instrumentation program has, as a major goal, the development of methods for measuring strain at high temperature. Development work includes both improvements in resistance strain-gauge technology and, as an alternative approach, the development of optical techniques for high-temperature strain measurement.

One of the recognized optical techniques for measuring the strain on a surface involves measuring changes in the speckle patterns obtained from photographs of the surface under laser illumination. The photographs, which are taken before and after thermal or mechanical deformation of the surface, capture the surface distortion as a corresponding distortion of the laser speckle pattern. A comparison of the photographs are made on an interferometric photocomparator, which measures differential magnification, which, in turn, corresponds to strain. Under the direction of Dr. Karl A. Stetson, a laser speckle photogrammetry system based on this technique has been developed at United Technologies Research Center. The system consists of a specklegram recording assembly and a interferometric comparator for specklegram readout as shown in figures 1 and 2. This development was partly sponsored by NASA Lewis under contracts NAS3-22126, NAS3-23690, and NAS3-24615. The first of these contracts (NAS3-22126) was a study of methods for measuring static strain on burner liners at temperatures to 870 °C. Under this contract, the laser speckle photogrammetry system was shown to be capable of measuring the thermal expansion of a Hastelloy X sample at temperatures up to 870 °C under laboratory conditions. The test arrangement is shown in figure 3, and some test results are shown in figure 4. Under the second contract (NAS3-23690) the laser speckle photogrammetry system was applied to the measurement of strain on a burner liner operating in a high-pressure, high-temperature, burner test facility at UTRC. A photograph of the combustor liner used in the test is shown in figure 5. The test cell arrangement is shown schematically in figure 6.

One of the problems in the use of this technique is optical distortion caused by turbulent high pressure gas within the viewing path. Although the effects of this distortion can be analyzed if the distortion is precisely known, the turbulence encountered around an operating burner is random and not well documented. One of the objectives of the experimental work in contract NAS3-23690 was to evaluate this problem. The results indicated that, in its present state of development, speckle photogrammetry can only be used at pressures below approximately 3 atmospheres. At higher pressures, turbulence of the gas within the viewing path causes the speckle patterns to blur (see fig. 7) and fail to correlate between photographs.

The objective of the third contract (NAS3-24615) was to demonstrate the use of the UTRC specklegram photogrammetry system on the burner liner cyclic fatigue rig at

NASA Lewis (fig. 8). In this rig flat plate samples of burner liner material are subjected to cyclic stresses in order to study phenomena such as thermomechanical deformation and fatigue. Because the rig operates at ambient pressure, distortion due to turbulent gas was not expected to be a problem. The contract involved the temporary use of the UTRC specklegram recording system at NASA Lewis to record specklegrams that were subsequently processed for strain data at UTRC using their automated interferometric comparator. Specklegrams were recorded at ambient temperature and at increments of approximately 100 °C up to 900 °C and back down to 120 °C. Following this, three pairs of specklegrams were recorded while cycling between the temperature extreme, and this was followed by a final recording at ambient temperature. Temperature at each data point was monitored by thermocouples and an infrared thermal scanner. The plates from the data run were developed at NASA Lewis. A typical speckle photograph is shown in figure 9. In three data runs 72 specklegrams were recorded and examined. The first set of 24 specklegrams lacked correlation, which was traced to out-of-plane warping and tilting of the sample in the test rig.

Based upon information from UTRC data evaluation of the first run, tests were performed by NASA personnel to check for tilting of the sample. A small spot in the center of the sample was illuminated by a CW laser, and a television camera, focused at infinity, was directed at this spot. The aperture at the center of the telecentric lens was imaged on the camera sensor and appeared on the TV monitor. Speckles were observed within the aperture, and they were seen to move horizontally as the sample was heated. A video recording was made of this speckle pattern for a sequence of heating and cooling of the sample, and this recording was sent to UTRC for evaluation. Between maximum and minimum temperatures, speckles were noted to move about four aperture diameters. This indicated excessive tilting about a vertical axis in the order of 6° due to heating. After mounting the sample more securely, two additional data runs were performed, one at the same temperatures as the first data run and the second with reduced temperature increments. Both of these runs also exhibited correlation problems although to a lesser degree.

The data obtained in these tests show an erratic pattern of strain (see fig. 10). This is particularly true for the data obtained by comparison of the sample before and after a temperature cycle. The important question is whether these data provide a valid description of the strain induced in the sample as a result of the thermal cycling or whether they are the result of turbulence or other artifacts of the specklegram recording system.

In summary at the present state of development, the laser speckle strain measuring system has a demonstrated capability to measure strain at 870 °C in the laboratory. The specklegram recording system has a demonstrated capability of withstanding a test-cell environment and successfully recording specklegrams. The most recently completed tests show that the system is sensitive to extraneous movement of the surface under study. This sensitivity may limit the applicability of the system to experiments in which the surface is precisely located. For applications in more nearly "engine condition" experiments, the limitations imposed by distortion due to turbulent, high-pressure gas within the viewing path, and extraneous movement of the surface under study will have to be overcome. In addition, further work to define the static error boundaries for this measuring system is required. Finally, the development of convenient optical techniques to measure test surface movement, especially out of plane movement and tilting of the surface, is desirable.

OPTICAL LAYOUT FOR SPECKLEGRAM RECORDING

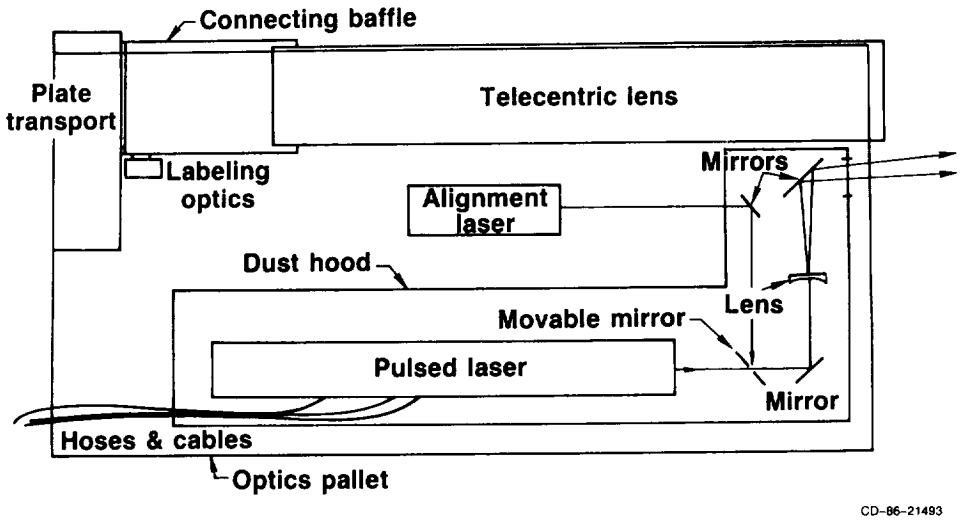

Figure 1

INTERFEROMETRIC COMPARATOR FOR HETERODYNE READOUT OF SPECKLEGRAM HALOS

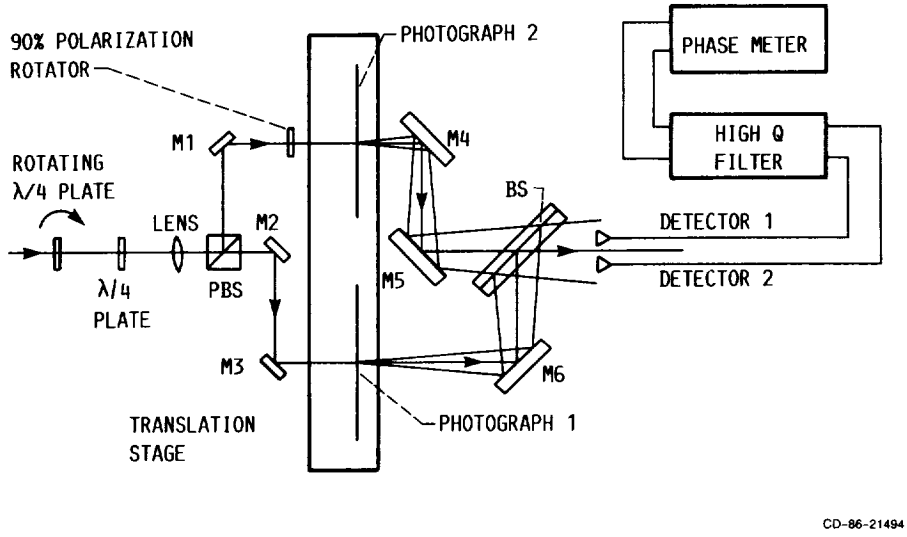

Figure 2

LABORATORY FURNACE AND SPECKLEGRAM RECORDING SYSTEM

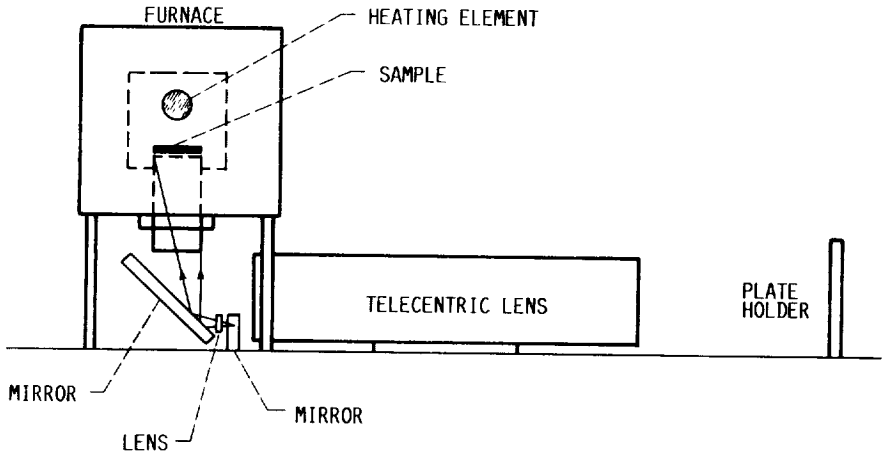

Figure 3

STRAIN HISTORY OF UNCONSTRAINED SAMPLE OF BURNER LINER MATERIAL

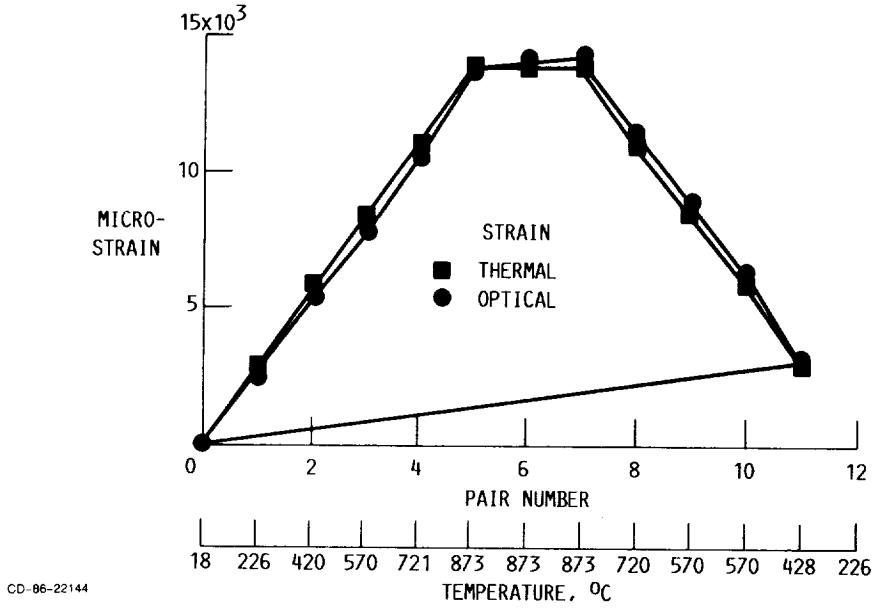

Figure 4

BURNER CAN WITH INSTRUMENTED SECTION REINSTALLED

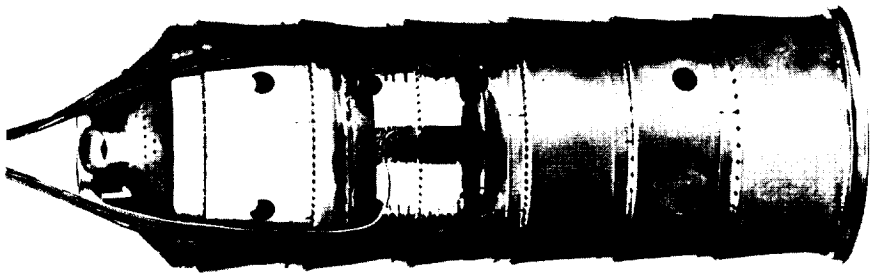

CD-86-22143

Figure 5

TEST CELL ARRANGEMENT

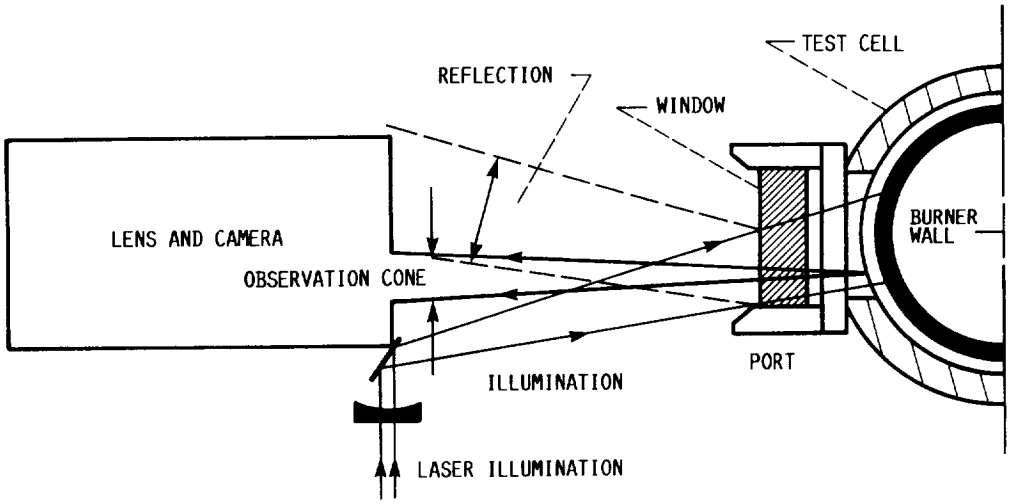

CD-86-21492

Figure 6

SPECKLEGRAM IMAGES WITH FOURIER TRANSFORM FILTERING

NO FLOW

FLOW

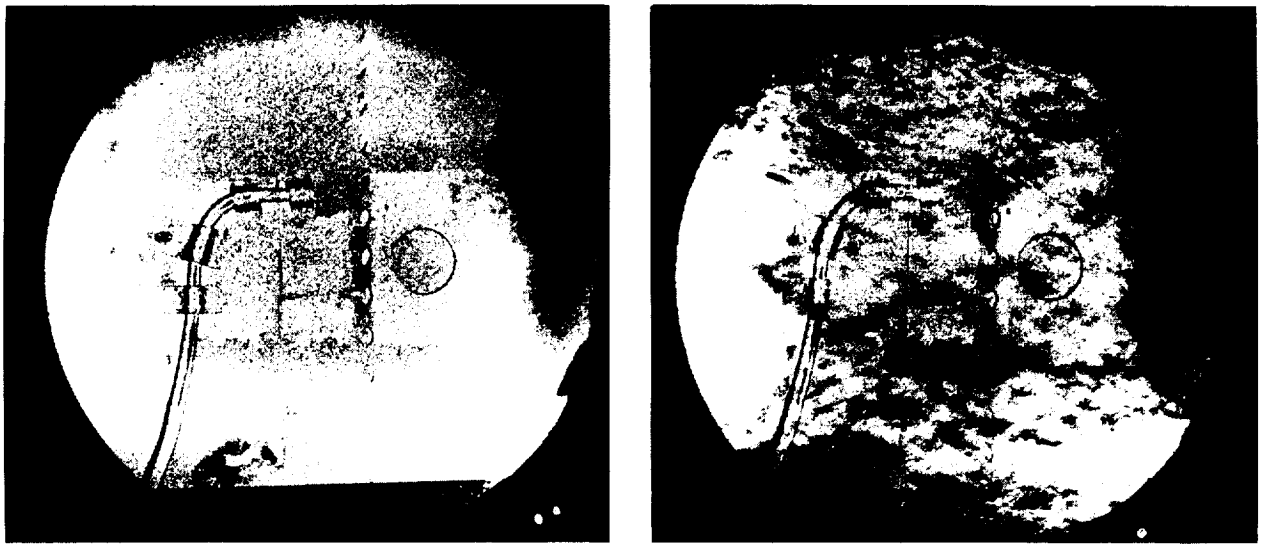

CD 86-22142

Figure 7

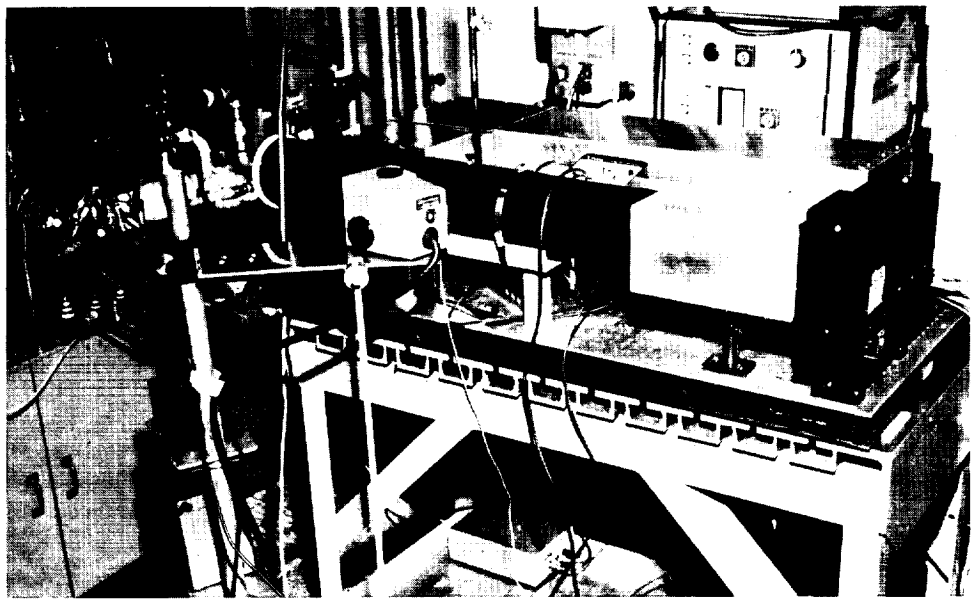

CD-86-22141

Figure 8

SPECKLE PHOTOGRAPH

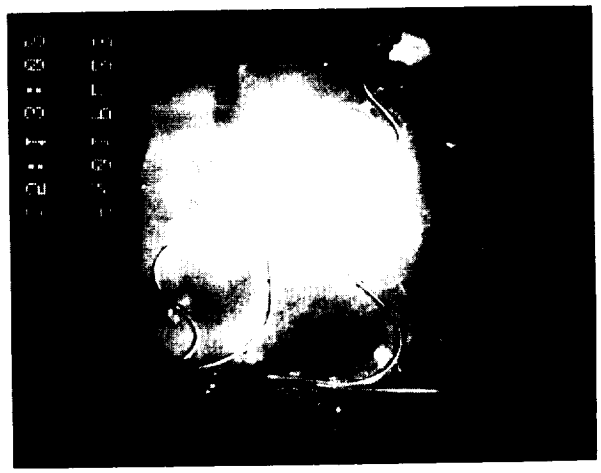

CD-86-22140

Figure 9

STRAIN DISTRIBUTION AT TWELVE LOCATIONS

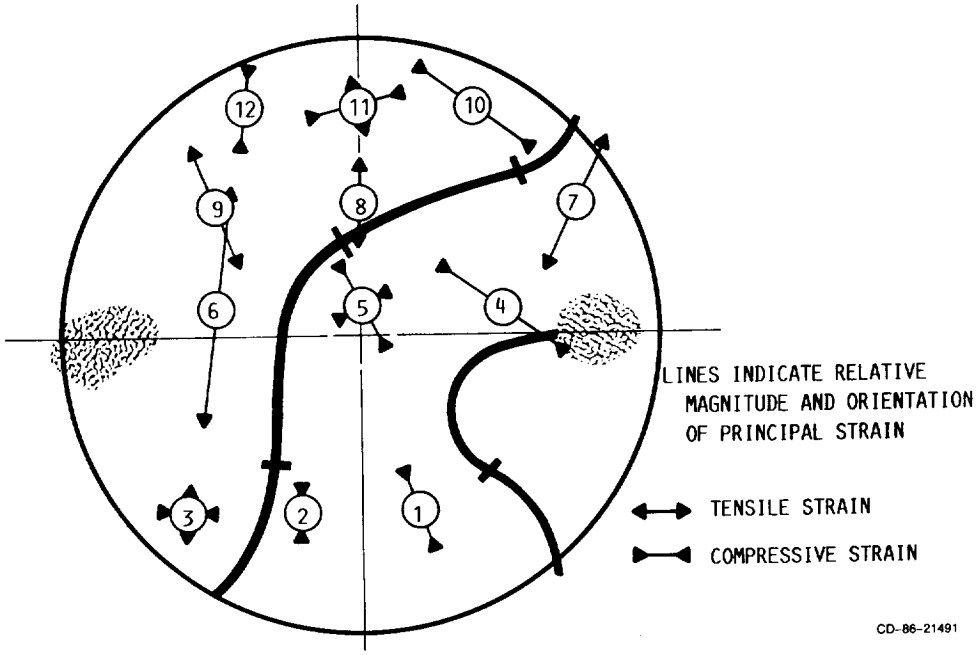

CD-86-21491

Figure 10

AEROTHERMAL MODELING PROGRAM--PHASE II*

ELEMENT A: IMPROVED NUMERICAL METHODS FOR TURBULENT VISCOUS RECIRCULATING FLOWS

K.C. Karki, H.C. Mongia, S.V. Patankar†, and A.K. Runchal‡
Allison Gas Turbine Division
General Motors Corp.

The main objective of the NASA-sponsored Aerothermal Modeling Program, Phase II--Element A, is to develop an improved numerical scheme for predicting combustor flow fields. This effort consists of the following three technical tasks. Task 1 has been completed and Task 2 is in its final stage.

Task 1--NUMERICAL METHOD SELECTION

Task 1 involved the selection and evaluation of various candidate numerical techniques. The criteria for evaluation included accuracy, stability, boundedness, and computational efficiency. These schemes were used to solve a number of simple test problems. On the basis of these preliminary results, the following three schemes were chosen for detailed evaluation:

(i) flux-spline techniques
(ii) CONDIF
(iii) bounded flux-spline

To make the solution algorithm more efficient, it was decided to evaluate the performance of a fully coupled approach in which the continuity and momentum equations are solved directly, rather than sequentially as in SIMPLE or SIMPLER (ref. 1).

Task 2--TECHNIQUE EVALUATION

Task 2, currently in progress, involves an in-depth evaluation of the selected numerical schemes. The numerical accuracy and computational efficiency were judged using the test cases that have either analytical solutions, fine-grid numerical solutions, or experimental results. The following three classes of test problems were investigated:

(i) convection-diffusion (scalar transport)
(ii) laminar flows
(iii) turbulent flows

The results for each of these groups are summarized in the following paragraphs.

---

*Work done under NASA Contract NAS3-24350.
†University of Minnesota.
‡Analytical and Computational Research, Inc.

Convection-Diffusion

The test problems for convection-diffusion included (a) the transport of a step change in a scalar in a uniform velocity field, and (b) recirculating flow in a cavity with prescribed source for temperature. For both these problems, the higher-order schemes (flux-spline and CONDIF) give more accurate results than the hybrid scheme over the entire range of Peclet numbers (see Figures 1 through 4). For the transport of the step change in the scalar, the flux-spline schemes exhibit undershoots and overshoots.

Laminar Flows

Two selected laminar flow test cases are: (a) driven cavity and (b) flow over a backward facing step.

The driven cavity problem was solved using a 22 x 22 uniform grid and the results were compared with a 82 x 82 hybrid solution. The higher-order schemes give much better accuracy and show substantial advantage over the hybrid scheme (see Figures 5 and 6). Computations for the flow over a backward facing step were made at two Reynolds numbers (Re = 100 and 715) and the results were compared with the experimental data (ref. 2).

At Re = 100, there is negligible false diffusion and the results of all schemes compare well with experiments. At Re = 715, the higher-order schemes predict a longer reattachment length, compared to the hybrid scheme, indicating smaller numerical diffusion. There is, however, disagreement between the numerical and experimental results. These deviations are probably due to the presence of three-dimensional effects in the experiments (ref. 2).

Turbulent Flows

The selected schemes were used to compute the Stanford Conference test case 0421 (flow over a backward facing step) (ref. 3). The computed reattachment lengths from various schemes are listed in Table I. In these computations, plug flow was assumed at the inlet. It is seen that the flux-spline scheme approaches a grid-independent solution with fewer grid points than the hybrid scheme. The improvement shown by the flux-spline technique, however, is not as large as in laminar flow cases. A similar trend in the results was noticed when the experimentally measured velocity profile was specified at the inlet.

Performance of the Coupled Solution Approach

The efficiency of a numerical technique based on the primitive variables depends to a great extent on the manner in which the velocity-pressure coupling is treated. The iterative methods (e.g., SIMPLE, SIMPLER) derive an equation for pressure and solve the momentum and pressure equations in a sequential manner. The convergence of such an approach is found to be slow. An alternative to this sequential approach is the direct solution of the whole set of continuity and momentum equations (ref. 4 and 5). This study evaluates the performance of a direct or coupled approach in conjunction with a flux-spline scheme for convection-diffusion.

In the present approach, the discretized continuity and momentum equations are treated as simultaneous equations and solved using the Yale Sparse Matrix Algorithm (YSMP) (ref. 6). The nonlinearities in the equations are handled using the successive substitution technique. In turbulent flow computations, the solution of the flow equations (using YSMP) is followed by the solution of the equations for the turbulence quantities (k and ϵ). The equations for k and ϵ are solved sequentially in a decoupled manner using a line-by-line tridiagonal matrix algorithm (TDMA). The sequence of calculations is as follows: (1) the continuity and momentum equations are solved using YSMP, (2) with the given velocity field, the k and ϵ equations are solved to provide a new viscosity field for the momentum equations. This procedure is repeated until convergence.

Preliminary Results

The details of the test problems selected for the evaluation of the coupled solution approach are given in Table II. The number of iterations required for convergence and the execution times for the coupled solver are compared with those for the SIMPLER approach in Table III. The results indicate that the direct solver gives a speed-up factor of about three for laminar flows and five for turbulent flows. Further evaluation on a finer grid is under progress.

TASK 3

The convection-diffusion scheme with superior performance in Task 2 and the direct solver will be incorporated in the NASA 3-D elliptic code (COM3D). A test case will be run to assess the accuracy and computational efficiency of the selected scheme/algorithm for three-dimensional situations.

REFERENCES

1. Patankar, S. V., Numerical Heat Transfer and Fluid Flow, Hemisphere, 1980.
2. Armaly, B. F., Durst, F., Pereira, J. C., and Schonung, B., "Experimental and Theoretical Investigation of Backward Facing Step Flow," Journal of Fluid Mechanics, Vol 127, 1983, pp 473-496.
3. Kline, S. J., Cantwell, B. J., and Lilley, G. M. (eds), The 1980-81 AFOSR-HTTM Stanford Conference on Complex Turbulent Flows, Stanford University.
4. Vanka, S. P., "Block Implicit Calculation of Steady Turbulent Recirculating Flows," International Journal of Heat and Mass Transfer, Vol 28, 1985, pp 2093-2103.
5. Braaten, M., Development and Evaluation of Iterative and Direct Methods for the Solution of the Equations Governing Recirculating Flows, Ph.D Thesis, University of Minnesota, May 1985.
6. Eisenstat, M. C., Gursky, M. C., Schultz, M. H., and Sherman, A. H., "Yale Sparse Matrix Package, II, The Nonsymmetric Codes," Research Report No. 114, Yale University, Department of Computer Science, 1977.

Table I.
Calculated reattachment lengths [x_R/h] (plug flow at the step).

Grid	Hybrid	CONDIF	Flux-spline
32 x 32	4.4	4.2	4.6
40 x 40	5.0	4.5	5.3
57 x 57	5.2	---	5.3

Table II.
Laminar flow test cases.

Case No.	Flow	Reynolds number	Grid (uniform)
1	Driven cavity	400	22 x 22
2	Driven cavity	1000	22 x 22
3	Sudden expansion	400	22 x 12
4	Sudden expansion	400	22 x 22
	Turbulent flow test cases		
5	Backward facing step	5.6×10^5	22 x 22

Table III.
No. of iterations required and execution times.

Case No.	No. of iterations		Execution times (seconds)	
	SIMPLER	Direct	SIMPLER	Direct
1	62	17	18	6
2	84	30	24	8
3	106	47	16	5
4	122	48	35	10
5	800	39	408	79

IBM 3084

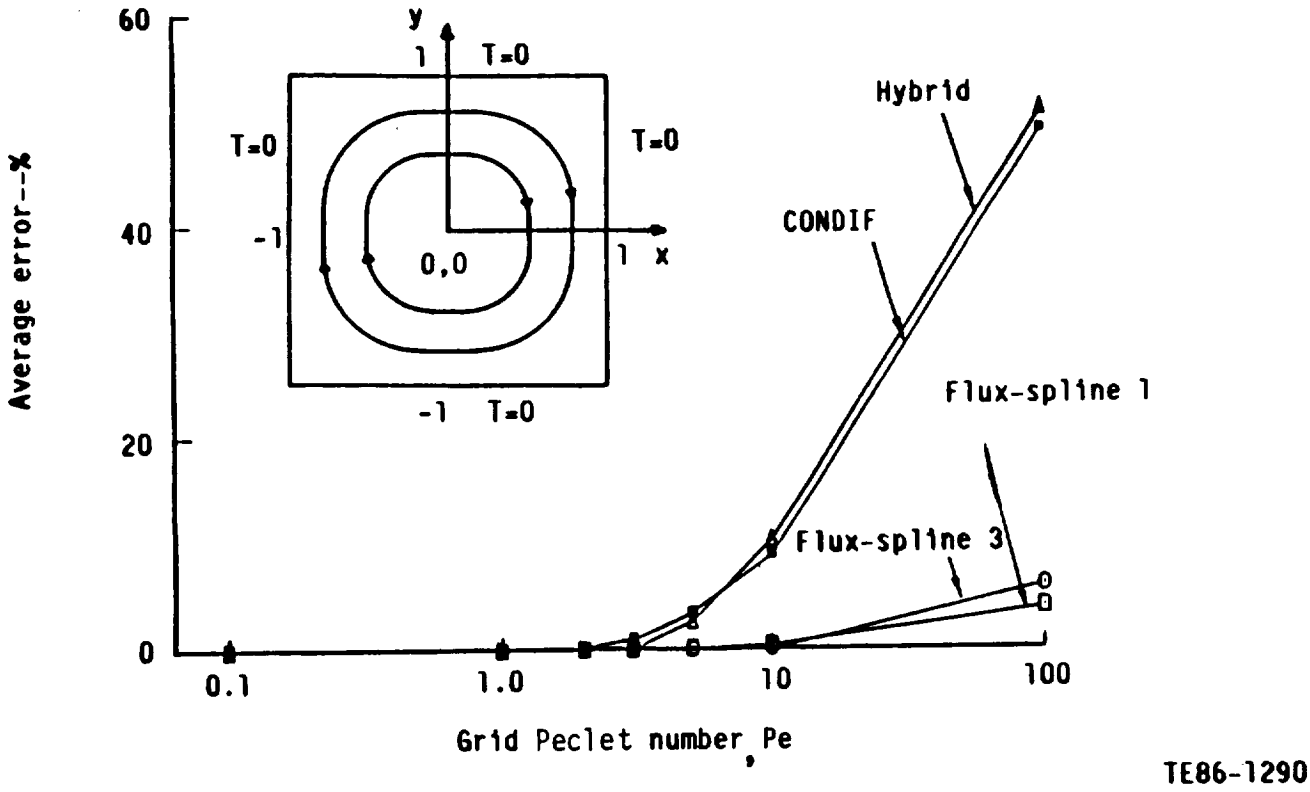

Figure 1. Comparison of the average error in the temperature calculated using different schemes. Recirculating flow with prescribed source for temperature.

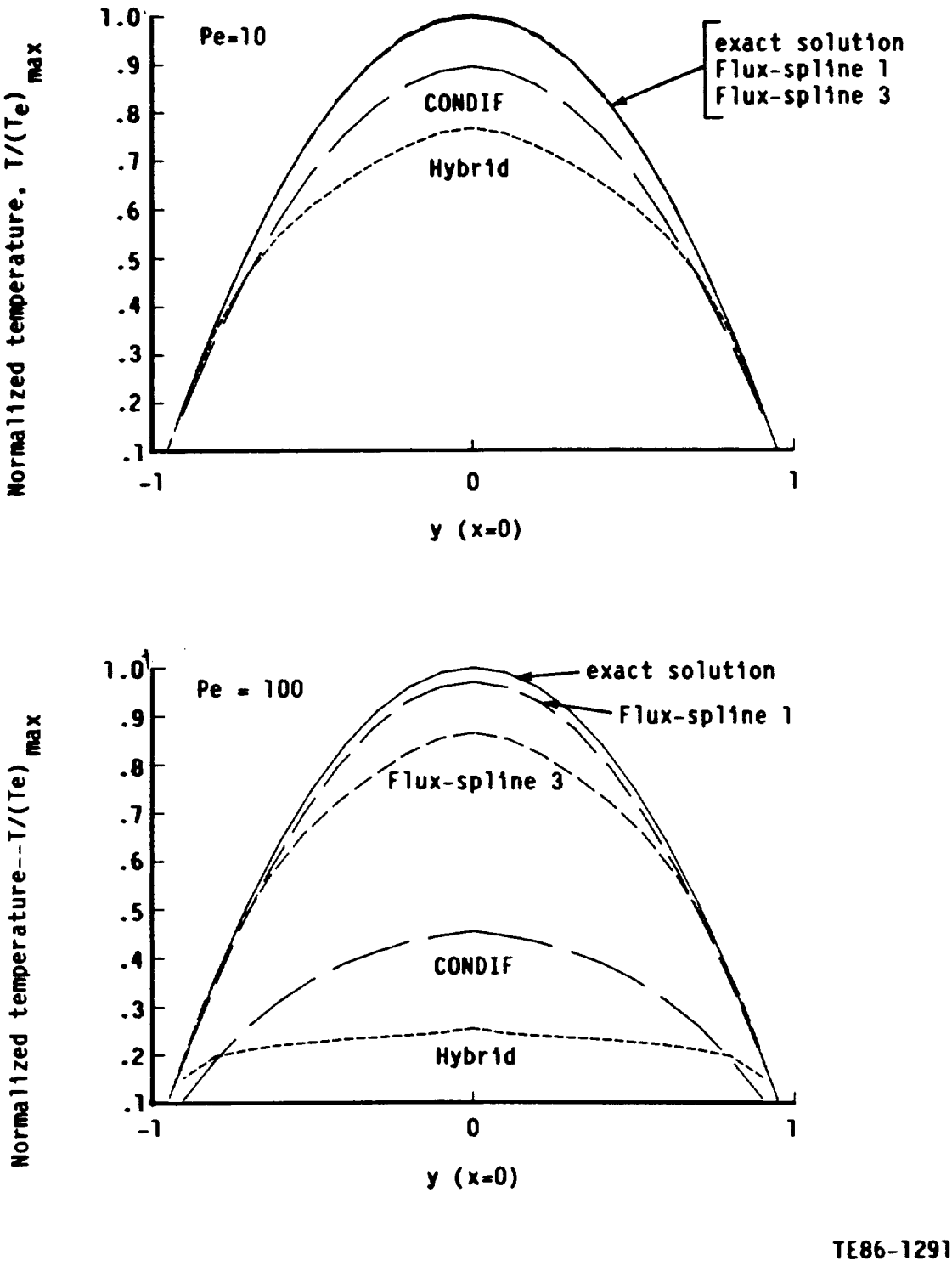

Figure 2. Comparison of the temperature profiles calculated using different schemes, with the exact solution. Recirculating flow with prescribed temperature source and velocity.

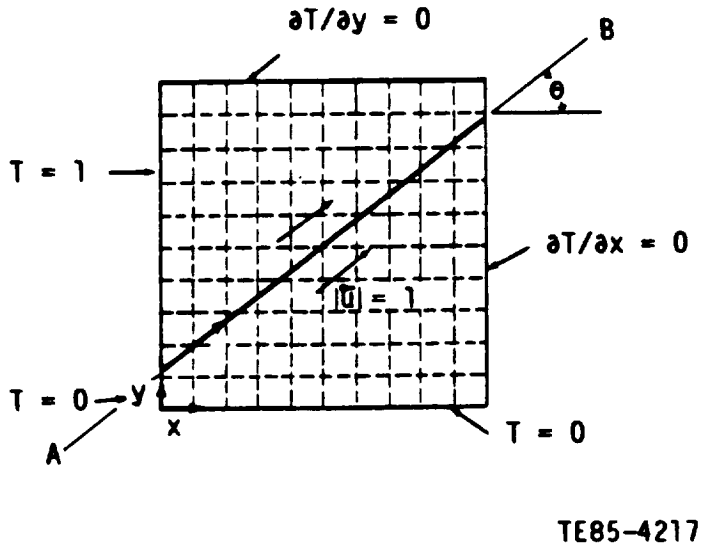

Figure 3. Transport of a step change in temperature in a uniform flow field.

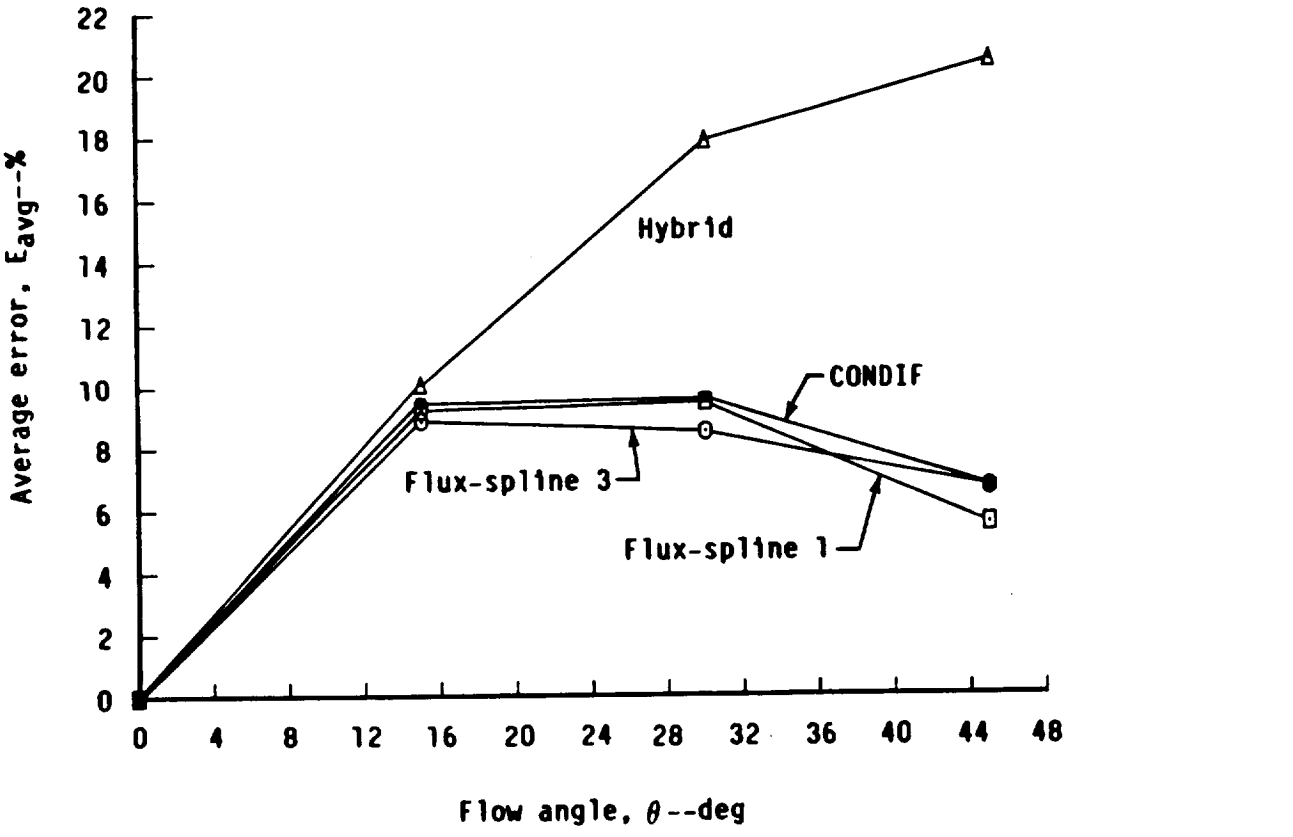

Figure 4. Comparison of the average error in the temperature calculated from the different schemes.

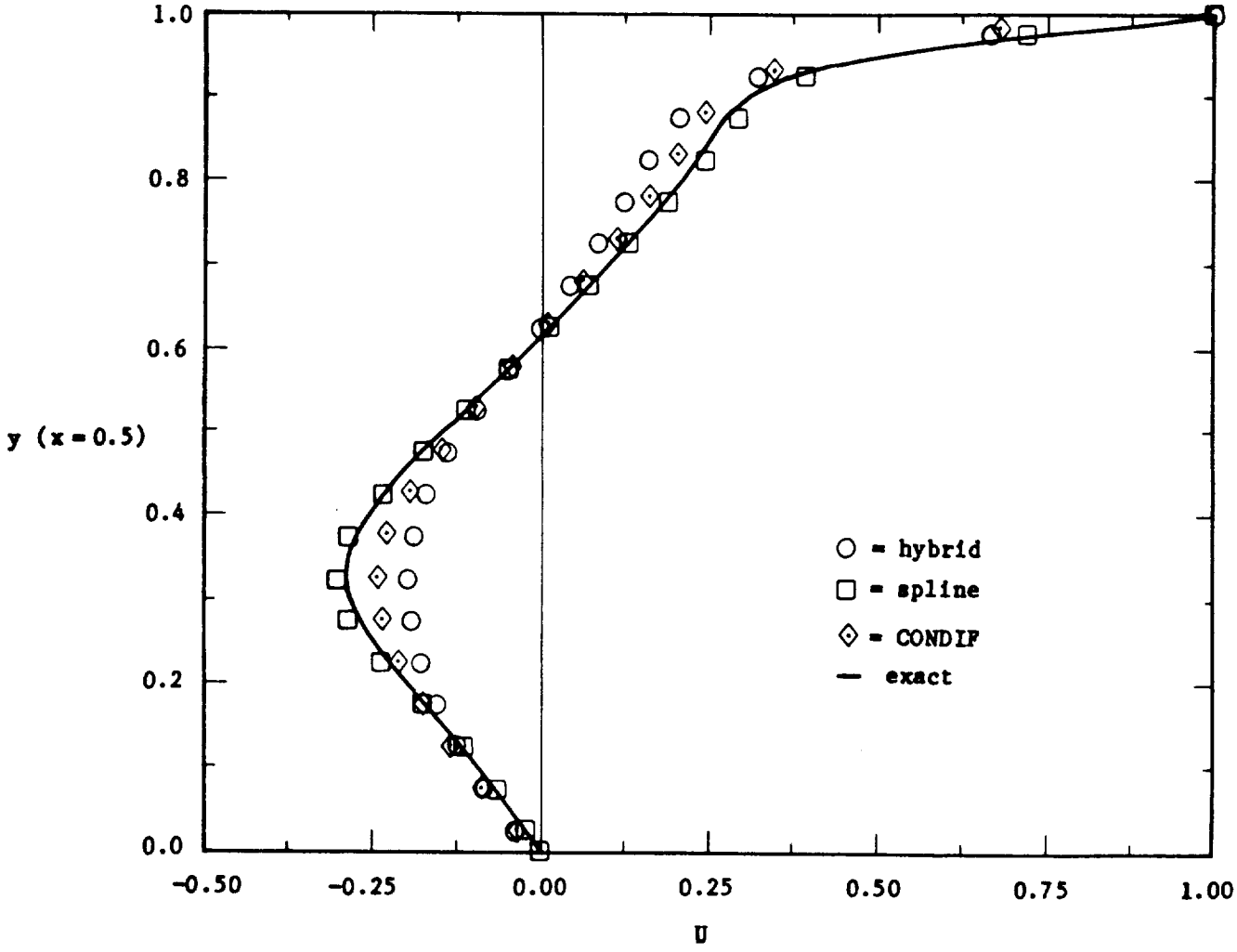

Figure 5. Normalized U-velocity at x = 0.5.

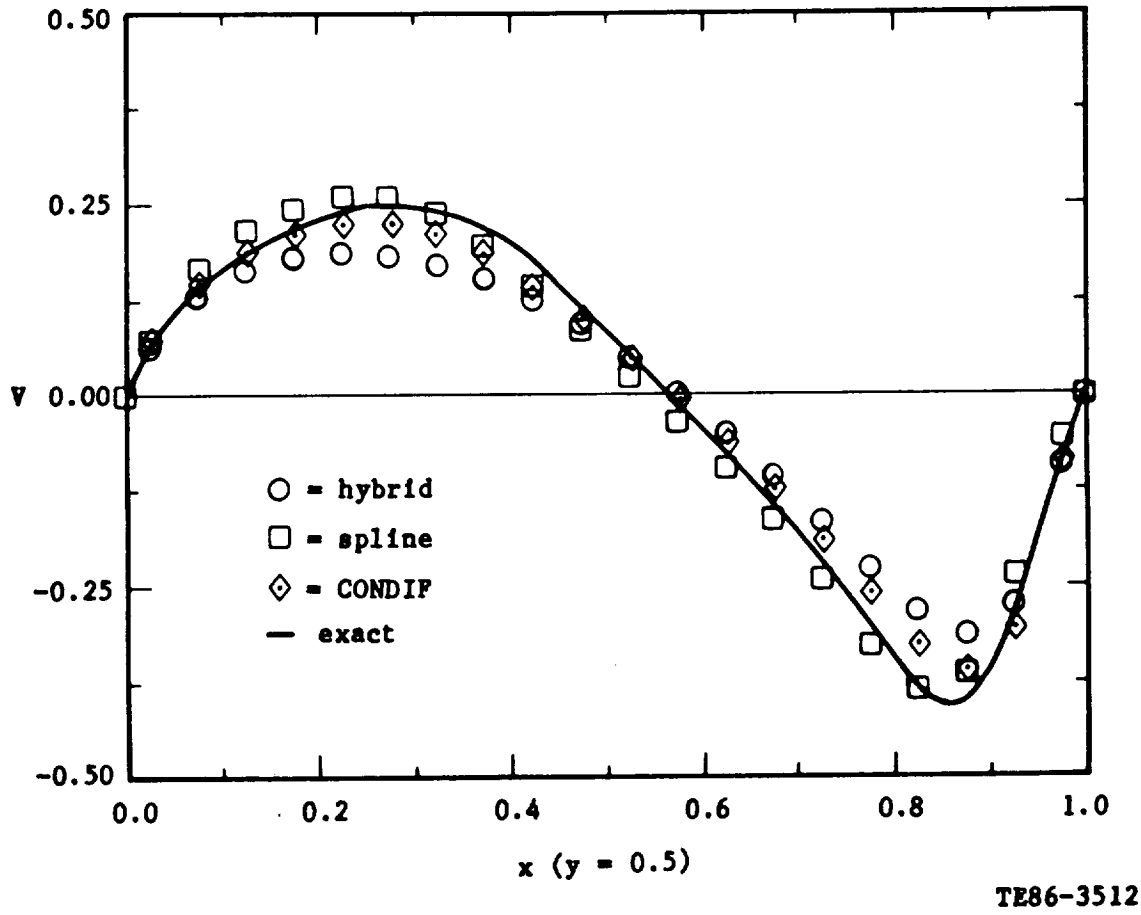

Figure 6. Normalized V-velocity at y = 0.5.

AEROTHERMAL MODELING PROGRAM--PHASE II*

ELEMENT B: FLOW INTERACTION EXPERIMENT

M. Nikjooy, H.C. Mongia, S.N.B. Murthy†, and J.P. Sullivan†
Allison Gas Turbine Division
General Motors Corp.

INTRODUCTION

This research is conducted as part of the NASA Lewis Research Center program to improve the design process and enhance the efficiency, life, and maintenance costs of the turbine engine hot section. Recently, there has been much emphasis on the need for improved numerical codes for the design of efficient combustors. For the development of improved computational codes, there is a need for an experimentally obtained data base to be used as test cases for the accuracy of the computations.

The purpose of Element-B is to establish a benchmark quality velocity and scalar measurements of the flow interaction of circular jets with swirling flow typical of that in the dome region of annular combustor. In addition to the detailed experimental effort, extensive computations of the swirling flows are to be compared with the measurements for the purpose of assessing the accuracy of current and advanced turbulence and scalar transport models.

The Allison program for Element B has five major tasks:

1. Experimental Configuration
2. Modeling
3. Measurements
4. Results and Analysis
5. Model Improvement

*Work done under NASA Contract NAS3-24350.
†Purdue University.

EXPERIMENTAL CONFIGURATION

This task involved preliminary design of the test section, its detailed design for fabrication and the experimental plan for data acquisition. The test section is of rectangular cross-section (15 in. x 3 in.) and extends 10 duct heights (30 in.) downstream from the head plate (Figure 1). The test section is constructed of glass and plexiglass to facilitate optical access for the laser Doppler velocimeter (LDV). The main flow is established using five swirlers and the primary jets are injected in cross-flow. Each swirler consists of an actual swirler from the production of the Allison 570-K turboshaft gas turbine engine. These are 60 degree angle flat vane swirlers with 12 vanes. They have an outer flow diameter of 1.459 in. and inner flow diameter of 1.084 in. The center swirler region is that of interest for taking data. The two swirlers on either side of the center are to remove side-wall effects inherent to the model but not in an actual combustor. Under this task, two similar rigs - one using air for LDV measurements, and the other using water for flow visualization have been designed. The detailed test matrix for the flow interaction program is given in Table 1 and the corresponding flow configurations are shown in Figure 2. These tests are designed to determine the effect of jet downstream location, number of jets, mass flow, and position relative to the swirl axis.

MODELING

A three dimensional code (COM3D) using the current turbulence model (k-ε) was employed to simulate different flow configurations for a preliminary study of the flow fields. The primary objective of the task has been in highlighting different flow regions in the flow field that would be taken into account during LDV measurements so as to resolve these regions of steep velocity gradient. Results indicate that these configurations offer interesting flow fields for the final verification/validation of models against the data base. The predicted results were qualitatively reasonable and the interaction of the jets and swirling flow was clearly seen.

MEASUREMENTS

Under Task 3, two test rigs and various test configurations have been fabricated and assembled. Initial check out runs have been made to ensure that the rig, instrumentation, and data reduction software are performing well. For the flow configurations identified in Task 1, measurements will be made to obtain the following:

- o detailed wall static pressure distribution
- o mean velocity and Reynolds stress components using two-color, two-component LDV system
- o fluctuating and mean concentration measurements for assessing scalar transport models.

In doing some flow visualization, it was later discovered that there are two exit flow regimes. These are shown in Figures 3-5. At low mass flow rates, the exit flow expands outward at an angle considerably less than 90 degrees, and is not attached to the head plate. At high mass flow rates, the exit flow remains attached to the head plate all the way out to the side wall. With moderate flow rates, a bistable flow situation is set up. That is, the flow will oscillate between the two regimes. Detailed velocity measurements are underway and some of the results will be presented during the meeting.

RESULTS AND ANALYSIS

Measurements of velocity and smoke concentration will be analyzed to determine the probability density function and auto- and cross-correlations .

MODEL IMPROVEMENT

Due to limited success with the standard $k-\varepsilon$ model and its modifications, work must continue in improving advanced turbulence and scalar transport models.

Turbulent closure of the mean flow equations is obtained by adopting a non-equilibrium and an equilibrium model for the Reynolds stresses using different pressure-strain models (ref. 1). In addition, performance of a high and a low Reynolds number model for combustor flow calculations using Reynolds-stress closures is investigated (ref.2-3). As for the turbulent scalar flux calculations, two different models are presented (ref. 3). One solves the algebraic equations for the scalar fluxes, while the other employs the transport equations for their respective scalar fluxes. The accuracy of the model is determined by comparing the results with measurements.

REFERENCES

1. Nikjooy, M., So, R. M. C. and Hwang, B. C., "A Comparison of Three Algebraic Stress Closures for Combustor Flow Calculations,"ASME -85-WA/FE-3.

2. Nikjooy, M., So, R. M. C., and Peck, R. E., "Modeling of Jet - and Swirl - Stabilized Reacting Flows In Axisymmetric Combustors," ASME - Winter Annual Meeting, 1986.

3. Nikjooy, M., "On the Modeling of Non-reactive and Reactive Turbulent Combustor Flows," Ph.D. Thesis, Arizone State University, 1986.

TABLE 1

TEST MATRIX

Test No.	Configuration	ε_j/H	X_j/H	M_j/Ms	Tracer	Jets/Swirler
1	BC1	-	-	-	NO	-
2	BC2	-	-	-	NO	-
3	A	1.0	0.5	0.75	NO	2
4	B	1.0	0.5	0.75	NO	2
5	C	1.0	0.5	0.75	NO	2
6	D	1.0	0.5	0.75	NO	2
7	E	0.5	0.5	1.50	NO	4
8	F	0.5	0.5	1.50	NO	4
9	A	1.0	1.0	0.75	NO	2
10	B	1.0	1.0	0.75	NO	2
11	E	0.5	1.0	1.50	NO	4
12	F	0.5	1.0	1.50	NO	4
13	A	1.0	0.5	1.50	NO	2
14	A	1.0	0.5	0.75	YES	2
15	B	1.0	0.5	0.75	YES	2
16	E	0.5	0.5	1.50	YES	4
17	F	0.5	0.5	1.50	YES	4

TEST SECTION GEOMETRY

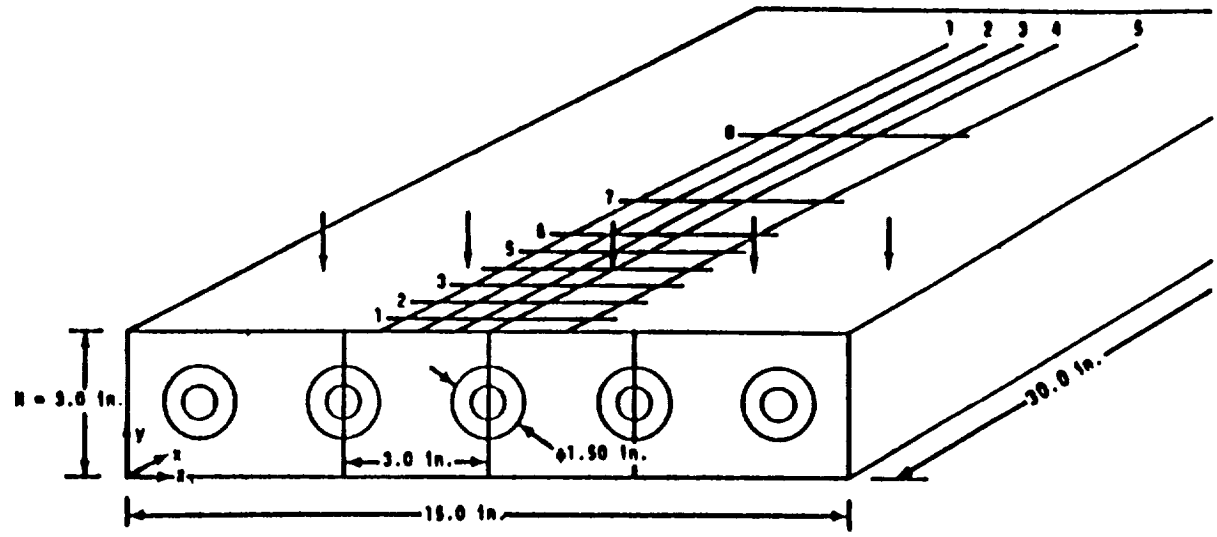

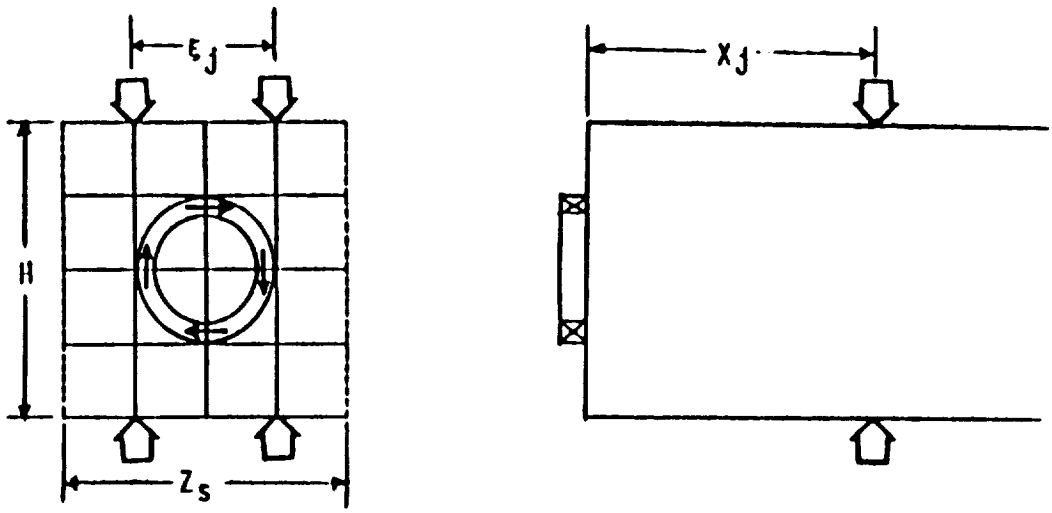

FIGURE 1

FLOW CONFIGURATIONS

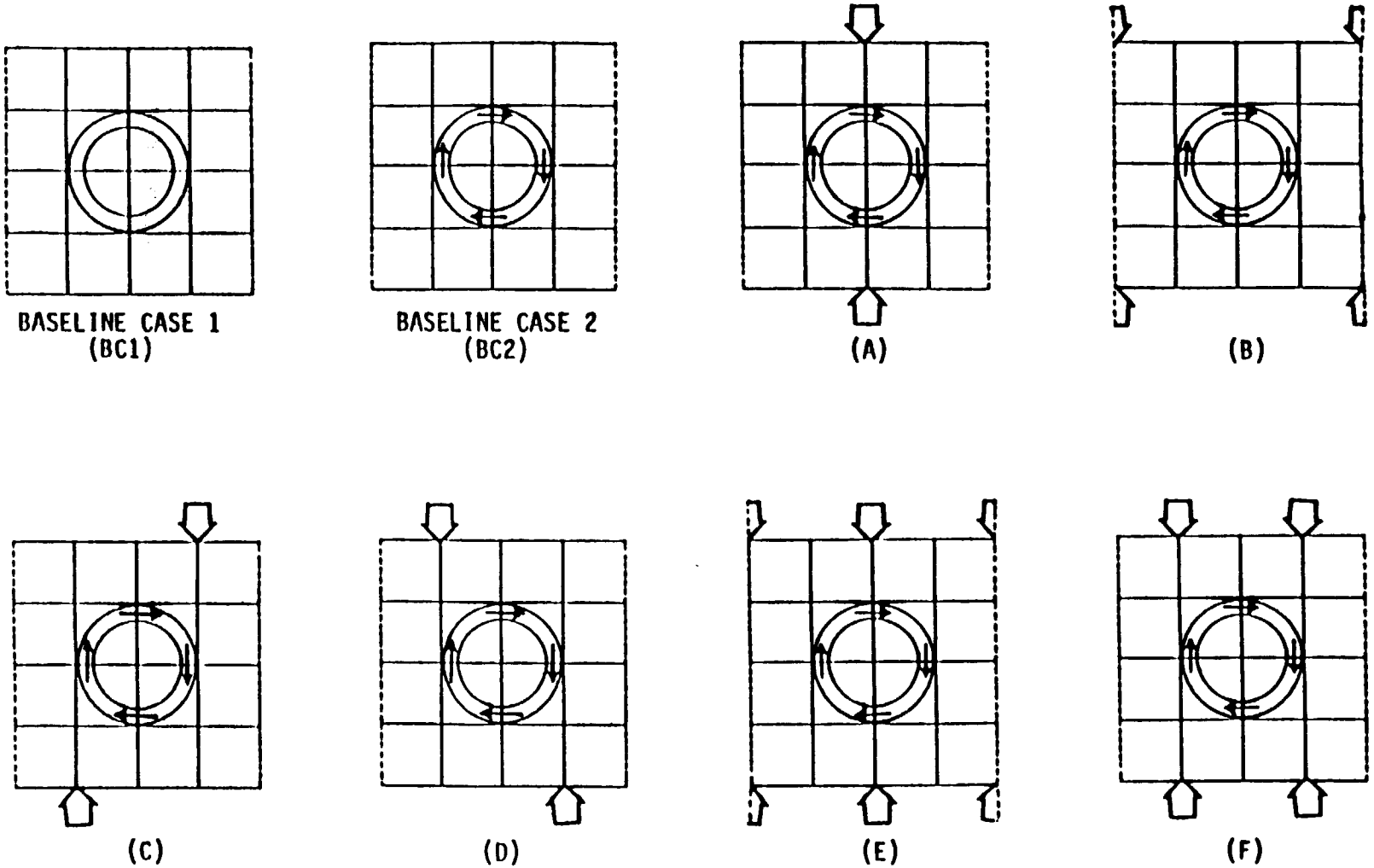

FIGURE 2

CONCENTRATION MEASUREMENTS (LOW REYNOLDS NUMBER)

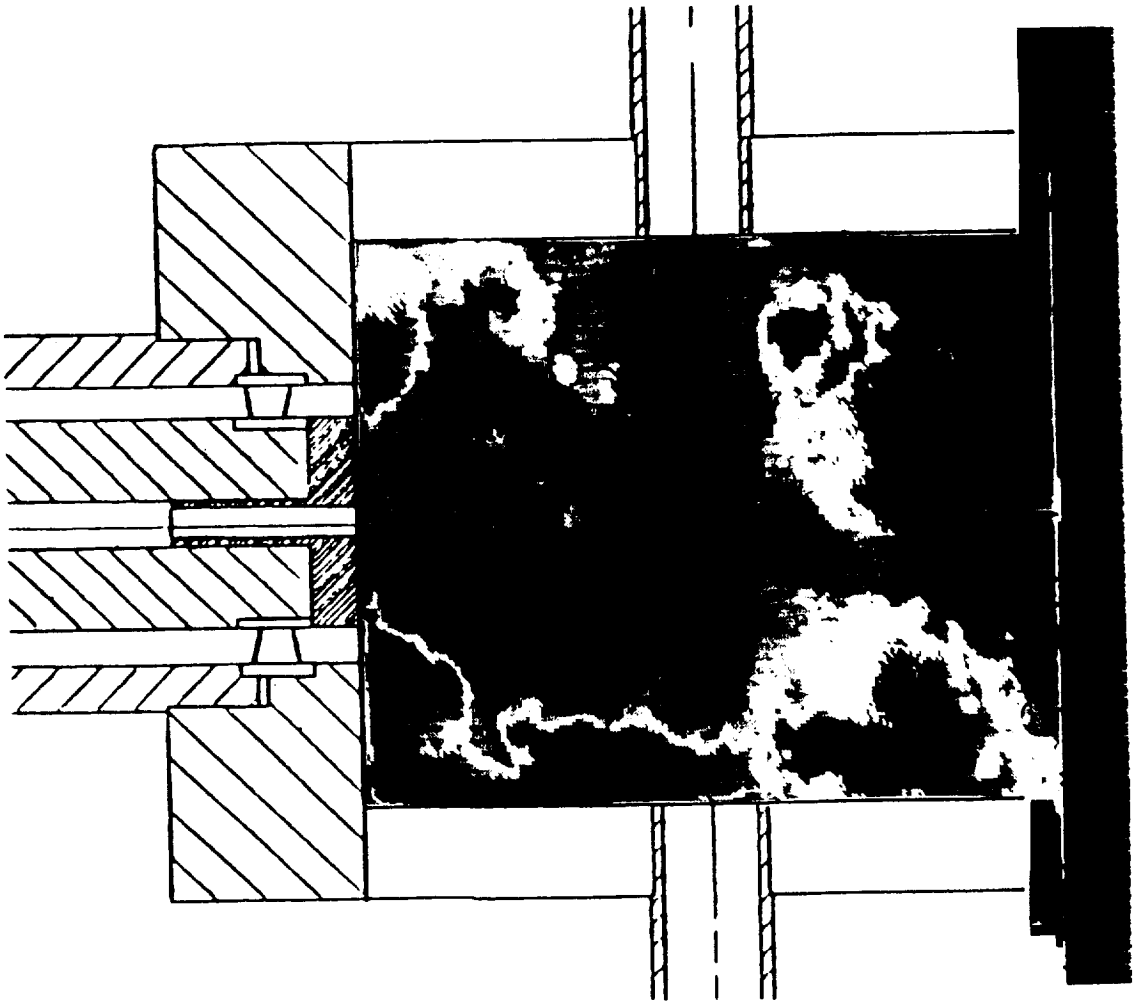

FIGURE 3

CONCENTRATION MEASUREMENTS (HIGH REYNOLDS NUMBER)

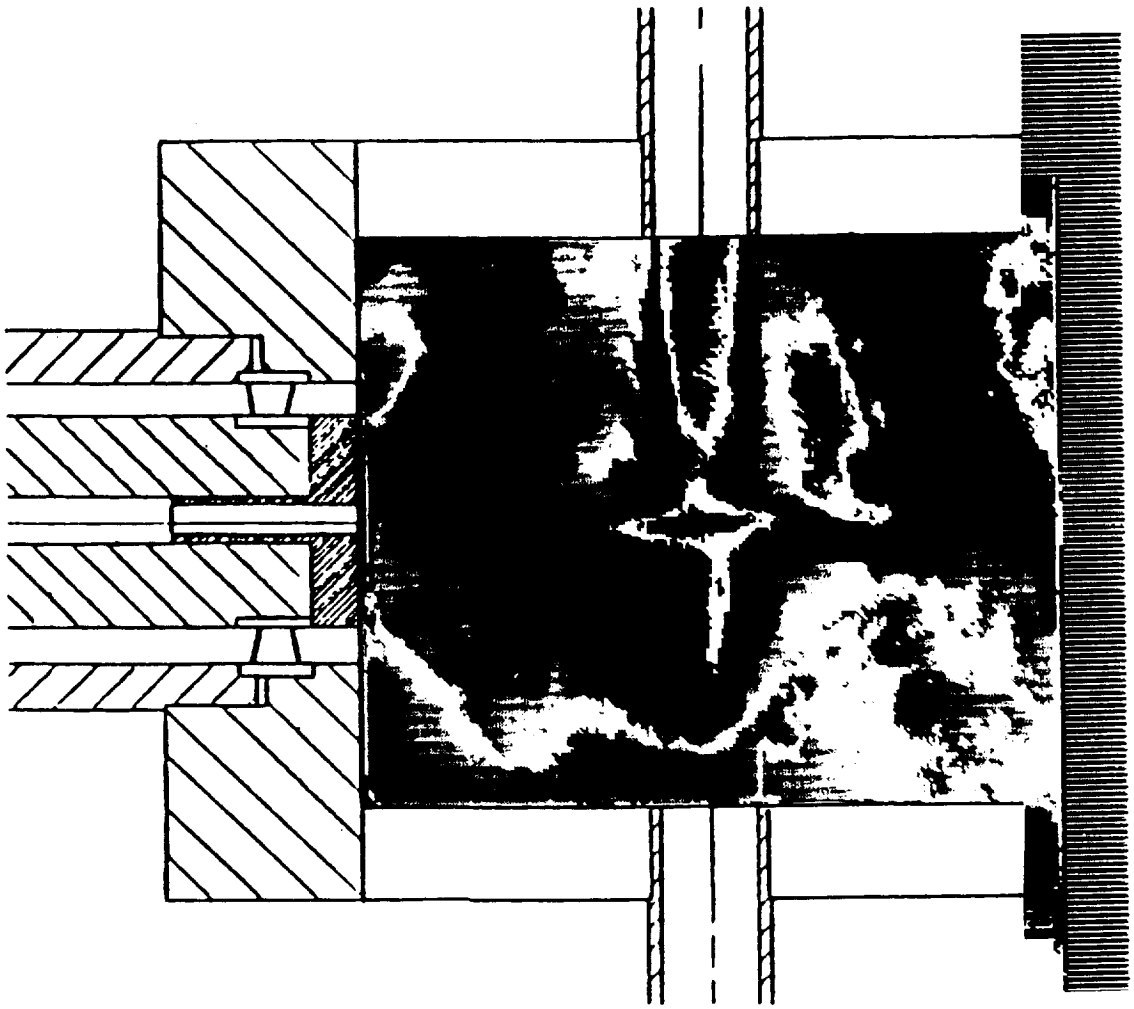

FIGURE 4

CONCENTRATION MEASUREMENTS (BISTABLE FLOW SITUATION)

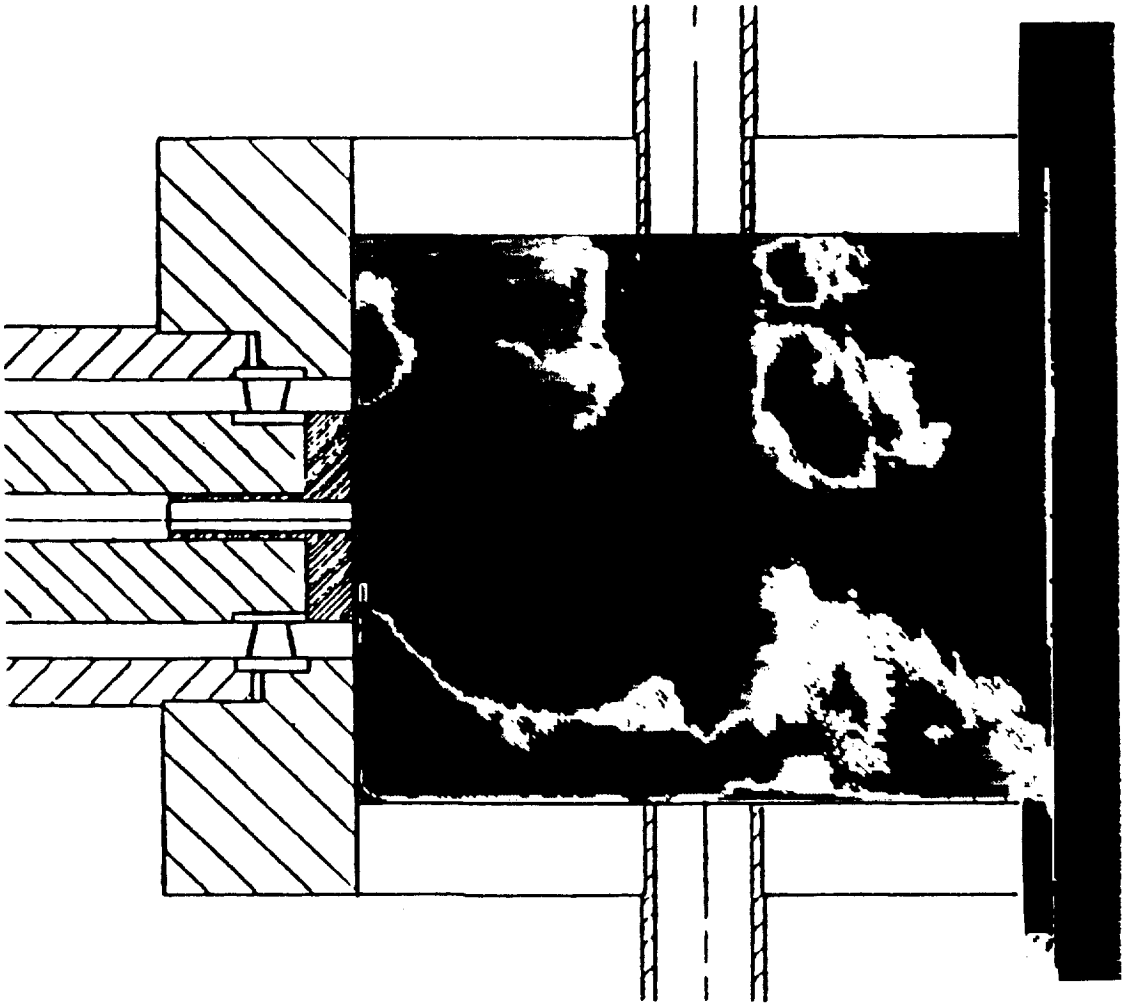

FIGURE 5

AEROTHERMAL MODELING PROGRAM--PHASE II*

ELEMENT C: FUEL INJECTOR-AIR SWIRL CHARACTERIZATION

A.A. Mostafa, H.C. Mongia, V.G. McDonnell†, and G.S. Samuelsen†
Allison Gas Turbine Division
General Motors Corp.

The main objectives of the NASA-sponsored Aerothermal Modeling Program, Phase II Element C, are experimental evaluation of the air swirler interaction with a fuel injector in a simulated combustor chamber (Figure 1), assessment of the current two-phase models, and verification of the improved spray evaporation/dispersion models.

This experimental and numerical program consists of five major tasks. Tasks 1 and 2 have been completed. Brief descriptions of the five tasks are given in the following paragraphs.

TASK 1--EXPERIMENTAL CONFIGURATION

This task involved preliminary design of the test section, its details for fabrication, and the experimental plan for data acquisition.

The aim of the experiment is to collect benchmark quality data to study the interaction of the fuel spray with a swirler typical of current use in aircraft turbine engines.

The fuel nozzle and swirler combination is operated at both unconfined and confined conditions (152 mm duct). The experimental plan covers a wide range of tests of varying complexity, with the constituent flows measured separately and then in combination. The duct is designed in such a way to enable the required measurements to be taken at the inlet plane and at seven axial locations downstream of the swirler-fuel injector combination. The measurements include the following quantities: the three components of mean and root mean square (rms) gas velocity as well as Reynolds stresses, the three components of mean and rms droplet velocity, Sauter mean diameter, droplet size distribution, spatial distribution of droplets, cone angle, fraction of liquid evaporated in the duct (vapor concentration), the static pressure along the wall of the duct, and the inlet air temperature.

All the test configurations (Figure 2) are first operated free of injected particles (except for the laser anemometer seed), second with injected monodisperse solid particles (50-micron glass beads) through a diameter jet tube, 24 mm, then with injected solid particles of two sizes (50 and 100 μm glass beads), and finally with a fuel spray (methanol) through an aircraft-type airblast atomizer.

*Work done under NASA Contract NAS3-24350.
†University of California at Irvine.

TASK 2--MODELING SENSITIVITY ANALYSIS

Allison had run its 2-D codes (parabolic and elliptic) to predict the distribution of the flow field variables for all proposed flow and geometry test conditions of the experimental test matrix. The main purpose of this task was to determine if the planned experiment is sensitive to the significant variables and which variable and boundary conditions had to be measured.

This effort resulted in two main modifications in the original test plan. First, the 457.2 mm duct that is concentrically located around the nozzle/swirler assembly to simulate the unconfined conditions was replaced by one made of screen mesh. The reasoning was that the permeable wall would permit the entrainment of air that would otherwise necessitate recirculation. Second, the flow rates through the fuel nozzle and the swirler and the low velocity stream of confinement were optimized to avoid spray impingements on the tube wall within the measurements region.

TASK 3--MEASUREMENTS

The efforts of this task have been directed to (1) the testing of the facility, (2) the verification of the two-component laser interferometer diagnostics (see Figure 3), and (3) the acquisition of test data in the spray chamber.

The utility, applicability, and accuracy of phase Doppler (PD) has been tested in a series of experiments in which the technique has been compared to visibility/ intensity validation and laser diffraction using a Malvern (see ref. 1 and 2). The PD compared well to the visibility technique with intensity validation (VIS/ IV), and exhibits major advantages in the dynamic range of both droplet size and droplet velocity. In trials with laser diffraction using a commercial Malvern analyzer, the composite line-of-sight measurement of spatial-SMD deduced from the PD measurements compares favorably to the single line-of-sight Malvern measurement of spatial-SMD. It is noteworthy that the two measurements are best aligned for the Model-Independent algorithm of the Malvern rather than the Rosin Rammler.

Example data for both the injection of 50 μm beads and the methanol spray are presented in Figures 4 and 5. Although data are taken at seven axial locations, only four are shown for clarity. The glass bead data (Figure 5a) display the axial mean velocity of both the bead and gaseous phase velocity, as well as the bead number density. The centerline hump in the bead number density is clearly discernable in the photograph (Figure 4a). The methanol spray data (Figure 5b) reflect the strong influence of the swirl in both the radial spread of the spray and the radial profiles of both SMD and mean axial velocity.

TASK 4--RESULTS AND ANALYSIS

Experimental data of Task 3 will be reduced and presented in a format suitable to make direct comparison with model predictions and to quantify the effects of the flow and geometric variables in various transport processes.

TASK 5--MODEL IMPROVEMENT

A mathematical model for turbulent evaporating sprays based on the recent work in that area (ref. 3-5) will be validated in this effort. This model will include improved submodels for spray injection, turbulence/droplet interaction, and droplet evaporation.

REFERENCES

1. Jackson, T. A., and Samuelsen, G. S., "Spatially Resolved Droplet Size Measurements," Journal of Engineering for Gas Turbines and Power, Vol. 108, No. 1, pp. 196-205, 1986.

2. Jackson, T. A., and Samuelsen, G. S., "Droplet Sizing Interferometry: A Comparison of the Visibility and Phase Doppler Techniques," Applied Optics, in press.

3. Mostafa, A. A., and Elghobashi, E. E., "A Two-Equation Turbulence Model for Jet Flows Laden with Vaporizing Droplets," Int. J. Multiphase Flow, II, pp. 515-533, 1985.

4. Rizk, N. K., Mostafa, A. A., and Mongia, H. C., "Modeling of Gas Turbine Fuel Nozzles," Symposium on Calculations of Turbulent Reactive Flows, ASME 107th Winter Annual Meeting, Nov. 30 - Dec. 5, 1986, Anaheim, California.

5. Mostafa, A. A., and Mongia, H. C., "Eulerian and Langrangian Predictions of Turbulent Evaporating Sprays," AIAA Paper No. 86-0452, 1986.

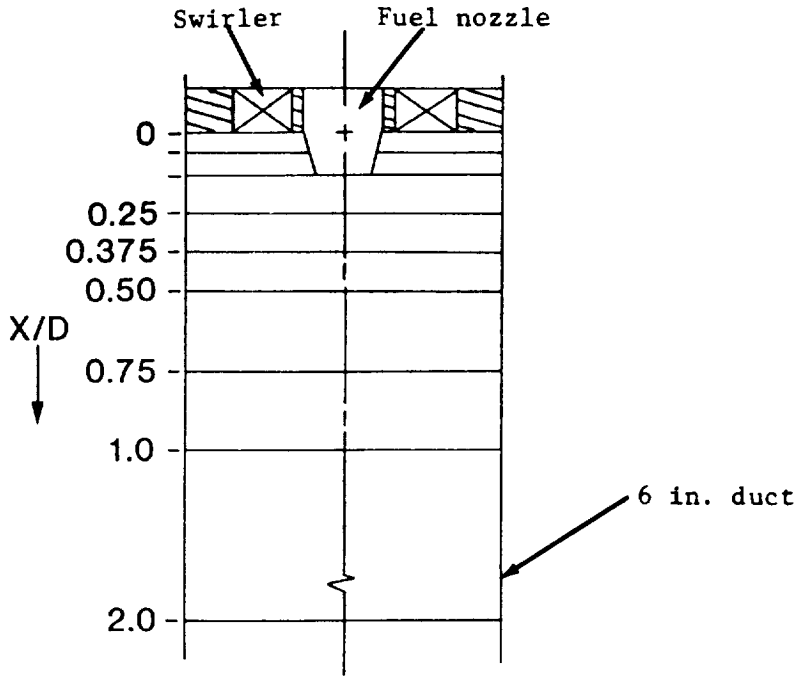

Figure 1. Experimental configuration for confined flow with liquid fuel injection and swirl.

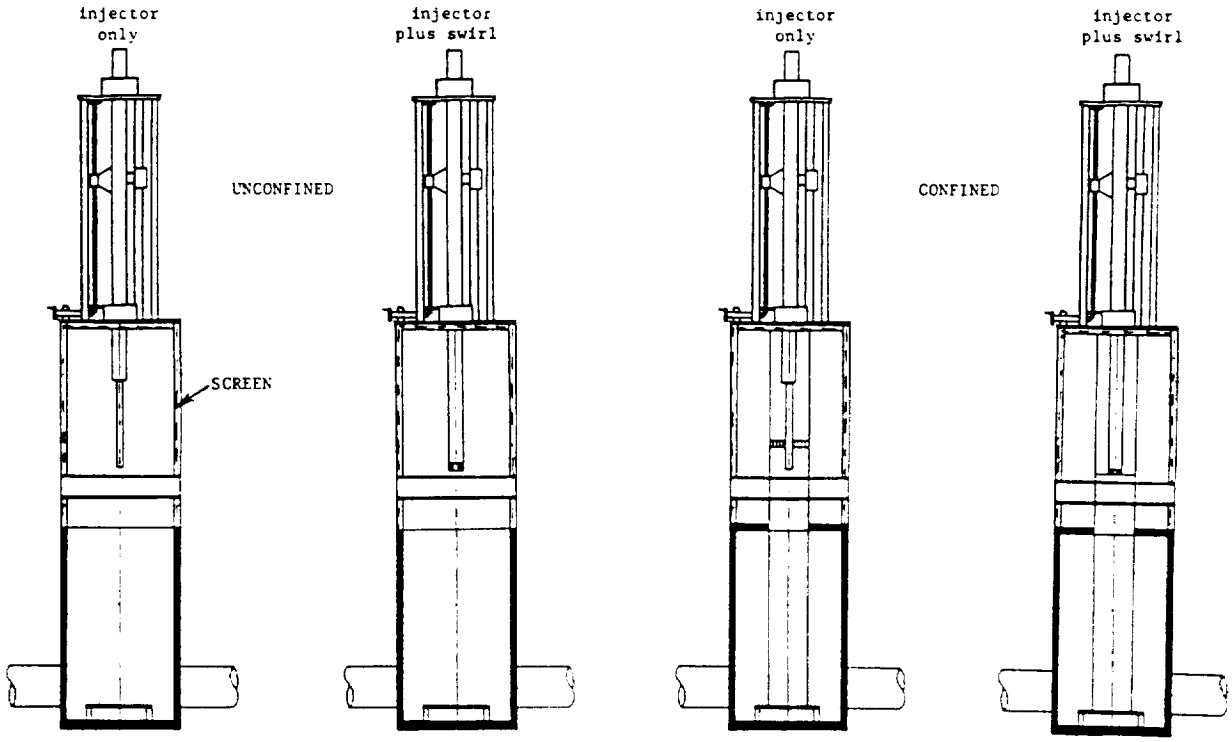

Figure 2. Experimental configurations.

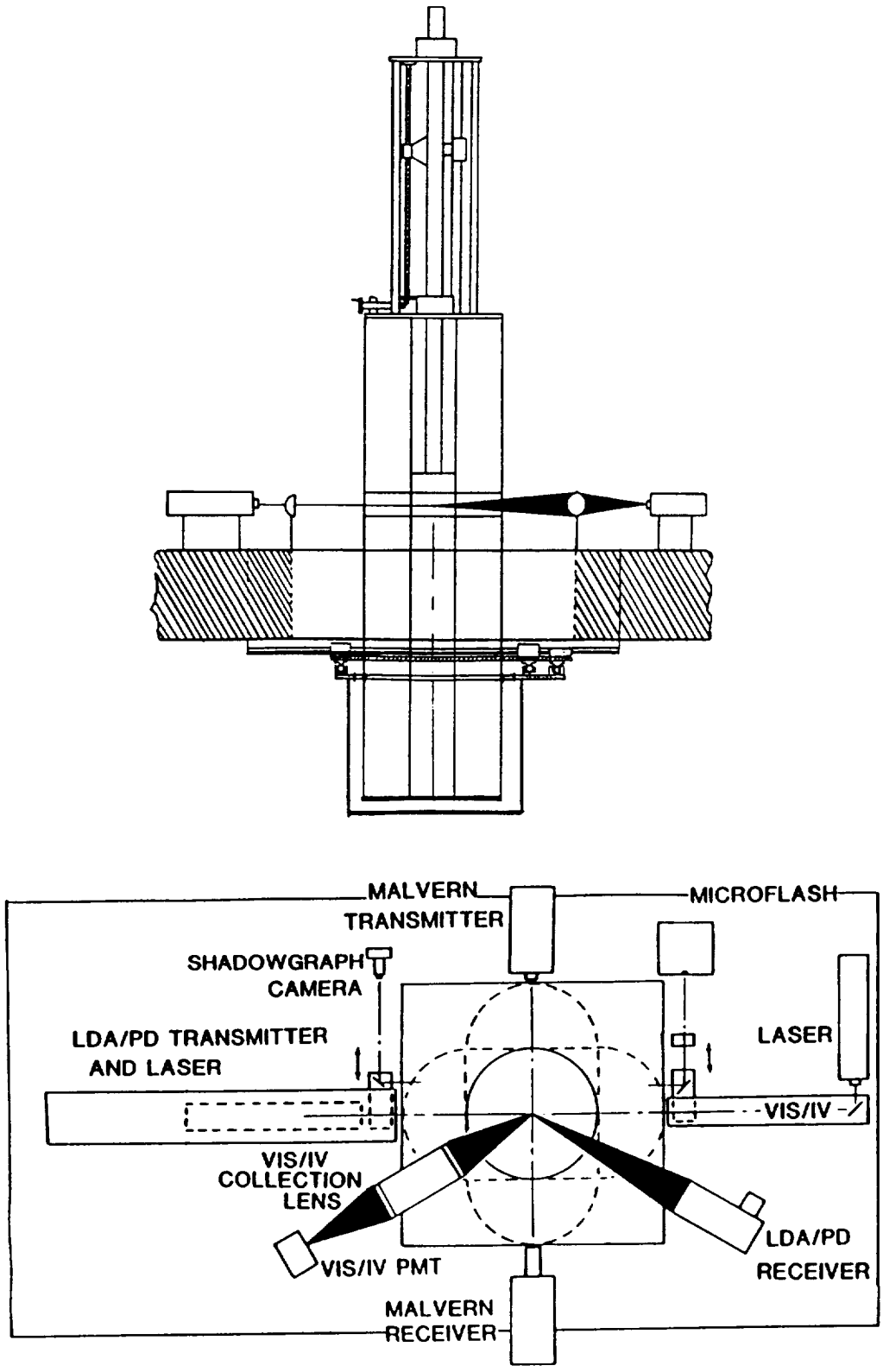

Figure 3. Flow facility and optical arrangement.

a) 50 μm beads (unconfined; without swirl)

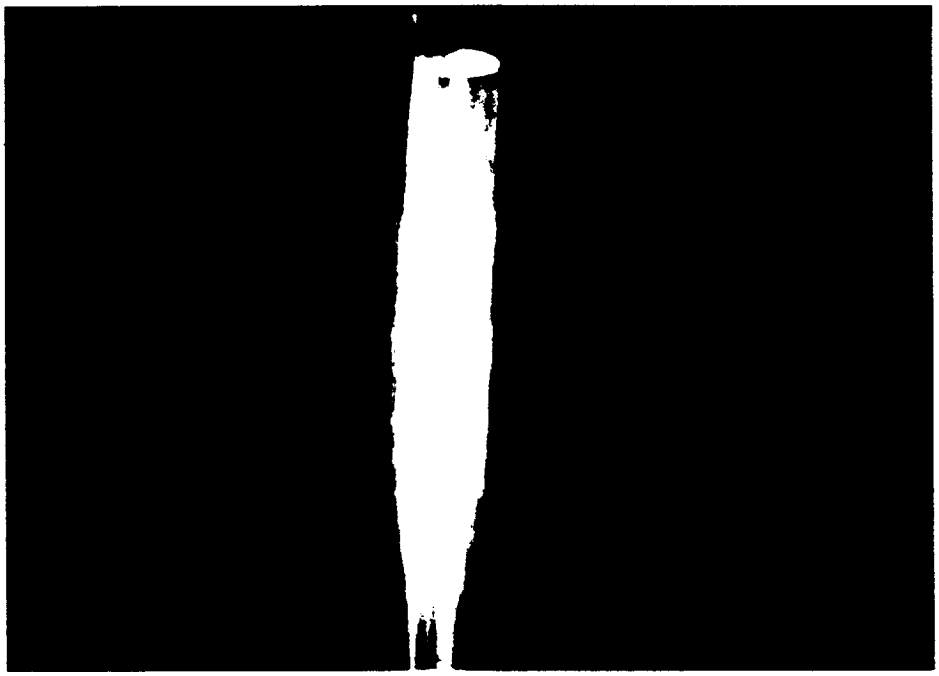

b) Methanol spray (unconfined; without swirl)

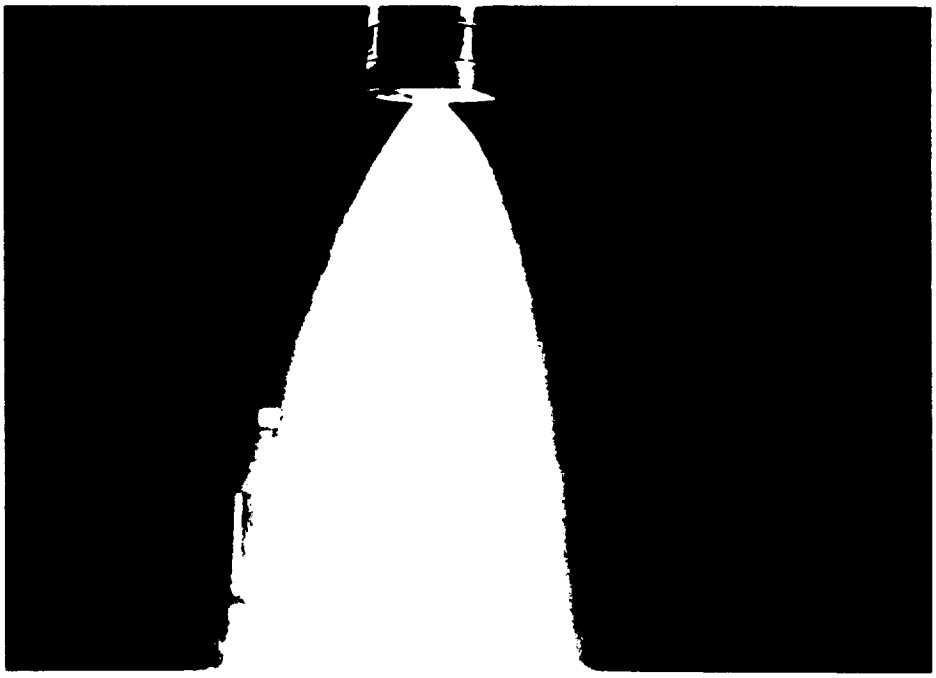

Figure 4. Representative data: photographs.

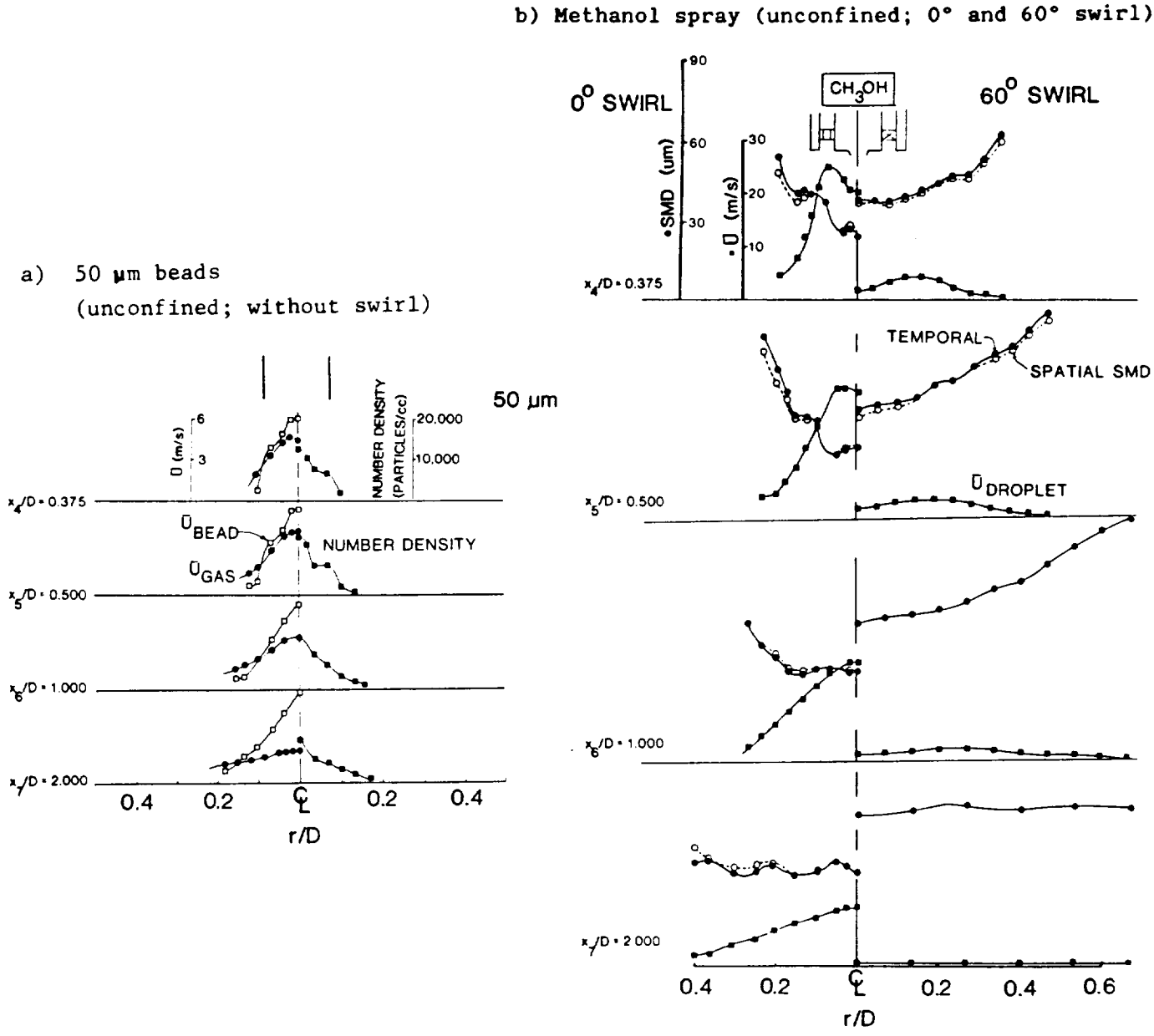

Figure 5. Representative data: radial profiles.

COMBUSTOR DIFFUSER INTERACTION PROGRAM

Ram Srinivasan and Daniel Thorp
Garrett Turbine Engine Co., Phoenix

INTRODUCTION

Advances in gas turbine engine performance are achieved by using compressor systems with high stage loading and low part count, which result in high exit Mach numbers. The diffuser and combustor systems in such engines should be optimized to reduce system pressure loss and to maximize the engine thrust-to-weight ratio and minimize length. The state-of-the-art combustor-diffuser systems do not meet these requirements. Detailed understanding of the combustor-diffuser flow field interaction is required for designing advanced gas turbine engines.

An experimental study of the combustor-diffuser interaction (CDI) is being conducted to obtain data for the evaluation and improvement of analytical models applicable to a wide variety of diffuser designs. The CDI program consists of four technical phases:

Phase I - Literature Search
Phase II - Baseline Configuration
Phase III - Parametric Configurations
Phase IV - Performance Configurations

Phase II of the program is in progress.

OBJECTIVES

Objectives of the Phase II efforts are to:

- Identify the mechanisms and the magnitude of aerodynamic losses in the prediffuser, dome, and shroud regions of an annular combustor-diffuser system
- Determine the effects of geometric changes in the prediffuser, dome, and shroud wall on aerodynamic losses and loss mechanisms
- Obtain a data base that can be used to assess advanced numerical aerodynamic computer models for predicting flowfield conditions in an annular combustor-diffuser system
- Assess the ability of current analytical models to predict flowfield characteristics in annular combustor-diffuser systems, including pressure distributions
- Upgrade the analytical models based on the experimental data for flowfield

*Work done under USAF Contract F33615-84-C-2427.

DESCRIPTION OF TEST CONDITIONS AND RIG

The test rig is a 60-degree sector of a full annular combustor-diffuser system whose cross-sectional details are shown in Figure 1. Air flow through the rig is established by connecting discharge ducts to vacuum lines. The airflow rate in each of the three lines is controlled to produce the desired flow split and a rig inlet Mach number of 0.35. The test rig performance evaluation is being made for 15 different flow conditions as shown in Table 1.

RESULTS

Water flow visualization tests were performed for all 15 flow conditions. The streamline patterns were photographed and compared with predicted results, which showed good agreement. A typical comparison is shown in Figure 2 for one of the test conditions. Subsequent to the flow visualization tests, detailed pressure and wall shear stress distribution measurements were made for these flow conditions. The instrumentation for pressure measurements are shown in Figure 3.

Shear stress distributions were measured only along the prediffuser walls (Figure 4). These data are being processed. The three-component LDV system (Figure 5) has been set up, and LDV measurements in the CDI test rig will be initiated to obtain detailed velocity field and turbulence quantities. Analytical model assessment and upgrade efforts will be performed in conjunction with the LDV measurements. Design efforts of the test rig for Phase III (Parametric Configurations) are underway. Figure 6 shows the configurations which will be test evaluated during this phase.

TABLE 1. FLOW CONDITIONS USED DURING PHASE II TESTING

	Percent Flow Split		
Test No.	Outer Annulus	Dome	Inner Annulus
1	32.9	20.0	47.1
2	40.0	20.0	40.0
3	48.0	20.0	32.0
4	55.0	20.0	25.0
5	60.0	20.0	20.0
6	26.8	35.0	38.2
7	32.5	35.0	32.5
8	39.0	35.0	20.3
9	44.7	35.0	20.3
10	48.8	35.0	16.2
11	20.6	50.0	29.4
12	25.0	50.0	25.0
13	30.0	50.0	20.0
14	34.4	50.0	15.6
15	37.5	50.0	12.5

DESCRIPTION OF THE BASELINE TEST RIG.

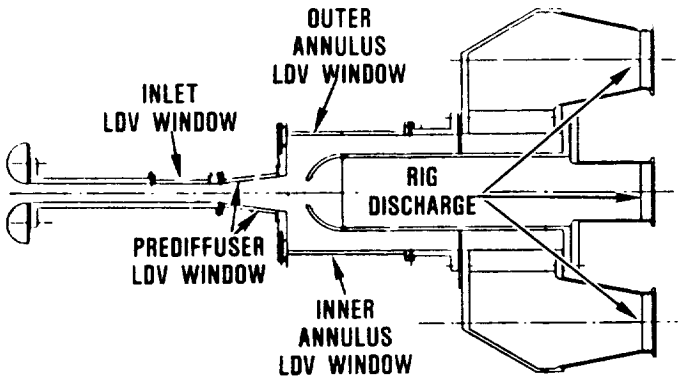

INNER TO OUTER DIAMETER RATIO AT PREDIFFUSER INLET	0.92:1
PREDIFFUSER AREA RATIO	1.86:1
PREDIFFUSER LENGTH TO INLET HEIGHT RATIO	3.778:1
WALL DIVERGENCE ANGLE	6.5 DEGREES
RATIO OF DUMP GAP TO PREDIFFUSER EXIT HEIGHT	0.52
RATIO OF COMBUSTOR CHANNEL HEIGHT TO INLET DUCT HEIGHT	3.10
RATIO OF OUTER TO INNER ANNULUS AREA	1.5

FIGURE 1.

FLOW VISUALIZATION TEST RESULTS AND PREDICTED STREAMLINES.

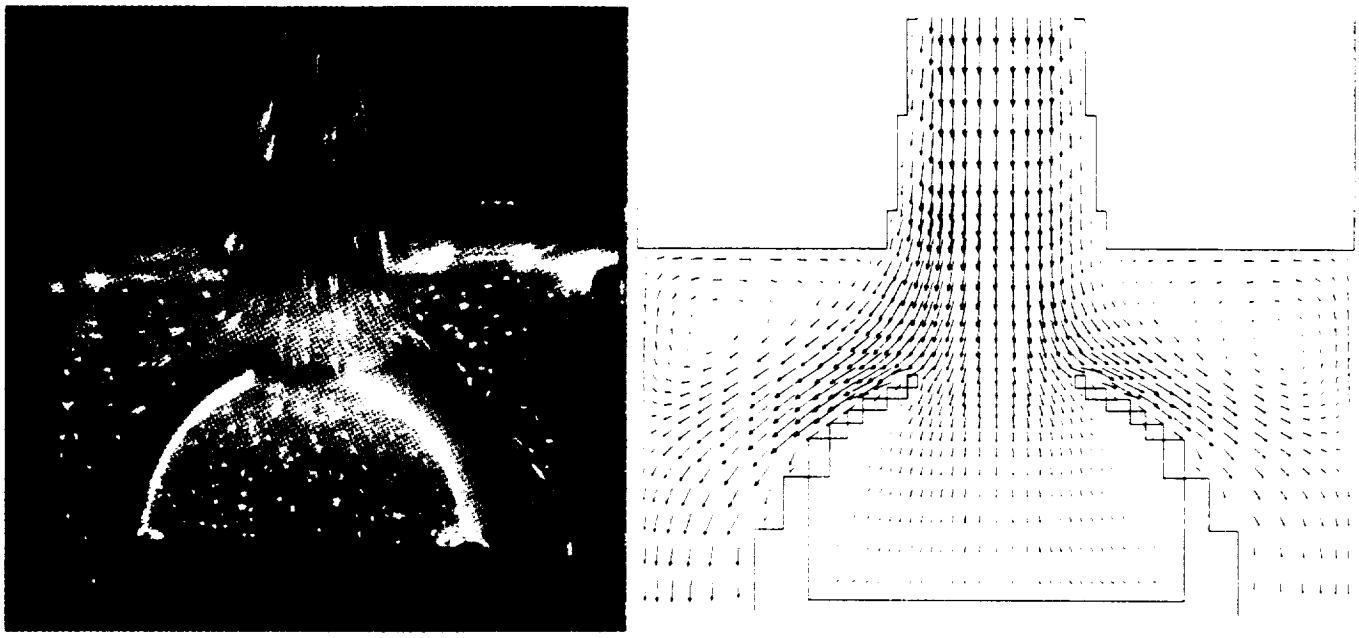

TEST CONDITION NO. 6

FIGURE 2.

WALL STATIC, TOTAL PRESSURE RAKE, AND PRESSURE SURVEY LOCATIONS.

▲ STATIC PRESSURE PROBE (3 PROBES AT EACH LOCATION CIRCUMFERENTIALLY UNLESS NOTED) 132

■ TOTAL PRESSURE RAKE-5 PROBES 4

● THERMOCOUPLE 4

x LOCATION OF PRESSURE SURVEY

— INLET, 10 LOCATIONS

— DIFFUSER EXIT, 20 LOCATIONS

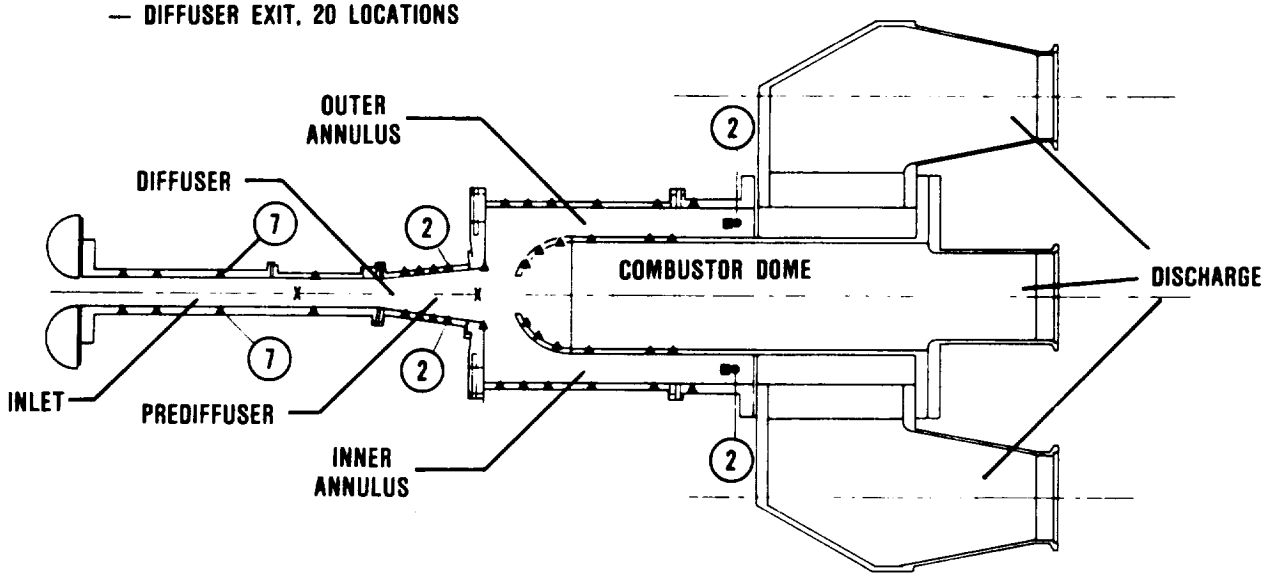

FIGURE 3.

LOCATIONS OF FLUSH-MOUNTED HOT FILM SENSORS USED TO DIRECTLY MEASURE WALL SHEAR-STRESSES IN THE PREDIFFUSER.

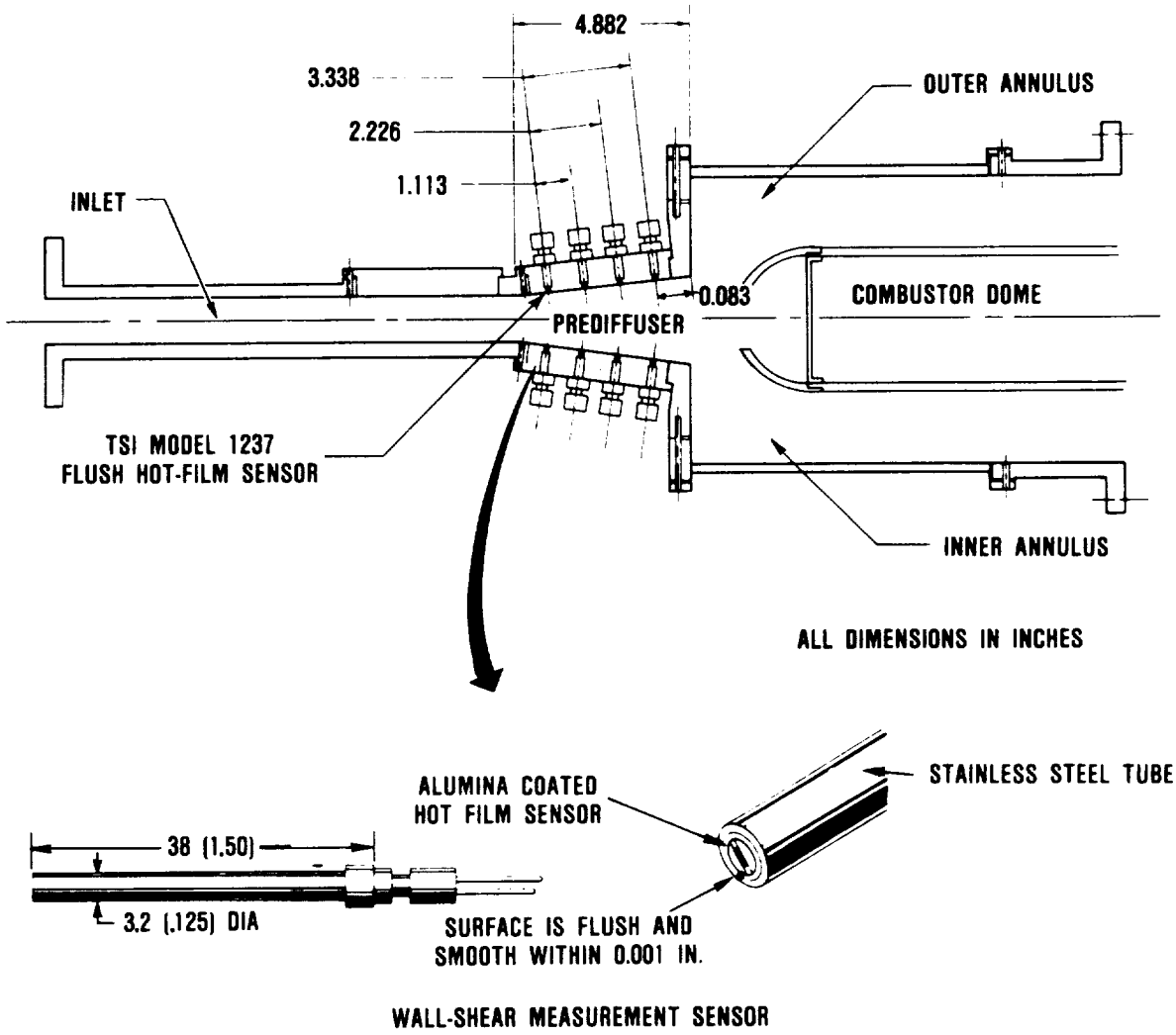

FIGURE 4.

SCHEMATIC OF THE THREE-COLOR, THREE-COMPONENT LDV SYSTEM.

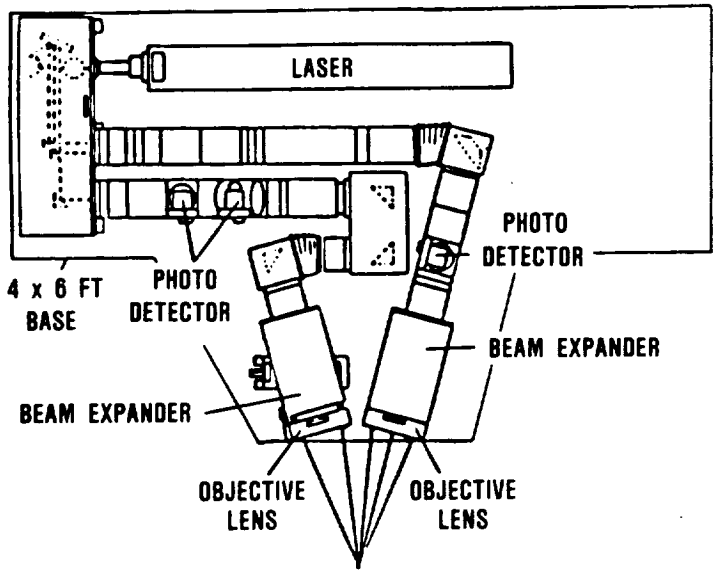

SYSTEM DESCRIPTION

- CHANNEL SEPARATION BY 3-COLOR
- 3.75x BEAM EXPANSION
- 450mm FOCAL LENGTH, 152mm OBJECTIVE LENSES
- OFF-AXIS BACKSCATTER COLLECTION
- DISPERSION PRISM COLOR SEPARATION
- 150 M Hz BAND WITH SIGNAL CONDITIONING
- 3-AXIS COMPUTER CONTROLLED TRAVERSIGN SYSTEM
- PROBE VOLUME SIZE
  - — DIAMETER = 0.6mm
  - — LENGTH = 0.22mm
- ESTIMATED ACCURACY ON VELOCITY COMPONENTS ABOUT 1 PERCENT WITH 30° SEPARATION ANGLE
- VELOCITY RESOLUTION 0.25% AT 40 M Hz OR 0.037 M/S AT 150 M/S

FIGURE 5.

SCHEMATICS OF PARAMETRIC CONFIGURATIONS FOR PHASE III TEST EVALUATION.

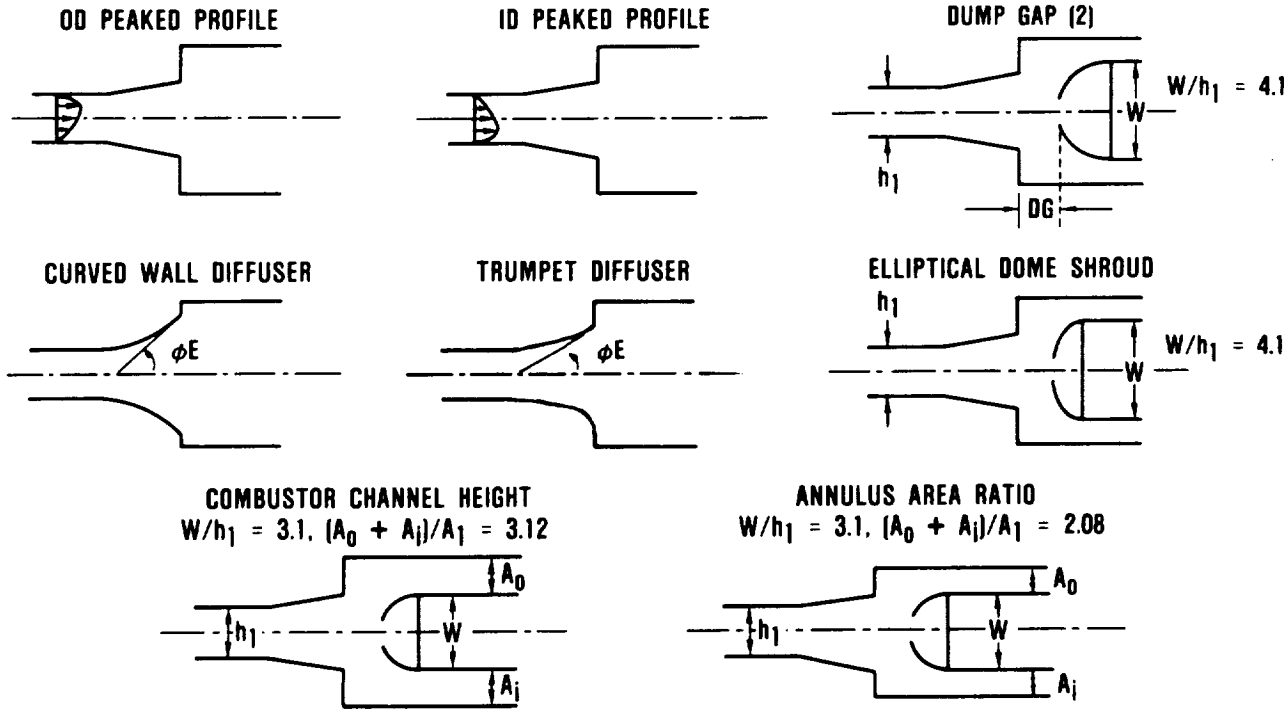

FIGURE 6.

EFFICIENT NUMERICAL TECHNIQUES FOR COMPLEX FLUID FLOWS*

Suhas V. Patankar
Department of Mechanical Engineering, University of Minnesota

INTRODUCTION

The use of computational methods for the prediction of multi-dimensional recirculating flows has been continuously increasing over the recent years. As the numerical techniques become more powerful, they are being applied to even more challenging problems encountered in combustion chambers, gas turbines, rotating machinery, heat exchangers, and other devices. Although computation is far less expensive than full-scale testing, the cost of a computational run is still substantial. Therefore, attempts are continually being made for improving the accuracy and efficiency of numerical techniques so that the predictions of a given accuracy can be obtained at a modest cost.

The central feature in any flow prediction method is the treatment of the coupling between the momentum and continuity equations. In natural-convection flows, the energy equation also becomes strongly coupled with the momentum equations. Because of the nonlinear nature of the coupling, these equations are solved iteratively. Iterative methods are often prone to slow convergence, divergence, and extreme sensitivity to underrelaxation factors.

The aim of the present research is to develop more efficient and reliable solution schemes for the coupled flow equations. Such schemes will significantly reduce the expense of computing complex flows encountered in combustion chambers, gas turbines, heat exchangers, and other practical equipment.

In the work completed so far, a technique employing norm reduction in conjunctine with the successive-substitution and Newton-Raphson techniques has been developed. Also, a block-correction procedure for the flow equations is currently being formulated and tested.

NORM REDUCTION TECHNIQUES

The development of a number of methods for solving strongly coupled equations has been reported in reference 1. The recommended method there is a combination of the successive-substitution and Newton-Raphson methods coupled with a norm reduction technique.

The central idea of the method will now be described. The linearized discretization equations are solved by a direct method, such as the sparse-matrix LU decomposition. The linearization can be of two kinds. If the unknown coefficients are simply evaluated from the currently available values of the dependent variables, the linearization is called successive substitution. In the Newton-Raphson method, the anticipated change in the coefficients is taken into account via their first derivatives with respect to the dependent variables.

* Work done under NASA Grant NAG 3-596

The solution of the linearized equations predicts a change in the values of the variables. However, instead of accepting this change as is, it is multiplied by a constant. (This constant can be imagined to be a kind of under- or over-relaxation factor.) The value of this constant multiplier is found by requiring that the norm of the residual vector (i.e., the sum of the squares of the residuals of all the equations) be a minimum. This minimization search produces a kind of "optimum" underrelaxation of the dependent variables.

The norm minimization (or reduction) can be used with either successive-substitution or Newton-Raphson linearization. When the current estimates are close to the final solution, the Newton-Raphson technique is very efficient. But for initial guesses that are far from the solution, the technique often diverges. Therefore, the practice found satisfactory for all the flows tested was to employ the successive-substitution linearization until the norm became less than a small quantity and then to switch to the Newton-Raphson linearization until the final convergence. Because of the combination of the two linearization practices, the technique is called the hybrid method in reference 1.

The hybrid method and many other alternative schemes (some of which are based on the Broyden methods described in reference 2) were tested on two flow configurations: the flow in a driven cavity at different Reynolds numbers and the natural convection flow in an enclosure with hot and cold walls at different Rayleigh numbers.

For the driven cavity problem, solutions were obtained by the hybrid method in at least one-third the computer time required for the iterative method SIMPLER. For the natural convection problem, most methods either diverged or converged extremely slowly as the Rayleigh number was increased. The hybrid method, however, converged rapidly and required a very modest amount of computer time. By using the hybrid method, it was possible to obtain convergence in 25 iterations at a Rayleigh number of 10^7 when a zero initial guess was used for all variables. If the results for a lower Rayleigh number could be used as the initial guess, it was possible to obtain solutions at a Rayleigh number of 10^9. It is believed that, for the first time, solutions have been obtained for such a high Rayleigh number (with a Prandtl number of 0.71). Iterative methods such as SIMPLER failed to converge even after 1000 iterations.

BLOCK CORRECTION TECHNIQUE

Work is currently in progress on another approach for accelerating the convergence rate of an iterative procedure such as SIMPLER. In the proposed technique, the velocity and pressure values are adjusted through a block correction procedure. Here the calculation domain is considered to be composed of several large blocks. Each block contains a number of grid points (and hence control volumes). It is proposed that the values of a variable for grid points within a given block will receive a uniform correction. These corrections are calculated such that the integral conservation of momentum and continuity is satisfied for each block. The block-correction equations thus resemble the discretization equations for momentum and continuity but are formulated on much coarser grid. The solution of these equations by a direct or iterative method is rather straightforward.

Initial testing of this apprach shows that, for fine grids, there is a noticeable improvement in the computational effort required to obtain a converged solution.

REFERENCES

1. MacArthur, J. W.: Development and implementation of robust direct finite-difference methods for the solution of strongly coupled elliptic transport equations. Ph.D. Thesis, University of Minnesota, Minneapolis, May 1986.

2. Broyden, C. G.: Quasi-Newton Methods in Optimization Methods in Electronics and Communications, ed. Cattermole, R. W. and O'Reilly, J. J., Pentech Press, 1984, pp. 105-110.

IMPROVED NUMERICAL METHODS FOR TURBULENT VISCOUS RECIRCULATING FLOWS*

J.P. Van Doormaal+, A. Turan and G.D. Raithby+
AVCO Research Laboratory, Inc.

INTRODUCTION

The objective of the present study is to improve both the accuracy and computational efficiency of existing numerical techniques used to predict viscous recirculating flows in combustors. This paper presents a review of the status of the study along with some illustrative results.

The effort to improve the numerical techniques consists of the following three technical tasks:

(1) selection of numerical techniques to be evaluated
(2) two-dimensional evaluation of selected techniques
(3) three-dimensional evaluation of technique(s) recommended in Task 2.

SELECTION OF NUMERICAL TECHNIQUES

Based on the citeria of accuracy, stability and boundedness the following discretization schemes were selected for evaluation in two-dimensional problems:

(1) Second Order Upwind (SOU) differencing
(2) Operator Compact Implicit (OCI) differencing
(3) improved Skewed Upstream Differencing Schemes (SUDS).

To enhance computational efficiency the methods selected for two-dimensional evaluation include the Strongly Implicit Procedure (SIP), for solving for the pressure correction of SIMPLE or its variants, accelerated by the following techniques:

(1) Conjugate Gradient (CG) acceleration
(2) Block Correction (BC) acceleration
(3) Additive Correction Multigrid (ACM) acceleration.

TWO-DIMENSIONAL EVALUATION OF SELECTED TECHNIQUES

Accuracy Improvement

Each of the selected techniques for improving accuracy was implemented adopting a conservative control volume approach and boundedness improvement strategies which ensured unique solutions and which posed no solution difficulties. The evaluation of the techniques for improving accuracy were carried out on a number of test problems including

(1) transport of a scalar with a step profile at the inlet and uniform flow
(2) transport of a scalar with a smeared step profile at the inlet and curved flow

* Work done under NASA contract NAS3-24351
+ Advanced Scietific Computing Ltd.

(3) transport of a scalar with a unit source and uniform flow
(4) transport of a scalar with a distributed source and uniform flow
(5) laminar shear driven flow in a square cavity
(6) laminar flow over a backward facing step
(7) turbulent coannular flow.

For illustrative purposes results of problems 2 and 4 are presented in this paper. For problem 2, the predicted outlet profiles of the scalar, shown in Figure 1, are used to illustrate the degree to which each discretization scheme exhibits smearing of gradients and/or non-physical overshoots or undershoots (ie lack of boundedness). The results of problem 4, as shown in Figure 2 illustrate the accuracy and rate of convergence with grid refinement of each of the discretization schemes.

Implementing SOU in a conservative framework results in a scheme with negative influence coefficients which, in turn, introduce the possibility of overshoots and undershoots in the numerical solution, see Fig. 1. Some attempts, including the one described in reference 1, have been made to reduce or eliminate this unboundedness of SOU. However, all attempts to date result in schemes which either are not conservative or do not guarantee unique numerical results. Also, as shown in Fig 1., SOU results can exhibit smearing of gradients when relatively coarse grids are used. Figure 2 illustrates the second order rate of convergence of SOU on fine grids. However, the level of error of SOU is notably higher than that of other second order schemes evaluated in the present study.

At the outset of the present study there were several OCI schemes with a formal accuracy of fourth order available in the literature. However, these schemes were not conservative. The development of a conservative Control Volume based OCI (CV-OCI) was undertaken in this study. The result of this effort was a CV-OCI scheme of exponential type which exhibits a second order rate of convergence with grid refinement, see Fig. 2. Bounded CV-OCI solutions can be ensured for one-dimensional problems, but, as illustrated in Fig. 1, a CV-OCI scheme which ensures bounded one-dimensional solutions is not guaranteed to produce bounded solutions for multi-dimensional problems.

For problems where the Peclet number is high, both the SOU and CV-OCI schemes can be viewed as corrected Upwind Differencing Schemes (UDS). The corrections to UDS that are employed in these schemes are necessary to eliminate the numerical diffusion of UDS and its variants. However, for multi-dimensional flows, it can be shown that these corrections are responsible for the unbounded nature of the schemes. An alternative to the corrected UDS approach is to use SUDS. Although the numerical solutions of the original SUDS of Raithby exhibitted no numerical diffusion, significant non-physical overshoots and undershoots were noted for some problems. also, the original SUDS was only a first order scheme. Recently, both Raw and Huget, see references 2 and 3, have proposed improvements to the original SUDS. These improvements include a Physical Advection Correction (PAC) to SUDS and, a flux element approach with two integration points per control volume face and a Linear Profile (LP) assumption along the flux element edges. The PAC is designed to improve the accuracy of SUDS by including the effects of diffusion and source terms on the advection term. The flux element approach was adopted to improve the boundedness of SUDS as well as to simplify the implementation of SUDS. The effectiveness of these improvements and other refinements developed throughout the course of this study are illustrated in Figures 1 and 2. Note the minimal overshoot and undershoot of LP-SUDS-PAC as well as its second order rate of convergence and low error levels.

In spite of the efforts to reduce overshoots and undershoots and to improve the accuracy of the discretization schemes, the SOU, CV-OCI and LP-

SUDS schemes are not sufficiently bounded to be used for predicting the turbulent kinetic energy and dissipation. It is essential that solutions for these turbulence quantities are bounded. Two schemes which ensure this boundedness are the bounded skew schemes BSUDS1 and BSUDS2, see reference 4. Unfortunately, since both schemes are bounded by including a sufficient component of UDS, accuracy improvements are noted only on relative fine grids. An alternative is to modify the LP-SUDS scheme to ensure that solutions are bounded. One such scheme is the Mass Weighted (MW) SUDS where the linear profile assumption along flux element edges is replaced by mass weighted averaging. Of course the boundedness of MW-SUDS, as illustrated in Fig. 1, is achieved at the expense of accuracy. Nevertheless, as can be seen in Figures 1 and 2, the accuracy of MW-SUDS is a significant improvement over the accuracy of UDS.

Computational Efficiency Improvements

The evaluation of the various techniques for enhancing computational efficiency were carried out on a number of problems including problems 5,6 and 7. Results for problems 5 and 6 are detailed in reference 5.

Preliminary evaluation of the convergence enhancement techniques revealed that conjugate gradient acceleration is very effective for coarse grids. However, it was found that the effectiveness of CG diminished significantly with grid refinement. This diminshed effectiveness arises because substantial improvements in the numerical solution occur only after a sufficient and often excessive number of iterations have been performed such that all of the dominant orthogonal basis vectors of the solution have been set up.

The BC accleration is, by design, effective when the solution for pressure correction is predominantly one-dimensional. Surprisingly, BC acceleration is also often effective even when a prodominant one-dimensional component of the solution is not evident. For instance, the use of BC for problem 5 with a 48x48 grid results in a 40 percent reduction in CPU requirements.

The additive correction multigrid acceleration technique is designed to systematically account for components of the solution in all directions by ensuring that conservation is satisfied on coarse grids. The use of ACM acceleration results in reductions in CPU requirements similar to those of BC.

In addition to the evaluation of the techniques used to accelerate the procedure for solving for pressure correction, additional methods for improving efficiency were considered. One computationally expensive aspect of the existing solution procedures for incompressible flows is the method chosen to account for the coupling between pressure and velocity. The current SIMPLE-like methods such as the PISO variant of SIMPLER require an appropriate amount of underrelaxation and an excessive number of costly coefficient iterations. To overcome these difficulties the solution strategy which is employed by most SIMPLE-like methods was modified. Instead of performing the calculations for velocity and pressure correction, u^*,v^* and p', only once before re-assembling coefficients, the SIMPLE-like method was repeated several times. Using this strategy, the parameter used to underrelax the momentum equations could be increased from 0.5 to 0.9 and the number of coefficient assembly iterations reduced by over 30 percent. Combining the new strategy with SIP-ACM reductions in CPU requirements of up to 70 percent were noted for laminar flows. For turbulent flows reductions in CPU requirements, ranging from 25 to 40 percent, were not as large.

RECOMMENDATION FOR THREE-DIMENSIONAL EVALUATION

Based on the results of two-dimensioanl evaluation outlined above it is recommended that the following techniques be implemented for three-dimensional evaluation

(1) modified SUDS to improve accuracy

(2) SIP-ACM to improve computational efficiency.

The implementation of modified SUDS will ensure that, on the coarse grids often used for three-dimensional predictions, signficantly more accurate solutions than UDS with little or, if required, no overshoots and undershoots present. The ACM technique is recommended over BC because the former technique is expected to have a wider range of applicability and is expected to provide even more dramatic reductions in CPU requirements for three-dimensional problems.

REFERENCES

1. Lai, C.H.; Bodvarsson, G.S.; and Witherspoon, P.A.: Second-Order Upwind Differencing Method for Nonisothermal Chemical Transport in Porous Media. Num. Heat Transfer, vol. 9, no. 4, 1986, pp 453-471.

2. Raw, M.J.: A New Control-Volume-Based Finite Element Procedure for the Numerical Solution of the Fluid Flow and Scalar Transport Equations. Ph.D Thesis, University of Waterloo, 1985.

3. Huget, R.G.: The Evaluation and Development of Approximation Schemes for the Finite Volume Method. Ph.D Thesis, University of Waterloo, 1985.

4. Syed, S.A.; Chiapetta, L.M.; and Gosman, A.D.: Error Reduction Program, Final Report. NASA CR-174776, 1985.

5. Van Doormaal, J.P.; Hutchinson, B.R.; and Turan, A.: An Evaluation of Techniques Used to Accelerate Segregated Methods for Predicting Viscous Fluid Flows. AIAA paper no. 86-1653, 1986.

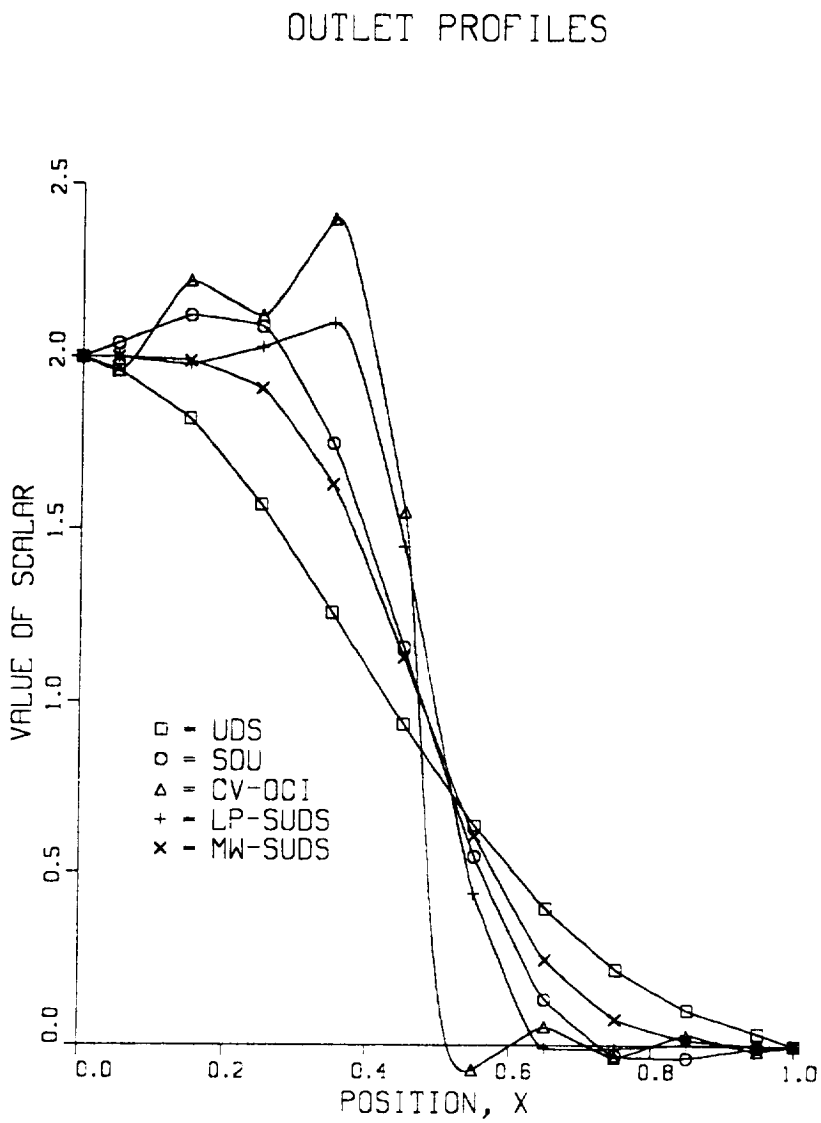

Figure 1: Outlet profiles for problem 2.

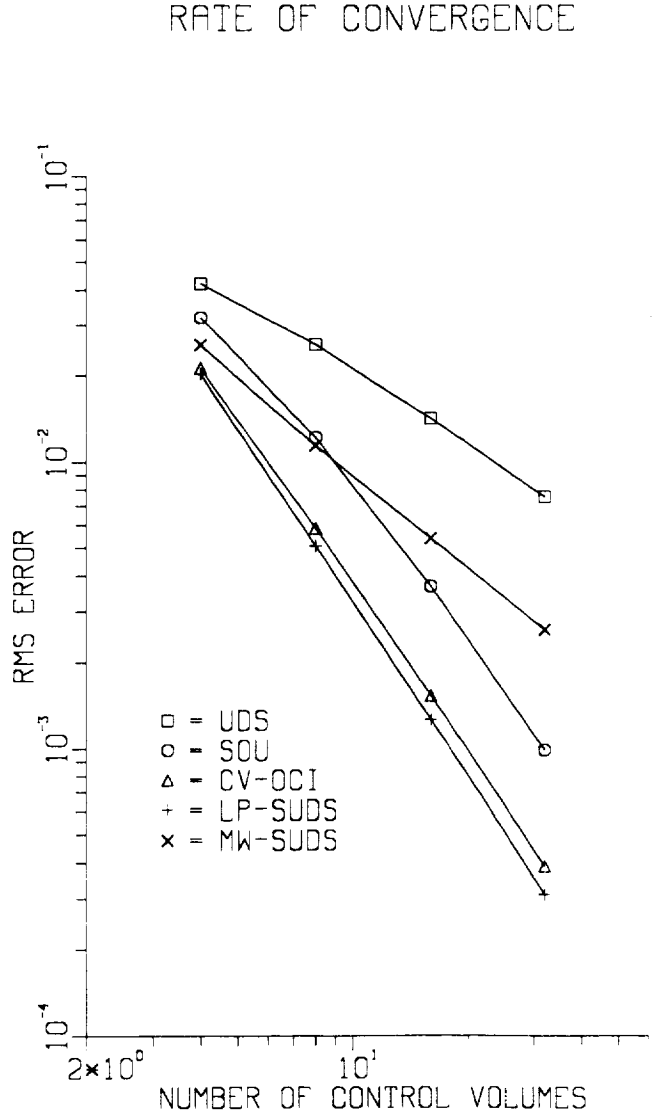

Figure 2: Convergence rate for problem 4.

INFLUENCE OF BULK TURBULENCE AND ENTRANCE BOUNDARY LAYER THICKNESS ON THE CURVED DUCT FLOW FIELD*

Roger A. Crawford and Carroll E. Peters
The University of Tennessee Space Institute
NASA Grant NAG3-617

INTRODUCTION

The objective of this investigation was the experimental evaluation of bulk turbulence and boundary thickness influence on the secondary flow development in a square, 90° turning duct. A three-dimensional laser velocimetry system was utilized to measure the mean and fluctuating components of velocity in the large curved duct facility developed under NASA Contract NAS3-23278. The entrance flow field was conditioned by a combination of increased inlet duct length and square bar turbulence generators. The results from this investigation, with entrance boundary layer thickness of 20-percent and bulk turbulence level of 6-percent, were compared with the thin boundary layer results documented in NASA CR-174811 (Ref 1.).

The three-dimensional development of the viscous shear layers in the curved duct has a strong influence on the complete flow field. Since ducted three-dimensional flows are found in many engineering applications, including gas turbine engines, and contain high turbulence levels and high wall heat transfer rates, they present a difficult challenge to computational fluid mechanics codes. Turbulence modeling remains one of significant constraints to CFD advances due to inadequate physical understanding and experimental definition of turbulent shear flows.

The results of this investigation expand the curved duct data base to higher turbulence levels and thicker entrance boundary layers. The experimental results provide a challenging benchmark data base for computational fluid dynamics code development and validation. The variation of inlet bulk-turbulence intensity provides additional information to aid in turbulence model evaluation.

FACILITY AND INSTRUMENTATION

The experimental facility features modular tunnel components which allow flow measurements every 15° in the 90° bend and at one duct width upstream and downstream of the bend. The 25.4 cm (10 in) square cross-section tunnel is constructed with 13 to 1 area-ratio bell mouth contoured to provide a uniform flow. An additional four duct widths of entrance duct length were fabricated and installed to provide the

*Work done under NASA Grant NAG3-617.

additional boundary layer thickness. Two square-bar turbulence generator grids were fabricated and tested for flow quality and level of turbulence intensity. A 42 percent blockage grid was selected for the experimental investigation, and it produced an average turbulence intensity of 8-percent, two duct widths downstream, and 6-percent, three duct widths downstream of the grid. Reference 2. provided the primary design data for the square bar grids. During the turbulence grid evaluation the curved duct static wall pressures were recorded to evaluate gross flow-field changes by comparison with previous wall pressure data. No significant wall pressure changes were observed.

The primary instrumentation was a three-component laser velocimeter which utilized two color beams and Bragg diffraction beam splitting/frequency shifting to separate the three simultaneous, orthogonal, velocity components. The laser velocimeter signal processors determine the values of velocity from water droplet seed particles crossing the moving fringe probe volume. The data is processed on-line by a minicomputer to yield real time values of mean and fluctuating velocity components, see Ref 1 for a complete description of the LV system. To assure data quality the laser velocimetry data was compared with pitot probe and hot-wire anemometer measurements in the entrance region.

EXPERIMENTAL INVESTIGATION

With the 42 percent blockage turbulence grid located three tunnel widths upstream of the entrance measurement station, detailed velocity surveys were conducted at six stations $(-1D, 0^o, 30^o, 60^o, 90^o, +1D)$. All data was taken at one Reynolds number corresponding to a tunnel bulk velocity of 10 meters/sec. At this test condition the wall boundary layers are fully turbulent ahead of the turbulence grid, and behind the grid typical wall turbulence levels of 10-15 percent remained with a core flow bulk turbulence of 6-8 percent.

The orthogonal laser velocimeter data was processed to yield mean velocity components U, V, W and the fluctuating components $u'v'w'$ calculated from the standard deviation on U, V, W. A minimum of 300 data samples was acquired for each flow field point. Data for each measurement station was acquired by computer controlled precision mill-bed traverse. All data was corrected to standard test conditions and nondimensionalized on duct bulk velocity.

This baseline set of data contains the influence of both thicker entrance boundary layer and bulk turbulence. To evaluate the separate influence of the thicker boundary layer on the downstream flow development,the 60^o station was measured without the grid installed. The two sets of data for the 60^o station contain the separate influences of boundary layer thickness and bulk turbulence.

DATA PRESENTATION AND DISCUSSION

Due the limited space in this paper, only the data from the 60° station will be presented. First it should be noted that both sets of data have very similar flow characteristics, thus the general flow field described by Taylor, Whitelaw, and Yianneskis in reference 3 has not been invalidated by addition of the turbulence grid. Figures 1 and 2 present respectively the axial velocity profiles for the thick boundary layer and thick boundary layer with bulk turbulence. Away from the wall shear layers, the nearly linear velocity gradient across the duct is nearly identical for both flows. The major axial velocity differences occurs in the strong viscous interaction region along the inner wall. The axial velocity results from this investigation and thin boundary layer investigation (Ref 1.) are nearly identical outside of the strong viscous wall interaction region. To satisfy continuity higher center-line velocities are associated with the thicker wall boundary layers. The secondary flow velocities V and W are much more sensitive to the entrance region boundary layer thickness.

The crossflow velocity vector plots for the 60° station show clearly the strong influence of boundary layer thickness on the magnitude of the crossflow velocity (Fig. 3 and 4.) The larger natural turbulent boundary layer produces a strong crossflow development with the "vortex" center located farther from the duct walls. The increased crossflow velocities may be related directly to the axial momentum deficit entering the curved duct. When the turbulence grid is introduced into the developing turbulent boundary layer, the boundary layer is partially re-energized resulting in reduced cross flow velocities as shown in figure 4.

The turbulence intensity distributions for the 60° station are compared in figures 5 and 6. The bulk levels of turbulence at the entrance station were 3 percent and 6 percent respectively for these two flows. The bulk turbulence level has decayed to 4-percent from a level of 8-percent just behind the grid as shown in Figure 6.

The results of this investigation are consistent with the turbulent transport of momentum models. The increase in entrance bulk turbulence from 3-percent to 6-percent has a significant influence on the axial velocity and crossflow development in the curved duct. The wall turbulence intensity and distribution matches the axial shear layer distribution and correlates well with the crossflow velocities, figures 1, 2, 3, 4, 5, and 6.

A complete summary of the data from this investigation has been documented in a NASA report soon to be published and distributed to the HOST participants. This report compares and analyzes the results from both the thick and thin entrance boundary layer investigations and expands the experimental benchmark data base for curved duct flows.

REFERENCES

1. Crawford, R.; Peters, C.; Steinhoff, J.; Nourinejad, J.; and Ramachandran, K.: Mean Velocity and Turbulence Measurements in a 90° Curved Duct with Thin Inlet Boundary Layer. NASA CR 174811, December 1985.

2. Blair, M.; Bailey, D.; and Schlinker, R.: Development of a Large-Scale Wind Tunnel for the Simulation of Turbomachinery Airfoil Boundary Layers. ASME Jol. Vol. 103, October 1981.

3. Taylor, A.; Whitelaw,J.; and Yianneskis, M.: Measurements of Laminar and Turbulent Flow in a Curved Duct with Thin Inlet Boundary Layers. NASA CR 3367, 1981.

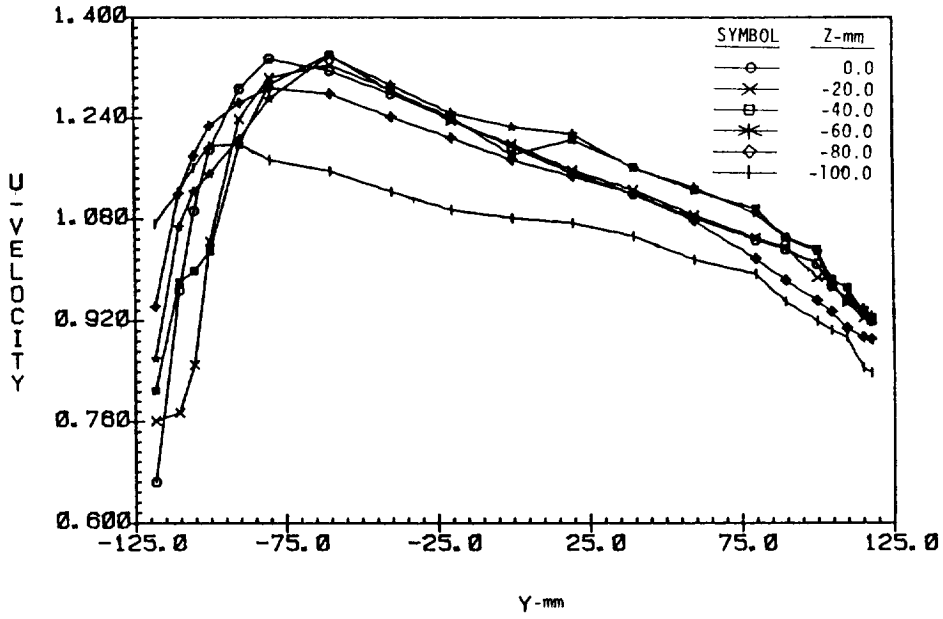

FIGURE 1. AXIAL VELOCITY, 60" STATION THICK TURBULENT BL NO GRID

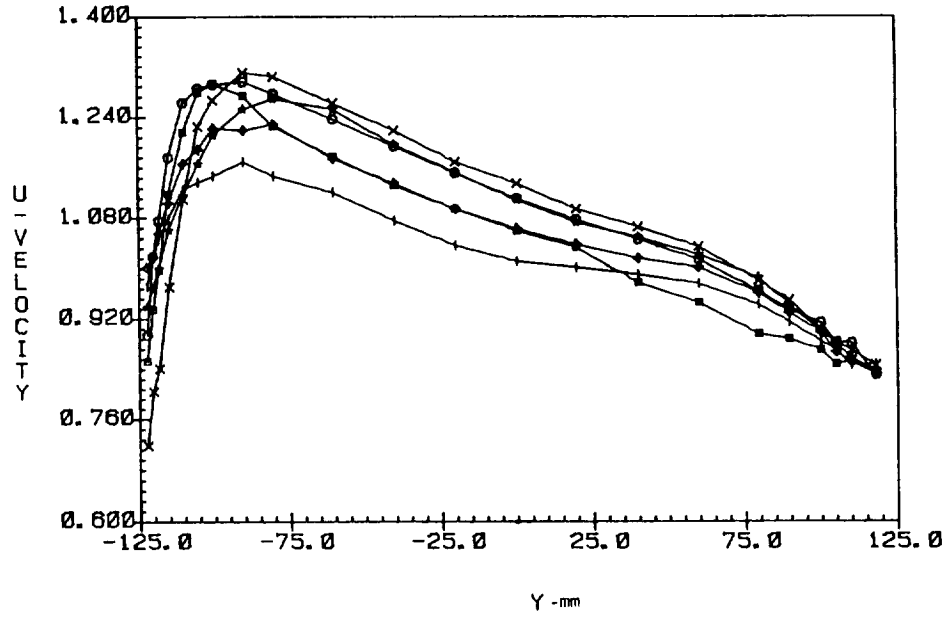

FIGURE 2. AXIAL VELOCITY, 60" STATION THICK TURBULENT BL WITH GRID

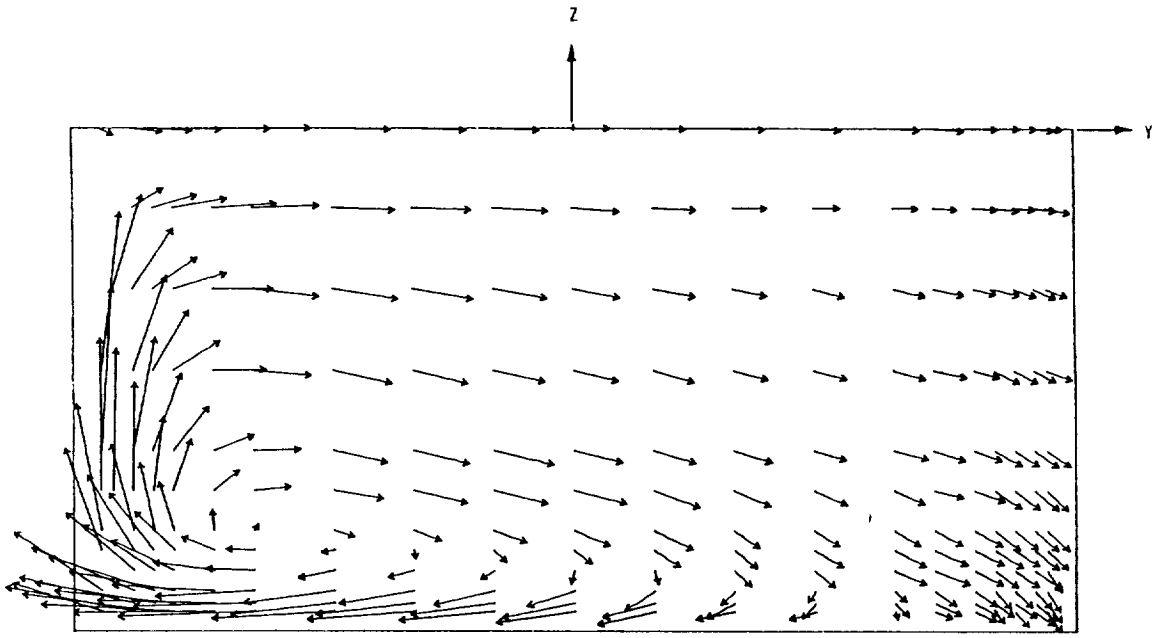

FIGURE 3. CROSS FLOW VELOCITY, 60° STATION THICK TURBULENT BL NO GRID

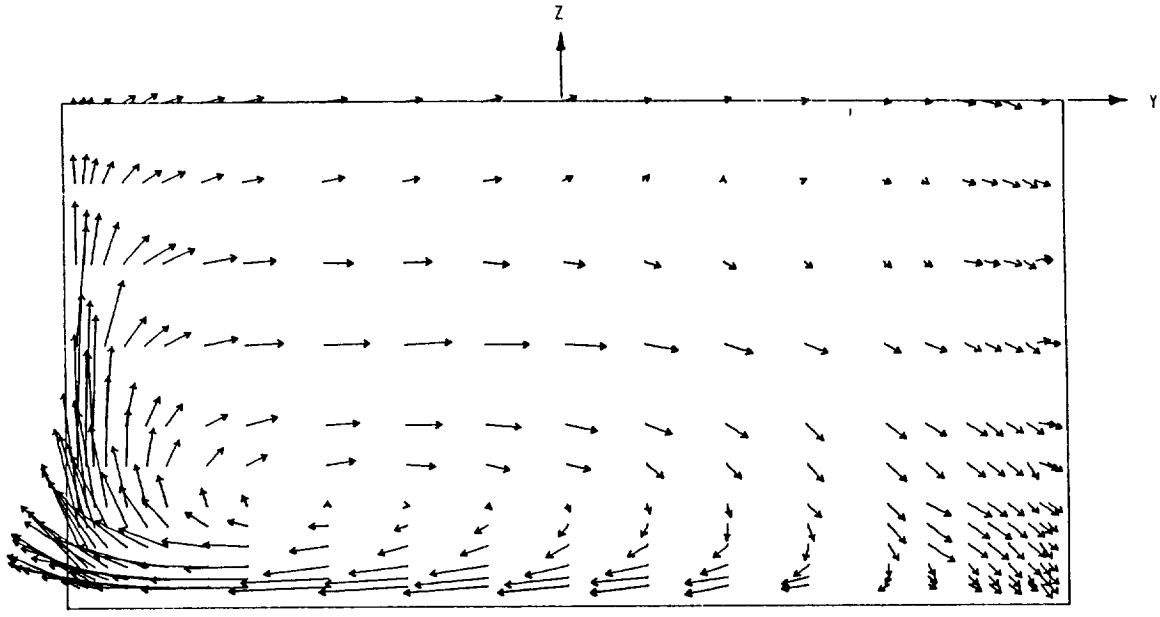

FIGURE 4. CROSS FLOW VELOCITY, 60° STATION THICK TURBULENT BL WITH GRID

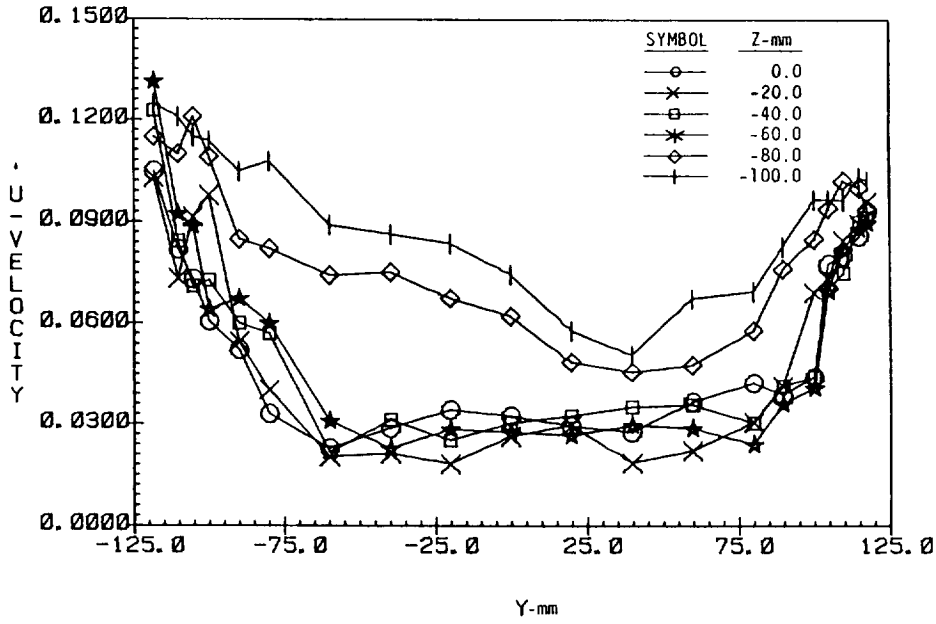

FIGURE 5. AXIAL TURBULENCE INTENSITY, 60° STATION THICK TURBULENT BL NO GRID

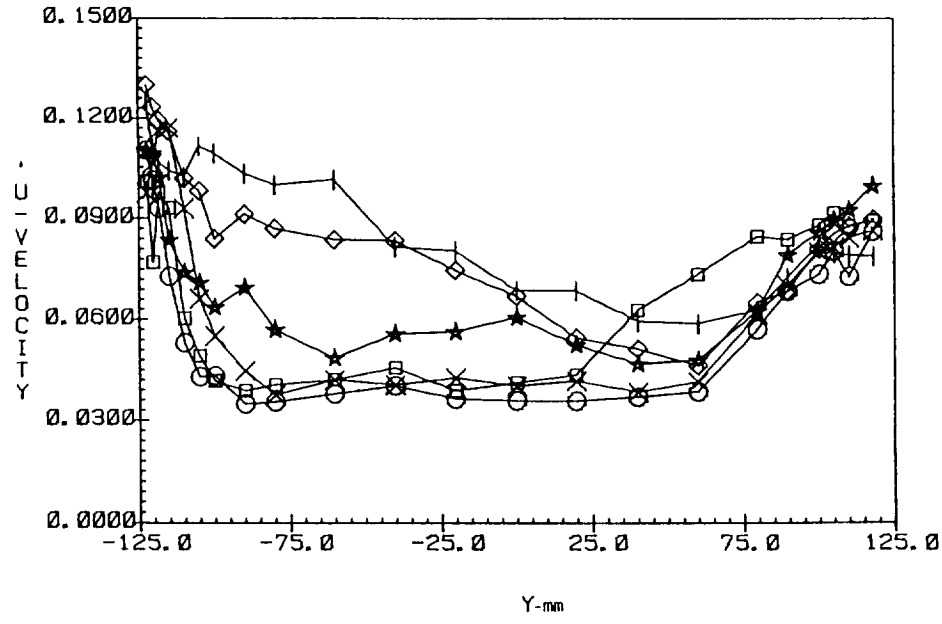

FIGURE 6. AXIAL TURBULENCE INTENSITY, 60° STATION THICK TURBULENT BL WITH GRID

N89-12897

MEASUREMENT OF AIRFOIL HEAT TRANSFER COEFFICIENTS ON A TURBINE STAGE*

Robert P. Dring
Michael F. Blair
H. David Joslyn

United Technologies Research Center
East Hartford, Connecticut 06108

INTRODUCTION

The Primary basis for heat transfer analysis of turbine airfoils is experimental data obtained in linear cascades. These data have been very valuable in identifying the major heat transfer and fluid flow features of a turbine airfoil. The question of major interest is how well all of these data translate to the rotating turbine stage. It is known from the work of Lokay and Trushin (Ref. 1) that average heat transfer coefficients on the rotor may be as much as 40 percent above the values measured on the same blades non-rotating. Recent work by Dunn and Holt (Ref. 2) supports the conclusion of Ref. 1. What is lacking is a set of data from a rotating system which is of sufficient detail as to make careful local comparisons between static cascade and rotor blade heat transfer. In addition, data is needed in a rotating system in which there is sufficient documentation of the flow field to support the computer analyses being developed today. Other important questions include the impact of both random and periodic unsteadiness on both the rotor and stator airfoil heat transfer. The random unsteadiness arises from stage inlet turbulence and wake generated turbulence and the periodic unsteadiness arises from blade passing effects. A final question is the influence, if any, of the first stator row and first stator inlet turbulence on the heat transfer of the second stator row after the flow has been passed through the rotor.

OBJECTIVES

The first program objective is to obtain a detailed set of heat transfer coefficients along the midspan of a stator and a rotor in a rotating turbine stage. These data are to be such that the rotor data can be compared directly with data taken in a static cascade. The data are to be compared to some standard analysis of blade boundary layer heat transfer which is in use today. In addition to providing this all-important comparison between rotating and stationary data, this experiment should provide important insight to the more elaborate full three-dimensional programs being proposed for future research. A second program objective is

*Work done under NASA Contract NAS 3-2317.

to obtain a detailed set of heat transfer coefficients along the midspan of a stator located in the wake of an upstream turbine stage. Particular focus here is on the relative circumferential location of the first and second stators. Both program objectives will be carried out at two levels of inlet turbulence. The low level will be on the order of 1 percent while the high level will be on the order of 10 percent which is more typical of combustor exit turbulence intensity. The final program objective is to improve the anlytical capability to predict the experimental data.

DESCRIPTION OF EXPERIMENTAL EQUIPMENT AND TEST CONDITIONS

The experimental portion of this study was conducted in large-scale (aproximately 5x engine), ambient temperature, rotating turbine model configured in both single stage and stage-and-a-half arrangements. A cross-sectional diagram of the turbine model in the stage-and-a-half configuration is presented in Figure 1. Heat transfer measurements were obtained using low-conductivity airfoils with miniature thermocoulpes welded to a thin, electrically heated surface skin. Heat transfer data were acquired for various combinations of low or high inlet turbulence intensity, flow coefficient, first-stator/rotor axial spacing, Reynolds number and relative circumferential position of the first and second stators. High levels of inlet turbulence were generated using a coarse biplane grid located 2 1/2 axial chords upstream of the stator leading edge plane(see Figure 1). Aerodynamic measurements obtained as part of the program include distributions of the mean and fluctuating velocities at the turbine inlet and, for each airfoil row, midspan airfoil surface pressures and circumferential distributions of the downstream steady state pressure and fluctuating velocities.

Time-mean velocity distributions at the inlet to the turbine model, obtained both with and without the turbulence grid installed, are presented in Figures 2a and 2b. These figures indicate that, both with and without the grid, the spanwise variations of mean velocity at each pitch location were quite small and that the pitchwise velocity variations were in excellent agreement with a potential flow prediction. The distributions of streamwise turbulence intensity measured with and without the grid are presented in Figure 3. As shown in Figure 3a, with the grid out the midspan region turbulence intensity was slightly greater than 1/2% with much higher levels in the endwall boundary layers. With the grid in, as shown in Figure 3b, the midspan turbulence intensity averaged 9.8%. Spectral measurements of the grid generated turbulence indicated that it was in excellent agreement with the von Karman isotropic spectrum.

RESULTS

Distributions of heat transfer along the various airfoil surfaces are presented as Stanton numbers based on exit conditions vs dimensionless

surface distance. Included in each figure are the specific flow coefficient and axial spacing for the data set and a note indicating whether the turbulence grid was IN or OUT.

Midspan first stator heat transfer distribution data obtained for the single-stage configuration for three Reynolds numbers and low inlet turbulence are presented in Figure 4. The experimental data are compared to distributions predicted by the UTRC two-dimensional finite difference boundary layer code (ABLE, Ref.3). Predictions for both fully laminar (L) and fully turbulent (T) flow (Cebeci-Smith, Ref.4) are included. On the pressure surface, agreement with the fully laminar prediction was excellent for all three Reynolds numbers. Evidence of possible boundary layer transition near the pressure surface trailing edge progressively decreased with decreasing Reynolds number. On the suction surface the agreement between the laminar prediction and the upstream half of the data was also excellent in all cases. A careful examination of the data near S/Bx=1 indicates that transition moved progressively, albeit slightly, downstream as Reynolds number decreased. Finally for S/Bx>1 both the highest andlowest Re data agreed very well with the two-dimensional fully turbulent prediction. For $Re=52x10^4$ an anamolous discrepancy of about 10% between theory and data resulted for this region. One possible explanation for this shift is that an undetected shift in model heater power occured during the process of automatic data acquisition.

The primary conclusion reached from Fig. 4 is that the facility, turbine model and instrumentation system all behaved as expected. As the Reynolds number changed for this relatively idealized first stator flow the data and two-dimensioinal theory remained in excellent agreement.

Rotor heat transfer distributions for the single-stage configuration are presented in Figure 5 for three Reynolds numbers. Again each data set is shown compared with the two-dimensional fully turbulent prediction for that particular Reynolds number. On the suction surface there was an increasingly significant, both in size and heat transfer level, transitional region as the Reynolds number dropped. For all cases, however, the heat transfer data agreed reasonably well with the two-dimensional, fully turbulent boundary layer prediction in the trailing edge region.

The rotor pressure surface heat transfer distributions shown in Figures 5 reveal a dependence on the Reynolds number. At the lightest Reynolds number the pressure surface heat transfer is significantly higher (50 to 80% higher) than the fully turbulent prediction. As the Reynolds number drops the data approach their respective predictions. Elevated levels of pressure surface heat transfer were observed for numerous airfoil-flow condition combinations in this investigation. Discussion of the phenomenon will follow as more examples are presented.

The effects on the first stage heat transfer distributions produced by raising the inlet turbulence intensity are shown in Figure 6. The impact of the high inlet turbulence on the first stator distribution was dramatic

with significant increases of heat transfer on the leading edge and along both suction and pressure surfaces. On the suction surface the increased turbulence moved the location of transition well upstream from S/Bx=1.0 to about S/Bx=0.3. For this high level of turbulence, then, transition occured in a region of accelerating flow instead of near the minimum pressure point. Another effect of the turbulence on the suction surface distribution was to produce considerably enhanced heat transfer in the fully turbulent region of the flow. The effect of the higher turbulence level was also very evident along the stator pressure surface. For the low turbulence case the heat transfer was essentially laminar while with high turbulence the measured heat transfer was as much as 60% greater than the two-dimensional fully turbulent prediction. The data of Figure 6a constitute another example of an airfoil-flow condition combination for which the measured/pressure surface heat transfer far exceeded fully turbulent levels.

On the rotor, Figure 6b, the effects produced by increasing the inlet turbulence were much less dramatic than for the first stator. A much smaller change to the heat transfer resulted for the rotor because even the baseline (low inlet turbulence) rotor flow is highly disturbed by the first stator wakes. The incremental change in the distrubance level produced by installing the grid was much less for the rotor than for the first stator. On the rotor suction surface, transition appears to have moved upstream to S/Bx$\sim$0.2 with the increased turbulence level. Changes downstream of transition in the fully turbulent region were negligible. The only region of the rotor pressure surface which showed any effects from the increased turbulence was from $-0.5<S/Bx<0$.

Figure 7 displays the impact of Reynolds number on the first stator heat transfer distributions with high inlet turbulence. On the suction surface Figure 7 shows an orderly, progressive downstream movement of the transition zone with decreasing Reynolds number. As the Reynolds number decreased the length of the near-laminar heat transfer zone increased and the length of the fully turbulent zone contracted. On the pressure surface the data show that for the highest Reynolds number the measured heat transfer greatly exceeded the turbulent prediction while for $Re < 4x10^5$ there was near agreement between theory and experiment.

A number of examples have been presented in which pressure surface heat transfer rates significantly exceeded two-dimensional, fully turbulent predictions. These results indicate that there can be an interaction between the effects of concave surface curvature, Reynolds number and the level of free-stream disturbance that may produce significant heat transfer enhancement. One possibility is that for certain critical combinations of surface curvature, Re_θ, acceleration and free-stream disturbance level, important Goertler vortex systems are produced in the boundary layer.

Rotor heat transfer distributions obtained for an extremely wide range of test flow coefficients are presented in Figure 8. These results reflect operation at severe off-design conditions and are included to demonstrate the impact on heat transfer for such extreme excursions. On the suction surface, for S/Bx<0.7, the local Stanton numbers decreased with Cx/U until

they approached laminar heat transfer rates. On the pressure surface there was a continuous, systematic increase in Stanton numbers through the entire range of test flow coefficients. The appearance of the distributions suggests that for Cx/U <0.5 the flow probably separated from the pressure surface. At these extreme negative incidence values the heat transfer was evidently dominated by a large, possible unsteady, pressure surface separation bubble.

Heat transfer distributions measured on the second stator are presented in Figure 9. These data were obtained for five relative circumferential positions of the first and second stators with and without the grid.

Probably the most striking feature of the second stator heat transfer distributions, both for the grid-in and grid-out are the very high values of Stanton number relative to the two-dimensional turbulent boundary layer prediction. On the pressure surface the heat transfer data are 50-100% above the prediction, a result which is in general agreement with most of the first stator and rotor pressure surface measurements. On the suction surface, however, the second vane heat transfer is entirely different from the first stage results. Not only are the suction surface heat transfer data well in excess of the two-dimensional prediction but the data and theory are diverging with increasing S. It appears that by the second stator the flow field has become so contaminated by secondary flow that a two-dimensional model is inappropriate. The effects associated with stator 1/stator 2 relative location appear to have been minor.

A detailed distribution of the heat transfer measured in the leading edge region of the first stator with the grid in is given in Figure 10. For these figures the heat transfer data are presented in the form of the Froessling number $Nu/\sqrt{Re_D}$ where the Reynolds number is based on the diameter of the leading edge. Locations are given as S/R_N, the surface distance divided by the nose radius. Note that, unlike a cylinder in crossflow, the theoretical heat transfer distribution is not symmetrical about the stagnation point. In addition, since the acceleration is very much stronger in the direction of the suction surface, the maximum predicted heat transfer rate is not at the stagnation point. The results of Figure 10 are quite surprising in that the heat transfer measured for the highly turbulent test flow was only about 20% greater than the predicted laminar levels. Data taken in a number of studies of cylinders in crossflows have indicated that freestream turbulence has a very strong effect on the stagnation region heat transfer (see Lowery and Vachon, Ref.5). It may be that the effects of turbulence are much larger for free cylinders than for airfoil leading edges.

A comparison of the heat transfer distribution measured in a previous investigation in a cascade (Ref.6) with the data obtained on the rotor of the present study is presented in Figure 11. These two data sets were obtained at somewhat different Reynolds numbers so predicted heat transfer distributions are given for both conditions. An examination of Figure 11 indicates that, on the suction surface, transition was somewhat earlier for the rotating case than for the blade cascade. This result is not

surprising as the disturbance level for the rotating blade was considerably higher than the 1% turbulence level at the entrance plane of the cascade. When allowance is made for the effect of Reynolds number, the post-transitional (S/Bx > 0.8) results for the rotating and cascade tests were practically identical. There was, however, a significant difference between the heat transfer distributions measured on the pressure surface with the cascade data falling well below the set from the rotating blade. This provides an additional piece of evidence which indicates that strong enhancement of fully turbulent, concave surface heat transfer may only occur for high levels of free-stream disturbance. Whatever the cause, the major difference between the rotating and non-rotating airfoil midspan heat transfer distributions was the considerably higher levels on the pressure surface of the rotating airfoil.

The heat transfer data measured in the leading edge region of the cascade airfoils are presented in Figure 12. Included in Figure 12 are the predicted laminar distributions for this airfoil as well as the comparable leading edge data from the rotating cases. Because of the instrumentaiton techniques employed the experimental uncertainty is considerably greater for the cascade leading edge data than for the rotating airfoil. Despite the data scatter associated with the cascade model it is still clear that the stagnation region heat transfer was reasonably well predicted by the laminar model. There was no evidence that the moderate (1%) free-stream turbulence in the cascade tunnel substantially enhanced the heat transfer in the leading edge region of the airfoil.

REFERENCES

1. Lokay, V. I., and Trushin, V. A.: Heat Transfer from the Gas and Flow-Passage Elements of a Rotating Gas Turbine. Heat Transfer-Soviet Research, Vol. 2., No. 4, July, 1970.

2. Dunn, M. G., and Holt, J. L.: The Turbine Stage Heat Flux Measurements. Paper No. 82-1289, AIAA/ASME 18th Joint Propulsion Conference, 21-23, June, 1982, Cleveland, Ohio.

3. Carter, J. E., D. E. Edwards and M. J. Werle: Coordinate Transformation for Laminar and Turbulent Boundary Layers, AIAA Journal, Vol. 20, No. 2, February 1982, pp. 282-284.

4. Cebeci T. and A. M. O. Smith: Analysis of Turbulent Boundary Layers, Academic Press, 1974.

5. Lowery, G. W. and Vachon, R. I.: The Effect of Turbulence on Heat Transfer From Heated Cylinders, IJHMT, Vol. 18, 1975, pp.1229-1242.

6. Graziani, R. A., M. F. Blair, J. R. Taylor and R. E. Mayle: An Experimental Study of Endwall and Airfoil Surface Heat Transfer in a Large Scale Turbine Blade Cascade, ASME Journal of Eng. for Power, Vol. 102, April 1980, pp. 257-267.

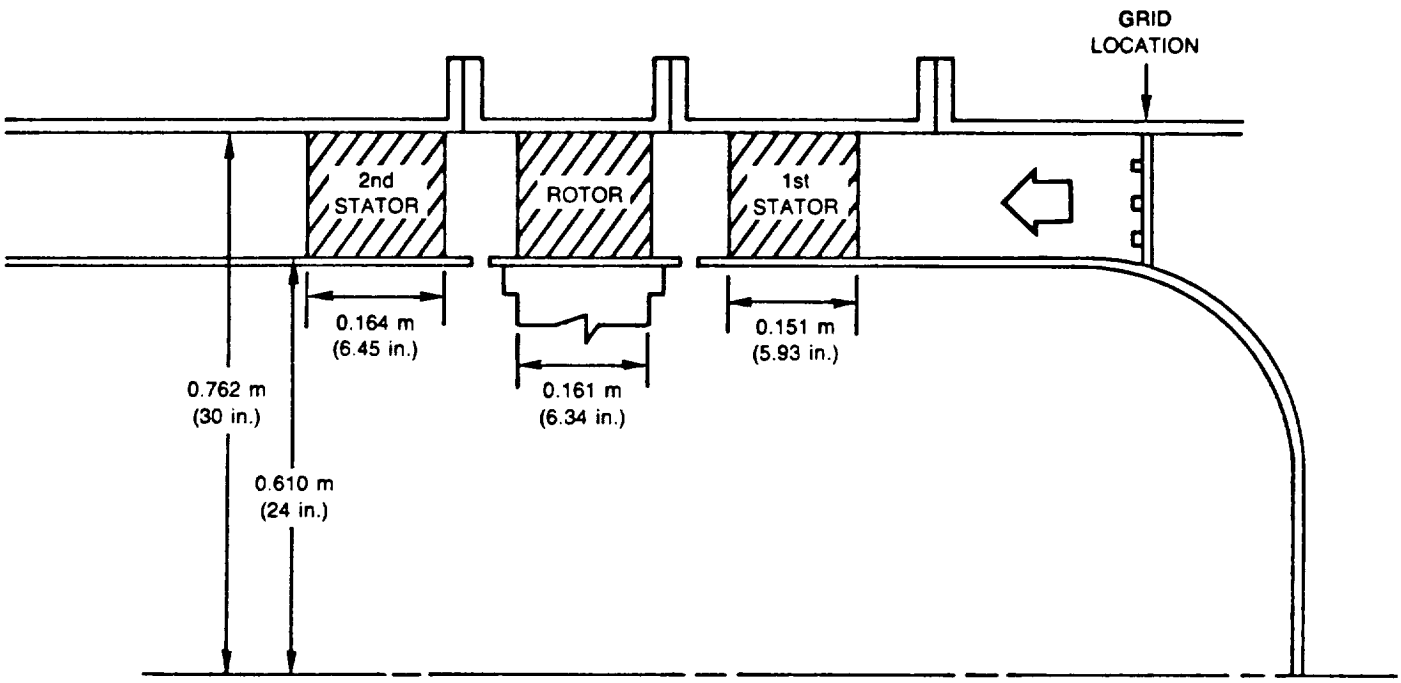

Figure 1 United Technologies Research Center Large Scale Rotating Rig.

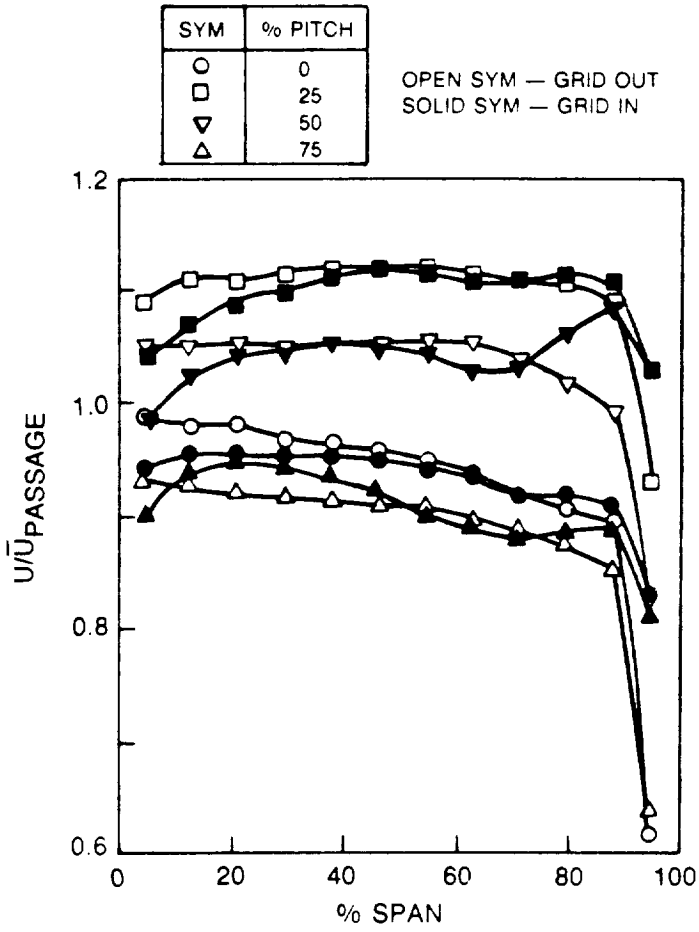

a) SPANWISE DISTRIBUTIONS OF THE TEMPORALLY AVERAGED STREAMWISE VELOCITY AT VARIOUS PITCH LOCATIONS

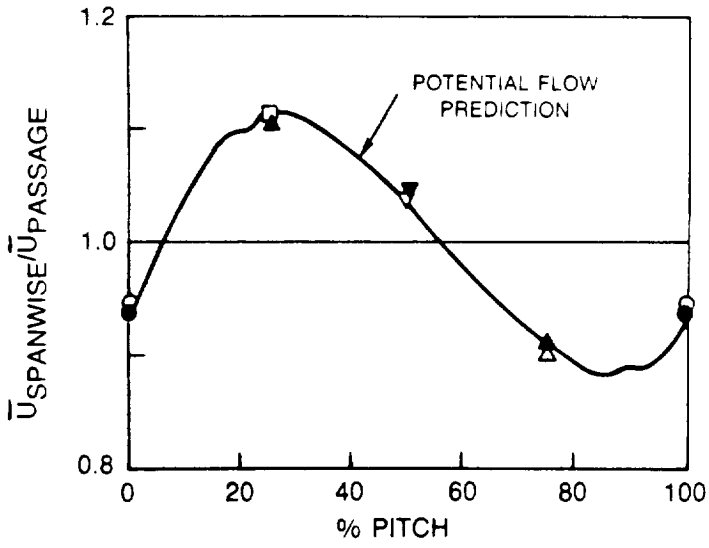

b) SPANWISE AVERAGED STREAMWISE VELOCITIES

Figure 2 Distributions of the Mean Velocity at X=-3.4cm (-23% Bx).

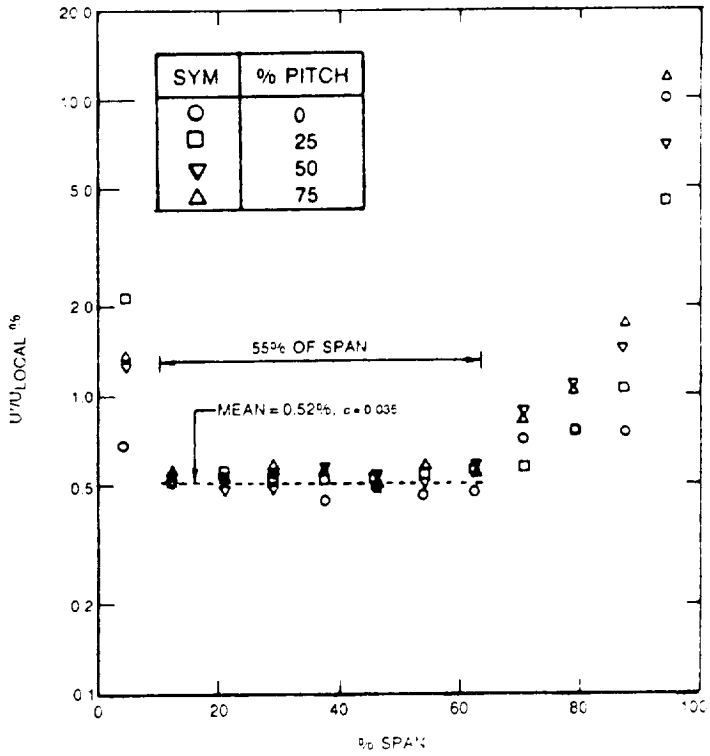

a) GRID OUT

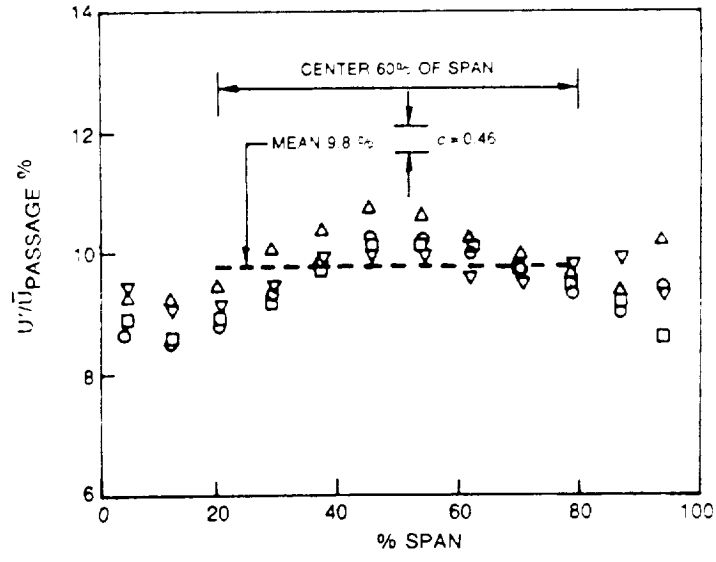

b) GRID IN

Figure 3 RMS Level of the Streamwise Component of Turbulence at X=-3.4cm (-23% Bx) at Various Pitch Locations.

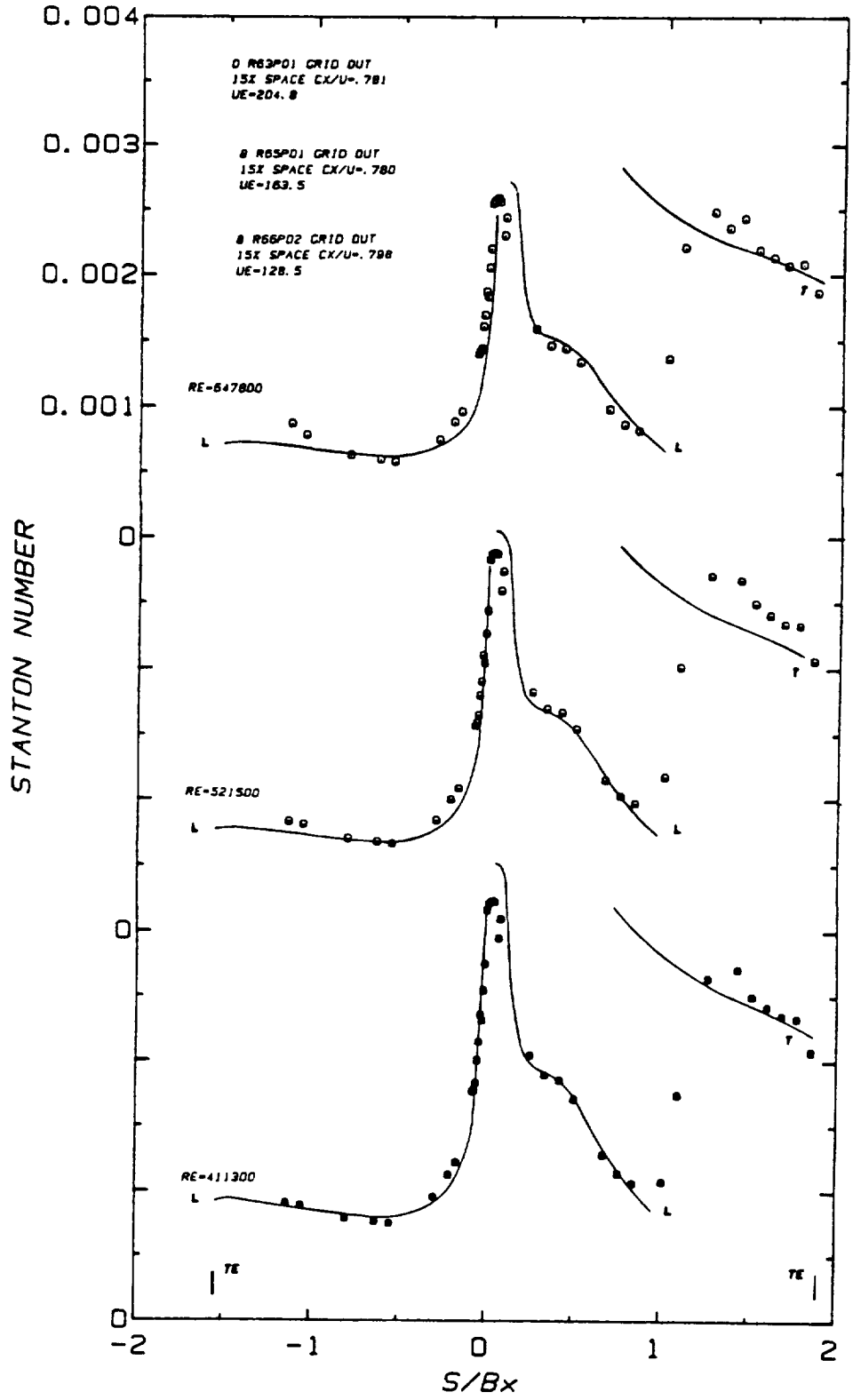

Figure 4 Effect of Reynolds Number on the Stator Heat Transfer, Grid Out.

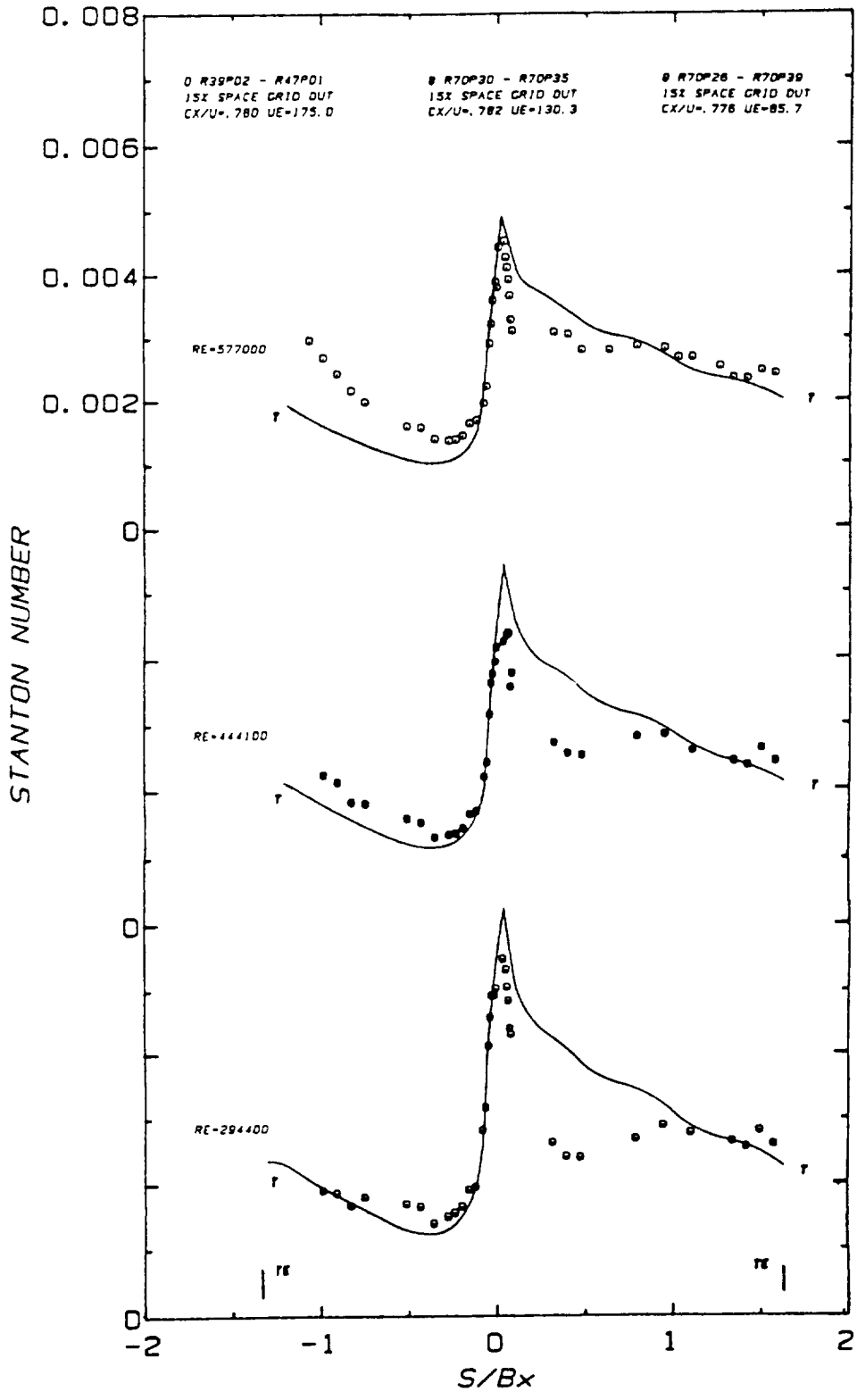

Figure 5 Effect of Reynolds Number on the Rotor Heat Transfer, Design Flow Coefficient, Grid Out.

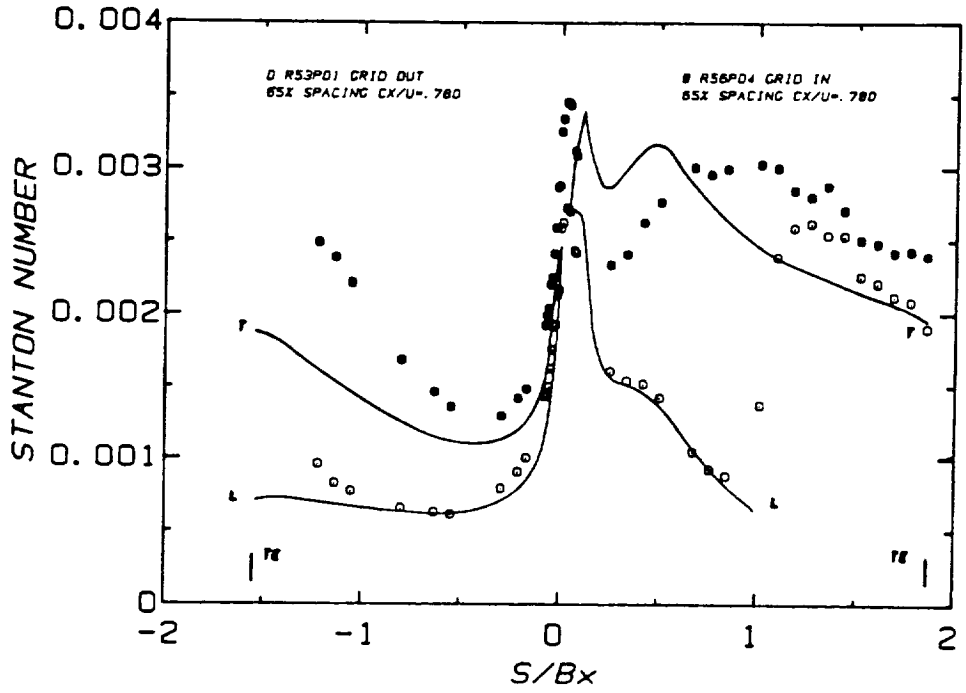

a) SINGLE-STAGE STATOR

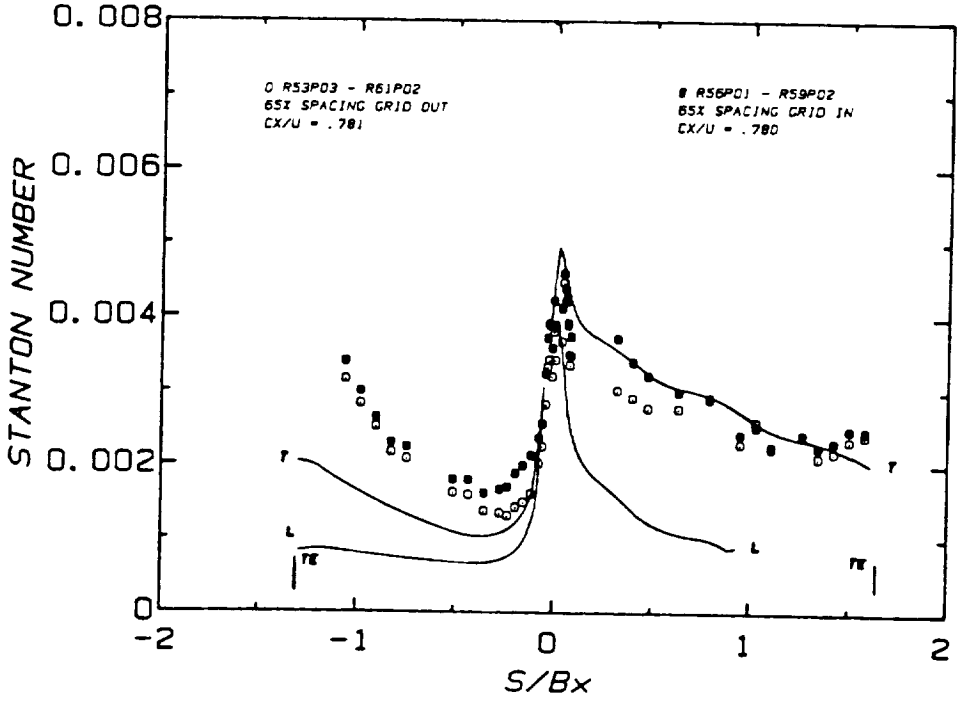

b) SINGLE-STAGE ROTOR

Figure 6 Effect of Free-Stream Turbulence on the Stator and Rotor Heat Transfer for the Single-Stage Configuration and Design Flow Coefficient.

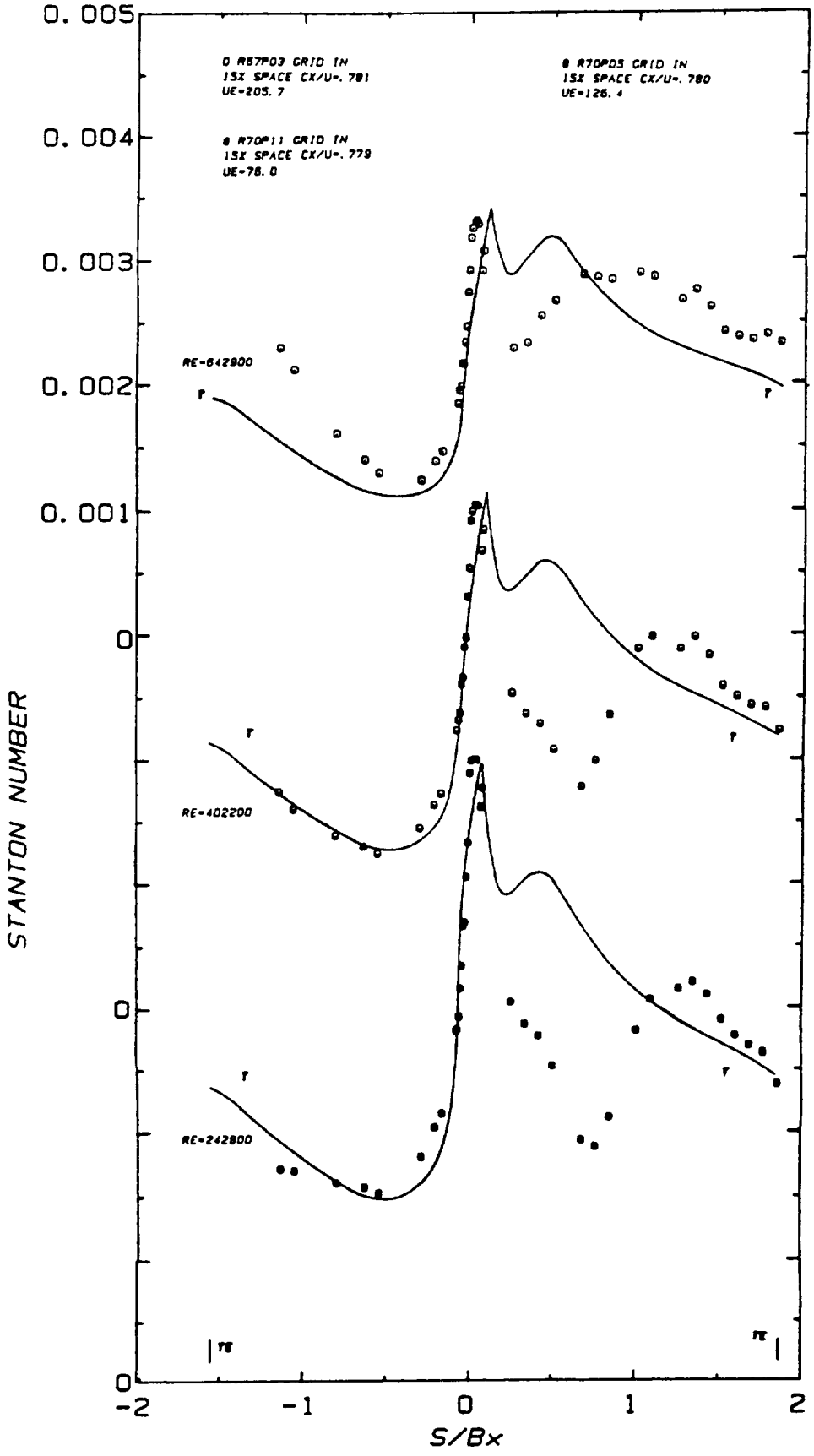

Figure 7 Effect of Reynolds Number on the Stator Heat Transfer, Grid In.

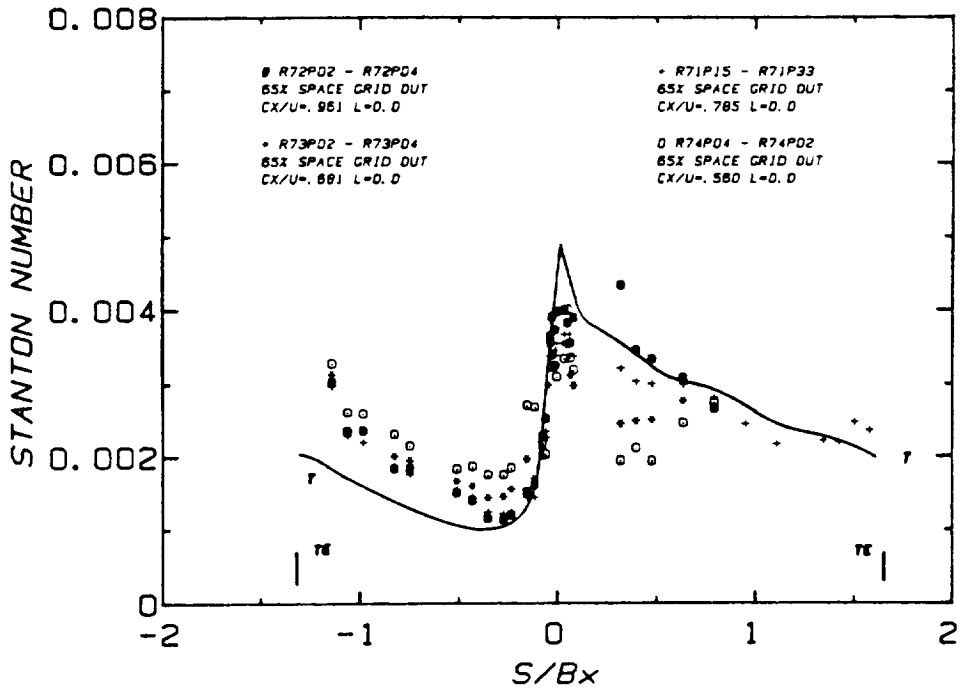

a) Cx/U = 0.96, 0.79, 0.68 and 0.56

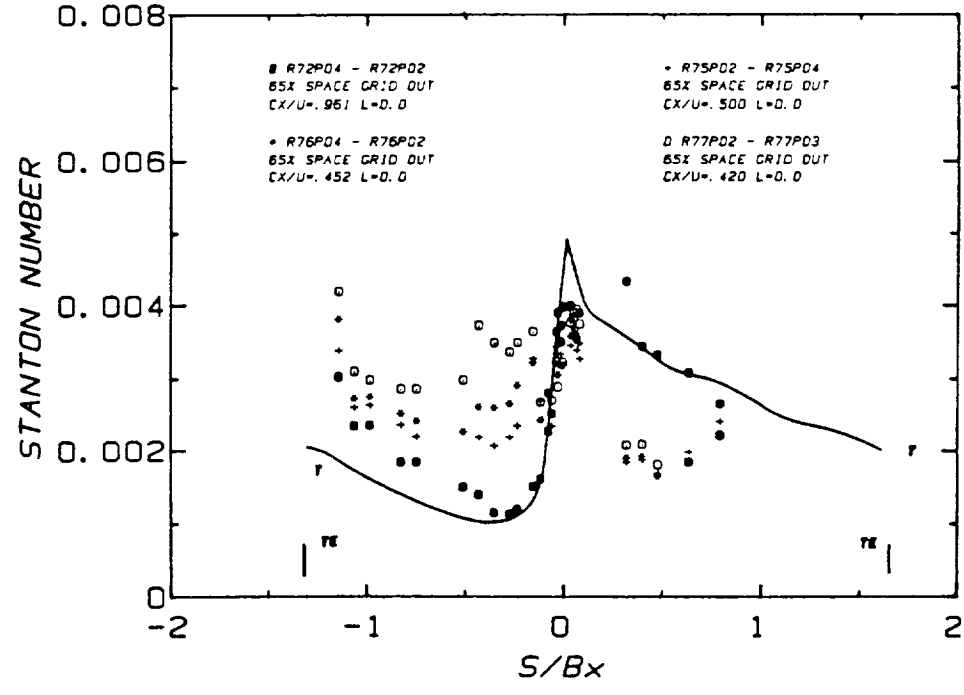

b) Cx/U = 0.96, 0.50, 0.45 and 0.42

Figure 8 Effect of Extreme Variation of the Flow Coefficient on the Rotor Heat Transfer Distribution, 1-1/2 Stage Configuration, Grid Out.

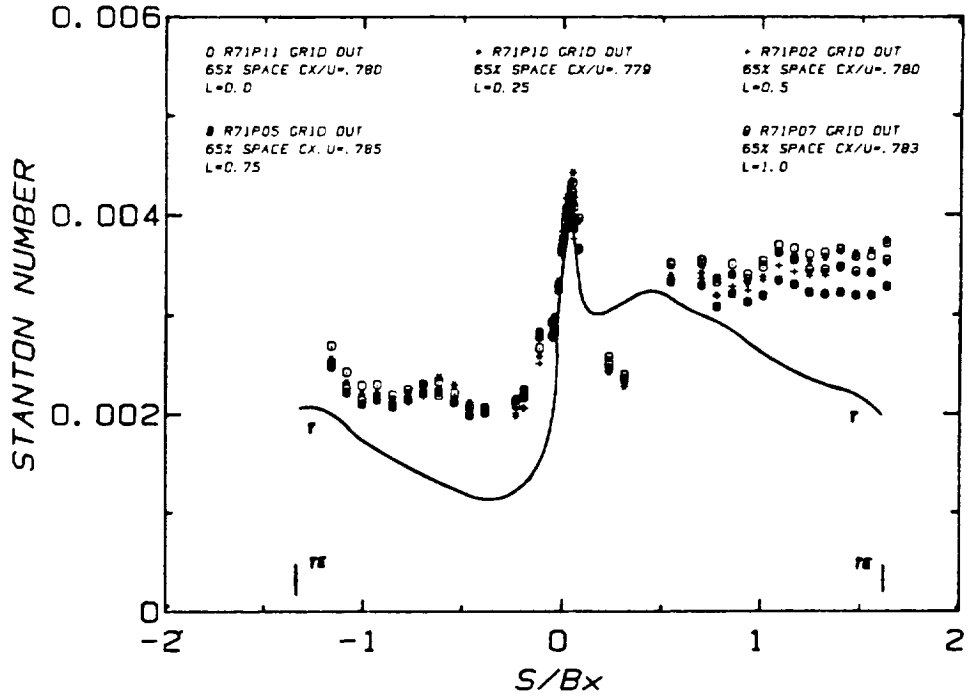

a) GRID OUT

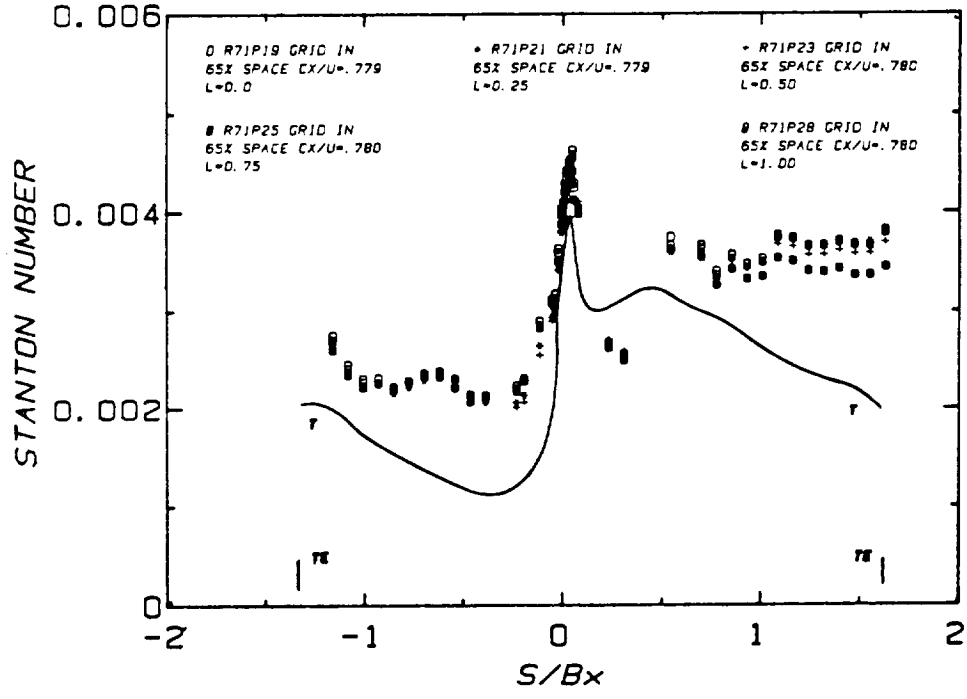

b) GRID IN

Figure 9 Effects of the Upstream Grid and the Relative Circumferential Positions of the First and Second Stators on the Second Stator Heat Transfer, 1-1/2 Stage Configuration, Design Flow Coefficient.

DATA SETS	Re_N RANGE	Re_{BX} RANGE
R66P05 R70P04 R67P02 R70P05 R67P03 R70P07 R70P02 R70P11	13280-36080	242800-642800

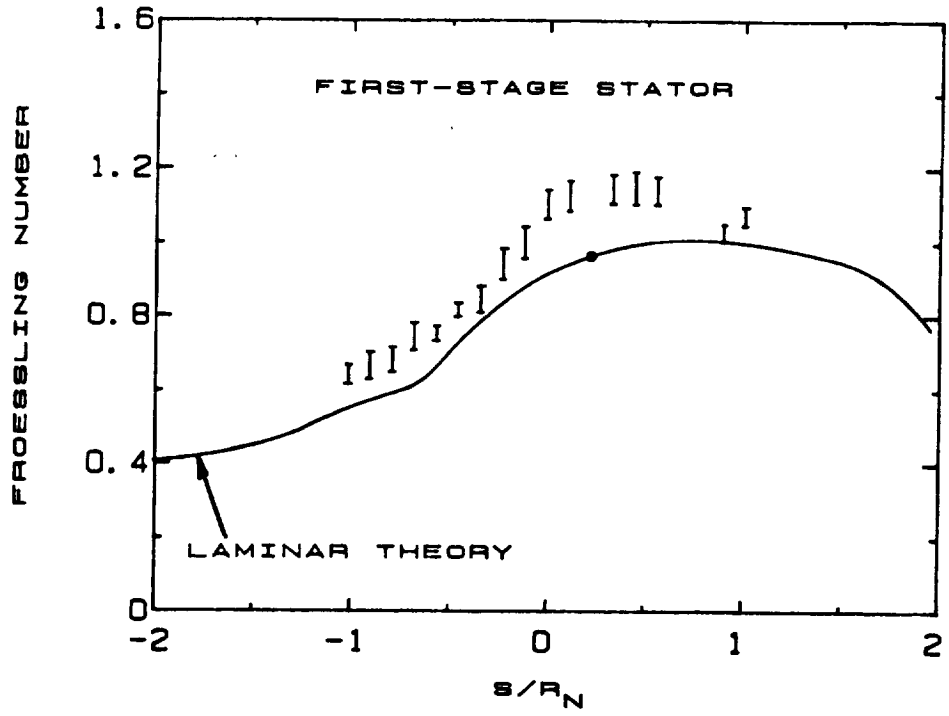

Figure 10 Measured and Predicted Heat Transfer Distributions for the Leading Edge Region of the First-Stage Stator. Data Obtained Over a Range of Reynolds Numbers With the Upstream Grid In.

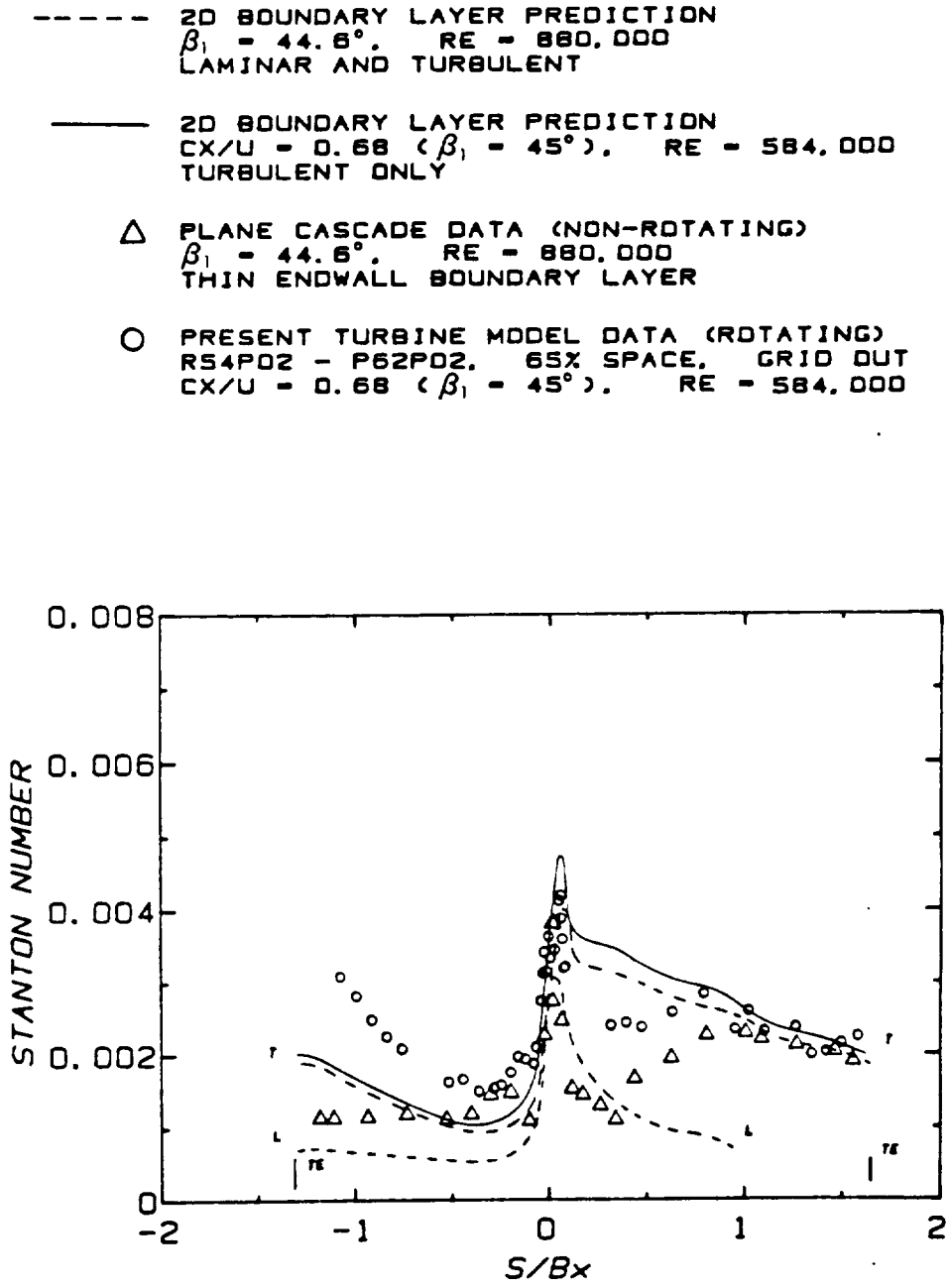

Figure 11 Comparison of Measured and Predicted Heat Transfer Distributions for the Rotor in the Present Rotating Turbine Model and the Same Airfoil Midspan Geometry Installed in a Plane Cascade (Non-Rotating).

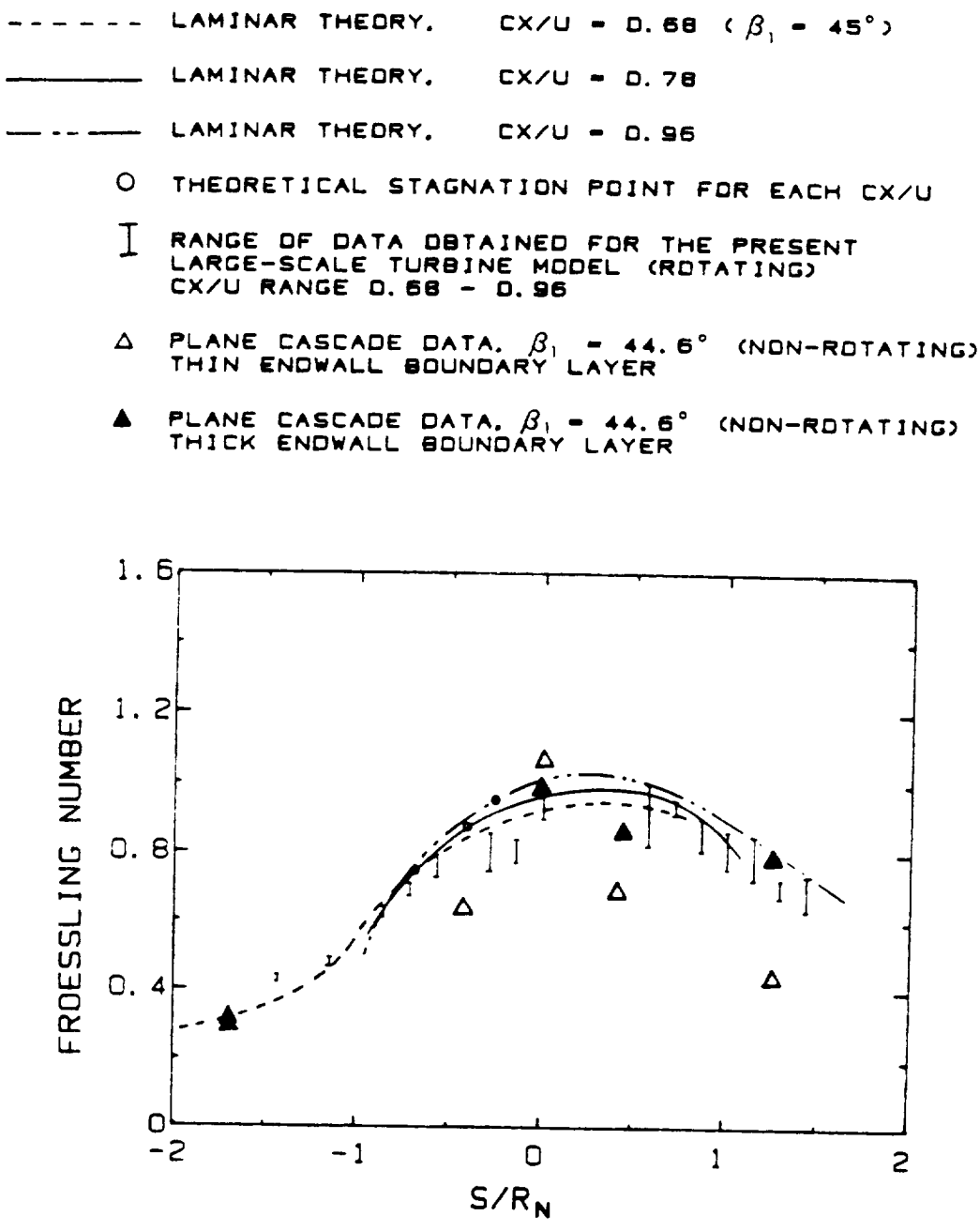

Figure 12 Comparison of Measured and Predicted Heat Transfer Distributions for the Leading Edge Region of the Rotor. Data Obtained on the Present Rotating Turbine Model and for the Same Airfoil Midspan Geometry Installed in a Plane Cascade (Non-Rotating).

HEAT TRANSFER IN THE TIP REGION OF A ROTOR BLADE SIMULATOR*

M.K. Chyu, H.K. Moon and D.E. Metzger
Mechanical and Aerospace Engineering Department
Arizona State University
Tempe, AZ 85287

INTRODUCTION

In gas turbines, the blades of axial turbine stages rotate in close proximity to a stationary peripheral wall (sometimes termed an outer ring or stationary shroud). Differential expansion of the turbine wheel, blades, and the shroud causes variations in the size of the clearance gap between blade tip and stationary shroud. The necessity to tolerate this differential thermal expansion dictates that the clearance gap cannot be eliminated altogether, despite accurate engine machining [1].

Pressure differences between the pressure and suction sides of a blade drives a flow through the clearance gap. This flow, often referred as the "tip leakage" flow, is detrimental to engine performance. The primary detrimental effect of tip leakage flow is the reduction of turbine stage efficiency, and a second important effect concerns the convective heat transfer associated with the flow. The surface area at the blade tip in contact with the hot working gas represents an additional thermal loading on the blade which, together with heat transfer to the suction and pressure side surface area, must be removed by the blade internal cooling flows [2].

Very limited information on turbine tip heat transfer and fluid flow has been reported to date [3-6], and almost all of the published work dealing with clearance gap flows involves consideration only of plain flat blade tips. However, a strategy commonly employed to reduce tip flow and heat transfer is to groove a single rectangular cavity chordwise along the blade tip. The groove acts like the cell of a labyrinth seal to increase the pressure drop and thus reduce the flow for a given pressure differential across the tip. The reduction of the flow will also act to reduce heat transfer. A schematic diagram representing the geometry of a grooved blade tip, viewed from a coordinate system fixed relative to the blade, is shown in Fig. 1. As seen in the figure, the outer shroud can be considered moving in the general direction from the suction side to the pressure side, with relative velocity equal to U_w. The leakage flow, its mean value denoted by $\bar{U}$, is driven by the pressure difference between two sides of the blade and flows in the direction opposite to the shroud motion.

*Work done under NASA Grant NAG 3-623

C-3

With this general configuration in mind, the grooved tip problem can be categorized as fluid flow and heat transfer over a shrouded rectangular cavity.

Both fluid flow and heat transfer over unshrouded, rectangular cavities have been the subjects of extensive investigation for many years [7]. The flow field over a cavity is characterized by flow separation and shear layer reattachment resulting in complex flow patterns with substantial effects on the friction drag and heat transfer. Most studies have relied on flow visualization techniques and/or heat and mass transfer data to obtain momentum and heat transfer information in cavity flow [8-10]. In all cases, the cavity problems studied have been considered as a flow system in which the cavity is open to a usually well-specified approaching flow over an otherwise smooth and stationary surface. The approaching flow may be a wall boundary layer for external flow or a well developed channel flow.

The grooved tip differs from the aforementioned unshrouded situation by virtue of the confined nature of the geometry as well as by the proximity of moving shroud. The degree of similarity between the heat transfer characteristics of the grooved tip and those of previous cavity studies has been unclear until recently. Metzger and Bunker [11], using a time-dependent paint coating technique, studied the heat transfer for flow through a confined narrow slot-type channel where one of the bounding walls contains a rectangular cavity. The effect of shroud motion is not included in this study. Details of heat transfer on the cavity surfaces are found to be largely dependent on the size of gap clearance and the cavity aspect ratio. A semi-empirical study by Mayle and Metzger [6], using a plain tip geometry, has argued that the heat transfer from the blade tip is essentially unaffected by the relative motion between blade and shroud. This speculation, however, has not been justified for the grooved tip situation. To gain further understanding of the convective heat transfer in cavities with various degrees of relative shroud motion is the primary objective of this study.

In the present work, experimental results concerned with the local heat transfer characteristics on all surfaces of shrouded, rectangular cavities are reported. The varying parameters include the cavity depth-to-width ratio, D/W, gap clearance-to-cavity width ratio, C/W, relative shroud moving speed, $U_w/\bar{U}$, Reynolds number, $Re = \bar{U}C/\nu$, and relative orientation between the leakage flow direction and shroud movement. Due to the problems associated with imperfect thermal insulation and temperature depression, local studies using direct heat transfer measurement are known to be difficult to perform and could induce significant error. The naphthalene ($C_{10}H_8$) sublimation mass transfer technique is instead employed herein facilitating better control of the experiment. The mass transfer results can be transformed into their counterparts in heat transfer by invoking an analogy between those two transfer processes. More detailed description of the analogy can be found in [12]. A brief discussion of the mass transfer system used in this study is given as follows.

SUBLIMING MASS TRANSFER SYSTEM

The mass transfer coefficient h_m is given by

$$h_m = \frac{\dot{m}}{\rho_{v,w} - \rho_\infty} \tag{1}$$

where, $\dot{m}$ is the mass transfer flux of naphthalene from a surface, $\rho_{v,w}$ is the vapor concentration of naphthalene at the surface, and ρ_∞ is the vapor mass concentration at the inlet of gap passage. In the present study, ρ_∞ is zero and Eq. (1) becomes

$$h_m = \frac{\dot{m}}{\rho_{v,w}} \tag{2}$$

In addition, as the mass transfer system is essentially maintained isothermal, the naphthalene vapor pressure and vapor concentration at the surface are constant. This corresponds to a constant wall temperature boundary condition in a heat transfer study.

Local mass transfer from a naphthalene surface can be evaluated from the change in naphthalene thickness. The change of thickness due to sublimation is given by

$$dy = \frac{\dot{m} \cdot dt}{\rho_s} \tag{3}$$

where ρ_s is the density of solid naphthalene ($\simeq 1.143$ gm/cm^3), and dy and dt represent the change in naphthalene thickness and the differential time duration, respectively. Note that dy and $\dot{m}$ are functions of the local coordinate of the subliming surface. Combining Eqs. (2) and (3), and integrating over the test duration yield the time-averaged, local mass transfer coefficient

$$h_m = \frac{\rho_s \cdot \Delta y}{\rho_{v,w} \cdot \Delta t} \tag{4}$$

The mass transfer Stanton number is defined by

$$St = \frac{h_m}{\bar{U}} \tag{5}$$

As it is often the case that the wall temperature varies slightly during test run, $\rho_{v,w}$ can be represented by the time-averaged naphthalene concentration at the surface. This is obtained from numerical integration of the concentration determined at the measured surface temperature. A correlation proposed by Ambrose et al. [13] is used to determine naphthalene vapor pressure, from this, $\rho_{v,w}$ is evaluated using the ideal gas law and the naphthalene surface temperature.

EXPERIMENTAL APPARATUS AND PROCEDURE

Fig. 2 displays schematic view of the test section. The entire construction is made of aluminum tooling plates. The shaded area in the figure, representing a cavity-like grooved tip, is the mass transfer active surface cast with a thin layer of naphthalene, approximately 2 mm in thickness. The cavity width, W, is maintained constant at 3.2 cm (1.25 inch) throughout the entire study. The desired values of C/W and D/W can be obtained accordingly, by fixing a pair of adjustable screws. A 1.6 cm width surface is extended both upstream and downstream of the cavity, forming the upstream gap and downstream gap, respectively. The cavity span normal to the streamwise direction is measured at 15.3 cm (6.0 inch) which is approximately four times of the streamwise width, W. Under this condition, although possible three-dimensional phenomena are expected, preliminary tests have shown that the mass transfer characteristics are very much two dimensional across at least 80% of the span. The moving shroud is modeled by a flat, seamless, Neoprene belt driven by a speed-adjustable, 3/4 HP. D.C. motor. The test assembly can be rotated in different orientation relative to the belt moving direction.

During a test run, the laboratory compressed air supply is first introduced to a plenum adjacent to the test cavity, then flows over the cavity, and subsequently discharges to the surrounding atmosphere. The entire test assembly including plenum and cavity is placed above and contacts the moving belt, with the cavity opening facing downward. Between the test assembly and the moving belt, there are several teflon pads mounted on the contacting surface of the test assembly to reduce dynamic friction and to prevent air leakage. An additional teflon plate is placed underneath and against the belt which effectively eliminates belt vibration as it moves over the test section. Preliminary tests at full anticipated belt speeds indicate that this design is very effective.

One of the most challenging aspects of the subliming mass transfer experiment is the surface profile measurement on the naphthalene surface. Mass transfer at a certain location is inferred from the change in naphthalene thickness at that location. In order to obtain the distribution of local mass transfer coefficient in the region of interest, the surface contour must be measured before and after each test run. Therefore, successful execution of local measurements in subliming mass transfer is critically dependent on precise positioning and accurate thickness change readings. In addition, to avoid errors caused by the extraneous naphthalene sublimation and human fatigue during a lengthy measurement requires rapid data acquisition. A computer-controlled, automated data acquisition system has been designed and used to fulfill all of these requirements. A block diagram giving a schematic view of the entire system is shown in Fig. 3. It consists of a depth gauge along with a signal conditioner, a digital multimeter, two-stepper-motor driven positioners, a motor controller, and a Zenith 150 microcomputer (IBM-PC compatible) as the measurement process controller. The Zenith microcomputer is also used for data storage and reduction. Details of the measurement system have been described in [14, 15].

RESULTS AND DISCUSSION

Most of the mass transfer results in this study are presented in form of Stanton number, St, as discussed in the previous section. For all the test runs, the uncertainty in the local St is estimated to be 5%, and the repeatability is considerably better than this value. Prior to the actual tests for grooved-tip geometries, mass transfer from a flat surface in the absence of cavity has been measured, and the results agree very well with those of heat transfer in the developing region for turbulent pipe flow with a sharp-angle entrance [16]. This validates the present experimental system and provides confidence in data accuracy.

A sample of results describing the local Stanton number distribution on the cavity floor and the surfaces of upstream and downstream of the cavity is shown in Fig. 4. The figure consists of four sub-figures, 4(a) to 4(d), representing $Re = \bar{U}C/\nu = 2.0 \times 10^4$, $C/W = 0.14$, and $D/W = 0.1$, 0.5, 1.0, and 1.5, $U_w/\bar{U} = 0.0$ and 0.46. It is noted in Fig. 4 that very non-uniform St distributions exist for all the cases tested. On the surface upstream of the cavity (i.e. the upstream gap), St increases with streamwise location, reaches a local maximum near the mid-point of the surface, and then decreases toward downstream. The characteristic of this St distribution is virtually identical to that of heat transfer near a channel entrance preceded by a sudden contraction. Typical value of the maximum St is approximately twice as that for the fully developed channel flow having the same Reynolds number.

Mass transfer characteristics on the surface downstream of the cavity (i.e. downstream gap) are similar to that of a newly developing boundary layer with zero angle of incidence. In contrast to the upstream gap, the highest St occurs near the leading edge of the surface, and the St decreases along the streamwise direction. However, it is speculated that a second local maximum St may exist somewhere downstream of the leading edge provided that the gap size is sufficiently large; a vortex region is expected to exist in the upstream portion of this surface. This second local maximum St has been reported in the literature for cavity flow without shroud presence [10].

Values of St on the cavity floor are in general smaller than that on surfaces upstream and downstream of the cavity. In addition, as shown in Fig. 4, the nature of the cavity-floor St distribution depends strongly on the cavity geometry, namely the cavity aspect ratio, D/W. For shallow cavities, say $D/W = 0.1$, the shear layer separated from the upper corner of the cavity upstream wall should have reattached the cavity floor. In the region near the reattachment point, generally accompanied with higher turbulence mixing, mass transfer coefficient reaches a local maximum. This effect is clearly observed in Fig. 4(a). For $D/W = 0.5$, according to a flow visualization study on unshrouded cavities [9], the entire cavity will be largely filled with a recirculating vortex resulting in a streamwise, monotonically increasing trend of mass transfer on the cavity floor, as shown in Fig. 4(b). For even deeper cavities,

D/W = 1.0 and 1.5, the values of cavity-floor St become smaller, and peculiar mass transfer characteristics exist, with more than one local maximum St being observed in Figs. 4(c) and (d). This is speculated to be attributable to the additional and strong degree of secondary-flow interactions near the cavity bottom.

For all the cases present in Fig. 4, the general trend of influence of relative shroud movement on the mass transfer from a grooved tip is found to be quite consistent. At each corresponding streamwise location, the mass transfer St on the surfaces of downstream gap and cavity floor are generally higher for $U_w/\bar{U}$ = 0.46 than that for stationary shroud situation (i.e. $U_w/\bar{U}$ = 0); while the reversed effect is observed on the surface of upstream gap. This is understandable that the shroud motion introduces more naphthalene-free air into the mainstream in the downstream portion of the test section, thus the bulk air flow in this region is less naphthalene-enriched than that without shroud motion. This in turn enhances the mass transfer. Opposite effect is expected for the upstream portion, resulting in a lower mass transfer driving potential. However, the difference in St affected by the different values of $U_w/\bar{U}$ is overall insignificant and, for majority of the data, the differences are in fact within the experimental uncertainty. The speculation raised in Ref. [6] that the relative shroud motion has a very minor effect on the flat blade-tip heat transfer may also be applied to the heat transfer to a grooved tip, at least for the present study range.

Mass transfer measurements are also made on cavity side walls, and Figs. 5 and 6 show typical results for the intermediate cases D/W = 0.25 and 1.0. The mass transfer from the cavity upstream wall (downstream-facing wall) is dominated by the vortex attached behind the wall and has the same order of magnitude of St as that on the upstream portion of cavity floor, which generally has low mass transfer rates. On the other hand, the fundamental mode of mass transfer mechanism for the cavity downstream wall (upstream-facing wall) is the impingement of the separated shear layer on the wall, in particular on the upper portion. As a result, the mass transfer coefficient is generally high near the top of the downstream wall. The influence of relative shroud movement on the mass transfer from the two side walls is found to be insignificant, the same finding shown in Fig. 4. However, the influence seems to be stronger for deeper cavity (D/W = 1.0) than for the shallower one (D/W = 0.25), and, as shown in Fig. 6, it affects oppositely on the mass transfer between upstream and downstream walls.

Fig. 7 shows the area-averaged mass transfer coefficient and the overall mass transfer rate for all the cases presented in Fig. 4. The left scale in Fig. 7 represents the Stanton number averaged over the entire mass transfer active region, $\overline{St}$; while the right scale gives the value of $\dot{M}_t/\rho_{v,w}$ normalized by the corresponding value for the case D/W = 1.0, where $\dot{M}_t$ is the time-averaged mass transfer rate over the entire mass transfer surface. As expected, the shroud motion has little influence on both results, with a less than 10% maximum variation caused by the difference in shroud movement. According to Fig. 7, $\overline{St}$ decreases with an increase in the value of D/W; however,

the value of normalized overall mass transfer rate remains almost constant for $D/W \leq 0.5$ and then increases for higher D/W values. This implies that, despite the lower mass transfer coefficient, the deeper cavities experience higher overall mass transfer rate than the shallower ones, due mainly to the additional mass transfer area present in the cavity side walls. If the heat transfer with tip leakage flow is of concern, it may be undesirable to groove a blade tip having a cavity aspect ratio, D/W, higher than 0.5. This result agrees favorably with the conclusion from Ref. [11] by Metzger and Bunker.

Another important parameter affecting the tip heat transfer is the size of gap clearance, namely C/W. Fig. 8 shows the typical results for cavities with $D/W = 1.0$, $Re = 2.0 \times 10^4$, and $U_w/\bar{U} = 0$. The general trend is that the larger the value of C/W, the higher the mass transfer coefficient. In addition to change in the magnitude of local St, the general characteristics of St distribution over the surfaces of upstream and downstream gap vary with different values of C/W. This variation may be understood by consideration of flow pattern in the gap, which, to a certain extent, is affected by the nature of sudden contraction as the fluids flow into the gap. Moreover, according to a recent study by Chyu et al. [17], the larger gap clearance permits the separated shear layer to grow thicker inducing higher turbulence level in the gap mainstream. The mass transfer on the downstream gap surface as well as on the cavity downstream wall are thus influenced by the characteristics of shear layer. In view of the results shown in Fig. 8, a recirculating vortex may exist in the downstream gap for $C/W \geq 0.2$., as a local minimum of St observed in the mid-portion of the surface.

Fig. 9 shows the Reynolds number effect on the tip mass transfer. While fixing the $D/W = 1.0$ and $C/W = 0.14$, the Reynolds number, defined as $Re = \bar{U}C/\nu$, varies from 0.38×10^4 to 3.6×10^4 by controlling the air flow from the laboratory compressor. Since the size of clearance is physically the same in these cases, the only variable in fact is the gap mean velocity. As shown in Fig. 9, within the present test range, the local St generally decreases with an increase of Re. However, the trend is attenuated and even reversed when $Re \geq 3.6 \times 10^4$. This peculiar tendency can be explained at least by consideration of the compressibility effect. For $Re = 3.6 \times 10^4$, Mach number in the gap is approximately equal to 0.4, and it may be inappropriate to consider the flow incompressible, and the mass transfer increases as the compressibility effect dominates.

The actual turbine blade involves curved surfaces, and at a certain location on blade tip, the relative direction between the leakage flow and the shroud movement may not be exactly opposite (180°). Complex secondary flow possibly with helix motions is expected in the tip groove under this condition. As a preliminary investigation of this phenomena, an attempt has been made to study this effect on tip leakage heat transfer by varying the relative orientation between the moving belt and the mass transfer test assembly. The angle varies from 180° to 112°. Fig. 10 displays the contours of constant Stanton number on the cavity floor with a 135° angle of mis-alignment,

C/W = 0.14, D/W = 1.0, $U_w/\bar{U}$ = 0.46 and Re = 2.0 x 10^4. To be noted is the fact that, except for the angle difference, the test condition and geometry are identical to that of results shown in Fig. 4(c). Comparing these two cases, the local mass transfer characteristics apparently are affected by the angle magnitude. However, the overall values of average Stanton number and mass transfer rate are virtually uninfluenced, as shown in Fig. 11.

Attention is now turned to the correlation between the area-averaged mass transfer and the affecting parameters as previously discussed. Using the power regression fit, $\overline{St}$ is found to vary with -0.24 power of D/W, and the power index becomes -0.28 if the area-averaged St over the cavity floor is only of concern. The latter is in good agreement with results from previous studies; -0.22 in Ref. [11] and -0.27 in Ref. [9]. It should be noted that, in Ref. [9], only the cavity floor was heated and the cavity side walls were kept adiabatic, whereas the present mass transfer system is equivalent to the situation with the entire cavity surface maintained at an isothermal wall condition. As for the gap clearance dependency, $\overline{St}$ groups well with C/W to a 0.32 power indicating that a greater influence on tip heat transfer than does the cavity aspect ratio, D/W. The same conclusion has also been found in Ref. [11]. The influence of Reynolds number on the entire tip mass (heat) transfer can be expressed as $\overline{St}$ proportional to $Re^{-0.36}$. In Ref. [9], for unshrouded cavities, the Stanton number averaged over the cavity floor is found to vary as the -0.5 power of Reynolds number. The difference may be attributed to the difference in the nature of cavity geometry, the boundary condition and the testing range of Reynolds number.

CONCLUDING REMARKS

The present study of heat transfer in the tip region of a rotor blade simulator is now in its second-year stage. The naphthalene mass transfer technique with the high-precision surface measurement system has demonstrated itself as a viable method to study the local transfer information in great detail. Parameters which influence the heat transfer in a grooved tip region have been identified, with their effects being investigated extensively. Further studies emphasizing actual blade airfoil shape may be desirable.

REFERENCES

1. Hennecke, D.K., "Heat Transfer Problems in Aero-Engines," Heat and Mass Transfer in Rotating Machinery, D.E. Metzger and N.H. Afgan, eds. Hemisphere, Washington, D.C., 1984, pp. 353-379.

2. Metzger, D.E. and Mayle, R.E., "Heat Transfer Gas Turbine Engines," Mech. Eng., 105, No. 6, June 1983, pp. 44-52.

3. Lakshminarayana. B., "Methods for Predicting the Tip Clearance Effects in Axial Flow Turbomachinery," J. Basic Eng, Trans. ASME, 92, 1970, pp. 467-482

4. Booth, T.C., Dodge, P.R. and Hepworth, H.K., "Rotor-Tip Leakage: Part I - Basic Methodology," J. Eng. for Power, Trans. ASME, 104, 1982, pp. 154-161.

5 Wadia, A.R. and Booth, T.C., "Rotor-Tip Leakage: Part II - Design Optimization Through Viscous Analysis and Experiment, J. Eng. for Power, Trans. ASME, 104, 1982, PP. 162-169.

6. Mayle, R.E. and Metzger, D.E., "Heat Transfer at the Tip of an Unshrouded Turbine Blade," 7th International Heat Transfer Conference, Munich, 3, 1982, pp. 87-92.

7. Aung, W., "Separated Force Convection," Keynote Paper, ASME/JSME Thermal Eng. Conf., Honolulu, March 20-24, 1983.

8. Haugen, R.L. and Dhanak, A.M., "Heat Transfer in Turbulent Boundary-Layer Separation over a Surface Cavity," J. Heat Transfer, 89, 1967, pp.335-340.

9. Yamamoto, H., Seki, N. and Fukusako, S., "Forced Convection Heat Transfer on Heated Bottom Surface of a Cavity," J. Heat Transfer, 101, 1979, pp. 475-479.

10. Chyu, M.K. and Goldstein, R.J., "Local Mass Transfer in Rectangular Cavities with Separated Turbulent Flow," Proceedings of 8th Int. Heat Transfer Conf., 3, 1986, pp. 1065-1070.

11. Metzger, D.E. and Bunker, R.S., "Cavity Heat Transfer on a Grooved Wall in a Narrow Flow Channel," ASME Paper 85-HT-57, 1985.

12. Eckert, E.R.G., "Analogies to Heat Transfer Processes," Measurements in Heat Transfer, ed. by Eckert, E.R.G. and Goldstein, R.J., Hemisphere Publication, Washington D.C., 1976.

13. Ambrose, D., Lawenson, I.J. and Sprake, C.H.S., "The Vapor Pressure of Naphthalene," J. Chem. Thermo., 7, 1975, pp. 1173-1176.

14. Goldstein, R.J., Chyu, M.K. and Hain, R.C., "Measurement of Local Mass Transfer on a Surface in the Region of the Base of a Protruding Cylinder with a Computer-Controlled Data Acquisition System," Int. J. Heat and Mass Transfer, 28, 1985, pp. 977-985.

15. Metzger, D.E., Chyu, M.K. and Moon, H.K., "Heat Transfer in the Tip Region of a Rotor Blade Simulator," NASA-Lewis 4th Host Workshop, Cleveland, Oct. 22-23, 1985.

16. Boetler, L.M.K., Young, G. and Iverson, H.W., "An Investigation of Aircraft Heaters XXVII - Distribution of Heat Transfer Rate in the Entrance Region of a Tube," NACA TN 1451, 1948.

17. Chyu, M.K., Metzger, D.E. and Hwan, C.L., "Heat Transfer in Shrouded Rectangular Cavities," AIAA/ASME Thermophysical and Heat Transfer Conference, June 2-4, 1986, Boston.

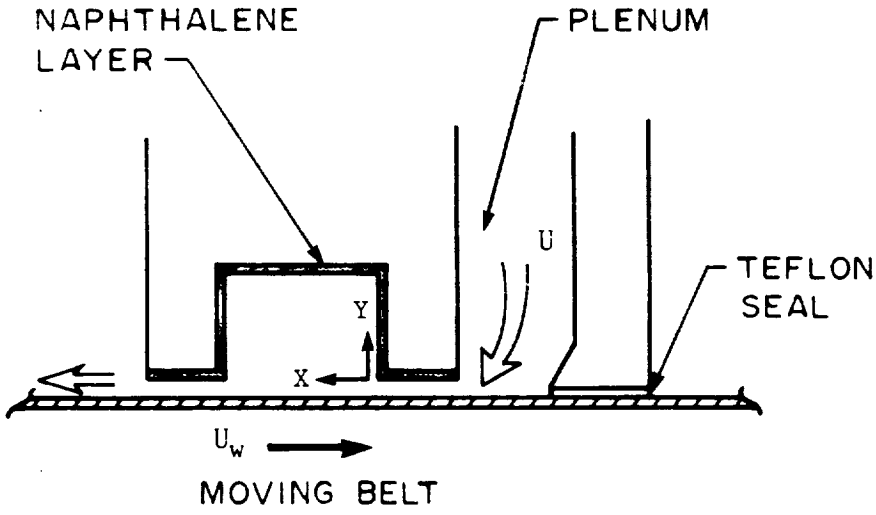

Fig. 1 Schematic View of Test Section

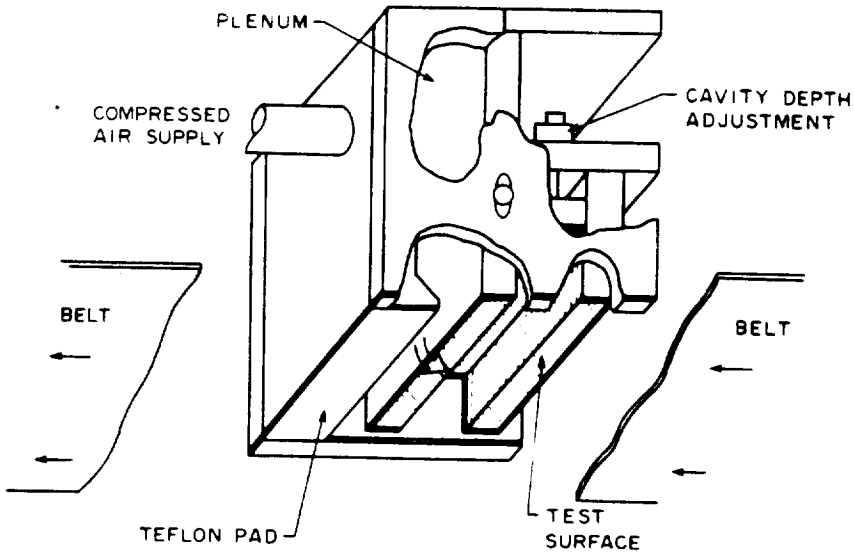

Fig. 2 Schematic View of Test Assembly

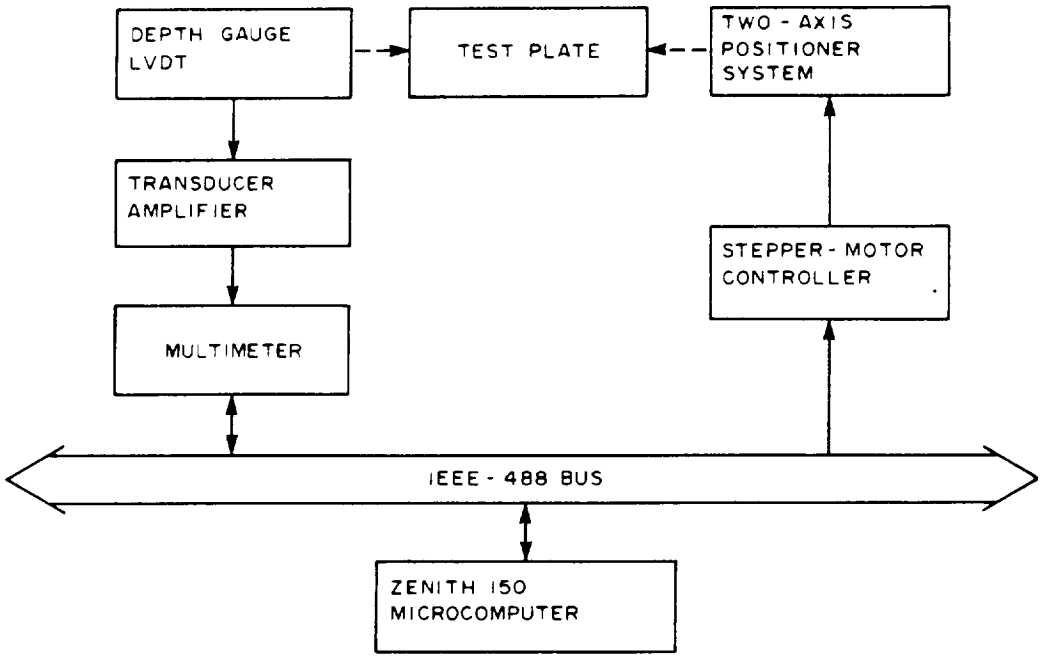

Fig. 3 Local Mass Transfer Surface Measurement System

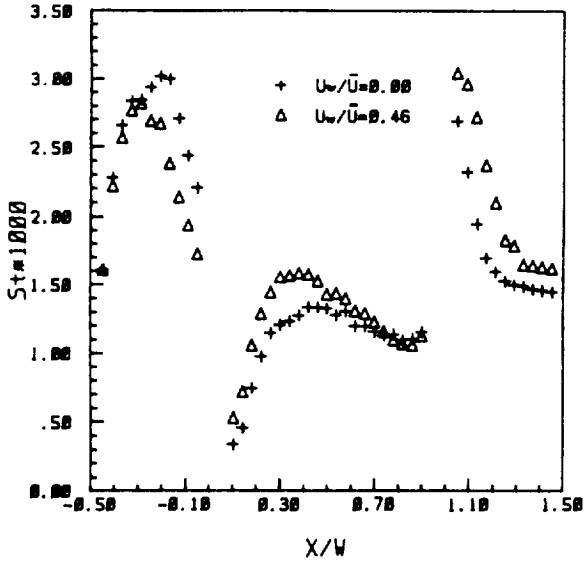

(a) D/W = 0.1

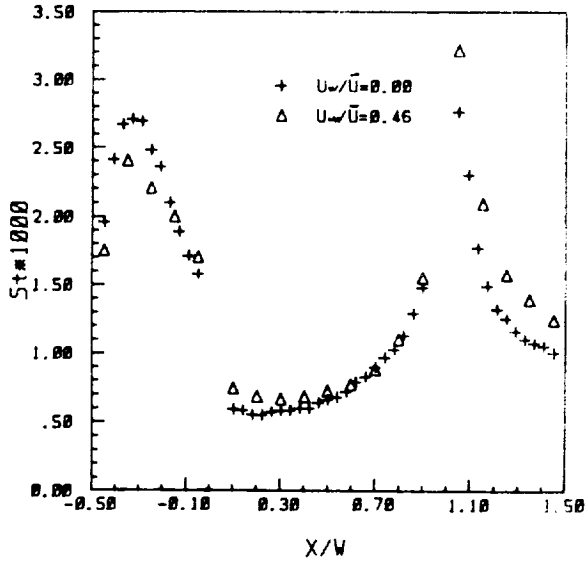

(b) D/W = 0.5

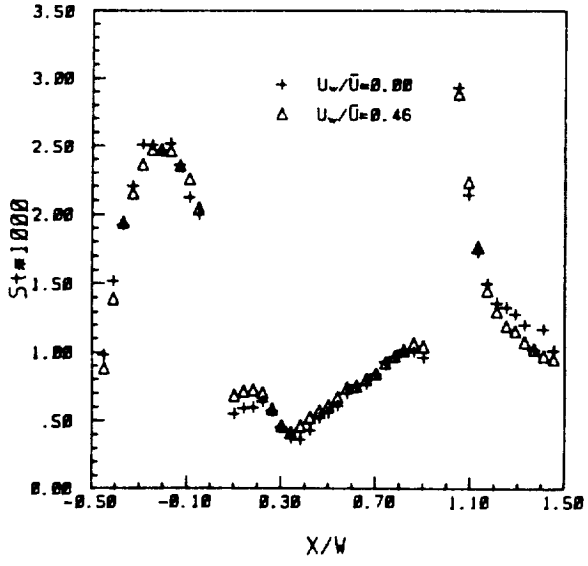

(c) D/W = 1.0

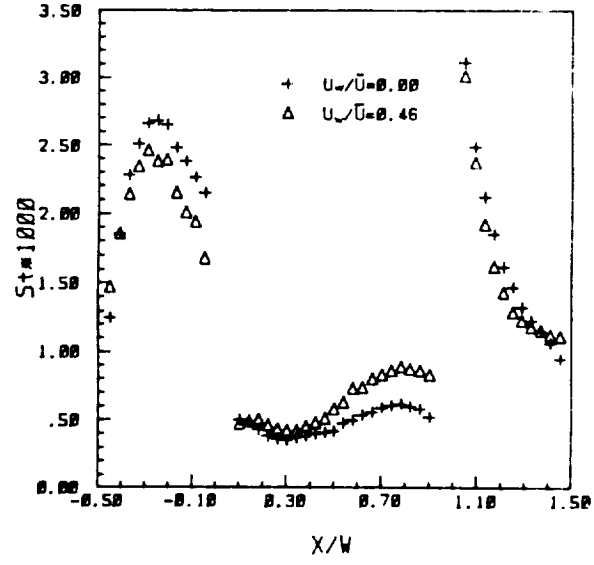

(d) D/W = 1.5

Fig. 4 Local St Distribution in Streamwise Direction; C/W = 0.14, Re = 2.0 x 10^4;

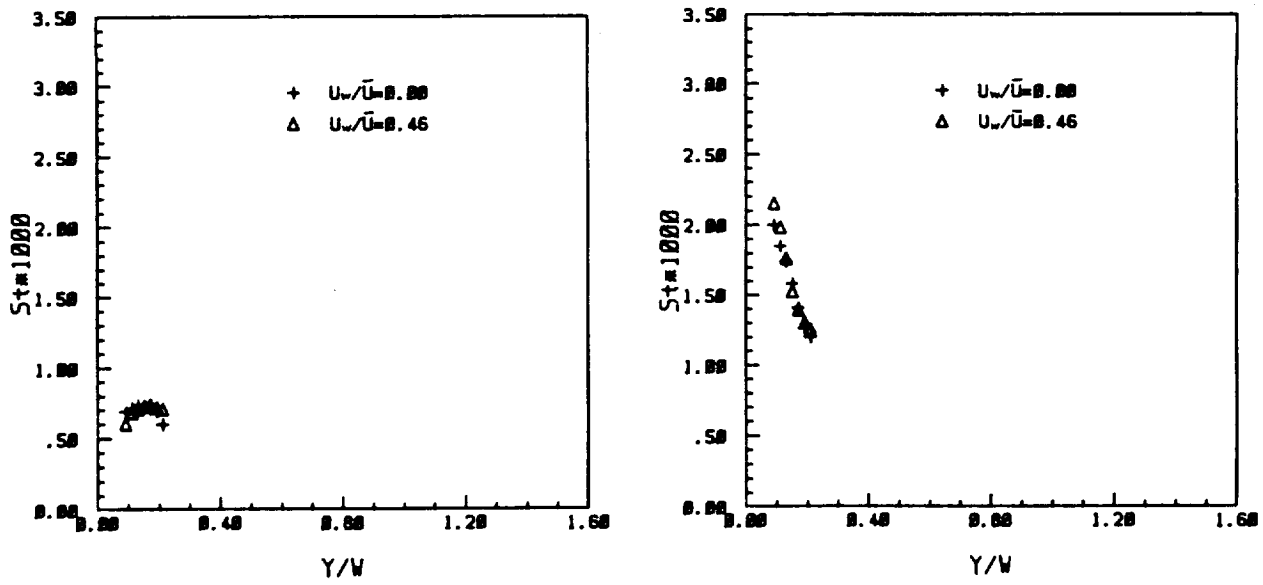

(a) Upstream Wall (b) Downstream Wall

Fig. 5 Local St Distribution on Cavity Side Walls; C/W = 0.14, D/W = 0.25, Re = 2.0 x 10^4

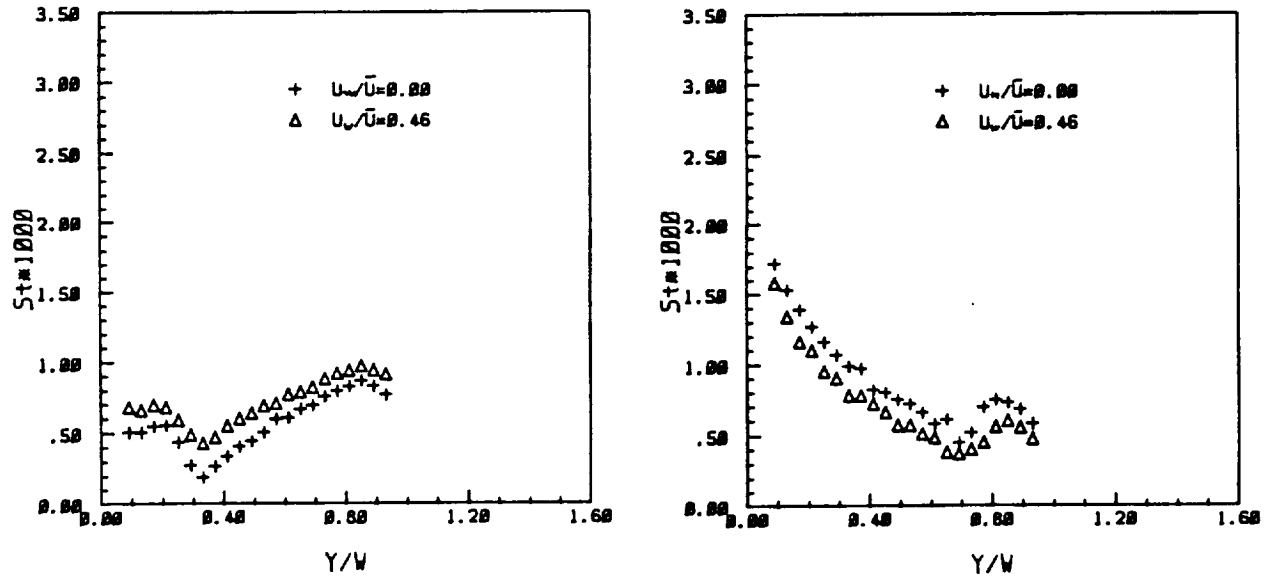

(a) Upstream Wall (b) Downstream Wall

Fig. 6 Local St Distribution on Cavity Side Walls; C/W = 0.14, D/W = 1.0, Re = 2.0 x 10^4

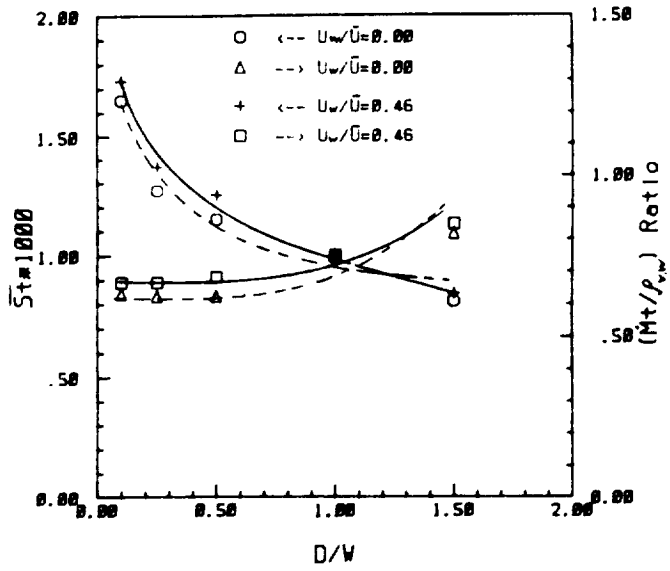

Fig. 7 Area-Averaged Mass Transfer;
C/W = 0.14, Re = 2.0 x 10^4

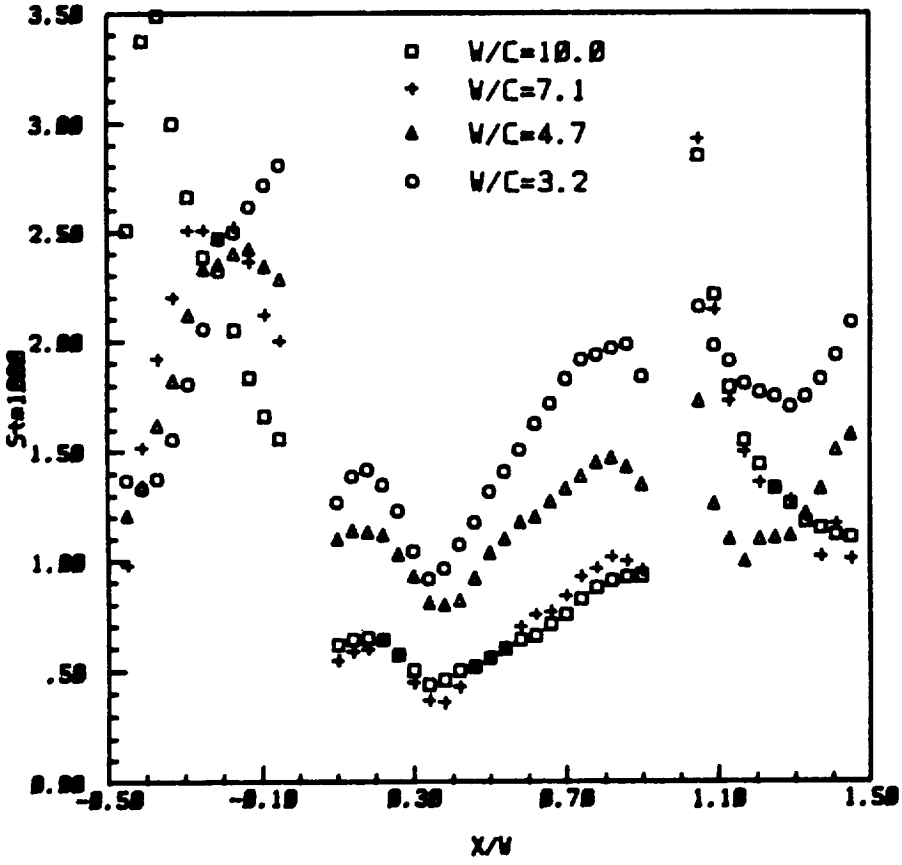

Fig. 8 Gap Clearance Effect on Mass Transfer;
D/W = 1.0, Re = 2.0 x 10^4, $U_w/\bar{U}$ = 0.0

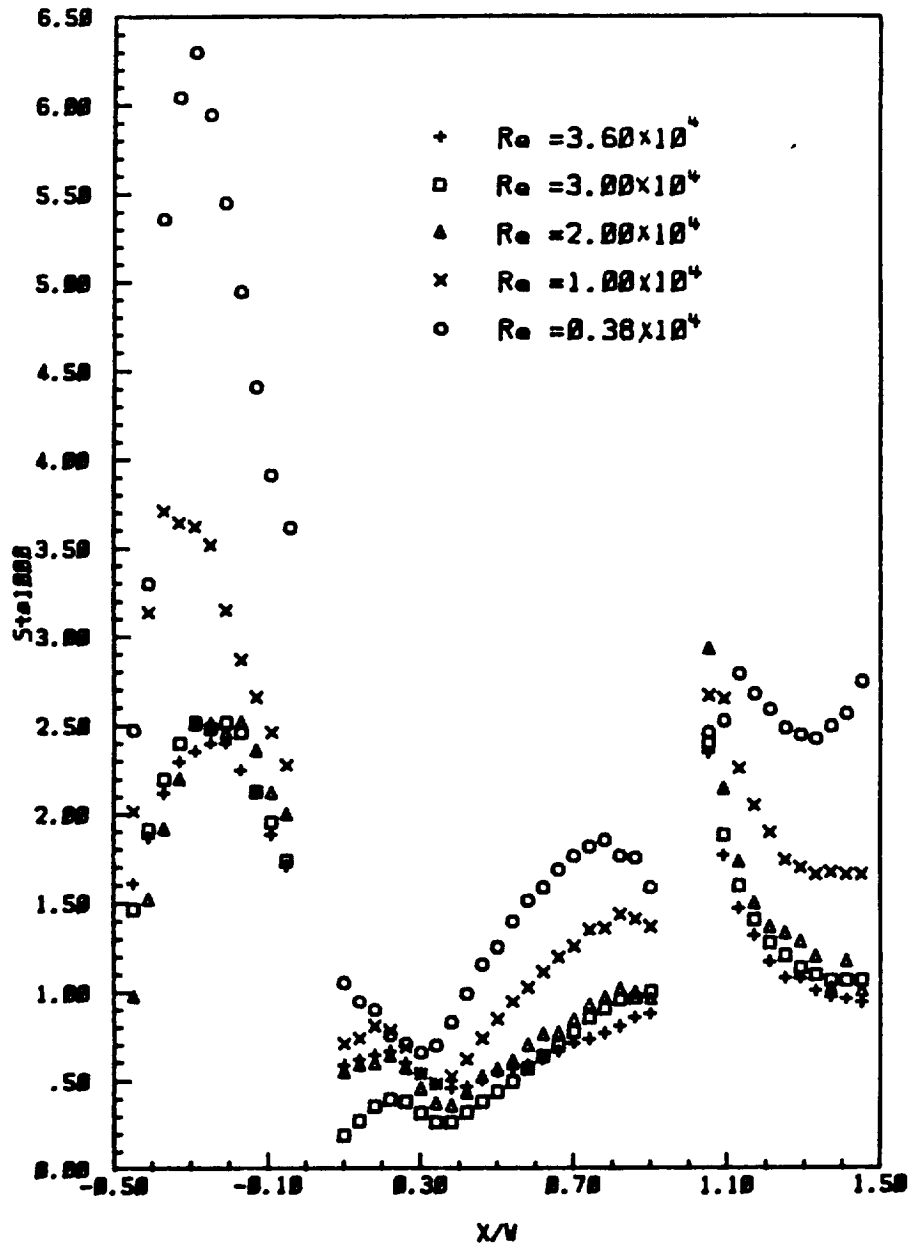

Fig. 9 Reynolds Number Effect on Mass Transfer; C/W = 0.14, D/W = 1.0, $U_w/\bar{U}$ = 0.0

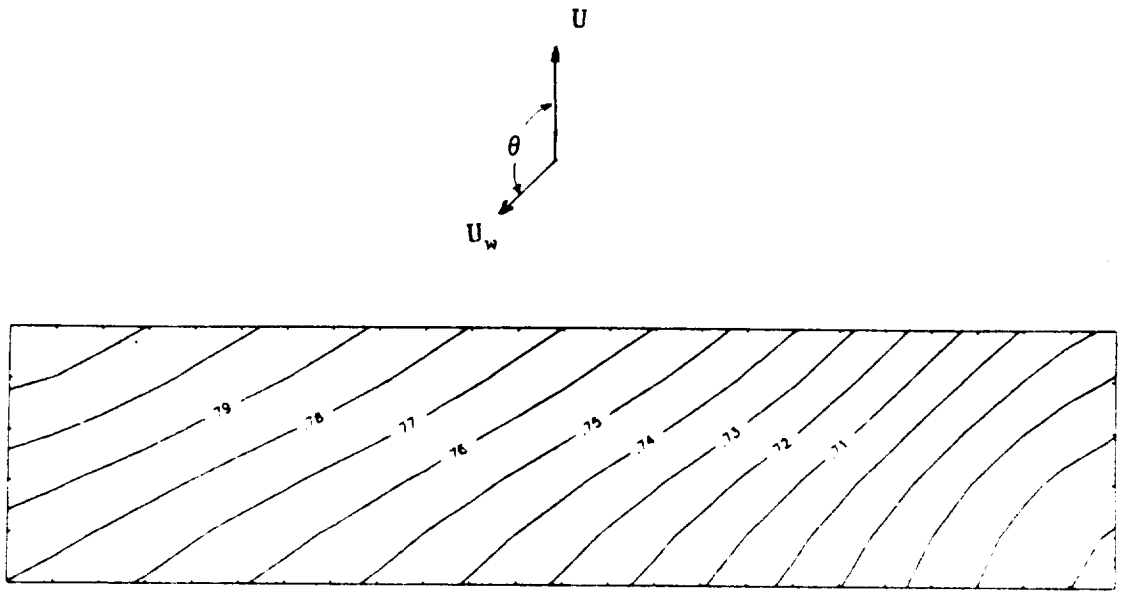

Fig. 10 Stanton Number (St x 10^3) Distribution on Cavity Floor; C/W = 0.14, D/W = 1.0, Re = 2.0 x 10^4, $U_w/\bar{U}$ = 0.46, θ = 135°

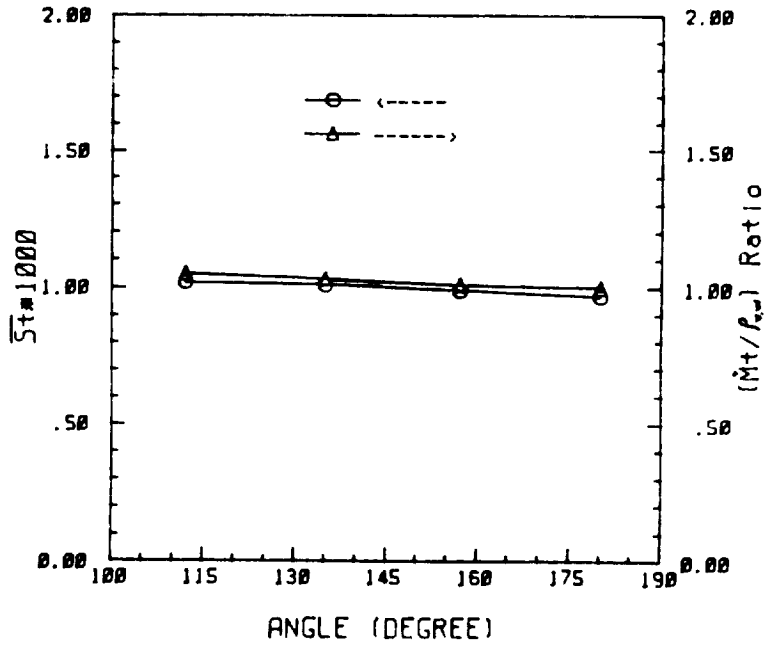

Fig. 11 Shroud-to-Cavity Orientation Effect on Mass Transfer; C/W = 0.14, D/W = 1.0, Re = 2.0 x 10^4, $U_w/\bar{U}$ = 0.46

COOLANT PASSAGE HEAT TRANSFER WITH ROTATION*

T. J. Hajek
United Technologies Corporation
Pratt and Whitney

J. Wagner and B. V. Johnson
United Technologies Research Center

In current and advanced gas turbine engines, increased speeds, pressures and temperatures are used to reduce specific fuel consumption and increase thrust/weight ratios. Hence, the turbine airfoils are subjected to increased heat loads escalating the cooling requirements to satisfy life goals. The efficient use of cooling air requires that the details of local geometry and flow conditions be adequately modeled to predict local heat loads and the corresponding heat transfer coefficients.

Improved turbine airfoil local temperature and hence, life predictions can be realized by accurately accounting for the effects of rotation on internal cooling. Although the effects of rotation which give rise to Coriolis and buoyancy forces can be large, they are currently not adequately included in the heat transfer designs of blades. Experimental data is particularly needed for the higher Rayleigh and Reynolds number conditions that are characteristic of turbine airfoils cooling passages. This data is crucial for development of design correlations and computer codes as well as their verification. Accurate prediction of local heat transfer coefficients enables the designer to optimize cooling configurations to minimize both metal temperature levels and thermal gradients. Consequently, blade life and engine efficiency can be significantly improved.

OBJECTIVE

The objective of this 36-month experimental and analytical program is to develop a heat transfer and pressure drop data base, computational fluid dynamic techniques and correlations for multi-pass rotating coolant passages with and without flow turbulators. The experimental effort is focused on the simulation of configurations and conditions expected in the blades of advanced aircraft high pressure turbines. With the use of this data base, the effects of Coriolis and buoyancy forces on the coolant side flow can be included in the design of turbine blades.

EXPERIMENTAL MODEL

The coolant passage heat transfer model features a four-pass serpentine arrangement designed to reflect the passages within a gas turbine blade. For the present experiments, the model was fitted with skewed turbulators, as indicated in figure 1. Figure 2 shows a schematic diagram of the model with the instrumentation and wall sections indicated. Heat transfer coefficients are obtained for each wall section element. These wall elements, numbered 1 to 64, consist of a copper block backed with a thin film electrical resistance type heater and instrumented with two thermocouples. The copper wall sections are 10.7 mm x 49.3 mm (0.42 in. x 1.94 in.). Each section is thermally isolated from the adjoining section by a 1.5 mm (0.060 in.) thick divider strip of low thermal conductivity G-11 composite material. The straight radial passages have a square cross section, 12.7 mm x 12.7 mm (0.5 in. x 0.5 in.).

*NASA Contract NASA-23691

DATA REDUCTION

Data acquisition/analysis consists of three general categories: equipment calibration, model heat loss measurement, and heat transfer coefficient calculations. The equipment calibration follows standard experimental procedures. Model heat loss measurements precede each test. These measurements are executed with no coolant flow and uniform wall temperature steady-state conditions, identical to the subsequent test less the coolant flow. Heat transfer coefficients are then calculated for each wall section element by applying the following procedure.

For each copper element the net energy convected to the fluid is calculated by subtracting the electrical line losses and conducted heat losses from the total energy supplied. Bulk fluid temperatures are then calculated based on an energy balance for each flowpath section as follows:

$$T_{b_{out}} = \frac{q_{net,\ 4\ walls}}{mc_p} + T_{b_{in}}$$

where the model inlet bulk temperature is measured. Once bulk fluid temperatures are determined, heat transfer coefficients are calculated from the equation:

$$h = \frac{q_{net,\ wall}}{A\ (T_w - T_b)}$$

where T_b is the average of the inlet and exit bulk temperatures. Thus for each test case, 64 heat transfer coefficients are calculated.

Table I shows the test conditions for which data were acquired with the skewed rough wall model. A total of 30 tests has been conducted to isolate the effects on heat transfer of rotation rate, flow rate, coolant-to-wall temperature variations, radius length and passage angle.

RESULTS

All of the experiments listed in Table I were completed to date. Measurements of both the passage heat transfer and the channel pressure drop were conducted. Due to the large number of data points obtained, comprehensive discussion of all the results is beyond the scope of this paper. Instead, the following paragraphs will mainly focus on comparisons between the smooth and the skewed trip strip channel data at specific operating conditions and physical locations within the model. This will facilitate better understanding of the underlying physical principles. It should also be noted that due to the complexity of the subject matter, many of the explanations presented herein are hypotheses and will require further substantiation.

In order to fully understand the channel heat transfer behavior under the influence of rotation, it is imperative that key differences between the smooth and the augmented channel be examined in stationary frame first. Figure 3 depicts a comparison between the smooth and augmented models for the baseline condition of Re = 25,000. In the first leg of the model, the smooth channel heat transfer exhibits classical thermal development behavior (decreasing Nusselt number with

distance), whereas the rough wall shows nearly constant augmentation (factor of 3) throughout the first leg. This is consistent with other Pratt & Whitney data.

Also quite different is the turn heat transfer. For the smooth wall case, classical heat transfer increase (factor of 2) is present. In the augmented channel turn, the Nusselt number decreases through the turns (note that it reaches values below the smooth duct). This is followed by an immediate increase, just downstream of the turn. Subsequently, the second leg heat transfer decreases along the passage. A similar pattern repeats for the second turn and the third leg. It is important to note that the second and the third passages exhibit progressively decreasing average Nusselt number. In fact, the third passage augmentation approaches levels expected from normal trip strips. Even though good understanding of this phenomenon has not been gained to date, it is clear that the first passage (with its well behaved inlet) acts very much like a straight duct, whereas the subsequent passages are strongly affected by the turn generated secondary flows. It is felt that this fact will play an important role in understanding the rotating results. Consistent with other results, the rough channel side wall (rib wall) heat transfer is augmented somewhat by the presence of the trip strips, but in general behaves similarly to the smooth duct rib walls.

Figure 4 shows comparison of heat transfer results for smooth wall and skewed trip rough wall at baseline rotating flow conditions of Ro = 0.24 and Re = 25,000. As was the case with the smooth passage, the rough wall leading surface heat transfer is significantly reduced (40-50% reduction) by the introduction of rotation. Because the trailing side shows heat transfer augmentation of only 30%, the average channel Nusselt number is reduced. While the rough model heat transfer in the first passage is strongly affected by rotation, the subsequent legs and turns show very little dependence. This fact is further supported by examining figure 5, where heat transfer ratios are presented for several rotation rates. In this figure, the first passage is again quite active, whereas the other channels exhibit very little variation with rotation. This finding further supports the hypothesis of turn generated secondary flows dominating the subsequent passages.

The influence of buoyancy on rotating channel heat transfer is depicted in figure 6. With the exception of the first leg, the leading (stabilized) wall shows very weak dependence on temperature (density) variations. The trailing surface, on the other hand, does show considerable dependence on ΔT. Better representation can be found in figure 7. Leading and trailing surfaces are plotted for the last heating element in the first leg. Note that the data at Ro = 0.0 do not coincide. This is a direct result of small manufacturing inconsistencies in the heating elements. The density (temperature) ratio is shown with flag symbols. It can be clearly seen that the trailing surface heat transfer is more sensitive to density variations than the leading surface. When the trailing side data are examined closely, it can be seen that the absolute heat transfer change due to temperature variations is approximately the same for both smooth and rough ducts. The rough wall leading surface, however, shows significantly smaller variation for a given ΔT change. This information indicates that the buoyancy forces do not play as important a role in augmenting heat transfer on "stabilized" surfaces for rough walls as they do for smooth walls. This fact is further supported in figure 8, where the same data is plotted against the Buoyancy Parameter. Both leading and trailing surfaces for smooth ducts as well as trailing surface for rough ducts correlate well with the Buoyancy Parameter. However, the leading surface data for the rough wall model do not collapse. Potentially, this may indicate that in addition to the buoyancy forces, some other process, as yet unexplained, is becoming important.

It should also be noted in figure 8 that at high levels of the Buoyancy Parameter, the heat transfer ratios are approaching an asymptotic limit. In the case of the smooth duct trailing surface, the limiting rough wall heat transfer level is only 20% higher.

In reality, the difference is only 10% if the rough wall convection area is corrected for the trip strip surface area. The important observation to be made here is that at low values of the Buoyancy Parameter, the rough wall has significant heat transfer advantage over the smooth wall. At high values of the buoyancy parameter, however, the trip strip advantage is significantly diminished.

WORK PLANNED

Detailed analysis and correlation of the skewed turbulator data will continue.

Currently the model is being modified to include normal turbulators on the leading and the trailing surfaces of the straight radial passages. A thirty point test matrix, similar to the one in Table I will be executed.

TABLE 1

TEST MATRIX FOR ROTATING HEAT TRANSFER EXPERIMENTS FOR SKEWED TURBULATORS

Test No.	UTRC Run No.	Dimensional Parameters						Basic Dimensionless Parameters				Secondary Dimensionless Parameters			
		P (psi)	Ω (rpm)	$\dot{m}$ (lb/sec)	ΔT (F)	H (in)	α (deg)	Re	Ro	$\frac{\Delta T}{T_{in}}$	$\frac{H}{d}$	$\frac{\Delta\rho}{\rho}\frac{\Omega H}{V}$	Gr/Re^2	$Grx10^{-8}$	Comments
201	6.7	147.7	0	0.013	81	25	0	25,337	0	0.15			0	0	No Rotation
202	9.9	147.8	0	0.006	80	25	0	12,490	0	0.15			0	0	
203	8.8	149.5	0	0.025	80	25	0	50,715	0	0.15			0	0	
204	10.8	145.0	0	0.024	80	25	0	75,348	0	0.15			0	0	
205			15		80	25	0	25,000	0.006				0.00	0.00	
206			145		80	25	0	25,000	0.06				0.01	0.13	
207			275		80	25	0	25,000	0.12				0.05	0.46	Vary Ro
208			412		80	25	0	25,000	0.18				0.12	1.06	Hold ΔT, Re
209			550		80	25	0	25,000	0.24				0.22	1.96	
210			825		80	25	0	25,000	0.35				0.45	4.22	
211			145		80	25	0	12,500	0.12				0.09	0.14	Vary Re
212			550		80	25	0	50,000	0.12				0.06	1.98	Hold ΔT, Ro
213			825		80	25	0	75,000	0.12				0.05	4.20	
214			275		160	25	0	25,000	0.12				0.14	0.87	High ΔT
215			550		160	25	0	50,000	0.12				0.14	3.49	
216			145		160	25	0	25,000	0.06				0.03	0.21	
217			412		120	25	0	25,000	0.18				0.17	1.55	
218			412		40	25	0	25,000	0.18				0.07	0.63	Vary ΔT, Ro
219			412		160	25	0	25,000	0.18				0.20	0.18	at Re=25,000
220			550		40	25	0	25,000	0.24				0.72	1.13	
221			550		120	25	0	25,000	0.24				0.30	2.73	
222			550		160	25	0	25,000	0.24				0.36	3.06	
223			825		40	25	0	25,000	0.36				0.28	2.39	
224			825		120	25	0	25,000	0.36				0.64	5.70	
225			825		80	25	45	25,000	0.34				0.42	3.66	
226			550		80	25	45	25,000	0.24				9.22	1.98	Angle
227			275		80	25	45	25,000	0.12				0.05	0.46	Variation
228			275		160	25	45	25,000	0.12				0.14	0.87	$\alpha = 45^0$
229			550		80	25	45	50,000	0.12				0.06	1.98	
230			550		160	25	45	50,000	0.12				0.14	3.49	

Streamwise location of test sections identified by A to R.
All four test section surfaces for streamwise locations A through R are heated.

- - - - - Leading test section surfaces

——— Trailing test section surfaces

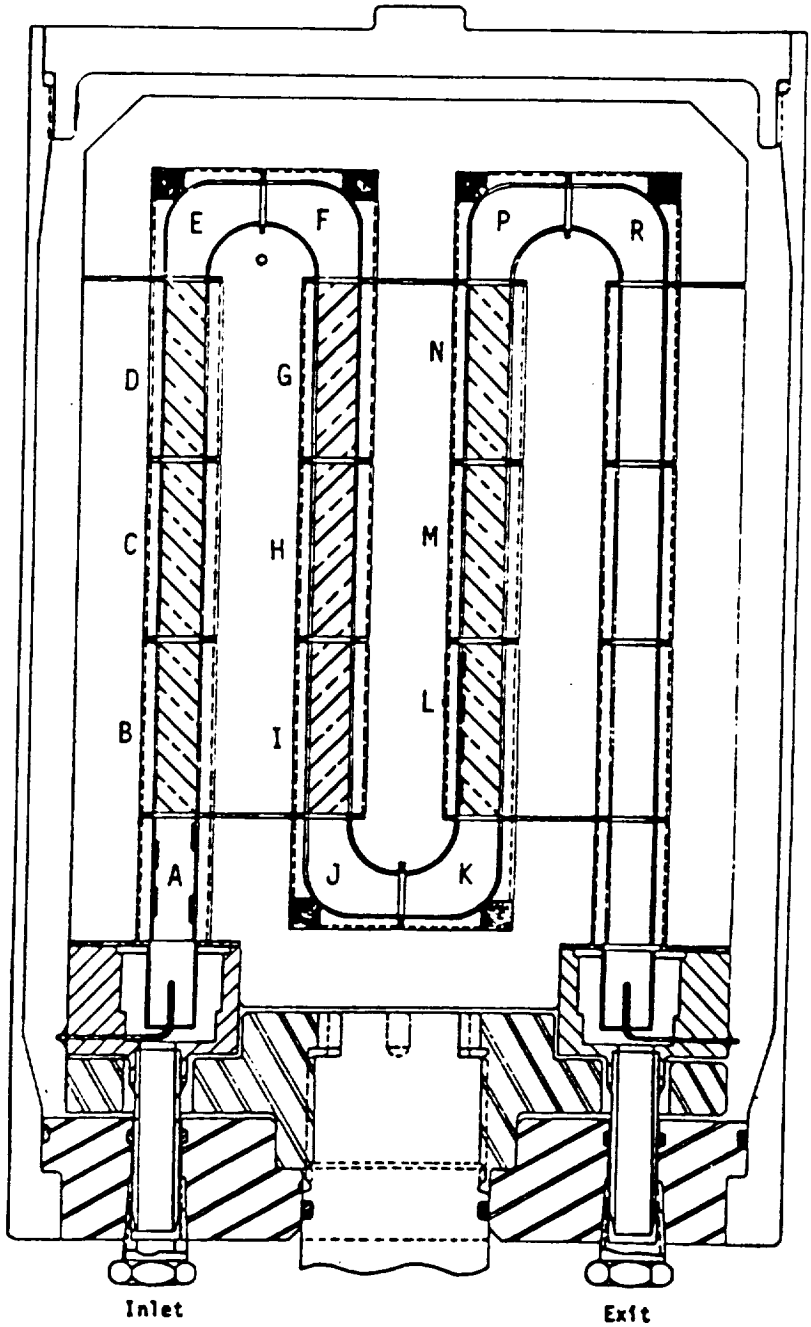

Figure 1 Cross Sectional View of Coolant Passage Heat Transfer Model Assembly With Skewed Trip Rough Walls

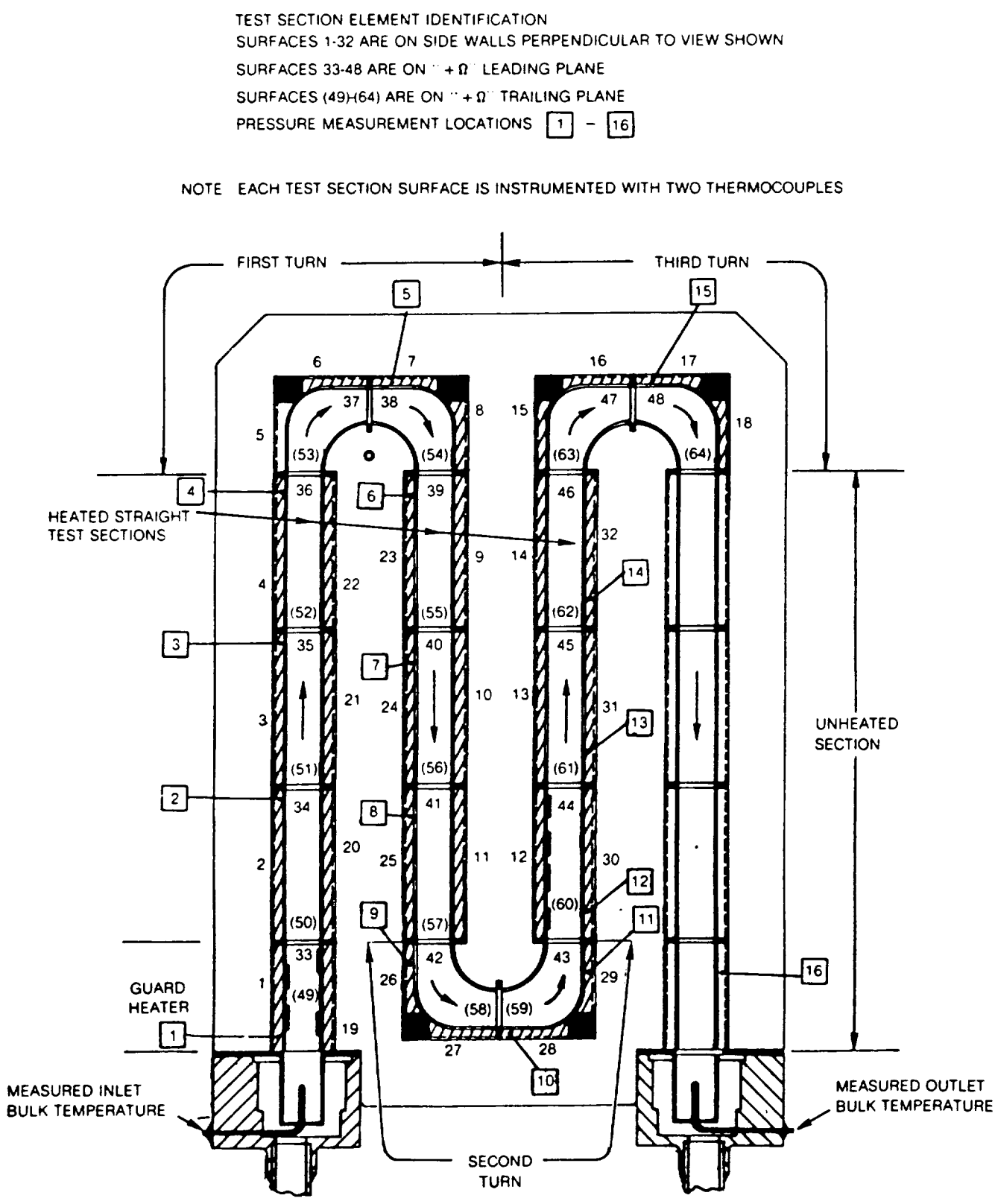

Figure 2 Instrumentation Plan for Coolant Passage Heat Transfer Model

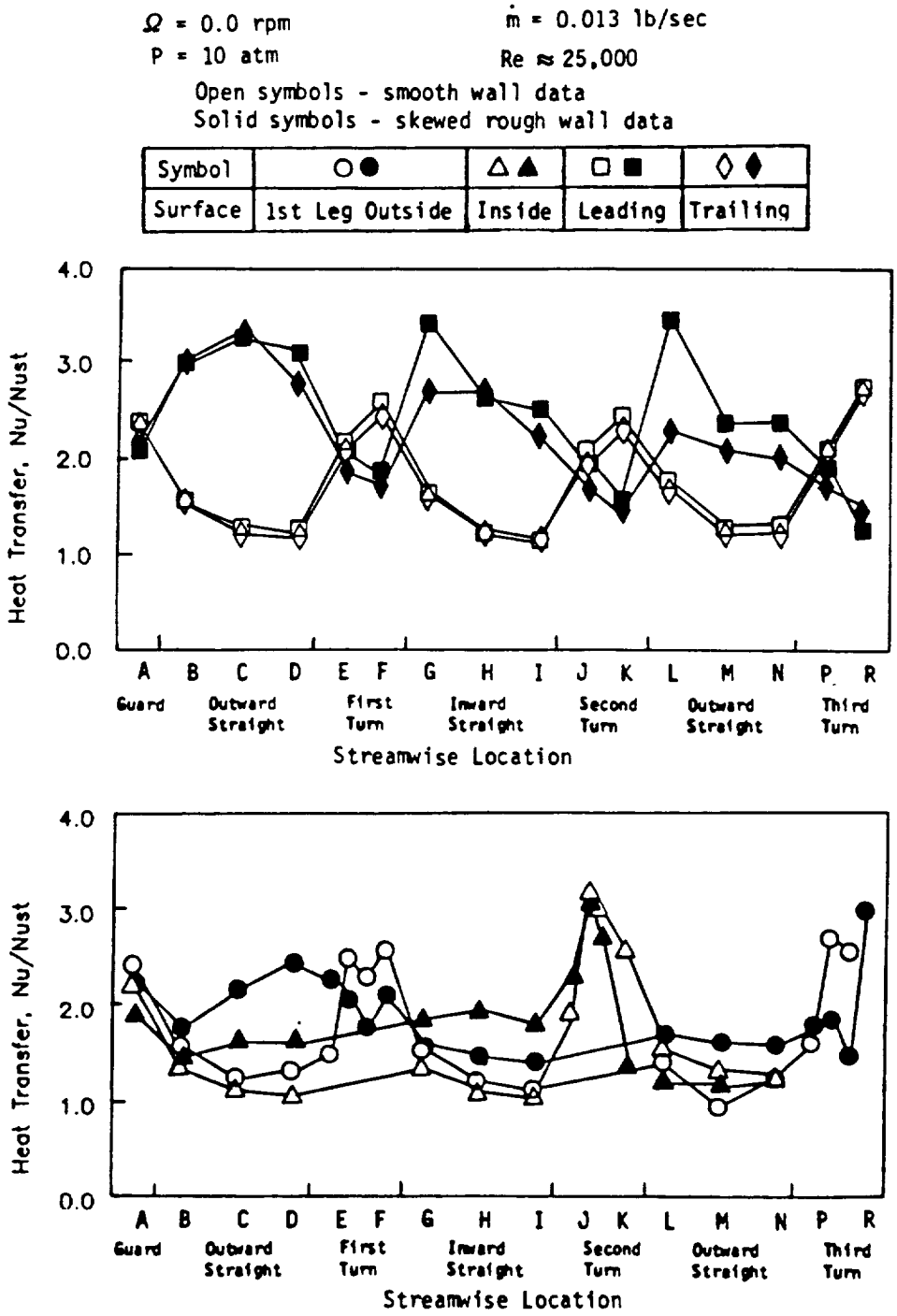

Figure 3 Comparison of Heat Transfer Results for Smooth Wall and Skewed Rough Wall at Baseline Stationary Flow Conditions

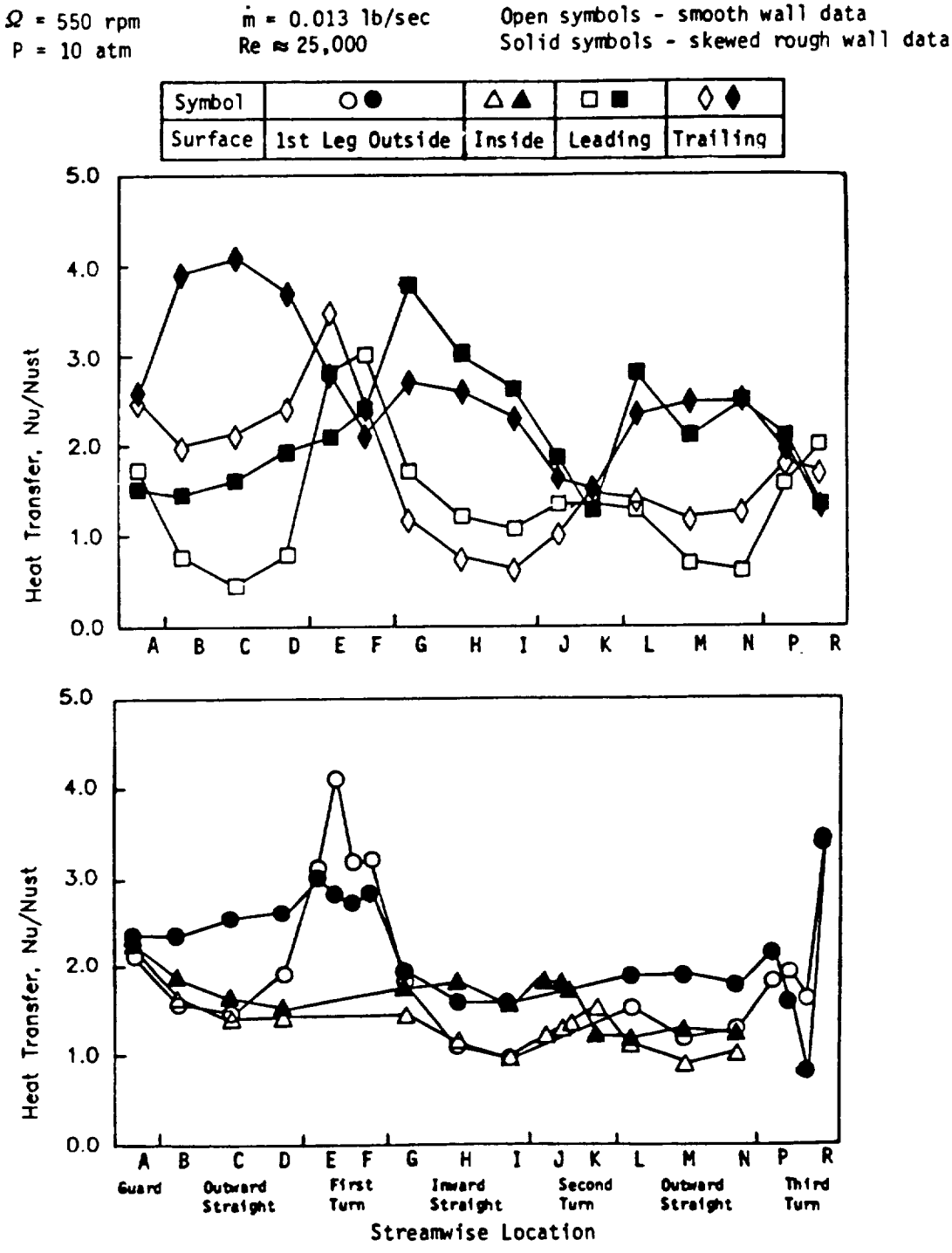

Figure 4 Comparison of Heat Transfer Results for Smooth Wall and Skewed Rough Wall at Baseline Rotating Flow Conditions

$\Delta T = 80^{0}$ F Re ≈ 25,000

Symbol	□	△	◇	×
Rotation Number	0	0.12	0.24	0.36
Speed (rpm)	0	275	550	825

a) Leading Surfaces 33-48

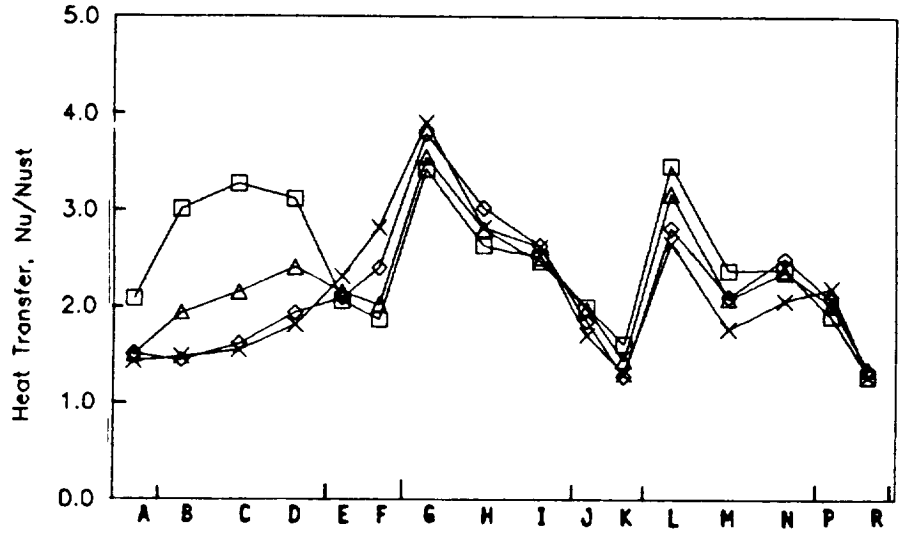

b) Trailing Surfaces 49-64

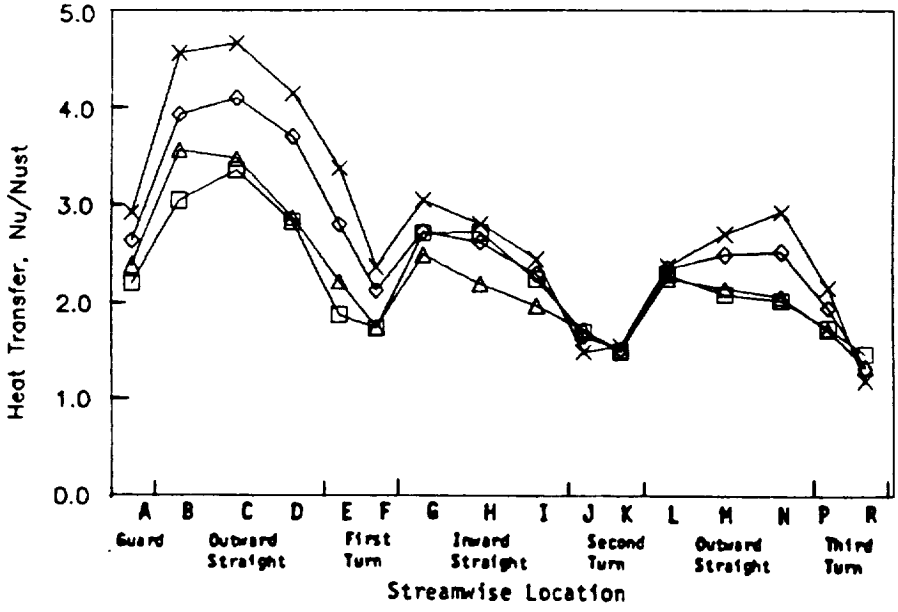

Figure 5 Effect of Rotation of Heat Transfer Results for Skewed Trip Rough Wall Model

$\Delta T = 80^{0}$ F Re ≈ 25,000

Symbol	□	△	◇	×
Rotation Number	0	0.12	0.24	0.36
Speed (rpm)	0	275	550	825

c) Side Wall Surfaces 1-18

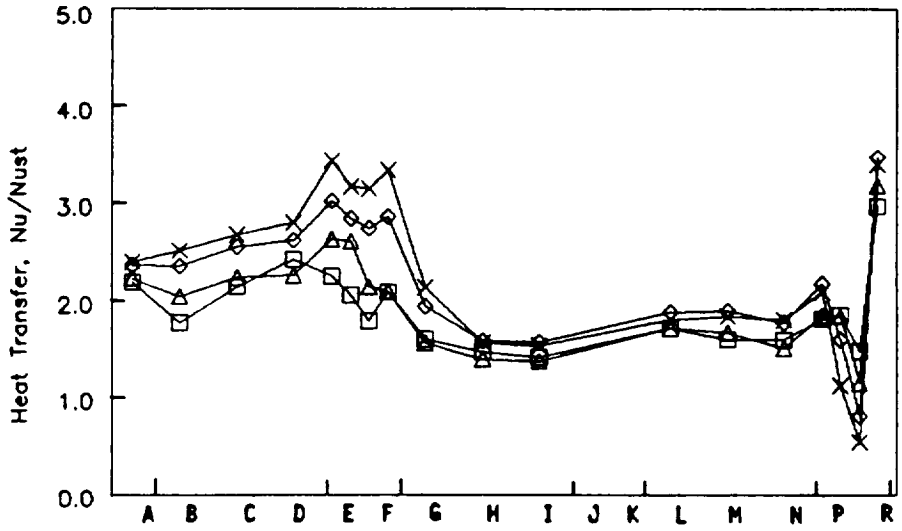

d) Side Wall Surfaces 19-32

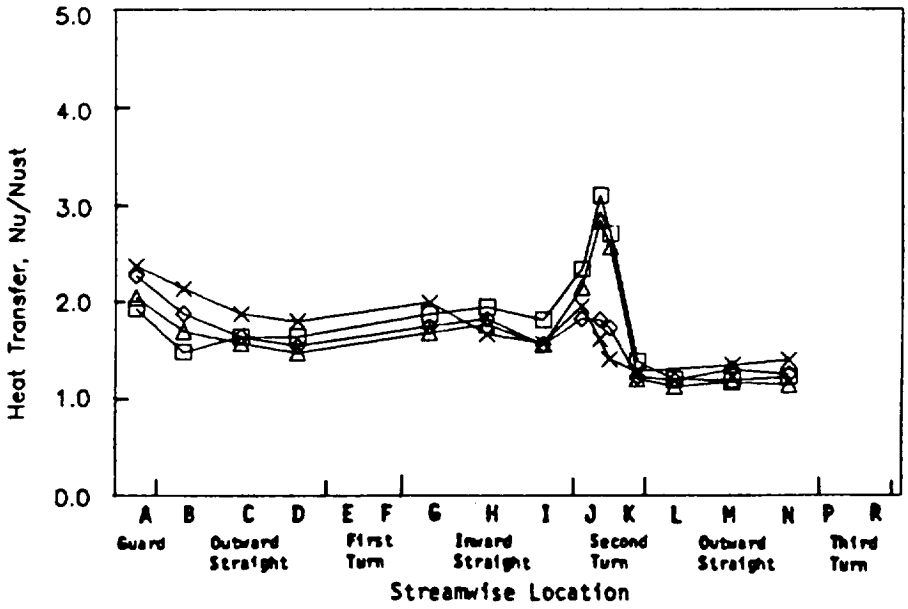

Figure 5 (Cont'd) Effect of Rotation of Heat Transfer Results for Skewed Trip Rough Wall Model

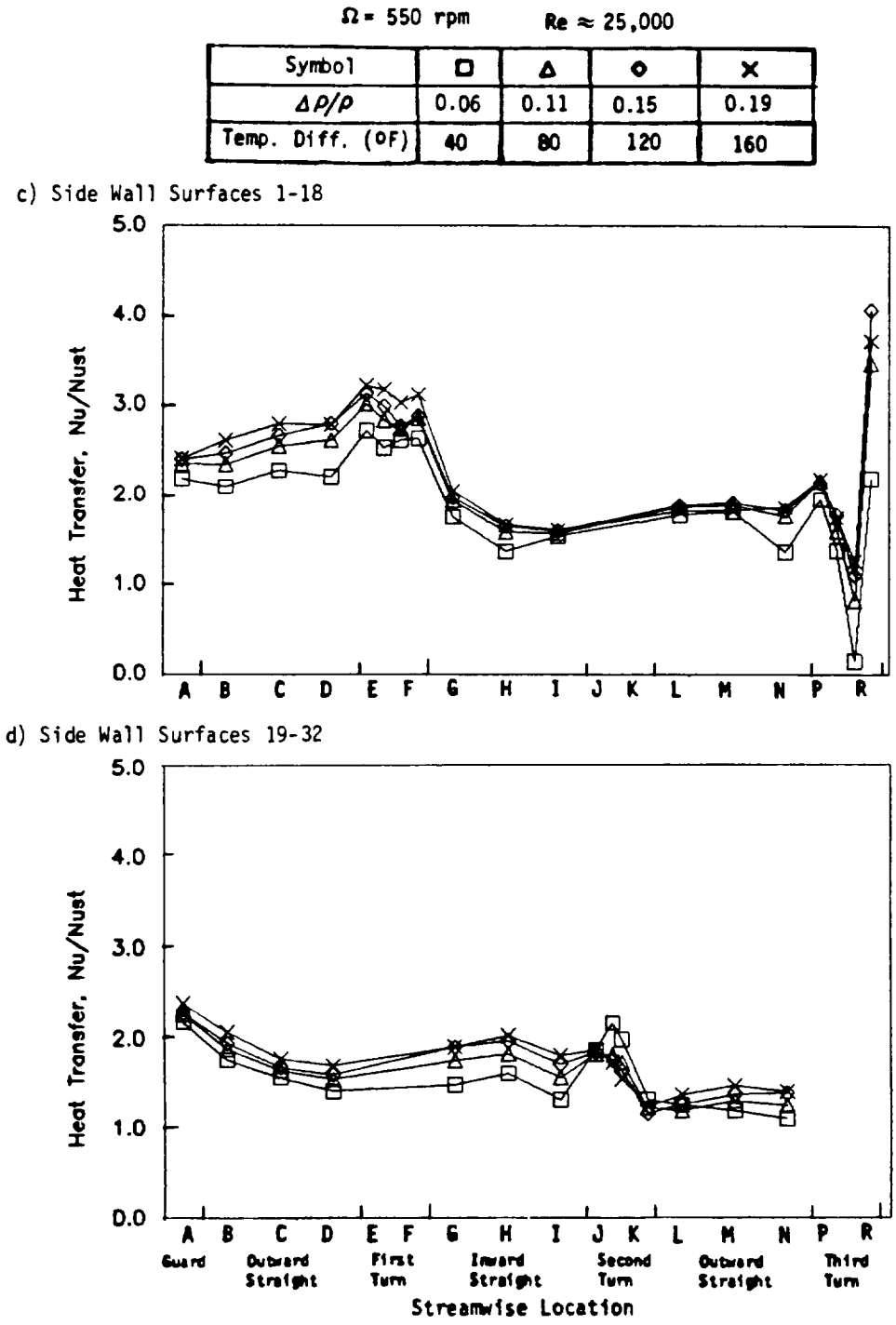

Figure 6 Effect of Density Ratio on Heat Transfer Results for Skewed Trip Rough Wall Model

Ω = 550 rpm Re $\approx$ 25,000

Symbol	□	△	◇	×
$\Delta\rho/\rho$	0.06	0.11	0.15	0.19
Temp. Diff. (°F)	40	80	120	160

a) Leading Surfaces 33-48

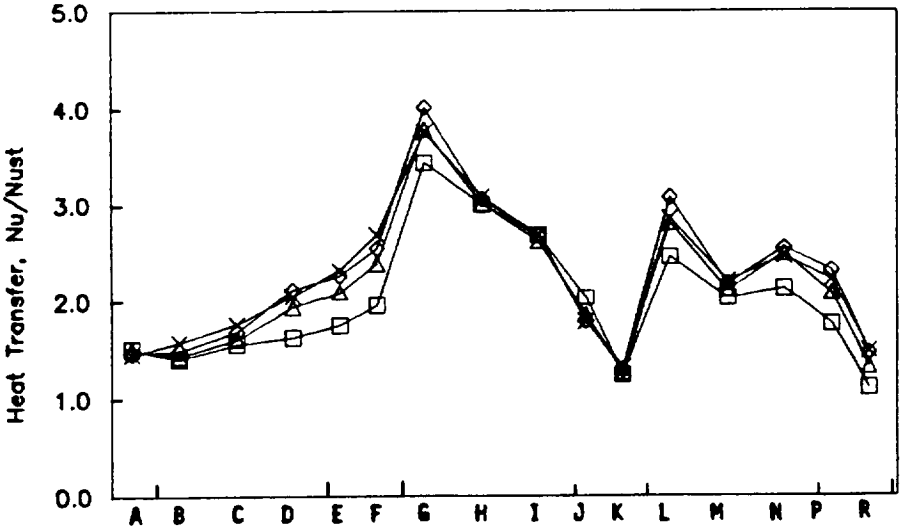

b) Trailing Surfaces 49-64

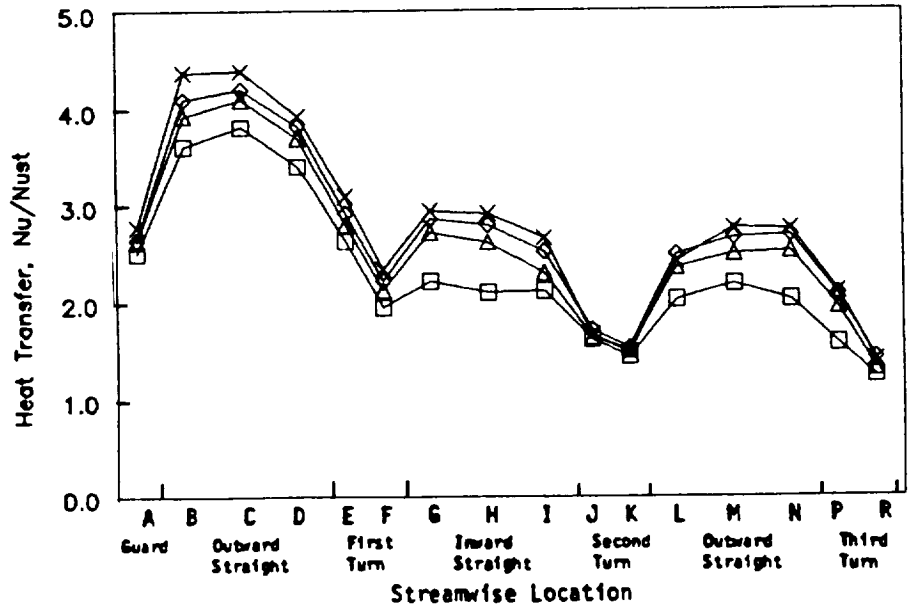

Figure 6 Effect of Density Ratio on Heat Transfer Results for Skewed Trip Rough (Cont'd) Wall Model

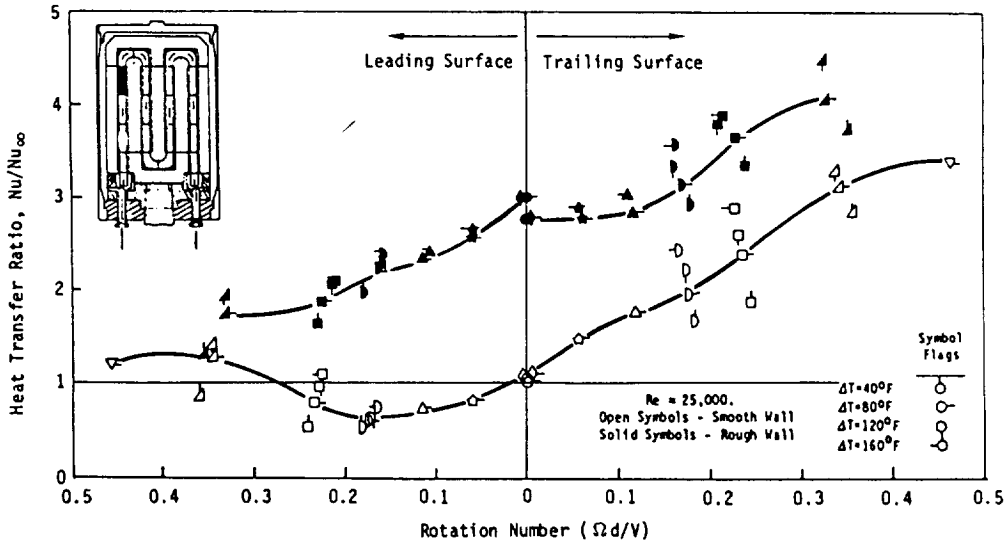

Figure 7 Effect of Rotation on Heat Transfer Ratio for Smooth Wall and Skewed Rough Wall Models

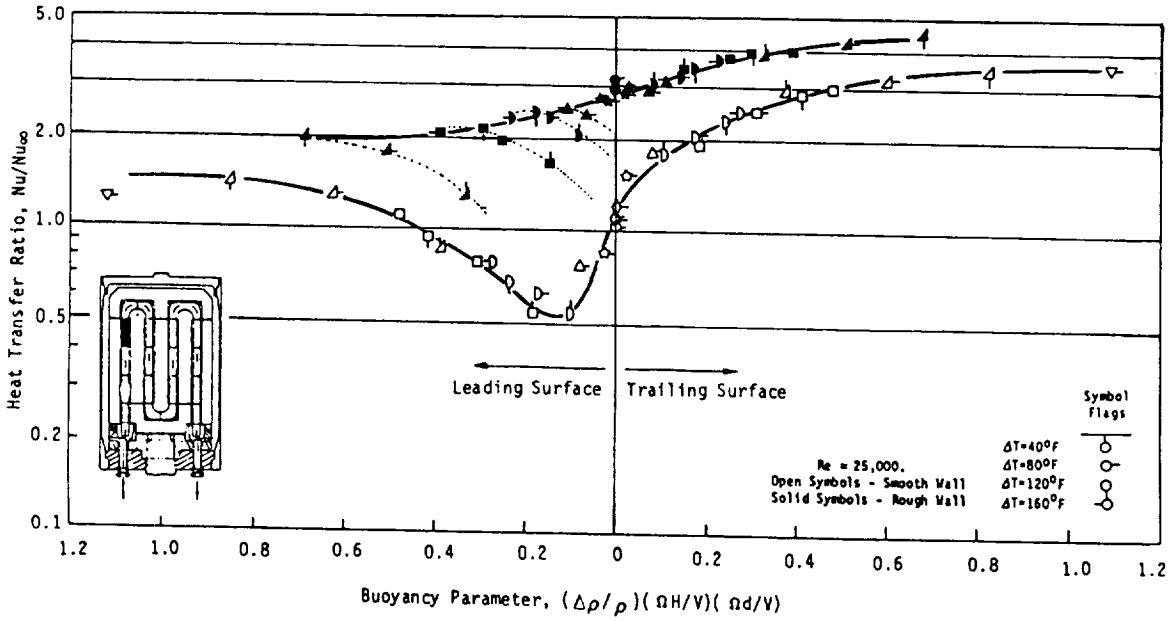

Figure 8 Effect of Buoyancy Parameter on Heat Transfer Ratio for Smooth Wall and Skewed Rough Wall Models

Heat Transfer with Very High Free-Stream Turbulence and Streamwise Vortices *

Robert. J. Moffat and Paul Maciejewski
John K. Eaton and Wayne Pauley

Department of Mechanical Engineering, Stanford University

Results are presented for two experimental programs related to augmentation of heat transfer by complex flow characteristics. In one program, high free stream turbulence (up to 63%) has been shown to increase the Stanton number by more than a factor of 5, compared with the normally expected value based on x-Reynolds number. These experiments are being conducted in a free-jet facility, near the margins of the jet. To a limited extent, the mean velocity, turbulence intensity, and integral length scale can be separately varied. The results to date show that scale is a very important factor in determining the augmentation. Detailed studies of the turbulence structure are being carried out using an orthogonal triple hot-wire anemometer equipped with a fourth wire for measuring temperature. The v' component of turbulence appears to be distributed differently from u' or w'. In the second program, the velocity distributions and boundary layer thicknesses associated with a pair of counter-rotating, streamwise vortices have been measured. There is a region of considerably thinned boundary layer between the two vortices when they are of approximately the same strength. If one vortex is much stronger than the other, the weaker vortex may be lifted off the surface and absorbed into the stronger.

Foreword

Most heat transfer research is conducted in low-turbulence tunnels, that is, with less than 0.5% turbulence, in flows especially refined to be spanwise uniform and steady. These conditions produce a "low-limit" estimate of heat transfer for a given mean flow and geometry. Free stream turbulence, or unsteadiness, or streamwise vortices increase heat transfer.

Even a small amount of free stream turbulence will advance the transition upstream, exposing more surface to turbulent heat transfer.

Free stream turbulence of 4 to 6% or larger may increase heat transfer even in fully turbulent regions [Blair, Ref. 1].

Streamwise vortices can thin the boundary layer, increasing heat transfer.

Most research studies of the turbulence effects use grids and let the turbulence relax until nearly homogeneous and isotropic before heat transfer studies are made [e.g. Blair, 1983].

* This work was performed under NASA NAG 3-522

Gas turbines, on the other hand, run with turbulence up to 20-30%, which is probably highly anisotropic and well laced with large coherent structures coming downstream from the combustion chamber. Dils and Follansbee [Ref. 2] measured up to 16% in the discharge of a laboratory scale combustor in a bench test. They reported increases in heat transfer of over 50% on the stagnation line of a cylinder in that flow. Other recent experiences (Rohde, [Ref. 3]) suggest 20 to 30% as a reasonable value for the relative turbulence near a typical first turbine nozzle ring.

The flow through a gas turbine may not look much like the flow most researchers have in mind when they think of "turbulence." It is not difficult to imagine, superimposed on the "normal" turbulent fluctuation a whole family of flow disturbances whose spatial and temporal characteristics are determined by the engine configuration upstream of the point observation.

Among the phenomena which may be present (either intermittently or steadily) are:

(1) large scale, low frequency quasi-coherent structures,
(2) streamwise vortices,
(3) wakes from upstream vanes or blades,
(4) regions of high turbulent shear stress.

This paper describes recent results from two programs at Stanford, one concerning the effects on heat transfer of very high free-stream turbulence and the second concerning the effects of streamwise vortices.

The high turbulence has, so far, been created by placing the test plate in the margin of a large diameter free jet. This exposes the plate to a flow in which the local turbulence intensity can be as high as 70%. Putting the plate at different distances from the jet exit, and at different distances from the axis of the jet allows a certain degree of independence in choosing the mean velocity, turbulence intensity, and the integral length scale.

There is no assurance that this flow is like that which exists in a gas turbine, but it need not be the same to provide clear evidence that chaotic, unsteady, and highly Turbulent (with a capital T!) flows can result in heat transfer rates far higher than predicted by the usual correlations. One objective of this program is to demonstrate how high the "upper bound" of turbulent heat transfer can be pushed, at a given x-Reynolds number based on mean velocity. This will not prove where the upper bound is in a gas turbine, but will show at least where the lower limit of that upper limit might be. A second objective is to identify the turbulence descriptors which best relate to the increased heat transfer. This latter issue is critically important, since we must know what aspect of turbulence best correlates with the increase in heat transfer before we can specify the measurements which must be made.

It would be very helpful to have a "good" description of the flow field in an engine, to guide the present experiments, but such data are not available. In fact, the present work has already raised some troubling questions about the sufficiency of the usual set of turbulence measures. The issue is, "What aspect of a turbulent flow field best correlates with the increase in heat transfer?" There is no assurance that measures of the mean velocity, turbulence intensity, and integral length scale will suffice to identify the heat transfer aspects of a flow. In fact, the work reported at HOST last year already contained evidence that fixing these three parameters <u>did not</u> fix the heat transfer. Until we know what aspect of the flow to measure, we cannot even enter a sensible request for "Engine Data."

The second program reported here concerns streamwise vortices, and their effect on heat transfer to turbulent boundary layers. This issue has attracted much attention over the last several years, chiefly with regard to the end-wall heat transfer. Several different vortical structures have been identified by flow visualization, but characterization of their effect on heat transfer has been slow in coming. This report describes some of the hydrodynamic features of a streamwise vortex pair which might relate to their effect on heat transfer. These results are described in the section entitled Phase II -- The Effects of Streamwise Vortices.

Phase I: The Effects of High Turbulence

During the past year, effort on this project has been concentrated on expanding the range of variable covered in the free-jet facility, documenting the turbulence structure in the free-stream and in the boundary layers, and designing an internal flow facility to run in parallel with the free-jet facility. The results will be presented in that order: first, the heat transfer measurements, then the turbulence measurements, and lastly, the plans for the new facility.

Figure 1 is reproduced from the 1985 HOST report and shows a schematic of the free-jet facility used in these studies. The test plate is 0.60 m wide and 2.5 m long, divided into 8 test plates, each 0.3 m long. Each test plate is of 1 cm thick Aluminum, equipped with 5 thermocouples in a cross-pattern, and a single-panel electric heater which covers the entire back face of the plate. The back face is protected with 6 cm of Fiberglass insulation, to minimize heat loss.

The test plate was checked for repeatability and baseline values by installing it in a closed-loop, low turbulence heat transfer tunnel. Data from the test plate agreed with the accepted correlation for a constant wall temperature turbulent boundary layer within +/- 4%. The test plate was then installed twice into the free jet, at the same nominal position coordinates and flow conditions. The two sets of results agreed within better than +/- 2%. By these three tests, the credibility of the test plate as a heat transfer device was established, as well as the reproducibility of the data in the free jet. These results were presented at the 1985 HOST meeting.

Figure 2 is also reproduced from the 1985 HOST report, and shows the effects of free stream turbulence up to 48%. The envelope within which the Stanton number may lie is bounded on the bottom by the usual low-turbulence correlations for laminar and turbulent boundary layers. At 48% turbulence, the Stanton number lies above the usual correlation by about a factor of 4 and has a discernibly lower slope, in log coordinates.

During the past year, we have extended the turbulence level of the tests from 48% to 63%, with runs over a range of mean velocities from 0.5 to 5 m/sec, with integral length scales between 4 cm and 17 cm. A total of 60 different combinations have now been run.

Results of the high turbulence heat transfer taken to date are summarized in Figure 3, in coordinates of St/Sto vs. Re_x. Each line of symbols represents one run. The points are measurements on the individual plates. St/Sto is the ratio of the Stanton number with high turbulence to the Stanton number which would have existed at the same mean-flow x-Reynolds number, but with no turbulence. On any one line of data, or comparing any two lines having the same mean velocity, this ratio is a direct measure of the heat transfer augmentation caused by the free-stream turbulence. It is not so direct to compare two line of different mean velocity.

The results shown cover the entire range of test conditions: various combinations of free stream velocity (.47 to 2.89 m/s), Tu (22% to 63%) and integral length scale (4-17 cm).

It is apparent, from Figure 3, that the effects of turbulence are not simple to correlate: No simple proposal orders the data. For example, turbulence intensity alone does not explain the comparison between Runs 1 and 3 (numbering down from the top of the figure): those two runs have approximately the same turbulence intensity, but the augmentaion is far higher for the low velocity than the high. Also, examining Runs 2 and 3, we see two runs at about the same mean velocity (0.87 compared with 0.89), and about the same integral length scales (9.0 and 10.0 cm), but significantly different turbulence intensities (48% and 63%), yet the two flow conditions produce almost exactly the same heat transfer augmentation: about 3/1. This same "insensitivity" is displayed by Runs 4 and 5, which differ by 10% in their turbulence intensities, but hardly at all in their heat transfer responses.

Several One-Parameter suggestions have appeared in the literature in the past 10 years, usually expressing the heat transfer augmentation in terms of turbulence intensity. Based on the present results, it appears that these cannot succeed, at least for the highly disturbed flow we are dealing with here. A broader treatment is required.

A stepwise multiple linear regression program was used on the present data set, a program which sought the most significant parameter from a list of candidates provided, and extracted its effect before seeking the next most important parameter. The coefficients were not forced, not was the order of parameter selection.

The program generated the following relationship:

$$St^{*} = 0.440 = \frac{St}{Re_{\lambda}^{-0.395}\left(\frac{\Delta}{\lambda}\right)^{-0.204}\left(1-\frac{y}{x_1}\right)^{-0.43}}$$

The correlation coeffient, R^2, for this relationahip was 0.95.

In this relationship λ is the integral length scale, y is the distance from the test plate to the centerline of the jet (at the leading edge), and x_1 is the distance from the leading edge of the test plate to the nozzle exit plane.

Of the 420 data points recorded, none lie more than 18% from that line, or more than 20% from a simpler, perhaps more physically satifying form:

$$St^{**} = 0.405 = \frac{St}{\left[Re_x\left(1-\frac{y}{x_1}\right)\right]^{-0.2}\left[Re_{\lambda}\left(1-\frac{y}{x_1}\right)\right]^{-0.2}}$$

Such results are useful, but dangerous if misinterpreted or misapplied. Any correlation arrived at by such a purely formal means must be viewed with caution, and its limitations kept in mind. It is not a predictor of expected results for tests outside the present operating envelope. It may not even be a good interpolator by which to predict the results of new tests whose conditions lie within the envelope, but which involve new combinations of the variables, combinations not included in the data base. It is a correlation which describes the existing data, and nothing more: 420 data points taken from 60 runs, each with 7 data points, for the

combinations of conditions we have run. We plan to investigate the robustness of these correlations by testing their predictions against a set of runs not included in the present correlation-generating base, but these tests have not yet been done. We hope these correlations will lead us to something more physically based.

Note that turbulence intensity does not appear in either of these correlations. If forced in, Tu appears with an exponent of +0.03: a very nearly insignificant effect. If only Re and Tu are offered as candidates, but not λ, the resulting correlation has a much lower value of R^2.

The high value of R^2 suggests that all of the significant variables are included, somehow, in this correlation. A constant value of the "position" parameter $(1 - y/x)$ must surely correspond to some invariant combination of the hydrodynamic parameters of the free jet. We haven't found what those are, yet, but we are working on identifying them.

In parallel with these heat transfer tests, detailed hydrodynamic studies have been made of the turbulence distributions within the boundary layer, by hot-wire anemometry. Previous hot-wire results reported from this project have come from a single wire, parallel to the test surface. This simple system was used to characterize the free stream turbulence, for the purpose of ordering the heat transfer data sets. For the detailed studies within the boundary layer, a more sophisticated system was introduced. An orthogonal triple-wire probe was used for the boundary layer studies, with real-time analog processing of the linearized signals from the three individual wires yielding real time, instantaneous U, V, and W velocity components in laboratory coordinates. The system has been used (and reported) before [Ref. 4]. It produces both time averaged and instantaneous values of U, V, W, u', v', w', u'v', u'w', and v'w', and products of these terms. A fourth wire, for temperature measurement, has been added under this project. The temperature signal is used in a fourth channel of analog processing which is connected to the velocity circuitry so as to compensate the instantaneous velocity signals for the instantaneous temperature, as well as to display the temperature fluctuation, t'. Thus, turbulence data can be taken in a heated boundary layer, without contamination of the velocity signals from the temperature fluctuations. In addition, the turbulent heat flux, v't' can be directly measured. We have not yet completed the qualification tests of the direct measurement of v't', but the preliminary results were good..

Figures 4, 5, and 6 show typical distribution of the mean velocity, the turbulence components (u' , v' , w' , and q), and the turbulent transport of momentum, -u'v'.

The mean velocity distribution is plotted against the y-position normalized on the momentum thickness of the boundary layer. The present results are compared with a seventh-power profile, for illustrative purposes. The present data are more sharply "squared off" than the usual turbulent boundary layer--indicative of higher shear stress (and heat transfer) at the wall. The distributions of q^2, $\overline{u'^2}$, and $\overline{w'^2}$ are similar in shape, rising exponentially from zero to the free stream value. The $\overline{v'^2}$ distribution is qualitatively different from the others.

The distributions of turbulent heat flux and shear stress are similar in shape and both indicate the existence of a very thin layer near the wall, wherein the shear strees and heat flux are constant. The quad-wire probe is too large to get data very close to the wall: those studies will have to be done with more conventional probes.

We are continuing the quad-wire study, and intend to document the structure of these layers for each of the conditions which has a significantly different effect on heat transfer and try to identify which aspect of turbulence is most closely associated with high augmenatation of heat transfer.

For the next year, we will move a part of the effort into a closed loop tunnel, generating high turbulence using a combustion chamber simulator. The objective, once again, will be to first identify flows with very aggressive turbulence characteristics, judged by their effect on heat transfer, and then to measure those characteristics. The combustion chamber simulator will be a rectangular box with replaceable sides, closed at the upstream end. It will be installed at the upstream end of the test section, extending upstream into the present nozzle. All 5 faces (4 sides and the upstream end) will have replaceable panels. Holes of different diameters will be used to adjust the larger scales of turbulence. Similar patterns of holes will be used for all sizes. A bypass gate will allow the test section mean velocity to be reduced, at constant turbulence kinetic energy. Prototype tests have show significant enhancements of heat transfer near the leading edges of flat plates in such a flow, but no detailed data have been taken.

From a comparison of the free jet and the internal flow results we hope to be able to identify which aspects of turbulence are responsible for the large increases in h and, perhaps, how to manage them by hardware design.

Phase II -- The Effects of Longitudinal Vortices

The objective of the second phase of the work is to examine the heat transfer effects of longitudinal vortices embedded in otherwise two-dimensional turbulent boundary layers. This simple case is meant to model the effects of embedded vortices which can be introduced by fixed support struts, cooling air jets, and transverse or longitudinal curvature. The experimentation couples spatially resolved heat transfer measurements with detailed mean velocity and turbulence measurements.

Earlier work, under separate funding examined the effect of single vortices of moderate strength [see Eibeck and Eaton, refs. 3 and 4]. The single vortex was found to produce substantial local augmentations of the heat transfer coefficient in the downwash region of the vortex. Fluid dynamics measurements showed that the effect of the vortex was simply to locally change the boundary layer thickness. Structural changes in the inner part of the boundary layer were minimal.

The work is presently being extended to pairs of vortices which are a common occurence in practical situations. The experiments are conducted in a two-dimensional, boundary-layer wind tunnel with a freestream velocity of 16 m/s and typical momentum-thickness Reynolds numbers of about 2000. The heat transfer coefficient is measured on a constant-heat-flux surface using 160 thermocouples to obtain good spatial resolution. All three mean velocity components and all components of the Reynolds stress tensor are measured using miniature five-hole probes and cross-wire anemometers. Counter-rotating vortex pairs are generated using pairs of half- delta-wing vortex generators which protrude from the wall.

To date, we have completed the acquisition of mean velocity and skin friction data for 12 different vortex configurations. Typical data are shown in Figure A. The striking feature is the broad region of boundary layer thinning and augmented skin friction between the two vortices. Clearly, this vortex pair would cause a very large increase in the average skin friction and heat transfer coefficients. Cases for which the common flow between the vortices is directed away from the wall have a

different behavior; the vortices propel each other out of the boundary layer and the effect on the heat transfer coefficient is minimal. One case involved a pair of vortices with unequal strengths, a rough model for the vortices on a turbine endwall. The vortices were swept towards each other by their image vortices, then the weaker vortex began to lift above the stronger. After a short distance, the weaker vortex lost its identity as it was absorbed into the stronger vortex.decreased on the other.

We are presently acquiring full planes of Reynolds stress data for two representative cases. Following that, heat transfer data will be obtained for all fifteen cases.

REFERENCES

1. Blair, M. F., "Influence of Free-Stream Turbulence on Turbulent Boundary Layer Heat Transfer and Mean Profile Development. Part I: Experimental Data," Journal of Heat Transfer, 105: 33-41, February 1983.

2. Dills, R. R., and Follansbee, P. S., "Heat Transfer Coefficiency around Cynlinders in Crossflow in Combustor Exhaust Gases," Jn. Eng. for Power, October 1977.

5. Rohde, J., "Personal Communication," 1984.

4. Frota, M. M. "Analysis of the Uncertainties in Velocity Mesurements and Techniques for Turbulence Measurements in Complex Heated Flows with Multiple Hot Wires". Stanford University PhD Dissertation, Department of Mechanical Engineering, August 1982.

5. Eibeck, P. A. and Eaton, J. K., "An Experimental Investigation of the Heat-Transfer Effects of a Longitudinal Vortex Embedded in a Turbulent Boundary Layer," Report MD-48, Department of Mechanical Engineering, Stanford University, November 1985.

6. Eibeck, P. A. and Eaton, J. K., "Heat Transfer Effects of a Longitudinal Vortex Embedded in a Turbulent Boundary Layer," J. Heat Transfer, in press, 1986.

FIGURE CAPTIONS

Fig. 1. Schematic of the free jet facility.

Fig. 2. High turbulence effects on heat transfer

Fig. 3. Summary of high turbulence heat transfer results.

Fig. 4. Representative profile of the mean streamwise velocity, U.

Fig. 5. Representative distributions of turbulence.

Fig. 6. Representative distribution of turbulent shear stress.

Fig. 7. Effects of a typical embedded vortex pair on mean velocity and skin friction.

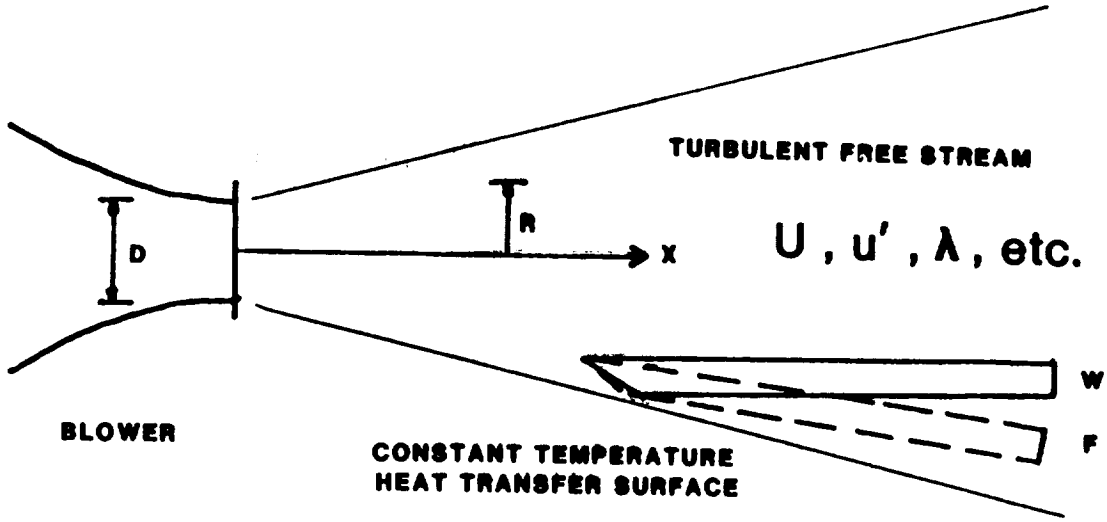

Fig. 1. Schematic of the free jet facility.

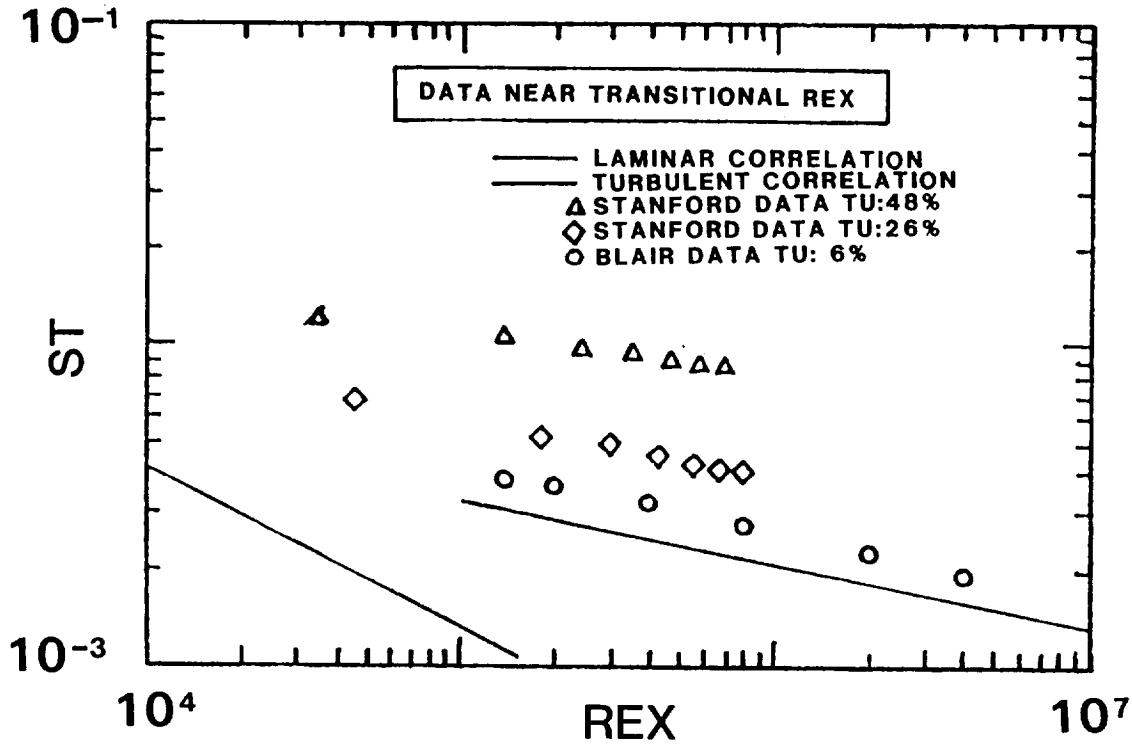

Fig. 2. High turbulence effects on heat transfer

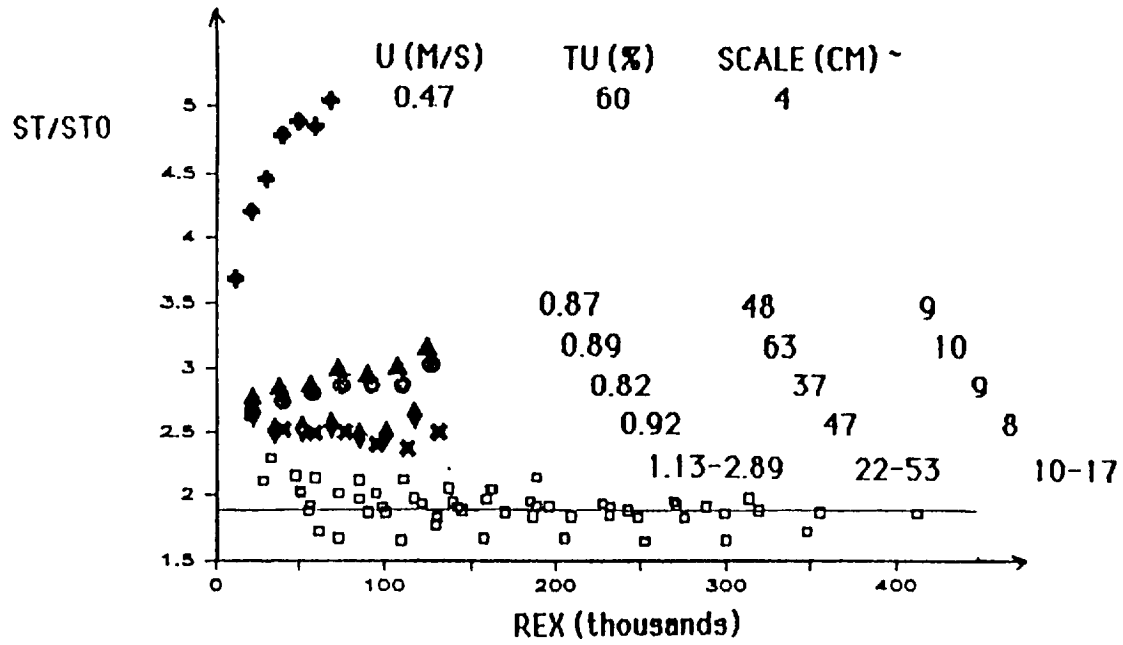

Fig. 3. Summary of high turbulence heat transfer results.

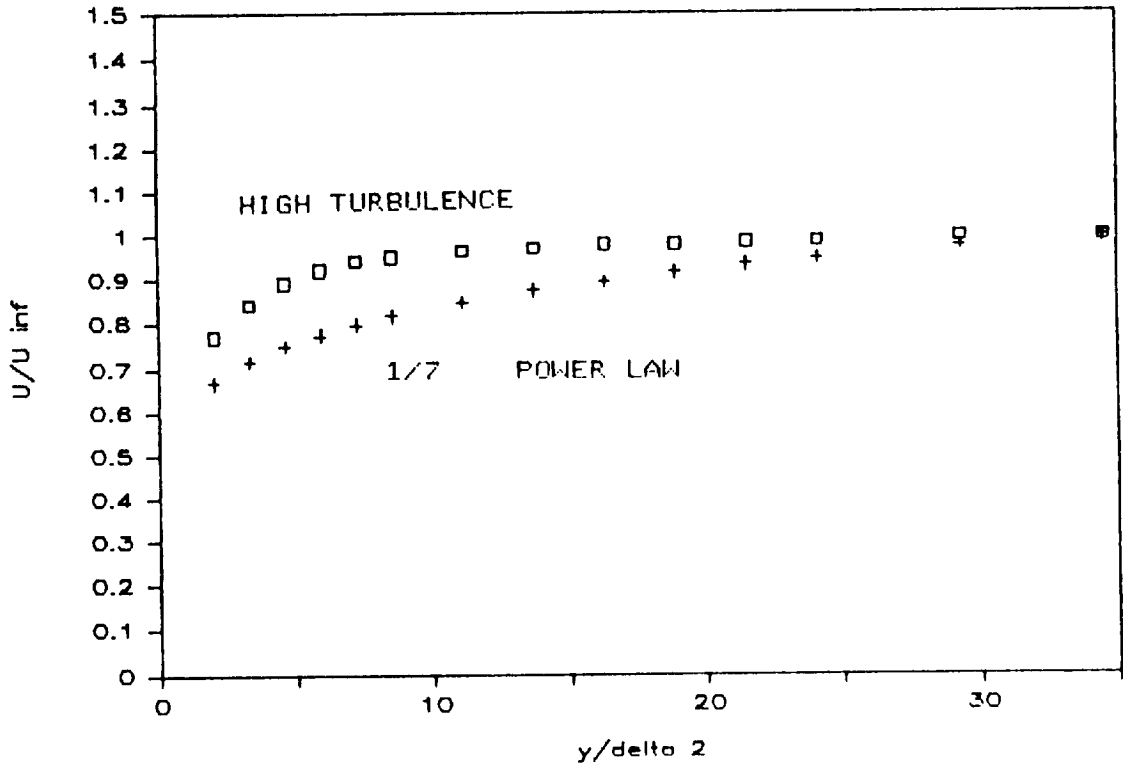

Fig. 4. Representative profile of the mean streamwise velocity, U.

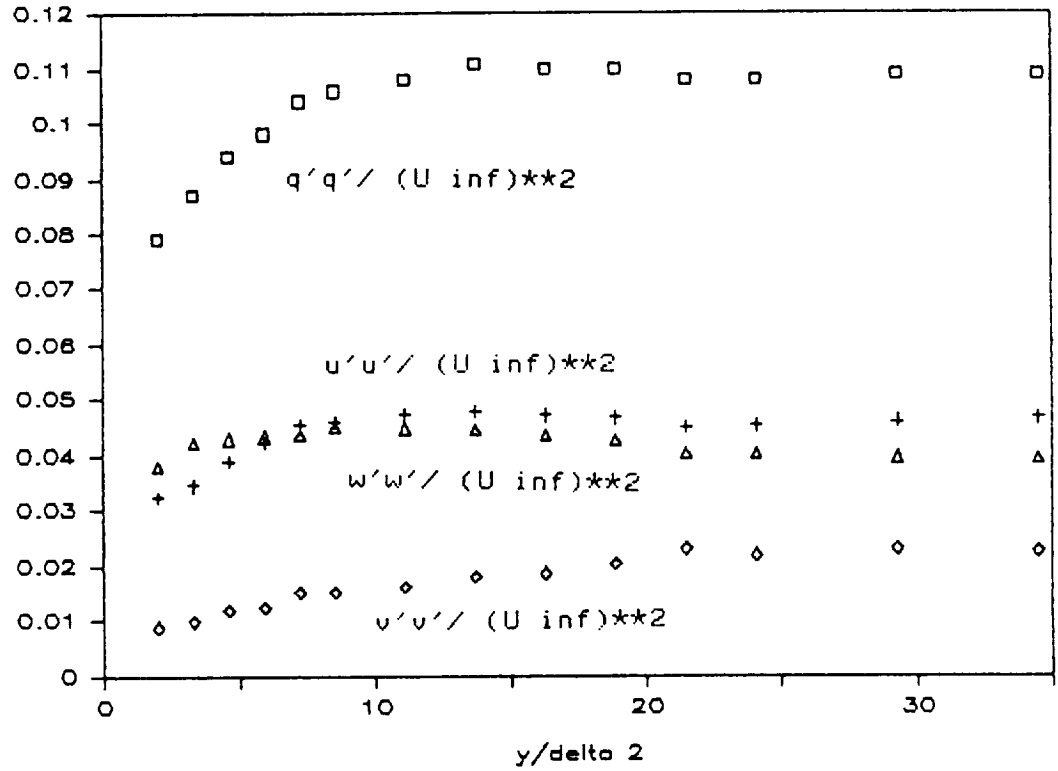

Fig. 5. Representative distributions of turbulence.

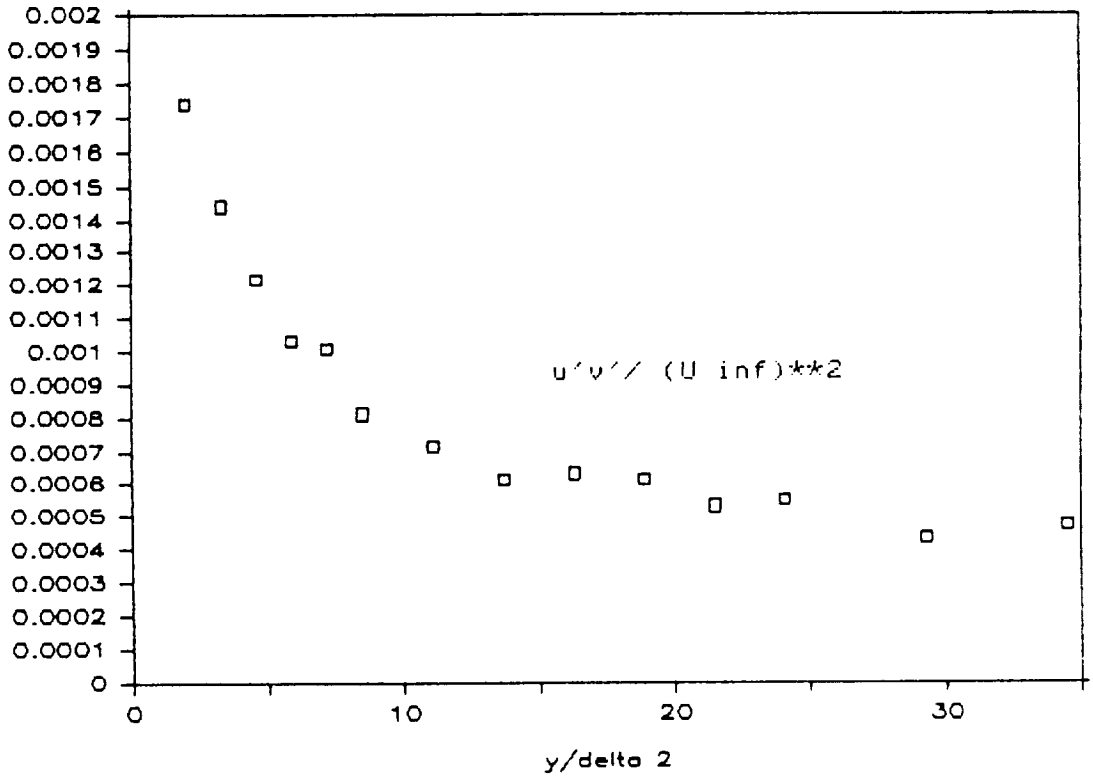

Fig. 6. Representative distribution of turbulent shear stress.

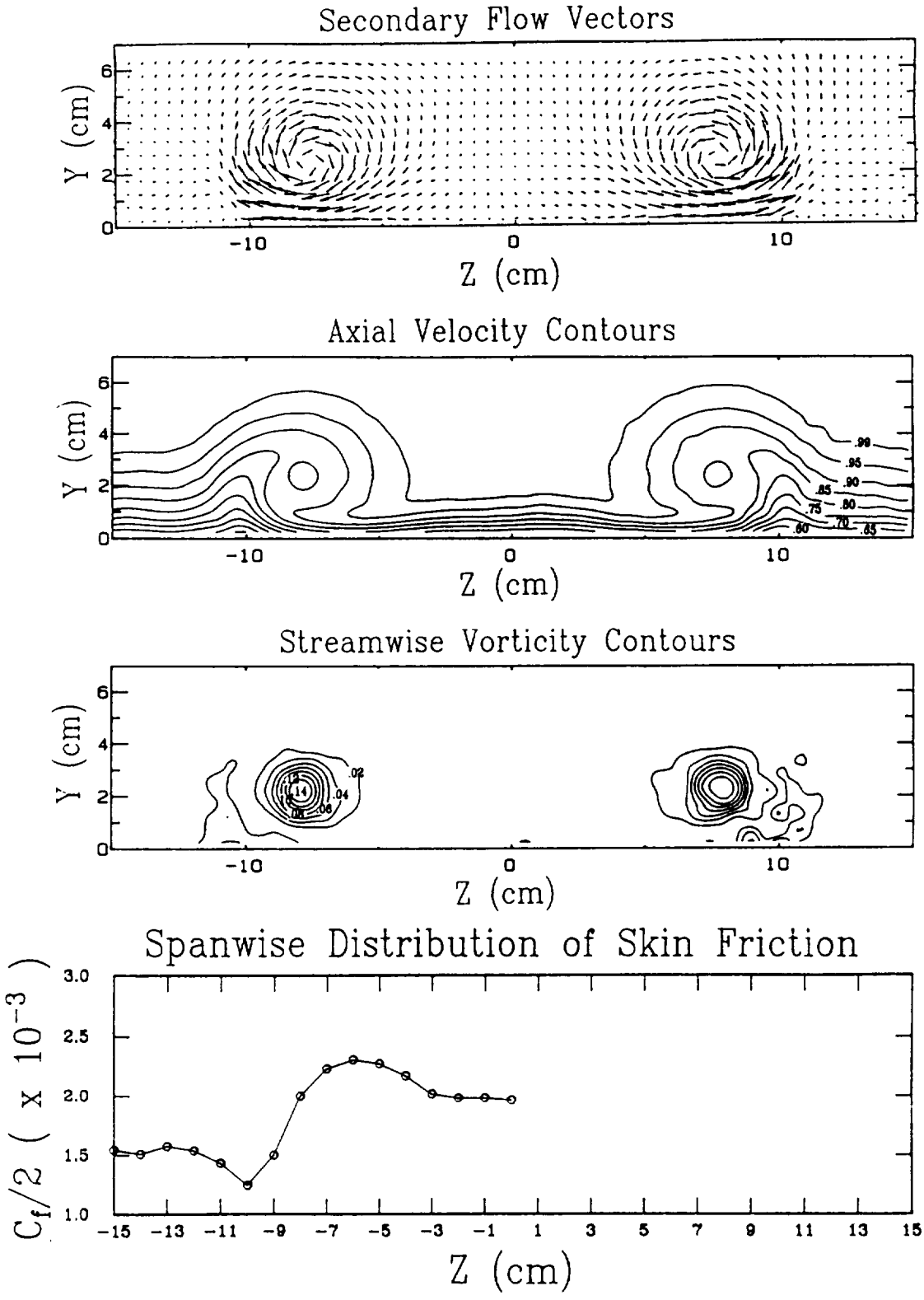

Fig. 7. Effects of a typical embedded vortex pair on mean velocity and skin friction.

DEVELOPMENT OF LOW REYNOLDS NUMBER TWO EQUATION TURBULENCE MODELS FOR FOR PREDICTING EXTERNAL HEAT TRANSFER ON TURBINE BLADES*

Suhas V. Patankar and Rodney C. Schmidt
Department of Mechanical Engineering, University of Minnesota

INTRODUCTION

A research effort has been underway to study the use of two equation low Reynolds number tubulence models in predicting gas side heat transfer on turbine blades. The major objectives of this ongoing work are basicly threefold.

(1) Study the predictive capabilities of two equation low Reynolds number turbulence models under the conditions characteristic of modern gas turbine blades.
(2) Explore potential improvements to the models themselves as well as to the specification of initial conditions
(3) Provide a comparison of the predictions of these models with the experimental data from a broad range of recently available turbine cascade experiments.

This work is particularly concerned with the problems associated with predicting the boundary layer transition from laminar to turbulent flow, as this may be the most serious deficiency of current modeling techniques.

The work has proceeded in a number of phases or steps, and several of these of been completed. The purpose of this report is to briefly discribe the results and conclusions of the first two phases of this work.

PHASE ONE

Evaluation of the transition prediction characteristics of current low Reynolds number two equation models for flat plate zero pressure gradient boundary layers under the influence of free stream turbulence.

Research has shown that the dominant factor influencing the location and length of transition is the free stream turbulence intensity [1]. It has also been shown that the effects of free stream turbulence on skin friction and heat transfer can be correlated reasonably well with two parameters, the free stream turbulence intensity (Tu_e), and the free stream turbulence length scale (L_e) [2,3]. These same two parameters are directly related to the two quantities whose behavior is modeled in most two equation turbulence models, ie. the turbulent kinetic energy (k), and the turbulence dissipation rate (ε). With the recent development of low Reynolds number versions of these models, it has seemed reasonable to hope that with refinement, these models would be capable of predicting the influence of free-stream turbulence on boundary layers in both the laminar and the turbulent regimes, and also on transition.

The application of some of these models by a number of independant workers has verified that at least qualitatively, these models do predict the major effects of free stream turbulence on transition [5,6]. However, a detailed quantitative study has not been available to the knowledge of the authors. The purpose of this phase of the research was to more carefully evaluate the transition prediction capabilities of two relatively popular low Reynolds number versions of the stardard k-ε two equation turbulence model. The models chosen were those of Lam and Bremhorst [7], and Jones and Launder [8].

The computations were performed using the Patankar Spalding method [9] for boundary layer flows. A variable grid using 88 nodes was used for all calculations and was found to be sufficiently fine to produce essentially grid independant results.

* Work done under NASA Grant NAG-3-579

Sensitivity to Initial Conditions

Figure 1 shows the results of varying the initial profiles of k and ε on the location of transition for a zero pressure gradient flat plate flow where Tu_e=3% (note that the subscript e will always refer to free stream conditions). The model used was the Lam-Bremhorst model. Run "A" follows the initial profile recommendations of Rodi and Scheuerer [4] , where

$$k=k_e*(U/U_e)^n \quad , n=2 \qquad (1)$$

$$\varepsilon=a_1*k*\partial U/\partial Y \quad , \varepsilon > (k_e)^{1.5}/L_e \quad , a_1(Tu=3.\%) = .375 \qquad (2)$$

Run "B" was begun with essentially zero kinetic energy within the boundary layer. This was accomplished by setting n=8 and a_1=2.0. Both A and B were begun at $Re_x=2.27 \times 10^4$, corresponding to a momentum thickness Reynolds number (Re_θ) of 100. Runs C and D correspond to A and B except for the initial starting location, which was moved upstream to $Re_x=10^3$. This figure illustrates the following general characteristics of both low Reynolds number models.

(1) At a given starting location, a k=0 initial profile results in the onset of transition begining at the farthest downstream location.

(2) The sensitivity to initial profiles decreases with decreasing initial Re_x. Below some critical value, the location of transition becomes essentially independant of initial Re_x.

An important result to understand is that it is possible to specify profiles at $Re_x=2.27 \times 10^4$ such that the curves A and B are reproduced. However, it is not possible to specify any set of profiles at $Re_x=10^3$ and yield transition as per C or D.

Sensitivity to Initial Starting Location

To further explore the sensitivity of the prediction to the initial starting location, a set of calculations were made with identical initial profiles, but at different initial Renolds numbers ($Re_{x,i}$). The k=0 initial profile explained above was used for all cases, as this always yielded the higher limit on $Re_{x,trans}$. Figure 2 shows the results of these calculations. For the Lam Bremhorst model, the location of transition is strongly dependant on $Re_{x,i}$ for $Re_{x,i} > 10^3$, but basically independant for $Re_{x,i} < 10^3$. The Jones Launder model shows a somewhat lower critical value, with the location of transition not significantly changing until $Re_{x,i}<10^2$.

Sensitivity to different free stream turbulent intensities

Figure 3 shows the results of calculations at free stream turbulence intensities ranging from 1.0 to 6 %. The calculations were all started at $Re_x=10^3$ (where for the Lam Bremhorst model the initial profiles of k and ε were unimportant). A Tu_e=1% calculation for the Lam Bremhorst model is not shown because it was found that transition was not predicted by this model for Tu=1%. This agrees with the experience of Rodi and Scheuerer [5].

As can be seen, the qualitative characteristics of the variation of C_f during transition are predicted reasonably well. Also, the onset of transition moves progressively upstream with increasing Tu_e as it should. However, significant differences between the predictions of the two models occur at higher

Tu_e. In Figure 4 the momentum thickness Reynolds number at the start ($Re_{\theta S}$) and the end ($Re_{\theta E}$) of transition are plotted and compared with the correlation of Abu-Ghannam and Shaw [10]. Two major quantitative problems are apparent in this figure. First, the onset of transition is generally predicted too early for both models.This is especially true at higher Tu_e. Second, the predicted length of transition is much too short.

Summary

Tests have been made of the transition prediction characteristics of two low Reynolds number two equation turbulence models. The major items of interest learned include the following;

(1)Both models tested showed, as expected, the ability to correctly model the basic qualitative aspects of transition, ie. the continuous transition from laminar to turbulent flow, the onset of which moves upstream with increaseing Tu_e.

(2)The onset of transition is moderately sensitive to the initial profiles specified for k and ε. This sensitivity decreases with decreasing $Re_{x,i}$.

(3)For any given $Re_{x,i}$, there is a limit to how far downstream the onset of transition can be predicted. This limit is reached by specifying the initial profile of k=0.

(4)The onset of transition is very sensitive to the location at which the calculations are started. This sensitivity decreases with decreasing $Re_{x,i}$.

(5)For calculations started at low $Re_{x,i}$ (where the sensitivity to the initial profiles for k and ε becomes small), the onset of transition occurs at unrealistically early locations for both models tested.

(6)Both models predict transition lengths significantly shorter than experiment.

(7)The Lam Bremhorst model does not predict transition for free stream turbulence intensities of about 1.1% and lower.

(8)Because of the above deficiencies, the transition predictions of both models compare rather poorly with the correlation of Abu-Ghannam and Shaw.

PHASE TWO

Modifications to improve the transition prediction characteristics of the Lam Bremhorst low Reynolds number turbulence model.

A fairly ideal transition model for boundary layer flows would be one which, given any physically realistic velocity, pressure, free stream turbulence and length scale distribution with x , and the profiles for U, k, and ε at some given x_i, would consistantly predict the correct location and length of transition. The agreement with experiment should be at least as good as the correlations currently available relating the effects of these parameters on transition. Furthermore, the results should be invariant with the initial starting location (x_i), as long as the profiles for k and ε were specified correctly.

That the two models tested do not adequately approach this ideal is quite obvious from the results presented earlier. However, there is another difficulty with striving to achieve this ideal. That problem centers around the lack of experimantal data concerning the nature of the "correct" profiles for k and ε at any point prior to transition. Although our models require this as input, insufficient knowledge is currently known about the values of these turbulent quantities within the quasi-laminar region just prior to the onset of transition. Thus previous researchers have had to rely on add-hoc methods with

little more than the known boundary conditions and intuition to guide them [5, 6].

In searching for ways to improve on the current models, we must be content (for the present) with "reasonable" profiles in this region, and try to minimize the sensitivity of the predictions to small variations in them.

The Lam Bremhorst model was chosen as the model to begin work with. This was done for basicly three reasons. First, the favorable results of the study by Patel et al [11] . Second, the previous use of this model by Rodi and Scheuerer in working on this same problem. And third, the simpler form of the source terms present in the k and ε equations, a result of the form of the dissipation rate variable used in this model.

Stability Considerations

The physical process by which an initially laminar boundary layer undergoes transition to a fully turbulent state is a very complex problem, but is unseparably tied to stability considerations. Fundamental to the process is the response of the flow to the introduction of small disturbances, from whatever source. Under some conditions, a disturbance will decay, it's small energy being absorbed into the mean flow. Under other conditions, a disturbance will be amplified, and energy will be extracted from the mean flow to feed this growth. It is only under these "unstable" conditions that the onset of transition can occur.

Linear stability theory gives some insight into the conditions underwhich a boundary layer becomes unstable. Solutions to the well known Orr-Sommerfield equation for a Blasius velocity profile yield a critical Reynolds number based on momentum thickness, $Re_{\theta,c}$, below which infinitesimal disturbances will not be amplyfied (Commonly quoted as 163 due to an approximate solution, more accurate solutions have shown it to be equal to 201).

Experiments have shown that under the infuence of high free stream turbulence, transition can begin to occur at Re_θ even less than this stability limit [10]. This is due the nonlinear behavior which the high Tu_e introduces. However, there does appear to be a lower limit, as the data seems to bottom out at about Re_θ=160. Consequently, Abu-Ghannan and Shaw have proposed Re_θ=163 as a lower limit below which transition will not occur even at high turbulence intensities.

Stability considerations are not a part of either of the low Reynolds number turbulence models that we have looked at. The k and ε equations are simple advection diffusion equations with a particular set of nonlinear source terms. From this context, it is not particulaly surprising that the deficiencies previously discribed exist.

Method of Rodi and Scheuerer

The most helpful previous work in this area that this author is aware of is the recent work presented by Rodi and Scvheuerer [5,6]. They apparently recognized many of the problems previously discussed and recomended a particular procedure to deal with it. They chose to begin all calculations at a momentum thickness Reynolds number of Re_θ=100. This in essence is their answer to the stability problem discussed earlier. They then proposed particular forms for the k and ε profiles (see eq. 1,2) which seemed reasonable, and which gave them a simple constant (a_1) with which to tune their results (a_1 was correlated with Tu_e).

Figure 5 shows the results of following this procedure for a range of Tu_e of 1.5 to 6 %. These conditions are identical to those used for the runs presented in Figure 3, and the results show improvement as compared to the previous Lam-Bremhorst model calculations. However, the results are still relatively unsatisfactory when compared to the correlation of Abu-Ghannan and Shaw. Although some improvement has been made with respect to the onset of transition, the short length of transition is still a problem. Furthermore, since the model itself has not been changed, we are still left

with the undesirable situation where, if we needed to start our calculations just a little farther upstream, we would be unable to find any profiles for k and ε which would yield similar results.

The mechanism by which the model simulates transition

Before attempting to consider ways to improve the transition prediction characteristics of the model, it is important to consider carefully how the process occurs in the model as it stands.

Figure 6 shows the typical development of the turbulent kinetic energy profiles as the model proceeds from a laminar to a turbulent state. Turbulent kinetic energy from the free stream initially begins to diffuse into the boundary layer. As this continues, the production term, $\mu_t(\partial u/\partial y)^2$, starts to become significant. This in turn increases the local value of k, and thus μ_t. Thus process feeds on itself, causing the rapid increase in k shown until the paramaters achieve a relatively stable state due to the low Reynolds number functions and the wall boundary conditions.

The key term in this entire process appears to be the production term in the turbulent kinetic energy equation. This is the term which in the model, simulates the amplification of free stream disturbances and the resulting eventual transition to a turbulent state.

Proposed modification to the production term

A variety of different modifications to the model were explored and compared to try and find a method which would satisfactorily alleviate the problems previously identified. These will not be discussed individually. Only the method found to be the most satisfactory (at this point) will be discribed.

The method developed focuses on two ideas. First, that some means of incorporating stability considerations into the calculational procedure must be provided. Second, that the process by which the model simulates transition, once started, must proceed at a finite rate and in accord with experiment. It will be referred to as the "PTM3" modification (an acronymn for Production Term Modification 3).

The modification is based on the following hypothesis.

(1) Since the production term is the term in the model which simulates the amplification of purtibations, below some critical momentum thickness Reynolds number ($Re_{\theta,c}$), the production term in the k equation should be insignificant.

(2) The rate at which P_k can change is assumed to have some finite limit. The form of that limiting growth rate, $\partial P_k/\partial t$, is assumed to be a simple linear function of P_k , as per equation 3 below, and as shown in Figure 7.

$$\left[\partial P_k/\partial t\right]_{max} = A*P_k + B \qquad (3)$$

Guided by linear stability analysis and the results of experiments at a variety of free stream turbulent intensities, the value of $Re_{\theta,c}$ was set at 125, and was assumed constant. Although admittedly somewhat arbitary, it is based on the fact that no experiments known to this author have indicated the onset on transition occuring for Re_θ lower than about 130-140. Thus, in the model, for $Re_\theta<125$, the production term in the k equation (the ε equation remains unchanged) was set equal to zero.

The values of A and B are assumed to be functions of the free stream turbulence intensity, and were found by optimizing the results of numerous numerical experiments to the correlations of Abu-Ghannam and Shaw. Figure 8 illustrates the dependence of A and B on Tu_e found from this work.

It should be noted that the form of this modification is such that the fully turbulent predictions of the unmodified Lam-Bremhorst model are not affected, becoming completely transparent once transition has occured.

Results of the Proposed Modification

In Figure 9, the sensitivity of the model to initial starting location is shown. Once again, a series of calculations at Tu_e=3% were made at different initial locations, just as was done and presented in Figure 2. As can be seen, the sensitivity is greatly reduced, with all calculations started at $Re_{x,i}$ less than 10^4 being virtually identical. Variations due to initial starting profiles for k and ϵ were also negligible for runs initiated below this limit.

In Figure 4 the predicted momentum thickness Reynolds numbers at the start and end of transition for the PTM3 calculations, the correlation of Abu-Ghannam and Shaw, and the previous unmodified calculations presented earlier.

In Figure 10, the behavior of the predicted variation of C_f with Reynolds number is shown for free stream turbulence intensities of from 1.5 to 8 %. The improvement is excellent as compared to figures 3 and 5.

In Figure 11 the heat transfer results for calculations using the PTM3 form of the Lam-Bremhorst model are compared with an experiment of Wang,Simon and Buddhavarru. Also shown is a calculation by Park and Simon (paper submitted to 2nd ASME/JSME Thermal Engineering Conference, Mar. 1987) using standard mixing length type transition modeling as per Abu- Ghannam & Shaw [10] and Dhawan & Narasimha [12]. The agreement is excellent, and an improved simulation of the transition path as compared to mixing length type models is indicated.

In Figure 12, the heat transfer data from three experiments of Blair [3] are compared with the calculations. Excellent agreement is found except for the grid 2 case, where the calculations predict transition somewhat upstream of the experiments.

Although the difference between the calculation and the experiment for grid 2 is not greater than the scatter indicated in the original correlation by Abu-Ghannam and Shaw, it was nevertheless disappointing. A plausible explaination for this error relates to the difference between the "total" free stream turbulence intensity, and the three componants from which it is found, ie. u', v', w'. Blair's experiments report the variation with x of both the total value of Tu_e, as well as each of these components. For this experiment, the u' component is about 1/2 % lower than the average of them all. Since many of the results reported in the literature report only u', isotropic conditions must be assumed in order to obtain a value for k_e. Thus it may be that the model is slightly biased toward u'. This would naturally manifest itself most clearly in the medium Tu range for the following reasons. First, the assumption of isotropic turbulence generally improves significantly with decreasing turbulence intensities. And second, the sensitivity of the location of transition to the magnitude of Tu_e decreases very strongly as Tu becomes higher. Thus, at moderate levels of Tu_e, we would expect the most sensitivity to a potential bias of this sort. Although just conjecture at this point, it was confirmed that when the calculations were repeated by assumming a free stream turbulence based on u' only, the results were in much closer agreement. This is also shown in Figure 12.

Conclusions

It has been found that the proposed modification, as applied to the calculation of transition on zero pressure gradient boundary layers under the influence freestream turbulence, has the following improved characteristics.

(1) The model is insensitive to variations in starting location for $Re_{x,i} < 10^4$.

(2) The model is insensitive to any reasonable specification of the initial profiles for k and ϵ for starting locations below $Re_{x,i} < 10^4$.

(3) For free stream turbulence intensities of from 1.3 to 8 % the model predicts transition starting and ending at momentum thickness Reynolds numbers in accordance with the correlation of Abu-Ghannam and Shaw.

(4) The path by which transition occurs, as manifest in the variation in skin friction or surface heat transfer, is in closer agreement with experiment than standard mixing length type transition models.

It was also found that,

(5) The modifications become completely transparent after transition occurs, reverting to the standard Lam-Bremhorst model.

REFERENCES

1. Graham, R. W., "Fundamental Mechanisms that Influence the Estimate of Heat Transfer to Gas Turbine Blades", ASME Paper 79-HT-43
2. Hancock, P. E., Bradshaw, P., "The Effect of Free Stream Turbulence on Turbulent Boundary Layers", J. of Fluids Engineering, Vol 105, Sept. 1983, pp. 284-289
3. Blair, M. F., "Influence of Free-Sream Turbulence on Turbulent Boundary Layer Heat Transfer and Mean Profile Development, Part 1 - Experimental Data", ASME J. of Heat Transfer, Vol. 105, Feb. 1983, pp. 33-40
4. Rodi, W., Scheuerer, G., "Calculation of Heat Transfer to Convection-Cooled Gas Turbine Blades", J. of Engineering for Gas Turbines and Power, Vol 107, July 1985, pp. 620-627
5. Rodi, W., Scheuerer, G., "Calculation of Laminar-Turbulent Boundary Layer Transition on Turbine Blades", AGARD-CPP-390
6. Wang, J. H. et al, "Airfoil Heat Transfer Using Low Reynolds Number Version of a Two Equation Turbulence Model", ASME Paper 84-GT-261
7. Lam, C.K.G., Bremhorst, K., "A Modified Form of the k-e Model for predicting Wall Turbulence", J. of Fluids Engineering, Vol. 103, Sept. 1981, pp. 456-460
8. Jones, W.P., Launder, B. E., "The Calculation of Low Reynolds Number Phenomena With a Two-Equation Model of Turbulence", Int. J. of Heat and Mass Transfer, Vol 16, 1973, pp. 1119-1130
9. Patankar, S.V., Spalding, D.B., Heat and Mass Transfer in Boundary Layers, 2nd. ed., Intertext, London, 1970
10. Abu-Ghannam, B.J., Shaw, R., "Natural Transition of Boundary Layers - The Effects of Turbulence, Pressure Gradient, and Flow History", J. of Mech. Eng. Science, Vol. 22, No 5, 1980, pp. 213-228
11. Patel, V.C., et al., "A Review and Evaluation of Turbulence Models for Near Wall and Low Reynolds Number Flows" , AIAA Journal, Vol 23, 1985, p. 1308
12. Dhawan, S., Narasimha, R., "Some Properties of Boundary Layer Flow During Transition from Laminar to Turbulent Motion", J. of Fluid Mech., Vol 3, 1958, pp. 418-436
13. Wang, T., Simon, T.W., and Buddhavarapu, J., "Heat Transfer and Fluid Mechanics Measurements in Transitional Boundary Layer Flows", J. of Eng. Gas Turbines and Power, Trans. ASME, Vol 107, No 4, pp. 1007-1015

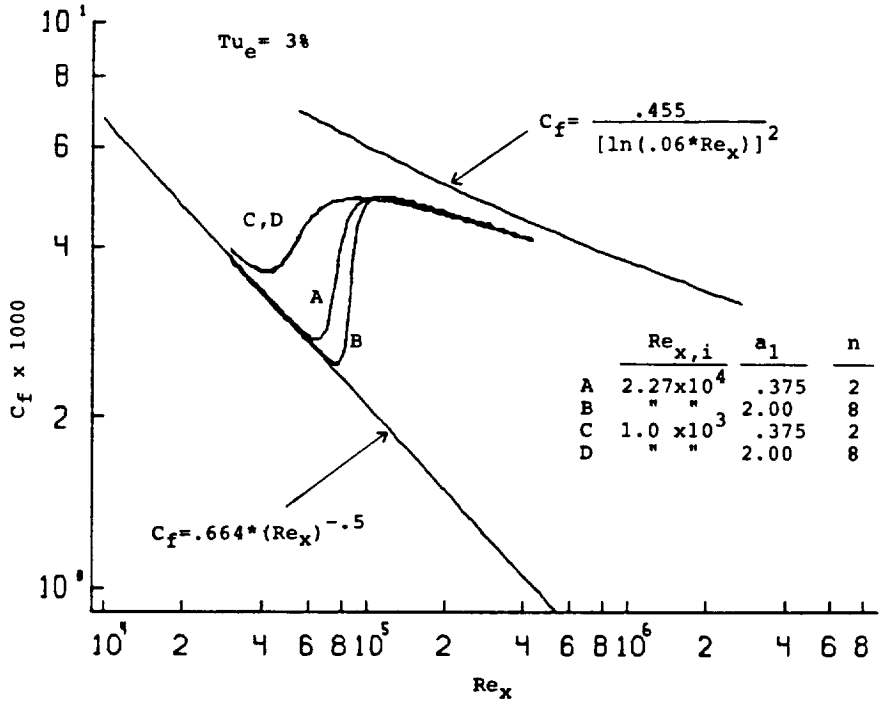

Figure 1 Plot of C_f vrs. Re_x showing the sensitivity to the initial profiles of k and ε of the Lam-Bremhorst model

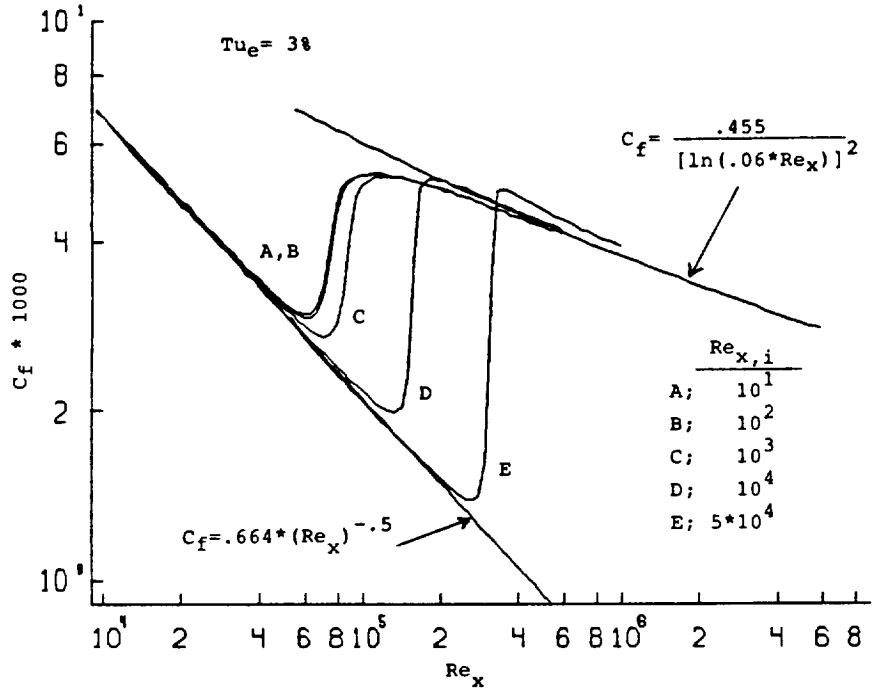

a) Jones Launder model

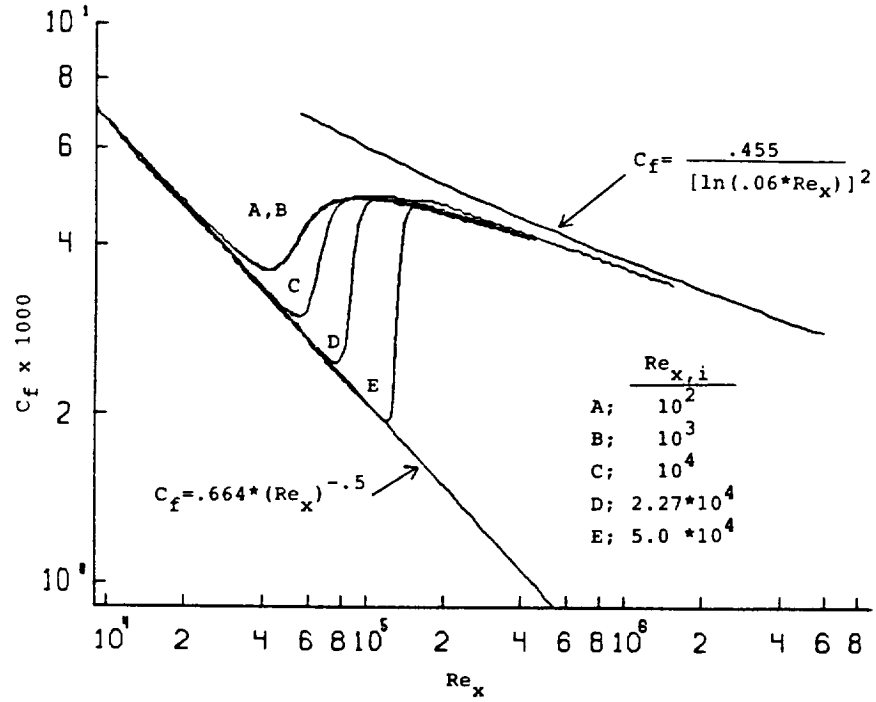

b) Lam Bremhorst model

Figure 2 Plot of C_f vrs. Re_x showing the sensitivity to the initial starting location

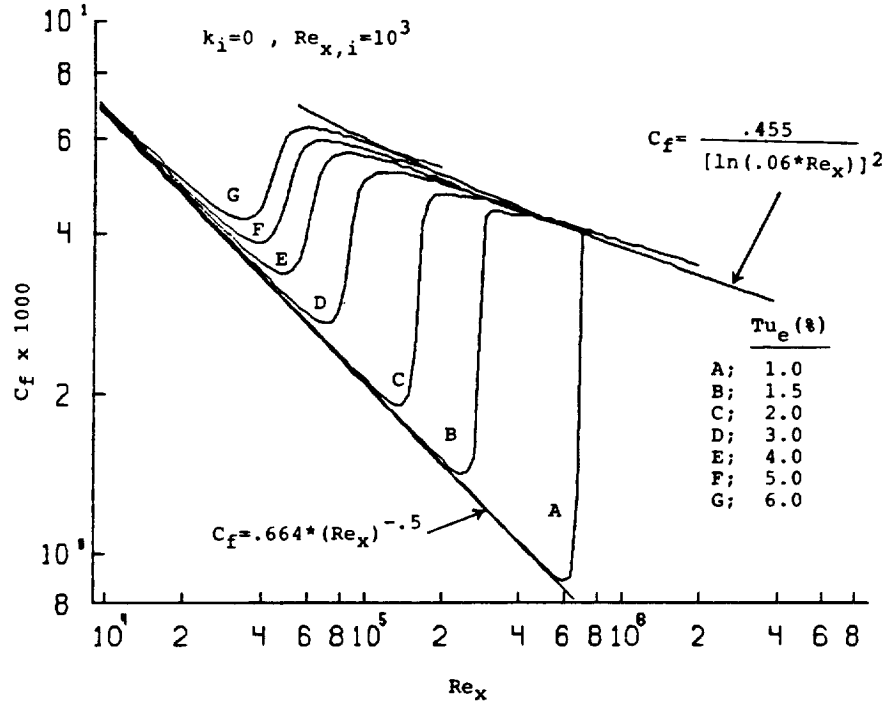

a) Jones Launder model

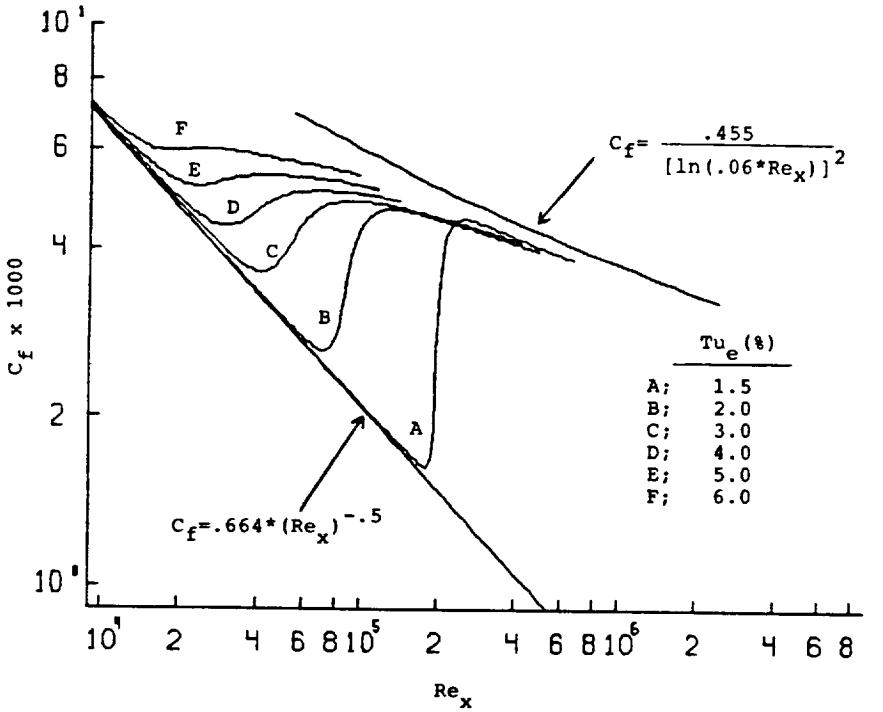

b) Lam Bremhorst model

Figure 3 Plot of C_f vrs. Re_x showing effect of free stream turbulence intensity on the prediction of transition

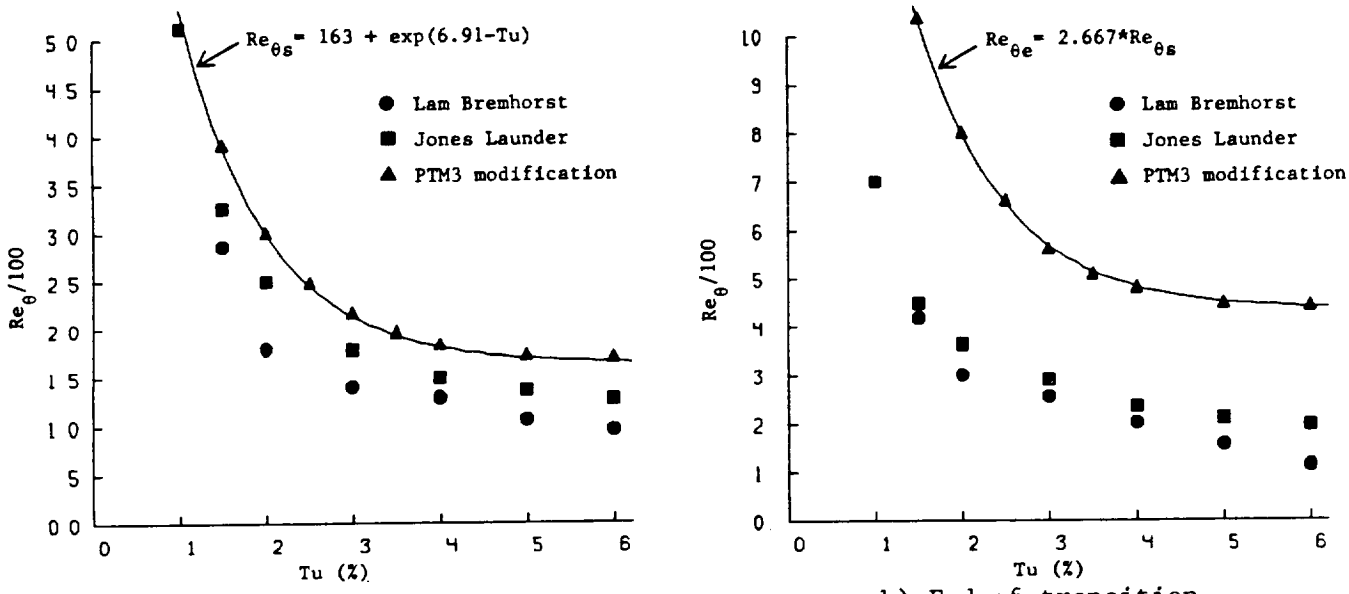

Figure 4 Momentum thickness Reynolds numbers at the start ($Re_{\theta s}$) and end ($Re_{\theta e}$) of transition.

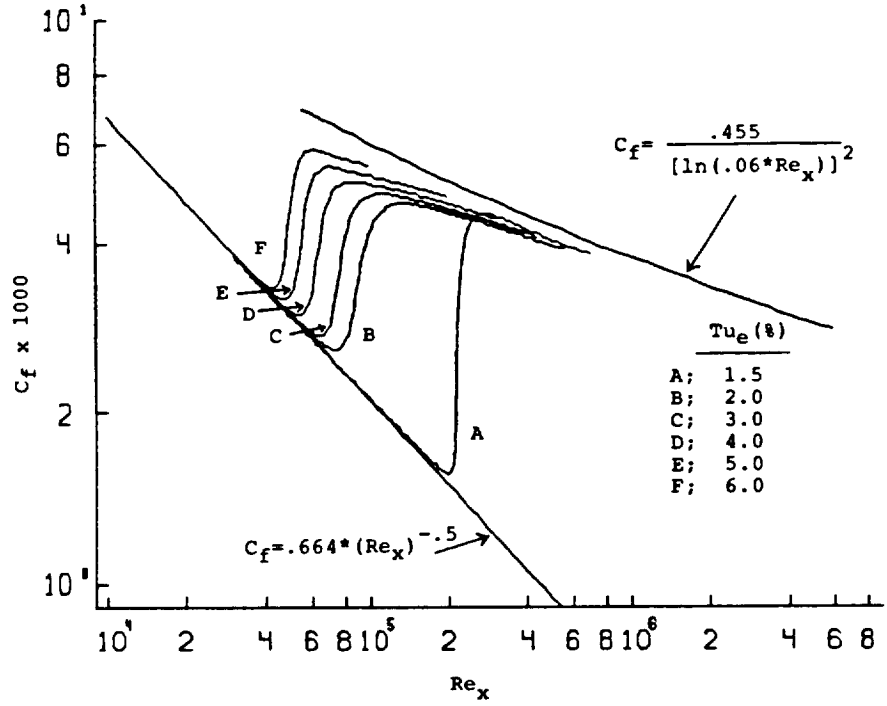

Figure 5 Plot of C_f vrs. Re_x showing effect of free stream turbulence intensity on the location of transition predicted by the Rodi-Scheuerer application of the Lam-Bremhorst model

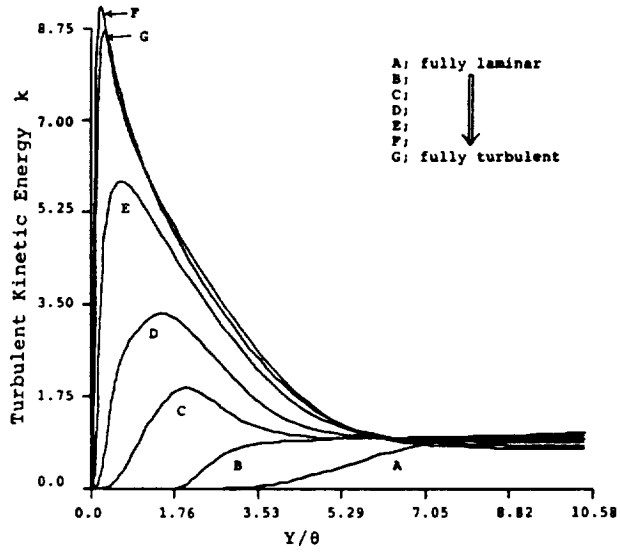

Figure 6 Typical development of the turbulent kinetic energy profiles through transition. Lam Bremhorst model

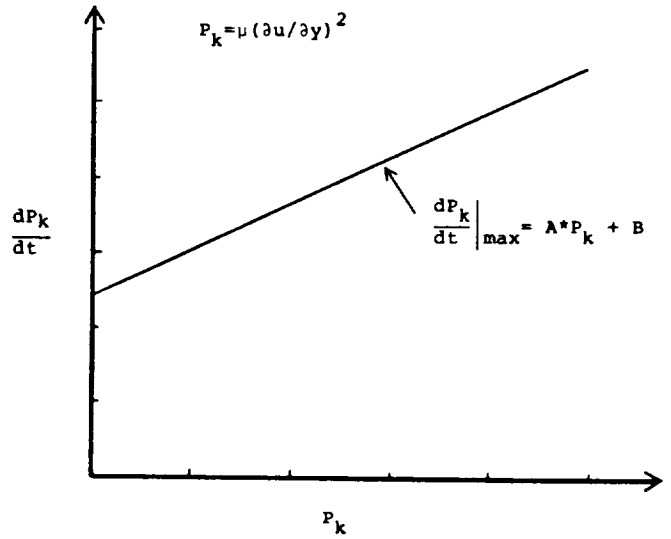

Figure 7 Limiting the growth rate of the production term in the k equation by the proposed model

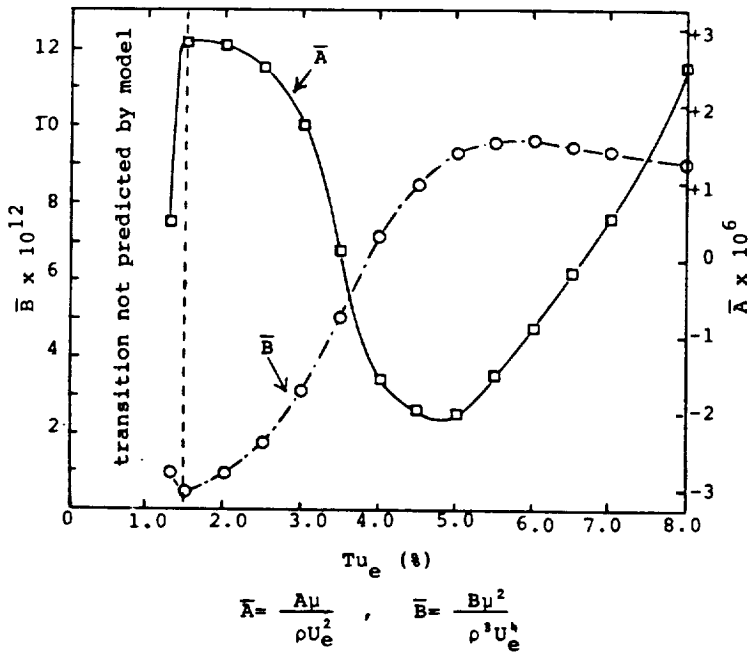

Figure 8 Variation of "A" and "B" with free stream turbulent intensity in the "PTM3" model

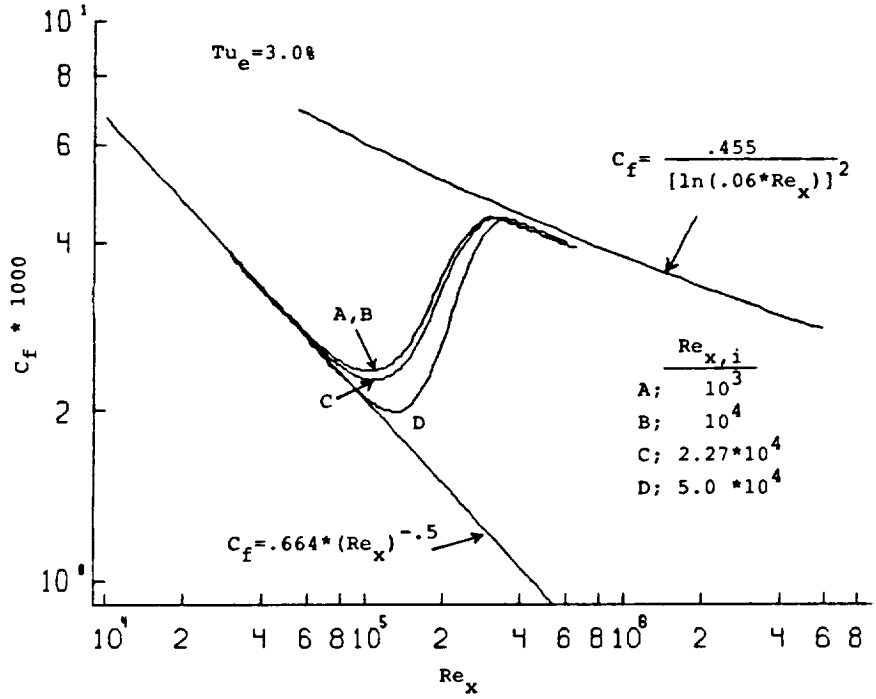

Figure 9 Plot of C_f vrs. Re_x showing the sensitivity to the initial starting location. "PTM3" modified form of the Lam Bremhorst model. Initial conditions set as per Rodi and Scheuerer

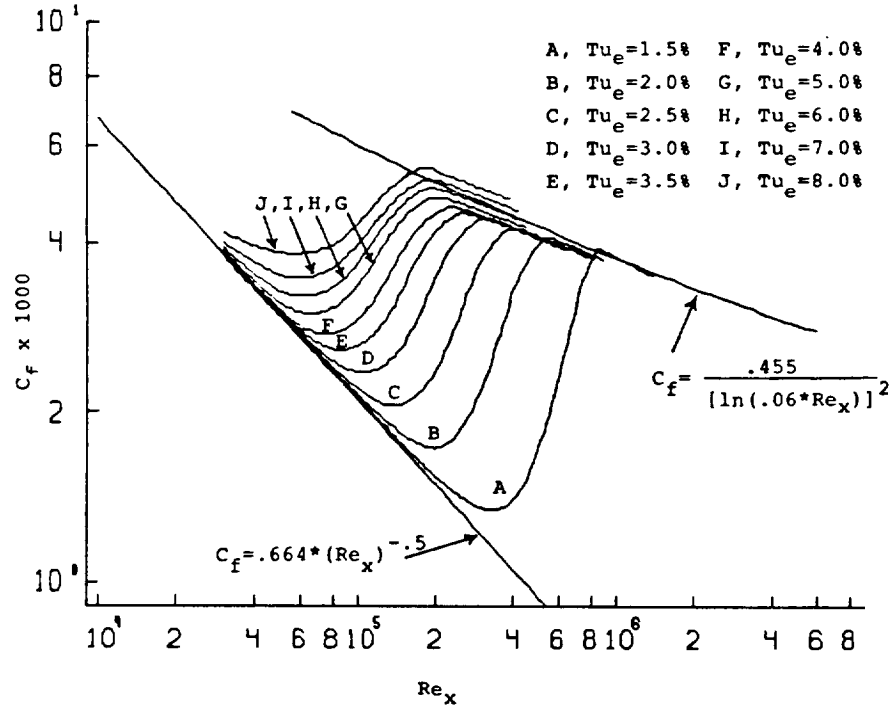

Figure 10 Plot of C_f vrs. Re_x showing the effect of free stream turbulence intensity on the location of transition as predicted by the "PTM3" modified form of the Lam Bremhorst model

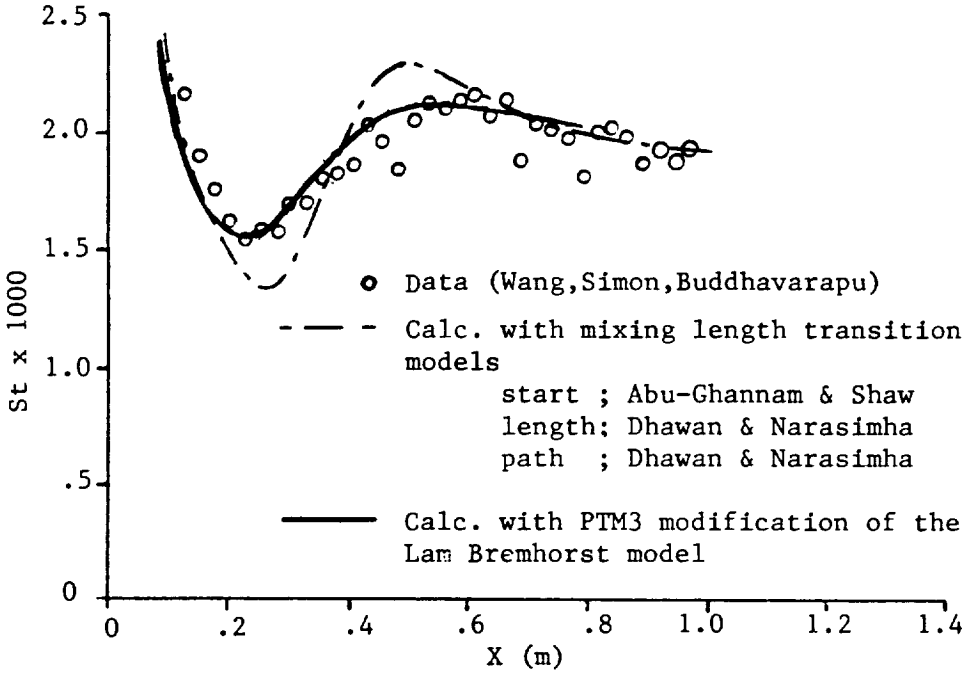

Figure 11 Comparison of the predicted heat transfer through transition with the data of Wang, Simon, and Buddhavarapu

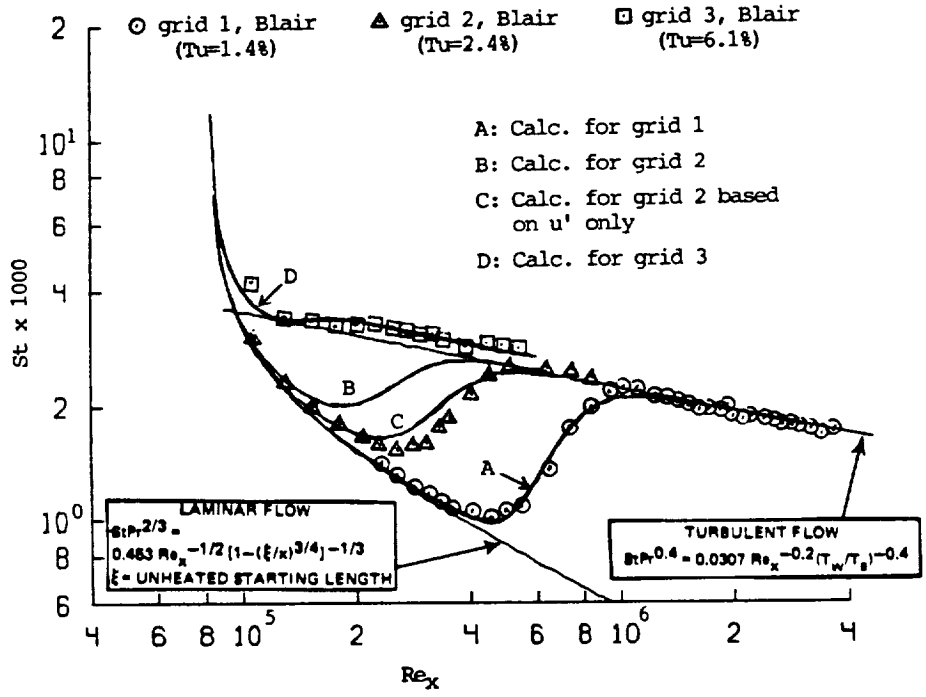

Figure 12 Comparison of the predicted heat transfer during transition with the data of Blair. "PTM3" modification of the Lam-Bremhorst model

TURBINE STATOR FLOW FIELD SIMULATIONS*

R.C. Buggeln, W.R. Briley, S.J. Shamroth and H. McDonald
Scientific Research Associates, Inc.

INTRODUCTION

The increased capability and accessibility of modern computers, coupled with increasingly sophisticated and accurate numerical and physical modeling, has led to a marked impact of numerical simulations upon current turbine design and research problems. The turbine section represents a considerable challenge as it contains significant regions of complex three-dimensional flow, including both aerodynamic and heat transfer phenomena. In particular, the turbine flow field contains several features which make its analysis a formidable problem. These include complex geometry, multiple length scales, three-dimensional effects, possible strong secondary flows, possible flow separation at off-design operation, possible transonic effects and possibly important unsteady effects.

As a result of the particularly difficult nature of the turbine cascade flow field, not nearly as much effort has been focused upon Navier-Stokes turbine simulations as upon many simpler problems. Much of the work performed to date has focused upon two-dimensional simulations. Although these can yield valuable information and insight, the actual problem is a three-dimensional one, and a three-dimensional approach is required to capture many of the important flow field properties.

The focus of the present effort is development of an efficient and accurate three-dimensional Navier-Stokes calculation procedure for application to the turbine stator and rotor problems. In particular, an effective procedure is sought which (i) adequately represents the flow physics, (ii) allows for sufficient resolution in regions of small length scale, and (iii) has sufficiently good convergence properties so as to allow use on a regular basis.

APPROACH AND BACKGROUND

The present approach solves the ensemble-averaged Navier-Stokes equations via the Linearized Block Implicit (LBI) technique of Briley and McDonald (Ref. 1). Boundary conditions for subsonic inflow and outflow (the usual case) set upstream stagnation pressure, upstream stagnation temperature, upstream flow angle, and downstream static pressure. Additional conditions used are density derivative on the inflow (upstream boundary), and velocity and temperature second derivatives on the downstream boundary. On the cascade blade no-slip conditions and a zero pressure gradient condition are applied along with either a specified temperature or a specified heat transfer rate. In general, the first grid point off the wall is taken so as to place a point in the viscous sublayer. The governing equations are written in general tensor form and solved in a body-fitted coordinate system. Details of the governing equations, numerical techniques, grid construction, turbulence model, etc. are given in Refs. 2-4.

* Work performed under NASA Contract NAS3-24358.

Using this approach has allowed simulation of a variety of flow fields. In particular, Refs. 3 and 4 describe work performed under a previous HOST contract showing favorable comparisons with experimental data for heat transfer and surface pressure distribution. More recent and yet unpublished work performed under NASC sponsorship shows favorable comparisons for surface pressure distribution, skin friction coefficient and velocity profiles, both on the blades and in the wake. References 3 and 4 also show demonstration calculations for a three-dimensional case formed by placing the C3X geometry between parallel endwalls. Finally, preliminary convergence studies for a Turner turbine cascade were presented by the present authors at the 1985 HOST meeting.

More recent convergence studies for the C3X cascade are presented in Figs. 1 and 2. Convergence history results for a two-dimensional laminar calculation are given in Fig. 1. The residual is defined as the imbalance of all steady terms and is normalized by the maximum residual in the field at the first time step. As can be seen, the residual drops five orders of magnitude in 150 time steps. It is also of interest to note that doubling the number of grid points did not significantly effect the convergence rate. The convergence rate for the three-dimensional case, is shown in Fig. 2. Again, rapid convergence is obtained; the solution was not continued to assess if the residual would continue to drop.

PRESENT EFFORTS

The focus of the present effort is demonstration of a two-equation turbulence model and demonstration of a three-dimensional turbulent case. In regard to the turbulence model, the code contains both a mixing length model and a $k-\varepsilon$ model, as described in Ref. 4. The C3X turbine cascade was chosen as a demonstration case for this capability. The calculation was run for a case having an inflow Mach number of 0.16, a Reynolds number of 3.4×10^5 and an inflow incidence of 0°. The calculation was initiated as a mixing length calculation and then continued with the two-equation model. Results showing pressure contours and velocity vector field are given in Figs. 3 and 4.

In addition to the turbulence energy calculation, present efforts are focusing upon three-dimensional turbulent calculations, in both stator and rotor configurations. The current problem being pursued is that of the C3X casade between parallel endwalls. A calculation is being made for the same flow conditions as in the two-dimensional case, using both mixing length and turbulence energy formulations.

REFERENCES

1. Briley, W.R. and McDonald, H.: Solution of the Multidimensional Compressible Navier-Stokes Equations by a Generalized Implicit Method. Journal of Computational Physics, Vol. 24, pp. 372-397, 1977.

2. Shamroth, S.J., McDonald, H. and Briley, W.R.: Prediction of Cascade Flow Fields Using the Averaged Navier-Stokes Equations. ASME Journal of Engineering Gas Turbines and Power, Vol. 196, pp. 383-390, 1984.

3. Yang, R.-J., Weinberg, B.C., Shamroth, S.J. and McDonald, H.: Numerical Solutions of the Navier-Stokes Equations for Two- and Three-Dimensional Turbine Cascades with Heat Transfer.

4. Weinberg, B.C., Yang, R.-J., McDonald, H. and Shamroth, S.J.: Calculations of Two- and Three-Dimensional Transonic Cascade Flow Fields Using the Navier-Stokes Equations. ASME Paper 85-GT-66, 1985.

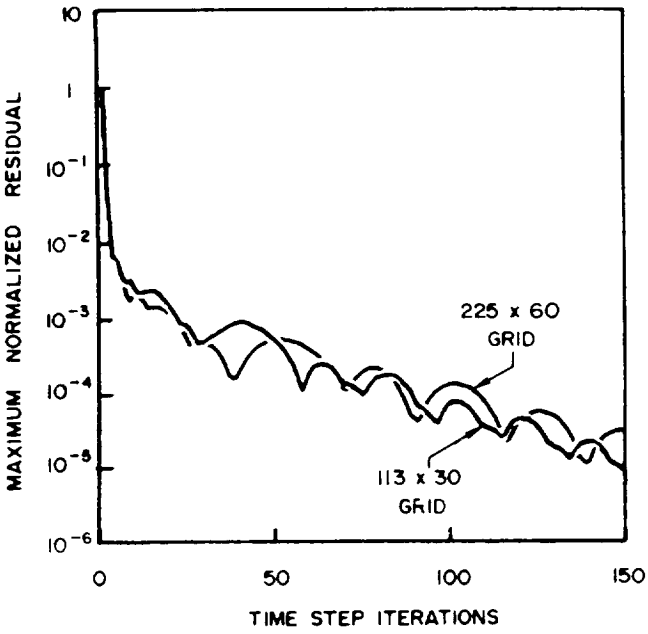

Fig. 1 - Convergence Behavior, C3X Laminar 2-D Cascade.

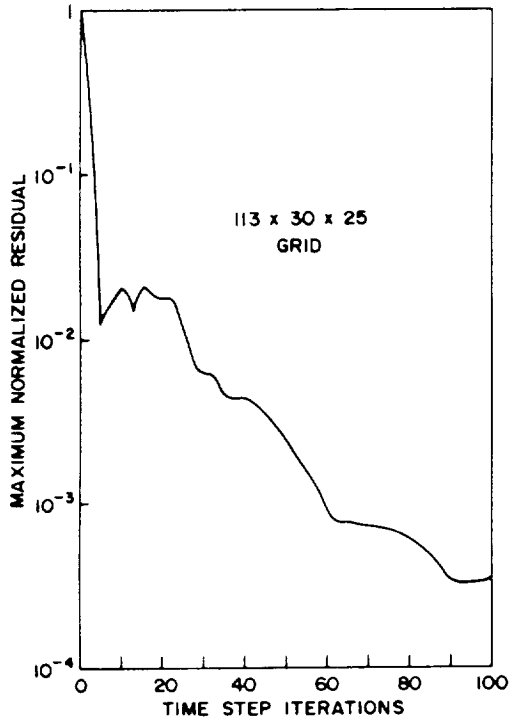

Fig. 2 - Convergence Behavior, C3X Laminar 3-D Cascade.

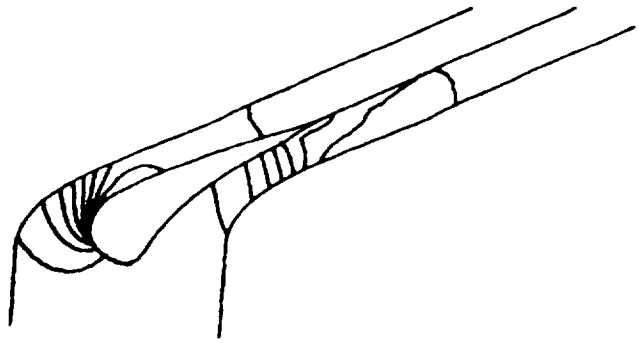

Fig. 3 - Pressure Contours, C3X Cascade, Turbulent Flow, k-ϵ Model.

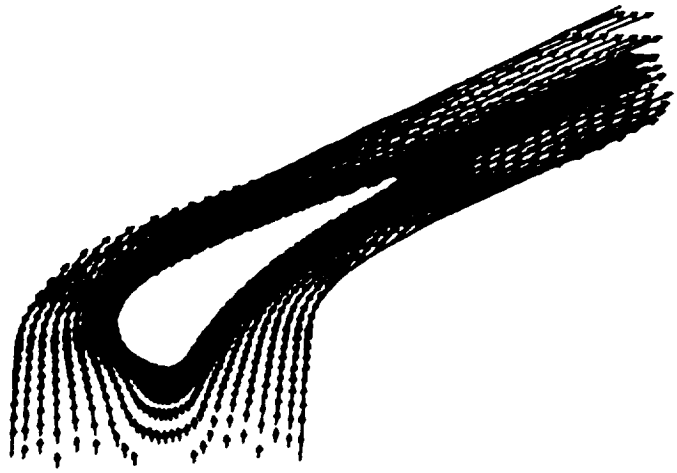

Fig. 4 - Velocity Vectors, C3X Cascade, Turbulent Flow, k-ϵ Model.

TURBINE AIRFOIL FILM COOLING*

Larry D. Hylton
Allison Gas Turbine Division
General Motors Corporation

INTRODUCTION

Emphasis is continuing to be placed on developing more accurate analytical models for predicting turbine airfoil external heat transfer rates. Performance goals of new engines require highly refined, accurate design tools to meet durability requirements. In order to obtain improvements in analytical capabilities, programs are required which focus on enhancing analytical techniques through verification of new models by comparison with relevant experimental data. The objectives of the current program are to develop an analytical approach, based on boundary layer theory, for predicting the effects of airfoil film cooling on downstream heat transfer rates and to verify the resulting analytical method by comparison of predictions with hot cascade data obtained under this program.

BACKGROUND

The overall approach to attaining the stated objective has involved a series of three programs. The initial program, performed under Contract NAS3-22761, assessed the capability of available modeling techniques to predict non-film cooled airfoil surface heat transfer distributions, acquired experimental data as needed for model verification, and provided verified improvements in the analytical models. This effort resulted in a baseline predictive capability and was reported in CR 168015 (ref. 1) published in May 1983.

The problem of heat transfer predictions with film cooling was broken into sequential efforts with the effect of leading edge showerhead film cooling being investigated first, followed by a program to study the effects of the addition of discrete site suction and pressure surface injection. The effort on showerhead film cooling was performed under Contract NAS3-23695 and was reported in CR 174827 (ref.2) published in July 1985. As part of that program, a five-row, simulated common plenum showerhead geometry was tested to determine differences between film and non-film cooled heat transfer coefficient distributions downstream of a leading edge, multiple hole film cooling array. Building on non-film cooling modeling improvements incorporated in a modified version of the STAN5 boundary layer code developed under Contract NAS3-22761, a program was developed to analytically model and predict differences resulting from leading edge mass injection.

The current program, being performed under Contract NAS3-24619, is intended to extend the analytical code development to include discrete site pressure and suction surface injection, with and without leading edge blowing, and to obtain relevant hot cascade data to verify the model improvements.

*This work is being performed under Contract NAS 3-24619

PROGRESS

Because of the long lead times associated with hardware design and fabrication, initial efforts on the program have been aimed at the experimental phase. The analytical efforts under the program are just beginning with the design mode analysis phase having started in August. This phase is intended to demonstrate the use of the base boundary layer method in a film-cooled turbine airfoil design system environment. This initial study is addressing details involved with method set-up procedures (e.g. defining initial and boundary conditions) and the qualitative behavior of the film cooling models for a relevant film-cooled airfoil design.

The experimental phase of the program will be an extension of the previous contract work. The hot cascade tests will utilize the same facility, cascade and experimental techniques used in the previous contract, with the instrumented airfoil in the cascade replaced with one containing suction surface and pressure surface film cooling arrays in addition to a leading edge showerhead film cooling array. Design of the film cooling arrays for the new airfoil has been completed and the fabrication and instrumentation of the airfoil is nearly complete.

The airfoil cooling design incorporates three separate film cooling supply plenums. One plenum will supply an array of leading edge showerhead film cooling holes. The geometry of this film cooling hole array will be identical to that utilized in Contract NAS3-23695. Two additional coolant supply plenums will be incorporated into the vane; one to supply an array of holes on the suction surface and the other to supply an array of holes on the pressure surface of the airfoil. The three separate plenums will allow independent control of the flow to each region of the airfoil.

The suction surface array will contain two staggered rows of holes centered at approximately 25.2% of the suction surface length from the leading edge. Based on the heat transfer results of the previous contract (NAS3-23695), this location will place the array midway between the points of boundary layer transition origin for the highest and lowest Reynolds number (Re) cases studied. This will result in the ability to move the boundary layer transition origin point across the array as the cascade operating conditions are changed. It is likely that the film cooling holes will act as trips, resulting in earlier transition for the low Reynolds number case.

In Figure 1, the two vertical lines between twenty and forty percent surface distance on the suction surface represent the location of the two rows of film cooling holes. This figure illustrates the position of the holes relative to the heat transfer coefficient distribution and clearly shows the suction surface holes located midway between the boundary layer transition origin points for the highest and lowest Reynolds number cases.

The location of the two rows of holes on the pressure surface are indicated by the two vertical lines on the pressure side in Figure 1. This array will be centered at 22.5% of the pressure surface length from the leading edge. As can be seen from Figure 1, this position is centered in the area of minimum heat transfer, at the point where the heat transfer begins to increase as you progress toward the trailing edge.

Details of the geometry for the film cooling arrays are summarized in Table 1. All hole diameters will be the same and will be identical to the showerhead hole diameters in the previous contract. The geometry of the showerhead array will be

identical to that tested in the previous contract. Both the suction and pressure surface arrays will consist of two staggered rows with row spacing-to-diameter ratios of 4.0. The hole spacing-to-diameter ratio of 3.0 will be the same on both the pressure and suction surfaces. The injection angle in the leading edge will be the same as in the previous contract where the holes were aligned normal to the surface in the chordwise direction and at a 45^{o} angle in the spanwise direction. The suction surface holes will be inclined at 35^{o} to the surface in the chordwise direction while the pressure surface holes will be at 20^{o} in the chordwise direction. Both arrays will be normal to the surface in the spanwise direction. These injection angles and the location of the film cooling arrays on the airfoil are illustrated in Figure 2.

Also shown in Figure 2 is the thermal barrier cutout region. This cut thermally isolates the film cooling supply plenums from the regions of the airfoil where heat transfer measurements are made, similar to the technique in the previous contract. The retaining bar shown in Figure 2 ensures that the airfoil profile is properly maintained after the thermal barrier cut is made.

PROGRAM PLANS

Fabrication and instrumentation of the film cooled airfoil should be completed late this calendar year. Cascade testing is currently planned to begin in late November and will extend through June 1987. Work on the analytical effort will include prediction of cascade results during the design mode analytical phase which is currently underway. While the cascade testing program is being performed, the analytical effort will focus on a methods characterization study which will determine the qualitative/quantitative capabilities of the proposed analytical method by comparing analytical predictions with experimental results from the cascade tests. Following completion of this effort, the analytical task will enter the method refinement/verification phase. This will address modeling deficiencies revealed in the first two phases of the analytical program and will develop an improved analytical code that will be verified by comparison with the experimental data obtained during the course of the contract.

REFERENCES

1. L. D. Hylton, M. S. Mihelc, E. R. Turner, D. A. Nealy, and R. E. York, "Analytical and Experimental Evaluation of the Heat Transfer Distribution over the Surfaces of Turbine Vanes", NASA CR-168015, May 1983.

2. E. R. Turner, M. D. Wilson, L. D. Hylton, and R. M. Kaufman, "Turbine Vane External Heat Transfer", Vol I, NASA CR-174827, July 1985.

TABLE 1. GEOMETRY OF FILM COOLING ARRAYS

	LEADING EDGE	SUCTION SURFACE	PRESSURE SURFACE
HOLE DIAMETER (IN.)	0.039	0.039	0.039
(CM.)	0.100	0.100	0.100
HOLE SPACING/DIAMETER	7.5	3.0	3.0
ROW SPACING/DIAMETER	4.0	4.0	4.0
HOLE ANGLE	45^{o} (Spanwise)	35^{o} (Chordwise)	20^{o} (Chordwise)
STAGGERED ROWS	Yes	Yes	Yes
LOCATION OF CENTER OF ARRAY (% SURFACE DISTANCE)		25.2	22.5

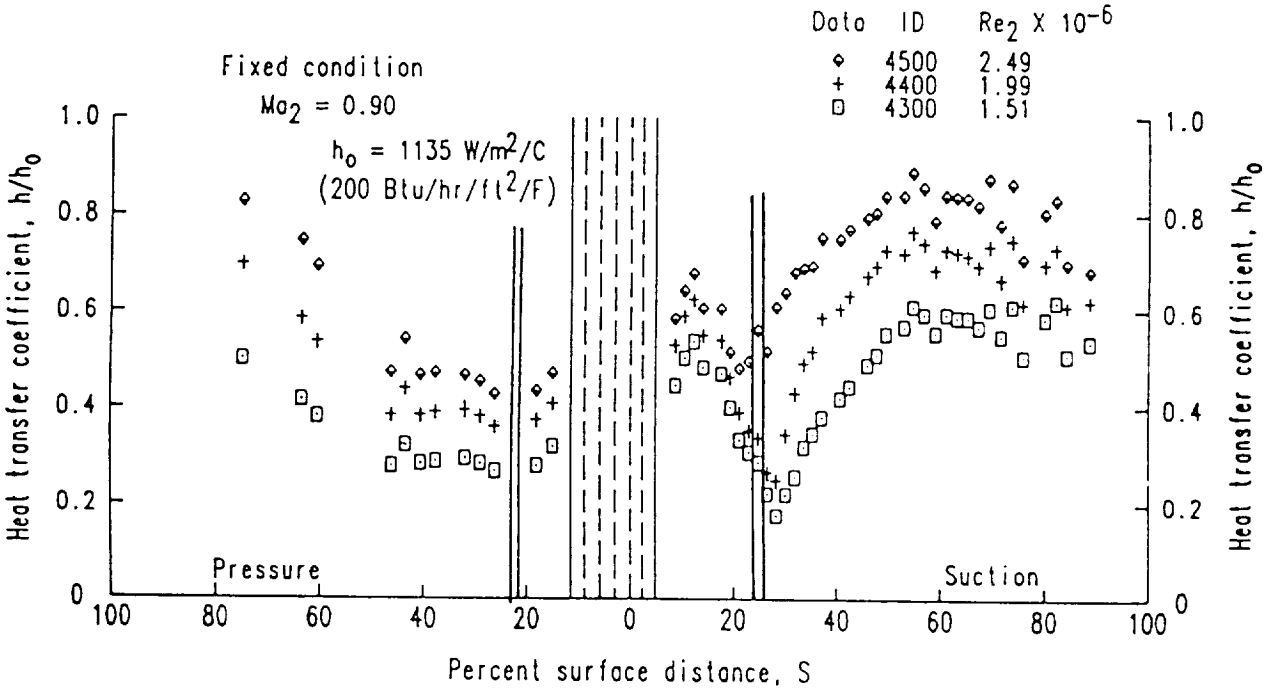

Figure 1. The effect of the exit Reynolds number variation on the C3X vane heat transfer coefficient distribution.

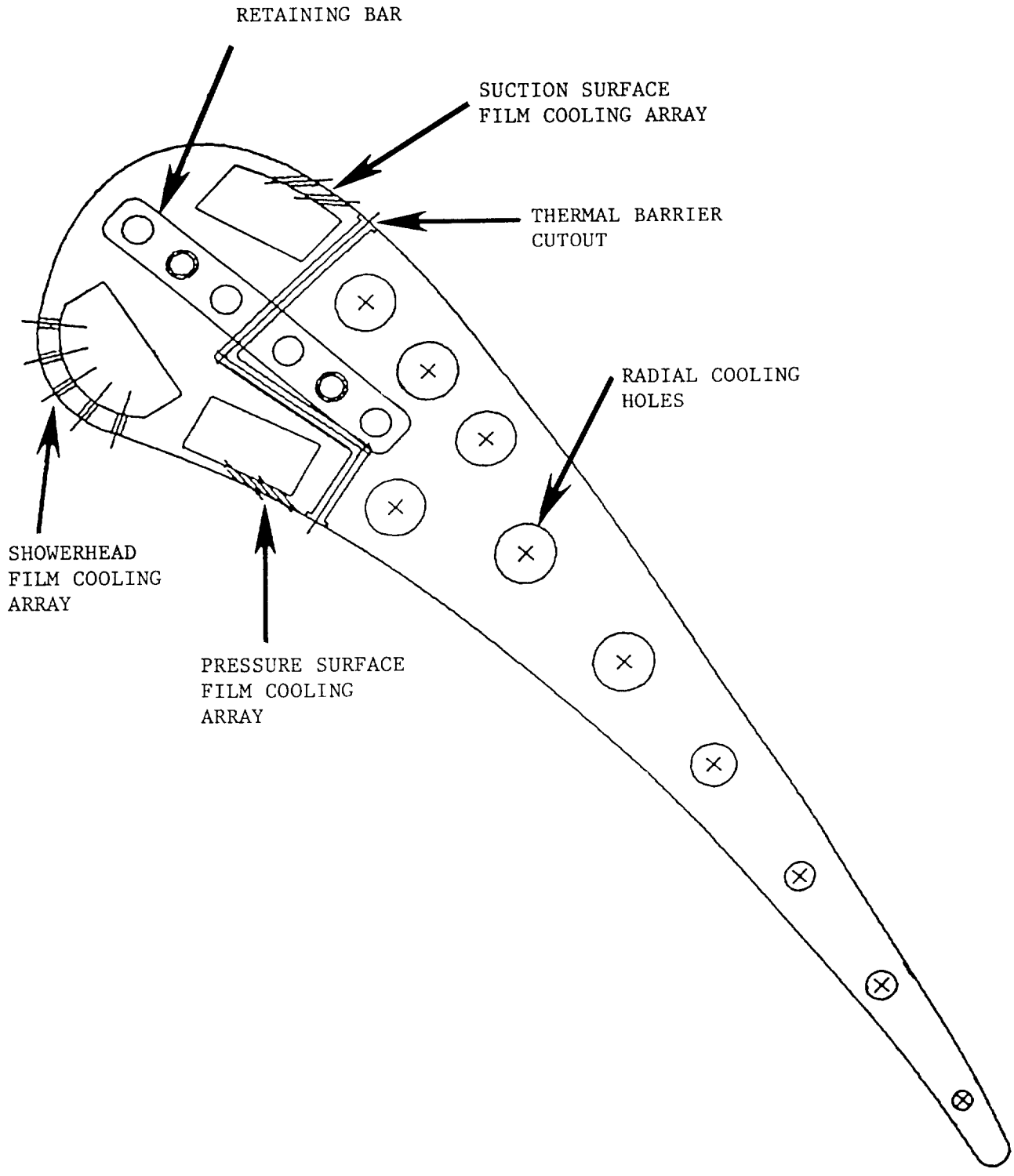

Figure 2. Airfoil geometry

CONSTITUTIVE MODELING FOR ISOTROPIC MATERIALS*

Ulric S. Lindholm and Kwai S. Chan
Southwest Research Institute

INTRODUCTION

The objective of the present program is to evaluate and further develop existing constitutive models for use in finite-element structural analysis of turbine engine hot section components. The class of constitutive equation studied is considered "unified" in that all inelastic deformation including plasticity, creep, and stress relaxation are treated in a single term rather than a classical separation of plasticity (time independent) and creep (time dependent) behavior. The unified theories employed also do not utilize the classical yield surface or plastic potential concept. The models are constructed from an appropriate flow law, a scalar kinetic relation between strain rate, temperature and stress, and evolutionary equations for internal variables describing strain or work hardening, both isotropic and directional (kinematic). This and other recent studies have shown that the unified approach is particularly suited for determining the cyclic behavior of superalloy type blade and vane materials and is entirely compatible with three-dimensional inelastic finite-element formulations.

In the first two years of the program, the unified constitutive models of Walker (ref. 1) and of Bodner and Partom (ref. 2) were demonstrated to yield good correlation for a nickel-base alloy (PWA designation B1900+Hf) for temperatures, strain rates, and strain range characteristic of cooled turbine vanes in advanced gas turbine engines. Experimental correlations were made with testing under uniaxial and biaxial tensile, creep, relaxation, cyclic, and TMF loading histories. Both models were incorporated into the MARC finite-element computer code. The code was then utilized to predict the high-temperature cyclic response of a notched-round tensile bar.

In this, the third year of the program, we have examined the behavior of a second nickel-base alloy, MAR-M247, and compared it with the Bodner-Partom model, further examined procedures for determining the material-specific constants in the models, and exercised the MARC code for a turbine blade under simulated flight spectrum loading. The third year results will be summarized in the following sections. Collaborators on this program have been staff of Pratt and Whitney Aircraft and Drs. Walker and Bodner.

TEST PROCEDURES AND APPLICATION TO MAR-M247 AND B1900+Hf

The details of both Bodner-Partom and Walker models and experimental facilities and test procedures are fully described in the Second Annual Status Report under this project (NASA CR-174980). Therefore, we will summarize only current results herein.

*Work done under NASA Contract NAS3-23925.

Uniaxial monotonic hardening. A major concern with the unified or any other comprehensive constitutive model is the determination of the material constants and the number of test conditions required in the process. Our previous work, to our surprise, had indicated that all constants could be derived from monotonic tensile tests alone conducted over the appropriate temperature and strain-rate ranges. It is usually assumed that cyclic data are required to separate the directional or kinematic hardening terms. However, it should be realized that hardening under any loading history results from both isotropic and directional components which may be separated if a model is available.

The monotonic tensile curves for MAR-M247 at several temperatures are given in Figure 1a with the Bodner-Partom model correlation below in Figure 1b. The hardening constants for the model correlation are determined from the construction given in Figure 2. Here the work-hardening rate, $\gamma = d\sigma/dW_p = d\sigma/\sigma d\varepsilon^p$, is plotted as a function of applied stress by differentiating the stress-plastic strain curve. A common assumption, used in the Bodner-Partom model, is that both isotropic and directional hardening progresses from an initial or current state to a satauration value ($d\sigma/dW_p = 0$) with large strain at a hardening rate determined by the parameter m. Such an evolutionary equation for hardening is

$$\dot{h} = m(h_s - h)\dot{W}_p$$

where h is the current state, h_s is the saturation value, and m is the rate parameter. One can show from the construction in Figure 2 that m_1 is the rate of isotropic hardening and that m_2 is the rate of directional hardening. Further, the saturation values, h_s, for both can be obtained from the stress intercept at $\gamma = 0$. Directional hardening saturates first and dominates at small strain, while the isotropic hardening dominates at large strains.

Figures 2b and 2c demonstrate similar hardening behavior for two other high-temperature alloys, B1900+hf and Hastelloy X.

Cyclic response prediction. The cyclic stress-strain curve predicted from the Bodner-Partom model and the monotonic tensile test data are given in Figure 3b along with the experimental curves in Figure 3a. Extensive similar correlations for B1900+Hf are given in NASA CR-174980 for cycles with varying strain range, R-ratio, hold-times, and temperature (TMF).

Biaxial response. Extensive biaxial tests have been conducted also on thin tubes under combined tension-compression and reversed torsion. Two examples will be cited. In Figure 4 we illustrate an experiment-model comparison for MAR-M247 tested at 982°C. Out-of-phase, strain-controlled loading is employed with the von Mises effective strain held constant during cycling but with periodic strain hold-times to observe the direction and magnitude of the stress relaxation. The Bodner-Partom model predicts the essential features except for the transient direction of the stress vector during relaxation. The model prescribes this direction to be radial toward the stress origin. The experiment shows that only asymptotically at long time is the relaxation vector in the direction of the origin. Also (not shown), the instantaneous direction of the strain-rate vector during the active cyclic portion of the loading is not radial (Bodner-Partom model prediction) but shows a small phase lag from the radial direction. An alternate model, such as that of Walker (ref. 1) which employs a "back-stress" type representation for directional hardening, does a more accurate prediction of these vectorial effects.

Figure 5 shows that for alloy B1900+Hf the cyclic hardening under out-of-phase and in-phase cycling was equal. The same result was found for MAR-M247 at all temperatures. This contrasts with previous results on Hastelloy X where the cyclic hardening under out-of-phase cycling was considerably greater than under in-phase (proportional) cycling.

Variable strain-rate tests. A series of tests was performed on MAR-M247 at several temperatures which included step-wise changes in strain rate. The results are illustrated in Figure 6. One purpose of these tests was to determine if both the hardening and rate-dependent constants in the Bodner-Partom model could be determined from a single test (specimen) at a given temperature. The result was partially successful in that the constants derived were used in the model correlations shown. However, the constants derived showed some differences from a set derived from multiple specimens each tested at a different strain rate. The latter procedure would be preferred, although a good first approximation can be obtained from the step-loaded single specimen.

HOT SECTION COMPONENT ANALYSIS

The component chosen for demonstration of the B1900+Hf unified model is the airfoil portion of a typical cooled turbine blade. The foil was analyzed using the MARC finite element program (ref. 3). The code was used at PWA with the Walker model and subsequently at NASA Lewis (ref. 4) with both the Walker and Bodner-Partom models for comparison. Figure 7a shows the finite element mesh used in the analysis. The bulk of the airfoil was modeled with 8-node solid elements with regions on the leading edge modeled with higher order 20-node solid elements. Figure 7b shows the temperature distribution during the cruise portion of the flight spectrum.

The loading and boundary conditions were chosen to simulate a typical commercial engine flight. The flight simulation is shown schematically in Figure 8 and includes periods of taxi, takeoff, climb, cruise, descent, taxi, and shutdown. The spectrum includes periods of transient loading (RPM) and temperature excursions as well as long steady-state or hold periods. The maximum temperature excursion is about 1000°C. Thus, the range of conditions exercises the constitutive model over a wide range of the state parameters.

PWA exercised the foil through three full flight spectra using the Walker model. Figure 9 shows the accumulation of inelastic strain at location A (Figure 7b) during all three flights. It is seen that the bulk of the inelastic strain is accumulated during takeoff of the first flight. At the end of climb some reversed inelastic strain is accumulated up to shutdown at this element. After the third flight the amount of inelastic strain accumulation appears to be stabilizing.

Using the PWA-developed code with identical mesh size and flight spectra, Kaufman et al (ref. 4) ran further simulations comparing a classical creep-plasticity model with both the Walker and Bodner-Partom unified models. The effective stress vs strain response at the airfoil critical location is compared in Figure 10 for all three constitutive models. The unified models yield very similar results but substantially different from the classical creep-plasticity model. Unfortunately, no experimental results are available or easily obtainable for this complex problem. It is noteworthy that a comparison of the CPU time requirements for these analyses on a Cray computer indicates that there is essentially no difference between the classical and unified approaches. For the problem cited, the CPU time was about 4000 sec with each model.

CONCLUSIONS AND FUTURE WORK

The results to date have further demonstrated the ability of the unified constitutive equations to model complex nonlinear, time- and temperature-dependent inelastic deformation under complex loading conditions. A methodology for evaluating the constitutive constants in the models from simple test conditions is evolving. The demonstration that these improved models can be used in a general-purpose, finite-element structural analysis code without penalty in computing time over existing methods is significant.

In the final year of the program we will examine further the effects of thermal history on the constitutive behavior of these nickel-base alloys with possible modifications to the models to include effects of strain aging, microstructural changes, and thermal history. Some experiments are also planned to assess the effect of a thermal-barrier coating on the response of thin-walled, biaxial tubular specimens.

REFERENCES

1. Walker, K. P.: NASA Contract Report NASA CR-165533, 1981.

2. Bodner, S. R. and Partom, Y: ASME J. of Appl. Mechs., vol. 42, 1975.

3. MARC General Purpose Finite Element Program, MARC Corporation, Palo Alto, California.

4. Kaufman, A., Saltsman, J. F., Halford, G. R., and Tong, M.: 3rd Symposium on Nonlinear Constitutive Relations for High Temperature Applications, Akron, Ohio, 1986.

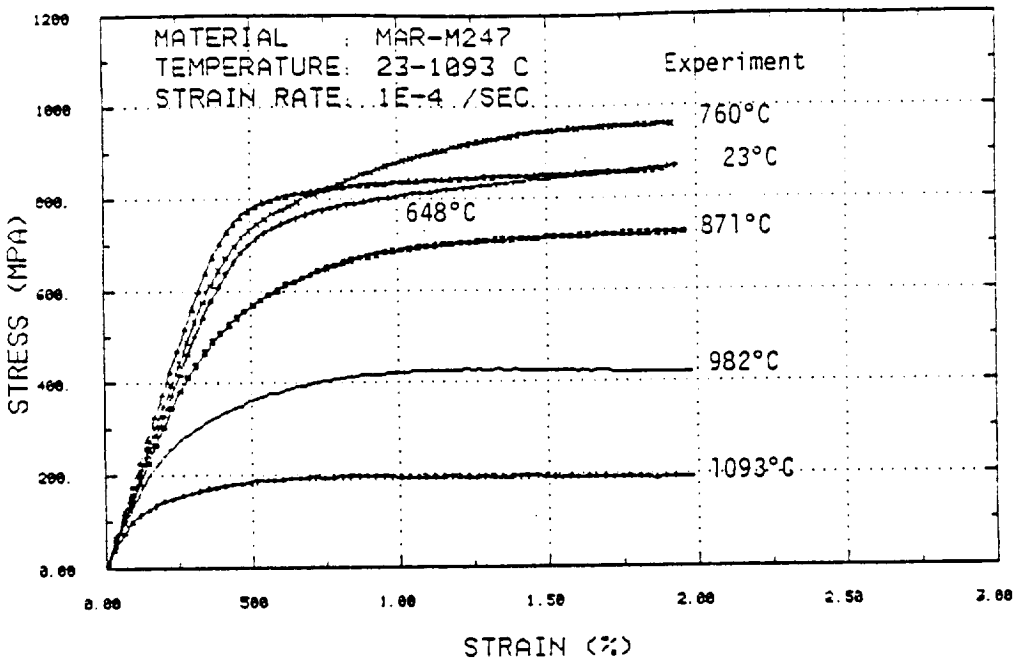

(a)

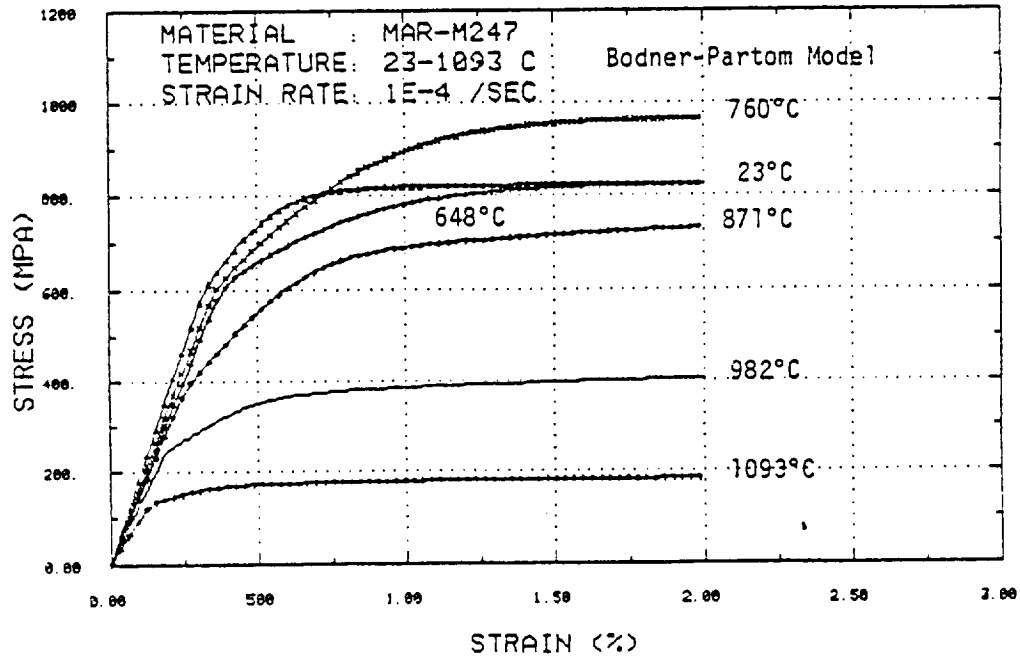

(b)

Figure 1. Correlation of Bodner-Partom model (b) with experimental tensile curves (a) for MAR-M247 at six temperatures.

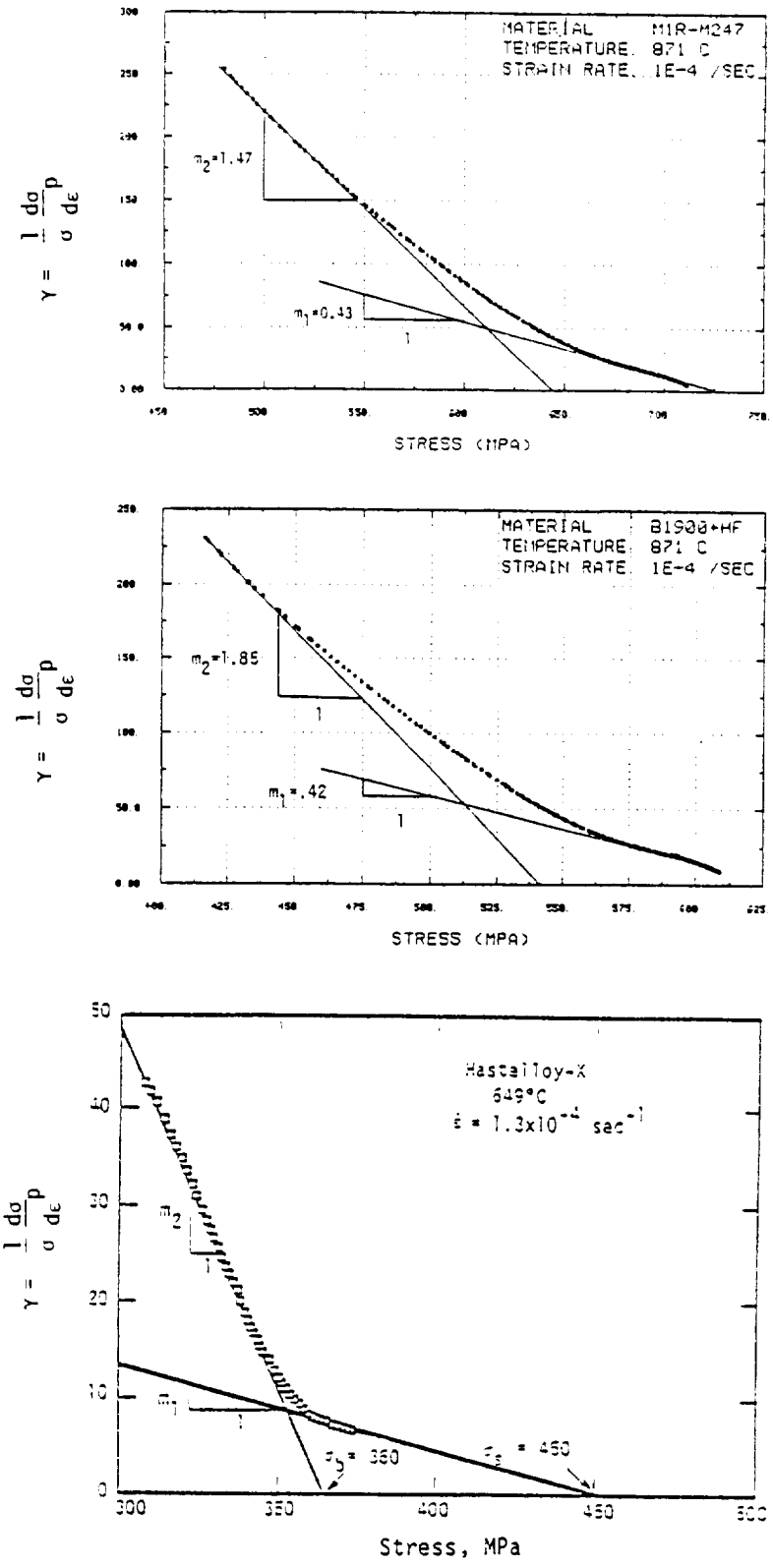

Figure 2. The work hardening curves for (a) MAR-M247, (b) B1900+Hf, and (c) Hastelloy X showing separation of isotropic and directional hardening parameters.

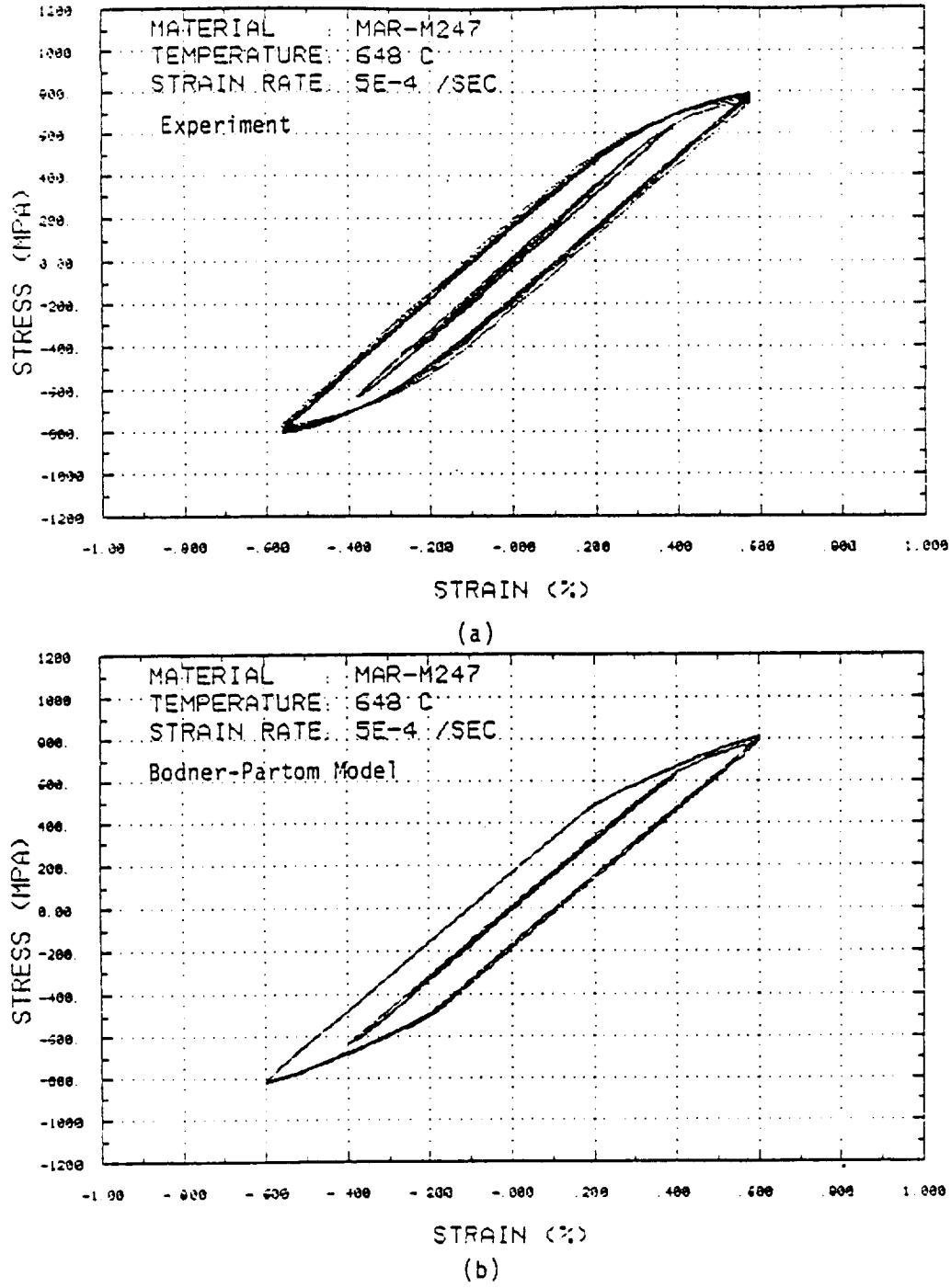

Figure 3. Comparison of model prediction (b) and experimental cyclic data (a) at 648°C for MAR-M247.

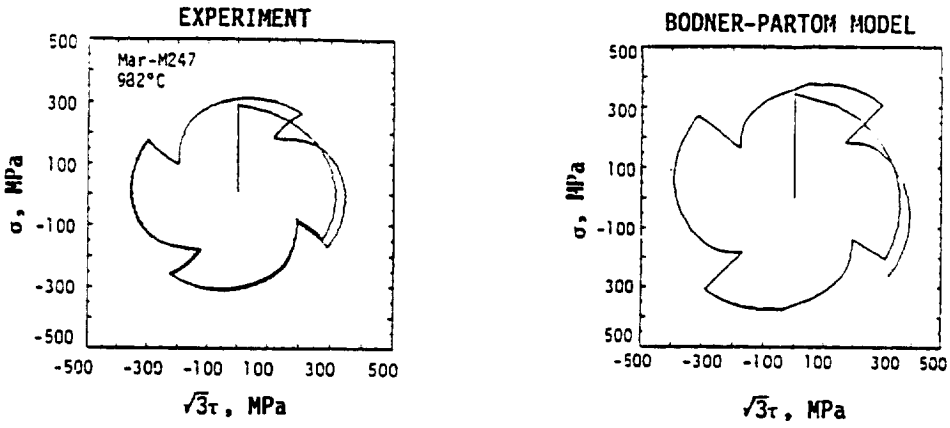

Figure 4. Comparison of model calculation and experiment for MAR-M247 under 90° out-of-phase cycling with hold time at 982°C.

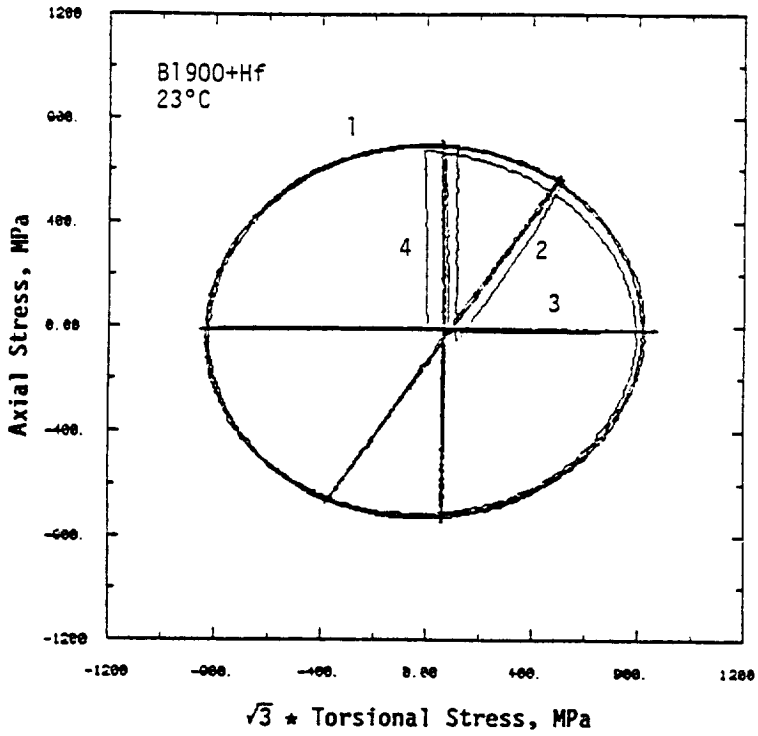

Figure 5. The stress response of B1900+Hf tested under (1) 90° out-of-phase axial/torsion, (2) in-phase axial/torsion, (3) torsion, and (4) axial. Effective strain and strain rate are ±0.4% and 4×10^{-1} sec^{-1}.

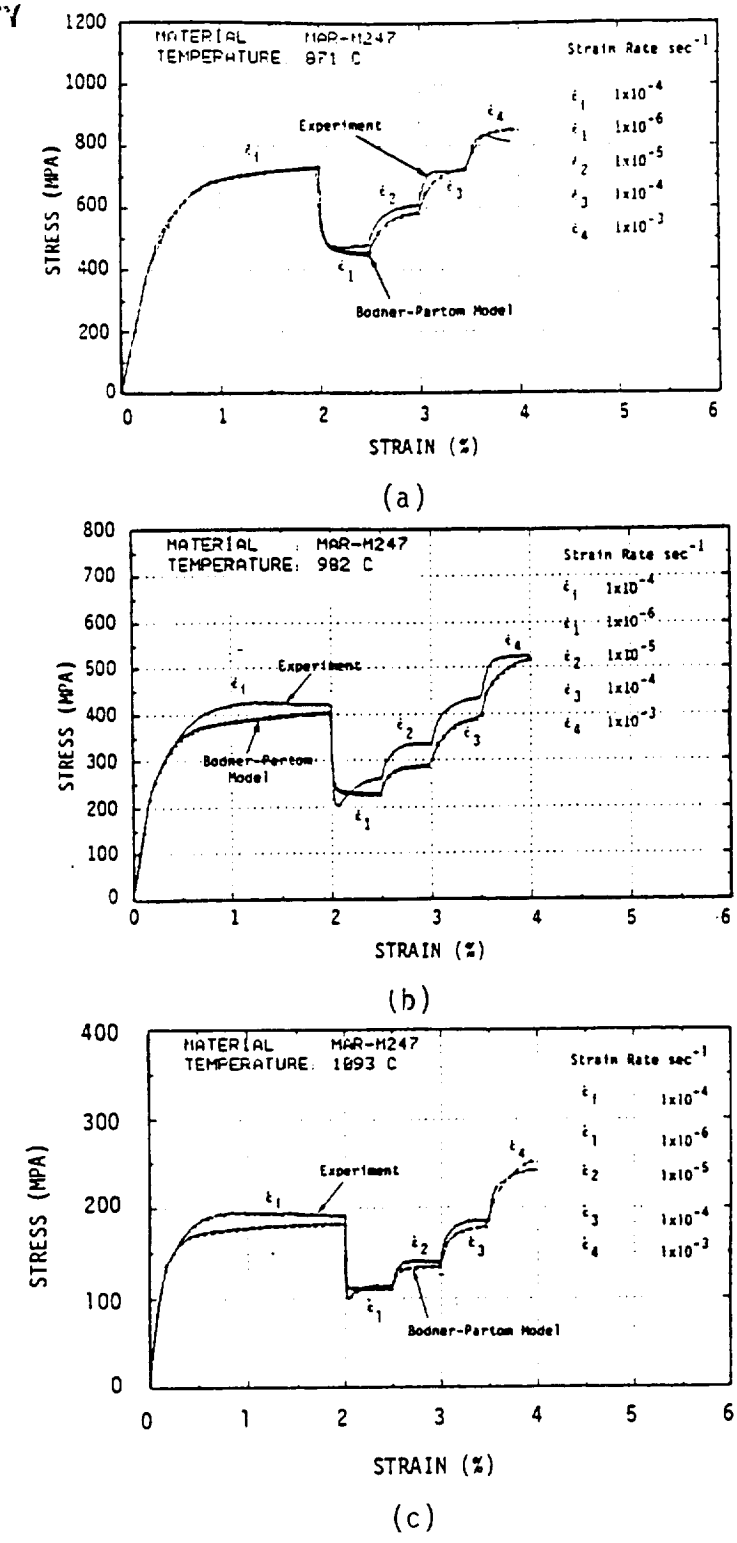

Figure 6. Comparison of model calculation and experiment for tensile test with step strain-rate changes; MAR-M247 at (a) 871°C, (b) 982°C, and (c) 1093°C.

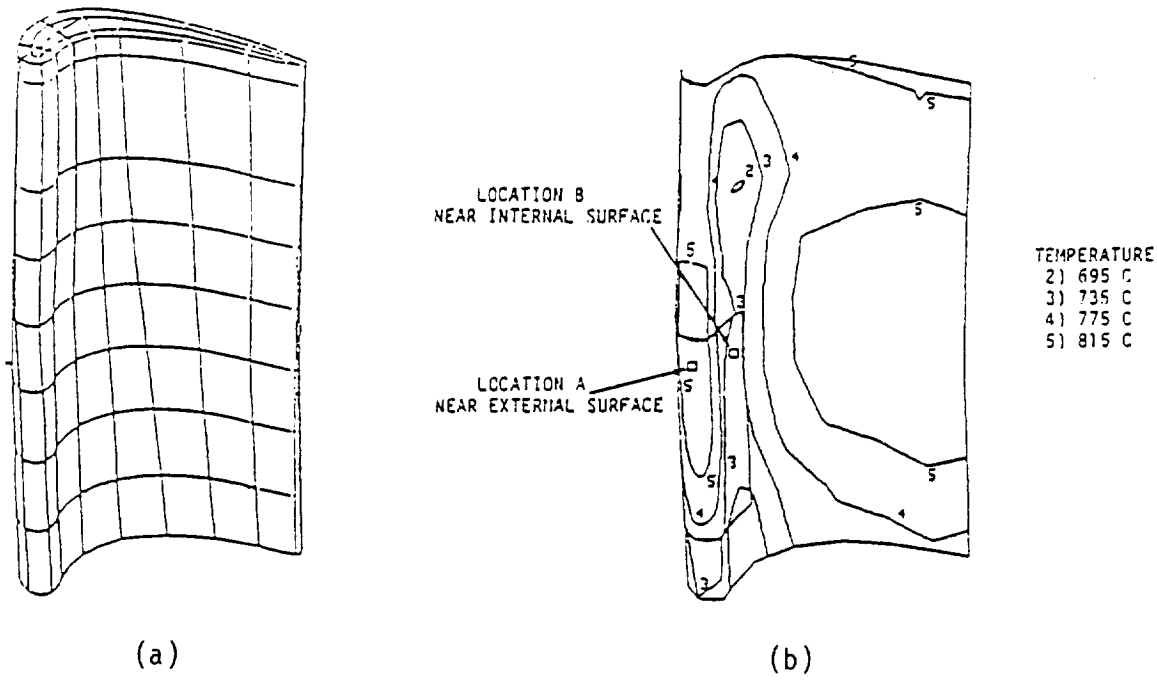

Figure 7. Finite element mesh used in calculation (a) and steady-state temperature profile during cruise (b).

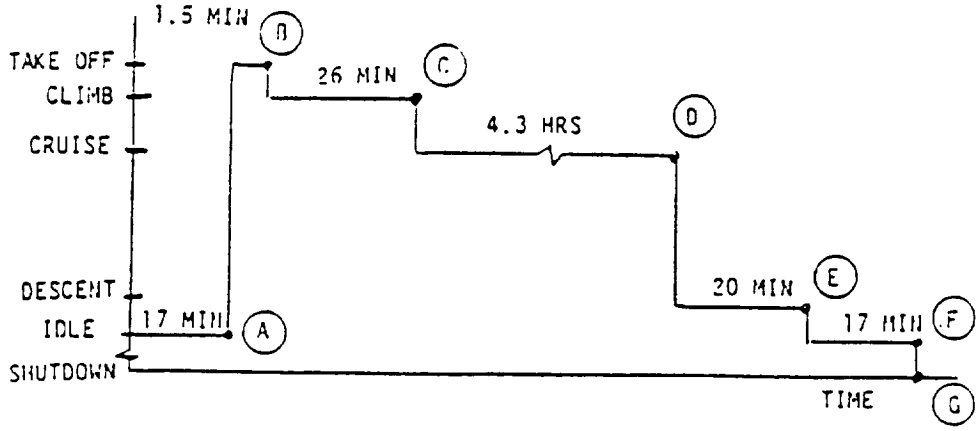

Figure 8. Simulated flight used in demonstration calculations

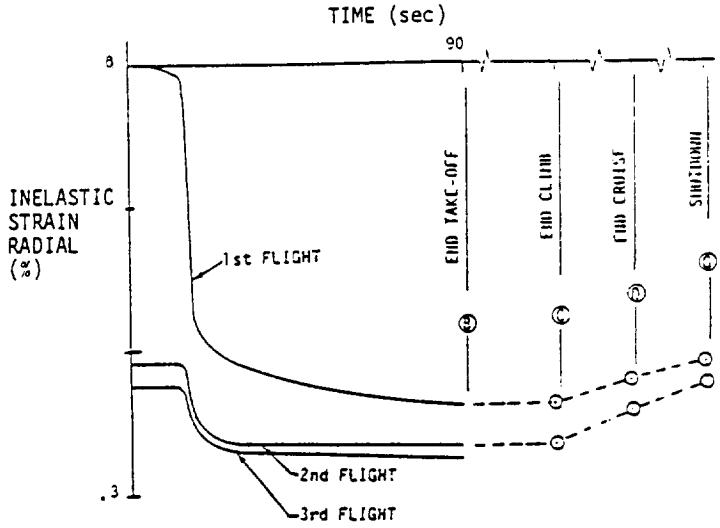

Figure 9. Accumulation of inelastic strain at location A (Figure 7) during all three flights.

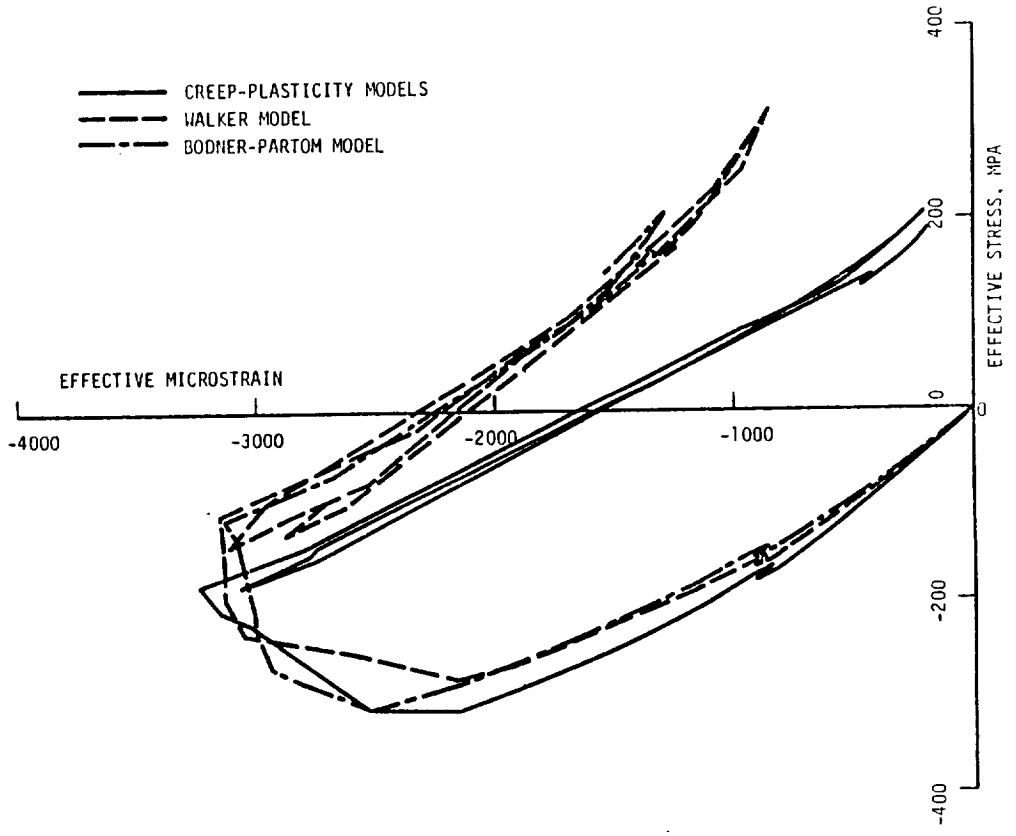

Figure 10. Airfoil calculations using the MARC finite-element analysis code from Kaufman et al (ref. 4).

3-D INELASTIC ANALYSIS METHODS FOR HOT SECTION COMPONENTS*

E. S. Todd
United Technologies Corporation
Pratt & Whitney

The objective of this program is to produce a series of new computer codes that permit more accurate and efficient three-dimensional inelastic structural analysis of combustor liners, turbine blades, and turbine vanes. Each code embodies a progression of mathematical models for increasingly comprehensive representation of the geometrical features, loading conditions, and forms of nonlinear material response that distinguish these three groups of hot section components.

Software in the form of stand-alone codes is being developed by Pratt & Whitney (P&W) with assistance from three uniquely qualified subcontractors: MARC Analysis Research Corporation (MARC), United Technologies Research Center (UTRC), and the State University of New York at Buffalo (SUNY-B). Special finite element models are being constructed by MARC, while mechanics of materials models and constitutive models are being assembled by UTRC. Development of advanced formulation (boundary element) models is being shared by P&W and SUNY-B. Verification of the various analysis packages is being done by P&W.

The technical effort of the Inelastic Analysis Methods program is divided into two 24-month segments: a base program, and an optional program exercised at the discretion of the government. The first year (Task I) of the base program dealt with linear theory in the sense that stresses or strains and temperatures in generic modeling regions are linear functions of the spatial coordinates, and solution increments for load, temperature and/or time are extrapolated linearly from previous information. The second half of the base program (Task II), as well as the option program (Tasks IV and V), extend the models to include higher-order representations of deformations and loads in space and time and deal more effectively with collections of discontinuities such as cooling holes and coating cracks. Work on Task IV (special functions theory) has been completed, and the results are given in the Third Annual Status Reports. Base program computer codes, hereafter referred to as MOMM (Mechanics of Materials Model), MHOST (MARC-HOST), and BEST (Boundary Element Stress Technology), have been developed and delivered to NASA-Lewis Research Center.

Three increasingly sophisticated constitutive models are employed by MOMM, MHOST, and BEST to account for inelastic material behavior (plasticity, creep) in the elevated temperature regime. The simplified model assumes a bilinear approximation of stress-strain response and glosses over the complications associated with strain rate effects, etc. The state-of-the-art model partitions time-independent (plasticity) and time-dependent (creep) in the conventional way, invoking the Von Mises yield criterion and standard (isotropic, kinematic, combined) hardening rules for the former, and a power law for the latter. Walker's viscoplasticity theory (ref. 1), which accounts for the interaction between creep/relaxation and plasticity that occurs under cyclic loading conditions, has been adopted as the advanced constitutive model.

In brief, MOMM is a stiffness method finite element code that utilizes one-, two- and three-dimensional arrays of beam elements to simulate hot section component behavior. Despite limitations of such beam model representations, the code will be useful during early phases of component design as a fast, easy to use, computationally efficient tool. All of the structural analysis types (static, buckling, vibration, dynamics), as well as the three constitutive models mentioned above, are provided by MOMM. Capabilities of the code have been tested for a variety of simple problem discretizations.

The MHOST code employs both shell and solid (brick) elements in a mixed method framework to provide comprehensive capabilities for investigating local (stress/strain) and global (vibration, buckling) behavior of hot section components. Over the last decade, in order to support their commercially available software, the MARC Corporation has accumulated a great deal of technical expertise creating new, improved algorithms that will significantly reduce CPU (central processing unit) time requirements for three-dimensional analyses. The MHOST code development has taken advantage of this expertise. The third generation (Task IV) MHOST code is operational and has been tested with a variety of academic as well as engine-related configurations.

Successful assembly of the all-new BEST code was possibly the most important accomplishment of the base program effort. The challenge of extending basic theory and algorithms to encompass inelastic dynamic effects in three-space was met by combining the special skills and efforts of the research and programming teams at SUNY-B and P&W. As with MHOST, the third version of BEST is executable and has been exercised with both small and large test cases. While MHOST and BEST are currently viewed as complementary, they are also competitors; and overall performance on large inelastic models will be watched with interest as the codes mature.

Work on Task V (general functions theory) and application of the codes to representative turbine blade and vane configurations is in process, and will be described at the Fifth Annual HOST Workshop.

REFERENCES

1. Walker, K. P.: "Research and Development Program for Nonlinear Structural Modeling With Advanced Time-Temperature Dependent Constitutive Relationships," NASA CR-165533, November 25, 1981.

3D INELASTIC ANALYSIS METHODS FOR HOT SECTION COMPONENTS*

R.L. McKnight, P.C. Chen, L.T. Dame, R.V. Holt
H. Huang, M. Hartle, S. Gellin, D.H. Allen
and W.E. Haisler
General Electric Company

INTRODUCTION

Accomplishments are described for the 2-year program, to develop advanced 3-D inelastic structural stress analysis methods and solution strategies for more accurate and cost effective analysis of combustors, turbine blades and vanes. The approach was to develop a matrix of formulation elements and constitutive models. Three constitutive models were developed in conjunction with optimized iterating techniques, accelerators, and convergence criteria within a framework of dynamic time incrementing. Three formulations models were developed; an eight-noded mid-surface shell element, a nine-noded mid-surface shell element and a twenty-noded isoparametric solid element. A separate computer program has been developed for each combination of constitutive model-formulation model. Each program provides a functional stand alone capability for performing cyclic nonlinear structural analysis. In addition, the analysis capabilities incorporated into each program can be abstracted in subroutine form for incorporation into other codes or to form new combinations.

OBJECTIVES

The objective of this research was to develop analytical tools capable of economically evaluating the cyclic time-dependent plasticity which occurs in hot section engine components in areas of strain concentration resulting from the combination of both mechanical and thermal stresses. The techniques developed are capable of accommodating large excursions in temperatures with the associated variations in material properties including plasticity and creep.

The overall objective of this research program was to develop advanced 3-D inelastic structural/stress analysis methods and solution strategies for more accurate and yet more cost-effective analysis of combustors, turbine blades, and vanes. The approach was to develop a matrix of formulation elements and constitutive models, three increasingly more complex formulation models and three increasingly more complex constitutive models.

*Work done under NASA Contract NAS3-23698.

CONSTITUTIVE MODELS

The three constitutive models were developed in conjunction with optimized iteration techniques, accelerators, and convergence criteria within a framework of dynamic time incrementing. These consist of a simple model, a classical model, and a unified model. The simple model performs time-independent inelastic analyses using a bilinear stress-strain curve and time-dependent inelastic analyses using a power-law creep equation. The second model is the classical model of Professors Walter Haisler and David Allen (Reference 1) of Texas A&M University. The third model is the unified model of Bodner, Partom, et al. (Reference 2). All models were customized for a linear variation of loads and temperatures with all material properties and constitutive models being temperature dependent.

FORMULATION MODELS

The three formulation models developed are an eight-noded mid-surface shell element, a nine-noded mid-surface shell element and a twenty-noded isoparametric solid element. Both of the shell elements are obtained by "degenerating" 3D isoparametric solid elements and then imposing the necessary kinematic assumptions in connection with the small dimension of the shell thickness (References 3 and 4). The eight-noded element uses Serendipity shape functions and the nine noded element uses Lagrange shape functions. The eight-noded element uses Gaussian quadrature for numerical integration, with nodal and surface stresses being obtained by extrapolation/mapping techniques. Lobatto quadrature is being used with the nine-noded element to effectively provide for direct recovery of the stresses and strains at the surfaces and node points. The eight-noded element has an excellent combination of accuracy and economy in the normal element aspect range encountered when modeling most hot section components. The nine-noded Lagrangian formulation overcomes the shear locking problem experienced when the element size-versus-thickness-aspect ratio becomes very large. The twenty-noded isoparametric element uses Gaussian quadrature.

COMPUTER PROGRAMS

A separate computer program has been developed for each combination of constitutive model-formulation model. Each program provides a functional, stand alone capability for performing cyclic nonlinear structural analysis. In addition, the analysis capabilities incorporated into each program can be abstracted in subroutine form for incorporation into other codes or to form new combinations. These programs will provide the structural analyst with a matrix of capabilities involving the constitutive models-formulation models from which he will be able to select the combination that satisfies his particular needs. The program architecture employs state-of-the-art techniques to maximize efficiency, utility, and portability. Among these features are the following:

(i) User Friendly I/O

- o Free format data input

- o Global, local coordinate system, (Cartesian, Cylindrical, Spherical)
- o Automatic generation of nodal and elemental attributes
- o User-controlled optional print out
  - Nodal Displacements
  - Nodal Forces
  - Element Forces
  - Element Stresses and Strains

(ii) Programming Efficiency

- o Dynamic core allocation
- o Optimization of file/core utilization
- o Blocked column skyline out-of-core equation solver

(iii) Accurate and Economical Solution Techniques

- o Right-hand side pseudoforce technique
- o Accelerators for the iteration scheme
- o Convergence criteria based on both the local inelastic strain and the global displacements

The ability to model piecewise linear load histories was also included in the finite element codes. Since the inelastic strain rate could be expected to change dramatically during a linear load history, it is important to include a dynamic time-incrementing procedure.

Three separate time step control criteria are used. These are the maximum stress increment, maximum inelastic strain increment, and maximum rate of change of the inelastic strain rate. The minimum time step calculated from the three criteria is the value actually used. Since the calculations are based on values readily available from the previous time step, little computational effort is required.

TEST CASES

These formulation models and constitutive models have been checked out extensively against both theory and experiment. Figure 1 shows the correlation between Bodner's model in the eight-noded and mid-surface shell element (MSS8) and

both experiment and other predictions (Reference 5). Figures 2 through 6 illustrate the predictability of the classical Haisler-Allen model. Figure 7 shows a comparison of both Bodner's model and the simple model to both experiment and independent predictions (Reference 6).

SOURCE CODE INFORMATION

These nine programs, both source (Fortran 77) and compiled, have been installed and checked out on the NASA-Lewis CRAY-1 machine. The interactive deck generator has been installed on the NASA-Lewis AMDAHL machine.

Table 1 shows the lines of source code for each of the nine computer programs. These numbers do not include the interactive deck generators.

TABLE 1. LINES OF SOURCE CODE

		Elements		
		20-Noded	8-Noded	9-Noded
Constitutive Models	Simple	8300	13,800	17,900
	Haisler-Allen	9200	16,300	19,000
	Bodner	7300	13,800	17,600

Since these programs use dynamic core allocation, they can be recompiled to size for any specific machine. They are presently loaded for 10^7 bytes of core. At this size, the maximum problem would be approximately 4000 nodes and 1000 elements, and 24000 degrees of freedom.

REFERENCES

1. Allen, D.H., and Haisler, W.E., "A Theory of Thermoplastic Materials," Computers and Structures, Vol. 13, pp. 129-135, 1981.

2. Bodner, S.A., Partom, I., and Partom, Y., "Uniaxial Cyclic Loading of Elastic-Viscoplastic Material," ASME J. Appl. Mech., Vol. 46, p. 805, 1979.

3. Chang, T.Y. and Sawamiphakdi, K., "Large Deformation Analysis of Shells by Finite Element Method," Comp. and Struct., Vol. 13, pp. 331-340, 1981.

4. Chang, T.Y. and Sawamiphakdi, K., "Nonlinear Finite-Element Analysis of Shells with Large Aspect Ratio," presented at the Nonlinear Structural Analysis Workshop, NASA-Lewis Research Center, April 19 and 20, 1983.

5. Stouffer, D.C., "A Constitutive Representation for IN100," Air Force Materials Laboratory, AFWAL-TR-81-4039, 1981.

6. Bodner, S.R., "Representation of Time Dependent Mechanical Behavior of Rene' 95 by Constitutive Equations," Air Force Materials Laboratory, AFML-TX-79-4116, 1979.

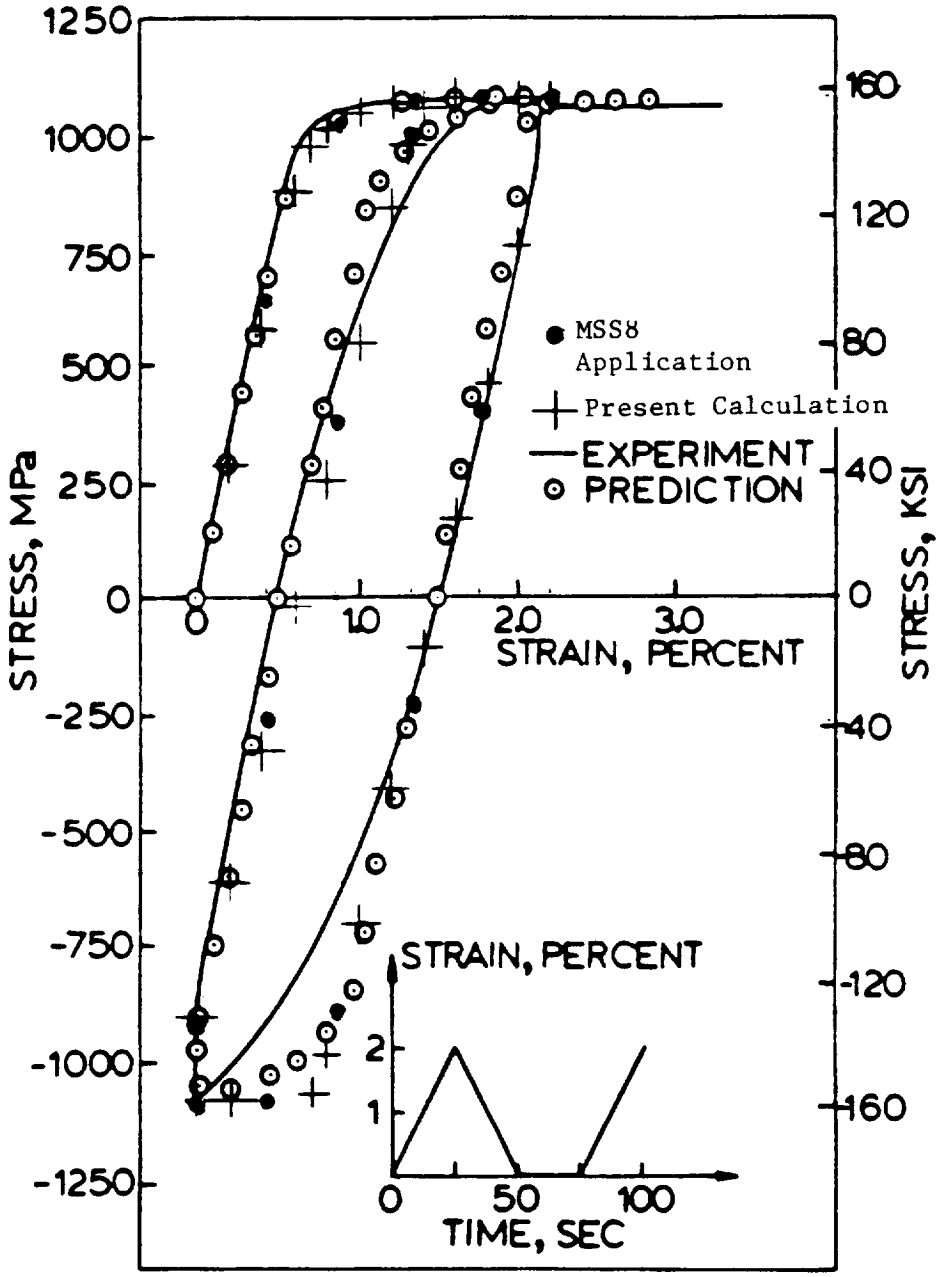

Figure 1. Displacement Controlled Cycling Results.

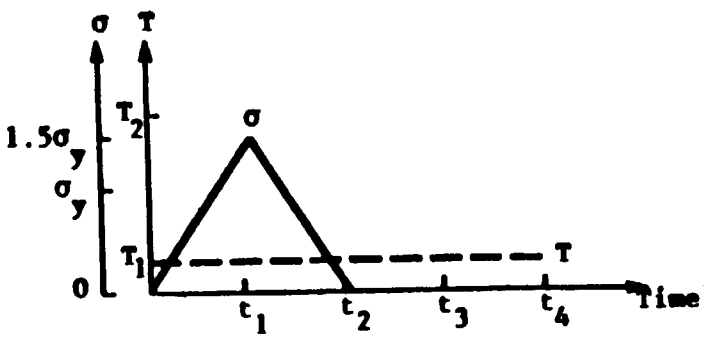

Case I

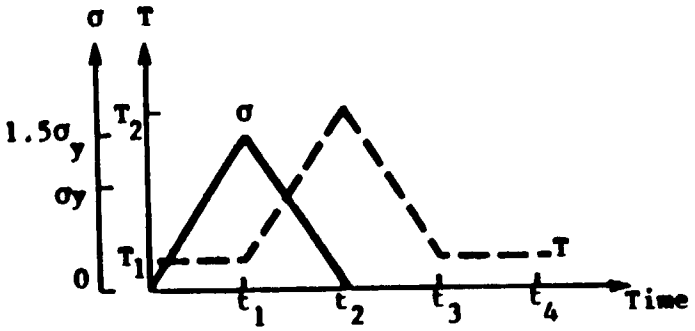

Case III

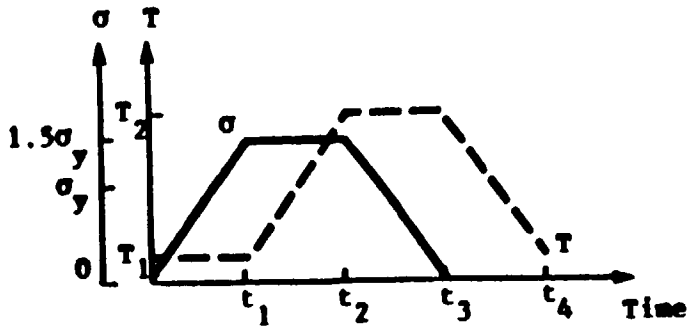

Case II

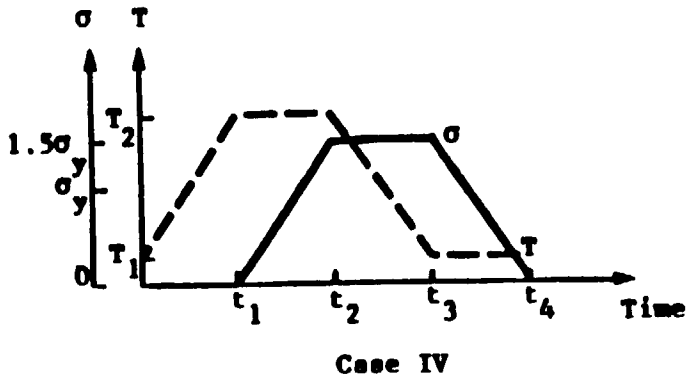

Case IV

Figure 2. Load Histories for Plasticity Example.

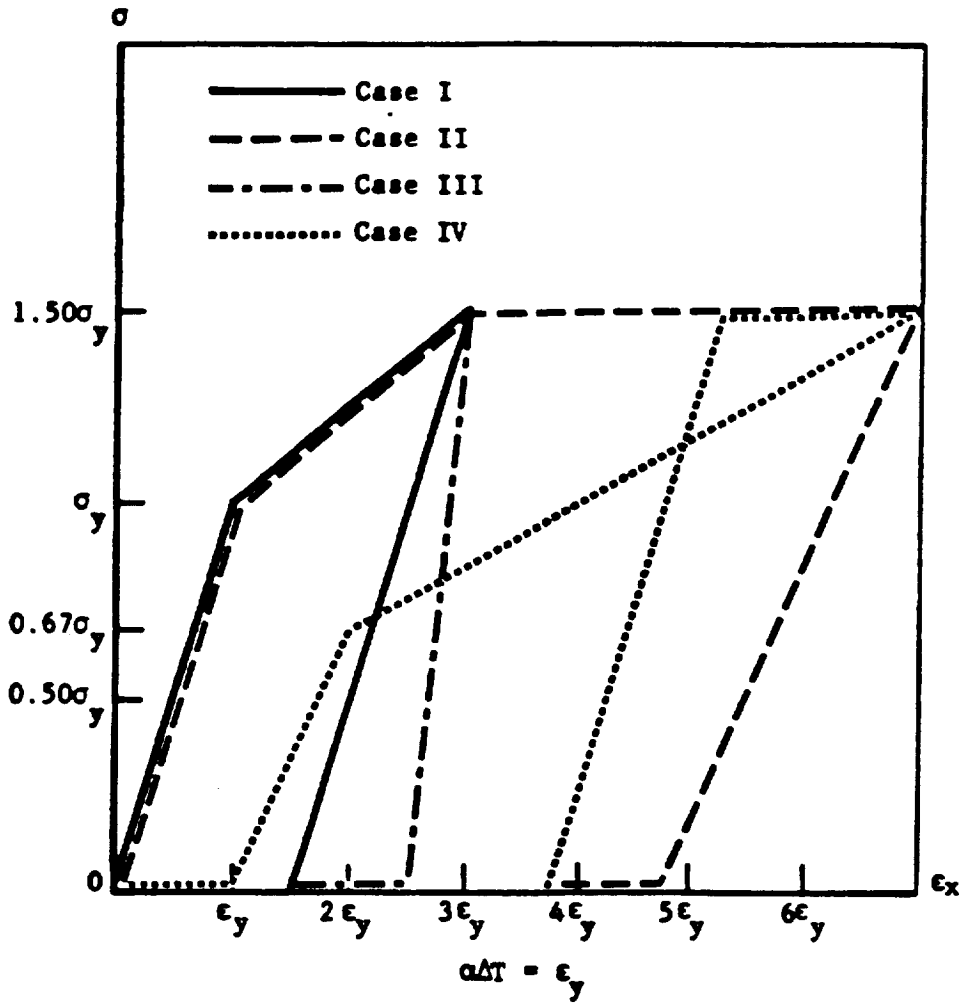

Figure 3. Results of Plasticity Example.

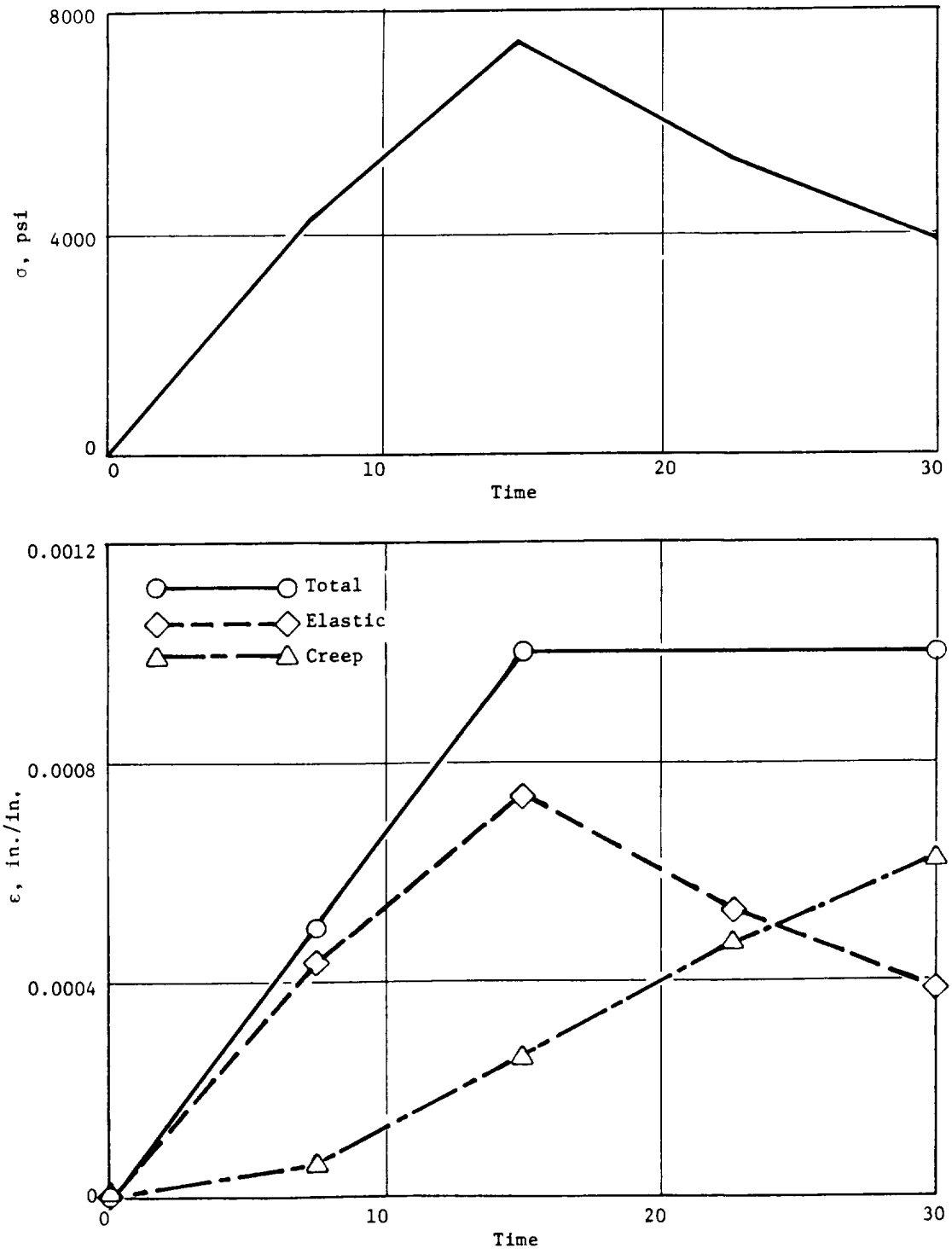

Figure 4. Strain Controlled Creep.

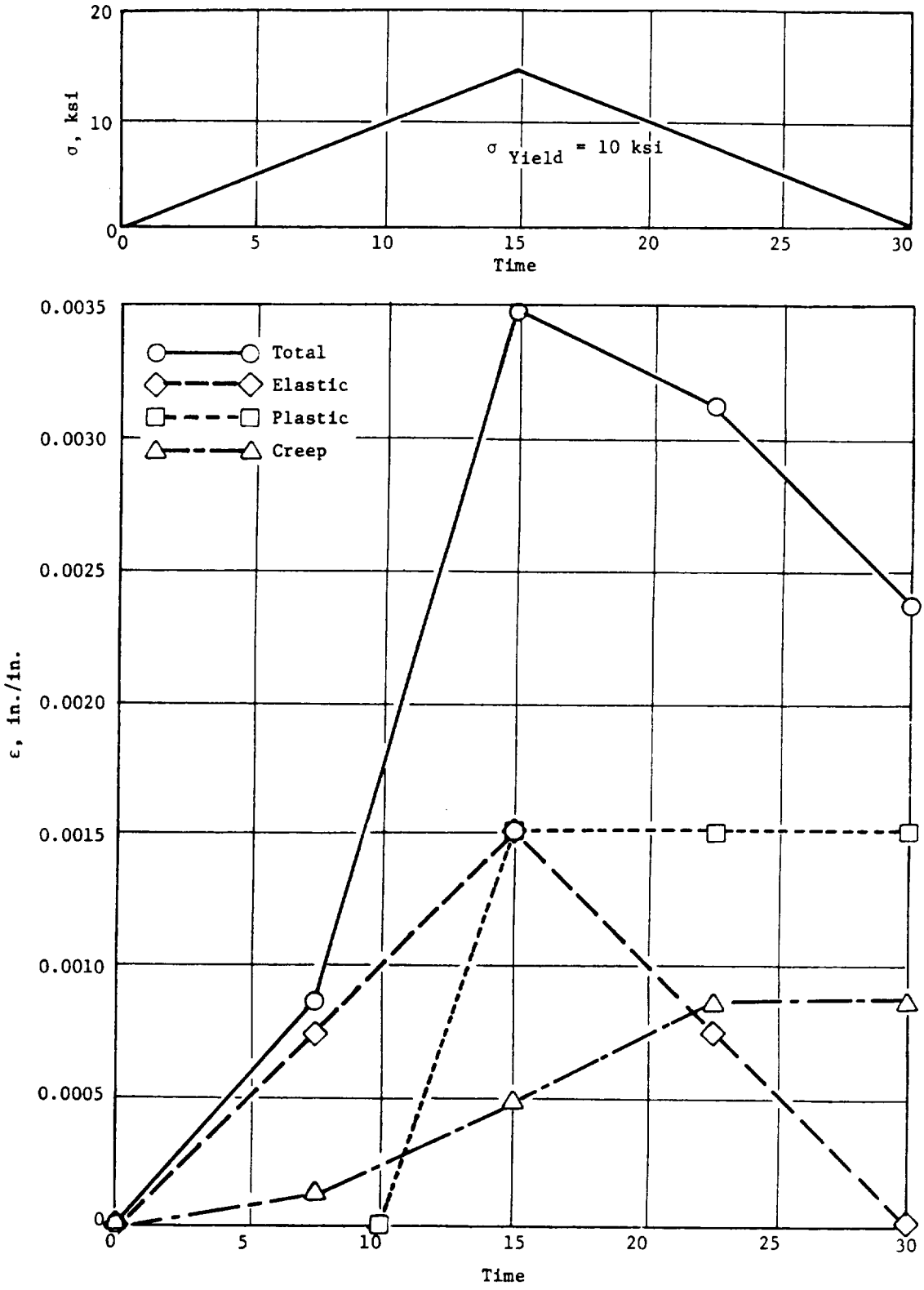

Figure 5. Stress Controlled Cycling with Combined Plasticity and Creep.

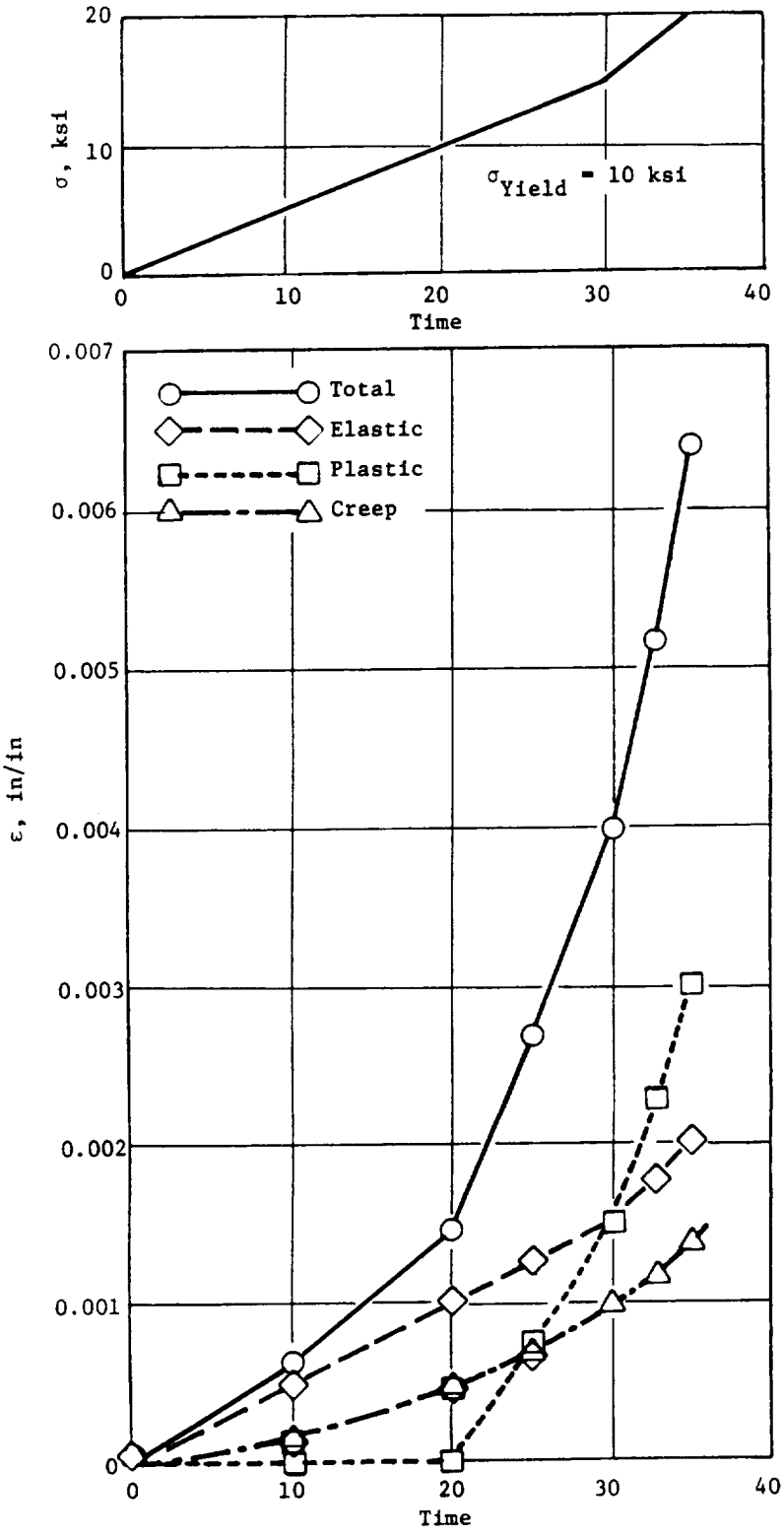

Figure 6. Stress Controlled Combined Plasticity and Creep.

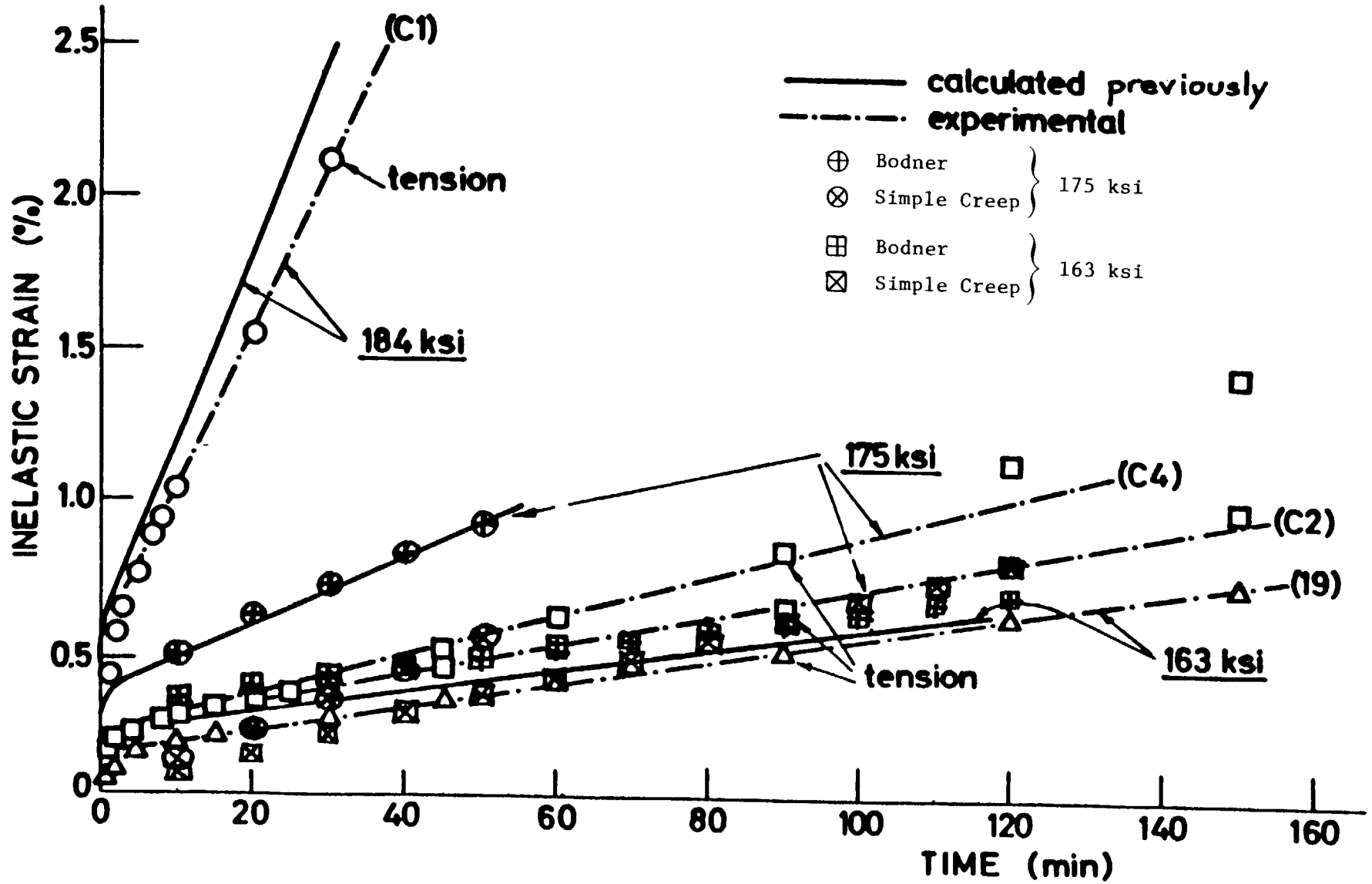

Figure 7. Comparison of Bodner Mode to Simple Creep.

COMPONENT SPECIFIC MODELING*

R.J. Maffeo, R.L. McKnight, M.T. Tipton, and G. Weber
General Electric Company

INTRODUCTION

The overall objective of this program is to develop and verify a series of interdisciplinary modeling and analysis techniques that have been specialized to address three specific hot section components. These techniques incorporate data as well as theoretical methods from many diverse areas including cycle and performance analysis, heat transfer analysis, linear and nonlinear stress analysis, and mission analysis. Building on the proven techniques already available in these fields, the new methods developed through this contract are integrated to provide an accurate, efficient, and unified approach to analyzing combustor burner liners, hollow air-cooled turbine blades, and air-cooled turbine vanes. For these components, the methods developed predict temperature, deformation, stress, and strain histories throughout a complete flight mission.

The base program for the component specific modeling effort is illustrated in Figure (1). Nine separate tasks were arranged into two parallel activities. The component specific structural modeling activity in Figure (2), was directed towards the development of the analytical techniques and methodology required in the analysis of complex hot section components. The component specific thermomechanical load mission modeling effort illustrated in Figure (3), provides for the development of approximate numerical models for engine cycle, aerodynamic, and heat transfer analyses of hot section components.

THERMODYNAMIC AND THERMOMECHANICAL MODELS

The Thermodynamic Engine Model (TDEM) and the Thermomechanical Load (TDLM) Model have been reported on extensively at previous HOST conferences. They have been installed on the NASA Lewis CRAY for over a year where they have been exercised by both GE and NASA personnel. Figures 4, 5 and 6 show representative pieces of input and output of these models. Figure 4 shows the input to the TDEM defining a specific mission. Figure 5 shows the output of the TDEM giving the engine parameters for a mission. This is then the input to the TDLM. Figure 6 shows a snapshot of a portion of the output of the TDLM for a combustor nugget showing the result of running the TDEM and TDLM to be local structural temperature and pressure loading on a component.

COMBUSTOR STRUCTURAL ANALYSIS

The emphasis in Phase I of this program has been on automating the COSMO procedure for the combustor liner. The COSMO procedure continues with the output

*Work done under NASA Contract NAS3-23687.

of the TDLM being structured as a data file for use in the combustor component specific model. Figure 7 defines the recipe which generates the combustor structural model. Figure 8 is a snapshot of a typical run of the combustor model when it was in the checkout phase as a free-standing code. As indicated, the model contains a default set of recipe parameters, only changes to this list need be given. After the recipe parameters have been set, only 5 parameters need be specified to generate a 3D sector model of a combustor to perform a hot streak analysis. The first parameter (shown as the number of exhaust nozzles) is required to divide the 360° combustor into the proper number of sectors. The next parameter (shown as the no. of circumferential elements) is used by the analyst to split up the circumferential sector into a number of slices, NS, for the 3D elements. Next, depending on the number of slices selected, the analyst can bias these slices by specifying NS-1 percents (program calculates final bias to total 100%). In this case the biasing selected, starting at the hot streak, was 5%, 15%, and 30% with the final slice being 50%. This is all the information that is required to generate a 3D finite element model consisting of 20-noded isoparametric elements. In this case the model consists of 648 elements, 3192 nodes and has 768 element faces with pressure loading. Figures 9 and 10 are graphical depictions of this 3D model. The combustor then maps the temperatures and pressures from the TDLM onto this model and generates data files for the structural analysis.

COSMO SYSTEM

Figure 11 shows a flow chart of the overall COSMO system including the action positions of the adaptive controls developed in this program. This system includes a bandwidth optimizer which is necessary to make the automatic remeshing/mesh refinement activity possible. For the combustor, the following adaptive controls have been incorporated into the system (the numbers are consistent with Figure 11).

1. time increment
2. load increment
3. plasticity tolerances
4. creep tolerances
5. number of master region elements
6. number of slices
7. position of slices
8. row refinement
9. element refinement

The first four adaptive controls are a function of the structural code being used. For this system the code and the controls are those developed under, "3D Inelastic Analysis Methods for Hot Section Structures." The other adaptive controls are keyed from a decision grid as indicated in Figure 12. The gradients in normalized stress, total strain, plastic strain, and creep strain will be used to rank requirements.

REFERENCES

1. McKnight, R.L., "Component Specific Modeling - First Annual Status Report," NASA CR-174765, 1983.

2. McKnight, R.L., "Component Specific Modeling - Second Annual Status Report," NASA CR-174925, 1985.

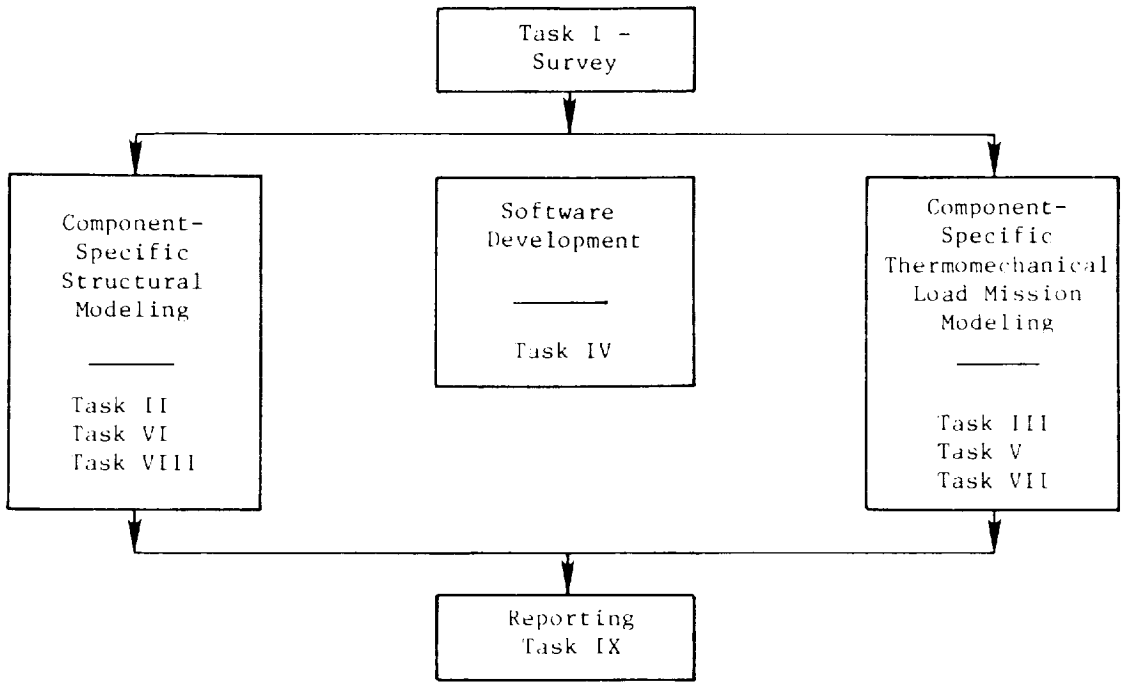

Figure 1. Component Specific Modeling Base Program.

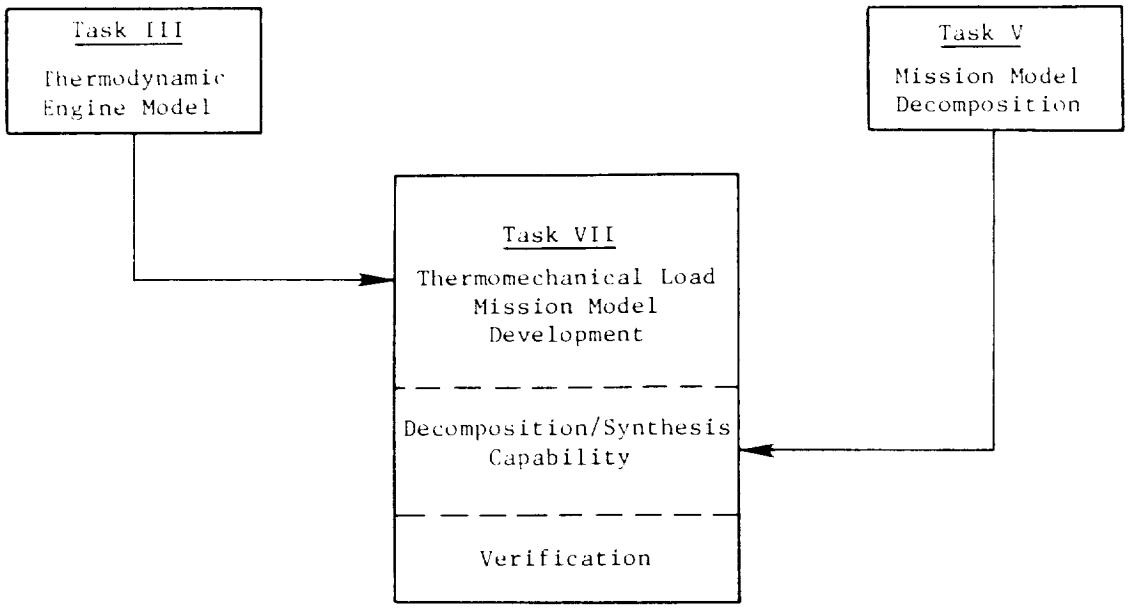

Figure 2. Component Specific Thermomechanical Load Mission Modeling.

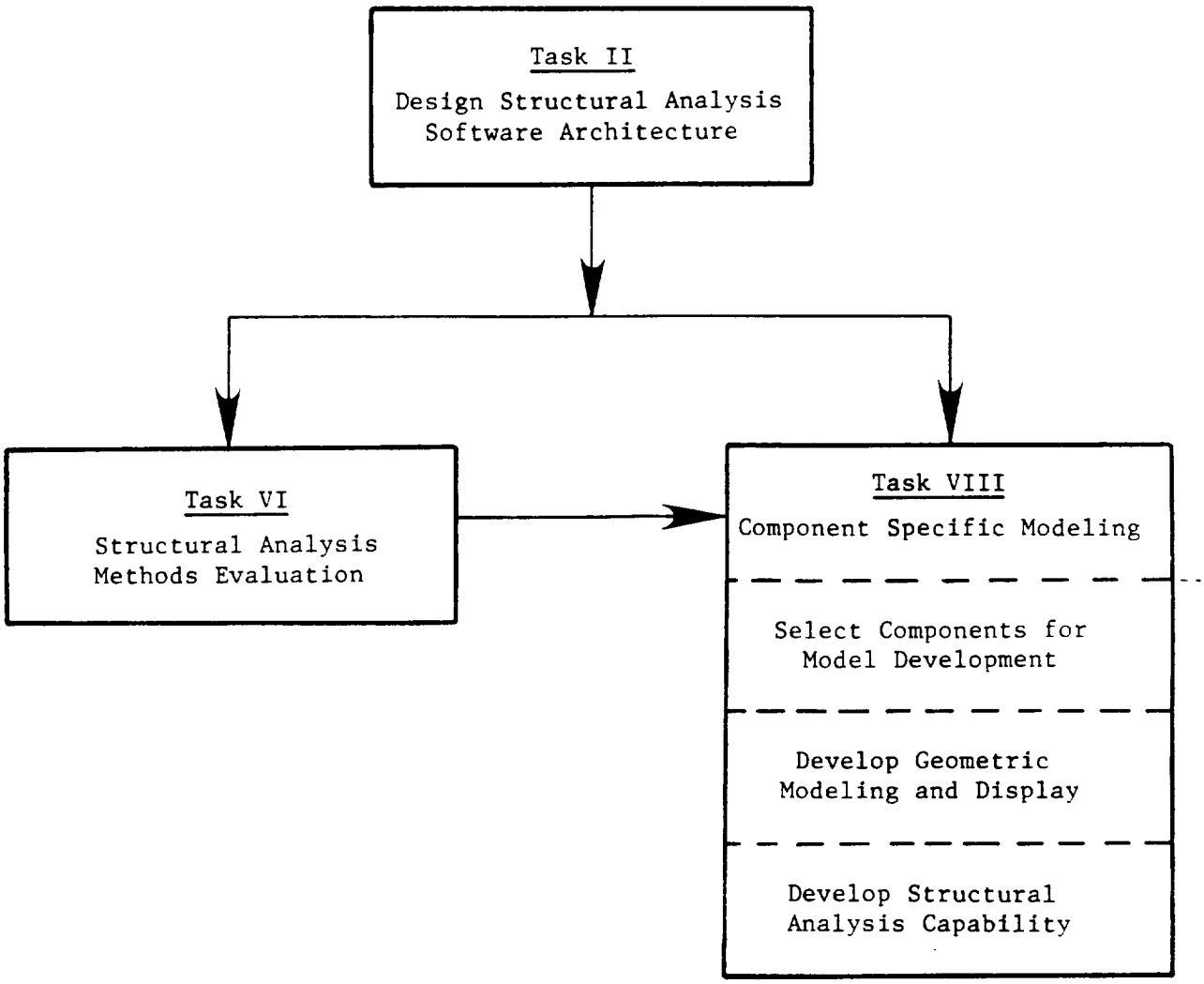

Figure 3. Component Specific Structural Modeling.

Case No.	Mach No.	Alt	Amb T Code	ΔTo	Power Code	Fan Speed	Bleed Code		No. Offset Instr	Special Ref. Case	Flt Phase
197	0.00	0.	10	0.	41	0.	-1.	-1.	0	197	ST
151	0.00	0.	10	0.	37	0.	-1.	-1.	0	0	GI1
152	0.00	0.	10	0.	22	3730.	-1.	-1.	0	0	TO1
153	.243	2000.	10	0.	22	3743.	-1.	-1.	0	0	TO2
154	.243	2000.	10	0.	22	3634.	-1.	-1.	0	0	CL1
155	.45	10000.	10	7.0	22	3634.	-1.	-1.	0	0	CL2
156	.58	11000.	10	7.0	22	3618.	-1.	-1.	0	0	CL3
157	.82	33000.	10	11.0	22	3724.	-1.	-1.	0	0	CL4
158	.82	33000.	10	11.0	22	3466.	-1.	-1.	0	0	CRU
159	.82	33000.	10	11.0	38	0.	-1.	-1.	0	0	D1
160	.61	11000.	10	7.0	38	0.	-1.	-1.	0	0	D2
161	.61	11000.	10	7.0	37	0.	-1.	-1.	0	0	D3
162	.42	6000.	10	2.0	37	0.	-1.	-1.	0	0	D4
163	.42	6000.	10	2.0	22	2798.	-1.	-1.	0	0	APPR
164	.24	0.	10	0.0	22	2798.	-1.	-1.	0	0	LDG
165	.18	0.	10	0.0	38	0.	-1.	-1.	0	0	FI
166	.18	0.	10	0.0	39	2968.	-1.	-1.	0	0	TR1
167	0.00	0.	10	0.0	39	2834.	-1.	-1.	0	0	TR2

Figure 4. Inputs to Thermodynamic Engine Model.

DATE - 07/16/85

* ENGINE PERFORMANCE DATA BY MISSION PHASE *

PHASE #	CASE #	P2	P25	P3	** ENGINE PARAMETER ** P4		P49	P5	P8	FNIN1	DTAMB	PHASE
1	197	14.696	14.696	14.696	14.696	0.	14.696	14.696	0.018	0.	0.	ST
2	151	14.696	15.531	73.295	69.860	0.	20.820	15.048	15.031	4538.261	0.	GI1
3	151	14.696	15.531	73.295	69.860	0.	20.820	15.048	15.031	4538.261	0.	GI1
4	152	14.696	32.353	422.356	402.822	0.	91.073	23.769	23.456	48907.753	0.	TO1
5	153	14.238	31.569	413.413	394.295	0.	89.075	23.105	22.796	37628.904	0.	TO2
6	154	14.237	30.207	388.387	370.358	0.	83.604	22.011	21.727	35094.032	0.	CL1
7	155	11.613	24.987	321.570	306.667	0.	69.312	17.822	17.580	24750.564	7.000	CL2
8	156	12.205	25.735	327.605	312.364	0.	70.500	18.211	17.966	22581.097	7.000	CL3
9	157	5.910	13.987	187.264	178.717	0.	40.557	10.415	10.275	11977.777	11.000	CL4
10	158	5.910	12.634	160.416	153.003	0.	34.522	8.872	8.752	9849.775	11.000	CRU
11	158	5.910	12.634	160.416	153.003	0.	34.522	8.872	8.752	9849.775	11.000	CRU
12	159	5.910	5.820	14.195	13.596	0.	5.152	3.878	3.876	-1602.839	11.000	D1
13	160	12.494	12.425	32.608	31.167	0.	12.205	9.855	9.850	-2438.477	7.000	D2
14	161	12.494	13.434	60.439	57.424	0.	15.634	10.153	10.136	-1434.762	7.000	D3
15	162	13.297	14.110	64.982	61.827	0.	17.506	12.153	12.137	-18.451	2.000	D4
16	163	13.296	19.957	205.245	195.282	0.	43.655	14.847	14.731	11991.389	2.000	APP
17	164	15.296	22.579	238.419	226.933	0.	51.135	17.924	17.793	16294.929	0.	LDG
18	165	15.032	15.298	42.036	40.353	0.	17.187	14.821	14.815	207.969	0.	FI
19	165	15.032	15.298	42.036	40.353	0.	17.187	14.821	14.815	207.969	0.	FI
20	166	15.033	23.122	261.537	249.111	0.	55.912	18.394	18.240	-11588.640	0.	TR1
21	167	14.697	21.554	234.321	223.144	0.	50.301	17.691	17.561	-4309.143	0.	TR2
22	151	14.696	15.531	73.295	69.860	0.	20.820	15.048	15.031	4538.261	0.	GI1
23	151	14.696	15.531	73.295	69.860	0.	20.820	15.048	15.031	4538.261	0.	GI1
24	197	14.696	14.696	14.696	14.696	0.	14.696	14.696	0.018	0.	0.	ST

Figure 5. Outputs From Thermodynamic Engine Model.

Pts 0.034 → 1.15 are Sufficient to Illustrate data

X	Y	T_H	T_A	ΔT_H	ΔT_A	ΔP
0.034	0.030	520.182	520.182	0.161	0.161	0.
0.094	0.030	521.284	521.284	0.263	0.263	0.
0.158	0.030	522.834	522.834	0.391	0.391	0.
0.208	0.030	523.901	523.901	0.463	0.463	0.
0.254	0.030	524.487	524.487	0.485	0.485	0.
0.288	0.030	524.935	524.935	0.499	0.499	0.
0.340	0.030	525.658	525.520	0.516	0.505	0.
0.404	0.030	526.519	526.002	0.523	0.489	0.
0.438	0.030	528.827	526.967	0.639	0.521	0.
0.584	0.040	530.446	527.690	0.735	0.562	0.
0.654	0.040	531.376	528.276	0.790	0.597	0.
0.764	0.040	531.686	528.758	1.032	0.800	0.
0.854	0.040	530.928	527.690	1.144	0.841	0.
0.934	0.044	529.826	527.311	1.310	1.014	0.
1.040	0.044	528.586	526.967	1.481	1.238	0.
1.074	0.040	527.828	526.726	1.461	1.284	0.
1.114	0.030	527.656	526.485	1.541	1.340	0.
1.150	0.030	527.518	526.381	1.613	1.405	0.

Figure 6. Outputs From Combustor Thermodynamic Loads Model.

Combustor Liner Parameter List

Code	Name	Default	Code	Name	Default
1	X_1	0.0	2	Y_1	0.0
3	α_1	0.0	4	L_1	10.5
5	L_2	2.0	6	L_3	0.5
7	L_4	6.0	8	L_5	0.8
9	L_6	1.0	10	L_7	2.0
11	T_1	0.5	12	T_2	0.7
13	T_3	0.5	14	T_4	0.65
15	T_5	0.5	16	θ_1	90.0
17	θ_2	90.0	18	R_1	1.0
19	R_2	1.0	20	R_3	0.75
21	R_4	1.5	22	R_5	1.5
23	R_6	1.5			

X = Coordinate

Y = Coordinate

α = Angle wrt, x - Axis

L = Length

T = Thickness

θ = Angle of Rotation

R = Radius of Curvature

(n)= Parameter Code Number

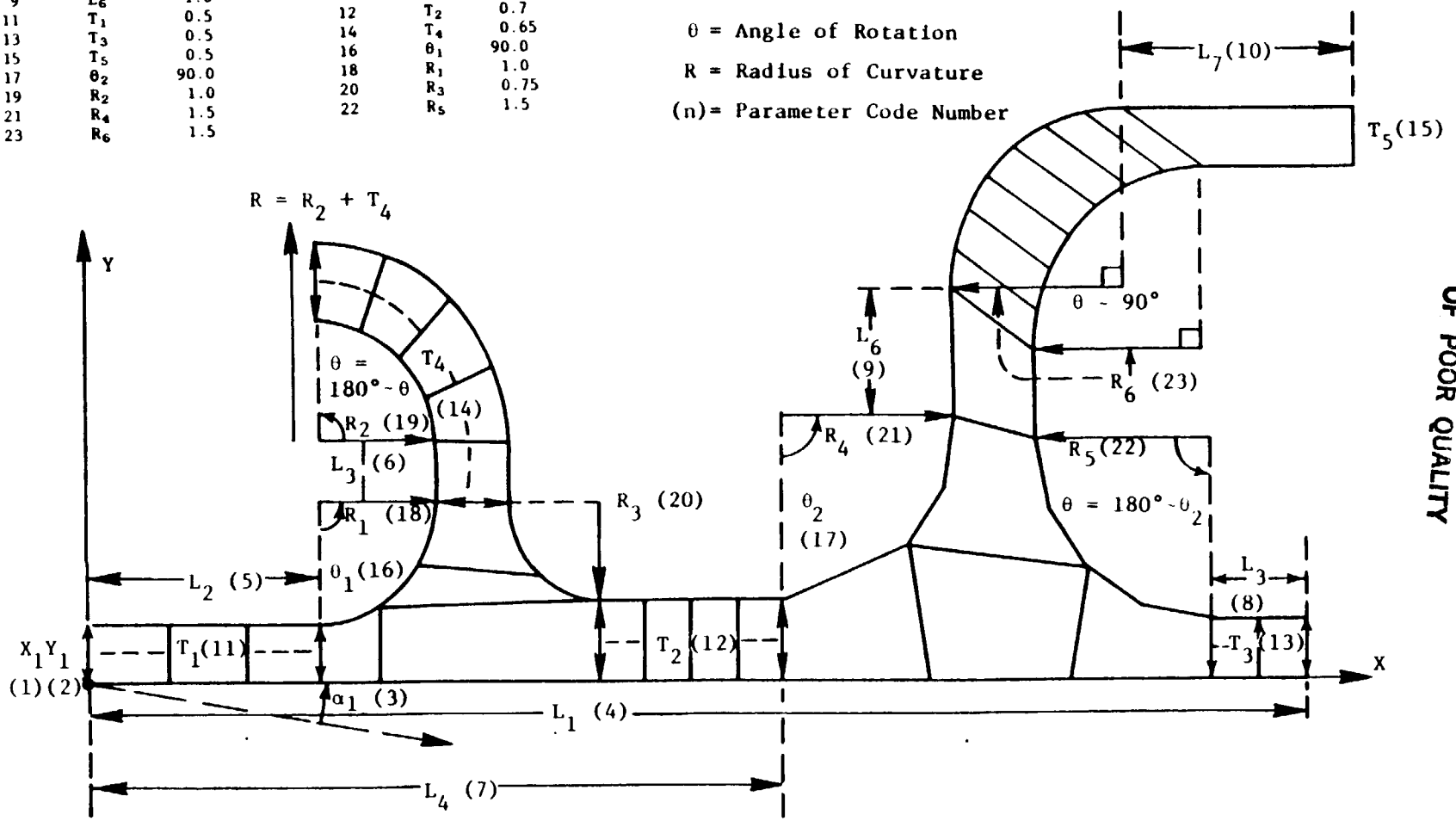

Figure 7. Combustor Liner Parameters.

```
8:RN /GN/NUGPRO

      NUGGET RECIPE    VERS.II 8/29/86

DO YOU HAVE A PARAMETER FILE 21? (0/1)
*
```

CODE	VALUE	CODE	VALUE
1	0.	2	0.
3	0.	4	1.16700
5	0.19200	6	0.04500
7	0.81000	8	0.06800
9	0.10000	10	0.20000
11	0.06000	12	0.08000
13	0.06000	14	0.06800
15	0.06800	16	110.00000
17	90.00000	18	0.06000
19	0.06300	20	0.12000
21	0.12500	22	0.08300
23	0.09500		

```
  ENTER PARAMETER CHANGES (ENTRY CODE, NEW VALUE)
      WHEN DONE ENTER     0 0

*0 0
```

CODE	VALUE	CODE	VALUE
1	0.	2	0.
3	0.	4	1.16700
5	0.19200	6	0.04500
7	0.81000	8	0.06800
9	0.10000	10	0.20000
11	0.06000	12	0.08000
13	0.06000	14	0.06800
15	0.06800	16	110.00000
17	90.00000	18	0.06000
19	0.06300	20	0.12000
21	0.12500	22	0.08300
23	0.09500		

```
 DO YOU WANT TO CHANGE PARAMETERS? (0/1)
*
READING FILE NUGCON
READING DONE
              27 ELEMENTS READ

ENTER ENGINE TEMPERATURE AND PRESSURE FILE NAME
*/GN/NUGINF
READING FILE /GN/NUGINF
READING DONE
              36 CENTROIDS READ

ENTER THE NUMBER OF EXHAUST NOZZLES
  AND THE NO. OF CIRCUMFIRENTIAL ELEMENTS
  BETWEEN T-AVE AND T-HOT (MAX NO.=10)
*3 4

ENTER THE  3 CIRCUMFIRENTIAL BIASING PARAMETERS
 -- ENTER AS PERCENTS, THE SUM BEING LESS THAN 100% --
*6 15 30

********  3192 NODES IN 3-D MODEL     ********
********   648 ELEMENTS IN 3-D MODEL  ********
********   768 FACES WITH PRESSURES   ********

 ### 2-D MODE  FILE IS TEMP FILE 20 ###
 ### PARAMETER FILE IS TEMP FILE 21 ###
 ### 3-D  UIF  FILE IS TEMP FILE 26 ###

*
```

FIGURE 8. TYPICAL PROGRAM RUN

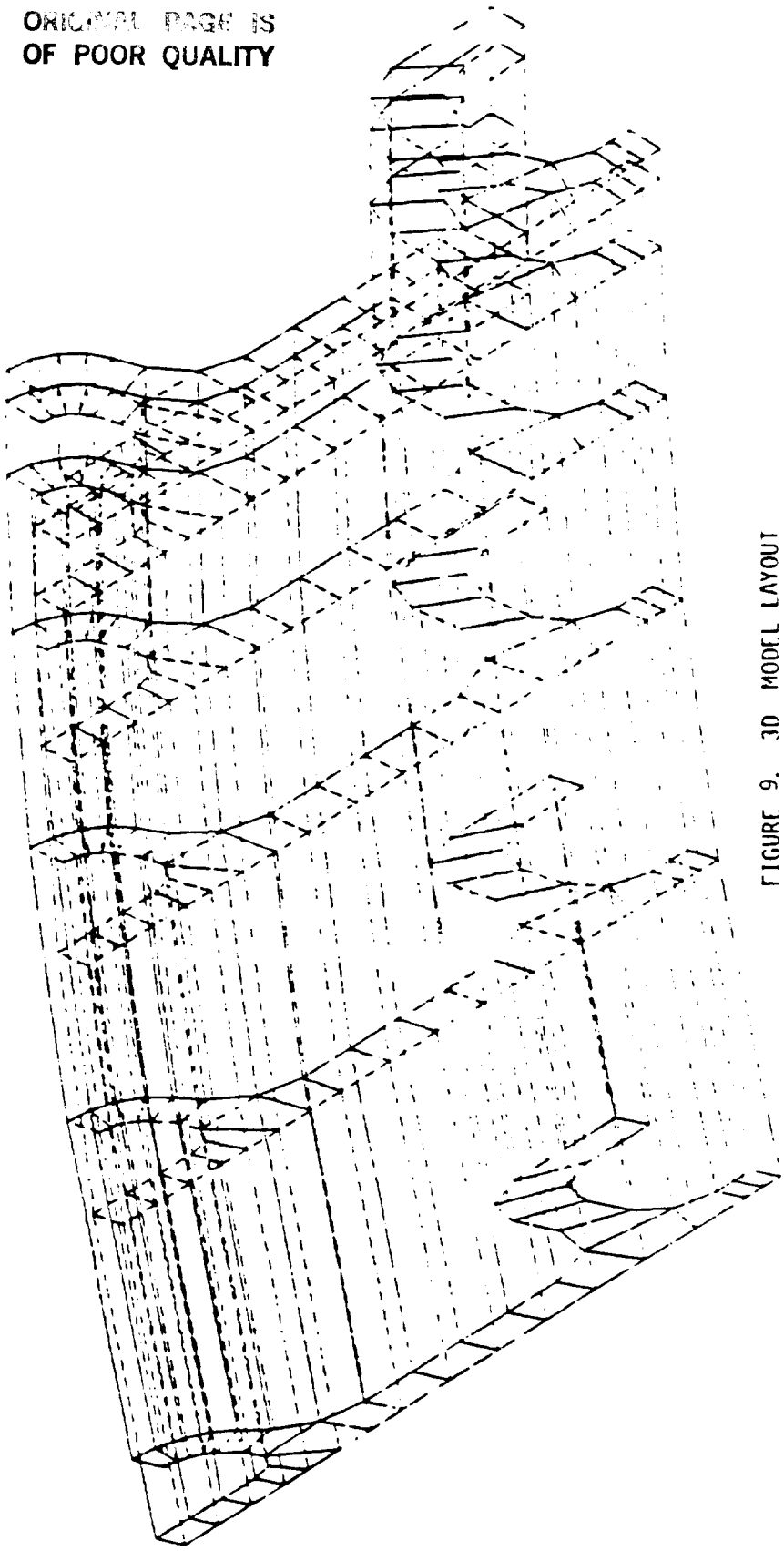

FIGURE 9. 3D MODEL LAYOUT

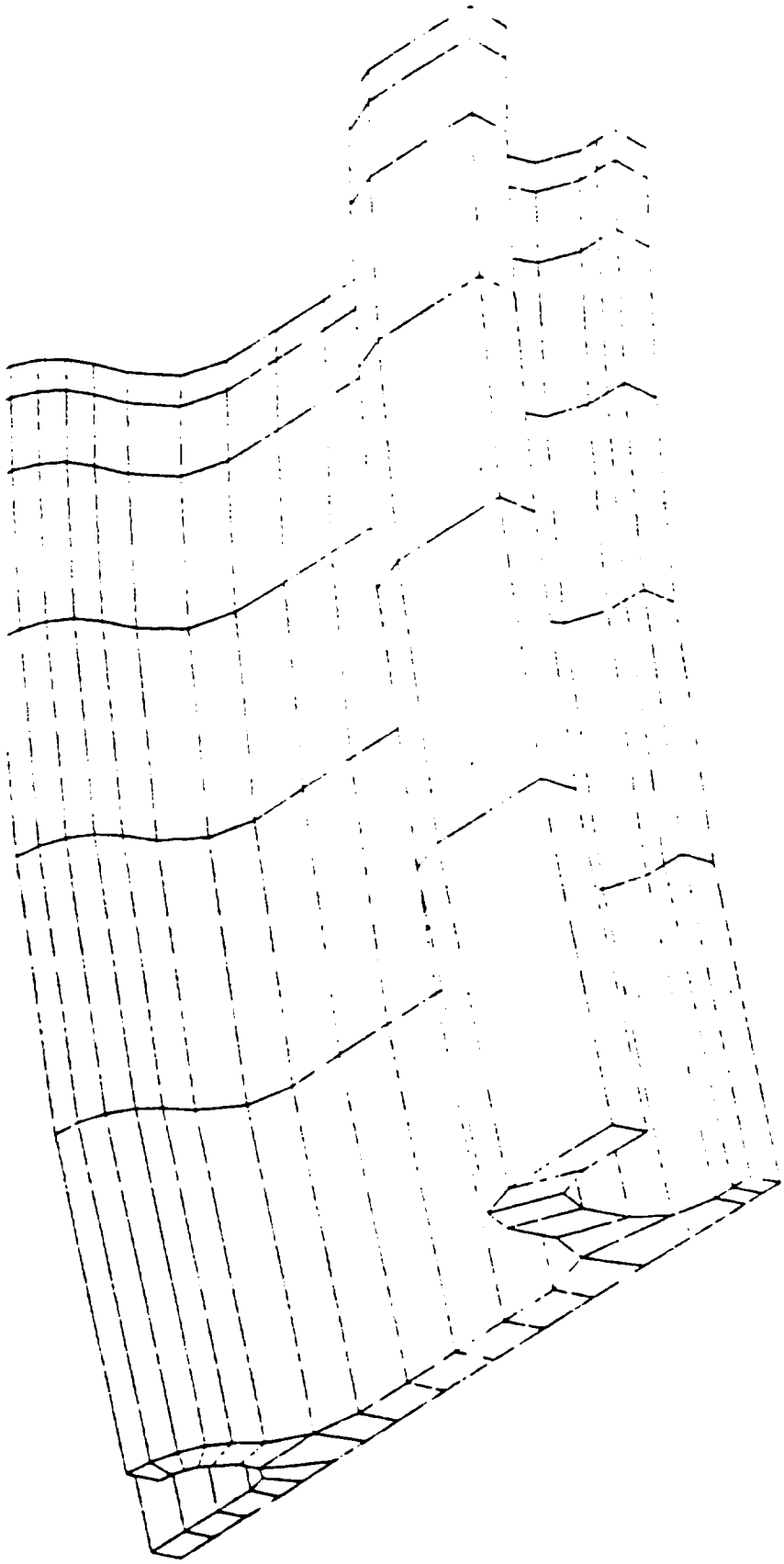

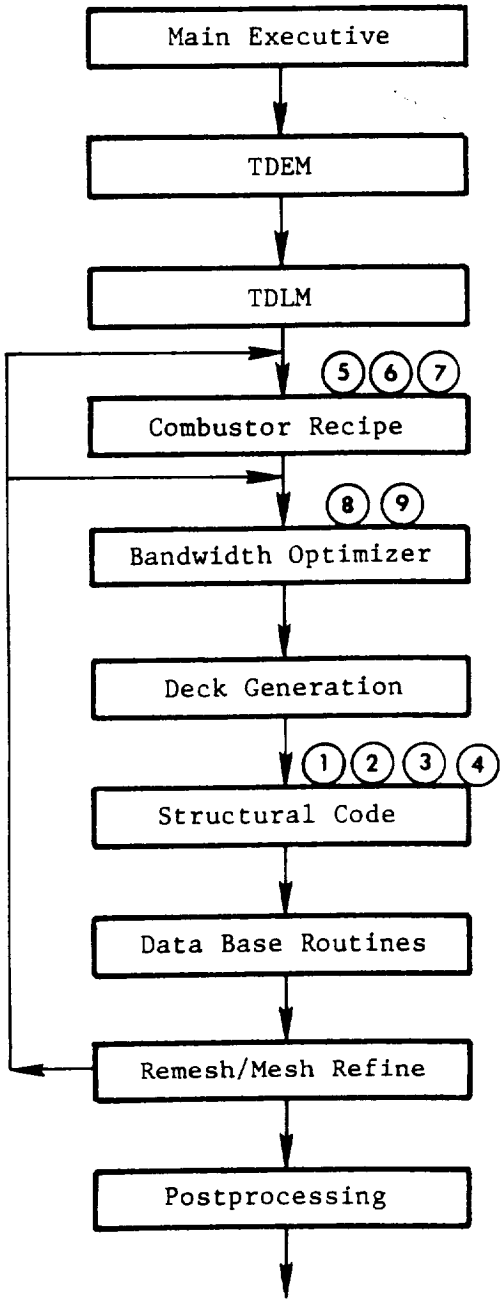

Figure 11. System Flow Chart Showing Adaptive Control Positions.

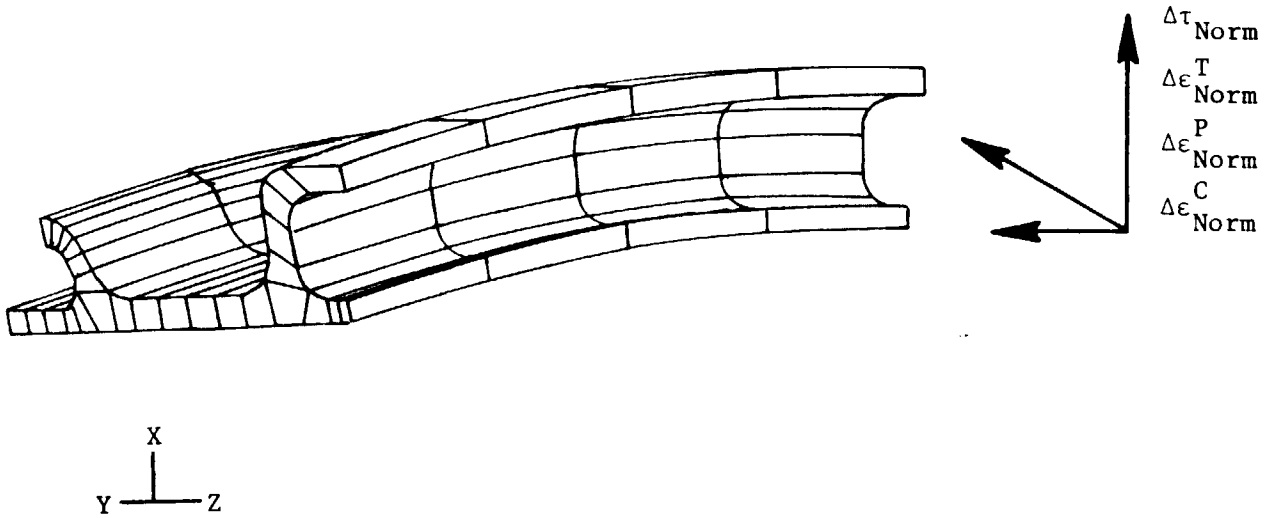

Figure 12. Combustor Nugget Decision Grid.

A MULTIAXIAL THEORY OF VISCOPLASTICITY FOR ISOTROPIC MATERIALS

D.N. Robinson and J.R. Ellis
The University of Akron
Akron, Ohio

INTRODUCTION

Many viscoplastic constitutive models for high-temperature structural alloys are based exclusively on uniaxial test data. Generalization to multiaxial states of stress is made by assuming the stress dependence to be on the second principal invariant (J_2) of the deviatoric stress, frequently called the "effective" stress. Testing other than uniaxial, e.g., shear, biaxial, etc., is generally done in the spirit of verification testing, not as part of the data base of the model.

If such a J_2 theory, based on uniaxial testing, is called upon to predict behavior under conditions other than uniaxial, say pure shear, and it does so poorly, nothing is left to adjust in the theory. The exclusive dependence on J_2 must be questioned.

For a fully isotropic material whose inelastic deformation behavior is relatively independent of hydrostatic stress, the most general stress dependence is on the two (non-zero) principal invariants of the deviatoric stress, J_2 and J_3. These invariants constitute what is known as an integrity basis for the material.

---

* This research was performed under NASA Grant NAG-3-379.

Here, we present a time-dependent constitutive theory with stress dependence on J_2 and J_3 that reduces to a known J_2 theory as a special case. The characterization of viscoplasticity can be made largely on uniaxial testing but the "strength" of the J_3 dependence must be determined by testing other than uniaxial, e.g., pure shear.

Earlier studies (refs. 1-3) have considered the inclusion of the invariant J_3 in the context of time-independent plasticity theory. The present time-dependent formulation is guided by the form of the yield function introduced in reference 1.

STATEMENT OF THE THEORY

As in references (4-6) the starting point is the assumed existence of a dissipation potential function

$$\Omega(\sigma_{ij}, \alpha_{ij})^* \tag{1}$$

with the generalized normality structure

$$\dot{\varepsilon}_{ij} = \frac{\partial \Omega}{\partial \sigma_{ij}} \tag{2}$$

$$-\dot{\alpha}_{ij}/h = \frac{\partial \Omega}{\partial \alpha_{ij}} \cdot \tag{3}$$

Here, σ_{ij} and α_{ij} denote the components of the applied and internal stress, respectively. $\dot{\varepsilon}_{ij}$ denotes the components of inelastic strain rate and h is a scalar function of the internal stress.

---

* The present treatment concerns only isothermal deformation, extension to nonisothermal conditions follows as in ref. 5.

We further assume, as in references (4-6), that the stress dependence enters through two scalar functions F and G, i.e.,

$$\Omega(F,G) \tag{4}$$

in which

$$F(\Sigma_{ij}) \tag{5}$$

and

$$G(a_{ij}) \tag{6}$$

Σ_{ij} in equation (5) denotes the stress difference

$$\Sigma_{ij} = S_{ij} - a_{ij} , \tag{7}$$

where S_{ij} and a_{ij} represent the deviatoric applied and internal stress, respectively.

As indicated earlier, for a fully isotropic material, F and G can depend only on the respective principal invariants of Σ_{ij} and a_{ij}, i.e.,

$$F(J_2,J_3) \tag{8}$$

and

$$G(\hat{J}_2,\hat{J}_3) \tag{9}$$

where

$$J_2 = \frac{1}{2}\Sigma_{ij}\Sigma_{ji}$$

$$J_3 = \frac{1}{3}\Sigma_{ij}\Sigma_{jk}\Sigma_{ki} \tag{10}$$

and

$$\hat{J}_2 = \frac{1}{2}a_{ij}a_{ji}$$

$$\hat{J}_3 = \frac{1}{3}a_{ij}a_{jk}a_{ki} \tag{11}$$

Guided by reference (1), we choose particular forms for F and G as

$$F(J_2,J_3) = \frac{(J_2^3 + CJ_3^2)^{1/3}}{K^2} - 1 \tag{12}$$

$$G(\hat{J}_2,\hat{J}_3) = \frac{(\hat{J}_2^3 + C\hat{J}_3^2)^{1/3}}{K^2} \tag{13}$$

Here, C indicates the "strength" of the J_3 contribution. Note that for C=0 the functions F and G reduce to the J_2 forms given in references (4 and 5).

Figure 1 shows plots of F=constant in a nondimensional normal/shear stress space for several values of C. Included are the special cases C=0(v.Mises-J_2), C=-4(Tresca) and C=-1.75(Drucker), the latter being the value taken in reference 1 for a yield function in time-independent plasticity. The experimental data points shown in figure 1 were obtained in preliminary experiments for determining the flow surfaces F=constant for a stainless steel (ref. 7). These few data suggest that the time-dependent behavior of this alloy may be somewhat stronger in shear than a J_2 material. A value of C=10 appears to fit the data reasonably well.

Using equations (4), (12), and (13) in equations (2) and (3) gives the flow law,

$$\dot{\epsilon}_{ij} = f(F)\Gamma_{ij} \tag{14}$$

in which

$$\Gamma_{ij} = J_2^2 \Sigma_{ij} + \frac{2C}{3} J_3 t_{ij} \tag{15}$$

and

$$t_{ij} = \Sigma_{ik}\Sigma_{kj} - \frac{2}{3} J_2 \delta_{ij} \tag{16}$$

The evolutionary law becomes

$$\dot{a}_{ij} = h(G)\dot{\varepsilon}_{ij} - r(G)\,\pi_{ij} \tag{17}$$

in which

$$\pi_{ij} = \hat{J}_2^2\, a_{ij} + \frac{2C}{3}\,\hat{J}_3\, g_{ij} \tag{18}$$

and

$$g_{ij} = a_{ik}a_{kj} - \frac{2}{3}\,\hat{J}_2\,\delta_{ij} \tag{19}$$

The functions f(F), h(G) and r(G) can be determined, as in references (4-6), from uniaxial testing. The value of C must be determined from a <u>non-uniaxial</u> test.

CALCULATED RESULTS AND DISCUSSION

Several calculations have been made using forms of the functions, f, h and r and associated material parameters that are typical of ferritic chrome-based and austenitic stainless-steel alloys. Qualitatively similar results can be expected for nickel-based alloys. Figure 2 shows predicted hysteresis loops over a constant strain range ($\Delta\varepsilon$=0.6%) and strain rate ($\dot{\varepsilon}$=.001/m). The curve in figure 2 labeled "uniaxial" can be thought of as having been carefully fit on the basis of uniaxial data. Predictions of pure shear response are also shown, corresponding to different values of C. That based on a J_2 theory is the curve labeled C=0. Even after tedious fitting of uniaxial cyclic data, if the shear prediction does not correlate well with shear data, nothing can be done in a J_2 theory short of compromising the uniaxial correlations. The present J_2, J_3 theory allows some flexibility in accurately predicting response other than uniaxial through the parameter C. Note that the hysteresis loop

labeled C=10, suggested by the data in figure 1, indicates a cyclic response that is about 20% stronger than the J_2 response (C=0).

Figure 3 shows predictions of creep response, i.e., behavior under constant stress. Here, the strain-time curve labeled "uniaxial and shear C=0" represents both the uniaxial response (using the strain scale on the left) and the shear response for a J_2 material (using the strain scale on the right). Each shear response corresponding to a particular value of C is to be measured using the right-hand shear strain scale. In creep, the effect of the J_3 dependence appears to be more pronounced than for strain cycling. Here, for C=10 the creep strain after 100 hours differs by a factor of 2 from that for the J_2 response (C=0).

REFERENCES

1. Drucker, D.C., ASME J. of Appl. Mech., Vol. 16, 1949.
2. Ohasi, Y., and Tanaka, E., ASME J. of Engr. Mat'ls. and Tech., Vol.103, 1981.
3. Chan, K.S., Lindholm, U.S., and Wise, J., ASME J. of Engr. Mat'ls. and Tech., Vol. 107, 1984.
4. Robinson, D.N., et.al., Proc. Specialists Meeting on High-Temp. Design Tech., IAEA, 1976.
5. Robinson, D.N., and Swindeman, R.W., ORNL/TM-8444, 1982.
6. Robinson, D.N., J. Nuc. Engr. and Des., Vol. 96, 1984.
7. Robinson, D.N., and Ellis, J.R., Proc. 5th Internat. Seminar on Inelastic Analysis, Paris, France, 1985.

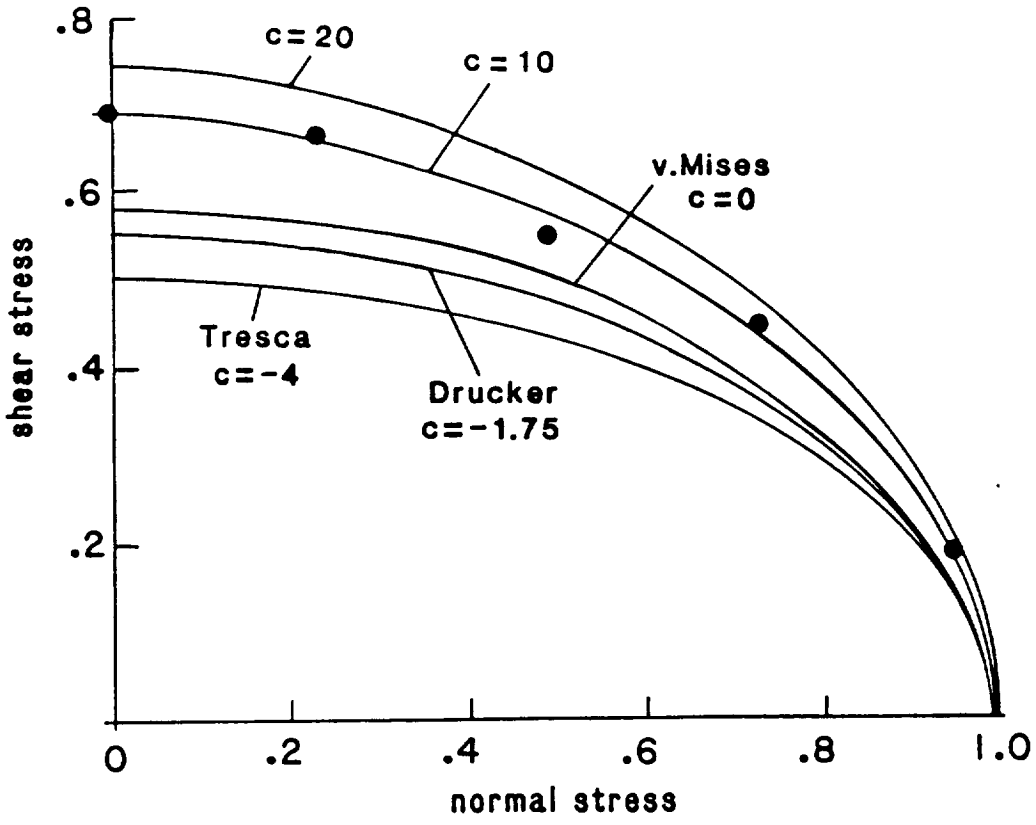

Figure 1 Plots of F=constant in normalized normal/shear stress plane for several values of C.

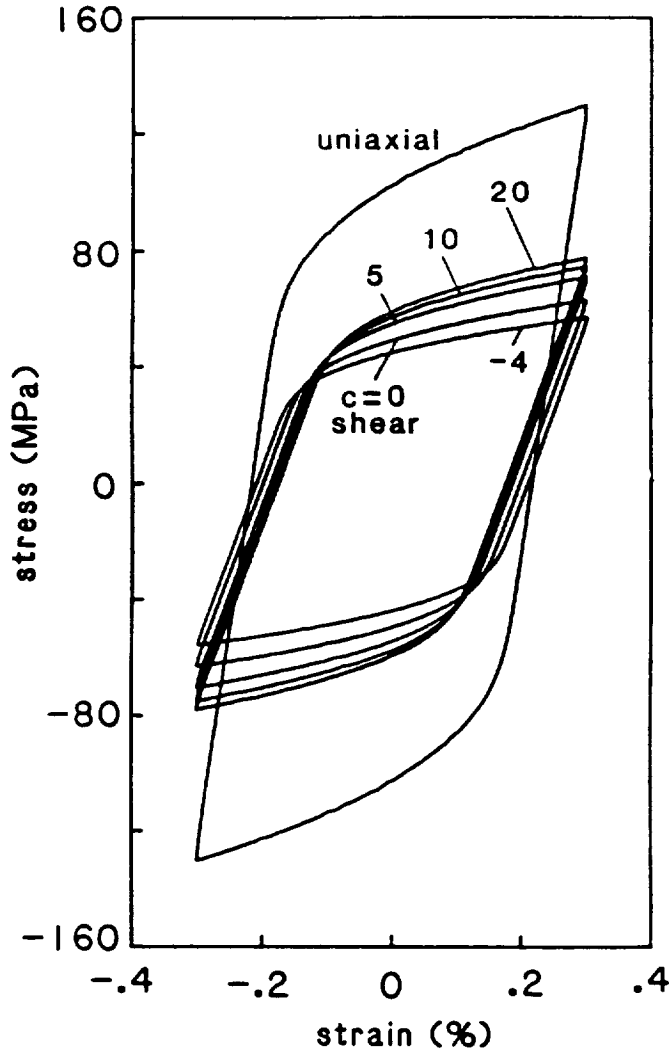

Figure 2 Saturated hysteresis loops for $\Delta\varepsilon$=0.6% and $\dot{\varepsilon}$=.001/m. Shown is uniaxial response and shear responses for several values of C.

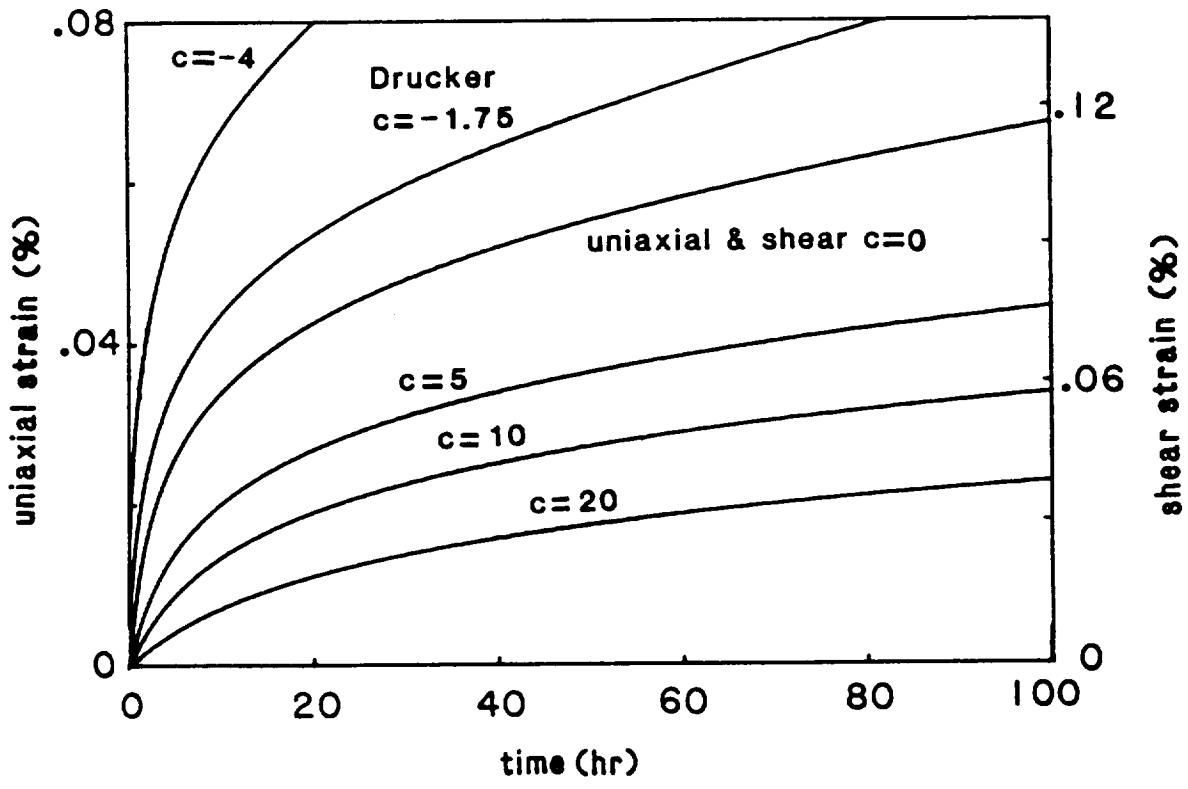

Figure 3 Creep response in uniaxial tension and shear for several values of C.

THERMOMECHANICAL CHARACTERIZATION OF HASTELLOY-X UNDER UNIAXIAL CYCLIC LOADING

J.R. Ellis*, P.A. Bartolotta, G.P. Allen, and D.N. Robinson*
NASA Lewis Research Center
Cleveland, Ohio

INTRODUCTION

In most high-temperature engineering applications, components are subjected to complex combinations of thermal and mechanical loading during service. A number of viscoplastic constitutive models have been proposed which potentially can provide mathematical descriptions of material response under such conditions (refs. 1 to 9). Implementation of these models into large finite element codes such as MARC has already resulted in much improved inelastic analysis capability for hot-section aircraft engine components.

However, a number of questions remain regarding the validity of methods adopted in characterizing these constitutive models for particular high-temperature materials. One area of concern is that the majority of experimental data available for this purpose are determined under isothermal conditions. This is in contrast to service conditions which, as noted above, almost always involve some form of thermal cycling. The obvious question arises as to whether a constitutive model characterized using an isothermal data base can adequately predict material response under thermomechanical conditions.

An experimental program was initiated within the HOST program at the NASA Lewis Research Center to address this particular concern (ref. 10). This paper describes the results of the most recent isothermal and thermomechanical experiments.

EXPERIMENTAL DETAILS

The equipment and procedures used in the isothermal experiments have been described in detail previously (ref. 11). These experiments were conducted under uniaxial loading on closed-loop, electrohydraulic test systems. The specimens tested had a 1.25-in. parallel working section with a 0.313-in. outside diameter. Strains were measured over a 1.0-in. gage length using an axial extensometer. The specimens were heated using an RF induction heater and considerable effort was expended in achieving uniform temperature profiles over the gage length. Usually, temperatures fell within ±5 °C of the nominal test temperature throughout the experiments.

The method of test system control and data acquisition is shown schematically in figure 1. Axial strain is programmed to follow a triangular waveform provided by a Wavetek 175 function generator. The corresponding stress-time response is monitored using strip chart recorders until fatigue failure occurs. In addition,

*The University of Akron.

stress-strain hysteresis loops are recorded automatically at predetermined intervals using a Bascom-Turner recording system.

In the thermomechanical experiments, specimens were again heated using an RF induction heater. Specimen cooling was by means of the test system's water cooled grips. This was the preferred approach as it allowed temperature profiles to be maintained within acceptable limits during the cooling process. Also to assist in this regard, the gage length over which strain measurements were made was reduced to 0.5 in. in these experiments. The net result was that temperatures in the specimen's gage length were within $\pm 10°$ C of programmed values during temperature cycling.

Another difference between the two sets of experiments is that a Data General S-20 computer was used for control purposes in the thermomechanical experiments. As indicated in figure 2, both axial strain and temperature were programmed to follow triangular wave forms, these waveforms being 180° out-of-phase in the subject experiments. As in the case of the earlier experiments, stress-time response was monitored until fatigue failure occurred. It is important to note that the same type of specimen, loading system, and heating system were used in the two series of experiments.

The material under investigation was Hastelloy-X in solution annealed condition. Two heats of material were obtained in 0.75-in. o.d. bar form meeting the requirements of Aerospace Material Specification (AMS) 5754H. As there was some question regarding the as-received condition of heat 1 material, specimens manufactured from this material were reannealed after fabrication and then micropolished to a surface finish of 8 rms. In the case of heat 2 material, reannealing and micropolishing was judged unnecessary. The as-machined surface finish of these specimens was 16 rms.

EXPERIMENTAL RESULTS

The results obtained in the isothermal experiments are shown in figures 3 to 6 as plots of stress range versus cycles. A logarithmic scale was selected for cycles as it allows the early stages of hardening, that occurring over the first 100 cycles, to be presented in a straightforward manner.

Another technique adopted to aid interpretation of the isothermal data was that of hardening curves determined at low, intermediate, and high temperatures were plotted separately. As indicated in figures 3 to 6, a single strain range, 0.6%, was used to generate the data presented here. Also as indicated, experiments conducted on Heat 1 material investigated a strain rate of 0.001 sec^{-1} while those conducted on Heat 2 material investigated strain rates of 0.001 and 0.0001 sec^{-1}.

In these exploratory experiments, no systematic attempt was made to investigate the repeatability of the data. However, in the experiments conducted at the slower strain rate, difficulties were encountered which meant that up to three attempts were necessary on occasion to successfully complete an experiment. The results of such repeat experiments are shown in figure 6 as they provide an indication as to the reproducability of the isothermal data.

The results of six out-of-phase thermomechanical experiments are shown in figure 7. The method of data presentation is identical to that described above for the isothermal data. Clearly in this case, however, the cyclic hardening curves apply

for temperature ranges rather than individual temperatures. Finally, thermomechanical and isothermal data determined at temperature in the range 400 to 600 °C (752 to 1112 °F) are compared in figure 8. These data were selected as they serve to highlight the differences in hardening behavior resulting from the two types of cyclic loading.

DISCUSSION

As a first step, the three sets of isothermal data were analyzed to establish general trends in the cyclic hardening behavior of Hastelloy-X. It was determined that individual hardening curves exhibit three types of hardening which will be termed early, transitional, and final in the following discussion.

In all three data sets, early hardening behavior, that occurring between cycles 10^0 and 10^2, is fairly systematic and repeatable. Over this cyclic range, hardening appears to be approximately linear in the plots shown in figures 3 to 5. The amount of hardening increases with temperature until reaching a maximum at 1200 °F (649 °C). At this temperature, the increase in stress range over the first hundred cycles is about double that occurring at the lower temperatures. As temperature is increased further, the amount of hardening decreases until at 1600 °F (871 °C) behavior is cyclically neutral. At still higher temperatures, the material exhibits small amounts of cyclic softening.

Material response during the transitional hardening stage is complex and almost certainly reflects aging processes occurring in the material during the experiments. In the case of heat 1 material, transitional hardening was evidenced between 10^2 and 10^3 cycles. In the tests conducted on heat 2 material, transitional behavior occurred over both earlier and later cyclic ranges. Up to 900 °F (482 °C), the slope of the hardening curves increase on the plots shown in figures 3, 4, and 5. At temperatures in the range 1000 to 1200 °F (538 to 649 °C), the hardening curves exhibit inflection points while at still higher temperature, the slopes of the hardening curves decrease.

Material response during the final stage of hardening is again more straightforward and is about linear on the semilogarithmic plots under discussion. Up to 1000 °F (538 °C), significant hardening is exhibited up to the point of fatigue failure. Between 1000 and 1200 °F (538 and 649 °C), hardening rates are drastically reduced which can result in the intersection of individual hardening curves. At higher temperatures, final hardening rates reduce until at 1600 °F (871 °C), behavior is essentially neutral.

It has already been noted that the cyclic hardening behavior of Hastelloy-X is complicated by thermal aging occurring during the experiments. This raises the possibility that some of the more subtle effects noted above might be sensitive to variations in the chemical composition of the material. Some feel for possible heat-to-heat variability can be obtained by comparing the heat 1 results shown in figure 3 with those for heat 2 shown in figure 4. Such comparisons show that the strain ranges achieved on the first cycle of the heat 1 experimental are less by about 100 MPa than those obtained in the heat 2 experiments. However, comparison of the two sets of curves shows that the general hardening characteristics of the two materials are very similar. The general trends of the data do not therefore appear sensitive to variability in material composition.

Questions also arise as to the role of strain rate in these isothermal experiments. Comparison of the data shown in figures 4 and 5 shows that cyclic hardening behavior at the two strain rates investigated is very similar up to 1300 °F (704 °C). Over this range, the rates of hardening in tests conducted at 0.0001 sec^{-1} are marginally higher than those obtained on tests conducted at 0.001 sec^{-1}. At higher temperatures, the most significant difference is that the stress range achieved on the first cycle of tests conducted at the slow rate are much reduced from those obtained at 0.001 sec^{-1}. Regardless of these first cycle differences, material response is essentially neutral at both strain rates for temperatures of 1600 °F (817 °C) and above.

One characteristic of the data which is of key concern to the experimentalist is that of repeatability. This is particularly the case when particular combinations of variables are characterized by single experiments only. The data shown in figure 6 provides some insight as to repeatability at least during the early and transitional stages of hardening. The most significant difference between repeated experiments is in first cycle response. Subsequently, the hardening behavior is very similar in the repeat experiments. At particular numbers of cycles into the test, stress ranges fell within about ±25 MPa of the mean. This is equivalent to percentage deviations of the order of ±5% for stress ranges around 500 MPa.

Having established a fair degree of confidence in the validity of the isothermal data base, the final and most important question addressed was what if any of the trends noted above carry over to thermomechanical conditions. As noted earlier, this is a major concern since service conditions usually involve thermomechanical loadings whereas the data usually available for material characterization is determined in isothermal experiments. A partial answer to this question can be obtained by comparing data shown in figures 5 and 7. At temperatures up to 900 °F (482 °C), the early hardening rates in the thermomechanical experiments can be seen to be about twice those obtained in isothermal experiments conducted over the same range of temperatures. The situation in the thermomechanical test conducted over the temperature range 400 to 600 °C (752 to 1112 °F) is somewhat different, as indicated in figure 8. Here, the early hardening behavior is similar for the two types of loading but the transitional and final stages differ significantly. Specifically, the hardening in the thermomechanical test is about three times that of the isothermal experiments. Clearly, the thermomechanical result could not have been predicted given the isothermal data shown. At temperatures above 1300 °F (704 °C), the isothermal and thermomechanicl results are similar. Thus, at these temperatures, the feasibility of predicting the thermomechanical results from an isothermal data base appears more practicable.

CONCLUSIONS

The following conclusions were drawn from the study of cyclic hardening in Hastelloy X under isothermal and thermomechanical conditions.

1. Cyclic hardening under isothermal conditions ranges from modest hardening, to drastic hardening, to modest softening as temperature increased. This highlights the importance of covering the entire temperature range of interest in characterization studies.

2. Cyclic hardening under isothermal conditions is extremely complex at temperatures in the range 1000 to 1200 °F (538 to 649 °C). At both higher and lower temperatures, behavior is less complex and it appears likely that the data can be modeled using fairly simple mathematical representations.

3. Cyclic hardening under isothermal conditions is not particularly sensitive to heat-to-heat variations and to strain rate effects, at least over the range 0.001 to 0.0001 sec^{-1}. Also, in terms of general hardening characteristics, the data are fairly repeatable.

4. Cyclic hardening under thermomechanical conditions differs significantly from that obtained in isothermal tests up to temperatures of about 600 °C (1112 °F). The hardening rates in the thermomechanical tests are factors of 2 and above greater than those obtained in isothermal experiments.

5. Cyclic response at temperatures above 600 °C (111 °F) is similar under both isothermal and thermomechanicl loading. In the limit, both types of loading exhibit behavior that is essentially cyclically neutral. Clearly under these conditions, an isothermal data base can be used more reasonably to model thermomechanical response.

FUTURE WORK

The emphasis of future testing will be in generating a more complete thermomechanical data base for Hastelloy X. Presently, experiments are being conducted under uniaxial loading over temperature ranges of 400 °C and this will be extended in later experiments to 800 °C. Also, it is planned to extend the investigation to the torsional form of loading. The advantage here is that apparent strains due to thermal expansion are second order effects in torsional strain measurements and so do not complicate interpretation of the data.

One deficiency of the data discussed in this paper is that it is presented entirely in the form of stress range versus cycles. Adopting this simplistic approach, no consideration is given to the inelastic material response which is occurring at various stages of individual cycles. This situation is being corrected by the use of more efficient data acquisition systems. Procedures are being developed which will allow the data to be reduced in a form more consistent with theoretical developments.

REFERENCES

1. Perzyna, P.: The Constitutive Equations for Rate Sensitive Plastic Materials. Quarterly of Applied Mathematics, vol. 20, 1963, pp. 321-332.

2. Bodner, S. R. and Partom, Y.: Constitutive Equations for Elastic-Viscoplastic Strain-Hardening Materials. Journal of Applied Mechanics, vol. 42, 1975, pp. 385-389.

3. Miller, A.: An Inelastic Constitutive Model for Monotonic, Cyclic, and Creep Deformation: Part 1 - Equations Development and Analytical Procedures. Journal of Engineering Materials and Technology, vol. 98, pp. 97-105.

4. Miller, A.: An Inelastic Constitutive Model for Monotonic, Cyclic, and Creep Deformation: Part II - Application to Type 304 Stainless Steel. Journal of Engineering Materials and Technology, vol. 98, pp. 106-112.

5. Hart, E. W.: Constitutive Relations for the Nonelastic Deformation of Metals. Journal of Engineering Materials and Technology, vol. 98, 1976, pp. 193-202.

6. Chaboche, J. L.: Viscoplastic Constitutive Equations for the Description of Cyclic and Anisotropic Behavior of Metals. Bulletin de l'Adacemie Polonaise des Sciences, vol. 25, no. 1, 1977, pp. 33-42.

7. Krieg, R. D., Swearengen, J. C., and Rhode, R. W.: A Physically-Based Internal Variable Model for Rate-Depednent Plasticity. Inelastic Behavior of Pressure Vessel and Piping Components, ASME/PVP-PB-028, 1978, pp. 15-28.

8. Robinson, D. N.: A Unified Creep-Plasticity Model for Structural Metals at High Temperature. Oak Ridge National Laboratory Report, ORNL/TM-5969, October 1978.

9. Walker, K. P.: Research and Development Program for Nonlinear Structural Modeling with Advanced Time-Temperature Dependent Constitutive Relationships - Final Report. NASA CR 165533 (Pratt & Whitney Research Center), November 1981.

10. Robinson, D. N. and Bartolotta, P. A.: Viscoplastic Constitutive Relationships with Dependence on Thermomechanical History. NASA CR-174836, (University of Akron), March 1985.

11. Bartolotta, P. A.: Thermomechanical Cyclic Hardening Behavior of Hastelloy-X. NASA CR-174999 (University of Akron), November 1985.

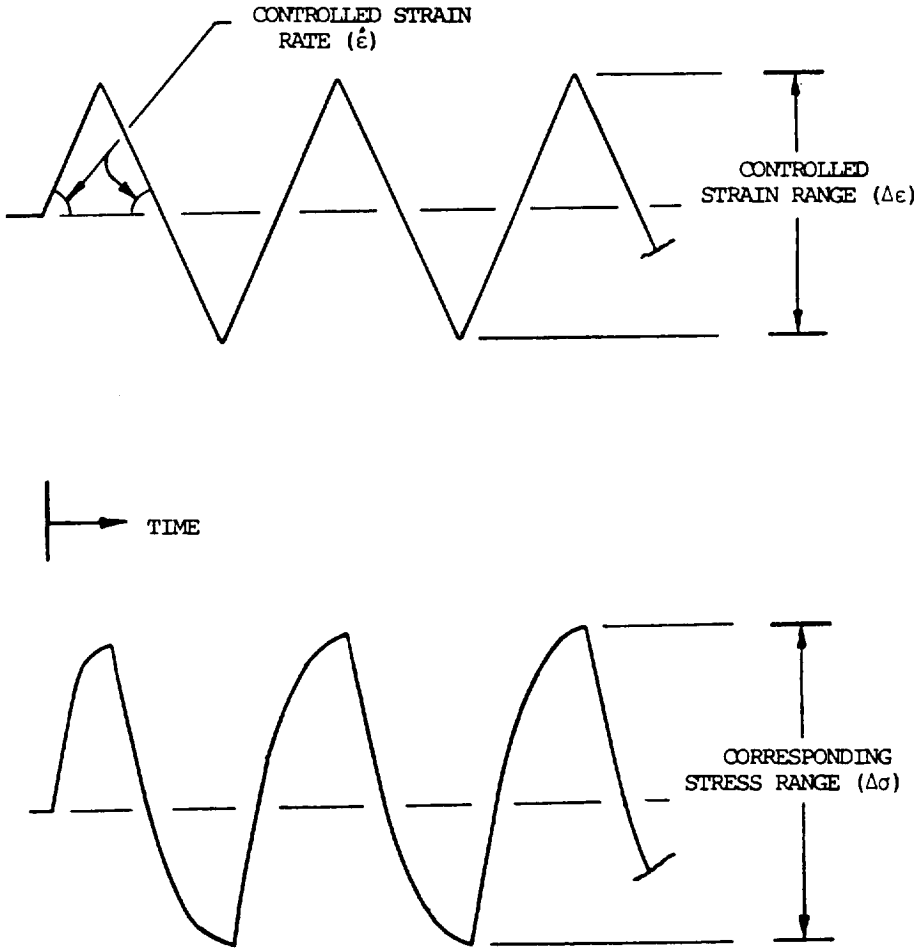

FIGURE (1) METHOD OF TEST SYSTEM CONTROL AND DATA ACQUISITION IN ISOTHERMAL EXPERIMENTS .

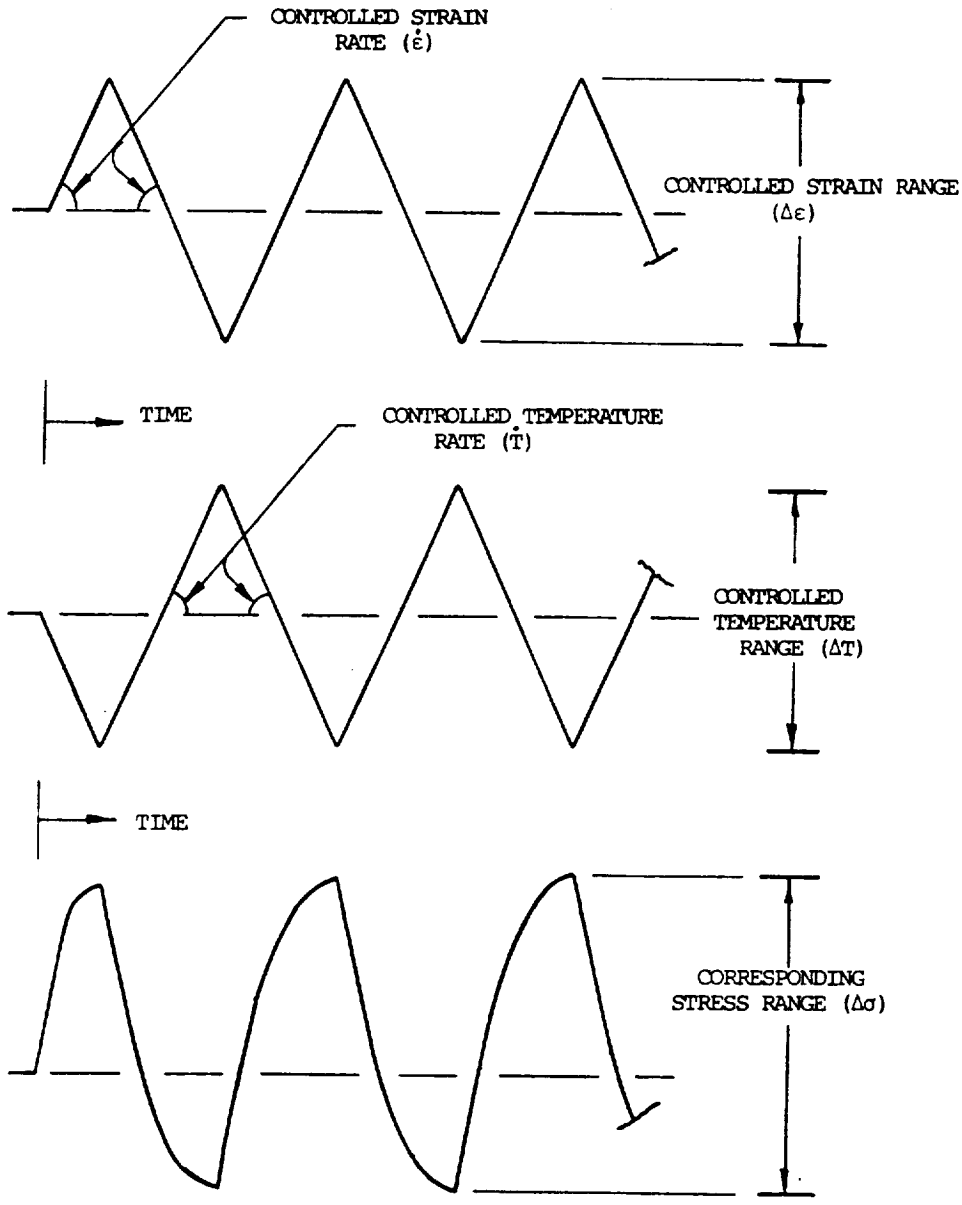

FIGURE (2) METHOD OF TEST SYSTEM CONTROL AND DATA ACQUISITION IN OUT-OF-PHASE THERMOMECHANICAL EXPERIMENTS.

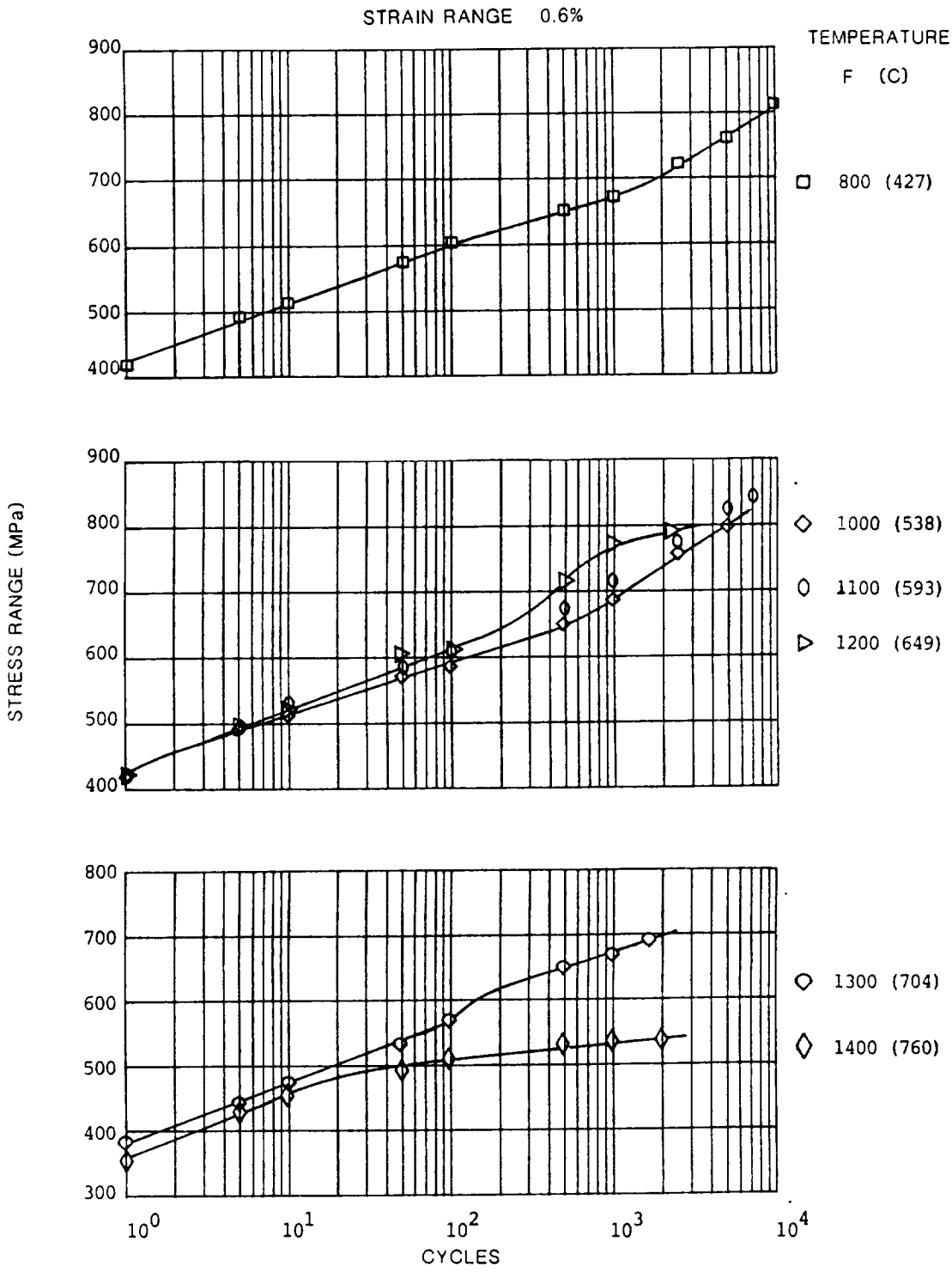

FIGURE (3) RESULTS OF ISOTHERMAL TESTS CONDUCTED ON HEAT (1) MATERIAL AT A STRAIN RATE OF 0.001/sec.

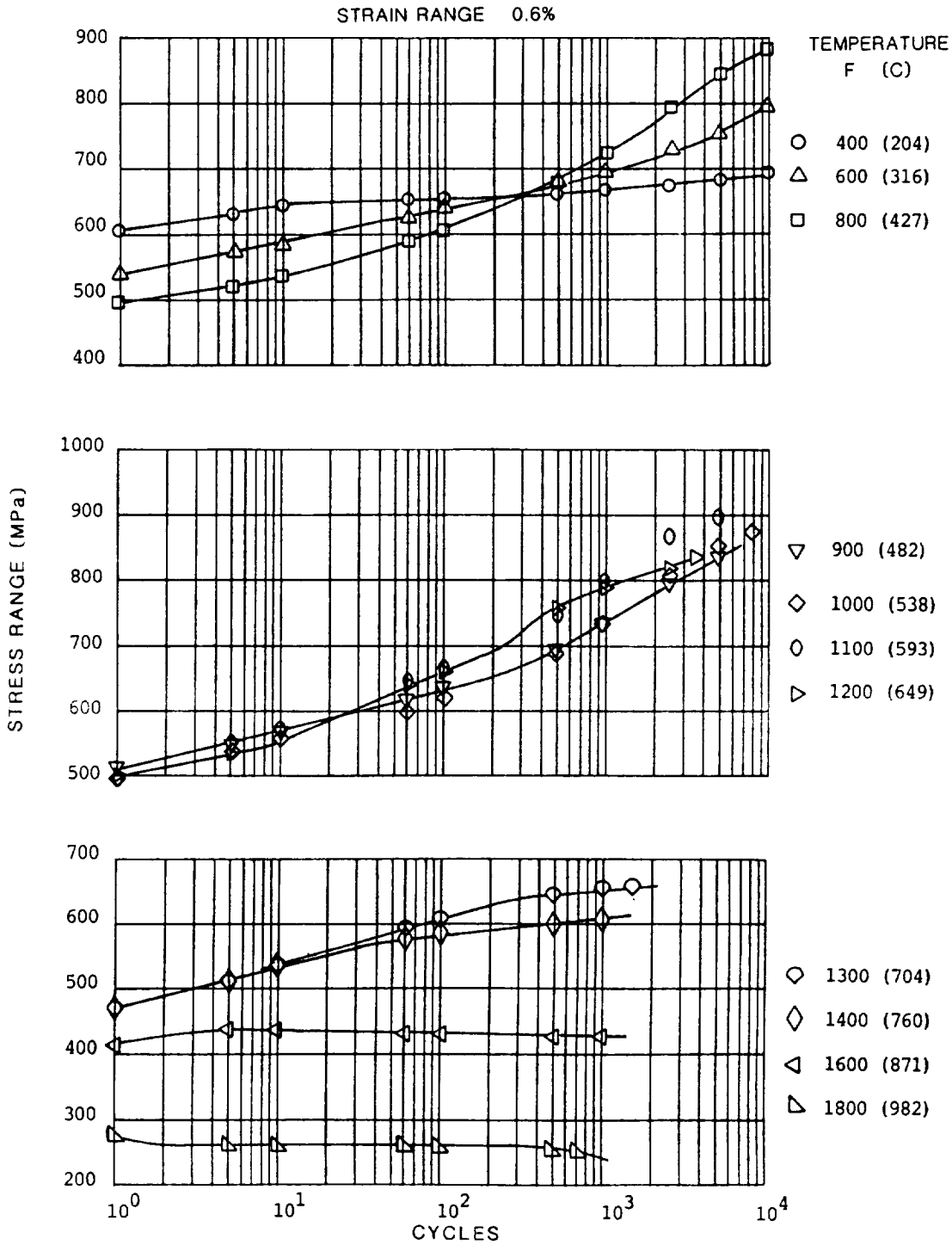

FIGURE (4) RESULTS OF ISOTHERMAL TESTS CONDUCTED ON HEAT (2) MATERIAL AT A STRAIN RATE OF 0.001/sec.

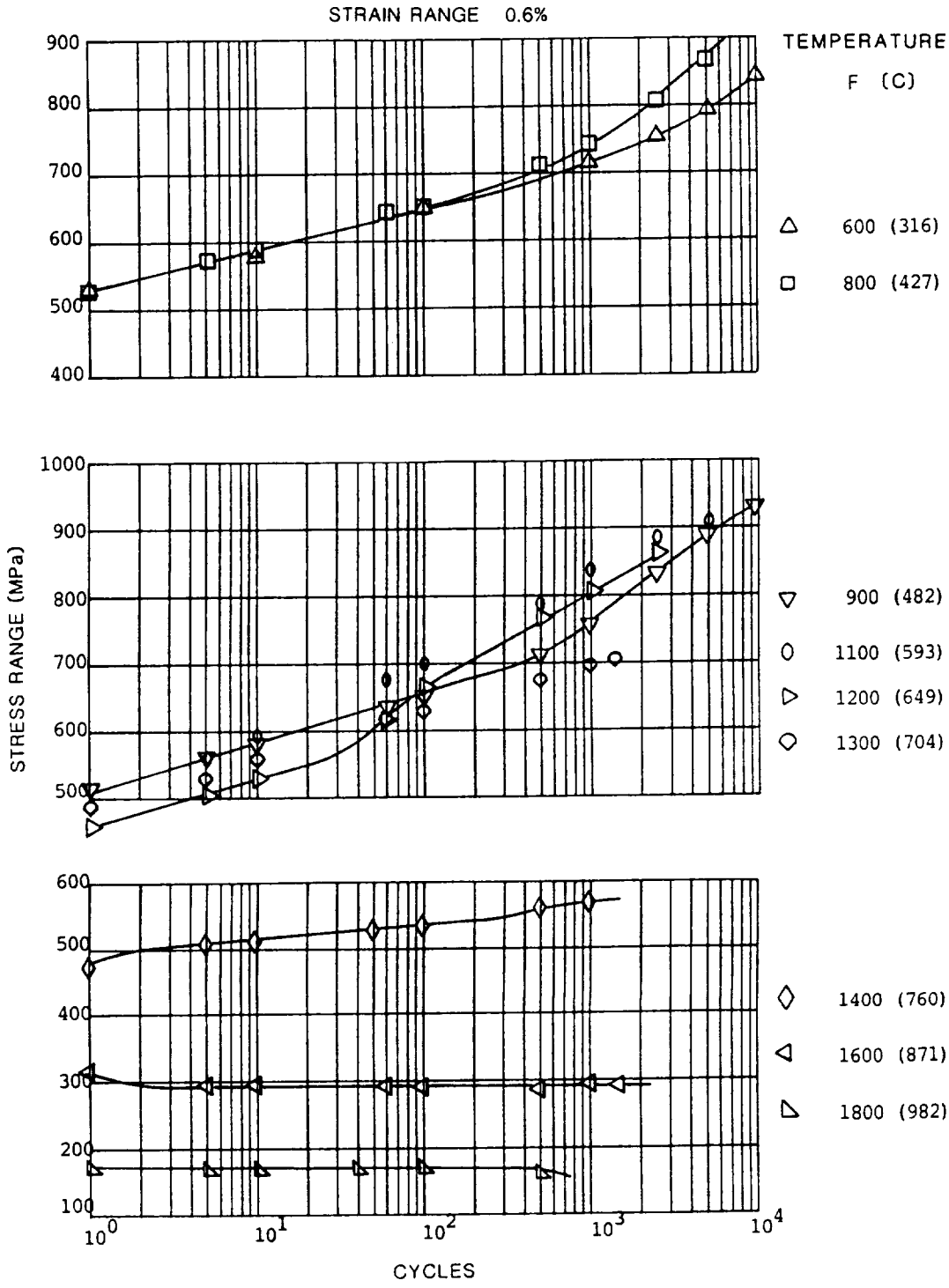

FIGURE (5) RESULTS OF ISOTHERMAL TESTS CONDUCTED ON HEAT (2) MATERIAL AT A STRAIN RATE OF 0.0001/sec.

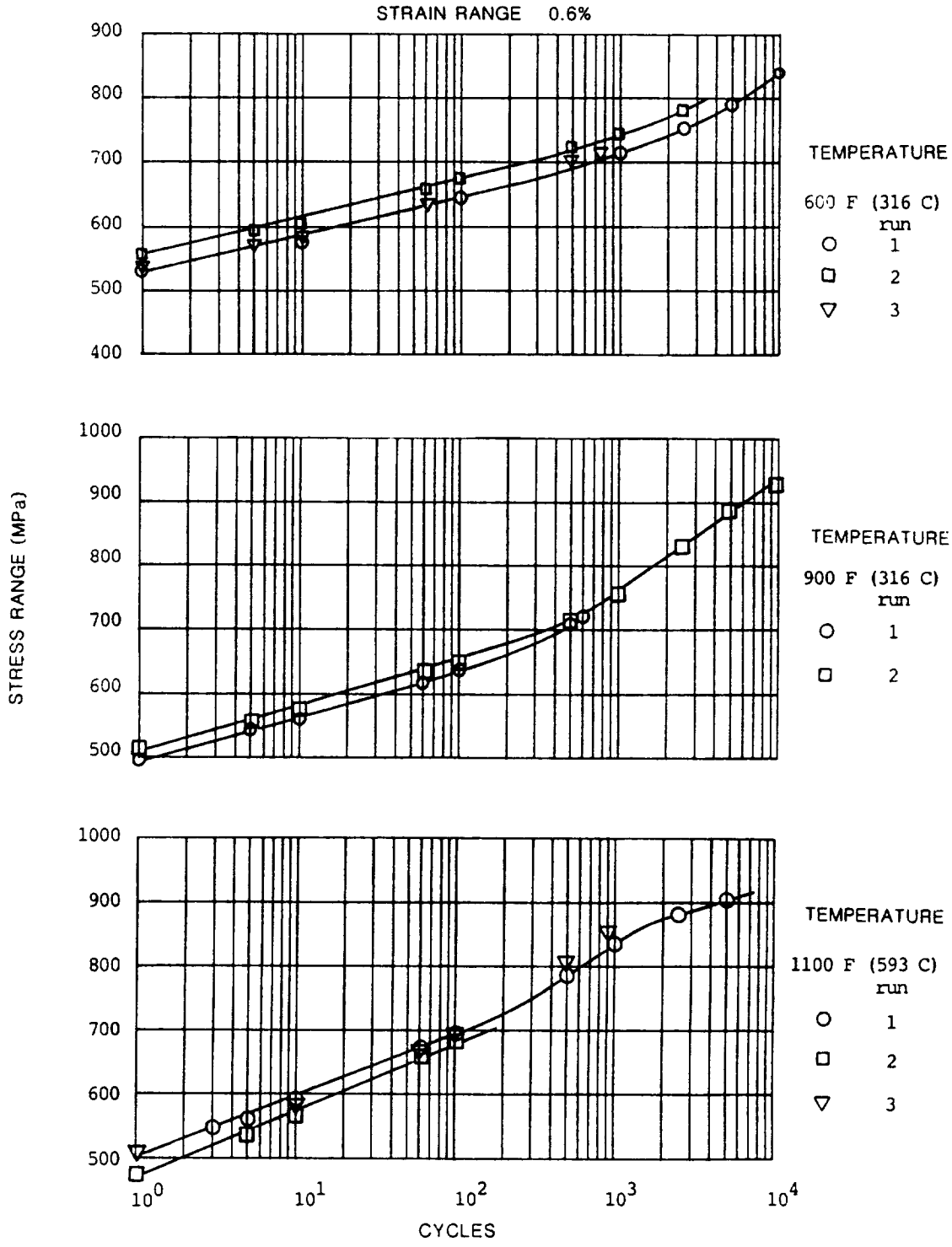

FIGURE (6) RESULTS OF REPEAT EXPERIMENTS CONDUCTED ON HEAT (2) MATERIAL AT A STRAIN RATE OF 0.0001/sec.

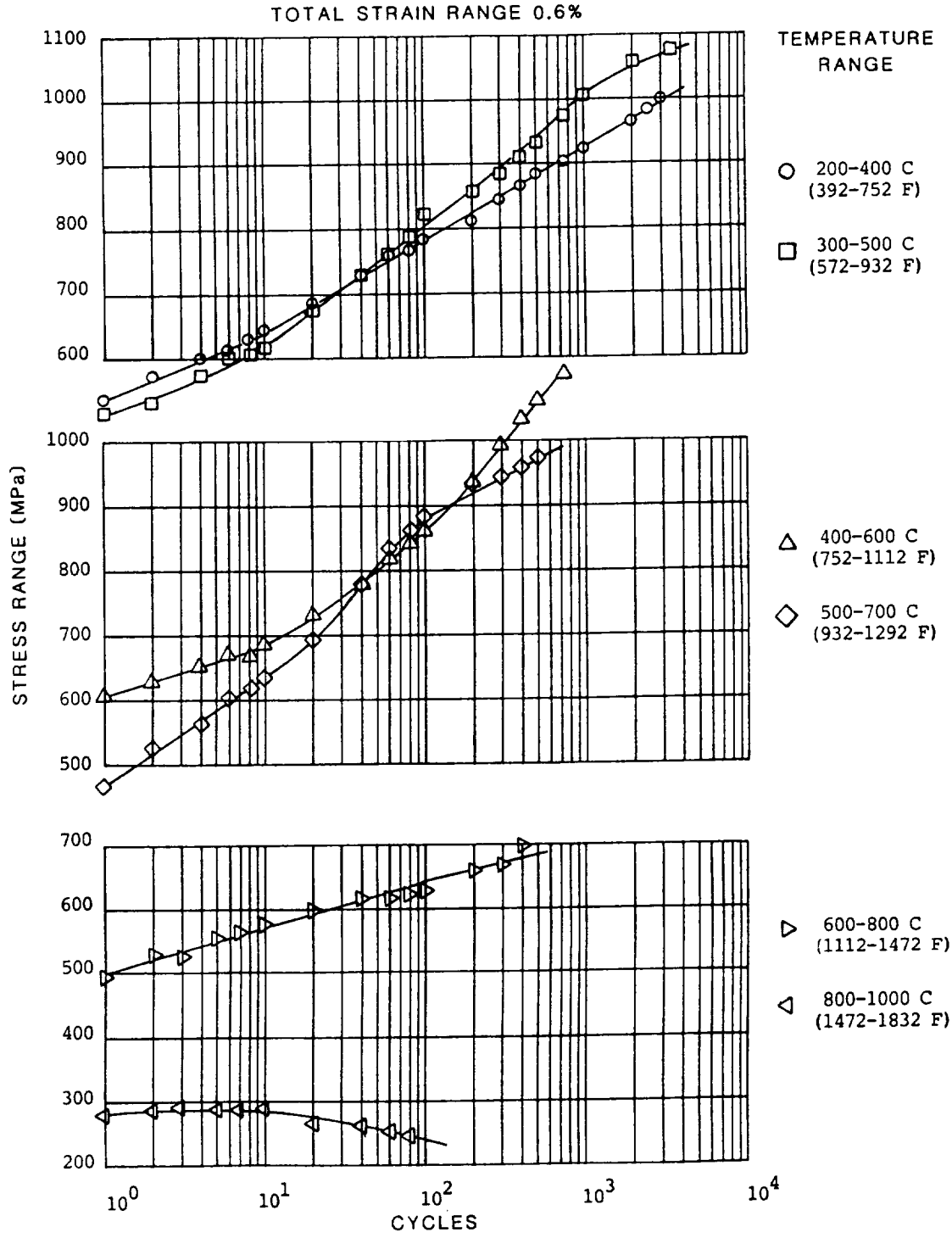

FIGURE (7) RESULTS OF OUT-OF-PHASE THERMOMECHANICAL TESTS CONDUCTED ON HEAT (2) MATERIAL AT A STRAIN RATE OF 0.00005/sec.

DETERMINATION OF SURFACES OF CONSTANT INELASTIC STRAIN RATE AT ELEVATED TEMPERATURE*

R. L. Battiste
S. J. Ball

Oak Ridge National Laboratory
Oak Ridge, Tennessee 37831

ABSTRACT

An experimental effort to perform special exploratory multiaxial deformation tests on tubular specimens of type 316 stainless steel at 650°C (1200°F) is described. One test specimen was subjected to a time-independent torsional shear strain test history, and surfaces of constant inelastic strain rate (SCISRs) in an axial/torsional stress space were measured at various predetermined points during the test. A second specimen was subjected to a 14-week time-dependent (creep-recovery-creep periods) torsional shear stress histogram SCISRs determinations made at 17 points during the test. The tests were conducted in a high-temperature, computer-controlled axial/torsional test facility using an Oak Ridge National Laboratory developed high-temperature multiaxial extensometer. The effort was successful, and for the first time the existence of surfaces of constant inelastic strain rate was experimentally demonstrated.

1. INTRODUCTION

In classical plasticity the concept of yield surfaces in multiaxial stress space plays a central role, not only in the definition of initial yielding but in determining subsequent plastic flow. At high temperatures the deformation behavior of structural alloys is strongly time dependent. Consequently, the significance of yield surfaces breaks down, and it has been proposed that in their place the concept of surfaces of constant inelastic strain rate might be utilized. Such surfaces, called SCISRs, can be shown to have a potential nature and thus constitute the basis of a rational multiaxial viscoplastic constitutive theory. To further pursue such a concept, exploratory multiaxial test results are required.

---

*Research sponsored by NASA-Lewis Research Center through Interagency Agreement No. 40-1447-84 with the U.S. Department of Energy and DOE's contract DE-AC05-84OR21400 with Martin Marietta Energy Systems, Inc.

The objective of this effort was to provide supporting data, in the form of surfaces of constant inelastic strain rate, for NASA's efforts to formulate constitutive theories.

A surface of constant inelastic strain rate (SCISR) is determined by loading the specimen at a constant effective stress rate in the two-dimensional axial/torsional stress state in various directions until a predetermined inelastic effective strain rate is reached. After each probe, the stress is returned to the initial starting point; thus a locus of points (surface or constant inelastic strain rate) is established.

Oak Ridge National Laboratory (ORNL) undertook the effort because of its experience in constitutive equation development and high-temperature testing and because of its existing multiaxial test facilities, including computer-controlled axial/torsional test machines and high-precision, high-temperature, multiaxial extensometers. This paper presents the experimental results of two SCISRs test series at 650°C (1200°F) on 316 stainless steel. One test investigated the effects of prior plastic "time-independent" deformations on subsequent SCISRs, while the second test investigated effects of prior creep "time-dependent" deformation.

The remainder of this paper is divided into four major sections. In the first, the multiaxial test facility and test specimen are briefly described. The software computer control programs are briefly described in the second section, while the third section contains a discussion of the test procedures, conditions, and data results. Finally, conclusions are stated in the last section.

2. TEST FACILITY AND SPECIMEN

The multiaxial test facility is a high-temperature facility designed to subject a tubular specimen to simultaneous axial and torsional loads as prescribed by a computer control system, function generator, or under manual control. The principal components of the multiaxial test facility (see Fig. 1) are an axial-torsional material testing system, a radio frequency induction heating system, a computer-based data acquisition and control system, a special ORNL-developed axial-torsional extensometer, and support equipment (plotters, filters, indicator, etc.).

The MTS model 810 material test system consists of an axial-torsional load frame, actuators, load cell, electronic control system, and hydraulic

power supply. The load frame and actuators are rated for maximum loads of 222 kN (50 kips) and 2.8 N-m (25,000 in.-lb). An MTS load cell with reduced rated maximum load capacity, 111 kN (25 kips) and 1.4 N-m (12,500 in.-lb), is used for greater accuracy and resolution. The control system is based on the standard MTS model 442 controllers which provide closed-loop servo-hydraulic control with a selectable feedback; load, strain, or stroke. The system includes a cycle counter, a function generator, a phase shifter, and several X-Y flatbed plotters. The controllers and load cell were calibrated using a secondary standard (traceable to National Bureau of Standards) to four selectable maximum loads for each channel, axial and torsional. These maximum loads were 89, 44, 22, and 9 kN (20, 10, 5, and 2 kips) axially and 1130, 565, 128, and 57 N-m (10,000, 5000, 2000, and 500 in.-lb) torsionally. The hydraulic power supply is a constant volume 0.19 L/S (3 GPM) MTS model 502.03 system.

A 5 kW Lepel model T-5-3-KC-BW high frequency generator heats the specimen. The generator is closed-loop controlled with a Babber-Colman model 520 temperature controller and an intrinsic Chromel-Alumel thermocouple mounted on the outside surface of the specimen in the center of the gage length. A water-cooled copper load coil is mounted around the specimen.

The major features of the computerized control and data acquisition system are shown in Fig. 2. Control voltage signals are sent to the integrators via the digital-to-analog (D/A) converters, where fixed input voltages to the integrators give ramp-function set-point outputs to the MTS system. Run, reset, and panic switches are provided. The axial and torsional strain signals from the MTS are first conditioned (low-pass filtered) and then sampled by analog-to-digital (A/D) converters, which have an integrating feature to reject 60 Hz noise. The two set-point signals are also sampled by A/D converters.

The computer utilizes an expanded version of the DEC FOCAL language, a high-level interpreter language similar in structure to BASIC. The control program as written for the present system is stored on three disk files, which are swapped in and out of the core as required to execute the various types of programs. The execution speed of the FOCAL program and the operations of the A/Ds and D/As and other peripherals are such that the required

computations can be accomplished for 1-s data sampling intervals. Extensive software programs developed to execute the SCISRs testing effort will be described in a later section of this paper.

An axial-torsional mechanical extensometer suitable for fatigue testing tubes at high temperature was developed several years ago at ORNL.[1,2] For the SCISRs tests, this original device was modified to provide greater accuracy, better resolution, minimal backlash, and minimal noise characteristics in a radio frequency environment. The extensometer in its present form is shown positioned on a test specimen in Fig. 3. The instrument's two quartz probes are located in indentations spaced 25.4 mm (1 in.) apart on the specimen. The differential axial displacement and differential rotation between the indentations are translated to proximity transducers through a system of Gimbal rings and swivels using flexural pivots for bearings. The flexural pivots eliminate backlash and reduce the friction to a constant small value. The HITEC Proximic proximity transducers are noncontacting, and their output using HITEC model 3200 signal conditioning units is a high-level signal, 0 to 10 DC volts for full-scale movement of 0.000 to 1.02 mm (0.000 to 0.040 in.). The electrical sum of two transducers gives a measure of axial strain while the difference of two transducers measures the torsional (one-half the engineering shear strain, γ) strain. Two additional ORNL-developed amplifier and filter modules are used to apply appropriate scaling factors to give a direct measure of axial and tensorial shear strain. The filter network is a three-pole low-pass Bessel filter with selectable time constants for reducing the inherent transducer noise and radio frequency induced noise.

These tests were conducted on tubular specimens fabricated from 51-mm (2-in.) bar stock of 316 stainless steel, ORNL reference heat 8092297. The specimens had a nominal 34.8-mm (1.37-in.) working section with a 26.04-mm (1.025-in.) outside diameter and a 1.91-mm (0.075-in.) wall thickness, as shown in Fig. 4. The specimens were solution annealed by heating to 1065°C (1950°F), holding for 30 minutes, and then forced-argon rapid cooled to minimize residual stresses. The heat treatment process was performed in an ert atmosphere of argon gas which produced no visible oxidation.

A room-temperature SCISR test was performed using the facility and procedures described in this paper to access the high-temperature extensometer system. A specimen was installed and aligned in the facility. The

axial and torsional extensometer outputs were adjusted to the equivalent strain readings of full bridge foil gage systems for both axial and torsional elastic load changes. The two crosstalk parameters between the extensometer channels were adjusted for their minimum values of ±3 με axial strain for approximately ±200 με tensorial shear strain and ±3 με tensorial shear strain for approximately ±300 με axial strain. Crosstalk strain-vs-strain loops averaged 3 to 5 με hysteresis at zero load or strain. The torsional stress-strain histogram shown in Fig. 5 was executed on the virgin specimen, and SCISRs were determined at the four indicated points. Only a description of the extensometer performance during this test will be presented since high-temperature test results are of most interest here. Analog load-strain plots of the extensometer outputs and the full bridge foil gage outputs were nearly identical for all probes and preloads. For example, during the preload from point 2 to 3, the torsional foil gage bridge read a change in strain of 0.8965% while the extensometer read a change of 0.8380%, for approximately a 6% difference. This is good agreement since the bridge was composed of 3.8-mm (0.125-in.) foil gages in a bending compensating configuration while the extensometer was essentially a quarter bridge 25.4-mm (1-in.) noncompensating device. Also, during the same preload, the axial foil bridge read a change of +27 με while the axial extensometer channel read a change of +63 με, thus verifying good torsional-to-axial crosstalk characteristics.

3. DESCRIPTION OF TEST CONTROL PROGRAM

The computer exercises control over the axial and torsional stress set point voltage inputs sent to the MTS system. Typically, a probe will begin at a point near the center of the surface of constant inelastic strain rate and proceed slowly outward at a prespecified rate and angle in the axial-torsional stress plane. The elastic strain rate is measured and used as a reference against which subsequent measurements are compared to determine the inelastic strain rate (ISR). When the measured (total) strain rate exceeds the elastic rate plus a specified ISR value (100 με/min for the tests described here), the stress and strain values at that point are recorded, and the set points are driven back to the starting point.

When the program is executed, the operator is first asked to supply scale factor information for the stress and strain signals, the values of

estimated elastic stress-to-strain ratios, the desired load rate (typically 10 ksi/min) and ISR (100 με/min), and (optionally) preload target information for up to two preload sequences to be run before the SCISR test.

After the set point ramps begin, the two strain signals are sampled once per second for eight seconds to determine, by a least-squares fit procedure, the individual strain rate values. From that point on, once every second the stress and strain signals are sampled, and a new measured effective strain rate, using RMS weighting of the axial and torsional rates, is calculated every 3 s. This process continues until the ISR exceeds the limit (typically 100 με/min).

When the limit is reached, the set point integrators' input voltages are set to zero (stopping the ramps), and the end point values of stresses, strains, and strain deviations are recorded. The stress set point trajectory is reversed (180°) immediately to minimize creep at the surface; then, after the set points reach their initial values, the program begins again at the next preprogrammed angle, etc., until all 16 probes are completed. All pertinent data from the runs are stored on hard disk (and later saved on mag tape) for further analysis.

3. TEST PROCEDURES, CONDITIONS, AND DATA RESULTS

Each specimen tested was instrumented with four rectangular strain gage rosettes prior to installation in the MTS axial-torsional test system. These gages were used for alignment purposes to ensure correct application of the loads. After alignment, the gages were calibrated in a full-bridge arrangement, which compensated for bending, to read axial and tensorial shear strain in order to check out and calibrate the high-temperature extensometer. Ten intrinsic Chromel-Alumel thermocouples were used to measure the temperature profile; six of these were mounted on the outside surface of the central 25.4-mm (1-in.) specimen gage length while four were attached to the 28.58-mm (1.125-in.) outside diameter shoulder. The induction heater load coil was adjusted to obtain a uniform temperature profile over the specimen gage length at 650°C (1200°F). Final calibration at 650°C of the extensometer in the elastic range was performed by adjusting its output to the calculated strain values using the **Nuclear Systems Materials Handbook**[3]

material property values for 316 stainless steel and the room-temperature measured strain values. These gage factor changes varied with the largest being approximately 5% and the smallest less than 1%.

Each of the two high-temperature tests was conducted using the above described control system and SCISR program with the MTS testing machine under load control. The target inelastic effective strain rate was 100 με/min) and the probe loading rate was 0.069 MPa/min (10 ksi/min) for both tests. The nominal torsional stress-strain histogram for the first 650°C SCISR test program was that shown in Fig. 5, with the SCISRs corresponding to the numbered points with one significant exception. After applying the initial preload shear strain of 0.5%, the initial probe for SCISR No. 2 was made in the positive shear strain direction (the same direction as the preload). Because the stress-strain curve was relatively flat, very abrupt yielding apparently occurred during the probe, and as a result an additional 0.34% shear strain was accumulated. Thus, the initial preload was effectively 0.84% rather than 0.5%, and the second SCISR surface corresponded to a preload of 0.84%. Following determination of SCISR No. 2, the specimen was returned to zero load and strain, and SCISR No. 3 was determined. The −0.5% preload was then applied and the test continued. Figure 6 shows the results for all the surfaces of this test. Note that two duplicate sets of probes were done for two of the SCISRs. The square symbols on these plots represent the initial probe results and the circles and triangles represent results from repeat probes which were occasionally done to check questionable points. Load changes during the preloads were conducted at a constant strain rate of 500 με/min.

The initial SCISR is smoothly defined by two separate sets of probes. The results show that the virgin specimen contained just a small amount of anisotropy (the initial SCISR is not quite centered at zero), but the SCISR is well described as a Mises type surface. Subsequent surfaces show a little less consistency, and they move (up or down) along the torque shear stress axis in the same direction as the last previous preload. The amount of bias varies from 15 to 35% while the width along that axis is relatively constant for the four surfaces.

A 14-week time-dependent SCISRs testing program at 650°C with torsional creep loads was subsequently executed on a new virgin specimen. Whereas the SCISRs determinations in the first test series were after "time-independent"

preloads, the emphasis of this second test was on time-dependent effects. Figure 7 depicts the planned or nominal program with a duration of 14 weeks (98 days) and 17 points of SCISR determinations. The test was executed with several exceptions to this planned program; therefore, the actual torsional stress vs time histogram for the time-dependent portion of the test is shown in Fig. 8.

A torsional stress level, τ_o, of 88.3 MPa (12.8 ksi) was chosen to produce an expected creep shear strain, $\gamma/2$, accumulation of about 0.5% in 1008 h (42 days) of testing. The virgin specimen was cycled at 650°C under strain control to introduce isotropic hardening and minimize the plastic strain on the initial loading. Forty-five cycles were performed with a tensorial shear strain range of ±0.173% and a strain rate of 0.05%/s. A constant axial compressive stress of approximately 24 MPa (3500 psi) was accidentally applied to the specimen during these cycles because of an inducted zero shift in voltage on the axial load channel. After the cycling, the axial load cell cable was rerouted away from a radio frequency cable which eliminated the zero shift. Peak-to-peak torsional shear stresses of ±90.1 MPa (±13.07 ksi) were attained by the last cycle.

The specimen was loaded to the target torsional stress level, 88.3 MPa, under MTS load control after determination of two initial SCISRs. A large plastic tensorial shear strain, which the cycling was supposed to prevent, occurred (approximately 0.43%) and a consequent large creep rate was obtained (approximately 0.05%/h after 4 hours). The torsional stress level was therefore lowered to 40 MPa (5.8 ksi) at the end of the fourth hour.

The test continued without incident until a plant power failure occurred between SCISR Nos. 9 and 10 (with no load on the specimen). The specimen was reheated and the test continued. Several subsequent surfaces after the power outage showed a definite bias in the negative axial direction. A possible explanation for this behavior is that an overload could have occurred in the negative axial direction during the power failure. This is possible since the hydraulic power supply provides some pressure while spinning down after a power loss, but control of the servovalve is immediately lost.

The torsional shear stress level was increased to 60 MPa (8.7 ksi) between SCISR Nos. 14 and 15 because most of the earlier surfaces were similar and more time-dependent creep deformation could be accumulated at

the higher stress. This increase led to exceeding the calibrated strain limit of 1%, but no strain measurement degradation was observed.

A total of 35 SCISRs was determined, at least two at each histogram point (see Figs. 7 and 8). Figure 9 shows the first initial surface (SCISR No. 1, Figs. 7 and 8), the last surface after the first creep period (SCISR No. 7, Figs. 7 and 8), the last surface after the recovery period (SCISR No. 13, Figs. 7 and 8), and the last surface after the final creep period (SCISR No. 17, Figs. 7 and 8). A small amount of contraction along the axial stress axis and slight movement in the plus shear stress direction of SCISR No. 7 relative to SCISR No. 1 can be observed. There appears to be no changes in the remaining surfaces, either quantitatively or qualitatively.

5. CONCLUSIONS

A key result of this testing effort is that surfaces of constant inelastic strain rate exist and can be determined or measured at an elevated temperature, 650°C. This conclusion is validated or deduced by the execution of the test programs and by the consistency of the surface results, especially the repeated surfaces. To our knowledge, this is the first successful determination of high-temperature surfaces of constant inelastic strain rate.

Although conclusions regarding the effect of these SCISRs data on different theories will be left to the constitutive equation developers, several results can be stated. First, the surfaces did not move or change shape in the axial/torsional stress state by any large significant amount. Second, by comparing Figs. 6 and 9, a deduction that plastic deformations have a larger effect than creep deformations can be stated. Last, SCISRs determined immediately after large plastic deformation (see Fig. 6) show more inconsistent results than SCISRs which have not undergone immediate prior plastic deformations. It is believed that this behavior is real and not a result of the testing system. Therefore, the state of the material may not have been in a steady-state condition at the time of the SCISR determinations.

Another conclusion of the effort is that the extensometer system and software control system performed extremely well in a difficult application. It was first necessary to measure high-temperature strains (axial and torsional) which were decoupled, then to differentiate these signals

with as little noise as possible to attain a reasonably small target inelastic strain rate, which, in turn, would minimize changes in state of the material during a surface determination. Plus, the above process took place in a noise generating radio frequency induction heating environment.

6. REFERENCES

1. K. C. Liu, **Low-Cycle Biaxial Fatigue of Annealed 2-1/4 Cr—1 Mo Steel at 538°C under In-Phase Load**, ORNL/TM-8641, Union Carbide Corp., Nuclear Div., Oak Ridge Natl. Lab., Oak Ridge, Tenn., July 1983.

2. J. R. Ellis and W. K. Sartory, "Evaluation of a Capacitance-Based Tension-Torsion Extensometer," pp. 35-51 in **High-Temperature Structural Design Program Prog. Rept. Dec. 31, 1982**, ORNL-5948, Union Carbide Corp., Nuclear Division, Oak Ridge Natl. Lab., Oak Ridge, Tenn.

3. U.S. Department of Energy, **Nuclear Systems Materials Handbook**, Oak Ridge Natl. Lab., Oak Ridge, Tenn.

Fig. 1. Multiaxial test facility used in SCISRs tests.

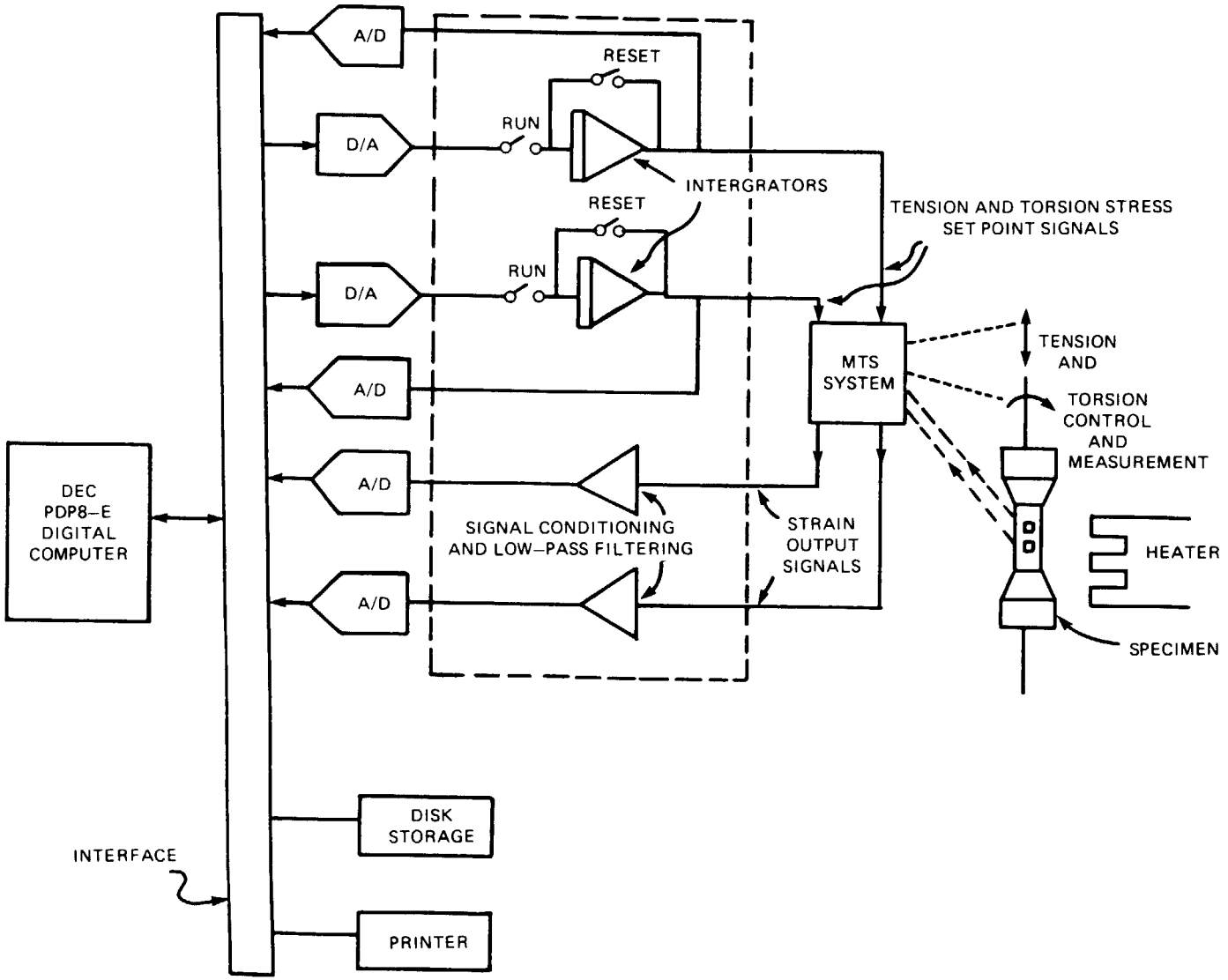

Fig. 2. Computer control system block diagram.

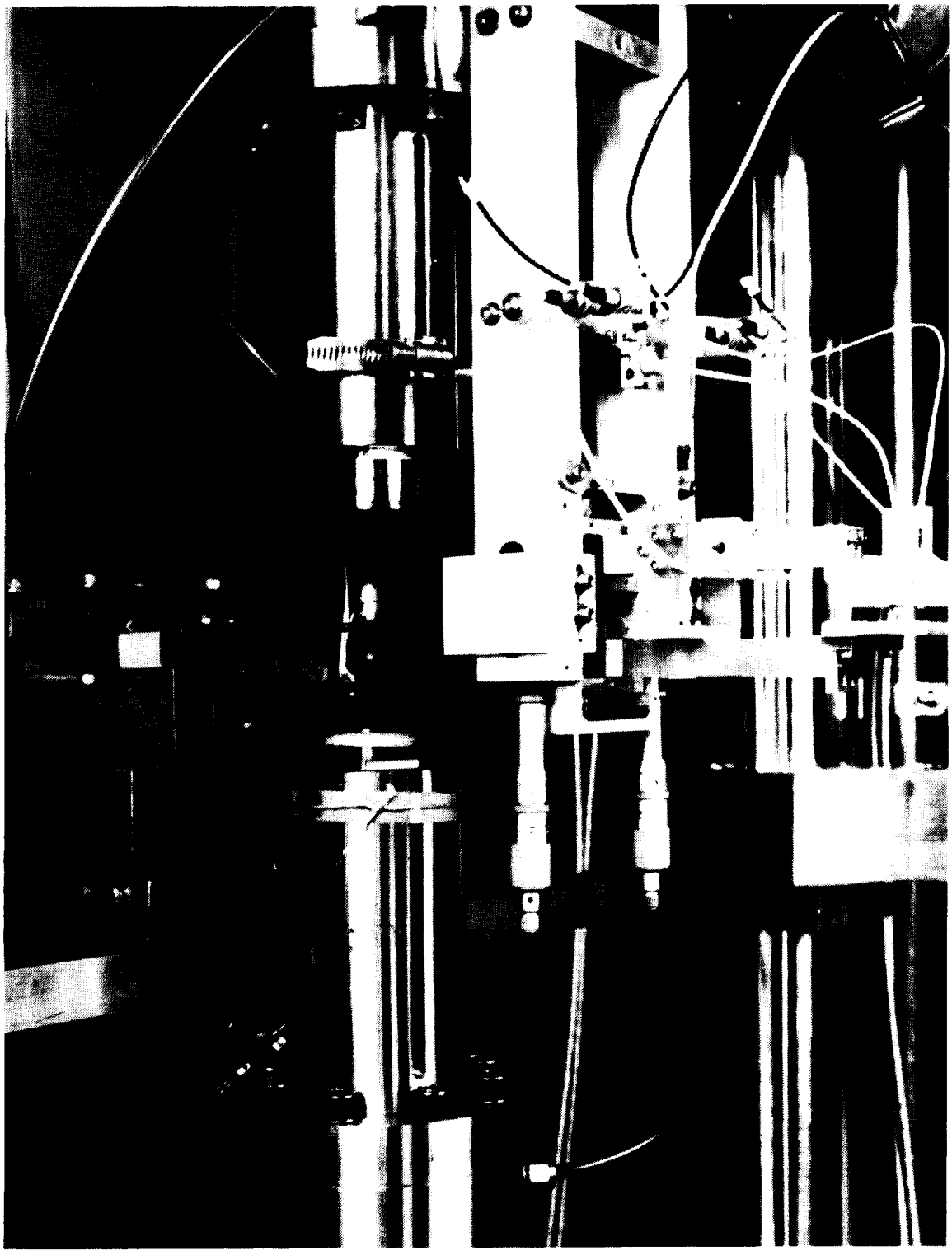

Fig. 3. Axial/torsional high-temperature extensometer mounted on the test specimen.

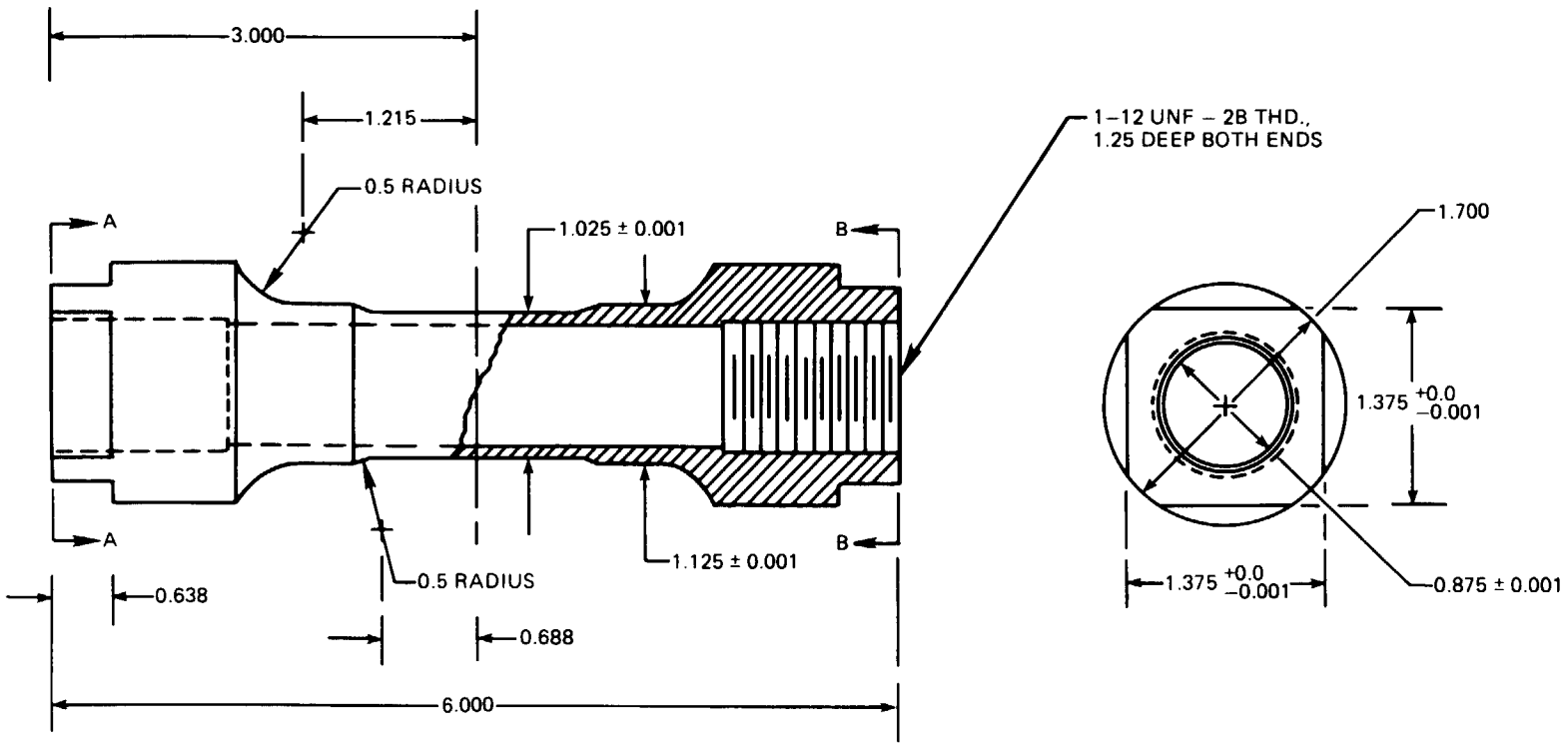

Fig. 4. Schematic of the test specimen. Dimensions in inches. (1 in. = 25.4 mm)

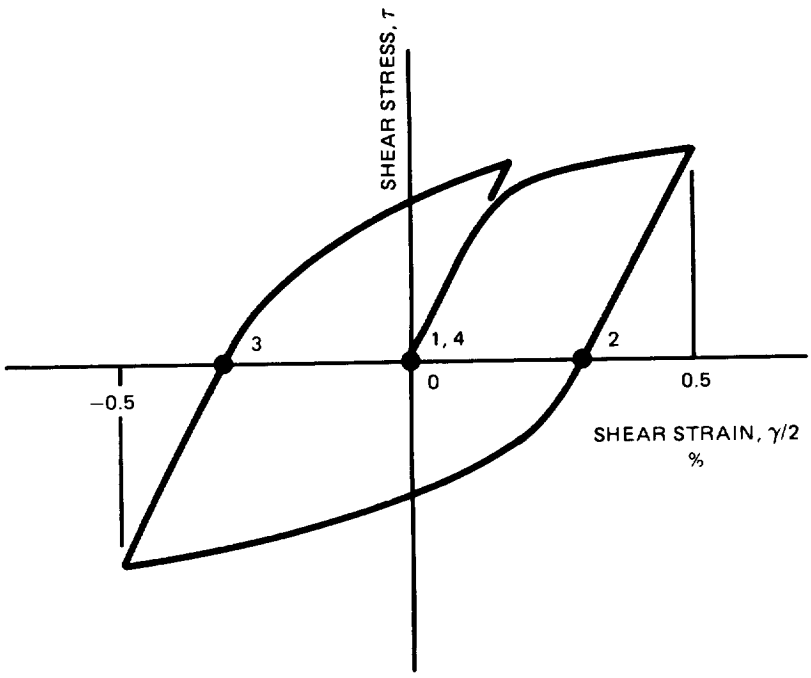

Fig. 5. Torsional stress-strain history for reference SCISRs test program. SCISRs were determined at the four labeled points. Each SCISRs measurement consists of 16 sequential probes to a maximum effective inelastic strain rate of 0.01%/min. The shear strain is tensorial strain (one-half the engineering shear strain, γ).

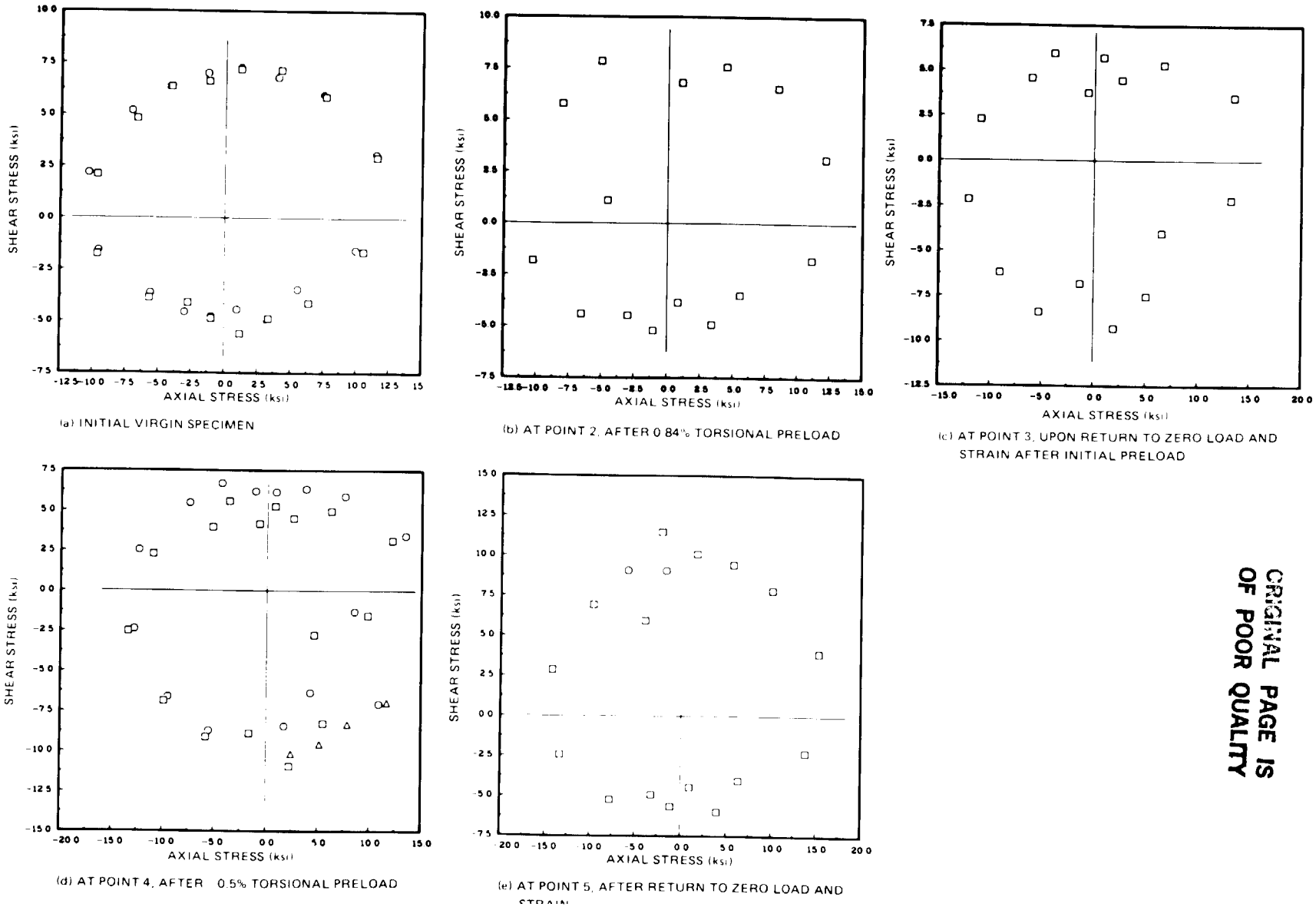

Fig. 6. Measured 650°C surfaces of constant inelastic strain rate for reference SCISRs test program. Note that the initial torsional preload was effectively 0.84% rather than 0.5% and that an extra SCISR (point 3) was determined.

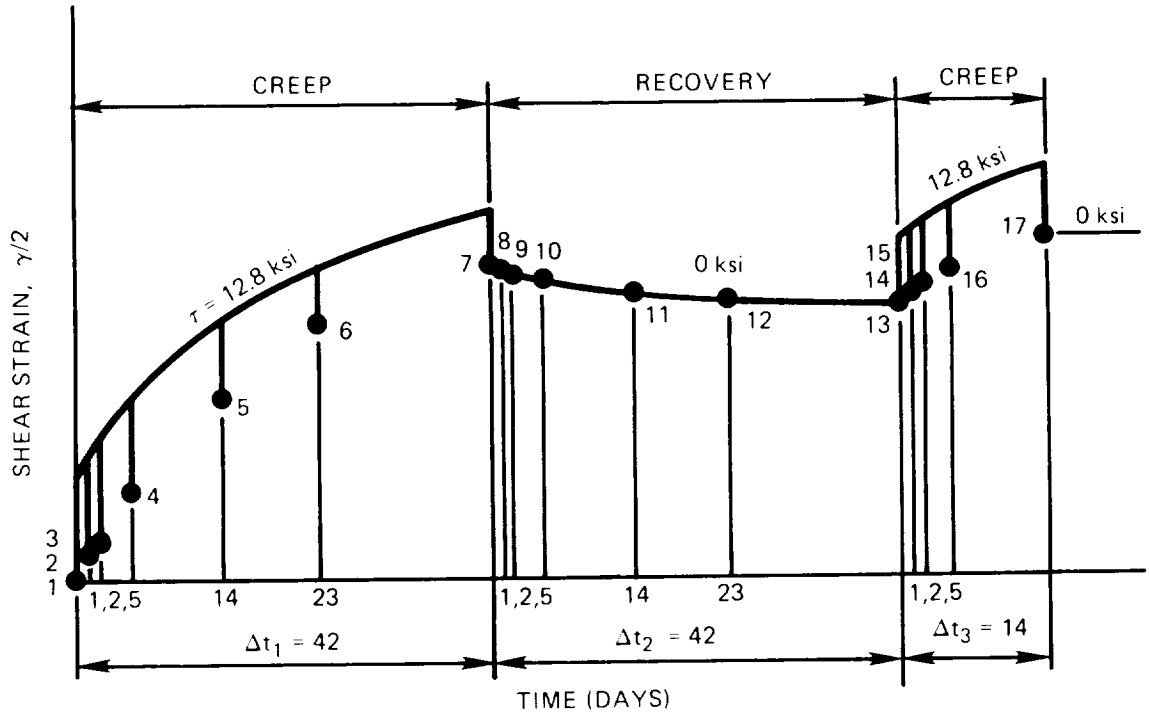

Fig. 7. Nominal time-dependent tensorial shear strain–time history for the second test program. SCISRs were to be determined at the 17 labeled points.

Fig. 8. Actual torsional shear stress–time history for the time-dependent test program. SCISRs were determined at the 17 labeled points.

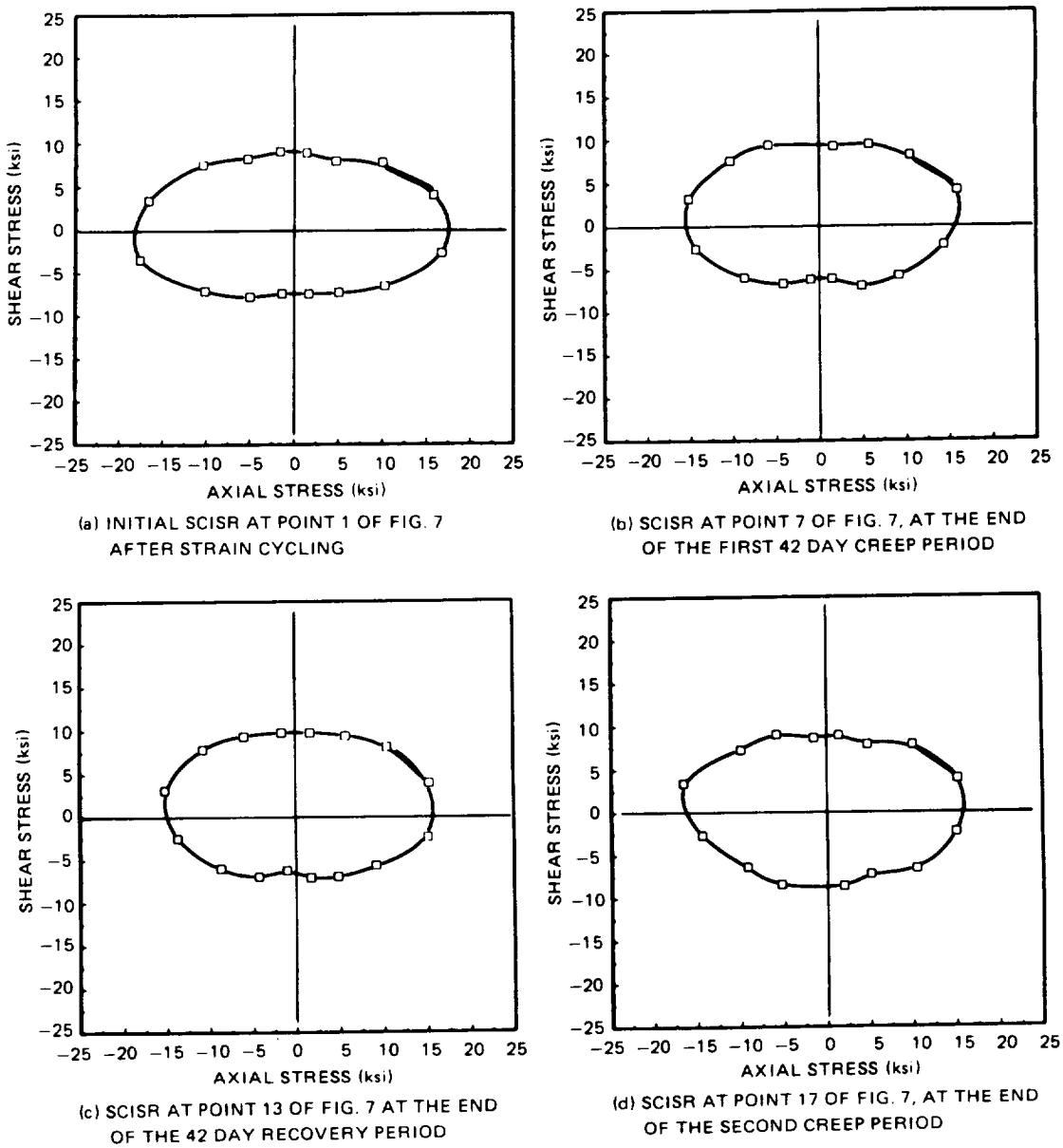

(a) INITIAL SCISR AT POINT 1 OF FIG. 7 AFTER STRAIN CYCLING

(b) SCISR AT POINT 7 OF FIG. 7, AT THE END OF THE FIRST 42 DAY CREEP PERIOD

(c) SCISR AT POINT 13 OF FIG. 7 AT THE END OF THE 42 DAY RECOVERY PERIOD

(d) SCISR AT POINT 17 OF FIG. 7, AT THE END OF THE SECOND CREEP PERIOD

Fig. 9. Measured 650°C surfaces of constant inelastic strain rate for the time-dependent test program. (1 ksi = 6.895 MPa)

CONSTITUTIVE MODELING FOR SINGLE CRYSTAL SUPERALLOYS*

D.C. Stouffer, N. Jayaraman, M. Sheh and D. Alden

University of Cincinnati

INTRODUCTION

The inelastic response of single crystal γ/γ' superalloys is quite different from the behavior of polycrystalline nickel base superalloys. Upto a critical temperature the yield stress of single crystal alloys is a function of the material orientation relative to the direction of the applied stress and the material exhibits significant tension/compression asymmetry [1]. This behavior is primary due to slip on the octahedral slip system. Above the critical temperature there is a sharp drop in the yield stress, cube slip becomes more predominant and the tension/compression asymmetry is reduced. Similar orientation and tension/compression asymmetry is observed in creep and secondary creep above the critical temperature is inferred to occur by octahedral slip [2]. There are two exceptions to this behavior. First loading near the [111] orientation exhibits cube slip at all temperatures, and; second, loading near the [001] orientation produces only octahedral slip at all temperatures.

LEVEL I CONSTITUTIVE MODEL

Earlier in the grant period, a constitutive model and finite element was developed for Rene N4 and verified using published results near the critical temperature [3].

In summary, the constitutive model is based on separating the total global strain into elastic and inelastic components. The elastic strains are calculated using cubic symmetry. The inelastic strain rate is calculated by summing the contributions of each slip system. The inelastic

*Work done under NASA Grant NAG3-511.

slip rate on each slip system is computed from a local inelastic constitutive equation that depends on local resolved shear stress components in each slip direction and local state variables. The orientation dependence and tension/compression asymmetry was incorporated using the "core width effect" proposed by Lall, Chin and Pope [4]. The constitution model for local slip also is based on a system of state variables to model the drag stress. Back stress was not included since this typically is associated with dislocation pile-ups at obstacles like grain boundaries which are absent in single crystals.

Typical calculations for an earlier chemistry of Rene N4, designated as VF 317 [5], were completed using the above equations imbeded in a twenty noded isoparametric brick. The combined constitutive equation and finite element was developed to model any piecewise linear load history and incorporated a dynamic time incrementing procedure. The calculated and experimental results are shown in Figure 1 for tensile tests at a constant strain rate of 8.33×10^{-5} sec^{-1} and three orientations. Tensile creep curves for seven specimens and the same three orientations is shown in Figure 2. The test temperature is $732^{o}C$ which is close to the critical temperature and the maximum orientation effect.

LEVEL II MODEL DEVELOPMENT

The above combined constitutive and finite element model was successful for predicting both the orientation dependence and tension/compression asymmetry for tensile and creep histories. The model proved to be inadequate for fatigue due to its simplicity. In particular, there is no means of capturing both the short time strain hardening and the long term cyclic hardening observed in fatigue. Further, there is evidence that

dislocations can pile-up at the γ-γ' interface at temperatures above the critical temperature. Thus, a set of local back stress state variables, similar to [6], have been incorporated into the model for both octhadedral and cube slip system. Further a set of computer programs have been written to evaluate the material parameters using a nonlinear optimization technique. The programs have been tested in a preliminary mode and they will be used in conjunction with the experimental program.

EXPERIMENTAL PROGRAM

The experimental program consists of approximately 50 tests at five temperatures, five orientations and several strain rates. In most cases the test will be stopped before failure to examine the active slip mechanisms in the strain range of interest. The work will primarily focus on monotonic tension at different strain rates and fatigue properties as a function of orientation. Creep will not be included in light of the above success with creep predictions. There will also be a group of nonstandard tests to evaluate the predictive capabilities of the model.

The initial phase of the experimental program is at 982°C (1800°F) since the earlier work was at 760°C (1400°F). This allows investigation of global strain resulting from the combined octahedral and cube slip mechanisms. The initial test matrix includes two tests each in the [001] and [111] orientations to isolate the octahedral and cube slip systems, respectively. The remaining tests are in the [123] and [110] orientations. This set of tests will be carefully evaluated before completing the test matrix at 982°C. The tests matrix for 760°C will be similar to that at 982°C. A few tests will be done at 1100°C, 870°C and 650°C.

These mechanical tests are being carried out on a closed loop MTS servohydraulic test frame. These are axial strain controlled tests in which

load, axial strain and diametrical strain are monitored. An induction heating unit with microprocessor temperature controller is used for heating the specimens to temperature. Typically, the temperature was found to have a maximum gradient of 3°F through the gage length of the sample at 892°F. An example, the axial and diametrical stress-strain response of a specimen oriented in the [011] direction is shown in Figure 3. The diametrical extensonmeter is in the $[01\bar{1}]$ direction. Notice that the elastic diametrical strain is positive which agrees with the values for the Poisson ratio shown in Figure 4.

REFERENCES

1. Pope D. and Heredra, F., "Tension/Compression Asymmetry in High $\dot{\gamma}$ Fraction Nickel Base Alloy Single Crystals," 5th International Symposium on Superalloys, ASM, Metals Park, Ohio 1984.
2. Shah, D., "Orientation Dependence of Creep Behavior of Single Crystal γ' (Ni_3Al)," Scripta Metallurgica, 17, pp 997, 1983.
3. Dame, L.T. and Stouffer, D.C., "Anisotropic Constitutive Model for Nickel Base Single Crystal Alloys: Development and Finite Element Implementation. NASA CR-175015, Lewis Research Center, March 1986.
4. Lall, C., Chins and Pope, D., "The Orientation and Temperature Dependence of the Yield Stress of $Ni_3(Al,Wb)$ Single Crystals" Metallurgical Transactions A, 10A, p 1323, 1979.
5. Wukuskick, C., "Directional Solidification Alloy Development," NADC-78136-60, Naval Air Systems Command.
6. Ramaswamy, V.G., "A Constitutive Model for the Inelastic Multiaxial Cyclic Response of a Nickel Base Superalloy Rene'80. NASA CR-3998, July 1986.

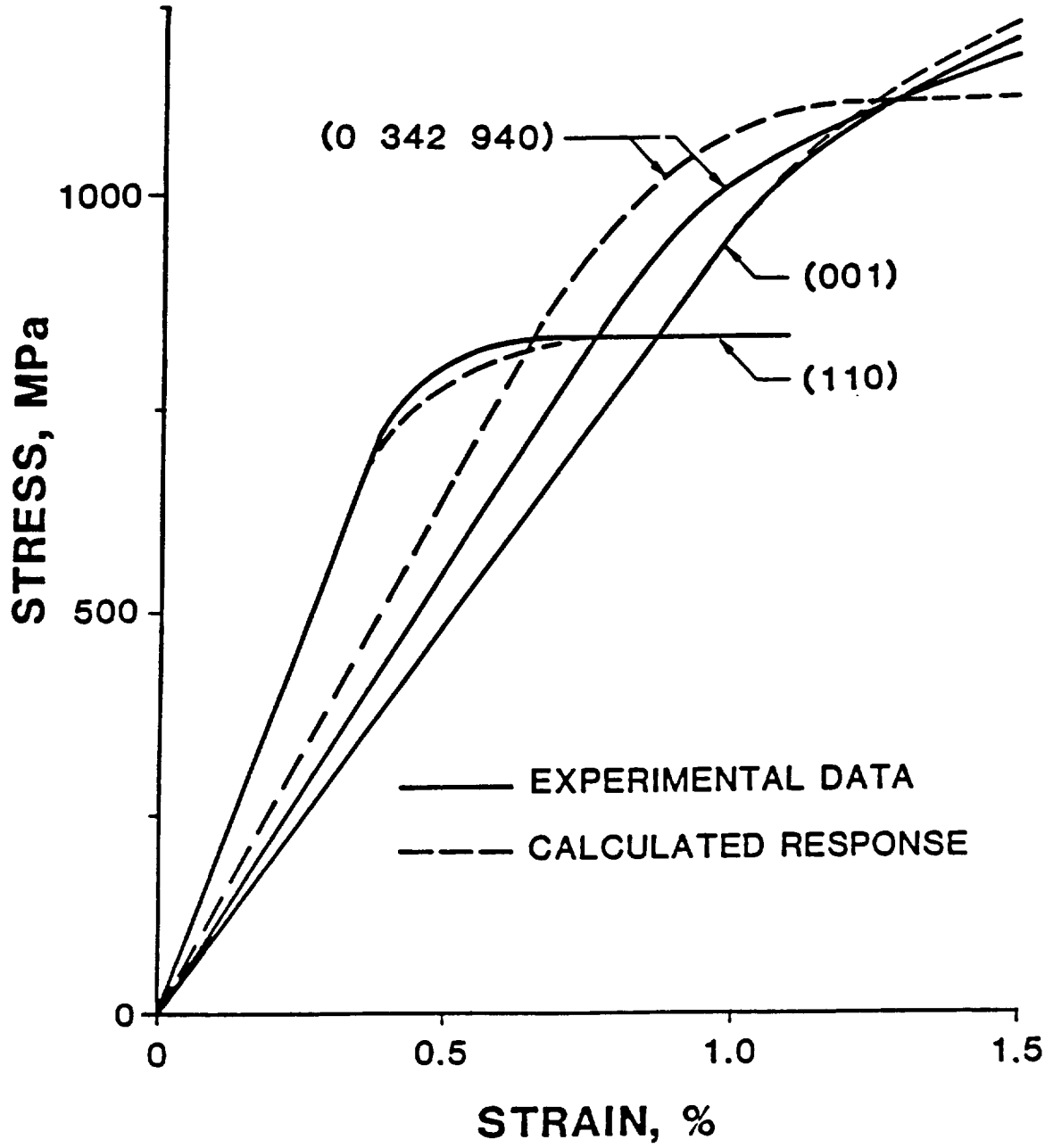

Figure 1. Predicted and experimental stress atrain curve for RENE N4 VF317 at 760°C.

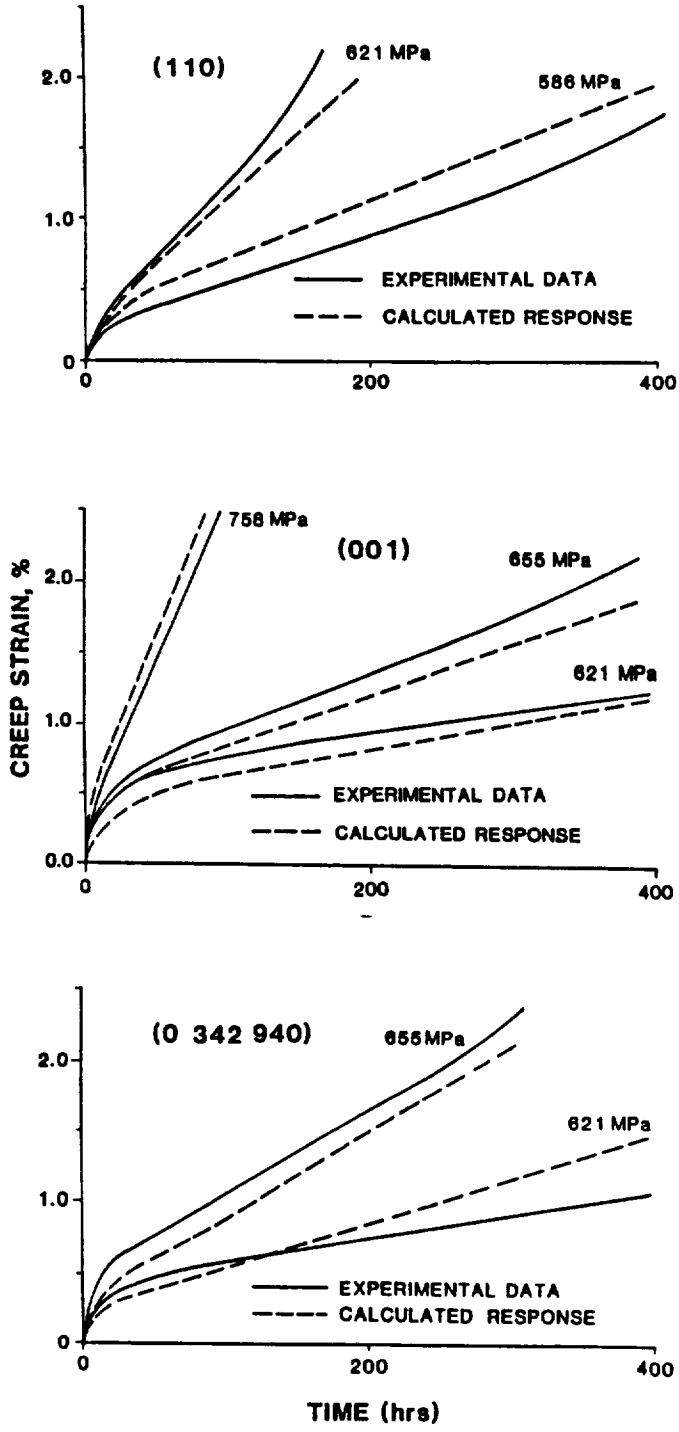

Figure 2. Predicted and experimental creep responses for RENE N4 loaded in different directions at 760°C.

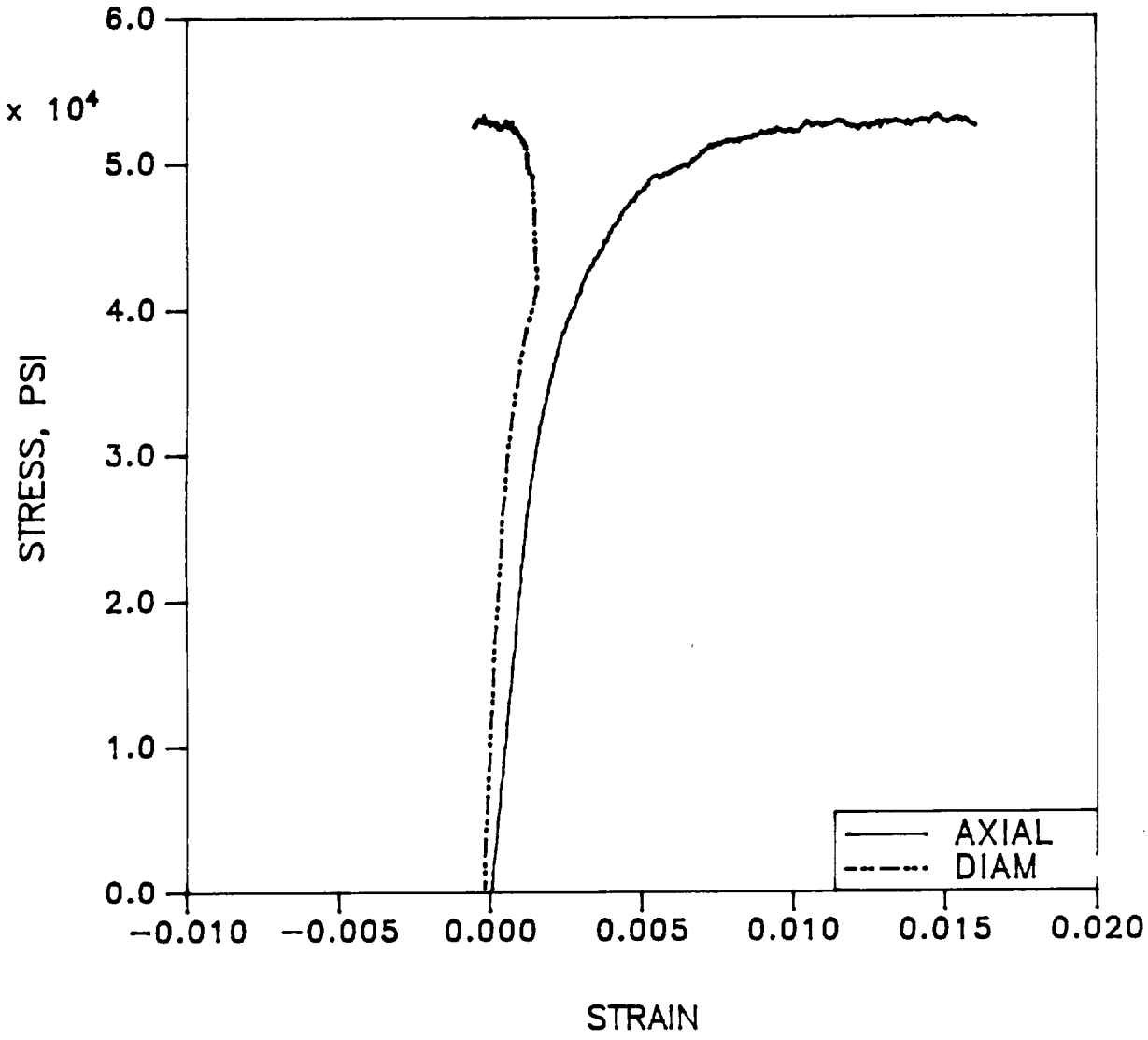

Figure 3. Tensile response of RENE N4 at 1800°F

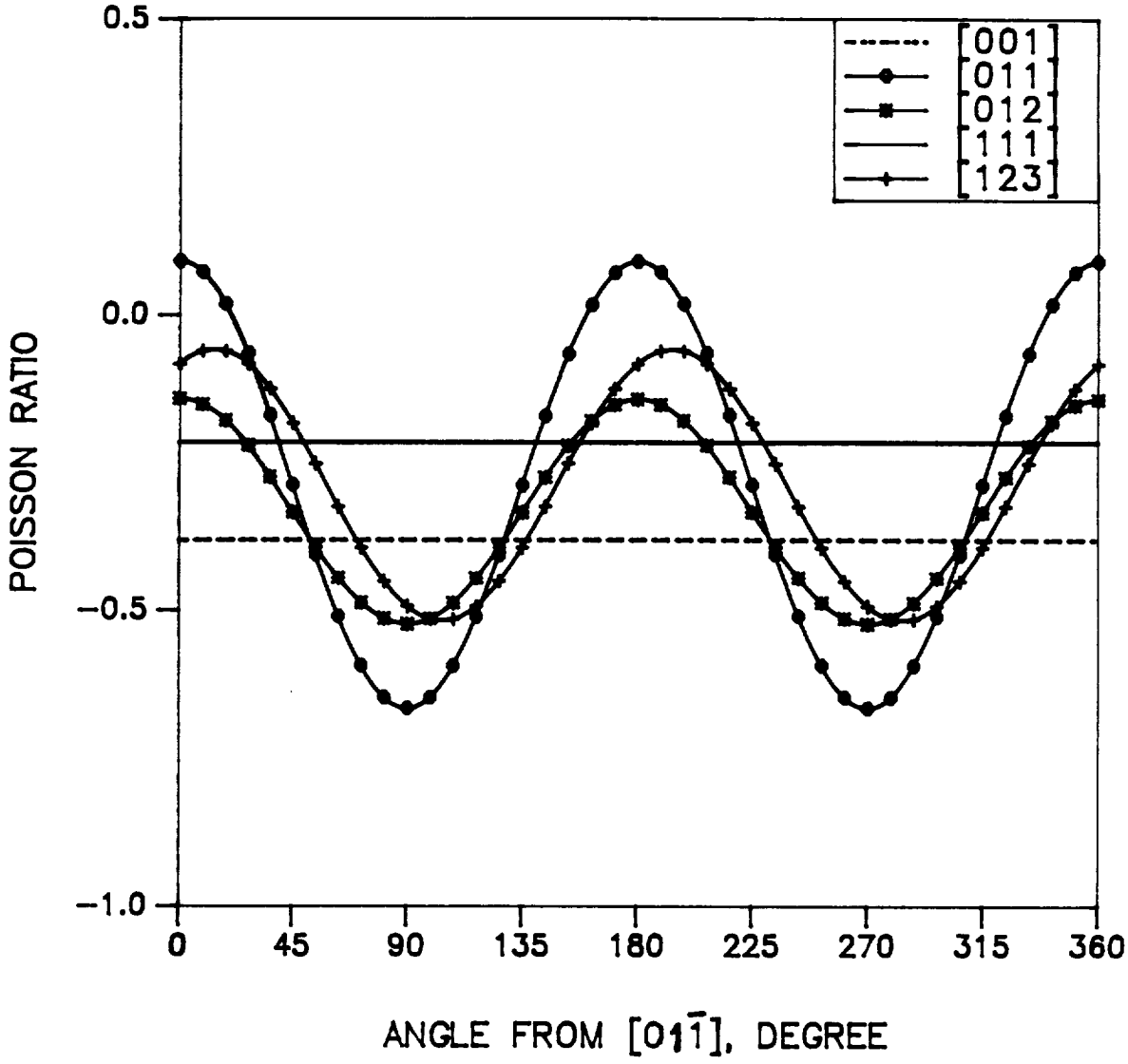

Figure 4. Variation in Poisson ratio with orientation for the five specimen orientations in the experimental program.

PROGRESS REPORT ON CONSTITUTIVE MODELLING OF SINGLE CRYSTAL AND DIRECTIONALLY SOLIDIFIED SUPERALLOYS*

E.H.Jordan** and K.P.Walker***

INTRODUCTION

The trend towards improved engine efficiency and durability places increasing demands on materials that operate in the hot section of the gas turbine engine. These demands are being met by new coatings and materials such as single crystal and directionally solidified nickel-base superalloys which have greater creep/fatigue resistance at elevated temperatures and reduced susceptibility to grain boundary creep, corrosion and oxidation than conventionally cast alloys.

This report discusses work carried out as part of a research program aimed at the development of constitutive equations to describe the elevated temperature stress-strain-time behavior of single crystal and directionally solidified turbine blade superalloys. The program involves both the development of suitable constitutive models and their verification through elevated temperature tension-torsion testing of single crystals of PWA 1480.

DISCUSSION

Two types of constitutive models have been developed to describe the deformation behavior of single crystal and directionally solidified superalloys. The first type makes use of a macroscopic continuum mechanics approach in which unified viscoplastic constitutive relations are developed for materials which exhibit cubic and transversely isotropic anisotropy. A second type uses crystallographic slip theory in an attempt to model the metallurgical processes governing the deformation behavior of single crystal and directionally solidified alloys.

The macroscopic models have the advantage of requiring relatively few material constants and they can be rapidly integrated over a given strain-time history. We have found, however, that they do not represent the deformation behavior of single crystal alloys as accurately as the micromechanical formulations based on

---

* Work Performed Under NASA-LEWIS Grant NAG3-512.

** University of Connecticut, Storrs, Connecticut, USA

*** Engineering Science Software, Inc., Smithfield, Rhode Island, USA

crystallographic slip theory. For example, the best correlation between theory and test results has been obtained by using a unified constitutive model in which the equilibrium stress (back stress or kinematic stress) hardens with inelastic strain in an anisotropic manner; that is, the equilibrium stress increments harden with inelastic strain increments through a fourth order tensor which exhibits cubic symmetry for the single crystal and transversely isotropic symmetry for the directionally solidified superalloys. This model gives reasonable predictions of the high temperature cyclic deformation behavior of single crystal specimens whose axes are oriented in the 001 and $\bar{1}11$ directions, since the material constants in the model were derived from specimens oriented in these directions. We have not yet tested the macroscopic model to predict the cyclic deformation behavior of specimens oriented in the 011 direction or to compare with the torsional behavior of specimens oriented in the 001 direction, but such comparisons are in progress.

The second type of model is based on crystallographic slip theory. Each slip system in the material is assumed to shear according to a unified viscoplastic constitutive relation. At temperatures below 750°C the single crystal alloy PWA 1480 deforms by octahedral glide of its crystallographic planes, while cube slip becomes an increasingly important deformation mode at temperatures above 750°C. We have found that both slip systems are required to model the constitutive behavior of PWA 1480 at 1600°F. The material constants for octahedral slip can be found by axial tension–compression testing of tubular specimens oriented in the 001 direction. This induces no cube slip in the specimens since the resolved shear stress promoting slip on the cube crystal planes is zero for axial tension–compression tests. The material constants for cube slip are then obtained by testing the 001 oriented tubular specimens in torsion, since this induces slip on both the octahedral and cube crystallographic planes. The cube constants may also be obtained from axial tension–compression testing of specimens oriented in the 011 and $\bar{1}11$ directions, since these tests also activate both the octahedral and cube slip systems. We have found that the material constants obtained from 001 and $\bar{1}11$ axial tests allow an accurate prediction of the axial behavior of 011 oriented specimens.

A model for directionally solidified alloys has been derived by embedding the single crystal formulation in a transversely isotropic self–consistent theory. This model has not yet been tested due to the lack of an experimental data base.

RESULTS

1. Single crystal viscoplastic constitutive models based on both macroscopic continuum mechanics and on crystallographic slip theory have been formulated and programmed as FORTRAN subroutines suitable for inclusion in the MARC nonlinear finite element program. Adapting the routines to other nonlinear codes is a trivial exercise.

2. Directionally solidified viscoplastic constitutive models based on both macroscopic continuum mechanics and on a self–consistent theory have been formulated, but

have not yet been tested or programmed due to the lack of a suitable experimental data base.

3. The macroscopic single crystal model is not as accurate as the model based on crystallographic slip theory. An anisotropic equilibrium stress state variable is needed in the macroscopic formulation to model the cubic anisotropy inherent in single crytal superalloys.

4. Both octahedral and cube slip systems are needed to model the deformation behavior of PWA 1480 single crystals at 1600°F. When the material constants are obtained from 001 axial tests and from either 001 torsion tests, or from $\bar{1}11$ axial tests, the model predicts accurate deformation behavior in the 011 tests. Predictions of axial strain rate dip tests for specimens oriented in the 001 direction are also of acceptable accuracy as shown in Figures 1–3.

5. Yield stress asymmetry is observed in PWA 1480. At temperatures below 750°C the yield stress asymmetry can be predicted according to the cross–slip theory of Takeuchi & Kuramoto, and by the Shockley partial constriction theory of Lall, Chin, Pope, Ezz, Paidar, Shah & Duhl. However, at 1600°F and above the preceding theories do not work. At temperatures below 750°C the preceding theories are in accord with the experimental results in showing that the yield stress in tension exceeds that in compression in the 001 corner of the stereographic triangle, with the reverse being true in the 011 and $\bar{1}11$ corners. At 1600°F and above, the yield stress in compression exceeds that in tension in all three corners of the stereographic triangle at strain rates above 10^{-4} sec^{-1}. The yield stress asymmetry also exhibits a strong rate dependence in which the yield stress is larger in tension than compression at low strain rates but is smaller at high strain rates. This dependence of the asymmetry on strain rate increases with increasing temperature, but cannot be modelled at present.

6. The material constants obtained from hysteresis tests at strain rates exceeding 10^{-6} sec^{-1} cannot model the deformation behavior observed in long term creep tests where the secondary creep rate is less than 10^{-7} sec^{-1}. It was hoped that this would not be the case. Leverant et al have proposed that primary creep occurs due to the dislocation motion of <112> slip systems on the octahedral {111} planes and that secondary creep occurs due to dislocation motion of <110> slip systems on the {111} planes. The present model cannot predict the long term secondary creep behavior based on the octahedral glide of the <110> systems. Possibly the <112> slip systems operate in both primary and secondary creep and we are investigating this behavior.

7. An experimental arrangement has been built and is now operational which allows biaxial tension–torsion experiments to be conducted under thermomechanical loading conditions. The software to input any given strain–temperature history has also been written and is now in operation. Experimental results are stored directly on floppy diskettes which can be used to drive the software for determining the material constants in the constitutive models.

8. In the last reporting period the material constants were determined by using the general purpose nonlinear optimization code CONMIN. A more suitable approach is now used in which the material constants are determined by a nonlinear least squares program developed specifically by the authors to determine material constants from experimental data files. This program requires the constitutive model to be integrated over the strain histories in the experimental data files, and the nonlinear least squares approach necessitates the use of an iterative technique. Because of the large amount of integration required it is necessary to integrate the single crystal constitutive model very rapidly. This is accomplished by casting the complicated three dimensional form of the model into three much simpler models which are suitable for the axial integration of specimens oriented in the 001 and $\bar{1}11$ directions, and for the torsional integration of specimens oriented in the 001 direction.

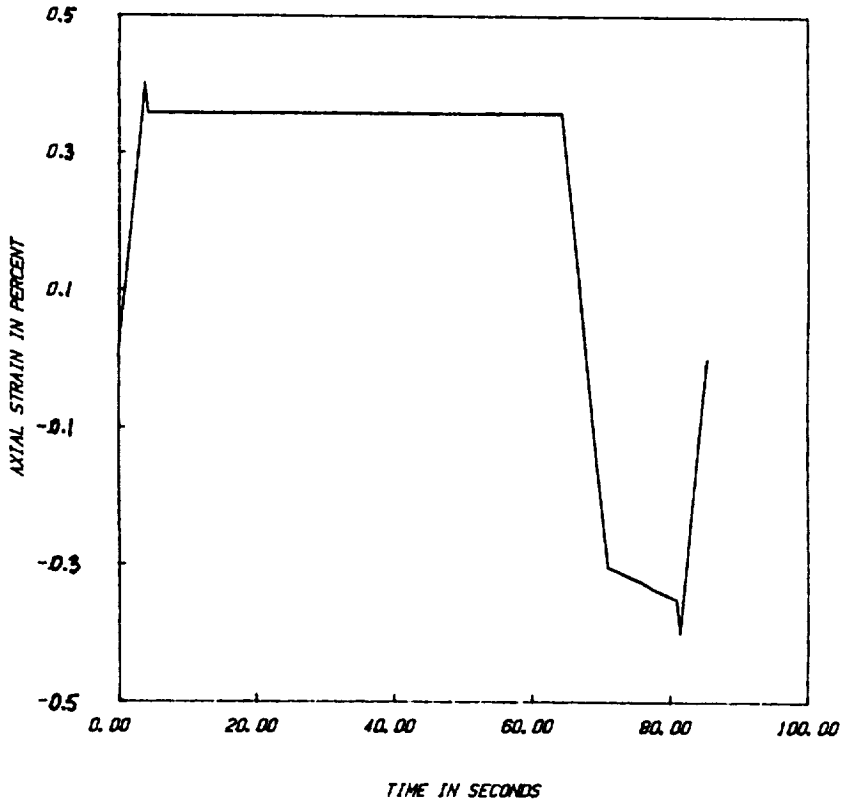

Fig 1. Experimental Strain-Time History For Dip Test On PWA 1480 at 1600F

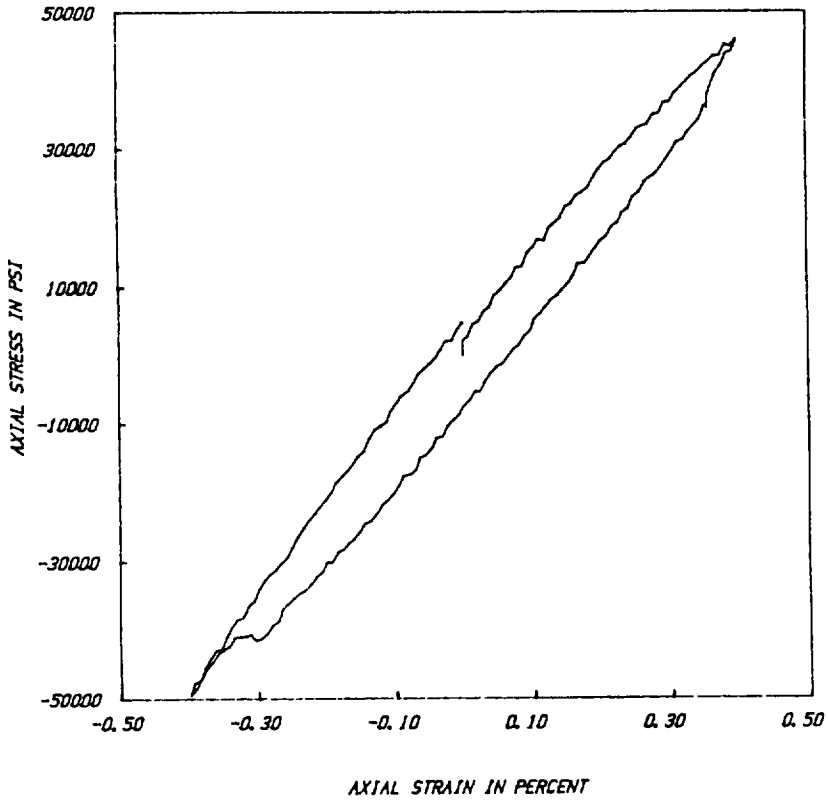

Fig 2. Experimental Stress-Strain Loop During Dip Test On PWA 1480 at 1600F

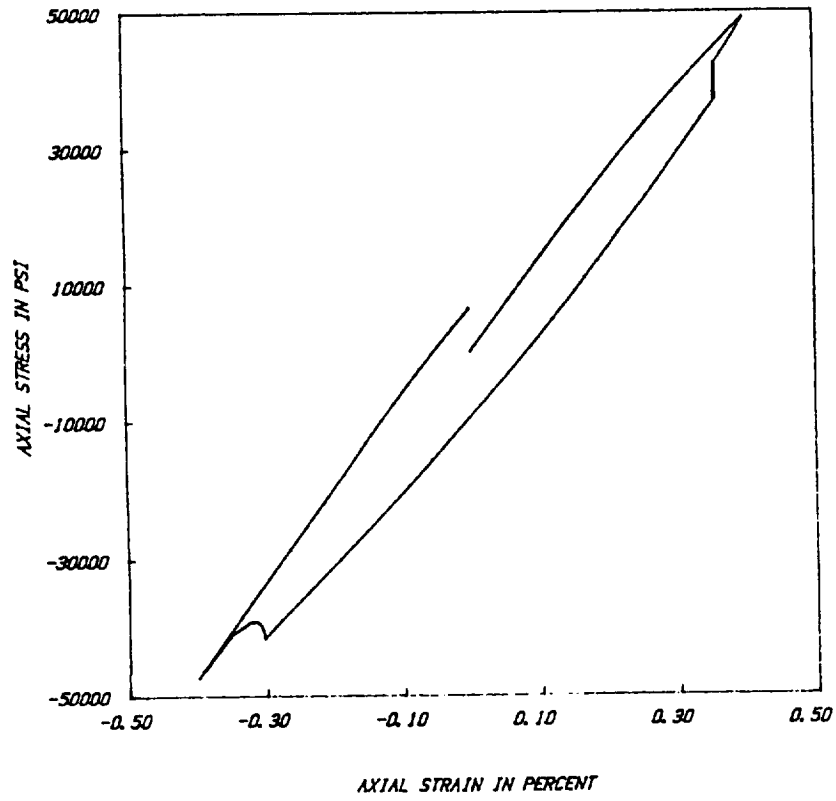

Fig 3. Predicted Stress-Strain Loop During Dip Test On PWA 1480 at 1600F

HIGH TEMPERATURE STRESS-STRAIN ANALYSIS

Robert L. Thompson and Paul E. Moorhead
NASA Lewis Research Center
Cleveland, Ohio

The objectives of the high-temperature structures program are threefold: to assist in the development of analytical tools needed to improve design analyses and procedures for the efficient and accurate prediction of the nonlinear structural response of hot-section components; to aid in the calibration. validation, and evaluation of the analytical tools by comparing predictions with experimental data; and to evaluate existing as well as advanced temperature and strain measurement instrumentation. As the analytical tools, test methods, tests, instrumentation, as well as data acquisition, management, and analysis methods are developed and evaluated, a proven, integrated analysis and experiment method will result in a more accurate prediction of the cyclic life of hot section components.

TEST FACILITIES

The two test facilities at Lewis which support the development of the analytical tools and the evaluation of advanced instrumentation are the high-temperature structures laboratory and the structural component response test facility. Both of these facilities have the capability to conduct controlled thermomechanical cyclic experiments under computer control. Small cylindrical bar and tubular specimens are tested in the high-temperature structures laboratory (see fig. 1) using uniaxial and biaxial test machines. Larger specimens such as flat plates, cylinders, and combustor liner segments are tested in the structural component response test facility, which consists of two rigs that operate at atmospheric pressures. Flat-plate specimens (5 by 8 in.) are tested in the bench-top quartz lamp rig (see fig. 2); large, cylindrical (20 in. diam.) and combustor liner specimens are tested in the annular quartz lamp rig (see fig. 3). The high-temperature structures laboratory, the bench-top quartz lamp rig, and the annular quartz lamp rig are operational.

High Temperature Structures Laboratory

Two uniaxial test machines (load capacity, ±20-kip) and two recently installed biaxial test machines (±55-kip load in tension/compression and 25-kip in torsional capacity) are used in the high-temperature structures laboratory for deformation testing. Two new uniaxial test machines have been purchased to replace the existing uniaxial machines. Each of these machines is computer controlled by an S20 Data General computer. A larger Data General computer (MV/4000) is used for data storage, management, reduction, and analysis. Five-kilowatt radiofrequency induction heaters are used with the uniaxial machines, and 50-kW audiofrequency induction heaters are used with the tension/torsion test machines. Instrumentation includes high-temperature water-cooled uniaxial extensometers for measuring strains on the uniaxial test machines. Two high temperature biaxial extensometers will be

tested and evaluated on the biaxial test machines. A third high-temperature biaxial extensometer has been evaluated as part of an interagency agreement with the Oak Ridge National Laboratory.

High-Temperature Laboratory Test Results and Constitutive Model Verification

One of the concerns about viscoplastic constitutive models, which for the most part are based on uniaxial isothermal test data, is their ability to accurately predict stresses and strains for cyclic thermomechanical conditions. To begin to assess this effects both in-phase and out-of-phase (temperature and strain) uniaxial nonisothermal tests have been conducted at NASA Lewis.

For illustration purposes, a comparison of out-of-phase uniaxial nonisothermal (TMD) experimental data with predictions from four unified models is shown in figure 4. The strain and temperature variations are linear (saw tooth) and 180° out-of-phase. The strain rate is 0.000046 in./in.-sec., the total strain range is ±0.3 percent, and the temperature range is 395 to 606 °C (743 to 1123 °F). The period is 295.3 sec/cycle. The temperature range selected is representative of a location on a combustor liner near the cooling holes, one of the several critical failure locations on a combustor liner. Qualitatively, the Walker and Bodner models predict reasonably well the uniaxial out-of-phase nonisothermal hysteresis response compared with the experimental data, but quantitatively, to accurately predict the shape and levels of the cyclic response, further refinements to the models are required. Additional tests are underway to expand the data base.

Bench-Top Rig

The major components of the bench-top quartz lamp rig are shown in figure 2. Four quartz lamps (6 kVA) are used to heat the plate specimens. The lamps are air cooled, and the test fixture is water cooled. A manifold provides cooling air to the top surface of the test plate. The cooling air to the plate can be preheated to 400 °F. A lamp-out detection system determines when a lamp has burned out.

A dual-loop programmable controller, a microprocessor, is used to control the power to the lamps. A specified power-time history is programmed into the microprocessor, and the cooling air temperature and flow rate are appropriately set so that when combined, the desired thermal cycle is imposed on the test plate.

Thermocouples and an infrared thermovision system are used to obtain surface temperatures on the plate. There are provisions for taking 30 thermocouple measurements. A viewport, consisting of a 5-in.-diameter quartz window, provides access for obtaining an infrared thermal image. Both thermocouple and thermal image data are obtained on the cool side of the test plate. Only thermocouple data are obtained on the hot side (facing the four quartz lamps) of the test plate. The thermocouple data provide temperatures at discrete points, while the infrared system provides detailed maps of thermal information about the test specimen.

During a test run both the facilities data (pressures. flows, power, etc) and the research data (primarily temperature) are acquired for each thermal cycle using the ESCORT II data acquisition system at Lewis. These data can be stored automatically once every second on the Amdahl computer. The software, however, does allow for varying the time at which data are taken during a thermal cycle. These data can be displayed on CRT's in the control room with about a 4-sec delay time.

To obtain real time readings of pertinent data, a strip chart recorder with nine channels is used.

The raw thermal images obtained from the infrared camera are stored on a VHS tape recorder, with the clock time superimposed on each image. Images of the test plate of from about 4 to about 1 in. in diameter (for finer resolution of temperatures) can be obtained with the zooming capability of the infrared system. Thirty thermal images are captured on tape every second. A computer system is then used to process, reduce, enhance, and analyze the transient temperature information. These data are also compared with the thermocouple data. Thermocouple data are used in the calibration of the infrared system.

Bench Top Rig Test Results

Some of the salient results of tests conducted on a Hastelloy-X flat plate, with dimensions of 8 by 5 by 0.05 in. are as follows: The plate temperatures are very repeatable from cycle to cycle. A 20-sec ramp time from low to peak temperature on the plate was achieved. The nominal life of the quartz lamps is 500 thermal cycles. Actual lamp life, however, varies depending on power settings (maximum or minimum, the hold times at those settings, and the ramp rates for a given thermal cycle. The infrared thermovision system provides a qualitative measure (maps) and, in some cases, a quantitative measure of transient surface temperatures. The experience, data, and other information obtained from the bench-top rig tests have benefited the tests conducted on the annular quartz lamp rig.

As an example of how the bench-top rig was used to evaluate a high-temperature strain measurement system for possible future use on the annular rig, a cooperative effort with UTRC and Lewis instrumentation personnel was undertaken to evaluate a laser specklegram system. The objective of the research program was to perform a demonstration test of laser speckle photographs by measuring strain on a flat plate. The demonstration test was a success; however, the inability to measure strain in some cases and accuracy of strain measurements in other cases were less than hoped for, but the system has potential. Preliminary temperature and structural analyses of the flat plate tested are underway and prediction of strains in the plate will be compared with the experimental data.

Another technique, high resolution photography, was employed to measure strain on plates in the bench rig. For this technique, a grid system of 0.5 in. squares was marked on the plate with a scribe or painted on with high temperature paint as shown in figure 5. The grid system is for the convenience of measuring strain, as strain can be measured between any two points which can be visually identified in the photograph. Technical Pan 2415 film was used which has a nominal resolution of 400 lines/mm. This would allow resolution of 0.0001 in. at 1X magnification. Photographs are made of the test plate in the original condition and at subsequent temperatures during the heating cycle.

In-plane displacements are determined by measuring the change in dimensions of the grid squares between two temperatures. A machinists microscope was used to measure these dimensions. The instrument used in this case reads out to 0.00005 in. With this system, measurements to 0.001 in. appear feasible and better accuracy is theoretically possible.

Out-of-plane distortion can be measured by placing boron fibers in front of the test plate (in the case on the quartz window) and using a single flash to illuminate

the plate. A sharp shadow is cast on the plate from the boron fiber. Lateral displacement of the shadow from one test condition to another indicates out-of-plane displacement of the test plate. The displacement is a function of the tangent of the angle of illumination. It may be noted that a curved plate gives a curved shadow.

Preliminary results comparing measured and calculated strains are

Strain direction	Comparison
X	From the twice calculated value up to 1 order of magnitude larger
Y	Close to calculated value and up to same order of magnitude

These results are encouraging and with refinements in measuring and computer codes, closer results may be expected.

Annular Rig

Figure 3 shows the annular quartz lamp rig installation and its major components. This rig is being operated under a cooperative agreement with Pratt & Whitney Aircraft (P&WA). G. Pfeifer and D. Sullivan are the P&WA coinvestigators on this project.

The quartz lamp heating system used to cyclically heat a test liner is shown in figure 6. One-hundred-twelve 6-kVA lamps configured circumferentially in 16 sectors, each having 7 lamps, are used to heat a 20-in.-diameter test liner. This system, in addition to drawing up to 672 kVA of 480-V power, requires 3.5 lb/sec of ambient temperature air at 5 psig, 1.5 lb/sec of ambient temperature air at 1 psig. and 80 gal/min of specially treated water for cooling the rig.

A natural-gas and air mixture is burned in a combustor can upstream of the test section to provide preheated cooling air to the test liner. Cooling air temperatures of from 400 to 600 °F can be obtained by varying the fuel/air mixture ratio. The cooling airflow rate is variable from about 4.0 to 7.5 lb/sec at 35 psig. Both the cooling-air temperature and flow rate can be varied to obtain the desired cyclic temperatures on the test liner.

The annular rig has six 5-in.-diameter viewports, three of which are spaced at 120° apart and are used to view the middle section of the test liner. The other three, also spaced at 120° apart, are used to view the upstream portion of the liner and its attachment piece. These windows are rotated 45° from the liner windows. The quartz windows are air and water cooled. Through these windows television cameras and the infrared camera are used to monitor and take temperature measurements on the liner. There are also provisions for having 140 thermocouples on the test liner.

The dual loop programmable controller system, the ESCORT II data acquisition system, and the infrared thermovision system, described previously for the bench-top rig application, are the same systems used for the annular rig. However, a more sophisticated lamp out detection system is used on the annular rig. It consists of

an IBM PC AT and other equipment to monitor voltages and current to each of the SCR's, as well as to the 16 lamp sectors. Results are displayed on the computer screen, and if an upper or lower limit is exceeded, an alarm is sounded.

Annular Rig Test Results

A power versus time curve was determined that simulated an actual engine mission thermal cycle on the test liner, a stacked-ring louver configuration fabricated from Hastelloy-X and supplied by P&WA.. The power history for the thermal cycle is shown in figure 7. The cyclic test conditions were a coolant flow rate of 5.5 lb/sec, a coolant flow temperature of 600 °F, a minimum power of 38 percent (actual), and a maximum power of 83 percent (actual). The total thermal cycle time was 2.2 minutes. The time was broken up into a 6-sec ramp up time from minimum to maximum power, a 60-sec hold time at maximum power, a 6-sec ramp down time. and a 60-sec hold time at minimum power. This power history was programmed into the dual-loop programmable controller. The controller was run in the set-point control mode.

Of the large quality thermocouple and IR temperature data base obtained, some typical thermocouple data are shown in figures 8 and 9. The data shown are the hot side and cool-side temperatures at maximum and minimum power. Figure 10 shows transient temperature response at three locations on louver 5 of the liner. For the 6-sec ramp up in power there was about a 25-sec time required for the liner temperature to reach equilibrium conditions, or about a 20-sec lag between the time to maximum power and stable peak liner temperatures. The 6-sec ram down-time results in an almost mirror image of the ramp up in terms of time for the liner to reach stable minimum temperatures. The ramp up and the ramp down times simulate the ascent and descent phases of an engine mission cycle, and the hold time represents cruise conditions, where the interaction of creep and plasticity occur simultaneously. These temperatures are used in the heat-transfer/structural analysis of the liner.

The infrared thermovision system is used to obtain a more detailed map of the cool-side liner temperatures. Figure 11 is an example of the IR data obtained. plotted are axial temperatures on the louver No. 4. Only the temperatures are shown for the maximum and minimum powers at steady-state conditions of the thermal cycle. Thermocouple data are also shown for comparison.With this system over 10^7 temperature measurements are obtained for each thermal cycle.

In addition to the temperature data obtained, dimensional measurements were made on the original liner and at several points during testing. Photographs were also taken which show the relative distortion of the liner as the test progressed. A plot of the relative radial displacement measurements on louver 5 at 300, 742, and 1800 cycles is shown in figure 12. Obtaining a set of these measurements is tedious and required several weeks of downtime for the test program. For this reason and to add to the overall information, photographs were made of the louvers between runs.

A composite photograph of the inside louvers of the liner after 1031 cycles is shown in figure 13. Very little distortion was evident and no cracks were found. Because of the minimal distortion of the liner, it was decided to increase the strain by increasing the maximum temperature reached in the test cycle. The maximum power setting for the test cycle was increased from 83% to 87%. This raised the overall thermocouple reading 70 to 1610 °F with one hot spot temperature jumping 180 to 1890 °F. As a result, the liner distortion was accelerated.

After 1603 cycles a crack developed in the liner as shown in figure 14. This crack occurred in a hot spot and was also in the vicinity of the weld on that louver. The hot spot developed because of closure of several cooling holes as shown in Figure 15. There was no thermocouple right at the hot spot but the maximum temperature was at least 1720 °F and could have been over 1890 °F.

A composite photograph of the liner after 1782 cycles is shown in Figure 16. This shows that most of the distortion occurs in louvers 4, 5, 6, and 7 in the 1 80° and 270° views. The top (0°) and 90° views show much less distortion.

The effect of this distortion on the air flow through the liner can be seen in figure 17. The distortion partially blocks the flow of air from the holes on the exterior of the liner. This results in hot spots and the attendant distortion.

The test program on this liner was terminated after 1782 cycles because the distortion of the louvers became severe enough to contact the frame of one of the quartz lamp banks. Measurements of the crack from the initial observation at 1603 cycles to 1728 cycles indicated 2% increase in length.

The distortion of the louvers is not atypical of liners run in service. The distortion shows some symmetry to the heat pattern of the lamps in that the peaks of distortion are at the longitudinal center of a lamp bank where the maximum heat flux occurred. It should be noted that a distortion peak was not formed at every bank of lamps.

Of the 112 original quartz lamps, only a few remained after the testing. Criteria for lamp replacement were excessive darkening of the glass envelope or sagging filaments. Based on the cumulative failures to date, a statistical analysis predicts a lamp half life of 65 hours.

TEST LINER ANALYSIS

The liner surface temperature measurements obtained from the thermocouples and the infrared thermovision system were used first to obtain the film coefficients on the cool and hot surfaces. Based on these coefficients, a heat-transfer analysis was performed using MARC, a general-purpose, nonlinear, finite-element heat-transfer and structural-analysis program. A two-dimensional. axisymmetric, transient, heat-transfer analysis of the louver was performed. Eight-node, heat-transfer finite elements were used in the analysis, and 107 elements and 522 nodes were used to model the louver. Comparisons between prediction and experimental data shows good agreement at the maximum power level, but at the lower power level the prediction was not quite as good.

The MARC program produces a tape which contains the temperature information The temperatures (or thermal loads) are then input to the structural-analysis program. The MARC program was also used to perform the structural analysis. A two-dimensional axisymmetric transient structural analysis of the louver was performed. Eight-node-structure finite elements were used in the analysis. The stress model was identical to the heat-transfer model. Symmetric boundary conditions were assumed at the ends of the louver. Walker's viscoplastic constitutive model was used in the analysis. This viscoplastic model, and others like it, accounts for the interaction between creep and plasticity, strain rate effects, time-independent and time-dependent effects, and other effects critical to a combustor-liner analysis and design.

Figure 18 shows hysteresis loops of hoop stress versus hoop strain for three locations on the liner: seam weld, lip, and knuckle. The data show a wide variation in strains, strain ranges, strain rates, as well as stresses and stress ranges. These data could be used to identify critical failure locations in a liner and provide for better damage or fatigue/failure predictions.

CONCLUSIONS

The high temperature structures laboratory is operational. A large quality data base on Hastelloy-X has been generated. The bench-top quartz lamp rig and the annular quartz lamp rig are also operational. Tests of a conventional sheet metal louver liner in the annular rig have been completed. Almost 1800 thermal cycles were accumulated on the liner before liner testing was terminated due to gross distortion on the liner. Liner temperatures were stable and repeatable not only for each thermal cycle but from test to test. Observed liner distortion simulated very well that of an in-service liner. By varying test conditions the distortion to the liner was accelerated. Cracking on the liner occurred at a seam weld between 1500 and 1600 thermal cycles. The cracks on the liner did not grow appreciably during the additional 200 or so thermal cycles. A large quality data base consisting of measured liner temperatures and displacements has been obtained. The temperature data obtained from thermocouples and the infrared camera are being analyzed and used in a preliminary heat-transfer analysis of the liner. Preliminary nonlinear, structural analyses are also being performed using as input the thermal loads obtained from the thermal analyses. A UTRC laser specklegram system and a high resolution camera system for measuring strain in a flat plate have been evaluated using the bench-top rig. The data are being reduced and analyzed. Preliminary 2-D thermal and nonlinear structural analyses of the test plate are being performed. In conclusion, both the annular and bench-top quartz lamp rigs are viable tools for high temperature cyclic structural testing of combustor liner segments and flat plates.

FUTURE RESEARCH

An advanced segmented combustor liner is being instrumented with 140 thermocouples. Testing of this liner in the annular rig should begin by December. Plans are also to test straight cylindrical specimens. Advanced, high-temperature strain gages and a high resolution camera system will continue to be evaluated on the bench-top rig. High-temperature torsional testing on a biaxial test machine is scheduled to begin in early November. A three-dimensional thermal/structural analysis of the conventional test liner will soon be underway.

HIGH-TEMPERATURE FATIGUE AND STRUCTURES LABORATORY

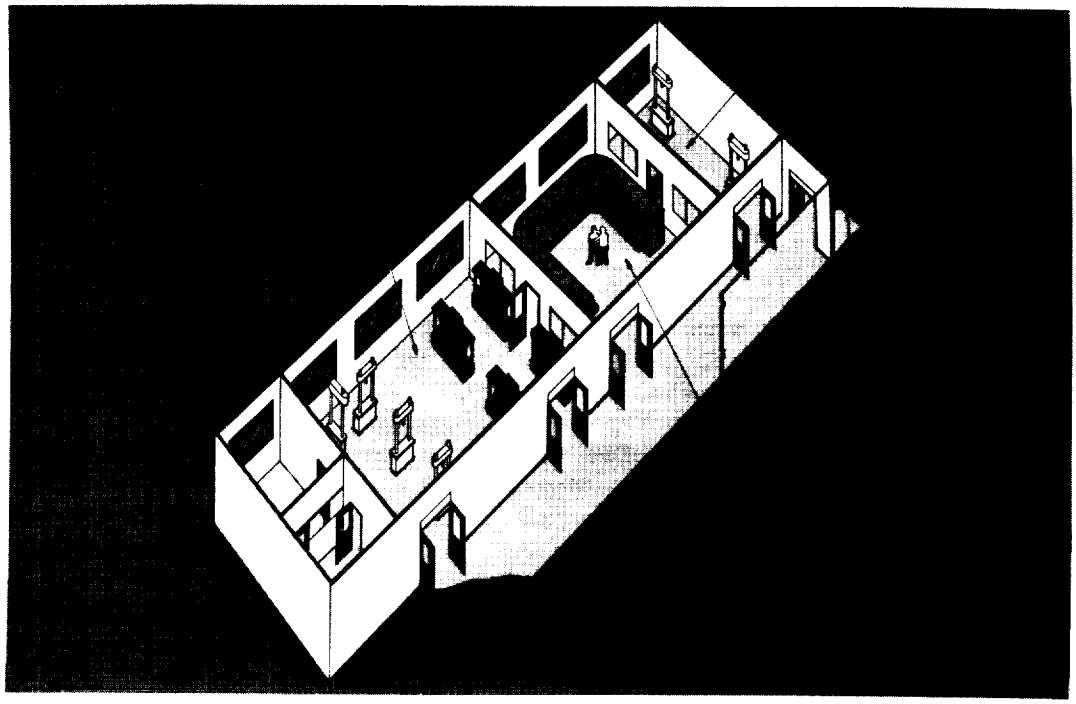

CD-86-22256

Figure 1

BENCH-TOP QUARTZ LAMP RIG

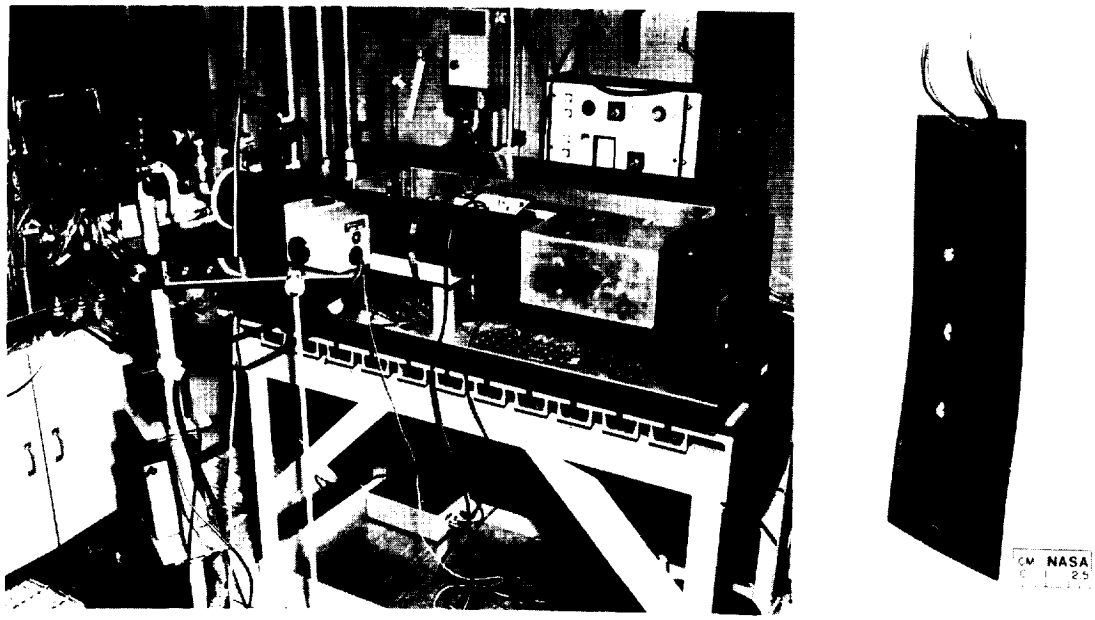

Figure 2

ANNULAR QUARTZ LAMP RIG

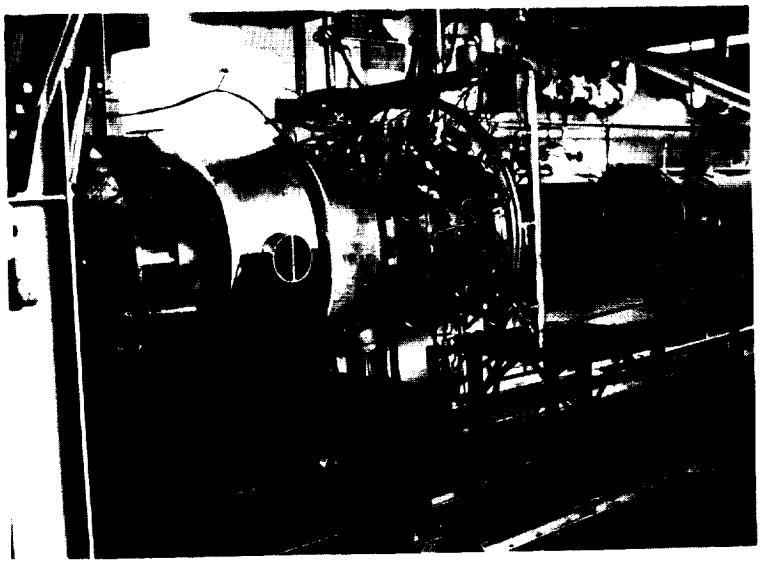

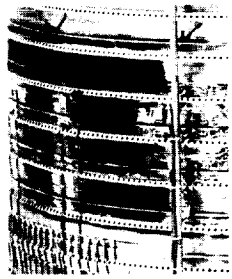

20-IN. DIAM CYLINDRICAL SPECIMEN

CD 86 22253

Figure 3

COMPARISON OF OUT-OF-PHASE UNIAXIAL THERMOMECHANICAL EXPERIMENTAL DATA AND UNIFIED MODEL PREDICTIONS

HASTELLOY X FOR TEMPERATURE RANGE OF 400 - 600 ^{o}C

(752 - 1112 ^{o}F); STRAIN RATE, 0.00005/SEC; 1 KSI = 5.9 MPA

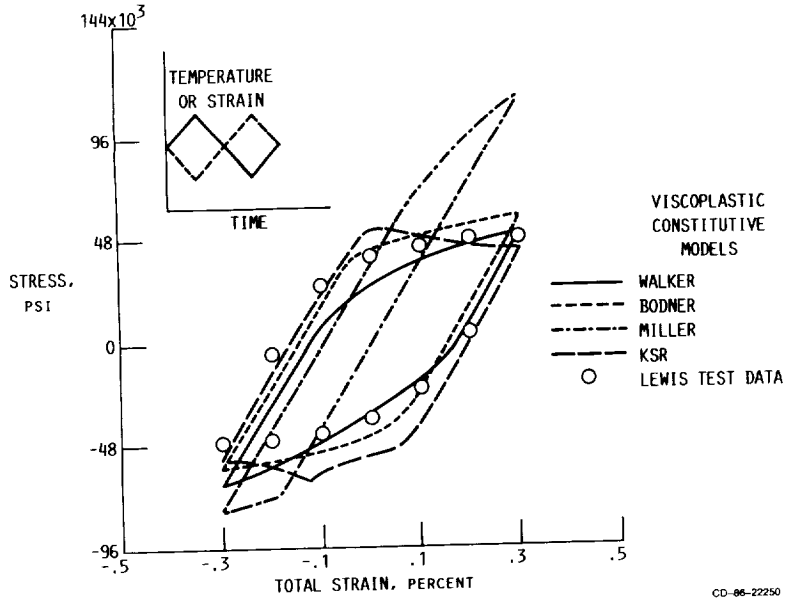

CD-86-22250

Figure 4

PLATE SHOWING GRID SYSTEM

NOTE BORON FIBERS AT 45° WITH SHADOWS ON PLATE

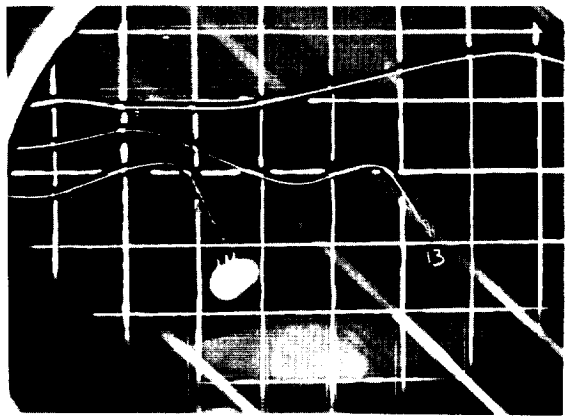

CO-86-22245

Figure 5

QUARTZ LAMP HEATING SYSTEM

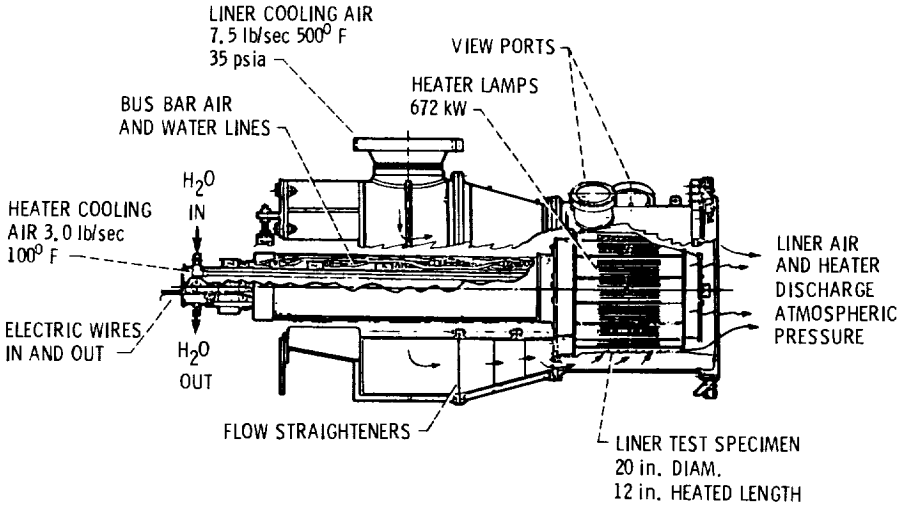

CS-85-3431

Figure 6

POWER HISTORY FOR THERMAL CYCLE

COOLANT FLOW RATE, 5.5/SEC; COOLANT FLOW TEMPERATURE, 600 ^{o}F

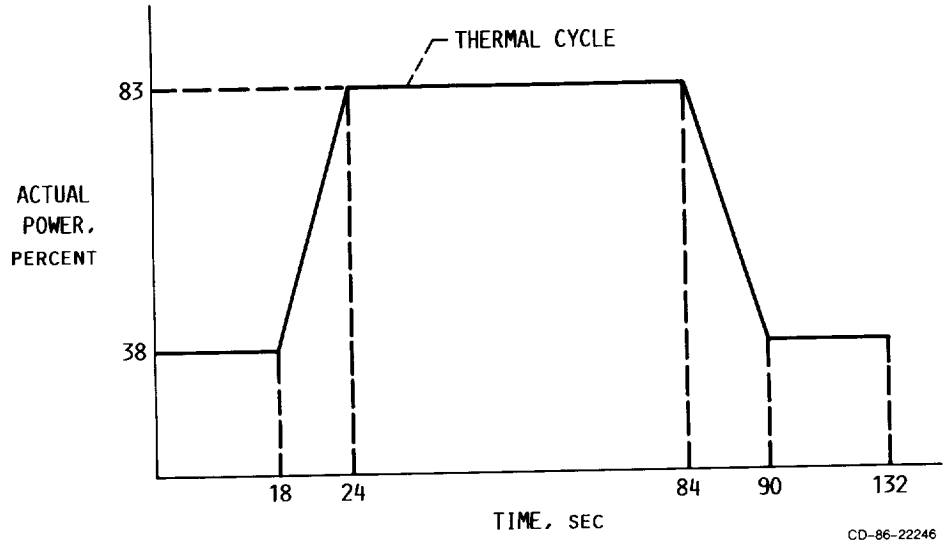

Figure 7

CYCLIC SURFACE LINER TEMPERATURES AT THREE LOCATIONS ON LOUVER 5

THERMOCOUPLE DATA

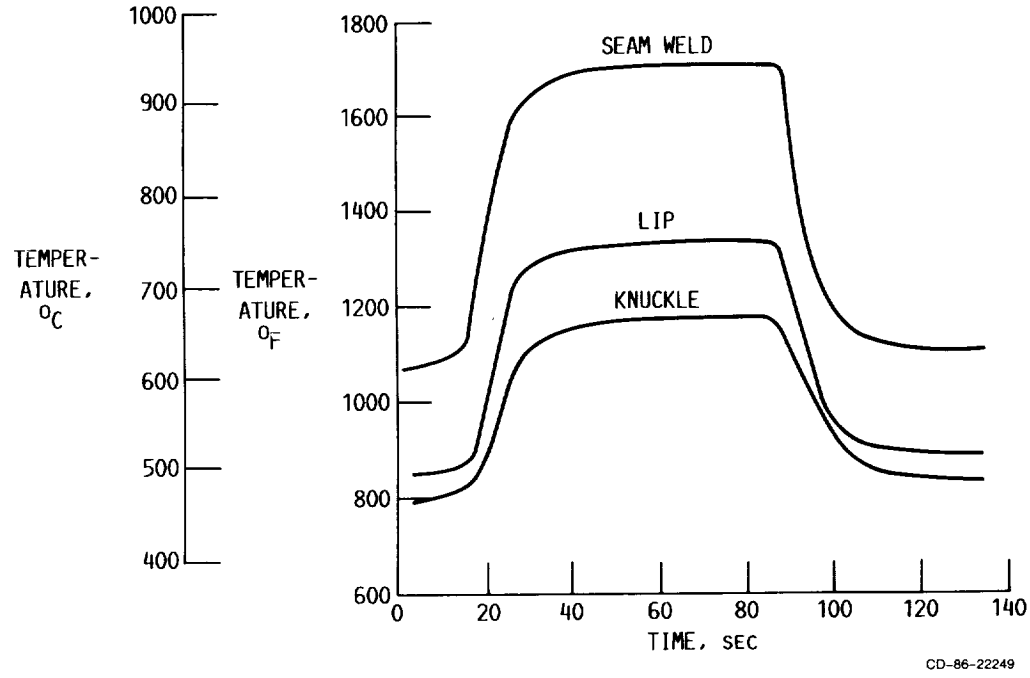

Figure 8

HOT SURFACE AXIAL LINER TEMPERATURES

LOUVERS 4 AND 5

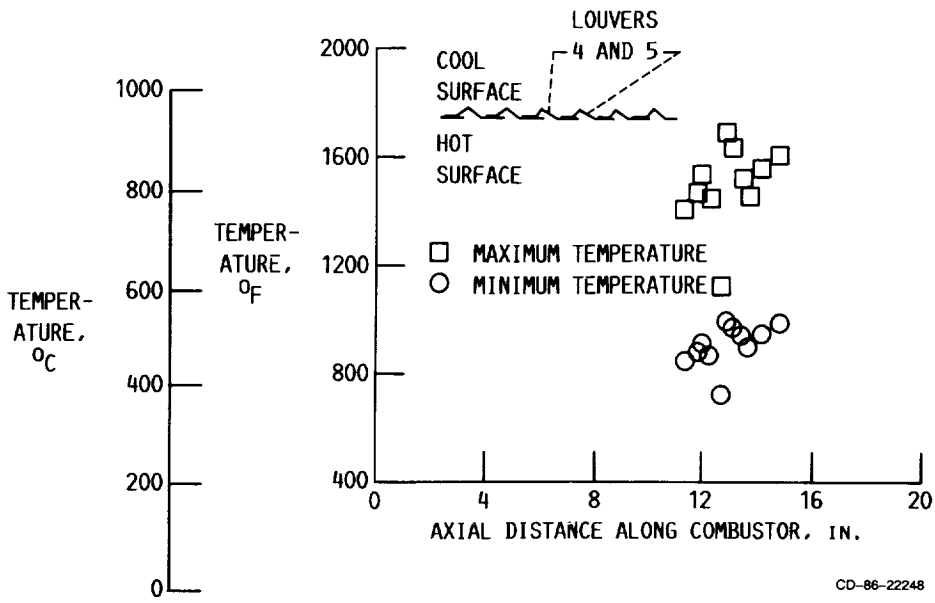

Figure 9

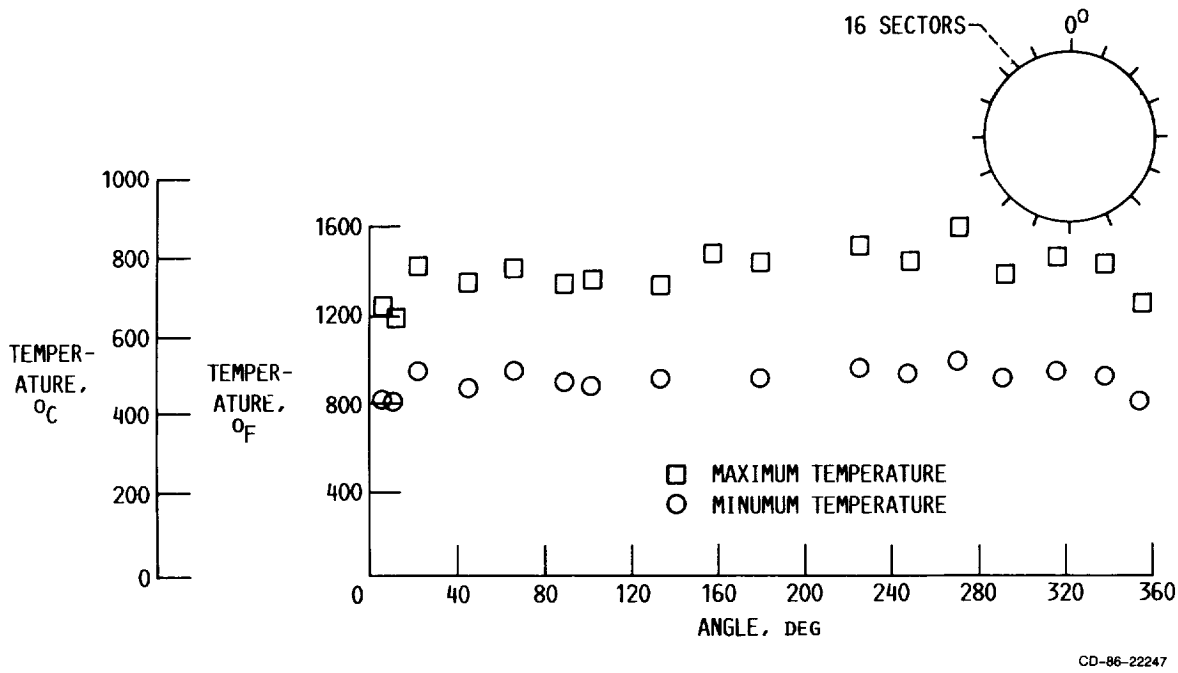

Figure 10

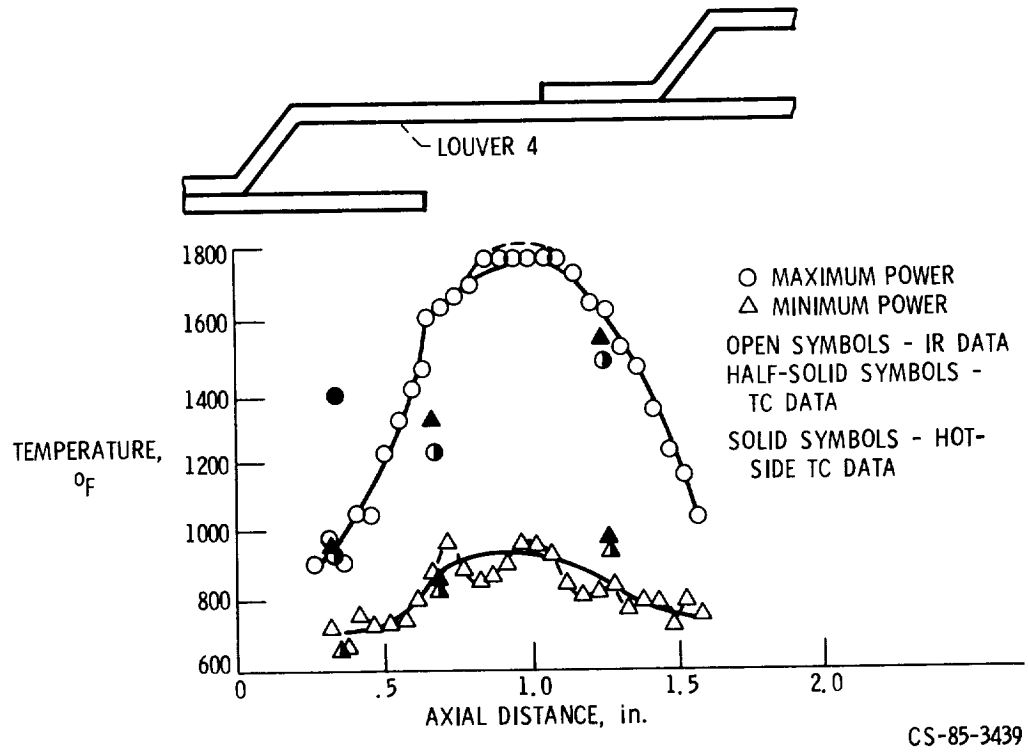

Figure 11

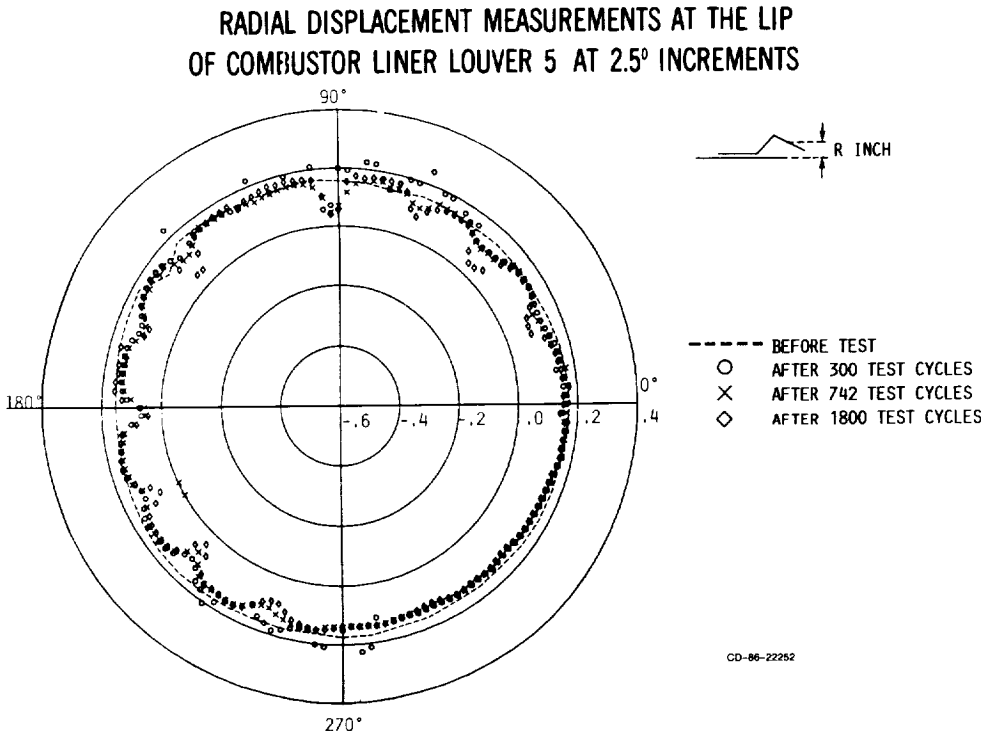

Figure 12

COMPOSITE PHOTOGRAPH OF LOUVERS INSIDE COMBUSTOR LINER AFTER 1031 CYCLES

NOTE THE RELATIVELY SMALL DISTORTION OF LOUVERS

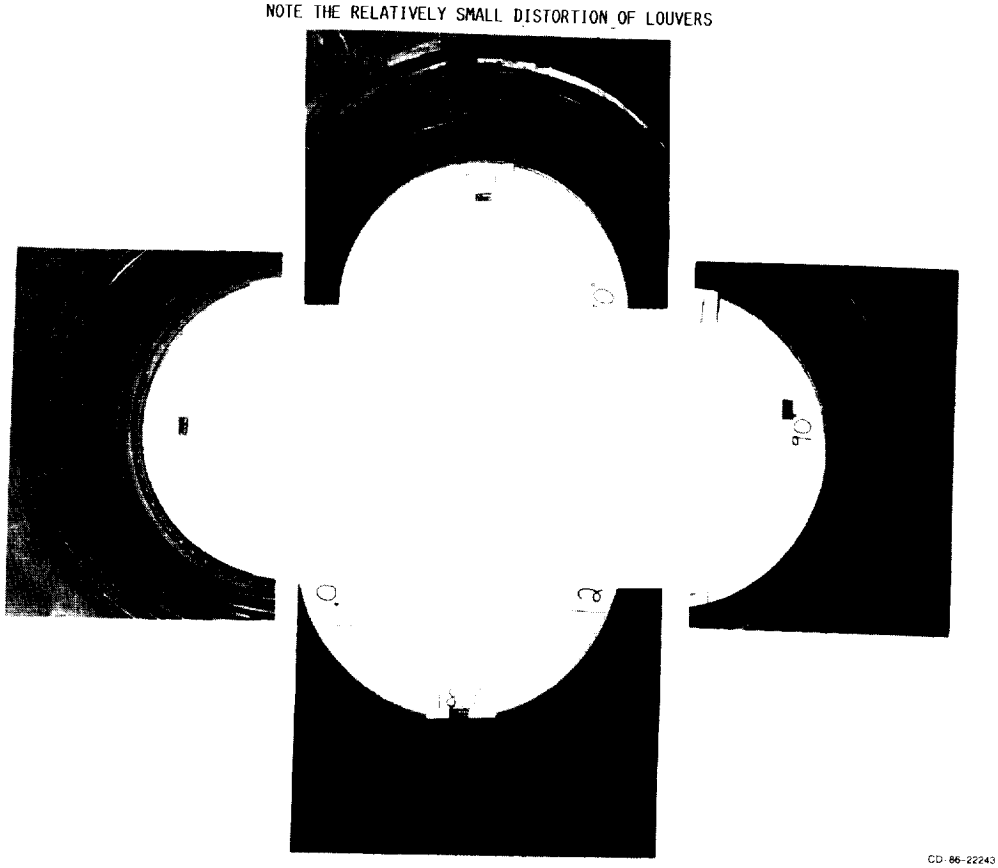

CD-86-22243

Figure 13

CRACK WHICH INITIATED IN LOUVER 5 BEFORE THE 1603rd CYCLE

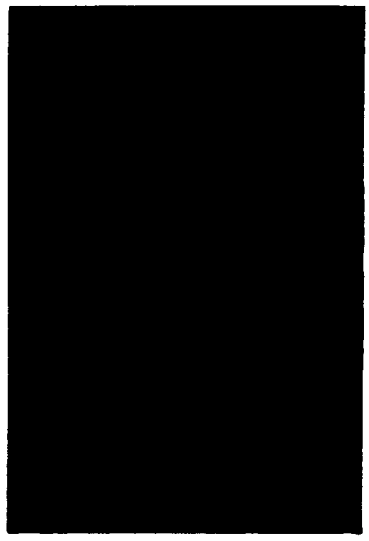

CD-86-22240

Figure 14

CLOSURE OF COOLING HOLES WHICH CAUSED HOT SPOT AND CRACK IN INSIDE LOUVER

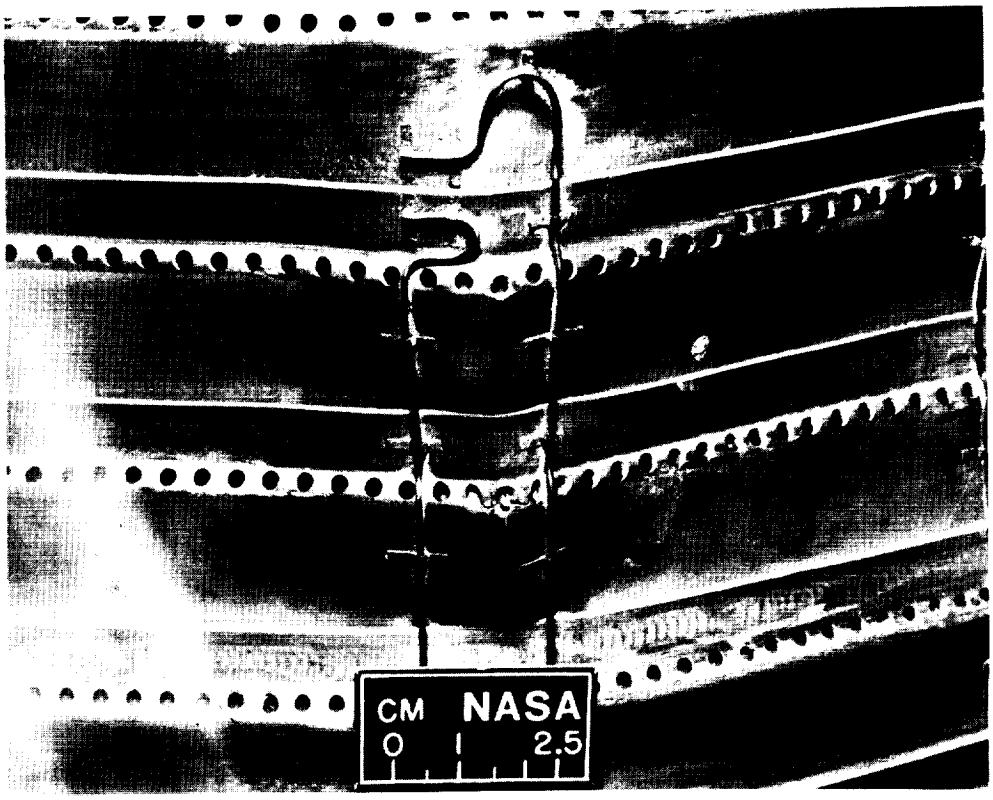

CD-86-22244

Figure 15

COMPOSITE PHOTOGRAPH OF LOUVERS AFTER 1782 CYCLES

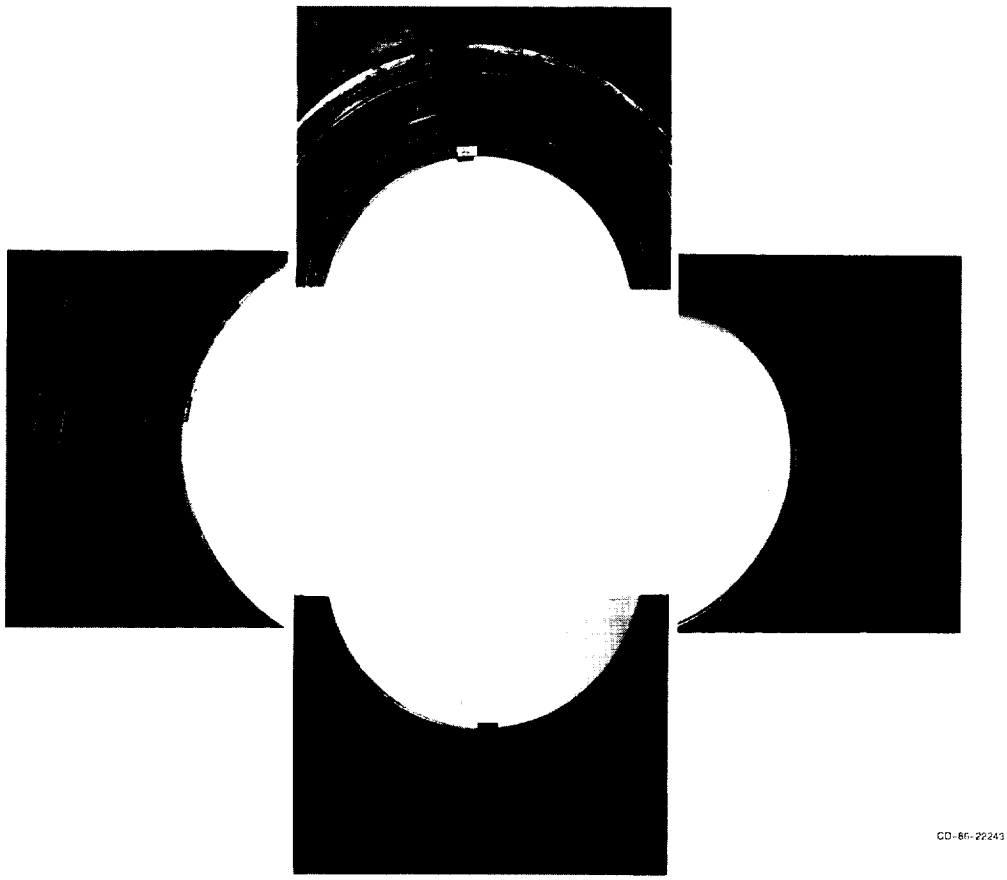

CO-86-22243

Figure 16

INSIDE OF COMBUSTOR
NOTE EFFECT OF DISTORTION OF LOUVERS ON AIR FLOW

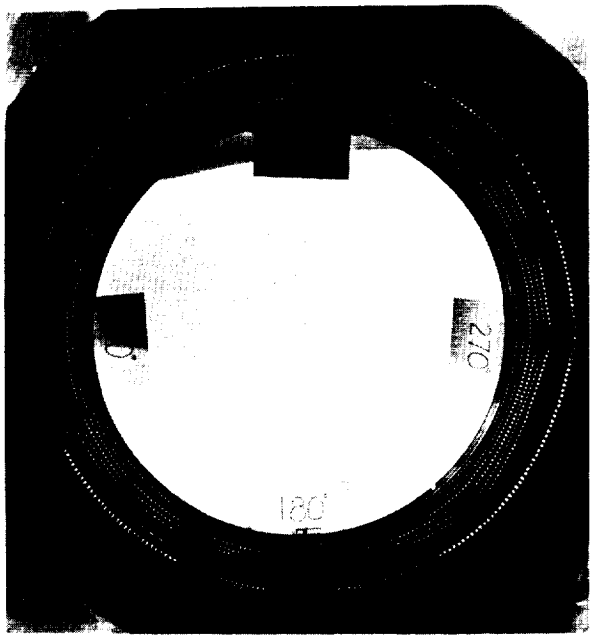

CD-86-22242

Figure 17

REPRESENTATIVE 2-D COMBUSTOR LINER HYSTERESIS LOOP PREDICTIONS OF LOUVER 5 USING THE WALKER MODEL

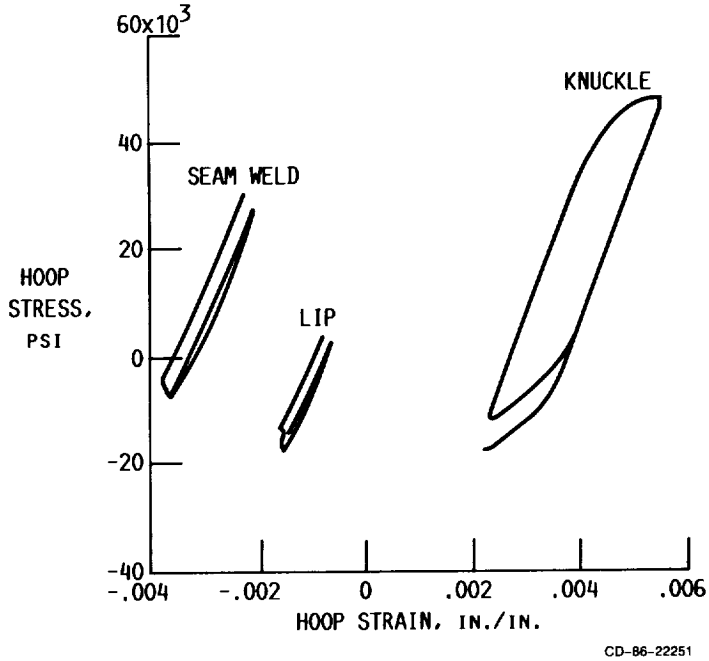

CD-86-22251

Figure 18

CREEP FATIGUE LIFE PREDICTION FOR ENGINE HOT SECTION MATERIALS (ISOTROPIC) - FOURTH YEAR PROGRESS REVIEW*

Richard S. Nelson and John F. Schoendorf
United Technologies Corporation
Pratt & Whitney

INTRODUCTION

As gas turbine technology continues to advance, the need for advanced life prediction methods for hot section components is becoming more and more evident. The complex local strain and temperature histories at critical locations must be accurately interpreted to account for the effects of various damage mechanisms (such as fatigue, creep, and oxidation) and their possible interactions. As part of the overall NASA HOST effort, this program is designed to investigate these fundamental damage processes, identify modeling strategies, and develop practical models which can be used to guide the early design and development of new engines and to increase the durability of existing engines.

This contract has recently been modified to be a 6-year effort, comprising a 2-year base program and a 4-year option program. Two different isotropic materials (B1900+Hf and INCO 718) will be utilized, along with two protective coating systems (overlay and diffusion aluminide). The base program (ref. 1), which was completed during 1984, included comparison and evaluation of several popular high-temperature life prediction approaches as applied to continuously cycled isothermal specimen tests. The optional program, of which two years have been completed, is designed to develop models which can account for complex cycles and loadings, such as thermomechanical cycling, cumulative damage, multiaxial stress/strain states, and environmental effects.

THERMOMECHANICAL MODEL DEVELOPMENT

A significant task under the optional program is the development of a damage model which is valid under conditions of thermomechanical fatigue (TMF). A total of 32 uncoated and 9 NiCoCrAlY overlay coated TMF specimen tests have been completed so far, covering variables such as strain range, temperature range, mean strain, cycle type, and hold times. Some of the non-standard cycle types used (such as elliptical and dogleg cycles) have demonstrated that TMF damage cannot always be predicted in the same manner as isothermal tests; the chosen model must be sensitive to accumulation of damage from several different sources throughout the cycle.

Six fully reversed TMF specimen tests have been completed at two nominal strain ranges, using both in-phase and out-of-phase cycling. The temperature range was 538-871°C. (1000-1600°F.), and the rate was 1 CPM. A plot of initiation life vs. total mechanical strain range is shown in figure 1, along with median life data from isothermal baseline tests at the same cyclic rate. As expected, the TMF results are lower in life than isothermal data from even the maximum cycle temperature. Note also that the difference in life between in-phase and out-of-phase cycling is a function of strain range; at lower strain ranges, the in-phase cycling produces higher life, while at the higher levels, the out-of-phase life is higher. Obviously, the number of data points in this set is limited, but this behavior has also been

*Work done under NASA Contract NAS3-23288

noted during other TMF testing. This serves to emphasize the need to understand and model the actual damage mechanisms active under these conditions; simple data correlations based on one or the other cycle type may not always give conservative predictions.

In order to provide insight into the relationship between mean strain and TMF life, a series of 7 tests was completed using one-way strain cycling. Five of these tests were run at R=0 conditions, and two were run using R=-infinity. Figure 2 shows a comparison between the results of the one-way tests and the fully reversed TMF data for out-of-phase cycling. The ordering of the life curves follows the expected trend, with the R=0 tests producing the lowest lives and the R=-infinity being the highest. However, as shown in figure 3, the R=0, in-phase tests showed no significant difference relative to the fully reversed in-phase tests; in fact, they appeared to be slightly higher in life. This may be due to inherent scatter in the limited data set, or it may be caused by competing damage mechanisms.

The dogleg TMF test (rapid strain cycling at minimum or maximum temperature, followed by strain hold in tension or compression during thermal cycling), was conceived as an intermediate step between an isothermal hold test and a traditional TMF test. Six specimens were tested using such cycles, and their initiation lives are shown plotted on figure 4 along with comparable isothermal and TMF (in-phase and out-of-phase) median test results. The dogleg tests with the hold in compression ("LC" & "HC") are about 2X higher in initiation life than the isothermal compression hold tests. However, the lives from the tension hold dogleg tests ("LT" & "HT") are nearly four times lower than those of similar isothermal tests. By using the median lives from the in-phase and out-of-phase TMF tests, the solid trend line shown on this figure can be drawn, and it is obviously opposite to what was found during the isothermal testing. It is therefore clear that the non-isothermal hold has a significant influence on specimen life, no doubt by activating different damage mechanisms as the temperature varies.

Perhaps the most interesting results obtained so far under this task are those from the elliptical cycle tests (strain and temperature are sinusoidal with time and shifted in phase by +/-135 degrees). Eight specimen tests were completed under this series, including both clockwise (CW) and counterclockwise (CCW) cycles. The CCW cycle is a good simulation of the strain-temperature history experienced by many actual hot section components. Although there are some components which have a CW movement around their strain-temperature history, the CW cycle results are most valuable when compared to the CCW results; the only apparent difference is the direction of motion around the loop. Figure 5 shows a plot of the elliptical test results, and it is clear that there is a large life difference between the two types of cycles. Note that life prediction methods based solely on the extremes of the cycle will not be able to predict this behavior, since they cannot distinguish between these two cycles. To account for such cycle dependent effects, an advanced incremental form of the CDA life prediction model is under development which can be integrated around any arbitrary strain-temperature history curve. This model is undergoing evaluation and refinement at the present time.

MULTI-AXIAL STRESS STATE MODEL

Another of the optional tasks is the development and verification of a multi-axial stress state creep-fatigue life prediction model. A fatigue test program which consists of 26 isothermal strain controlled tests utilizing B1900+Hf thin-walled tubular specimens is being conducted to provide crack initiation data. Four types

of strain cycles are employed in the tests: simple tension, simple torsion, combined tension-torsion in-phase (proportional loading) and combined tension-torsion 90° out-of-phase (non-proportional loading). The torsion to tension strain ratio in the combined strain tests is 1.5. The idealized strain paths in $\epsilon - \gamma$ space for these cycles are shown in figure 6. Two temperature levels, 871°C (1600°F) and 538°C (1000°F), and two frequency levels, 10 CPM and 1 CPM, are being investigated to determine their effect on the cracking behavior and possible changes in stress state dependence. The variation in fatigue life with strain range is also being investigated.

To date, a total of 16 multiaxial specimen tests have been completed. The results are presented in Table I. The tensile test results are similar to those obtained on solid cast uniaxial specimens tested in the base program. This demonstrates the capability of producing consistent fatigue data with the multiaxial test rig and specimen.

Multiaxial fatigue theories that relate to the physical damage processes have shown promise. Therefore, the resultant physical damage has been studied closely by monitoring fatigue crack initiation and growth during test through the use of cellulose acetate surface replicas and by post-test fractographic analysis. These observations indicate that for this material, multiaxial fatigue cracks initiate and grow mainly on planes perpendicular to the maximum normal strain under all loading conditions although some crack growth along maximum shear planes occurs at 538°C (1000°F). Therefore, a single parameter that is consistent with the cracking mode, maximum normal strain, has been used to correlate the test results (figure 7). It can be seen that there is considerable overall scatter in the two temperature groupings of data, but the results for the four strain cycles are intermingled. Other investigators (ref. 2) have consistently found out-of-phase tension-torsion loading to be more damaging, especially with a 90° phase angle, than in-phase loading. Damage from non-proportional loading may depend on a number of variables such as material, temperature level and strain amplitude and, therefore, may be difficult to characterize. Metallographic observations indicate that extensive rubbing of opposing fracture surface features occurred during the 90° out-of-phase tension-torsion tests; examinations of these specimens by SEM have not provided useful information concerning the crack initiation sites.

Trial data correlations have also been accomplished using other potential multiaxial fatigue parameters such as equivalent strain, maximum shear strain and plastic work per cycle (ref. 3) with limited success. None of the parameters produced an acceptable correlation of the test data, due in part to their inability to properly account for the pure torsion tests which resulted in significantly higher fatigue lives. In addition, during the determination of the plastic work, the hysteresis loops for B1900+Hf exhibited little plasticity even for fatigue tests that resulted in fairly low lives, as shown in figure 8. This situation caused plastic work calculations to be very critical, and fatigue life assessment to be extremely sensitive to small changes in experimental measurements or analytical calculations of cycle plasticity.

Part of the scatter in the data is due to the low life of the in-phase tension-torsion test of specimen 204 which may have been adversely affected by dross found at the initiation site (figure 9). Subsequent to this discovery, an inspection program was undertaken to screen 22 untested specimens using X-ray, fluorescent penetrant and visual inspection procedures. Although indications of minor subsurface shrinkage were found in most of the specimens, no surface or subsurface discontinuities were discovered that would disqualify these specimens.

Work is continuing to complete the 10 remaining specimen tests. Additional single and multiple parameters will be investigated to characterize the multiaxial fatigue behavior.

CUMULATIVE LOADING MODEL

Work under this task has been completed during the past year, based on the results of a total of 50 cumulative damage tests. These include block tests (one set of conditions for the first block of cycles, followed by a second set of conditions for the remainder), sequenced tests (alternating blocks of two different sets of conditions), and interrupted tests (fatigue cycling interrupted by periods of temperature exposure, either with or without load). The results of these tests show that some conditions obey a linear damage rule, while certain other conditions show a strong non-linear interaction. The non-linear damage accumulation method and the ductility fraction concept which were discussed at last year's workshop have been incorporated into the formulation of the CDA model to account for the observed interaction effects. It is expected that future refinements of these equations will continue to be made until the end of the optional program.

ENVIRONMENTAL ATTACK MODEL

An environmental creep-fatigue test program which consists of 27 tests utilizing B1900+Hf solid smooth baseline fatigue specimens has been determined for this optional task. Isothermal, fully reversed, strain controlled tests will be conducted in inert argon, in oxygen at partial pressures typical of that encountered in the engine hot section, and in laboratory air. The crack initiation results will be used to develop, evaluate and verify a model for prediction of environmental (oxidation) effects on the creep -fatigue life.

Test results from previous tasks were reviewed to determine test conditions that would activate the various damage processes, including oxidation. The program incorporates two temperature levels, 982°C (1800°F) and 871°C (1600°F), and two strain rates, 1.67×10^{-3} sec^{-1} and 1.67×10^{-4} sec^{-1}. Testing will be done in two stages: 1) screening tests will be run to determine the alternative environment (inert argon or pressurized oxygen) with the greatest effect, and 2) utilizing this alternative environment in conjunction with laboratory air by varying the length and order of exposure to demonstrate the effects of the environment at different stages in the development of a fatigue crack.

A stainless steel, low pressure test chamber (figure 10) has been designed and built to accommodate the planned environmental tests. The chamber has been subjected to an overpressure test which demonstrated its capability to withstand a maximum pressure at least 2X greater than the working pressure of 5 atmospheres.

The initial environmental experiments are scheduled to begin shortly using a test rig that is now being outfitted with the pressure chamber and other necessary accessories.

PROTECTIVE COATINGS MODELS

Under the modified version of this task, a total of 8 overlay coated specimens will be tested. Two such tests have been completed using one-way strain cycling: one at 1600°F and 10 CPM, and one at 1800°F and 1 CPM. The 1600°F test showed a significant increase in initiation life when compared to similar tests on uncoated specimens, but the separation life was essentially the same. However, the test which was

run at 1800°F showed approximately a 3X increase in both initiation and separation lives over the uncoated results.

CYCLIC MEAN STRESS MODEL

A total of 25 controlled mean stress tests are planned for this task, including five under TMF conditions. Two of these TMF tests have been completed using load control to achieve the desired mean stress. The mean stresses chosen were +30 and +10 KSI, and the resulting mean strain histories of these specimens are shown in figure 11. It can be inferred that a significant amount of creep damage occurred during these tests, and it is therefore not surprising that the lives were significantly reduced relative to strain controlled testing (by a factor of 40X for the +30 KSI test). The isothermal portion of this testing will be conducted at the University of Rhode Island by Professor Ghonem.

ALTERNATE MATERIAL TESTING

A rolled ring forging of AMS 5663 (INCO 718) material has been obtained for use in this portion of the program. A total of 70 isothermal tests (both monotonic and fatigue), 20 TMF tests, and 15 multiaxial tests are currently planned as part of this task. Machining of these specimens is well underway, and testing is scheduled to begin in the last quarter of 1986.

FUTURE TASKS

Further work is continuing on all the above tasks, with a view to producing a creep-fatigue model which is both practical and accurate. During the coming year, the focus of the efforts is planned to shift from generation of test data to analytical model development activities. The generation of CDA model constants for INCO 718 will be completed first, followed by additional refinement of the CDA life prediction model.

REFERENCES:

1. Moreno, V., Nissley, D. M., and Lin, L. S., " Creep Fatigue Life Prediction for Engine Hot Section Materials (Isotropic) - Second Annual Report," NASA CR-174844, March 1985.

2. Kanazawa, K., Miller, K.J. and Brown, M.W., "Low-Cycle Fatigue Under Out-of-Phase Loading Conditions", ASME Journal of Engineering Materials and Technology, Vol. 99, No. 3, July 1977, pp. 222-228.

3. Garud, Y.S., "A New Approach to the Evaluation of Fatigue Under Multiaxial Loadings, " ASME Journal of Engineering Materials and Technology, Vol. 103, April 1981, pp. 118-125.

TABLE I

MULTIAXIAL FATIGUE TEST RESULTS

Specimen Number	Temp. (°F)	Freq. (CPM)	$\Delta\epsilon$ (%)	$\Delta\gamma$ (%)	Phase Angle (Deg.)	Crack Initiation Life* (Cycles)
217	1600	10.0	±0.250	0.0	-	1150
222			±0.200	0.0	-	14,600
203			0.0	±0.404	-	8100
219			0.0	±0.361	-	40,000
204			±0.185	±0.260	0	350
218			±0.147	±0.220	0	6900
216			±0.250	±0.375	90	1250
205			±0.147	±0.220	90	11,700
220	1000		±0.338	0.0	-	1950
201			±0.260	0.0	-	4100
221			0.0	±0.675	-	1350
209			0.0	±0.500	-	20,100
223			±0.255	±0.382	0	2200
202			±0.338	±0.506	90	240
214			±0.250	±0.375	90	6100
215		1.0	±0.338	±0.506	90	500

*These lives are preliminary and subject to change as additional inspection data become available.

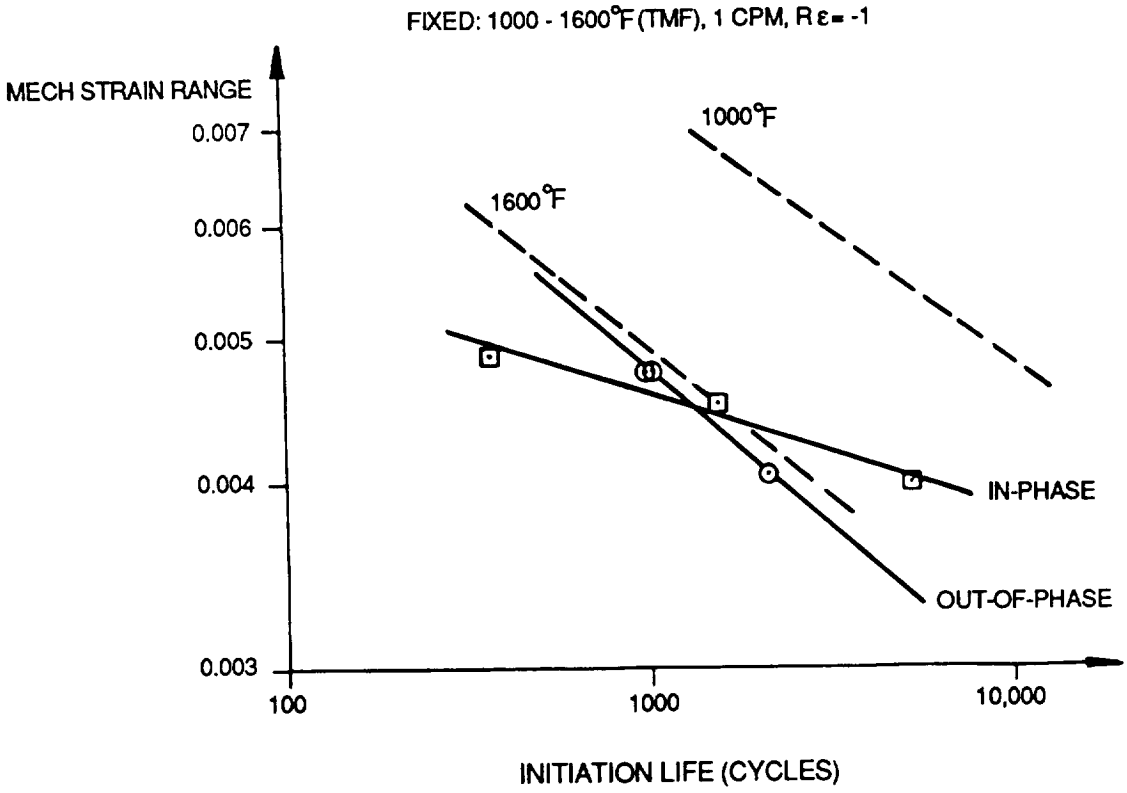

Figure 1 TMF Test Results for In-Phase and Out-of-Phase Cycles

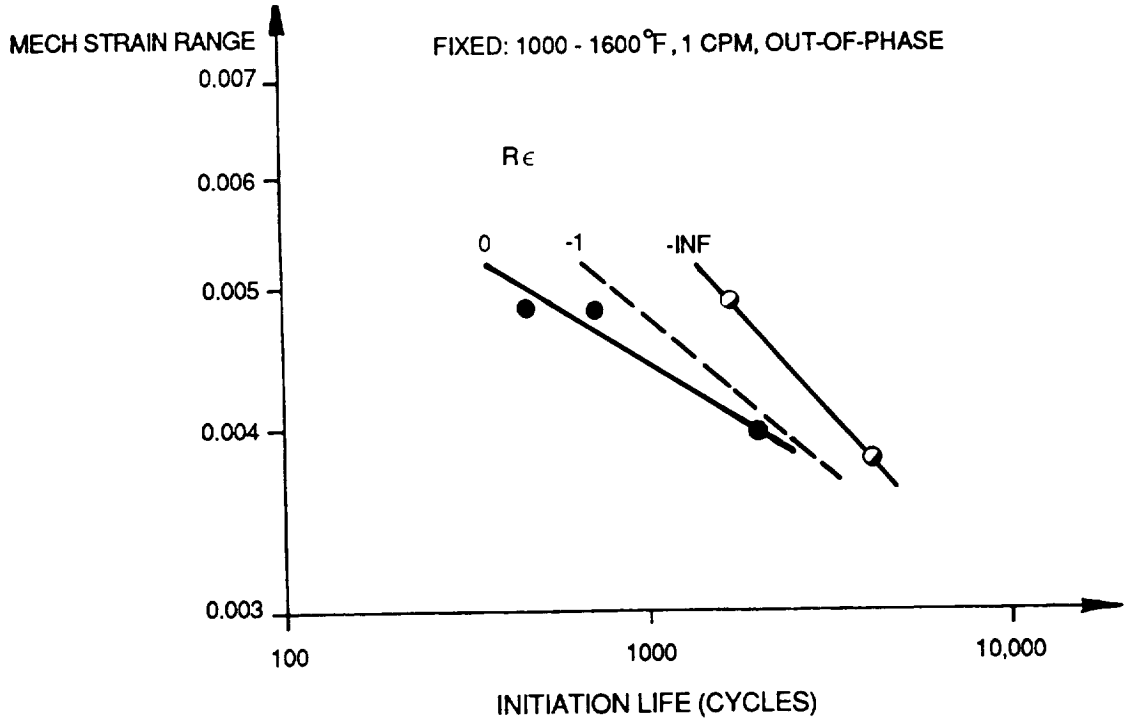

Figure 2 Strain Ratio Effect on Out-of-Phase TMF Tests

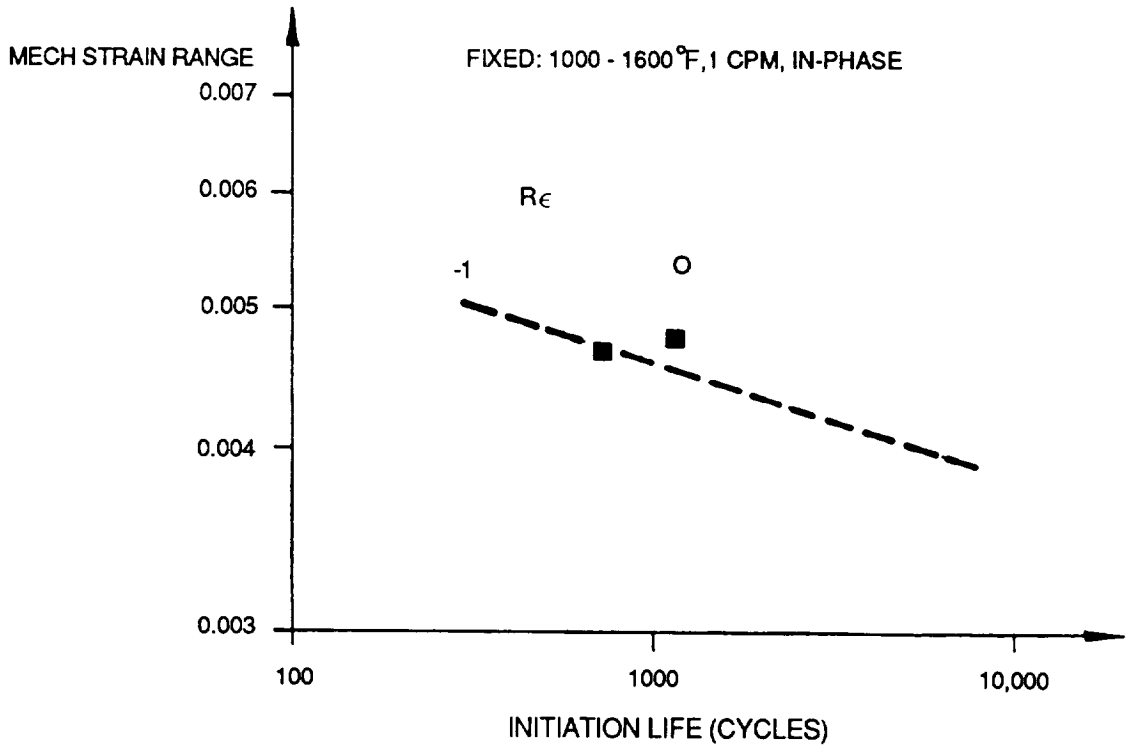

Figure 3 Strain Ratio Effect on In-Phase TMF Tests

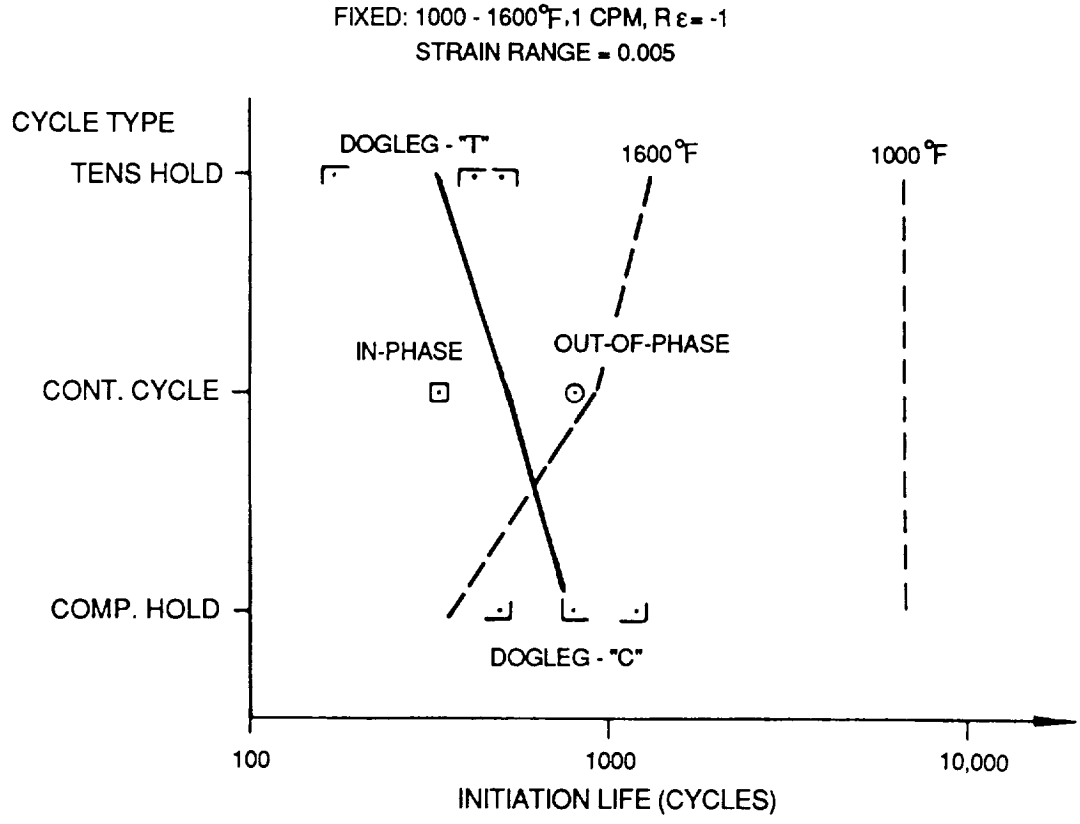

Figure 4 Dogleg TMF Test Results

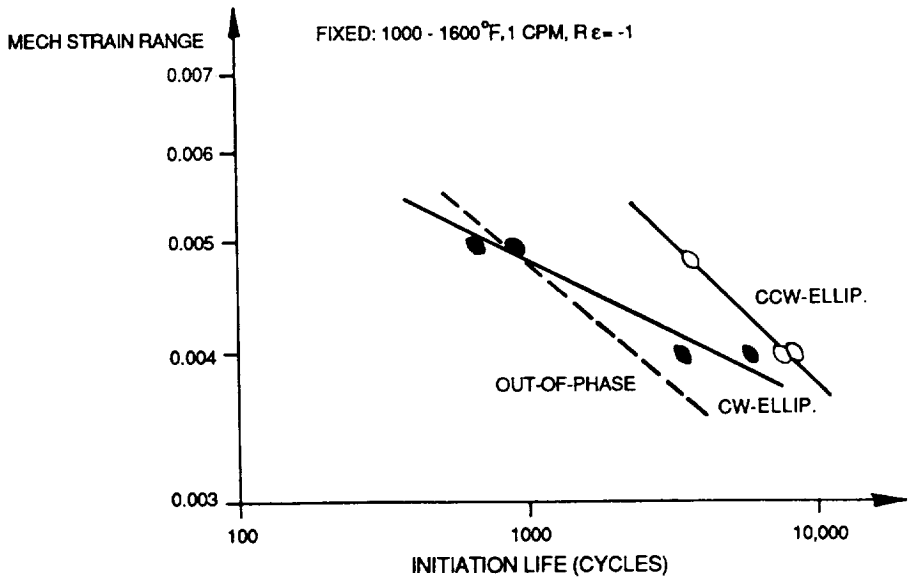

Figure 5 Elliptical Cycle TMF Test Results

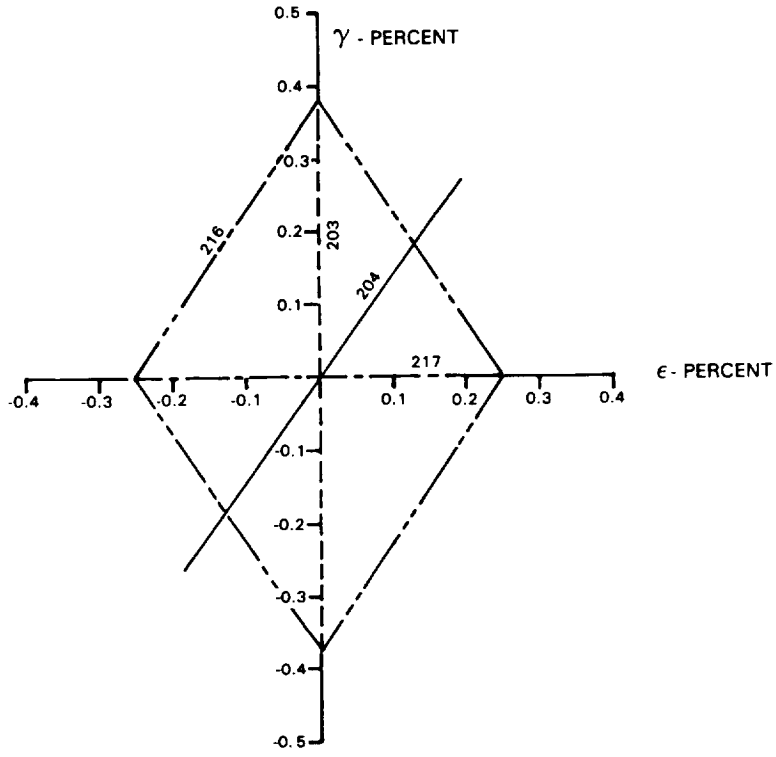

Figure 6 Multiaxial Test Specimen Strain Paths

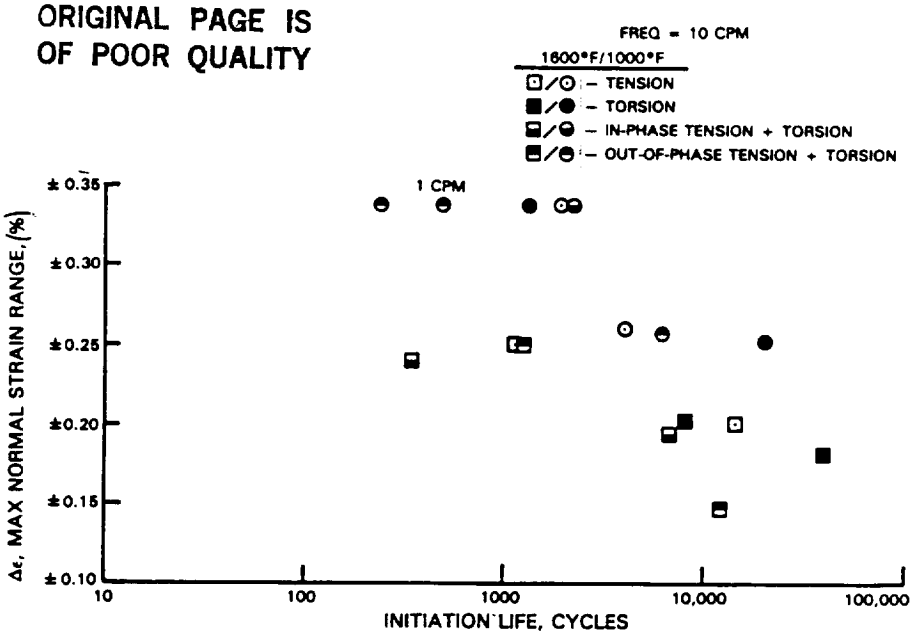

Figure 7 Maximum Normal Strain Range Versus Crack Initiation Life

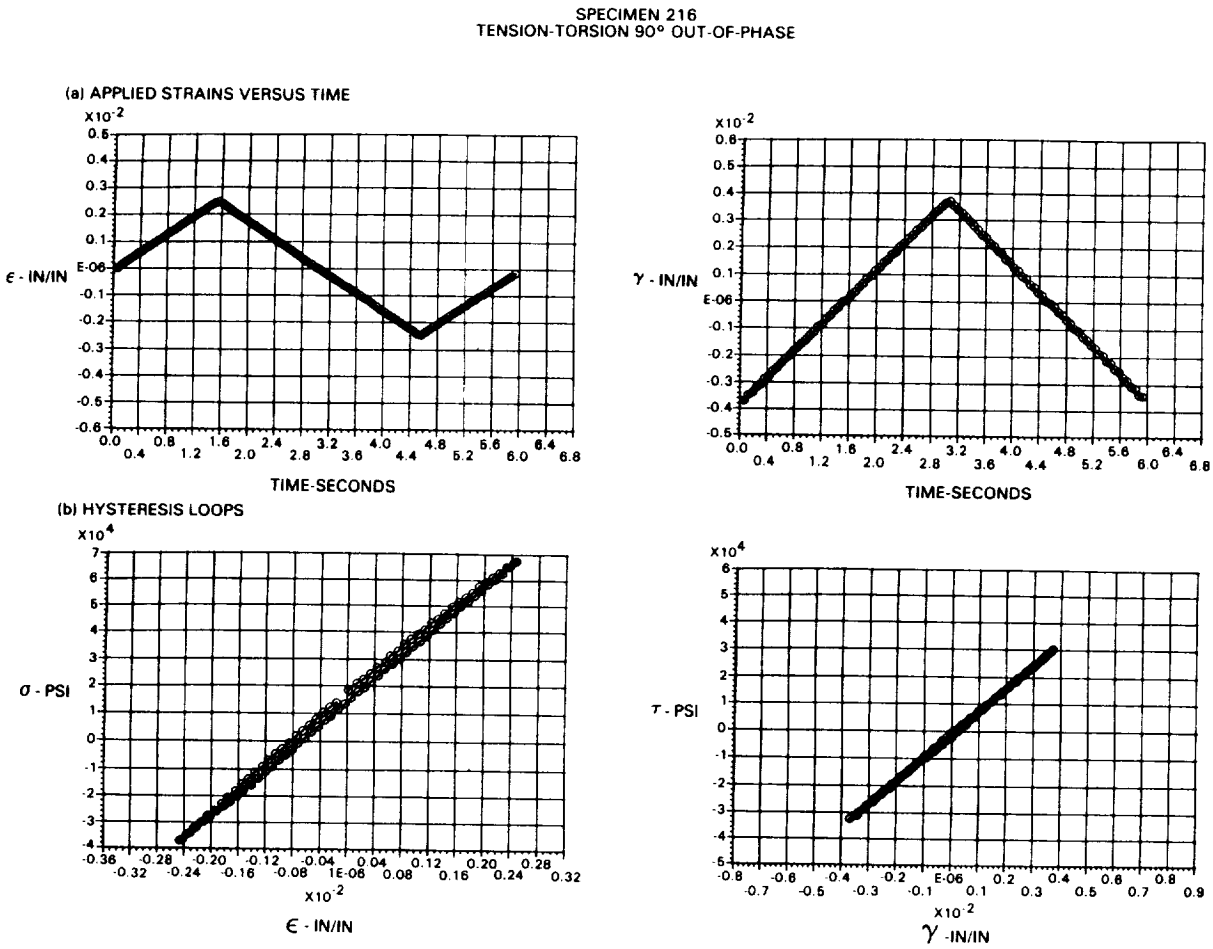

Figure 8 Specimen 216 Tension-Torsion 90° Out-of-Phase

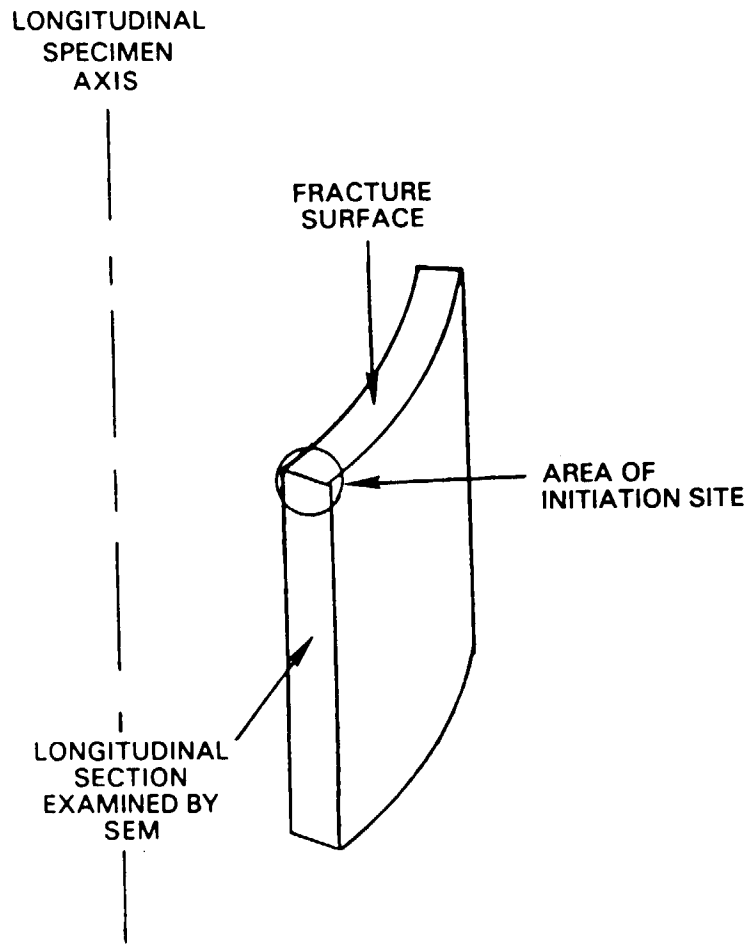

(a)

(b)

0.1 mm

Figure 9 Characterization of longitudinal section through initiation site.

(a) Schematic diagram showing orientation of section examined by SEM.

(b) SEM micrograph of longitudinal section at initiation site showing oxide buildup on fracture surface as well as in secondary crack.

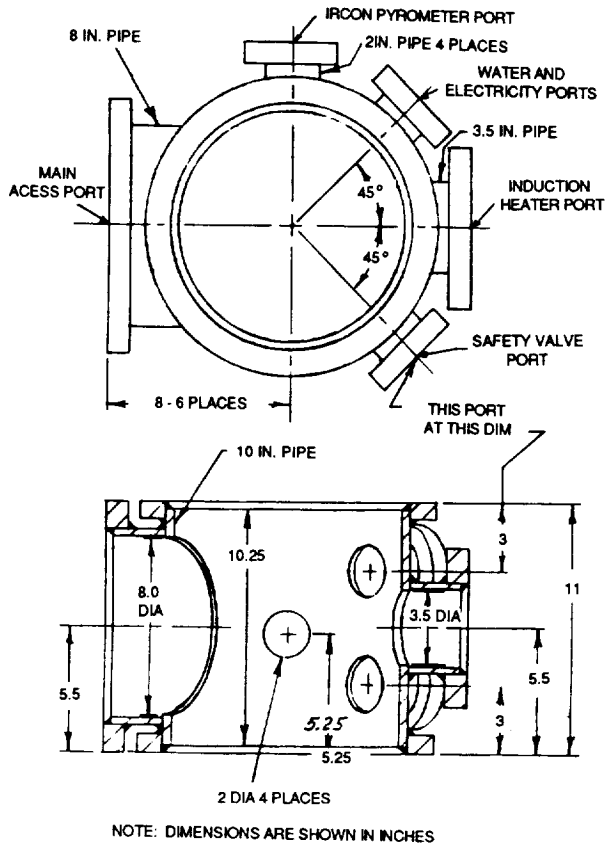

Figure 10 Environmental Test Chamber

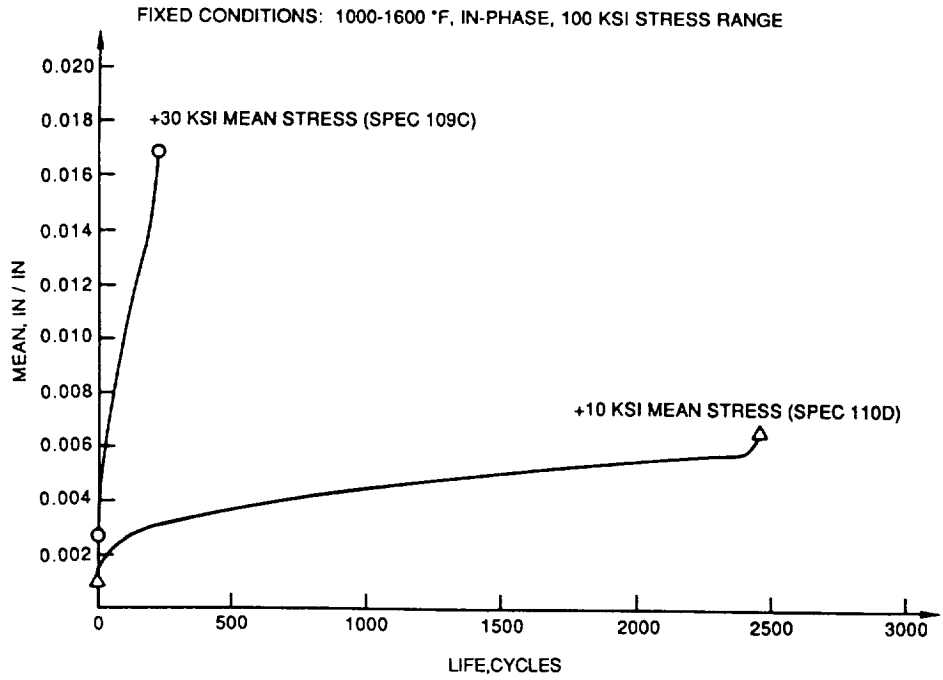

Figure 11 Mean Strain History for Controlled Mean Stress TMF

ELEVATED TEMPERATURE CRACK GROWTH*

S.N. Malik, R.H. Van Stone, K.S. Kim, J.H. Laflen
General Electric Company

INTRODUCTION

Critical gas turbine engine hot section components such as blades, vanes, and combustor liners tend to develop minute cracks during the early stages of operation. These cracks may then grow under conditions of fatigue and creep to critical size. Current methods of predicting growth rates or critical crack sizes are inadequate, which leaves only two extreme courses of action. The first is to take an optimistic view with the attendant risk of an excessive number of service failures. The second is to take a pessimistic view and accept an excessive number of "rejections for cause" at considerable expense in parts and downtime. Clearly is is very desirable to develop reliable methods of predicting crack growth rates and critical crack sizes.

To develop such methods, it is necessary to relate the processes that control crack growth in the immediate vicinity of the crack tip to parameters that can be calculated from remote quantities, such as forces, stresses, or displacements. The most likely parameters appear to be certain path-independent (PI) integrals, several of which have already been proposed for application to high temperature inelastic problems. A thorough analytical and experimental evaluation of these parameters needs to be made which would include elevated temperature isothermal and thermo-mechanical fatigue, both with and without thermal gradients.

Investigations of fatigue crack growth under elastic-plastic condition should consider the impact of crack closure on the appropriate crack growth model. Analytically, this requires the use of gap elements in a nonlinear finite element code to predict closure loads. Such predictions must be verified experimentally through detailed measurements; the best method for measuring crack closure has not been established in previous studies.

It is the purpose of this contract (NAS3-23940) to determine the ability of currently available PI-integrals to correlate fatigue crack propagation under conditions that simulate the engine combustor liner environment. The utility of advanced fracture mechanics measurements will also be evaluated and determined during the course of the program. These goals are to be accomplished through a nine task, combined experimental and analytical program. To date, an appropriate specimen design, a crack displacement measurement method, and boundary

* Work done under NASA Contract NAS3-23940.

condition simulation in the computational model of the specimen has been achieved. Computational verification of the path-independence of the proposed integrals has been demonstrated for isothermal and thermal gradient cases. Also, the experimental testing and data acquisition is continuing. Tensile and cyclic tests were run at several strain-rates so that an appropriate constitutive model could be developed. The experimental data include cyclic crack growth tests under isothermal, thermo-mechanical, and thermal gradient conditions.

EXPERIMENTAL PROGRAM

Alloy 718, a γ-γ" nickel-base superalloy, has been selected as the analog material for this program because over the temperature range from 800 to 1200°F, it shows very large changes in creep behavior. This permits the use of Alloy 718 to simulate the behavior of combustor liner materials while still performing experiments at a relatively low temperature. Tensile, creep and cyclic constitutive tests have been performed over the temperature range from 70 to 1200°F. Even though this material can experience large amounts of creep deformation at the upper end of this temperature range, the tensile and cyclic tests showed little evidence of strain rate sensitivity on constitutive response. Figure 1 shows the resultant tensile stress strain curves determined for 70, 800, and 1200°F. Tensile curves were also determined at 900, 1000 and 1100°F. These curves were used during the analysis of the temperature gradient tests which are described later in this paper.

The crack growth tests have been performed using a single edge notch (SEN) specimen with buttonhead grips. The width and thickness of the gage section is 0.4 and 0.1 inch, respectively. Detailed descriptions of the specimen, testing procedure and finite element analyses have been described previously [1]. The SEN tests were performed in a strain control mode with the experimental setup shown schematically in Figure 2. The controlling extensometer was mounted at the center of the 0.4 inch wide surface of the specimen. The other two displacement gages, one to monitor crack mouth opening displacement and one to monitor the back face deflection, were also used. The controlling and back face extensometers had a gage length of 0.5 inch and the crack mouth gage had a gage length of 0.03 inch. The crack length was monitored using a DC potential drop technique. The hysteresis loops from these tests [1] were open, indicative of large net section non-linear deformation (i.e., plasticity and creep). Figure 3 shows the data from four 1000°F, $A_c=\infty$ crack growth rate tests - single tests at strain ranges of 0.5 and 1.7% and duplicate tests at 1.15% strain range. The initial EDM notch depth was approximately 0.01 inch. Figure 3a shows the strong influence of strain range on the crack growth behavior. The results from the duplicate 1.15% tests are very similar. During these strain control tests, the maximum loads diminished as the crack grew. Figures 3b and 3c show the 1000°F crack growth rates (da/dN) plotted as a function of ΔK and K_{max}, respectively. These data show that these tests cover a range of conditions which can not be described by K, which is proportional to the crack tip stress field in linear elastic fracture mechanics. Comparison of

Figures 3b and 3c also shows that the crack growth rates are better described by K_{max} than ΔK. This suggests that when the final analysis of these tests is completed, the adjustments for crack closure will describe the behavior over the entire range of crack length.

Thermal gradient tests have been performed to evaluate the PI-integrals under non-isothermal conditions. The thermal gradient was established using a combination of induction heating and forced air cooling. At the front or cracked surface, the crack mouth opening extensometer prevented the use of cooling air so the crack was grown from the high temperature to the low temperature. Cooling air was applied to the back face of the specimen above and below the extensometer with cooling tubes and to the gage section with air forced through the cooling passages in the extensometer probes. This gradient technique was originally developed on a specimen which was monitored with fifteen thermocouples. Three sets of five thermocouples were attached to the specimen along the crack plane and at planes 0.25 inch above and below the crack plane. The two latter locations correspond to the positions where the arms of the two large gage length extensometers contact the specimen. On all three planes, a thermocouple was located at each edge of the specimen and at four equally spaced intervals. The presence of the thermocouples prevented the attachment of the three extensometers, so the temperatures were monitored along the plane of the crack in another specimen using an optical pyrometer attached to a traveling microscope. The results of the temperature measurements are shown in the Figure 4. The line connecting the "X" symbols represent the optical pyrometry measurements. These results show a small amount of temperature difference from specimen-to-specimen and along the gage length. This variation is within an acceptable range.

COMPUTATIONAL PROGRAM

Major computational accomplishment was the implementation, verification, and applications of the selected PI-integrals to uniform and non-uniform thermal gradients, and thermo-mechanical loadings for fracture mechanics analyses involving nonlinear material stress/strain behavior. A critical review [2] of the available J_X-integrals conducted under this program revealed that PI-integrals proposed by Ainsworth (J_θ), Blackburn (J^*), Kishimoto (J), and Atluri (T_p^* and T_p) are suitable for nonlinear thermo-mechanical response. The relative advantages and limitations of the various J_X-integrals for thermal gradient problems are discussed in-depth in Reference [2]. The traditional Rice J-integral becomes path-dependent and loses its physical significance for thermo-mechanical loadings due to presence of the mechanical (rather than total) strain energy in its formulation and, also, due to the absence of thermal strains contribution and non-homogeneous (temperature dependent) material properties.

Verification of the implemented thermo-mechanical J_X-integrals was carried out by prescribing a linear temperature gradient through the width of the SEN (single edge notch) crack specimen which was gradually loaded with far-field

uniform normal stress. The crack length to specimen width ratio (a/W) is 0.25 and the specimen length to width ratio (L/W) is 1.25. The specimen edge at crack face was kept at 1200°F temperature and the back-face edge had a temperature of 1000°F. All properties of the material were kept temperature dependent and, as such, they varied through the specimen width. Therefore, the material properties are non-homogeneous along the direction of thermal gradient.

Nonlinear, thermo-mechanical, finite element (FEM) analyses of the SEN specimen were carried out for several values of the applied uniform stress, resulting in thermo-elastic to thermo-elastic/plastic response. Figure 5 shows the far-field normal displacement (Uy) variation which is linear in nature through the specimen width for all the load cases considered. A significant amount of plastic yielding is taking place ahead of the crack for the larger values of the applied stress as seen in Figure 6 which shows the effective stress contours in the specimen. The FEM analyses results were then used in the post-processor PI-integral computer code to determine the various J_x-integrals for several integration paths around the crack tip. Table 1 shows a typical variation of the various J_x-integrals along four paths spanning extreme plasticity to pure elastic regions near the crack. It could be seen that the Rice J-integral values are path dependent for the thermo-mechanical load case. The other five J_x-integrals shown in Table 1 are path-independent. A few of these thermo-mechanical PI-integrals are plotted in Figure 7 for various applied normal stress values. These integrals show excellent agreement with isothermal Elastic-Plastic Fracture Mechanics (EPFM) Handbook [3] and Tada/Paris [4] analytical solutions for lower values of applied stresses. For higher values of applied stress, the thermo-mechanical PI-integrals attain larger values as compared to analytical isothermal J-integral. These results demonstrate implementation and verification of the thermo-mechanical PI-integrals considered here.

To minimize the finite boundary effects, the specimen L/W ratio used in verification analysis was 1.25. For the actual specimen, however, the L/W ratio is only 0.78. Therefore, in order to investigate the influence of finite boundary on J_x-integrals, the same linear thermal gradient analysis was carried for the actual specimen. Typical results as shown in Figure 8 indicate a maximum deviation of 3% on PI-integrals for the prescribed applied stresses.

The actual thermal gradient developed in the SEN specimen gage-section can be approximated as trilinear relationship, as shown in Figure 9. It is approximately constant at 1200°F for the first 0.175 inch along the specimen width; it then linearly drops to 1050°F for the next 0.14 inch of the width; and, finally, it varies linearly to 900°F in the remaining 0.08 inch of the width. Stress analysis of the specimen with the measured temperature dependent material properties and the prescribed trilinear thermal gradient was performed. An interesting result was observed for the pure thermal gradient load case (zero applied load/deflection). For an a/W ratio of 0.25, a crack mouth opening displacement of 0.00015 inch was predicted. The corresponding far-field normal displacement for pure thermal expansion load case is shown in Figure 10 for two

cross sections - one at y = 0.31 inch (end of gage length), and the other at y = 0.25 inch (location of extensometer probes). These free-thermal-expansion normal displacements vary nonlinearly, through the specimen width, due to a combination of the temperature dependent material properties and the trilinear thermal gradient. It has been shown previously that the far-field mechanical displacement in the specimen varies linearly along the specimen width at the end of gage-section. Figure 11 shows the normal stress variation ahead of the crack-tip for the pure thermal gradient load case. The normal stress has a value of 20 ksi near the crack-tip and it drops sharply to -8 ksi at x = 0.175 inch and then gradually increases to 12 ksi by the end of the specimen width. This normal thermal stress is self-equilibrating in nature since there is no mechanical load applied. This fact is further elaborated in Figure 12 which shows the contour plots of the normal stress in the entire gage-section of the specimen. It could be seen that at the top surface (end of the gage-length) the normal stress is zero along entire width of the specimen. The whole specimen is in elastic state of stress with a maximum effective stress of 35 ksi. Since there exists a crack-tip stress field in the specimen for the measured thermal gradient load case, the various J_x-integrals were determined and found to be path-independent. The average value of these PI-integrals was 1.16 lbs/inch, which is equivalent to 5 ksi$\sqrt{\text{in}}$ thermal-K_I value.

Stress analyses were further carried out by prescribing uniform normal stresses superimposed on the actual specimen with the measured thermal gradient. Figure 13 shows the variation of the thermo-mechanical J_x-integrals with applied stress. It could be seen that the values of these integrals are very close to each other for lower values of the applied stress with very little plasticity in the specimen. When the level of plasticity increases, then the various PI-integrals have somewhat different values but remain path-independent.

CONCLUDING REMARKS

The analyses conducted for thermo-mechanical PI-integrals have been very successful and compare very well with the available results. Work is now in progress for computational simulation of the measured load-displacement plots for the thermo-mechanical response of the specimen. In addition, computations are also to be performed for reversed plastic loading to simulate crack-closure. These results will be compared with crack growth experimental measurements to identify path-independent integrals which can predict cyclic crack growth behavior under isothermal, TMF, and thermo-mechanical loading conditions.

REFERENCES

1. Malik, S. N., Van Stone, R. H., Kim, K. S., and Laflen, J. H., "Elevated Temperature Crack Growth," pp. 329-340, NASA Conference Publication 2405, Turbine Engine Hot Section Technology Conference, NASA Cleveland, Oct. 1985.

2. Kim, K. S. and Orange, T. W., "A Review of Path-Independent Integrals in Elastic-Plastic Fracture Mechanics," ASTM 18th National Symposium on Fracture Mechanics, ASTM STP-945, 1986.

3. Kumar, V., German, M., and Shih, C. F., "An Engineering Approach for Elastic-Plastic Fracture Analysis," EPRI Report NP-1931 (R.P. 1237-1), Electric Power Research Institute, Palo Alto (CA), 1981.

4. Tada, H., Paris, P. C., and Irwin, G. R., "The Stress Analysis of Cracks Handbook," Second Edition, Paris Production, Inc. and Del Research Corp., St. Louis (MO), 1985.

TABLE 1: Thermo-Mechanical J_x-Integral Values for SEN Specimen Under Linear Temperature Gradient and Uniform Applied Stress

σ Appl = 65 ksi, L = 0.5 in, (a/w) = 0.25, (L/W) = 1.25

J_x-Integral Load Case #7	For Path 1 (lbs/in)	For Path 2 (lbs/in)	For Path 3 (lbs/in)	For Path 4 (lbs/in)	J_x-Average (lbs/in)
Rice	194.29	201.30	204.00	204.252	201.086
Ainsworth	136.58	138.12	138.10	138.27	137.793
Blackburn	163.50	163.46	163.50	164.25	163.678
Kishimoto	167.26	167.98	168.02	171.95	168.303
Atluri - T_p*	161.309	161.789	161.685	164.109	162.234
Atluri - T_p	308.179	308.644	308.5556	310.722	309.025
EPFM Handbook (1100F)	-	-	-	-	124.220

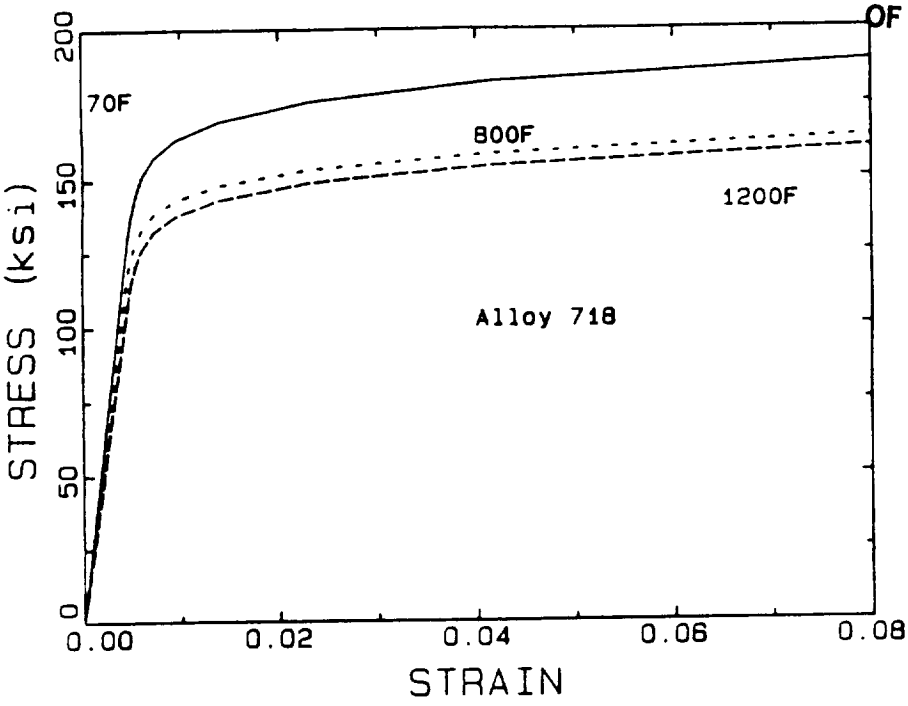

Figure 1: Tensile Curves for Alloy 718 at 70, 800 and 1200°F.

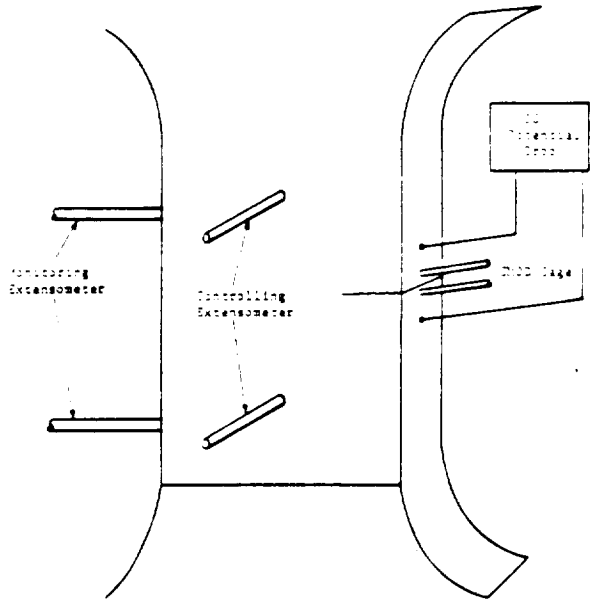

Figure 2: Schematic Drawing of SEN Specimen Test Method

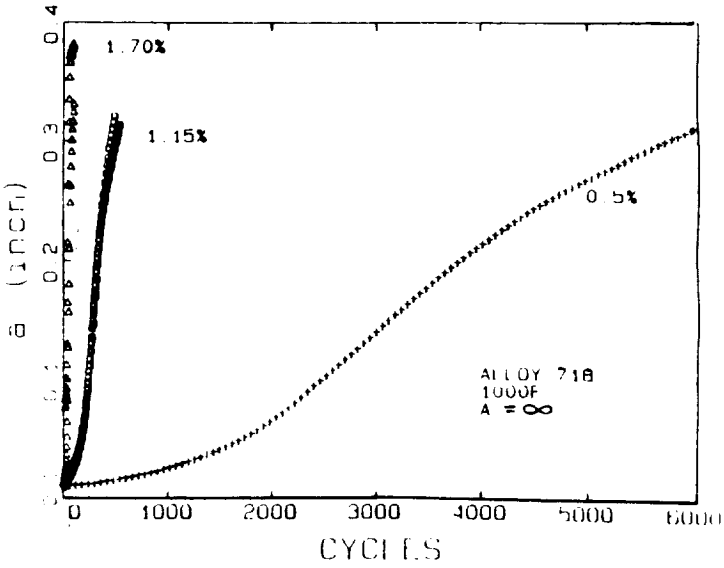

(a)

Results of 1000°F, Alloy 718

Displacement Control Tests

(a) crack depth versus cycles.
da/dN versus

(b) Δ K

(c) K_{max}.

ORIGINAL PAGE IS OF POOR QUALITY

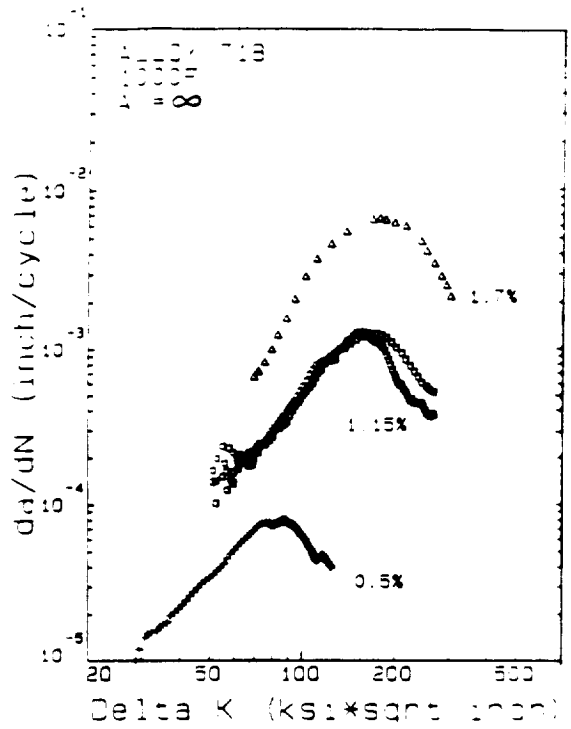

(b)

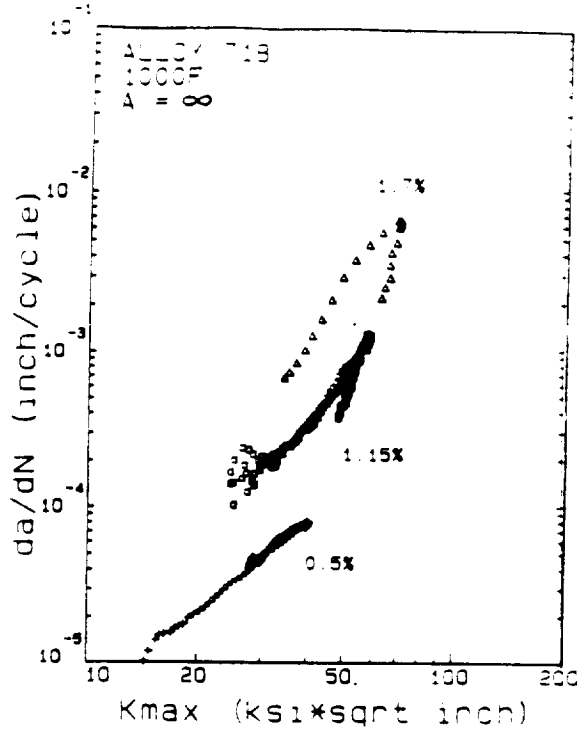

(c)

Figure 3

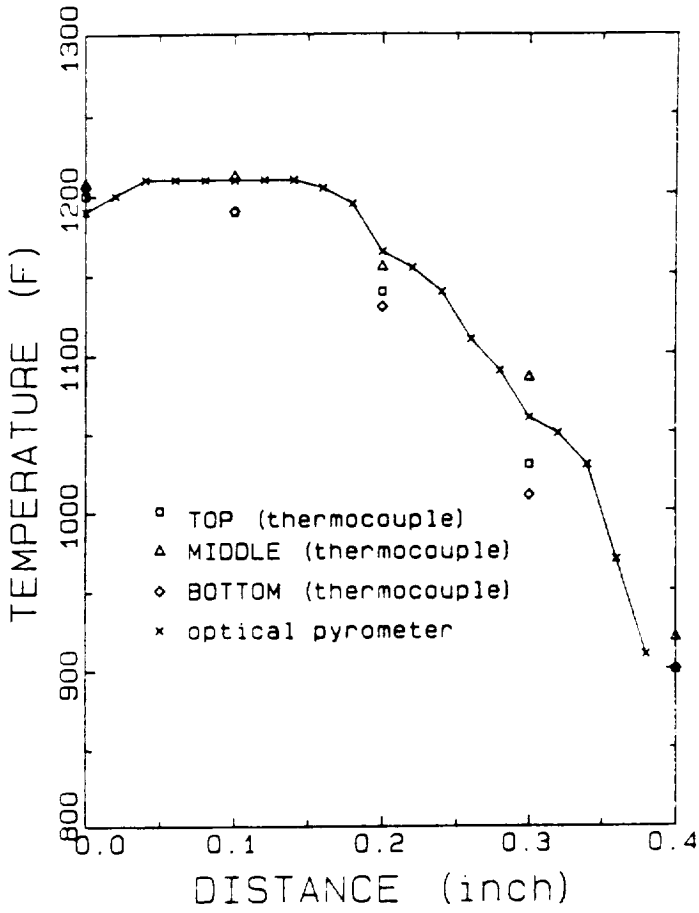

Figure 4: Temperature Profile in Thermal Gradient Tests

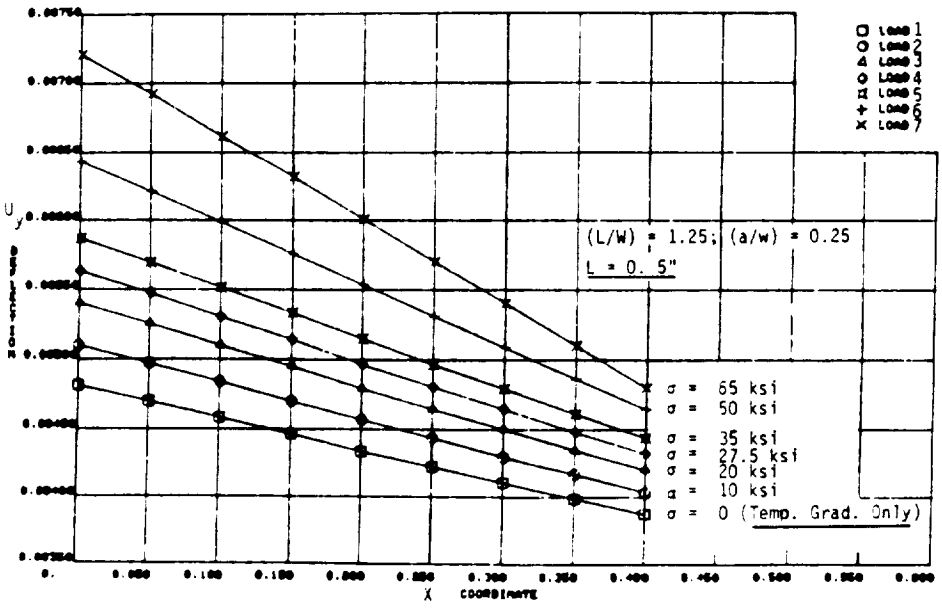

FIGURE 5: Far-Field U_y (y = 0.5") Displacement in SEN Specimen Under Linear Temperature Gradient and Applied Uniform Stress. (L/W = 1.25)

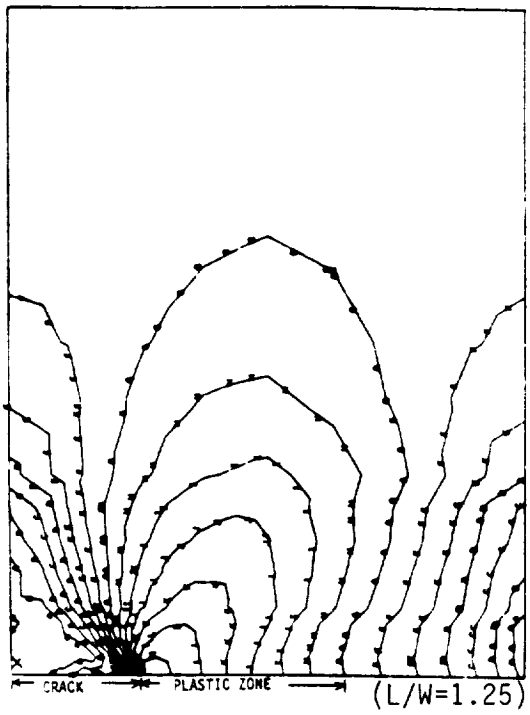

ORIGINAL PAGE IS
OF POOR QUALITY

FIGURE 6: Effective Stress Contours in SEN Specimen Under Linear Temperature Gradient and Applied Stress of 65 ksi.

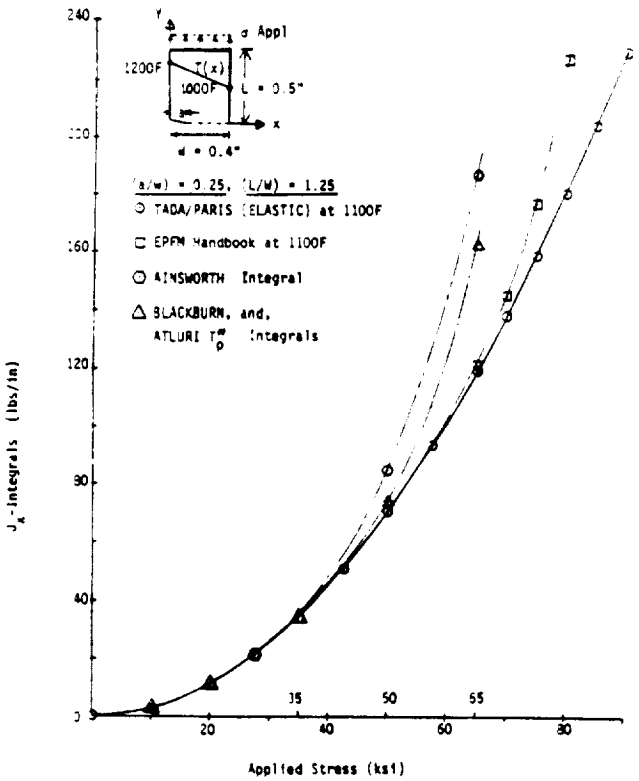

FIGURE 7: Thermo-Mechanical Elasto-Plastic J_x-Integrals in SEN Specimen Under Linear Thermal Gradient and Applied Uniform Far-Field Stress.

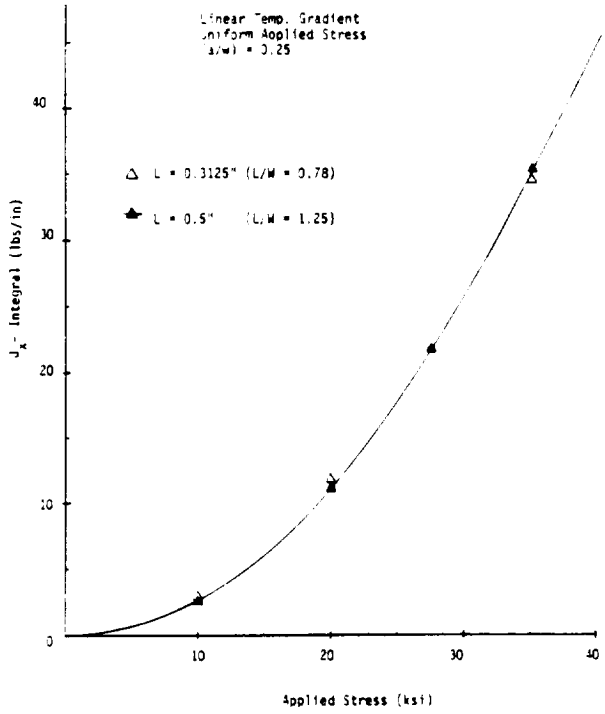

FIGURE 8: Thermo-Mechanical Kishimoto Integral in SEN Specimen

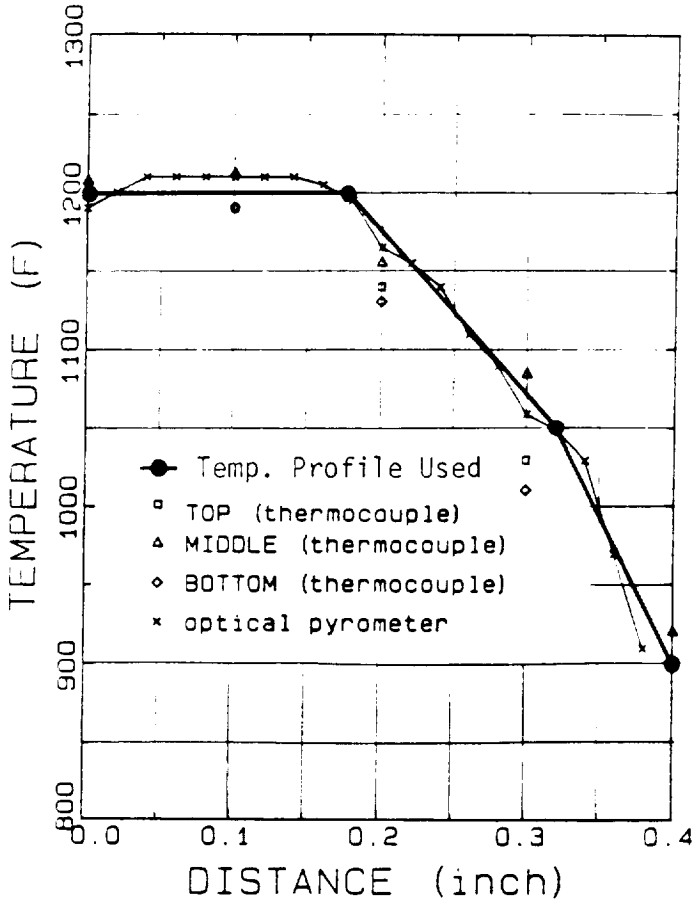

Figure 9: Trilinear Thermal Gradient Used in Analysis

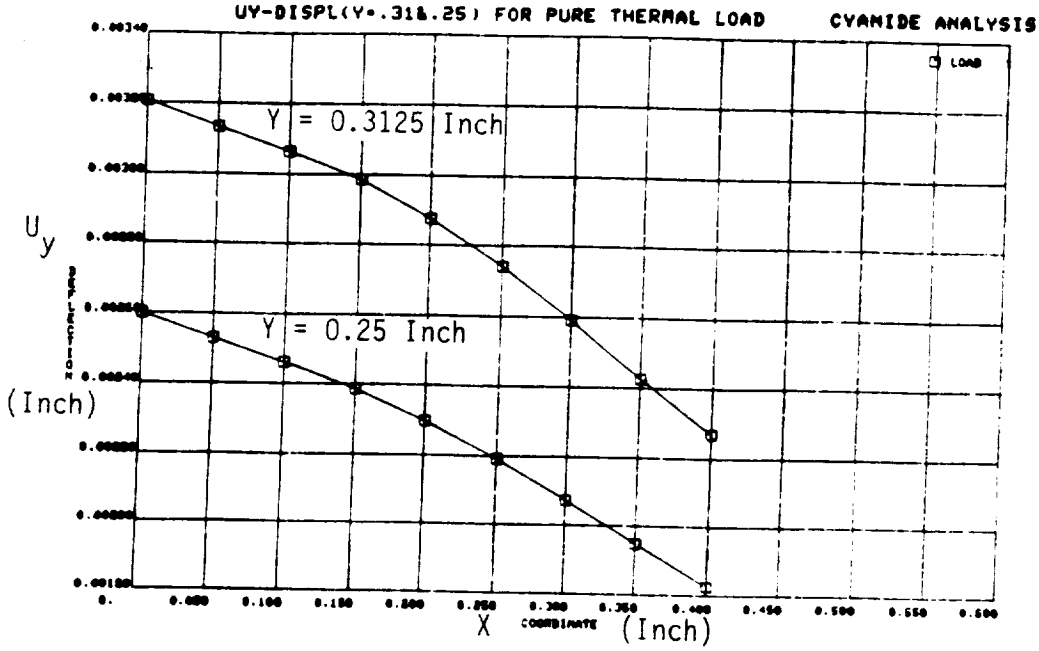

Figure 10: Far-Field Normal Displacement for Thermal Gradient

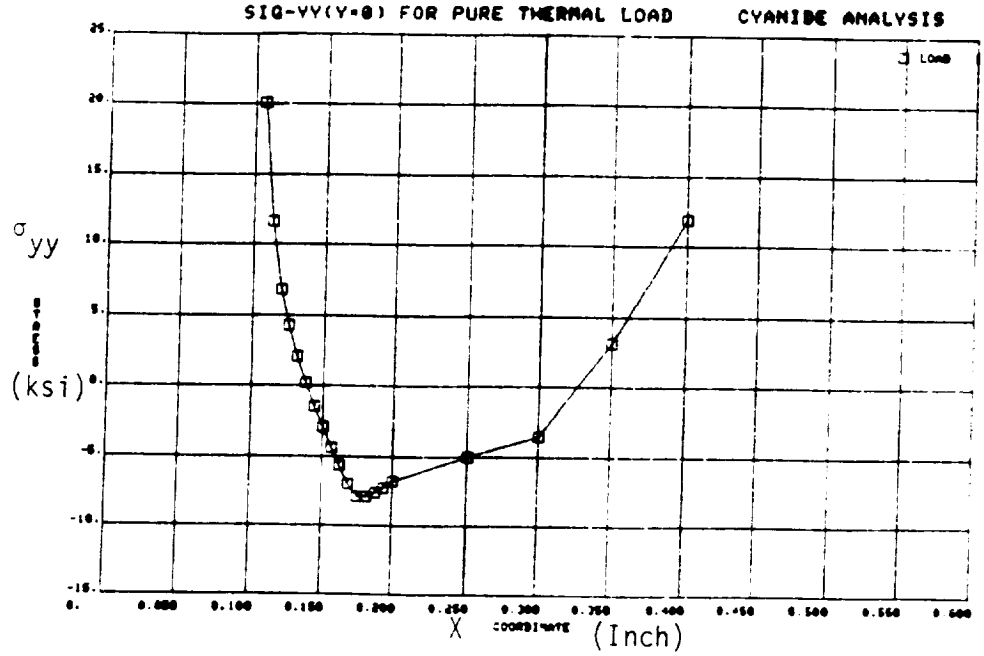

Figure 11: Normal Stress Ahead of Crack-Tip for Thermal Gradient

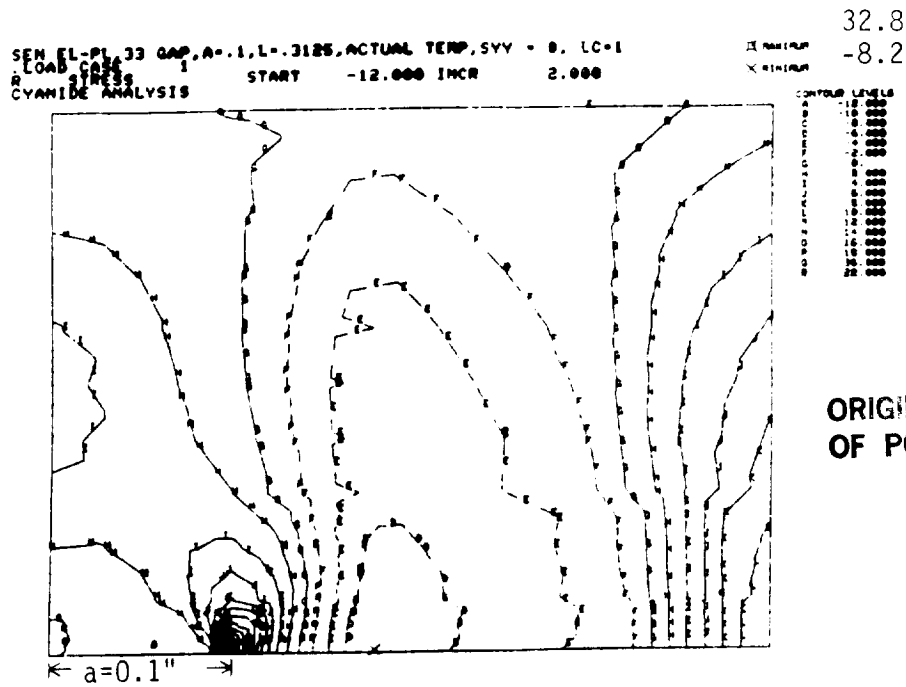

ORIGINAL PAGE IS
OF POOR QUALITY

Figure 12: Normal Stress (σ_{yy}) Contours for Thermal Gradient

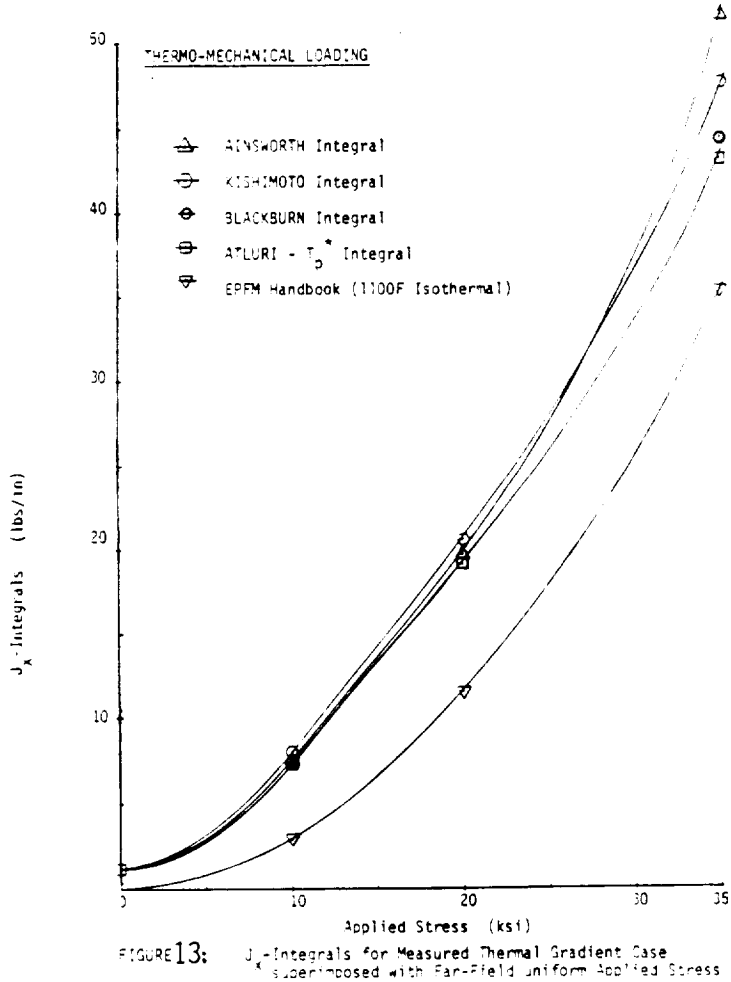

FIGURE 13: J_x-Integrals for Measured Thermal Gradient Case Superimposed with Far-Field Uniform Applied Stress

LIFE PREDICTION AND CONSTITUTIVE MODELS FOR ENGINE HOT SECTION ANISOTROPIC MATERIALS PROGRAM*

G.A. Swanson, T.G. Meyer, and D.M. Nissley
United Technologies Corp.
Pratt & Whitney

INTRODUCTION

The purpose of this program is to develop life prediction models for coated anisotropic materials used in gas turbine airfoils. In the program, two single crystal alloys and two coatings are being tested. These include PWA 1480, Alloy 185, overlay coating (PWA 286), and aluminide coating (PWA 273). Constitutive models are also being developed for these materials to predict the time independent (plastic) and time dependent (creep) strain histories of the materials in the lab tests and for actual design conditions. This nonlinear material behavior is particularly important for high temperature gas turbine applications and is basic to any life prediction system. This report will highlight some of the accomplishments of the program this year.

SINGLE CRYSTAL CONSTITUTIVE MODEL

Two separate unified constitutive models for single crystal PWA 1480 have been formulated and are in the final stages of development. The first model, the "microscopic model", computes the inelastic quantities on the crystallographic slip systems. This model achieves the required directional properties as a consequence of resolving the summed slip system stresses and strains onto the global coordinate system. The second model, the "macroscopic model", uses global stresses and strains directly and employs anisotropic tensors operating on global inelastic quantities to achieve the required directional properties. The two models offer a trade between accuracy and physical significance and computing time requirements. The microscopic model is more accurate and is more physically significant in its formulation than the macroscopic model. However the macroscopic model is more computationally efficient, because integration of the evolutionary equations is required only for the six global stress/strain quantities rather than for each of the slip systems.

Cyclic stress/strain data at 871C (1600F) will be used to illustrate the behavior of the models. Figures 1 and 2 show test data from uniaxial bars oriented in three crystal directions: <001>, <111>, and <011>. These three orientations represent the extreme ends of the possible crystal orientations.

* Work performed under NASA contract NAS3-23939.

The tests were conducted under controlled strain rates ranging from 0.001% per second to 1.0% per second.

The microscopic model models deformation on both the octahedral slip systems and the cube slip systems. The importance of including both slip systems can be shown by examining the results of inactivating the cube system terms. The model, thus modified, was fit to the <001> data and subsequently used to predict the <111> behavior. Figure 3 shows the correlation with the <001> data is quite good, but the prediction for the <111> data is poor. The good correlation with the <001> data could have been expected since for a tensile bar in this orientation, only the octahedral slip systems have nonzero resolved shear stresses. The resolved shear stress on the cube slip systems is zero for this orientation. In contrast, a tensile bar oriented in the <111> direction has nonzero shear stresses on both the octahedral and the cube slip systems. When cube slip terms are included in the model, the correlation with the <111> and <001> data is quite good as seen in Figure 4. The model constants in this case have been determined to best fit both the <001> and the <111> data. The accuracy of the full model is illustrated in Figure 5 by a prediction of data from a third orientation: the <011> orientation. Comparison with the test data in Figure 2 shows the prediction is very good. The maximum difference seen between the micro model and test data for all three orientations, for stress ranges up to 2100 MPa (305 ksi) and over three orders of magnitude of strain rate is less than 62 MPa (9 ksi).

In the macroscopic model being developed, a single set of evolutionary equations are written using the global stresses and strains directly (i.e. not resolving them onto slip systems). The orientation dependence is achieved by including anisotropic tensors in the evolutionary equations for both inelastic strain and back stress. If the anistropic tensor is included only in the equation for inelastic strain, the best correlation with <001> and <111> data resulted in a maximum stress error 2.5 times that achieved in the slip system based model. However, as shown in Figure 6, when the back stress components are allowed to evolve anisotropically, correlation of the <001> and <111> test data is comparable to that achieved with the slip system based model. The ability of the macroscopic model to predict other orientations is currently under investigation.

COATING CONSTITUTIVE MODEL

Five isotropic constitutive models were evaluated based on ability to correlate isothermal overlay coating behavior during stress relaxation and ability to predict thermomechanical behavior. The models evaluated were a classical formulation (e.g. Ref.1), Walker's isotropic formulation (Ref.2), a simplified form of Walker's isotropic formulation where back stress was assumed equal to zero, the Stowell model (Ref.3), and Moreno's Simplified Unified Approach (Ref.4).

Early evaluation of model correlation ability indicated little differences between the models. Additional isothermal cyclic stress relaxation tests were subsequently conducted to determine whether kinematic terms were necessary. To accomplish this, a 5 minute strain hold initiating at zero stress after unloading was incorporated into the test history. Experimental results from the test conducted at 649C (1200F) is presented in Figure 7. The positive relaxation observed during the 5 minute strain hold indicated that kinematic hardening was necessary to accurately represent the overlay coating response. As such, the 3 models which do not contain kinematic hardening formulations (i.e. classical, simplified Walker, and Stowell) were dropped from consideration.

Correlation of the isothermal stress relaxation information was best accomplished using the Walker model. The Moreno model as applied was generally unable to correlate the observed positive relaxation response largely as a result of the assumed back stress evolution equation:

$$\Delta\Omega = Ep\,\Delta\,\varepsilon in + \varepsilon in\,\Delta Ep$$

where:
$\Delta\Omega$ = back stress increment
Ep = strain hardening slope in uniaxial tensile test
$\Delta\varepsilon in$ = inelastic strain
$\Delta\varepsilon in$ = inelastic strain increment
ΔEp = change in Ep (with respect to temperature)

Moreno in his work on Hastelloy X (Ref.4) utilized a less rigorous back stress formulation which relied on a set of rules. This was considered cumbersome and, hence, the above formulation was adopted.

Prediction of an out-of-phase overlay coating hysteresis loop by the Walker and Moreno models is presented in Figure 8. Clearly, the Walker model is the more accurate, but the Simplified Unified Approach does predict the gross behavior and is also quite easy to apply, since only simple hand calculations are required.

Aluminide diffusion coating isothermal stress relaxation tests are in process. Because diffusion coatings depend largely on the substrate material, tests are conducted on 2 thicknesses of PWA 1480 material .13 and .25 mm (.005" and .010"). Initially, the overlay constitutive model (i.e. Walker) will be applied to both thicknesses and each material constant will then be plotted vs. PWA 1480 thickness and extrapolated to zero PWA 1480 thickness to obtain the "effective" coating material constants.

LIFE PREDICTION TESTS

Tests concentrated on gaining insight to coating/PWA 1480 substrate interactions during thermomechanical loading conditions. Critical fatigue experiments conducted on <001> and <111> PWA 1480 specimens with either overlay or aluminide coatings have shown that thermomechanical fatigue life is significantly influenced by the presence of a coating, coating structure (overlay or diffusion), substrate orientation, and strain-temperature-time path. Test results supporting these conclusions are presented in Figures 9 through 12. All lives are relative to specimen separation life, except in Figure 12 where coating cracking lives are also provided. Although not shown, coating cracking lives generally follow the same trends. Isothermal fatigue tests were primarily limited to overlay coated <001> PWA 1480 and were designed to provide initial life data for exercising life models. This particular coating/substrate orientation combination was chosen because it is the most understood from previous experience and material behavior standpoints.

The remainder of specimen coating/substrate orientation combinations are intended to obtain anisotropy and coating structure effects.

LIFE PREDICTION MODELS

Based on observed specimen cracking lives obtained from multiple acetate replications of each specimen, life must be separated into coating and substrate

components such as provided in the following equation:

$$Nsep = Nci + Nsi + Nsp$$

where: Nci = Number of cycles to generate a crack through the coating.

Nsi = Additional cycles for coating crack to penetrate a small distance into the substrate. Initially defined as .13 mm (.005").

Nsp = Additional cycles to grow crack to critical size.

Nsep = Specimen separation life (50% stress range drop).

Initially, simple correlations of overlay coating cracking life (Nci) were considered: Coffin-Manson, Ostergren, actual tensile hysteresis energy, and another hysteretic energy approach based upon the concept of effective temperature (Ref.5). In the latter approach, effective temperature was assumed to be the midcycle temperature of the loading condition (i.e. (Tmin+Tmax)/2). These four correlations are presented in Figure 13. In each case, the overlay coating correlating parameters were determined by analysis using a one-dimensional 2-bar mechanism. The correlation lines shown in the figure represent a "hand-fit" curve passing through all the out-of-phase TMF test conditions and are intended to serve as a reference to qualitatively judge the correlations. Of the four, the tensile hysteretic energy model is best able to correlate the lives of the varied test conditions.

PWA 1480 substrate life modeling depends upon what is considered crack initiation vs. propagation. The methodology applied in this program initially defines substrate crack initiation as a crack which has penetrated .13 mm (.005") into the PWA 1480. Assuming a penny-shaped crack, this is consistent with a .15 to .25 mm (.006" to .010") surface crack. To verify the relationship between acetate replica observations and actual substrate cracking, substantial optical and Scanning Electron Microscopy (SEM) fractography has been conducted. Such investigations have indicated that overlay coating cracks do not penetrate into the PWA 1480 substrate during tests conducted at high temperature. Figure 14 is a schematic of the demarkation between temperatures where coating cracks do or do not penetrate into the PWA 1480.

TMF of a coated specimen (or component) is particularly complex because thermal growth mismatch between coating and substrate introduce biaxial stresses and strains during thermal cycling. Final model(s) will consider such biaxial conditions and more rigorous statistical evaluations of the model(s) will then be performed.

FUTURE

In the coming year, additional cyclic tests are planned to assist in life prediction model development. Also, in Option 1 of the program, life model development will be extended to airfoil root attachment temperatures, stress levels, and notch stress concentrations.

ACKNOWLEDGEMENTS

The authors wish to recognize some of the individuals contributing to the progress of the program. Dr. Kevin P. Walker, of Engineering Scientific Software, Inc., originator and developer of the single crystal constitutive models and one of the coating constitutive models. At P&W, Messrs. Paul P. Norris, Indrik Linask, and many others are continuing to develop constitutive and life prediction models and overseeing and interpreting specimen tests; also, Messrs. Frank X. Ashland, Phillip D. Retzer, William A. Murphy, and Larry E. Durey for their support in specimen procurement and testing.

REFERENCES

1. Kraus, H.: "Creep Analysis", John Wiley & Sons, Inc., New York, Chapter 2, 1980.

2. Walker, K. P.: "Research and Development Program for Nonlinear Structural Modeling with Advanced Time-Temperature Dependence Constitutive Relationships", NASA CR-165533, November, 1981.

3. Stowell, E. Z., et al: "Predicted Behavior of Rapidly Heated Metal in Compression", NASA TR R-59, 1960.

4. Moreno, V.: "Development of a Simplified Analytical Method for Representing Material Cyclic Response", NASA CR-168100, January, 1983.

5. Pejsa, P. N. and Cowles B. A.: "Thermal Mechanical Fatigue Life Prediction for Advanced Anisotropic Turbine Alloys", Journal of Engineering for Gas Turbine and Power, vol. 108, July, 1986. ASME no. 86-GT-124.

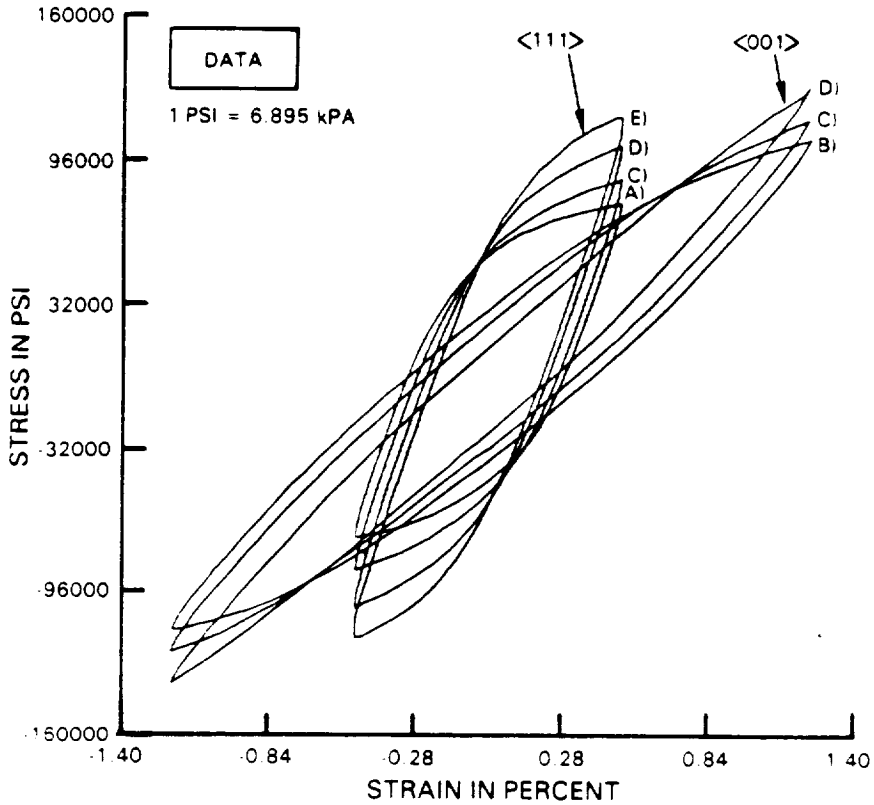

FIGURE 1 EXPERIMENTAL LOOPS IN <001> AND <111> DIRECTIONS AT 871C (1600F) AT STRAIN RATES OF A) .001% PER SEC, B) .0025% PER SEC, C) .01% PER SEC, D) .1% PER SEC, AND E) .5% PER SEC

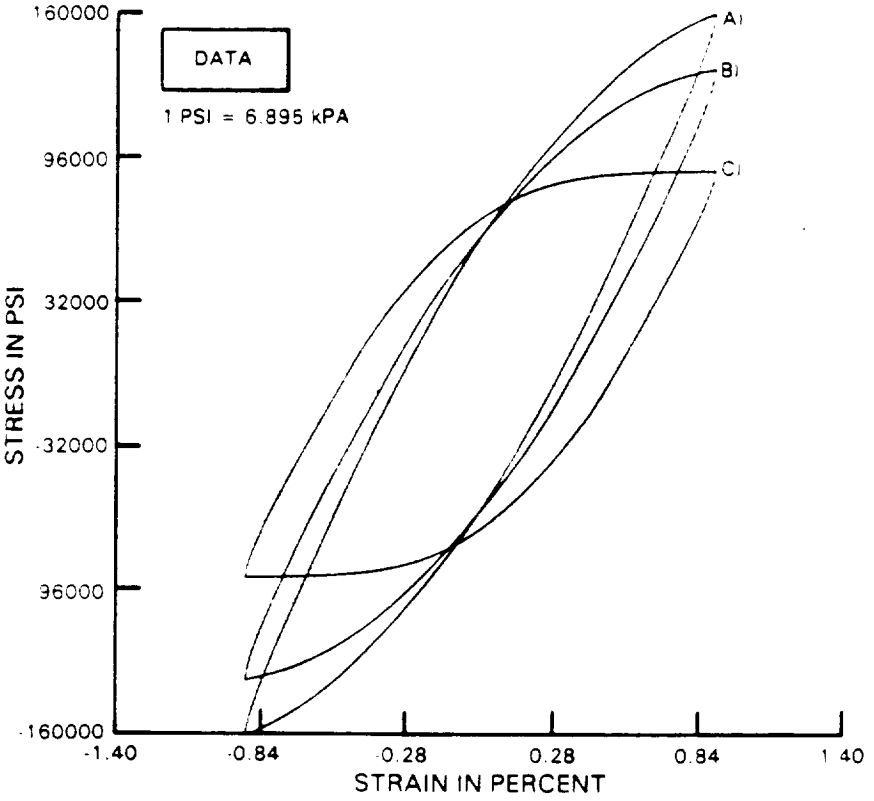

FIGURE 2 EXPERIMENTAL LOOPS IN <011> ORIENTATION AT 871C (1600F) AT STRAIN RATES OF A) 1.0% PER SEC, B) 0.1% PER SEC, AND C) 0.001% PER SEC

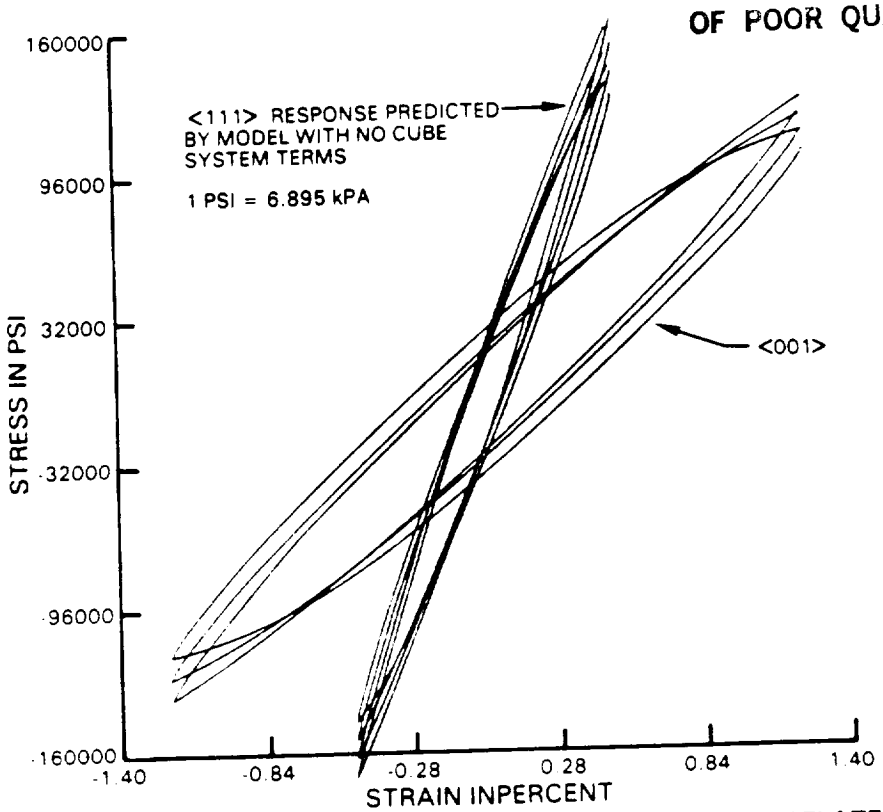

FIGURE 3 USING ONLY OCTAHEDRAL SLIP TERMS, THE <001> DATA IS CORRELATED WELL BUT SUBSEQUENT PREDICTION OF <111> RESPONSE IS POOR. COMPARE TO DATA IN FIGURE 1

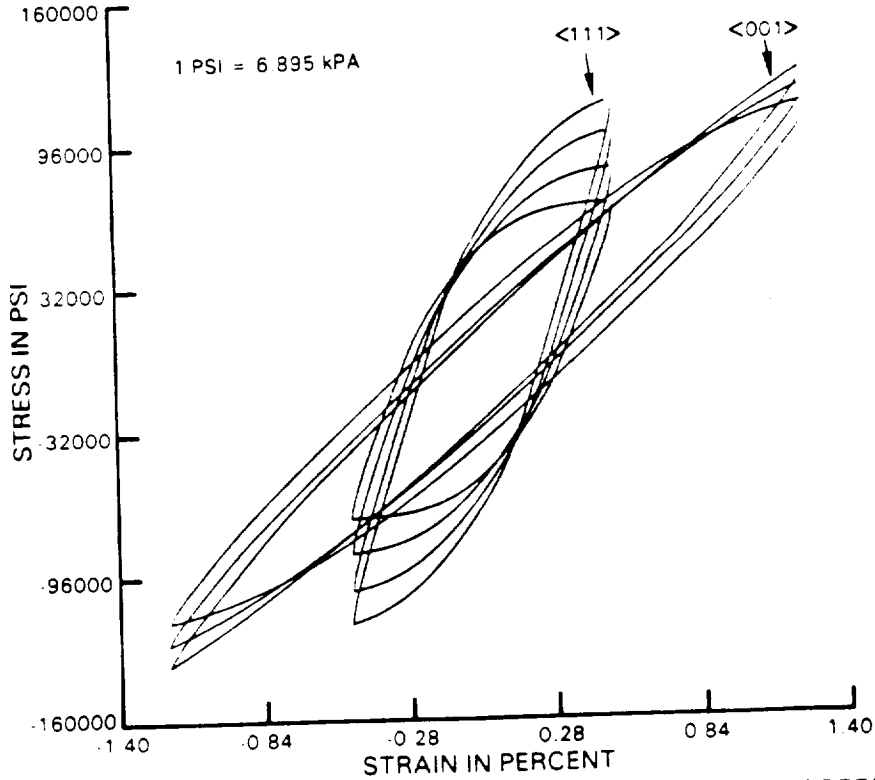

FIGURE 4 MICRO MODEL WITH BOTH OCTAHEDRAL AND CUBE SLIP TERMS CORRELATED TO <111> AND <001> DATA. COMPARE TO DATA IN FIGURE1

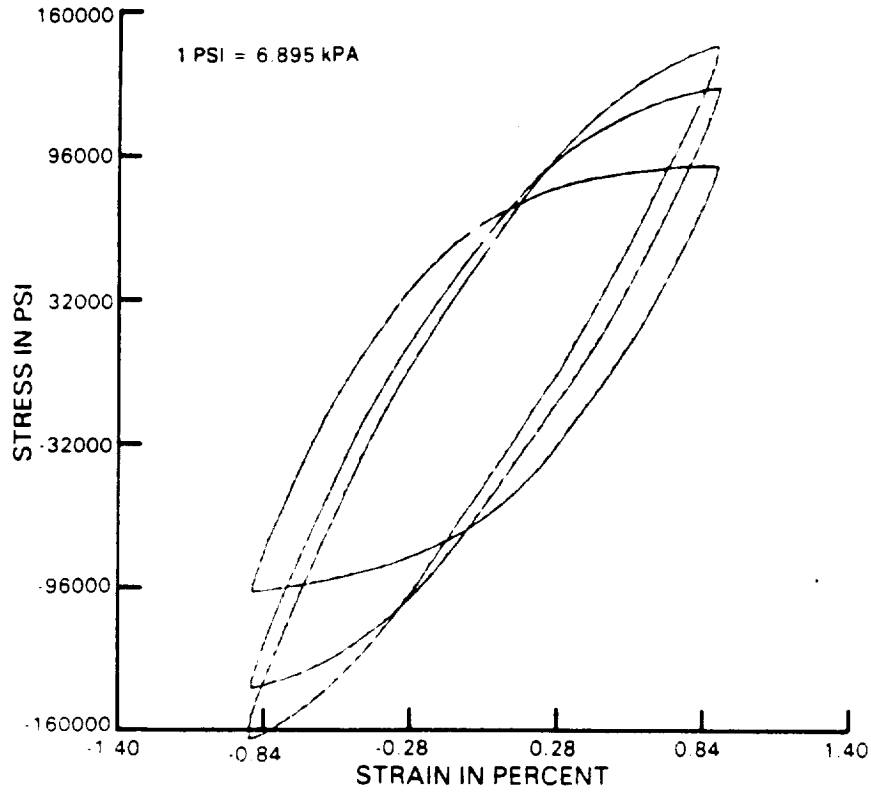

FIGURE 5 PREDICTED LOOPS IN <011> ORIENTATION AT 871C (1600). COMPARE TO DATA IN FIGURE 2

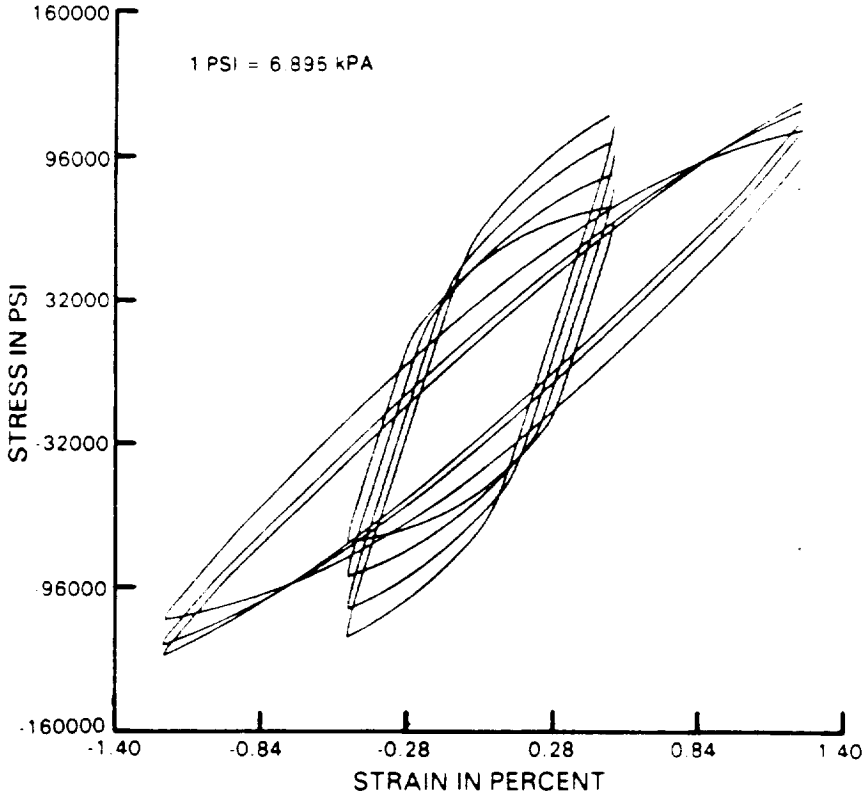

FIGURE 6 CORRELATION OF <001> AND <111> DATA WITH ANISOTROPIC BACK STRESS MODEL

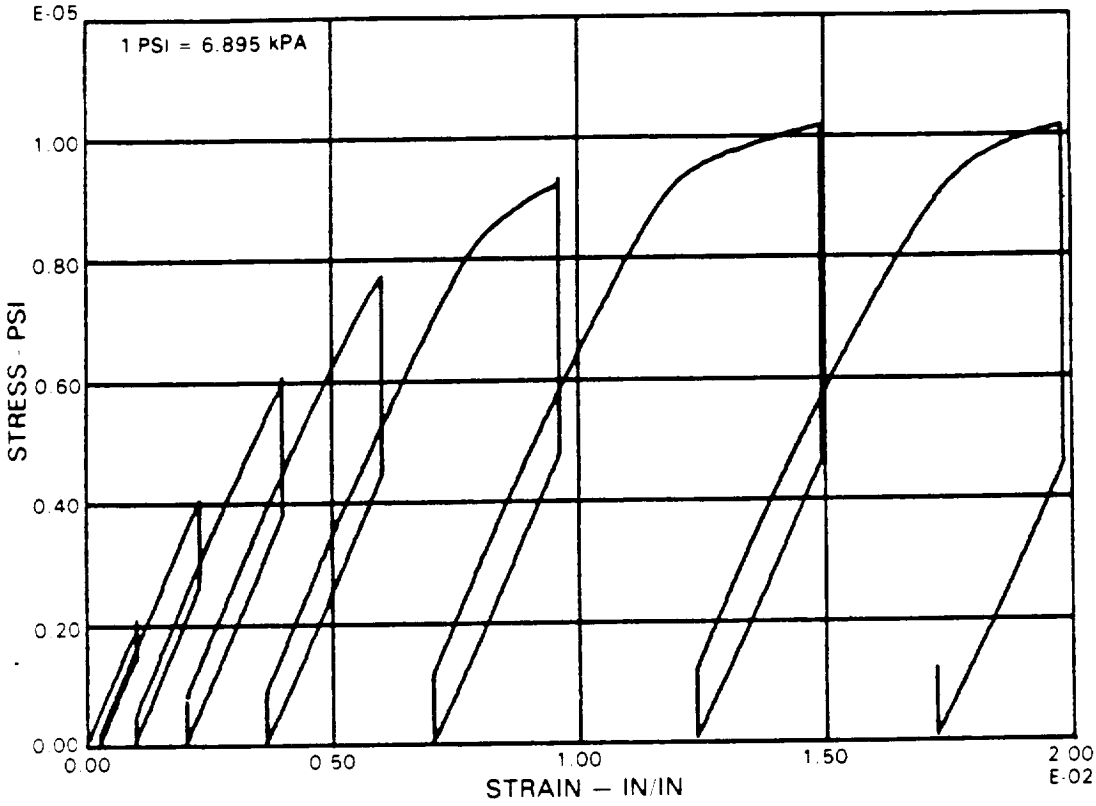

FIGURE 7 649°C (1200°F) STRESS RELAXATION TEST OF UNEXPOSED, BULK HIP'PED PWA286

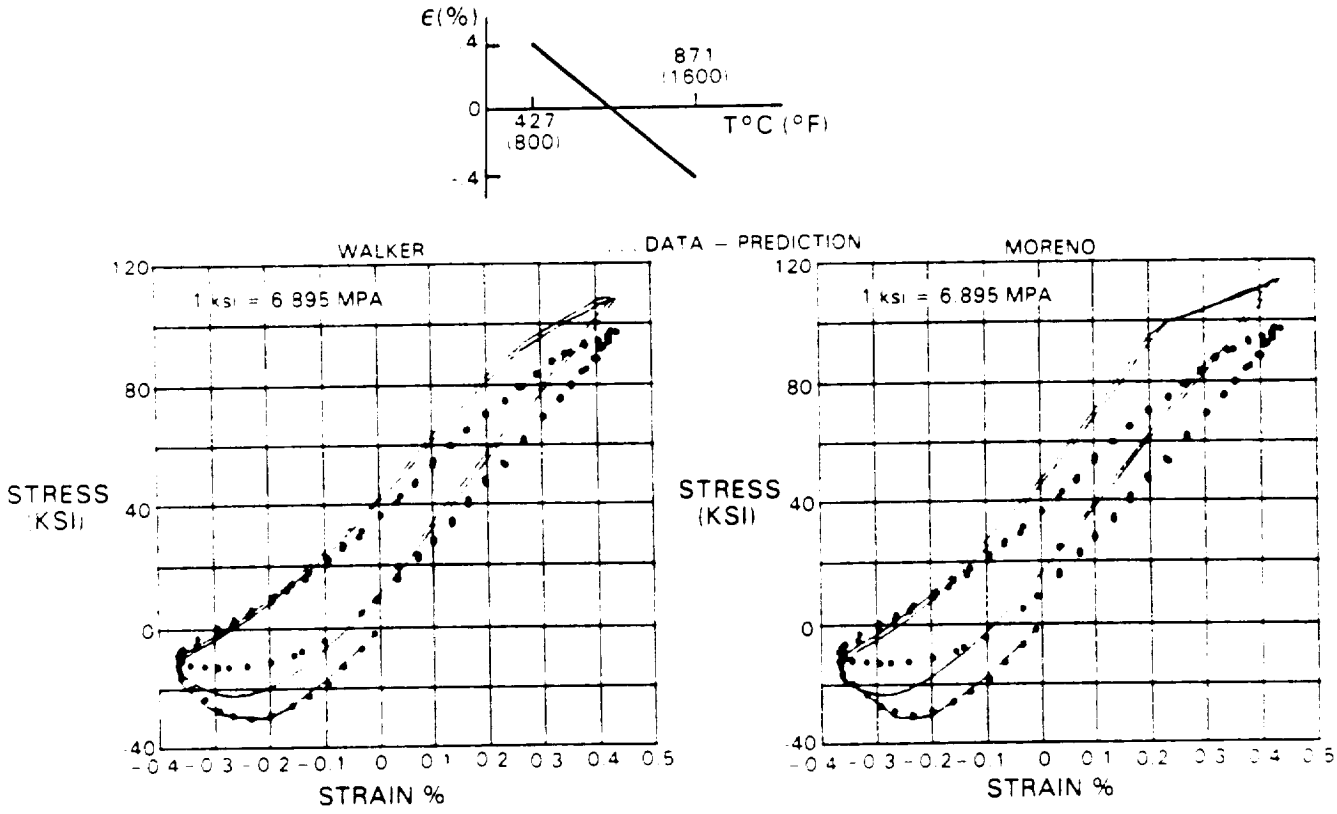

FIGURE 8 WALKER AND MORENO MODEL PREDICTION OF OUT-OF-PHASE TMF TEST

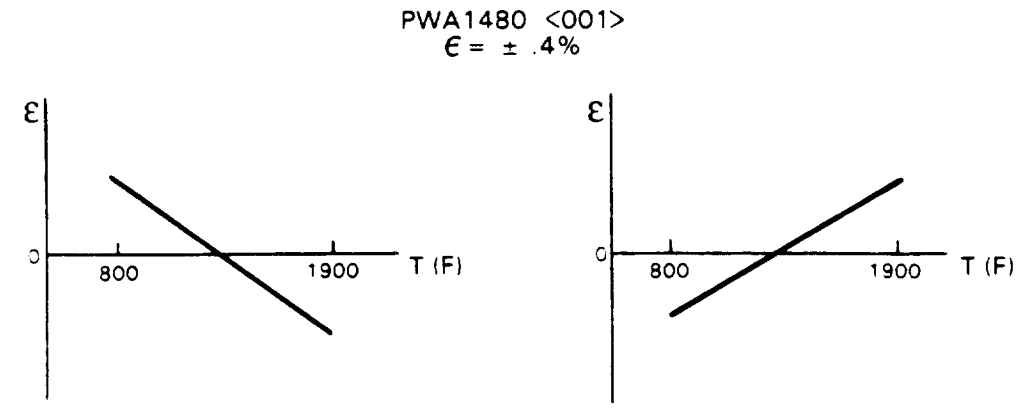

COATING		
NONE	1.00	2.35
PWA273 NiAl DIFFUSION	.22	4.00+
PWA286 NiCoCrAlY OVERLAY	.73	4.06

FIGURE 9 THERMAL MECHANICAL FATIGUE LIFE DEPENDS UPON COATING

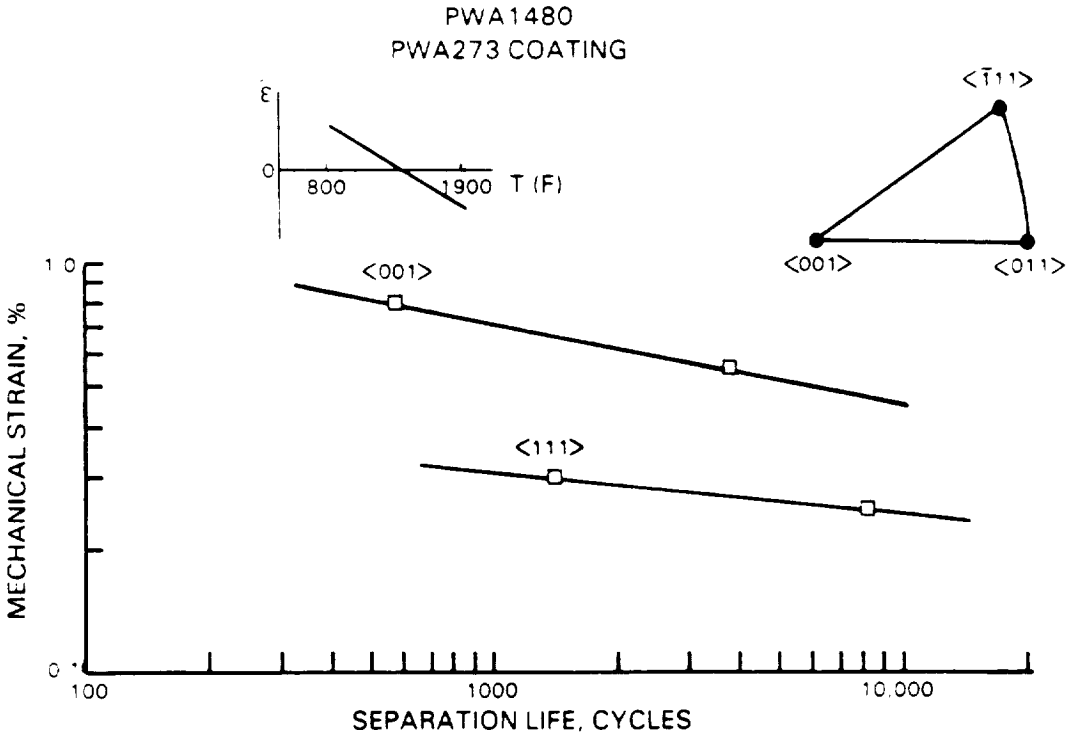

FIGURE 10 THERMAL MECHANICAL FATIGUE LIFE DEPENDS UPON SUBSTRATE ORIENTATION

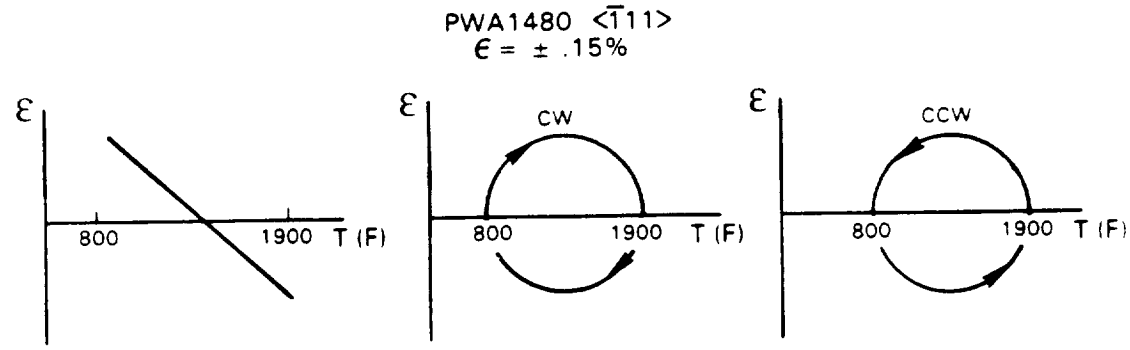

COATING			
PWA273 NiAl DIFFUSION	1.0	1.16	4.75
PWA286 NiCoCrAlY	1.0	1.23	3.85+

FIGURE 11 TMF LIFE DEPENDS UPON MECHANICAL STRAIN - TEMPERATURE PATH

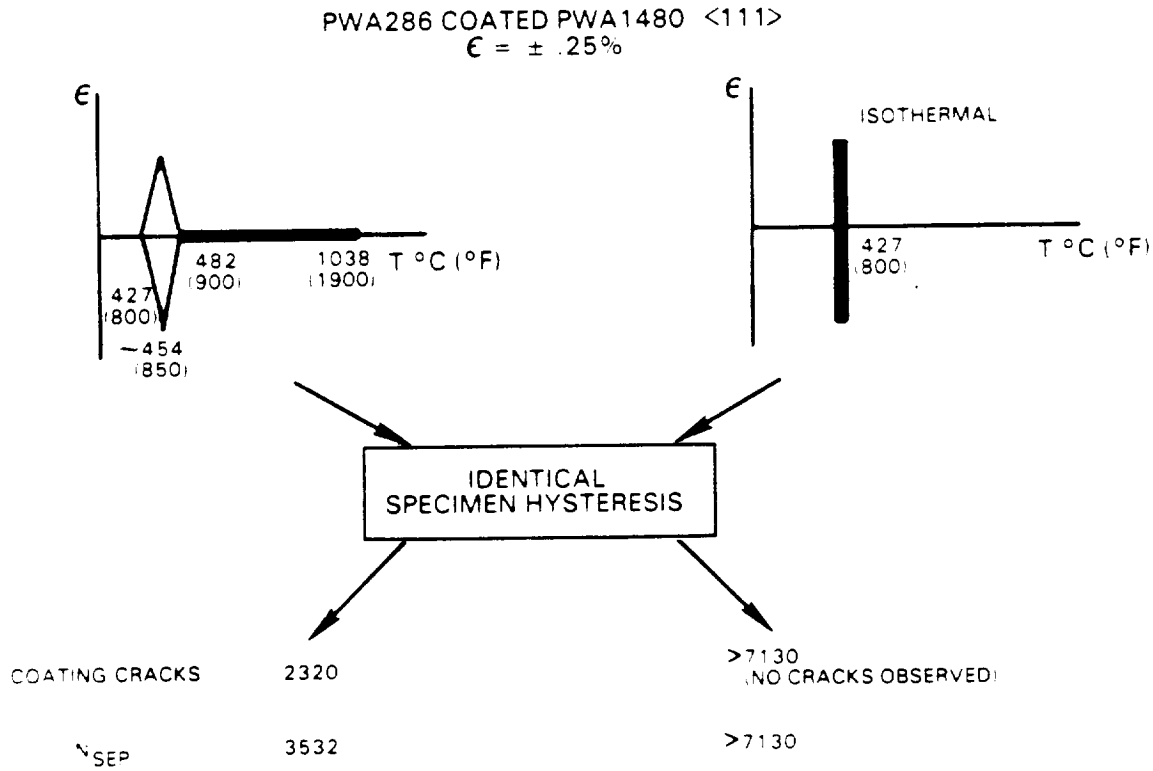

FIGURE 12 TMF LIFE DEPENDS UPON THERMAL CYCLE

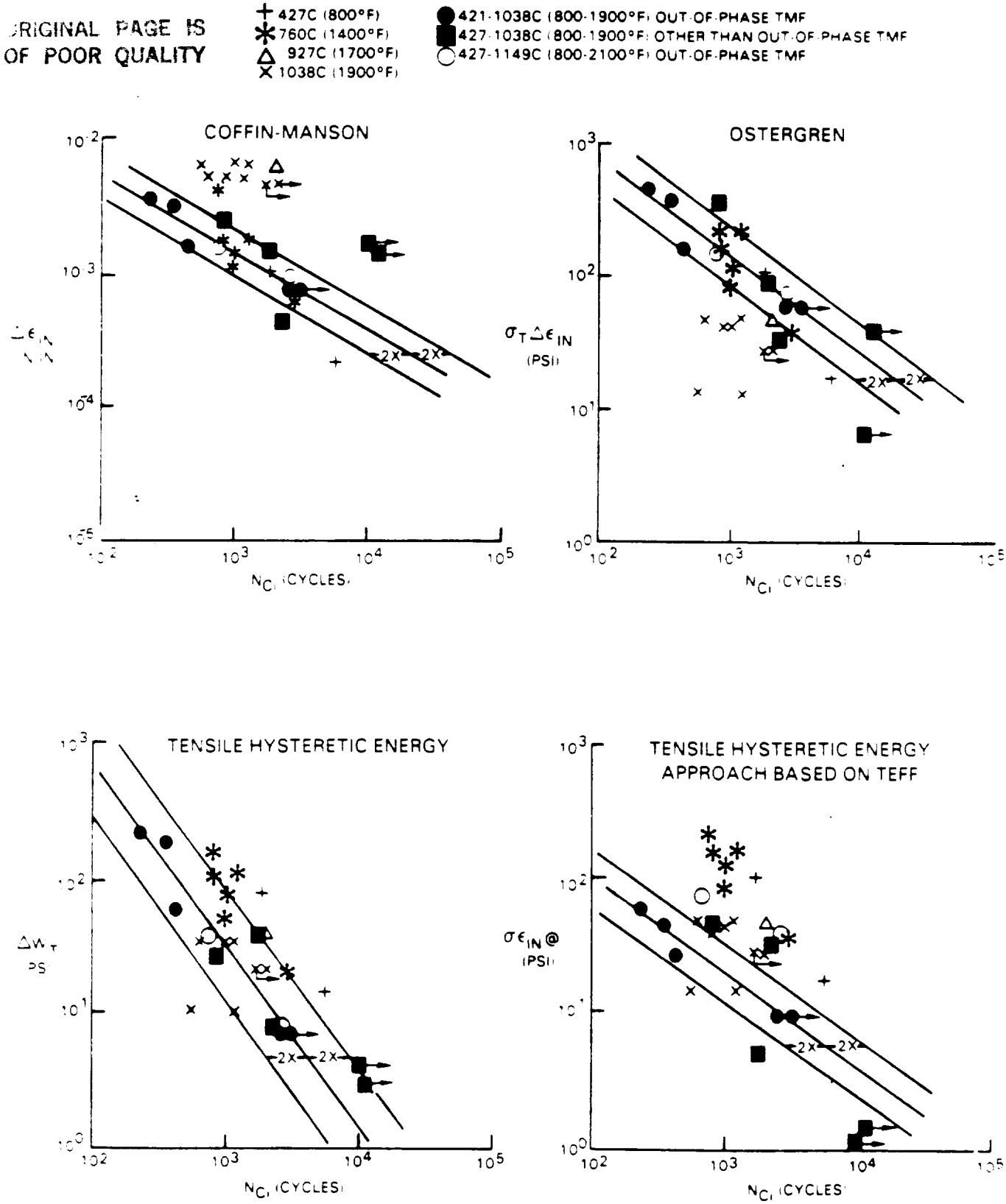

FIGURE 13 PWA286 OVERLAY COATING CRACKING LIFE CORRELATIONS

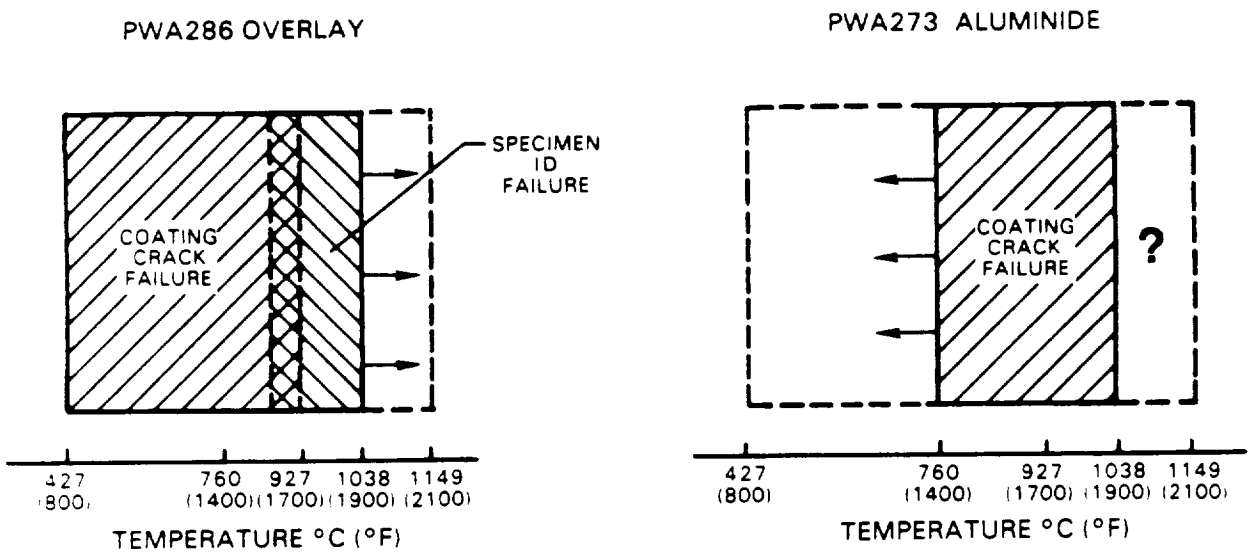

FIGURE 14 SCHEMATIC OF OBSERVED SPECIMEN FAILURES. AT HIGH TEMPERATURES PWA286 COATING CRACKS DO NOT PENETRATE INTO PWA1480.

AUTOMATION SOFTWARE FOR A MATERIALS TESTING LABORATORY

Michael A. McGaw and Peter J. Bonacuse
NASA Lewis Research Center
Cleveland, Ohio 44135

A comprehensive software system for automating much of the experimental process has recently been completed at the Lewis Research Center's high-temperature fatigue and structures laboratory. The system was designed to support experiment definition and conduct, results analysis and archiving, and report generation activities. This was accomplished through the design and construction of several software systems, as well as through the use of several commercially available software products, all operating on a local, distributed minicomputer system (fig. 1). Experimental capabilities currently supported in an automated fashion include both isothermal and thermomechanical fatigue and deformation testing capabilities. The future growth and expansion of this system will be directed toward providing multiaxial test control, enhanced thermomechanical test control, and higher test frequency (hundreds of hertz).

Research Project Model

A model of a typical research project was developed by examining the process used by researchers in the course of conducting materials behavior research (fig. 2). The principal emphasis of the automation effort at the Lewis Research Center has been on supporting the formulation and conduct of experiments, the analysis of the resulting data, and the reporting of research progress.

Hypothesis formulation is an intensely creative (human) process and therefore is not easily subjectable to automation. Whether this will remain true in the future is a topic of fervent debate and will not be discussed here, save to say that automation tools can do much to support this creative process. An identical statement can be made for the conclusion formulation process.

Experiment Formulation and Conduct

A basic model of this process is given in figure 3. The researcher, attempting to prove a hypothesis, first formulates an experiment or set of experiments. Having a suitable description (generally symbolic in nature), a parametrization is made to fix the precise nature of the tests desired. In this way all control parameters and measurement variables are defined, as well as their strategies. At this point these requirements must be translated into the form of a computer program in order that the desired test can be executed. Generally, this has meant the creation of unique programs, a consequence we are seeking to minimize.

Our present capabilities consist of a very general uniaxial, isothermal test-creation and control capability, as well as a number of unique programs for conducting thermomechanical tests. The unique programs are generated in the usual

sense; the general development process and supporting tools are described in figures 4 and 5. A program is developed and tested (to the maximum extent possible) on the host processor, where a full complement of tools are present to support such activities.

When the requirements of an experiment fall within the uniaxial, isothermal test catagory, an automated process is used. A set of command waveform and data acquisition requirements are generally related: a materials test command waveform and data acquisition requirement can always be decomposed into "blocks" where certain sequences of command and data acquisition are fixed in relation to one another and usually repeated as a block for a finite number of interations. These "blocks" differ from one to another based on changing data acquisition needs, control mode differences, command waveform differences, or a combination of these. At times, these blocks are concatenated, forming yet another "block". Because of this, a capability to nest a series of "blocks" exists. These test control requirements are implemented through the creation of a "control tree", an ordered path connecting elements, or nodes, of operations. There are five types of nodes, each possessing a set of usage rules for implementing its functions. A typical test, the constant-amplitude strain-controlled fatigue test, and its control tree are given in figure 6. As can be seen, node types exist for expressing repetition, command waveform character, and data acquisition parameters and strategies. This structure effectively provides for the creation of virtually any kind of test - it is adaptable to include other capabilities as well. In fact, the extensions of multiaxial test control, computed variable control and thermomechanical test control were incorporated into the basic data structure and program design and will be implemented in the future.

Once the control tree is generated, the actual experiment can be conducted. This is accomplished through a program which interprets the control tree and effects the operations called for. This multitasked and interrupt-driven program performs in real-time. The interface provides for the usual controls during execution: begin the test, pause, resume, status request, and abort. At this time, it is not possible to alter either the tree structure nor node (test) parameters dynamically other than through the aforementioned interface. This capability is latent in the basic design, however, and will be implemented in the future. A number of programs (an environment) support the creation and execution of tests using the control-tree approach (fig. 7). Support functions include capabilities to:

(a) Uniquely describe a given uniaxial materials testing system in terms of transducer complement, calibration data, etc.
(b) Create control trees from parametric descriptions of desired tests.
(c) Conduct materials tests from control trees previously generated.
(d) Produce formatted test reports from the data acquired during the execution of an actual test.
(e) Provide interface mappings between a given computer system and a given servohydraulic testing system.
(f) Provide general communications capabilities among the lab computer systems, including file transfer and virtual interface capabilities.

A more complete description of this environment as well as a thorough discussion of the control-tree concept will appear in a future paper.

A basic model of this process is given in figure 8. The usual procedure for analyzing experimental test results involves organizing the primative data, deciding how to analyze the results (task definition), and generating (unique) programs for the analysis. This procedure is quite lengthy and cumbersome, especially within the context of software available to automate much, if not all of this process. We have elected to use commercially available software systems for this portion of the research process; our choice of software includes a relational data base management system (residing on the host processor), and an integrated graphics/statistics/modeling program (residing on personal computers). Key features of these systems are shown in figures 9 and 10.

The manner in which these system are used in our laboratory is characterized by two separate environments: the relational DBMS resides on the host computer system and is the primary organizing and archiving system. Data acquired in the laboratory are loaded into this system after each experiment (or set of experiments). The interactive analysis system, residing on personal computers distributed throughout the building, accesses the data through the DBMS (all systems are networked over the Lewis CATV local area network). The user need not physically handle the data at all - electronic transfer of compatible data files throughout the laboratory computer system is possible. We have found this environment to be both powerful and efficient.

The final portion of the analysis process is reporting. For this function, we are using a variety of work processing and text editing programs: each individual is using his or her choice. The fundamental characteristic of this process, however, is the ability of these programs to exchange text files with the secretarial word processing systems.

CONCLUSION

The system in use for conducting research at the Lewis Research Center's high temperature fatigue and structures laboratory has been described. Those areas of the research process that could be automated in an effective manner through the use of commercially available software systems were. For those areas not effectively automated through commercially available systems, custom systems were developed. A key characteristic of the test conduct portion of the described system is the notion of a control tree, the principal means of describing and executing materials tests under computer control. The environment supporting the creation and execution of control trees was described. Finally, future extensions planned for enhanced control capability were described.

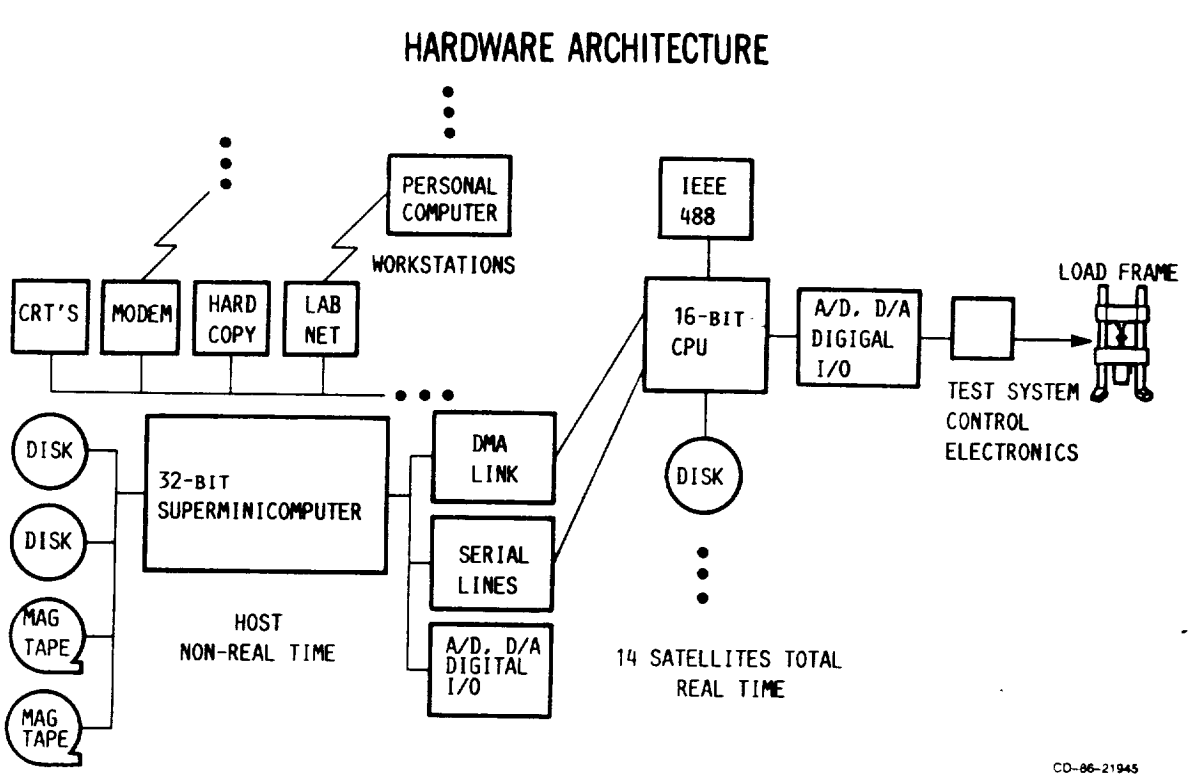

Figure 1

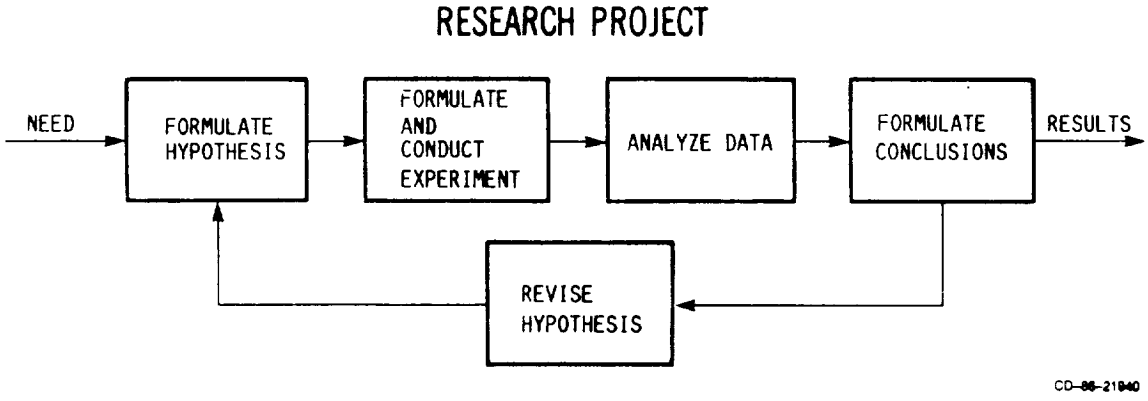

Figure 2

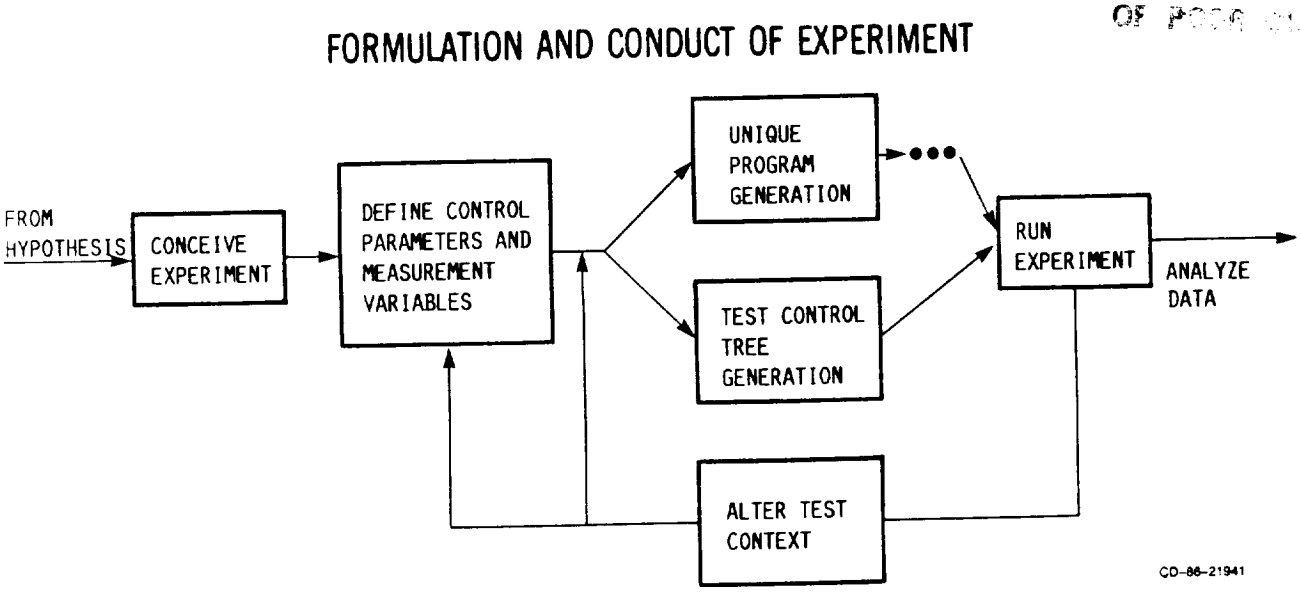

Figure 3

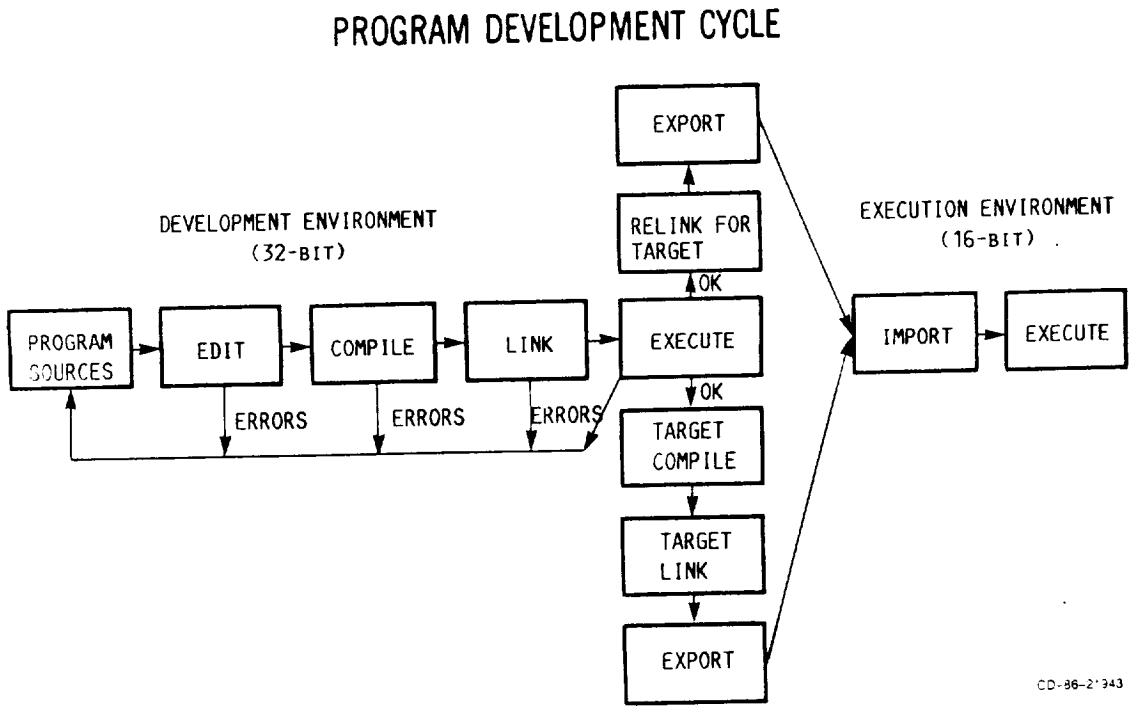

Figure 4

PROGRAM DEVELOPMENT TOOLS

- SOURCE EDITORS
- LANGUAGE PROCESSORS
  - ADA
  - PASCAL
  - FORTRAN-77
  - BASIC
  - ASSEMBLER
- LINKER
- MISCELLANEOUS TOOLS
  - CONFIGURATION CONTROL UTILITY
  - SYMBOLIC DEBUGGERS
  - LIBRARY EDITOR
  - FILE EDITOR
  - ETC.
- LIBRARIES
  - SENSOR INPUT/OUTPUT
  - MATHEMATICS
  - STATISTICS
  - GRAPHICS

CD-86-21939

Figure 5

TYPICAL FATIGUE TEST

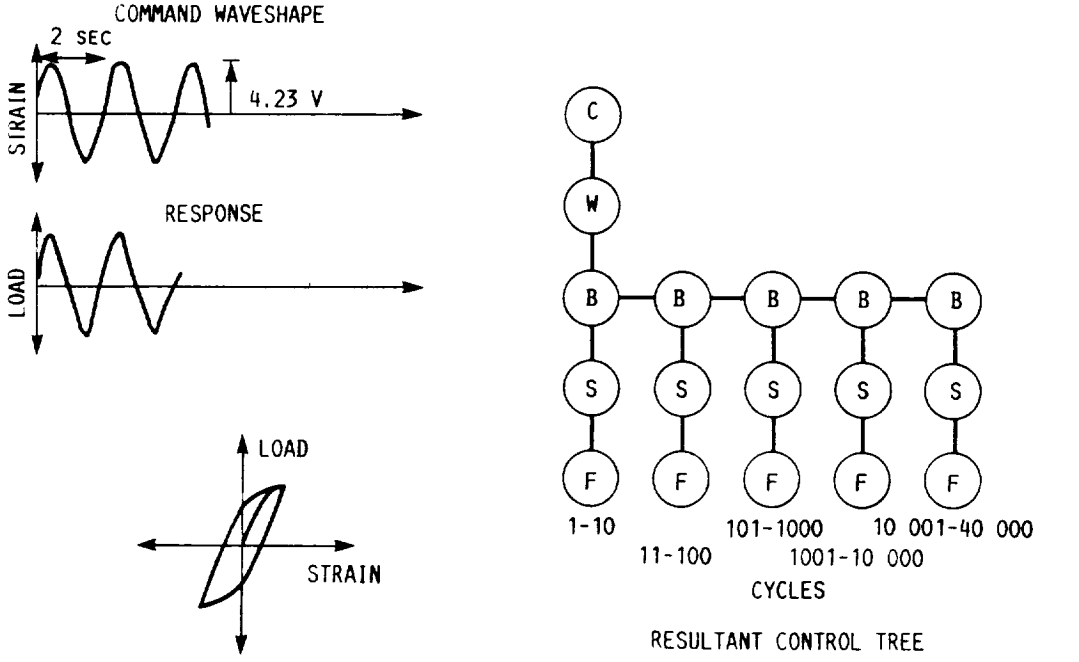

CD-86-21942

Figure 6

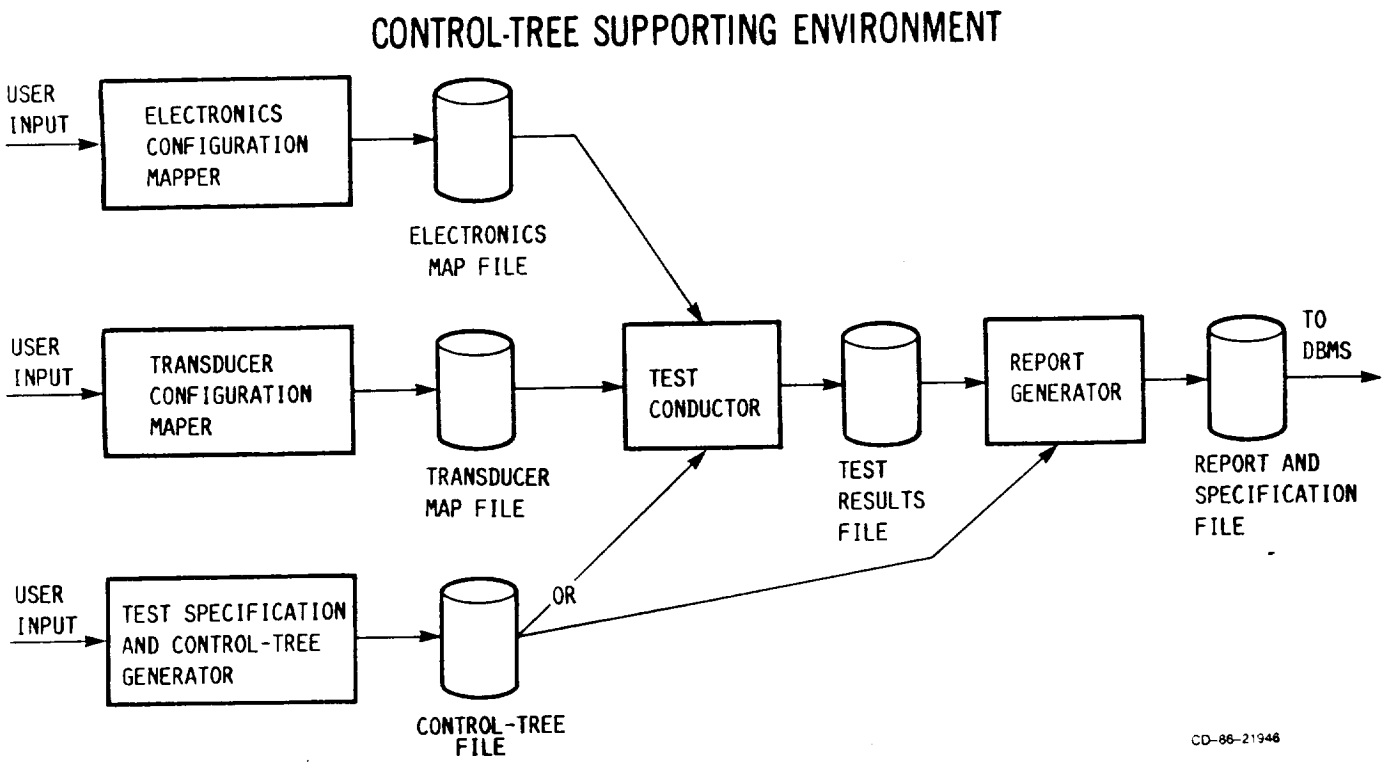

Figure 7

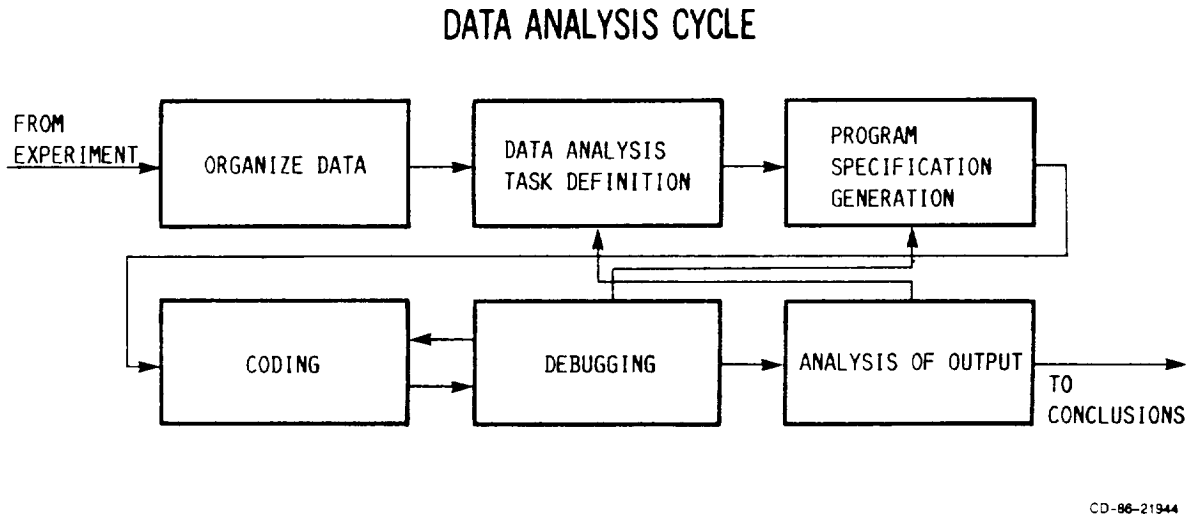

Figure 8

RELATIONAL DBMS

- MULTIUSER DATA ACCESS, SHARING
- RELATIONAL; USERS VIEW DATA AS COLLECTIONS OF TABLES
- SQL DATA MANIPULATION/DEFINITION LANGUAGE
- INTERACTIVE AND PROGRAM CONTROLLED ACCESS

CD-86-21938

Figure 9

INTERACTIVE ANALYSIS ENVIRONMENT

- DATA ENTRY AND RETRIEVAL FUNCTIONS
- DATA TRANSFORMATION AND ANALYSIS
- GRAPHICS: COLOR, 2- AND 3-D, DIGITAL PLOTTER
- CURVE FITTING
- STATISTICS
- ANALYTICAL MODELING
- INTERACTIVE OR PROGRAM-DRIVEN

CD-86-21937

Figure 10

N89-12918

Grain Boundary Oxidation and Its Effects on High Temperature Fatigue Life*

H.W. Liu and Yoshiki Oshida

Department of Mechanical and Aerospace Engineering
Syracuse University

INTRODUCTION

Fatigue lives at elevated temperatures are often shortened by creep and/or oxidation. Creep causes grain boundary void nucleation and grain boundary cavitation. Grain boundary voids and cavities will accelerate fatigue crack nucleation and propagation, and thereby shorten fatigue life.

Gibb's free energies of metal oxide formation are negative. No metal or alloy is stable when exposed to an oxidizing environment. Grain boundary is a path of rapid diffusion. Therefore, grain boundary oxidation rate is higher and grain boundary oxide penetration is deeper. Oxide is brittle and fractures easily when a tensile stress is applied. Grain boundary oxide crack may serve as a nucleus of a fatigue crack and the crack nucleus will grow by the subsequent cyclic fatigue load. Therefore, grain boundary may shorten fatigue crack nucleation life. Oxidation also accelerates fatigue crack propagation. Hence, grain boundary oxidation will shorten fatigue lives at elevated temperatures.

Both oxidation and creep have been shown as possible mechanisms for high temperature fatigue damage. Grain boundary void formation and cavitation are the result of surface diffusion and/or grain boundary vacancy diffusion, while grain boundary oxidation is primarily caused by the diffusion of oxygen. The kinetics of the diffusions of vacancies and oxygen atoms is shown schematically in Figure (1). One mechanism dominates in the high temperature region and the other dominates in the low temperature region. Therefore, the question is not which one of these two mechanisms causes high temperature fatigue damage. The problem is to define the different regions dominated by these two different mechanisms.

The functional relationships between the damage rate of fatigue crack nucleation and propagation and the kinetic process of oxygen diffusion depend on the detailed physical processes. In this study, the kinetics of grain boundary oxidation penetration was invetigated. The statistical distribution of grain boundary penetration depth was analyzed. Its effect on high temperature fatigue life will be disscussed. A model of intermittent micro-ruptures of grain boundary oxide was proposed for high temperature fatigue crack growth. The details of these studies are reported in references 1 and 2.

* Work done under NASA Grant NAG3-348

GRAIN BOUNDARY OXIDATION KINETICS AND ITS EFFECTS ON FATIGUE CRACK NUCLEATION

Cylindrical coupons of a nickel-base superalloy (TAZ-8A) were subjected to oxidation in air under the stress-free condition. The oxidized disk coupons were sectioned, each sectioned surface was examined under an optical microscope, and the maximum grain boundary oxide penetration depth, a_{mi} of the ith section was measured. Then a thin layer of coupon approximately 80μm was removed. Then the new surface was polished, and another a_{mi} of the new surface was measured. This process was repeated 12 times for each test coupon to collect enough data for the statistical analysis. Couling and Smoluchowski (ref. 3) and Turnbal and Hoffman (ref. 4) have found that grain boundary diffusion penetration is a function of the angle of (100) tilt boundaries. Therefore, it is expected that the grain boundary oxide penetration depth, a_m, is not uniform. It varies from one grain boundary to another. Figure 2 shows the Weibull plot of 480 data points for oxidation at 800°C for 500 hours. The data fits the Weibull distribution function very well.

$$[1 - P(a_{mi})] = \exp\left[-\left(\frac{a_{mi} - a_u}{a_o}\right)^b\right] = \exp\left[-\frac{(a_{mi} - a_u)^b}{\eta_a}\right] \qquad (1)$$

$P(a_{mi})$ is the probability of finding an oxide depth less than a_{mi} on a sectioned surface. The probability of finding a depth equal to or deeper than a_{mi} is $[1 - P(a_{mi})]$. For the data in Figure 2, b = 2.0, a_u = 40μm, and a_o = 31 μm.

Grain boundary diffusion is several orders of magnitude faster than bulk diffusion. If the flux due to bulk diffusion is neglected, grain boundary diffusion can be considered a channeled one-dimensional flow. With a constant oxygen concentration C_o at the "entrance" of the grain boundary, the oxygen concentration in the boundary is

$$C(x, t) = C_o\left[1 - \mathrm{erf}\left(\frac{x}{2\sqrt{D_{gb}t}}\right)\right] \qquad (2)$$

where erf is the error function, D_{gb} is the grain boundary diffusion coefficient. "Bulk" oxide will be formed when the oxygen concentration reaches a certain critical value, C_c. According to Equation (2),

$$C_c = C_o\left[1 - \mathrm{erf}\left(\frac{x_c}{2\sqrt{D_{gb}t}}\right)\right] \qquad (3)$$

x_c is the depth of the oxide penetration, where $C = C_c$. According to Equation (3), the quantity $(x_c/D_{gb}t)$ must be a constant, and x_c must be proportional to $\sqrt{D_{gb}t}$. Therefore, the grain boundary oxide penetration must be proportional to $\sqrt{t}$.

However, the model does not take the bulk diffusion and the chemical process into consideration. Perhaps it is reasonable to assume that a_{mi} is proportional to $(D_{gb}t)^n$. Therefore a_{mi} must have the form

$$\frac{a_{mi}}{B} = \beta\left(\frac{D_{gb}t}{B}\right)^n \qquad (4a)$$

or

$$a_{mi} = \alpha_i\, t^n \exp\left(-\frac{n\Delta H}{RT}\right) = \alpha_i\, t^n \exp\left(-\frac{Q}{RT}\right) \qquad (4b)$$

B is the magnitude of the diffusion jumping vector or interatomic spacing.

The grain boundary oxide penetration depths were measured at the oxidation temperatures of 600, 800, and 1000°C at the exposure time from 100 to 1000 hours. The regression analysis of the data gives the following empirical relation

$$a_{mi}(cm) = 1.34 \times 10^{-3}\, t^{0.25} \exp(-4.26/RT) \tag{5}$$

where t is in seconds, the activation energy in kcal/mol, and T in ^{o}K. The coefficient of auto-correlation is 0.96.

Assume the relation between a_{mi}, t, and T is deterministic. The deviation of each measured penetration depth from the empirical relation can be lumped into the term α_i in Equation (4b).

$$\alpha_i = a_{mi}\, t^{-n} \exp(\frac{Q}{RT}) \tag{6}$$

At any temperature T and exposure time t, with the measure a_{mi} known, the value of α_i can be calculated from Equation (6). The data of 144 values of α_i fit well the Weibull distribution function as shown in Figure (3).

$$[1 - P_i(\alpha)] = \exp\left[-\left(\frac{\alpha - \alpha_u}{\alpha_o}\right)^b\right] = \exp\left[-\frac{(\alpha - \alpha_u)^b}{\eta_\alpha}\right] \tag{7}$$

$P_i(\alpha)$ is the probability of finding an α-value less than α. The value of b, α_u, α_o are 1.85, 0.53×10^{-3} and 0.51×10^{-3} respectively.

The maximum α-value along the periphery of the i'th sectioned surface can be considered as the α_i-value of an exposed area of $\pi\delta d$ of a test coupon. δ is the coupon diameter and d is the grain size. Another sectioned surface at a distance one grain diameter away contains an entirely different set of grain boundaries and it is another independent sample.

If $P_s(\alpha)$ is the probability of finding an α-value less than α on an exposed area s. $P_s(\alpha)$ is related to $P_i(\alpha)$

$$[1 - P_s(\alpha)] = [1 - P_i(\alpha)]^{s/\pi\delta d} \tag{8}$$

The value of $P_s(\alpha)$ might be taken as the value of $P_s(a)$, the probability of finding a penetration depth less than a on an exposed surface area s. Therefore the data measured from the test coupons can be used to extrapolate to a much larger surface area of an engineering component.

Oxide is brittle and fractures easily under a tensile stress. Once an oxide crack is formed, the crack will continue to grow under a cyclic fatigue load. The oxide crack can be considered as a precrack. The remaining fatigue life, N_{fa_o} of a precracked specimen or a precracked engineering component is a function of the precrack size, a_o

$$N_{fa_o} = f(a_o) \tag{9}$$

The probability of having fatigue life N_{fa_o} is also the probability of having an oxide crack size a_o. Therefore, the statistical scatter of the fatigue lives at elevated temperatures may reflect the scatter of the oxide penetration depth.

A fatigue crack is often nucleated by cyclic plastic deformation. This nucleation mechanism is cylcle dependent. The damage mechanism by oxide crack formation is time dependent. Therefore, for a very low cyclic frequency, the oxide crack formation may preceed the fatigue crack nucleation by the cyclic plastic formation process. Thus the fatigue nucleation life (in terms of number of load cycles) might be shortened. Perhaps, the shortened fatigue life at elevated temperatures and the wide scatter of the fatigue life of engineering components are caused by grain boundary oxidation.

THE INTERMITTENT MICRO-RUPTURE MODEL FOR HIGH TEMPERATURE FATIGUE CRACK GROWTH

Figure (4) shows the frequency effect on fatigue crack growth rate for a number of high temperature alloys. For each data set, both ΔK and test temperature were maintained constant.

In the low frequency region, the fatigue crack growth rate, da/dN, of Inconel 718, Inconel X-750, Astroloy at 700 and 760°C, and Cr-Mo steels, are inversely proportional to frequency, ν. The time rates of the fatigue crack growth, da/dt = (da/dN)(1/ν) are constant. In this region, the fatigue crack growth is intergranular.

For constant-K tests at elevated temperatures, two crack growth features are common: (i) the time rate of crack growth is constant, (i.e. da/dt = constant) and (ii) crack growth is intergranular. Crack growth at constant-K is often referred to as creep crack growth. Fatigue crack growth in the low frequency region has these two same features. Therefore, fatigue crack growth in the low frequency region is often referred to as creep crack growth.

One question can be raised. Do the inverse relation between da/dN and ν and the intergranular crack growth preclude grain boundary oxidation as the underlying cause of the accelerated fatigue crack growth at elevated temperatures? In this section, a fatigue crack growth model, based on the fracture of grain boundary oxide, will be constructed. The model agrees with the inverse relation between da/dN and ν. The fracture path following the grain boundary oxide, is intergranular.

In Figure (4), the cyclic loading patterns are also shown. For Inconel 718 and Astroloy at 760°C, a hold time, Δt_H at K_{max} was applied. For Inconel X-750, Cr-Mo steels, and Astroloy at 700°C, a triangular loading pattern was used. The crack growth with a hold time will be analyzed first.

The oxygen arriving at a crack tip will have to diffuse into the region ahead of the crack tip in order to form oxide along the grain boundary. When the crack tip grain boundary oxide reaches a critical size, δa, the oxide will rupture and the crack will grow by the amount, δa. The critical size, δa, depends on the K-level during the hold time. Once the crack tip advances to its new position, this process of grain boundary diffusion, grain boundary oxidation, and the micro-rupture of the grain boundary oxide will be repeated again. This process of micro-rupture of crack tip grain boundary oxide can reoccur intermittently many times during a fatigue cycle.

During Δt_H at K_{max}, many micro-ruptures will take place. After each micro-rupture, the penetration of grain boundary oxide will have to start all over again

from "time" zero. Therefore, the time interval, δt necessary to reach the critical size δa is

$$\delta t = (B/D_{gb})(\delta a/\beta B)^{1/n} \tag{10}$$

The number of micro-ruptures during Δt_H is

$$m = \Delta t_H/\delta t = (\Delta t_H D_{gb}/B)(\beta B/\delta a)^{1/n} \tag{11}$$

m is linearly proportional to Δt_H and is inversely proportional to ν.

Fatigue crack growth per cycle is the sum of the micro-ruptures during Δt_H.

$$\frac{da}{dN} = m\delta a \tag{12}$$

From Equations (10, 11, and 12), we obtain

$$\frac{da}{dN} = \beta'\Delta t_H D_{gb} (B/\delta a)^{(1-n)/n} = \beta'(D_{gb}/\nu)(B/\delta a)^{(1-n)/n} \tag{13}$$

da/dN is inversely proportional to ν. For n=0.25, da/dN is inversely proportional to δa^3. Fatigue crack growth rate increases rapidly as δa becomes small. δa is smaller if the oxide is more brittle, if the flow stress of the material is higher, and if the crack tip stresses are in the state of plane strain.

Figure (5) shows the triangular loading patterns of two different frequencies. The time interval Δt_i at K_i is inversely proportional to ν. We treat Δt_i as the hold time at K_i. If the crack tip fields at K_i are the same at both of these two frequencies, the number of micro-ruptures during Δt_i is linearly proportional to Δt_i and is inversely proportional to ν. This must be true at every K_i-level. Fatigue crack growth is the sum of all of the micro-ruptures at all the K_i-levels during one fatigue cycle. Therefore da/dN is inversely proportional to ν. Fatigue crack growth follows the path of grain boundary oxide, therefore, it is intergranular.

We have shown grain boundary oxidation as a <u>possible</u> mechanism of high temperature damage that shortens fatigue life. Our work is only one of the many steps toward the construction of a quantitative model based on the physical damage processes caused by oxidation.

Only after the quantitative models of the physical processes of fatigue damage due to creep and oxidation are completed, we will be able to predict high temperature fatigue life accurately and with confidence. The quantitative relations between the diffusion rates of vacancies and oxygen, the rate of oxide rupture, the rate of nucleation and growth of voids and cavities, and the rate of fatigue damage have not yet been established.

Without a clear understanding of the underlying physical processes for the observed fatigue behaviors, it is difficult and unsafe to extrapolate a limited amount of experimental data for fatigue life predictions. For example, to extrapolate the crack growth rate in Figure (4), from the low frequency region into the high frequency region or vise versa will underestimate the growth rate. Therefore it is unsafe.

REFERENCES

1. Oshida, Yoshiki; and Liu, H.W.: Grain Boundary Oxidation and an Analysis of the Effects of Oxidation on Fatigue Crack Nucleation Life. To be published in the Proceedings of the ASTM Symposium on Low Cycle Fatigue: Direction for Future Research, Lake George, NY., Oct. 1985.

2. Liu, H.W.; and Oshida, Yoshiki: Grain Boundary Oxidation and Fatigue Crack Growth at Elevated Temperatures. To be published in the Jour. of Theoretical and Applied Fracture Mechanics.

3. Couling, L; and Smoluchowski, R.: Anisotropy of Diffusion in Grain Boundaries. J. Appl. Phys., 25, p.581, 1954.

4. Turnbull, D; and Hoffman, R.: The Effect of Relative Crystal and Boundary Orientations of Grain Boundary Diffusion Rates. Acta Met., 2, p.419, 1954.

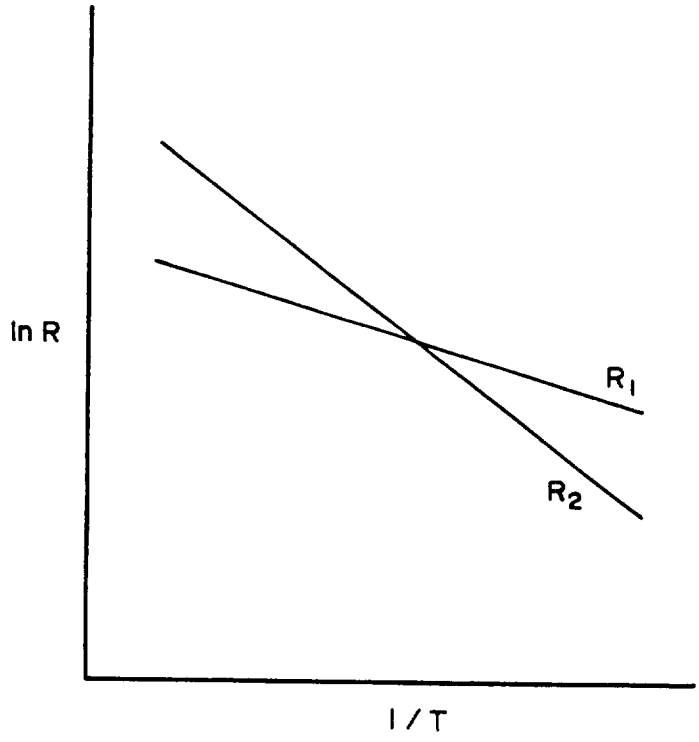

Figure 1. Schematic illustration of diffusion kinetics of vacancies and oxygen atoms

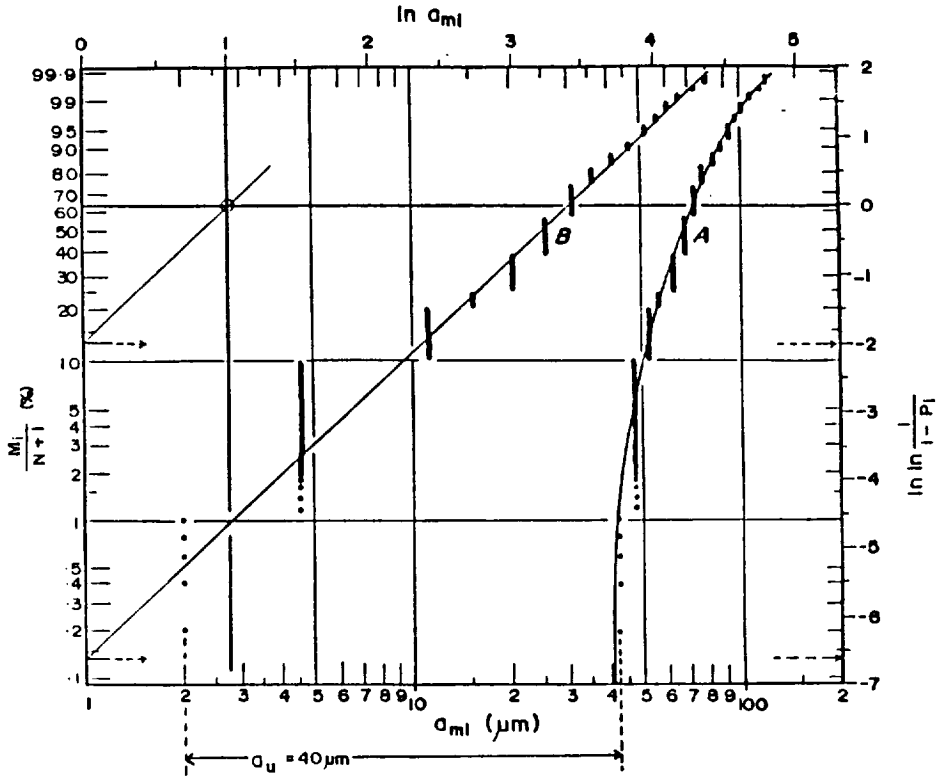

Figure 2. Weibull plot of a_{mi} (i = 480)

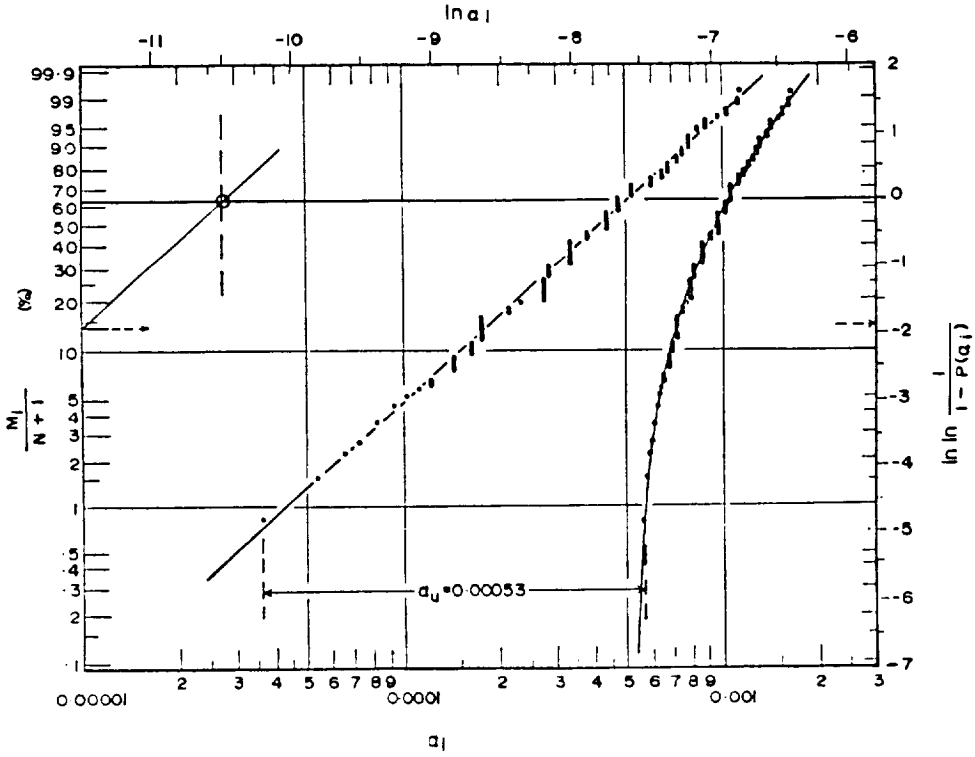

Figure 3. Weibull plot of α_i (i = 144)

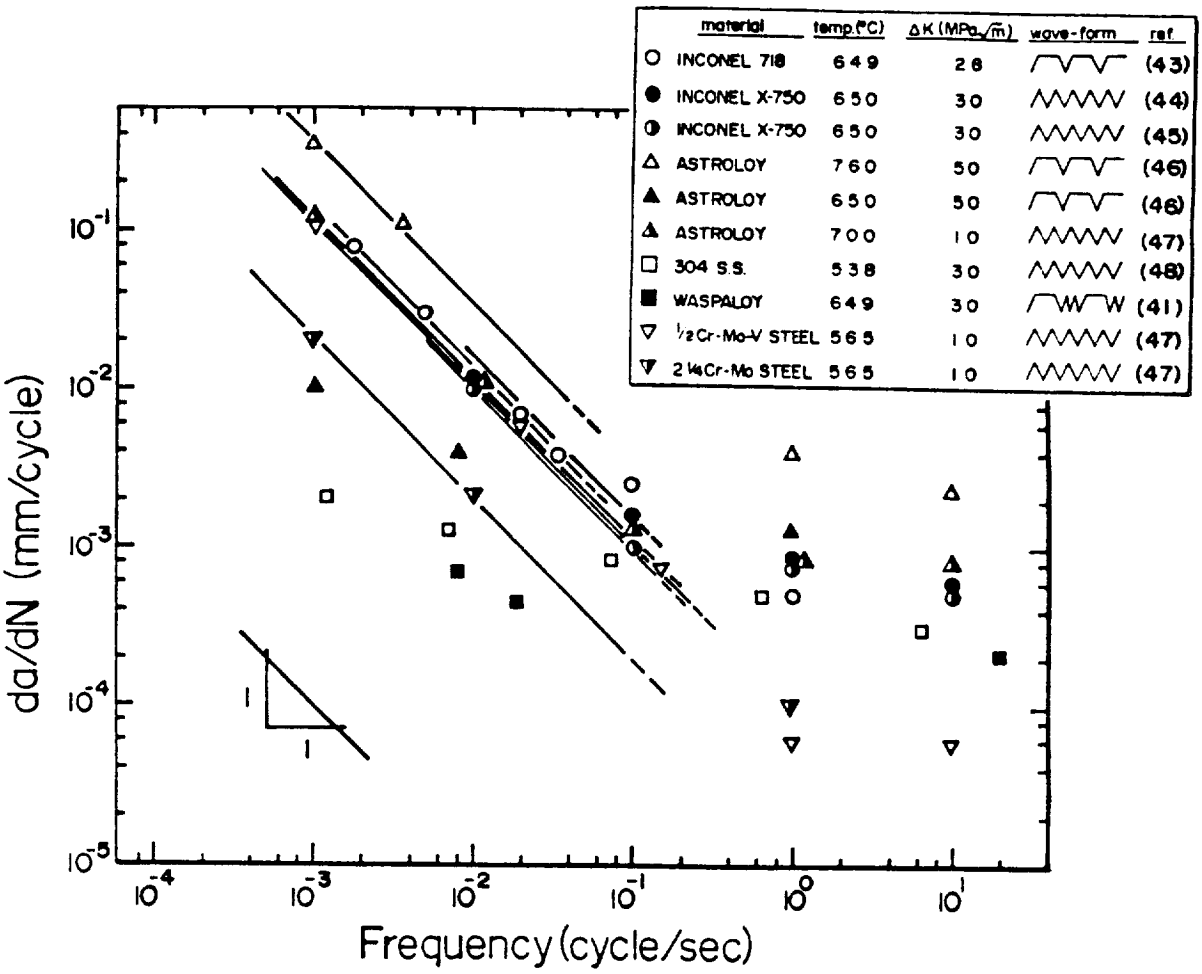

Figure 4. Frequency effect on fatigue crack growth

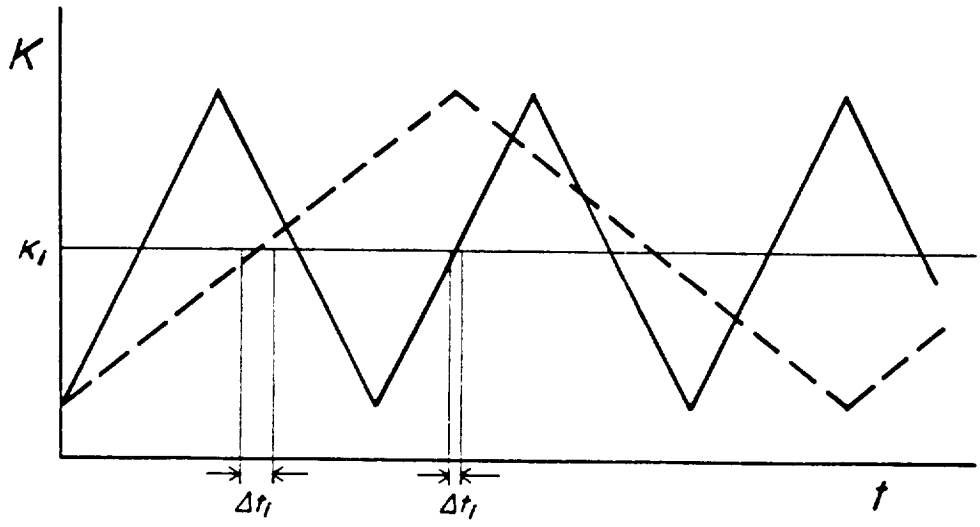

Figure 5. Triangular loading patterns of two different frequencies

A STUDY ON THERMAL BARRIER COATINGS INCLUDING THERMAL EXPANSION MISMATCH AND BOND COAT OXIDATION*

George C. Chang and Woraphat Phucharoen
Cleveland State University

Robert A. Miller
National Aeronautics and Space Administration
Lewis Research Center

1. INTRODUCTION

The present investigation deals with a plasma-sprayed thermal barrier coating (TBC) intended for high temperature applications to advanced gas turbine blades. Typically, this type of coating system consists of a zirconia-yttria ceramic layer with a nickel-chromium-aluminum bond coat on a superalloy substrate. The problem on hand is a complex one due to the fact that bond coat oxidation and thermal mismatch occur in the TBC, as reported in reference 1. Cracking in the TBC has also been experimentally illustrated in the same reference.

The purpose of this investigation is to help achieve a clearer understanding of the mechanical behavior of the TBC. The near-term objective is to study the stress states in a model thermal barrier coating as it cools down in air.

In this investigation, the powerful finite element method has been utilized to model a coated cylindrical specimen. Four successively refined finite element models have been developed. Some results obtained using the first two models have been reported in references 2, 3 and 4.

The present paper discusses progress in the current year. The major accomplishment is the successful development of an elastic TBC finite element model known as TBCG with interface geometry between the ceramic layer and the bond coat. An equally important milestone is the near-completion of the new elastic-plastic TBC finite element model called TBCGEP which yielded initial results. Representative results are presented in figures 11 through 22.

2. EXPERIMENTAL FINDINGS OF FRACTURING OF COATINGS

A number of researchers have reported their TBC work since the late 1970's. Most papers and reports dealt with testing of coated specimen ranging from cylindrical coupons to full-size turbine blades. Significant progress has been made, however, the central question of coating failure mechanism(s) has yet to be conclusively ascertained.

Of particular interest to the present investigation is the experimental work on TBC reported in reference 1. In that work, coated superalloy specimens were

* Research conducted under NASA-CSU Cooperative Research Agreement No. NCC-3-27

tested. The uncoated specimen which is illustrated in figure 1, had a radius of 0.65 cm. and a length of 7.60 cm. The specimens were plasma-sprayed in air with the zirconia-yttria (ZrO_2-8wt.% Y_2O_3) on a nickel-chromium-aluminum-zirconium bond coat. Coated specimens were next exposed to the combustion gases of a burner rig for varying periods of time before cooling took place. Most specimens went through many thermal cycles.

In reference 1, it was found that the coatings of all specimens tested in the air at temperatures high enough permitting bond coat oxidation eventually failed in spalling. The spalling which was visible had been examined by scanning electron microscopy (SEM) to be preceded by ceramic coating delamination. The TBC specimens invariably failed within the ceramic layer just above the bond coat on cooling in air from high temperatures. The same photomicrographs also showed the rough interface between the ceramic layer and the bond coat that contained oxides. More oxides were found in the region adjacent to the interface than the region away from the interface. Some interfaces were approximately sinusoidal with peak-to-peak and peak-to-valley dimensions up to 100 micrometers (μm).

These tests illustrated some TBC failure modes, and have led to the present analytical modeling effort.

3. FINITE ELEMENT MODELING OF A CYLINDRICAL THERMAL BARRIER COATING

To determine the quantitative nature of the stress (and strain) states associated with a TBC specimen, a general-purpose finite element program has been employed to model a cylindrical test specimen which is similar to the ones reported in reference 1. The modeling concept is illustrated in figure 1.

The test specimen is sufficiently long, as compared to its radius, that the problem can be approximated by a two-dimensional generalized plane-strain case. This approximation implies, as in the classical theory of elasticity, uniform strain in the axial (or z-) direction. The chief advantage of this approximation is to help keep the amount of computation to a manageable level on a super computer.

As shown in figure 1, a sinusoidal interface between the ceramic layer and the bond coat is introduced with a period of approximately 50 μm (0.0020 in.) and an amplitude of approximately 15 μm (0.0006 in.). This interface is much smoother than the one (50 μm) used for the results reported earlier in reference 4.

The three materials comprising the substrate, the bond coat, and the ceramic are assumed to be homogeneous and isotropic and elastic for the TBCG model. The bond material in the latest model, TBCGEP, however, is assumed to be elastic-plastic, following the classical theory of plasticity with von Mises' criterion for yielding or the onset of plastic flow. Strain hardening which has been built into the program, is controlled by the slope of the stress-strain curve. Up to four line segments can be used to specify the stress-strain curve associated with the bond material.

Each material, therefore, possesses its own temperature-dependent parameters, such as Young's modulus (E), Poisson's ratio (ν), and thermal expansion coefficient (α). In addition, the bond material has a plasticity parameter which

controls the yielding process (YP1). Finally, the bond material is capable of simulating oxidation effects in the manner discussed in reference 3 and 4, and elsewhere in this paper.

An overview of the more recent (third) model known as TBCG is given in figures 2 to 6. The model contains 1316 nodal points and 2140 elements, both triangular and quadrilateral. Particular attention has been given to the region in the vicinity of the model of fundamental interest in the discretization process. Most elements in the refined region are sized at several micrometers to insure fine resolution. Details of the refined region are shown in figures 7 to 10, where oxidized elements are shown in bold lines along the sinusoidal interface.

The actual modeling is done with the use of a general purpose computer program known as MARC (ref. 5) which is operational on a super computer (CRAY-I) at NASA Lewis Research Center.

The boundary conditions applied to the model are fully compatible with those normally required in the theory of continuum mechanics. More specifically, only radial displacements are allowed to take place along radial lines, OA and OB, in figures 2 and 3. Line AB is free to displace. Point O which represents the center of the unit slice or the z-axis of the cylindrical specimen, is fixed.

Model TBCGEP is identically the same as TBCG, with the exception of plasticity capability in the bond coat.

To simplify the complex problem on hand, only a uniform temperature field is imposed on the model specimen. The steady-state solution sought here will greatly aid in the interpretation of computational results.

4. STRESS STATES CAUSED BY THERMAL EXPANSION MISMATCH

With the use of the TBCG computer program, a problem simulating a cylindrical TBC specimen experiencing a temperature drop of 100°C from an assumed stress-free state at 700°C has been solved. This problem is referred to as Case B-2 which is identically the same as Case A-2 reported in reference 3 with only one difference. In the present case, a smoother ceramic-bond interface with an amplitude of 15 μm is specified. The corresponding magnitude for Case A-2 is 50 μm.

Material properties used for the present case are given in Table 1. Selected results of Case B-2 are shown in figures 11 through 13. The strains are of reasonable size and distribution, being analogous to the stresses. They are not presented here to keep the length of this paper to a proper limit.

From figure 11, it can be seen that stresses in the x-direction (or radial stresses) in the vicinity of the sine peak (asperity) are rather high and are tensile. Such high tensile stresses could easily initiate cracking at the asperities as the TBC specimen cools down. Note these stresses correspond to a temperature drop of 100°C. An additional temperature drop would produce proportionately increased stresses. Thus, there should be little doubt that micro-cracking could be initiated at the asperities at some point during the cooling process. This is especially convincing when one recalls that the occurrence of such

cracking may contribute to the acoustic emission observed as TBC specimens cool down (ref. 6).

The peak tensile radial stresses in figure 11 are only 55 percent as large as those found in Case A-2. The same is also true of the compressive radial stresses between the two cases. This reduction in stress buildup can be most logically attributed to the changing geometry between the two cases. A smoother interface causes less stress concentrations than a rougher interface.

The stresses in the y-direction (or hoop stresses), as shown in figure 12, are fairly uniform throughout the thickness of the ceramic layer. They are compressive, as expected. These stresses are only slightly smaller in magnitude than corresponding values for Case A-2. The reduction is in the range of about ten percent. The same is true of shearing stresses for both Cases B-2 and A-2. Again, the shearing stress maximizes near the interface where failure is observed in reference 1. At present, reliable data on allowable stresses from this ceramic material is lacking. It is therefore inappropriate to make any conclusive remarks about these two stresses, although the shearing stress is of significant magnitude (± 8 MPa).

5. STRESS STATES ASSOCIATED WITH BOND-COAT OXIDATION

Reference 1 reported that bond coat oxidation was seen to grow with thermal cycles when the test was conducted in the air. The failure of TBC was correlated with this oxidation of the bond coat. The oxide layer appeared to grow thicker with each exposure to the air at high temperature. The net effect is equivalent to inserting an extra oxide layer between the ceramic layer and the remaining unoxidized bond material. The oxide is largely alumina which is a very hard and strong material. As such, the stress state in the ceramic (and the bond) is expected to be severely impacted by the expanding oxide layer.

As a first attempt to model the effects of bond coat oxidation, the single layer of finite elements bordering on the sinusoidal interface have been assigned the properties of alumina. These are given in Table 1.

In this case, oxide growth has been represented by giving these elements an artificially large thermal expansion coefficient given by

$$\alpha_a = G \times \alpha$$

where G is a growth factor, and α is the usual thermal expansion coefficient of the oxide material (7.79×10^{-6}). Proper choice of G was discussed in reference 3.

For the present case, B-10, the growth factor, G, was set equal to -1000. A temperature drop of only 0.1°C was utilized to minimize thermal expansion mismatch stresses. This yielded a very modest expansion of 0.08% in the oxide layer. The resulting stresses due to this oxidation-like process are shown in figures 14 to 16.

The stresses obtained for Case B-10 are, in general, the reverse of those obtained for Case B-2. In figure 14, stresses in the x-direction are compressive near the peak of the asperity and tensile above the valley. Stresses in the

y-direction, as shown in figure 15, are positive near the peak of the asperity while still being negative elsewhere. Shearing stresses in figure 16, are, in general, in the opposite direction (opposite sign).

The magnitude of the above stresses are very large considering that only a very modest expansion of the oxide has been modeled. In particular, the size of tensile radial stresses in the ceramic above the valley is noteworthy. They are in the range of 6 to 10 MPa. Thus, the stress state due to oxidation can be expected to have a profound influence on the coating failure mechanism.

The present case is identically the same as Case A-10 reported in reference 3 with the only exception of interface geometry, the present case involves a smoother interface than Case A-10. As expected, radial stresses in case B-10 are approximately 15 percent lower than those of Case A-10. The overall pattern for radial stresses for Case B-10 is the same as that for Case A-10. The same can be said of patterns of hoop and shearing stresses between these two cases.

6. STRESS STATES RESULTING FROM THERMAL EXPANSION MISMATCH AND PRECRACKING

As radial stresses of large magnitude occur in the ceramic layer at the peak of the asperity accompanied by in-plane compressive stresses, such as shown in figures 11 and 12, cracking in the tangential (or hoop) direction may very well take place. Once cracks occur, the local stress states will be altered. The results of the TBCG calculation for a pre-selected, simulated crack are shown in figures 17 through 19. This problem is labeled Case B-14. The stresses correspond to a temperature drop of 100°C. The radial stresses in figure 17 have been redistributed in the presence of the crack. High tensile radial stresses continue to exist near crack tips, possibly causing additional circumferential cracking. Therefore, crack propagation is entirely expected. However, the magnitudes of such radial tensile stresses are expected to become progressively lower as the crack continues to grow in the circumferential direction. It is also noted that some compressive radial stresses do exist above the valley. Such compression is thought to be able to arrest (or at least slow down) the continued cracking in the absence of other forces (such as those resulting from oxidation) which promote crack growth. This stress phenomenon helps explain the previous observation made in reference 1, that TBC specimens which did not experience oxidation had a long thermal cycle life (e.g. in excess of 10,000 cycles).

Radial stresses at a considerable distance away from the pre-cracking are left almost unchanged from that of Case B-2, as expected. The same is also true with stresses in the y-direction and shearing stresses.

Results of a similar problem, Case A-14, were presented in reference 4. A comparison between the two sets of results indicates that stress patterns in both cases are very much similar, with the present case yielding a reduction of approximately 10 percent in stresses due to the presence of a smoother ceramic-bond interface. This observation is both logical and consistent with two other comparisons made earlier in this paper (in Sections 4 and 5).

7. PRELIMINARY RESULTS OF PLASTICITY IN THE BOND COAT

Initial operational capability of the newest computer program called TBCGEP was achieved in July 1986. This program has been designed to model the cylindrical TBC specimen with an elastic-plastic bond coat. By choice, the ceramic layer and the superalloy substrate remain elastic. Other than this plastic material property, all other features of TBCGEP are identically the same as those of the computer program TBCG.

Results of a preliminary elastic-plastic TBC run known as Case EP-2, are presented in figures 20 through 22. The problem parameters for the case under consideration are given in Table 1. The data used are nearly identical to those of Case B-2. However, a temperature drop of 0.1°C was utilized in this case on a trial basis. (This will also pave the way for successive calculations to accommodate plastic flow/strain hardening.) At the same time, the plasticity yield parameter (YP1) was arbitrarily set at 69 MPa for lack of proper data for the bond coat yielding behavior. (An experimental effort is underway to determine plastic behavior of a related bond coat material. Results from this particular testing are expected to be used for future TBCGEP runs).

The elastic-plastic results presented in figures 20 to 22 are necessarily preliminary in nature. The radial stresses in the bond coat are modest in magnitude. It is premature to draw any specific conclusions from these very limited numerical results of Case EP-2. However, the radial stress pattern in the ceramic, as shown in figure 20, is seen as somewhat similar to that of Case B-2, figure 11. The magnitudes of the elastic-plastic radial stresses in the ceramic are only a small fraction of that of the elastic case. Such low level of stresses could nevertheless be increased, or decreased, by the proper selection of the YP1 value for the bond coat material. As discussed in reference 7, it is generally understood that plasticity leads to the loss of energy in a loaded body, resulting in a somewhat lowered state of stresses than a similar elastic body subjected to the same loads and boundary conditions. In addition, the size of temperature drop will influence the state of stress as well. Thus, these radial stresses in the ceramic are presented here merely as an illustration of the plausible pattern. Considerable effort will be made to quantitatively interpret the meaning of several elastic-plastic runs in the future.

The same can also be said about the states of stresses in the y-direction and of the shearing stresses. Nonetheless, the low state of stress in the y-direction in the bond coat near the peak of asperity is noteworthy. Such a pattern is in clear contrast to that of the stress in the x-direction in the same region.

8. A PRELIMINARY MECHANISM FOR OXIDATION-INDUCED COATING FAILURE

In reference 3, a preliminary mechanism for oxidation-induced coating failure was proposed, as shown in figure 23. The results presented in preceding sections lend additional credibility to that proposed mechanism.

The proposed TBC failure mechanism is largely based on the elastic stress patterns. The actual mechanism would most likely be further complicated by the effects of inelasticity and anisotropy. Nevertheless, it appears that the current computer modeling effort has begun to provide important insights into the thermomechanical behavior of the thermal barrier coatings. Additional

elastic-plastic computer analyses planned for the next eight months will certainly contribute to the evaluation of the validity of the proposed mechanism.

9. CONCLUDING REMARKS

From the preceding discussions in Sections 4 through 6, it is not difficult to suggest that a rough ceramic-bond interface introduces states of higher stresses, as expected. This is a tradeoff the designer will have to deal with.

The capability to generate a reasonably useful set of data pertaining to the cylindrical TBC specimen now exists, along with a limited amount of data (presented here and in references 2, 3 and 4.) These are now available for use by designers or researchers who are interested in TBC failure by either oxidation or fracture caused stress intensities.

With the attainment of initial operational capability of the latest (and fourth) computer program called TBCGEP, several computer runs will be made to calculate stresses and strains in the cylindrical TBC specimen with an elastic-plastic bond coat capable of strain hardening following yielding. Experimental data on the strength and plastic behavior of the bond material, as well as the ceramic, would be of utmost usefulness to this modeling effort. The numerical data so generated by the TBCGEP model should be illustrative of the elastic-plastic behavior of the thermal barrier coating in a comprehensive way hitherto-before considered impossible. Such data could, in turn, guide the experimentalist and the designer in their work on the TBC.

The approach or methodology developed in this investigation is applicable to analyzing any TBC specimens or engine parts protected by related coatings. The latest program, the TBCGEP, can be modified to deal with more complex geometry, where necessary. The only limitation at present time is the computing power. Nevertheless, it is believed that a reasonable modeling effort of a coated turbine blade can now be attempted.

REFERENCES

1. Miller, R. A.; and Lowell, C. E.: Failure Mechanism of Thermal Barrier Coatings Exposed to Elevated Temperatures. Thin Solid Films, 95, 1983, pp. 265 - 273.

2. Chang, G. C.; and Phucharoen, W.: Finite Element Analysis of Thermal Barrier Coatings. NASA - Industry Workshop on Thermal Barrier Coatings, Middleburg Heights, May 1985.

3. Chang, G. C.; Phucharoen, W.; and Miller, R. A.: Thermal Expansion Mismatch and Oxidation in Thermal Barrier Coatings. NASA CP-2405, pp. 405 - 425, 1985.

4. Chang, George C.; Phucharoen, Woraphat; and Miller, Robert A.: Behavior of Thermal Barrier Coatings for Advanced Gas Turbine Blades. Surface and Coatings Technology, 1986 (in-print).

5. Anonymous: MARC Finite Element Program User Manual, Version K-1, MARC Analysis Research Corp., 1983.

6. Berndt, Christopher C.; and Miller, Robert A.: Failure Analysis of Plasma-Sprayed Thermal Barrier Coatings. NASA Technical Memorandum No. 83777, 1984.

7. Chang, George C.: Interaction of Plane Stress Waves With Lined or Unlined Tunnels in Elastic-Perfectly Plastic Media, Ph.D. thesis, University of Illinois, Urbana, Illinois, June 1966.

TABLE 1 MATERIAL AND OTHER PARAMETERS

PARAMETERS	Case B-2	Case B-10	Case B-14	Case EP-2
Young's Modulus (MPa)				
Substrate	$0.1758X10^{6}$	$0.1758X10^{6}$	$0.1758X10^{6}$	$0.1758X10^{6}$
Bond Coat	$0.1379X10^{6}$	$0.1379X10^{6}$	$0.1379X10^{6}$	$0.1379X10^{6}$
Oxide Layer	---	$0.3448X10^{6}$	---	---
Ceramic	$0.0276X10^{6}$	$0.0276X10^{6}$	$0.0276X10^{6}$	$0.0276X10^{6}$
Poisson's Ratio				
Substrate	0.25	0.25	0.25	0.25
Bond Coat	0.27	0.27	0.27	0.27
Oxide Layer	---	0.32	---	---
Ceramic	0.25	0.25	0.25	0.25
Coefficient of Thermal Expansion (/C)				
Substrate	$13.91X10^{-6}$	$13.91X10^{-6}$	$13.91X10^{-6}$	$13.91X10^{-6}$
Bond Coat	$15.16X10^{-6}$	$15.16X10^{-6}$	$15.16X10^{-6}$	$15.16X10^{-6}$
Oxide Layer	---	$-7.79X10^{-3}$	---	---
Ceramic	$10.01X10^{-6}$	$10.01X10^{-6}$	$10.01X10^{-6}$	$10.01X10^{-6}$
Cracks	NO	NO	YES	NO
Temperature Drop	-100°C	-0.1°C	-100°C	-0.1°C

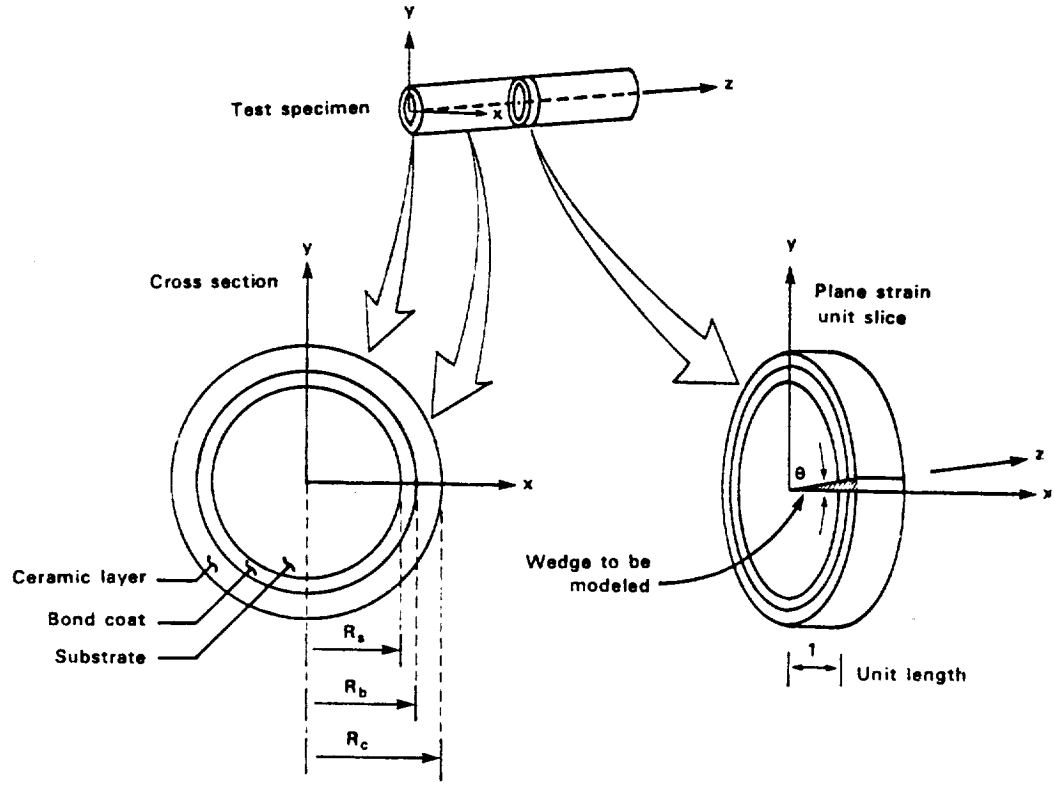

Figure 1. CYLINDRICAL TBC TEST SPECIMEN

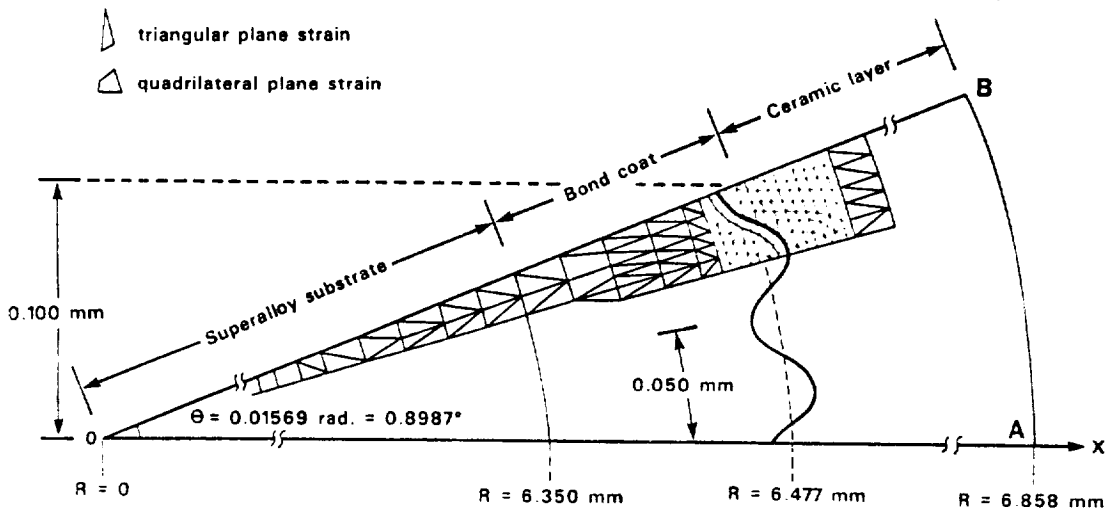

Figure 2. THE TBCG FINITE ELEMENT MODEL

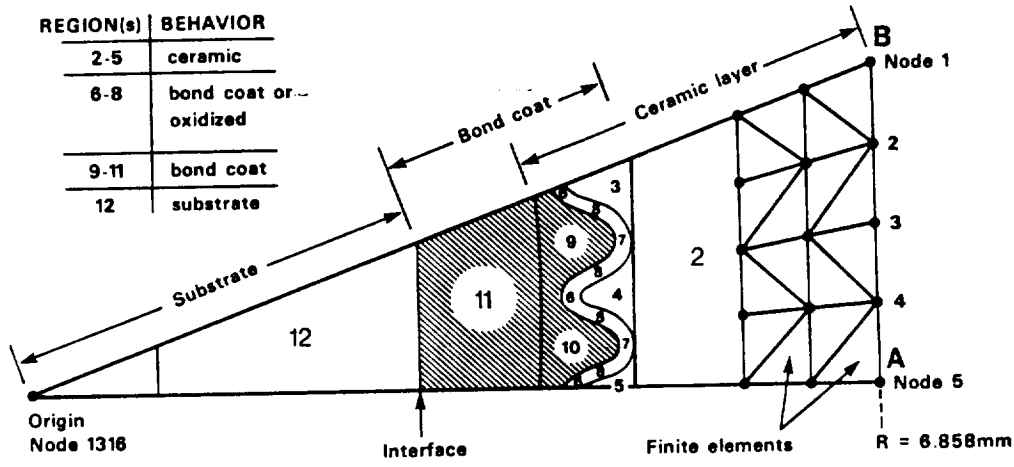

Figure 3. OVERVIEW OF THE ADVANCED TBCG MODEL

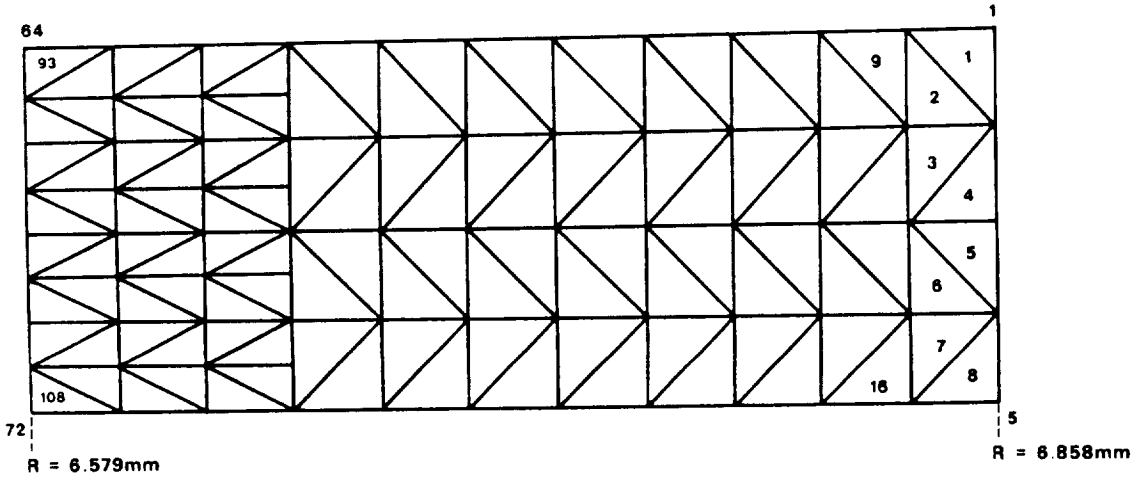

Figure 4. TBCG MODEL (Part 1)

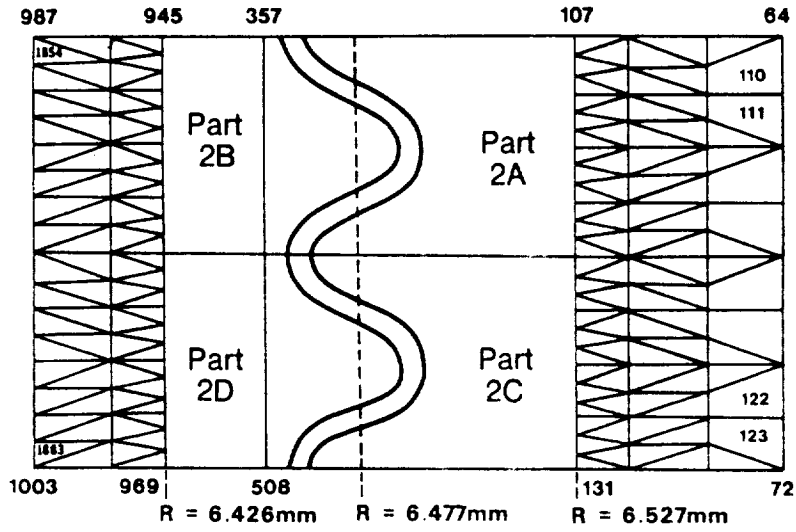

Figure 5. TBCG MODEL (Part 2)

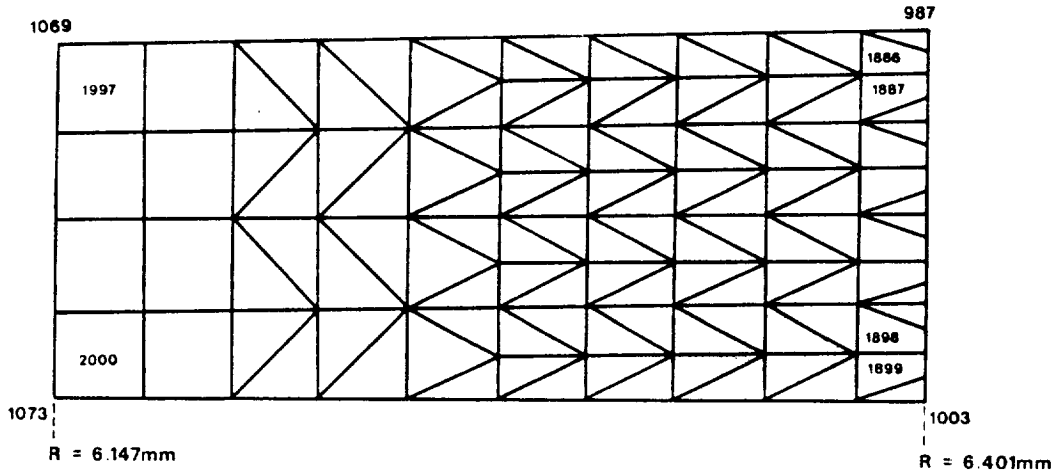

Figure 6. TBCG MODEL (Part 3)

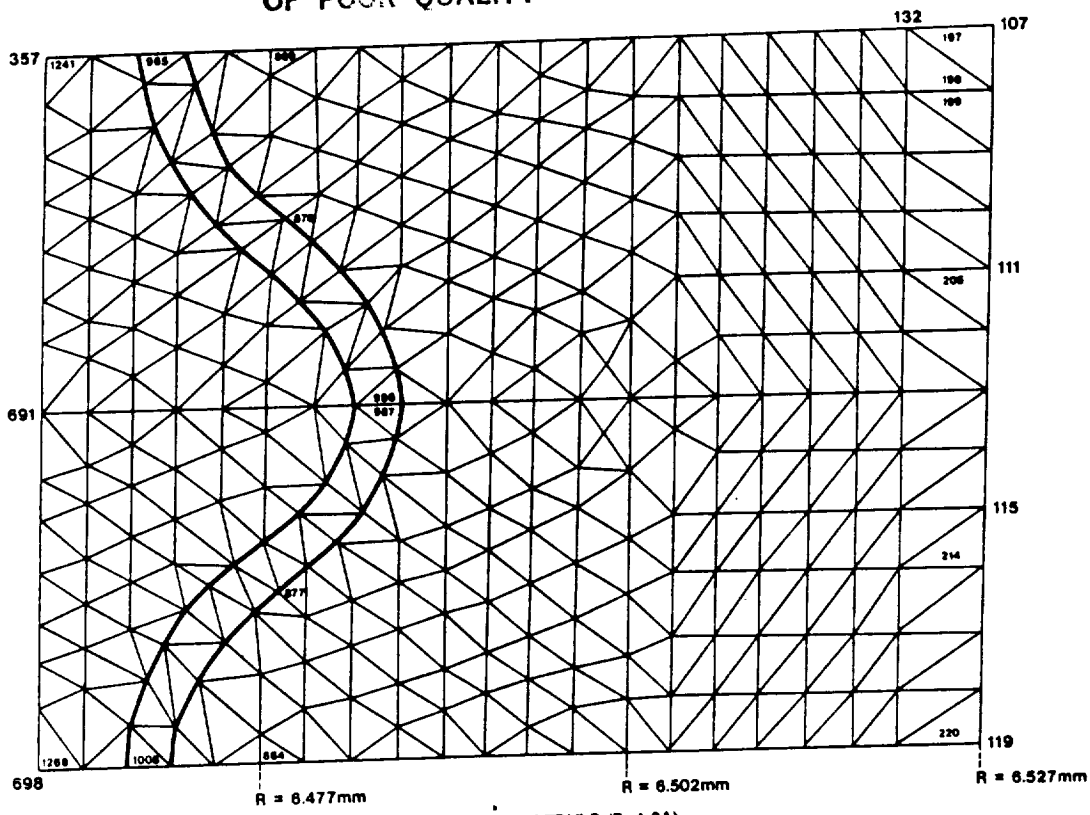

Figure 7. FINITE ELEMENT DETAILS (Part 2A)

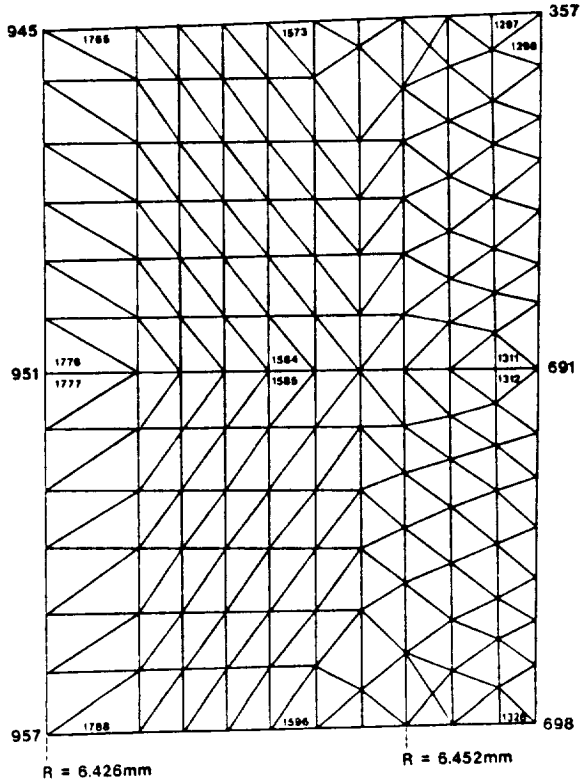

Figure 8. FINITE ELEMENT DETAILS (Part 2B)

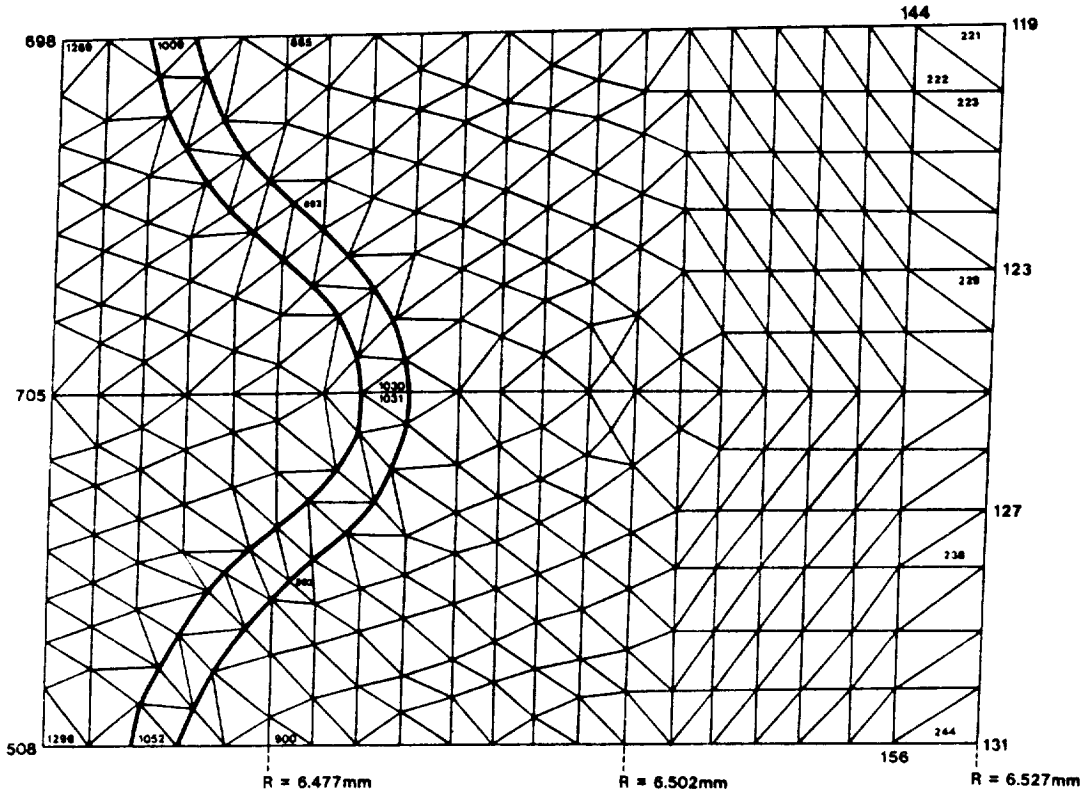

Figure 9. FINITE ELEMENT DETAILS (Part 2C)

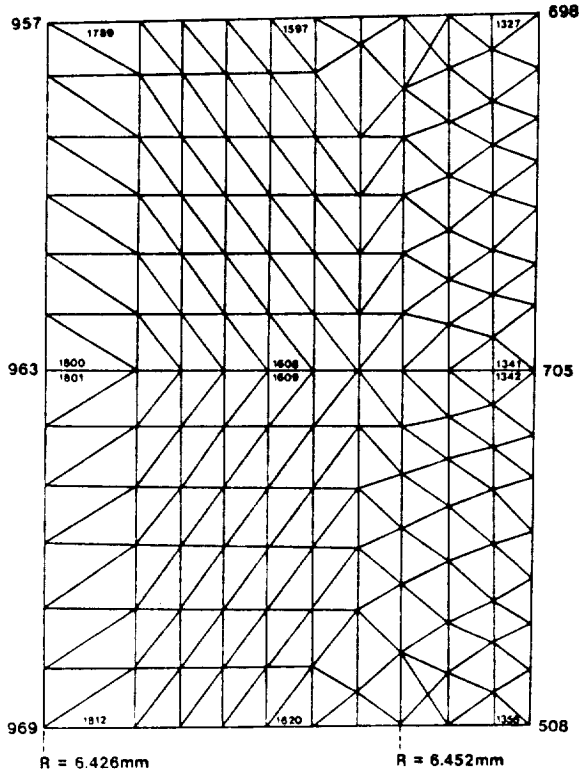

Figure 10. FINITE ELEMENT DETAILS (Part 2D)

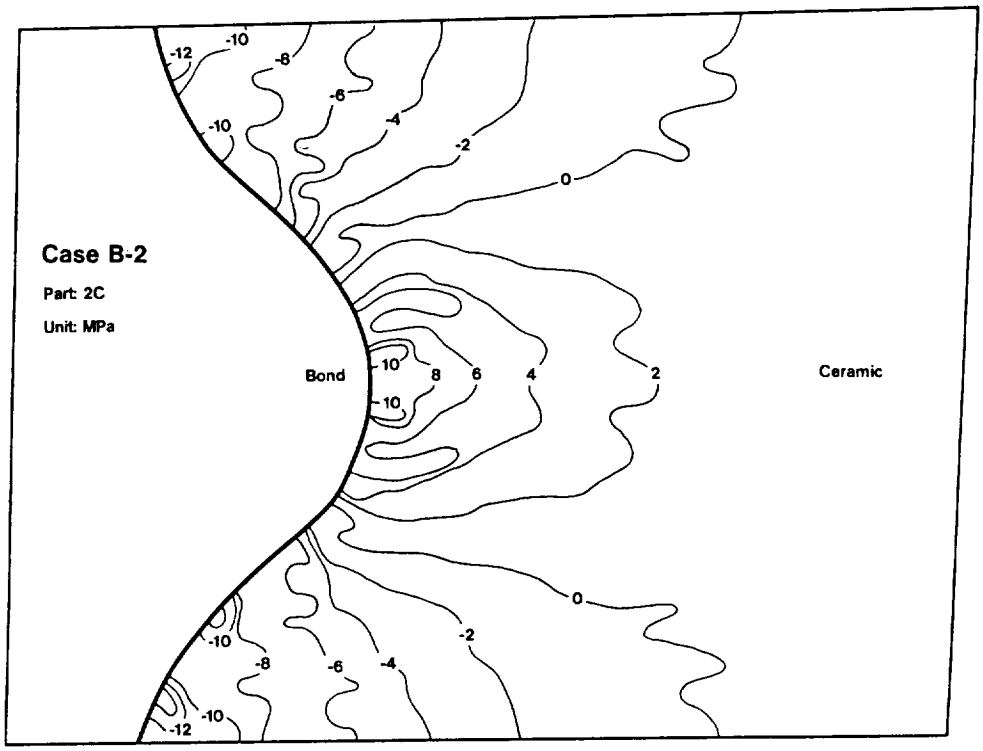

Figure 11. STRESS IN X-DIRECTION DUE TO THERMAL EXPANSION MISMATCH

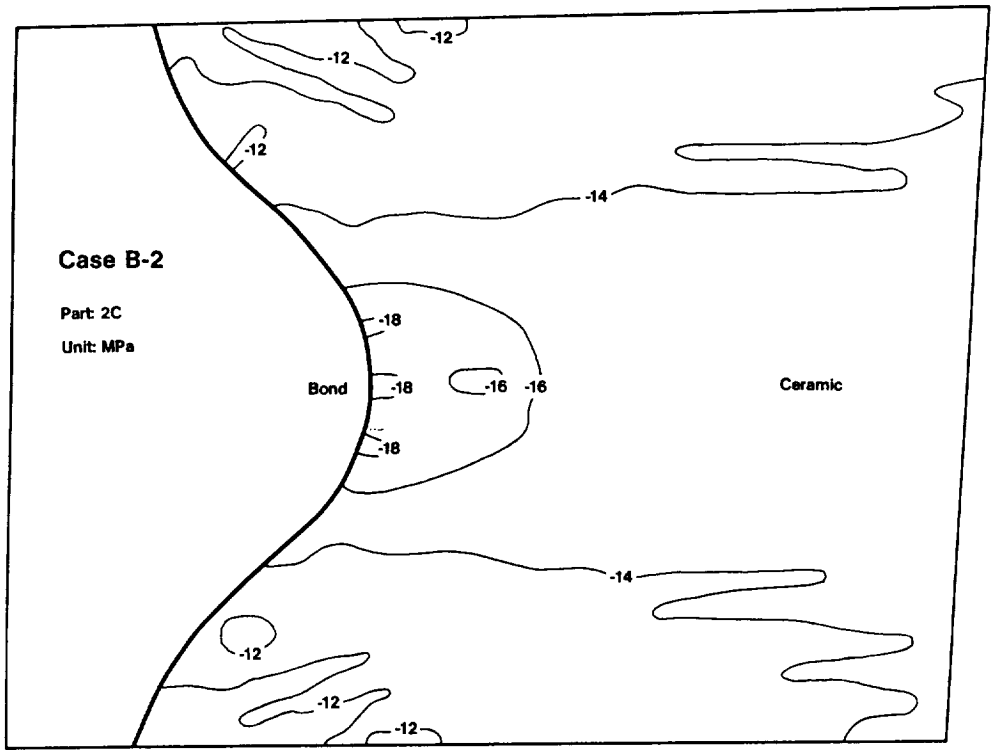

Figure 12. STRESS IN Y-DIRECTION DUE TO THERMAL EXPANSION MISMATCH

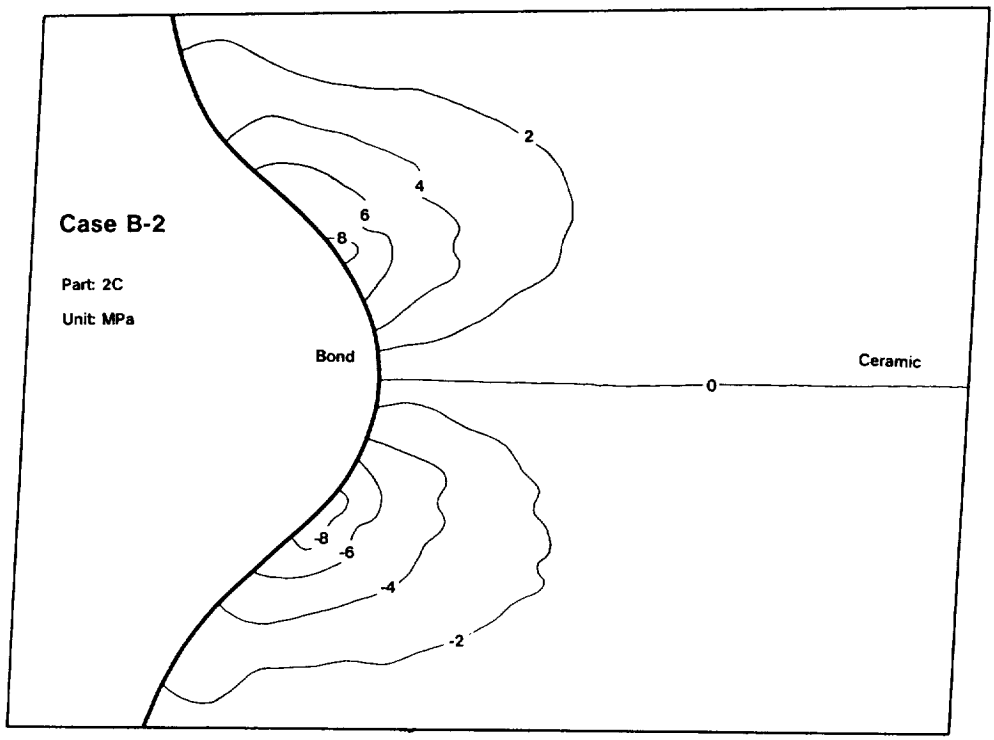

Figure 13. SHEARING STRESS DUE TO THERMAL EXPANSION MISMATCH

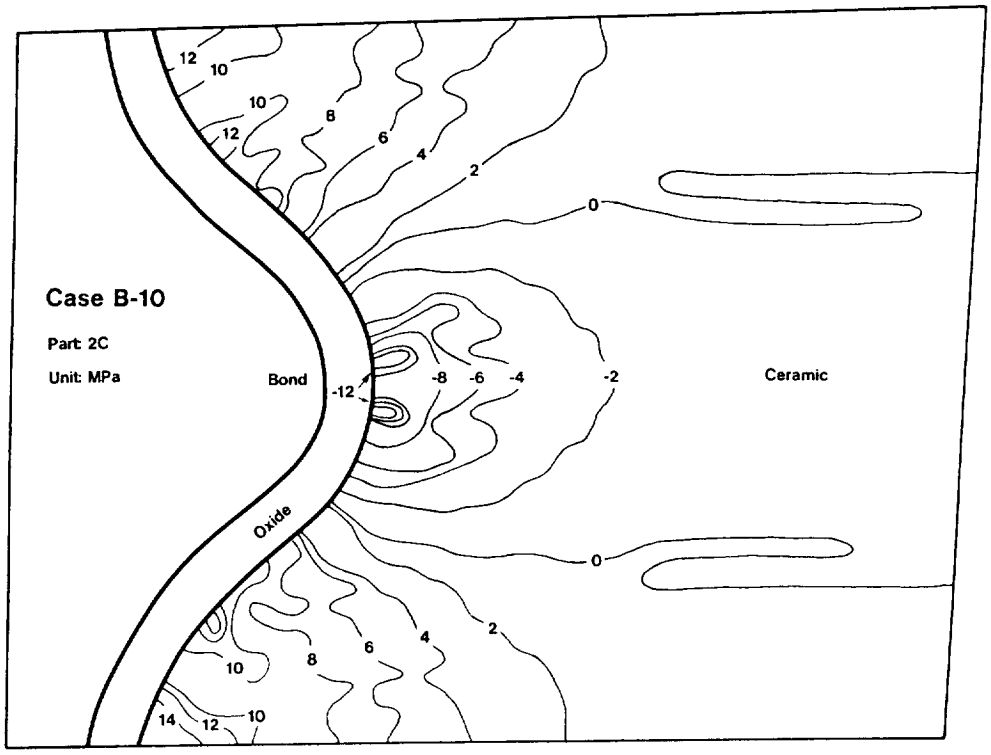

Figure 14. STRESS IN X-DIRECTION DUE TO OXIDATION

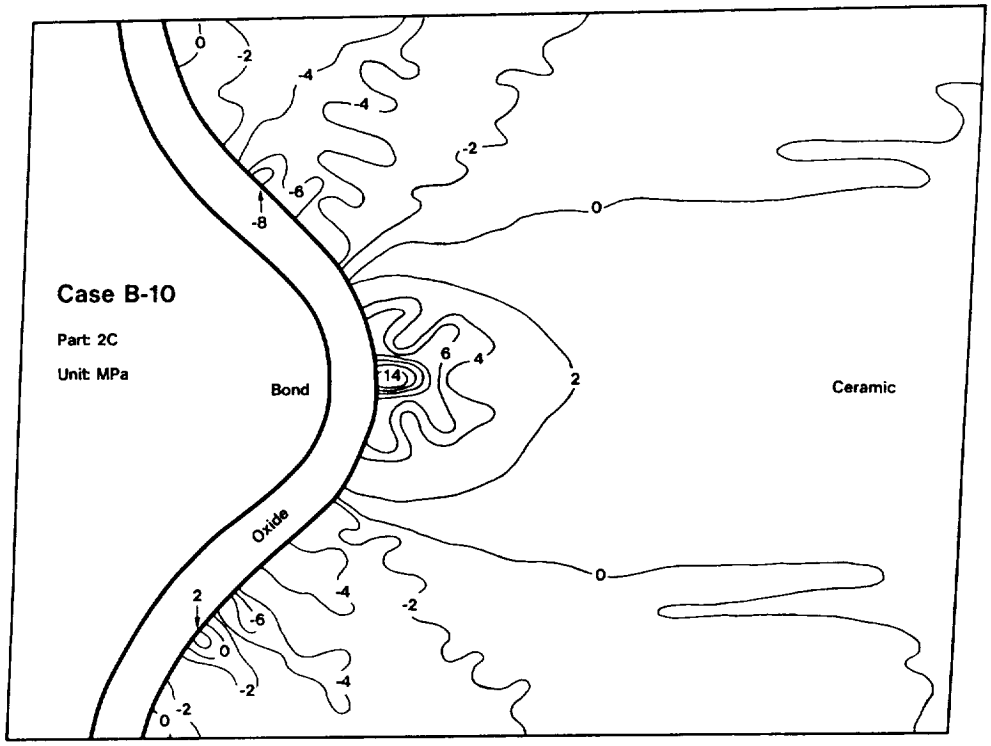

Figure 15. STRESS IN Y-DIRECTION DUE TO OXIDATION

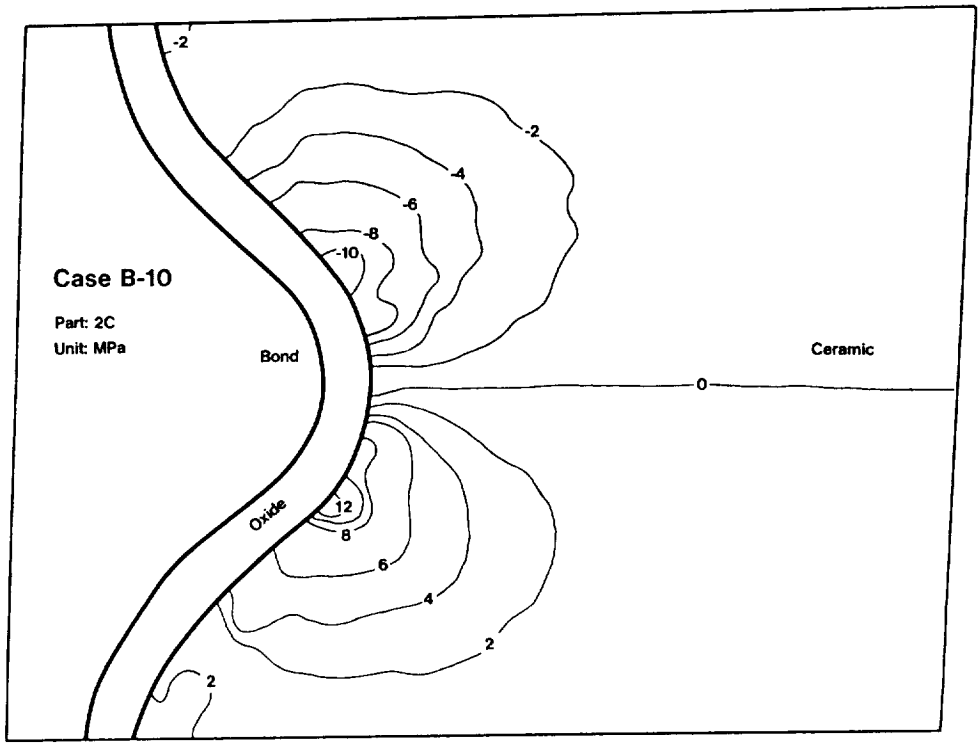

Figure 16. SHEARING STRESS DUE TO OXIDATION

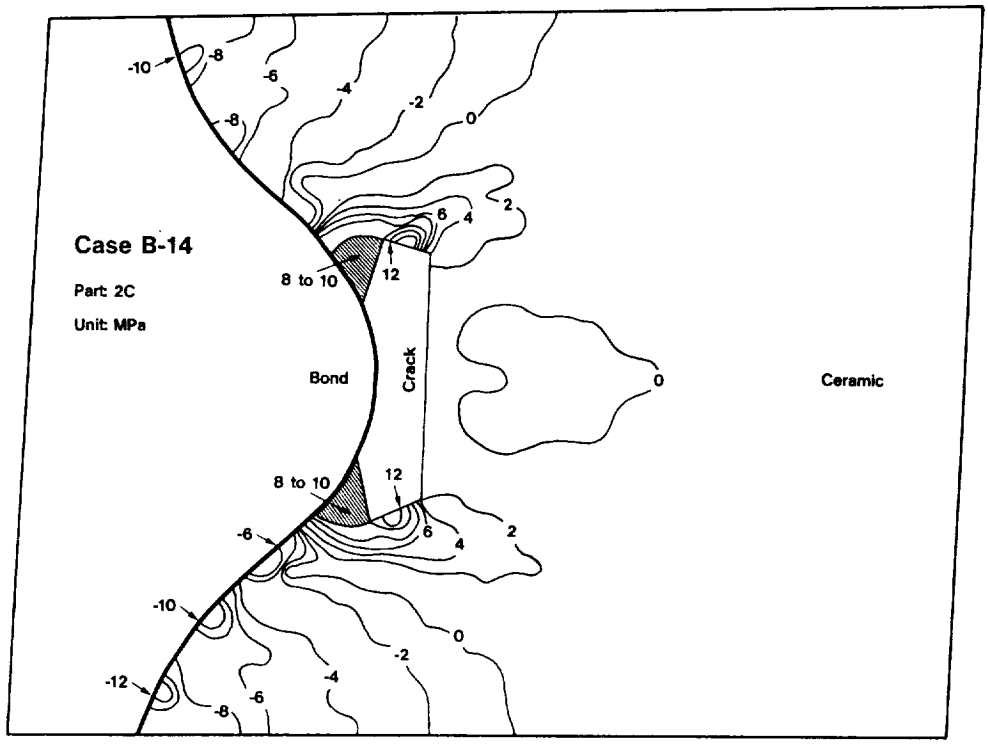

Figure 17. STRESS IN X-DIRECTION DUE TO THERMAL EXPANSION MISMATCH WITH PRECRACKING

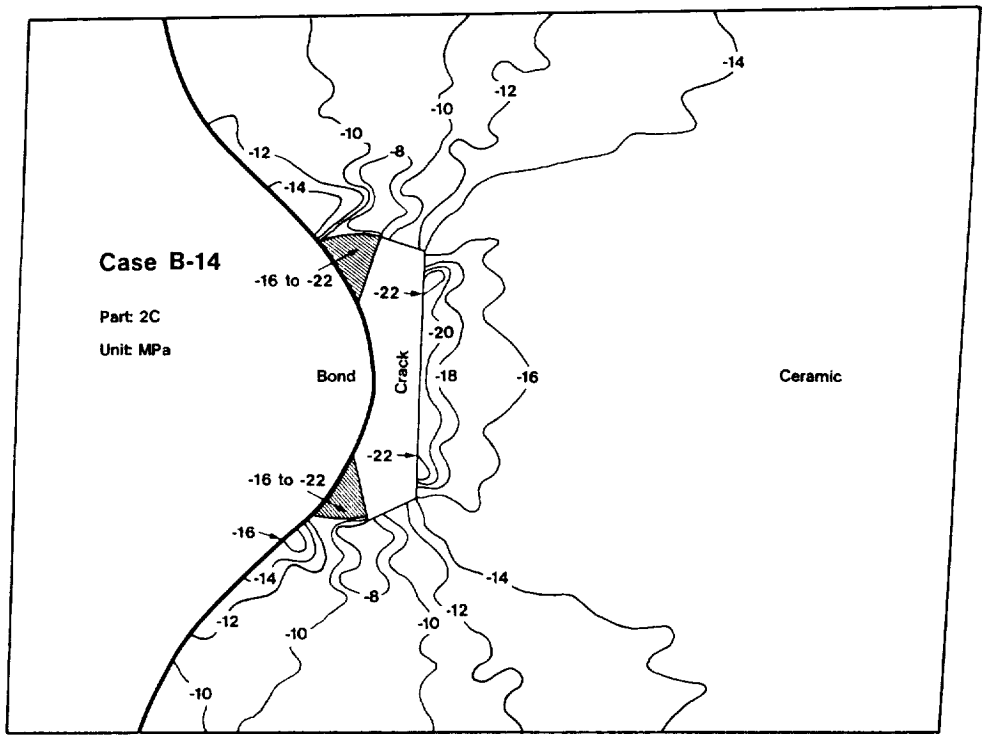

Figure 18. STRESS IN Y-DIRECTION DUE TO THERMAL EXPANSION MISMATCH WITH PRECRACKING

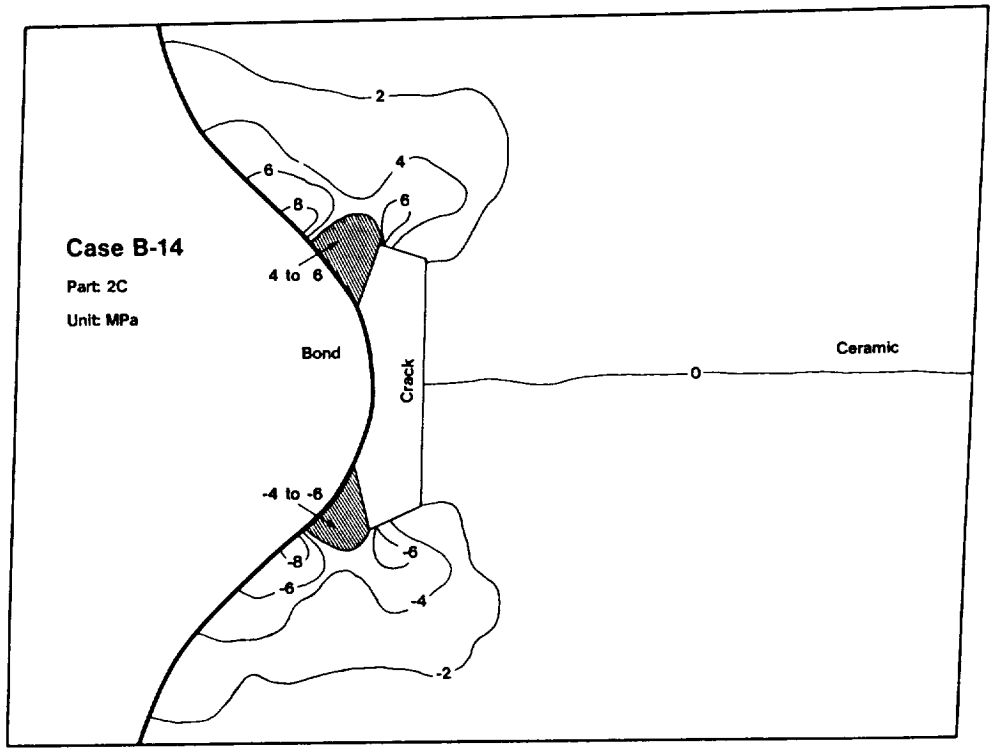

Figure 19. SHEARING STRESS DUE TO THERMAL EXPANSION MISMATCH WITH PRECRACKING

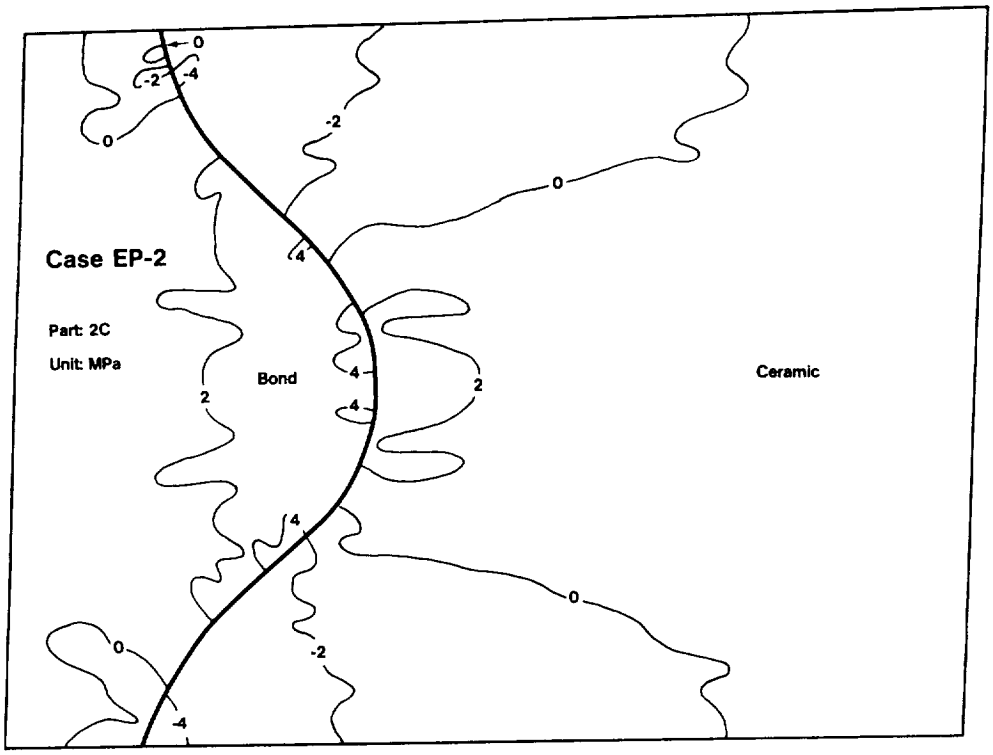

Figure 20. ELASTIC-PLASTIC STRESS IN X-DIRECTION DUE TO THERMAL EXPANSION MISMATCH

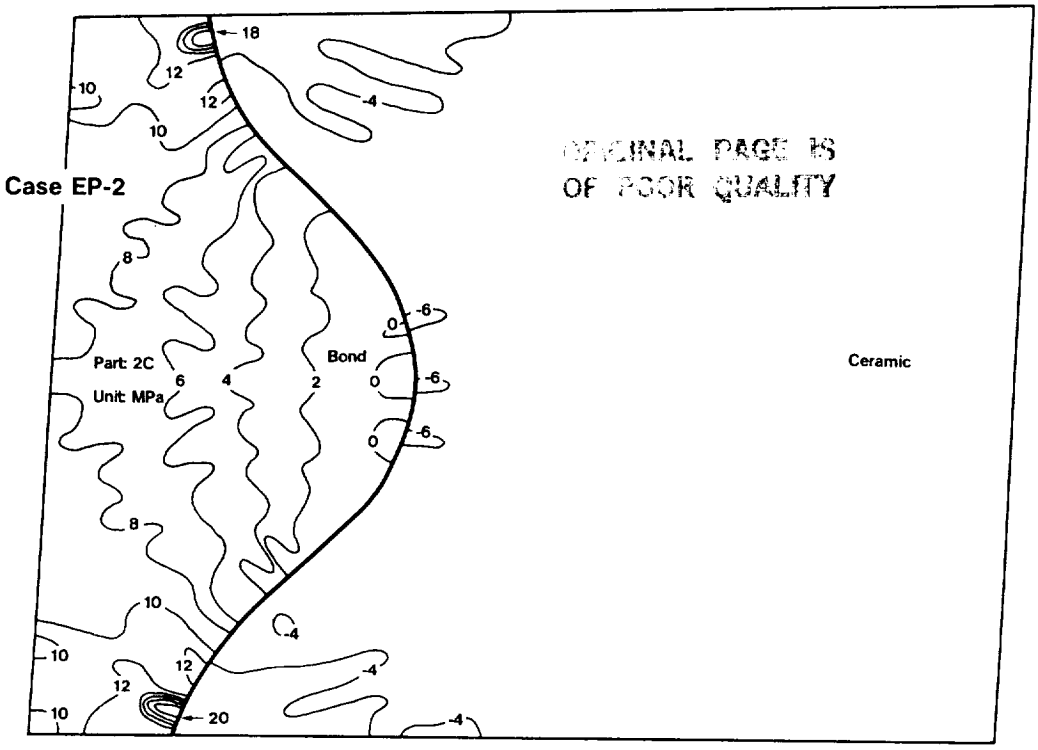

Figure 21. ELASTIC-PLASTIC STRESS IN Y-DIRECTION DUE TO THERMAL EXPANSION MISMATCH

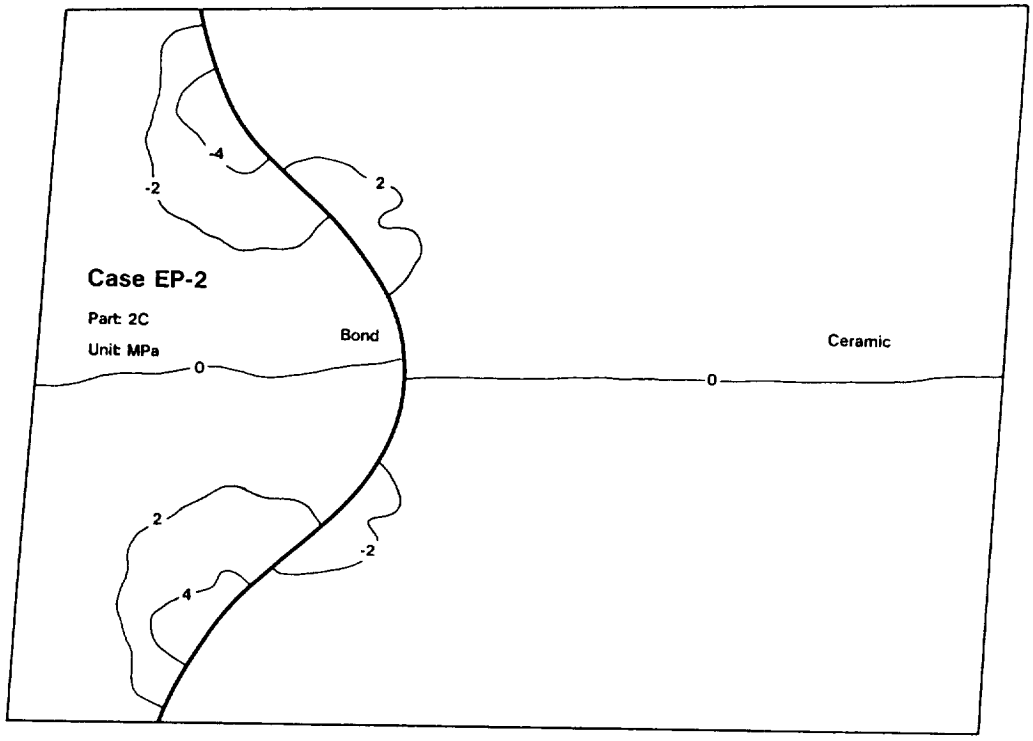

Figure 22. ELASTIC-PLASTIC SHEARING STRESS DUE TO THERMAL EXPANSION MISMATCH

THERMAL BARRIER COATING LIFE PREDICTION MODEL DEVELOPMENT*

T.E. Strangman, J.F. Neumann and A. Liu
Garrett Turbine Engine Company (GTEC)

Thermal barrier coatings (TBCs) for turbine airfoils in high-performance engines represent an advanced materials technology with both performance and durability benefits. The foremost TBC benefit is the reduction of heat transferred into air-cooled components, which yields performance and durability benefits (Figure 1). To achieve these benefits, however, the TBC system must be reliable. Mechanistic thermomechanical and thermochemical life models are therefore required for the reliable exploitation of TBC benefits on gas turbine airfoils. GTEC's NASA-HOST Program (NAS3-23945) goal is to fulfill these requirements.

This program focuses on predicting the lives of two types of strain-tolerant and oxidation-resistant TBC systems that are produced by commercial coating suppliers to the gas turbine industry (Figure 2). The plasma-sprayed TBC system, composed of a low-pressure plasma-spray (LPPS) or an argon shrouded plasma-spray (ASPS) applied oxidation resistant NiCrAlY (or CoNiCrAlY) bond coating and an air-plasma-sprayed yttria (8 percent) partially stabilized zirconia insulative layer, is applied by Chromalloy (Orangeburg, New York), Klock (Manchester, Connecticut), and Union Carbide (Indianapolis, Indiana). The second type of TBC is applied by the electron beam-physical vapor deposition (EB-PVD) process by Temescal (Berkeley, California).

The overall objective of Phase I of this program is to develop mechanistic mission-analysis-capable life prediction models for the predominant environmental and thermomechanical TBC failure modes for preliminary design analyses. Because the TBC must be considered early in the component design process in order to fully incorporate and exploit its benefits, an additional model goal is to drive the preliminary TBC life model with component thermal analysis data and simple snap acceleration-snap deceleration stress analysis data. This approach permits the designer to economically include TBCs into initial iterations of the blade and vane design process. More refined TBC analyses for final design lives are the subject of Phase II.

A comprehensive strategy to achieve this goal has been developed that includes the analyses of the TBC durability on both the TFE731-5 HP turbine blades (Figure 3) and the burner rig test specimens. Due to the complex nature of the problems involved, the finite element method is deemed to be most effective in promoting the in-depth understanding of the essential overall thermal/mechanical behavior of the TBC systems as well as the interactions between the individual material regimes and the interfacial conditions in the TBC systems. This approach also interfaces efficiently with existing airfoil design methods.

*Work done under NASA Contract NAS3-23945.

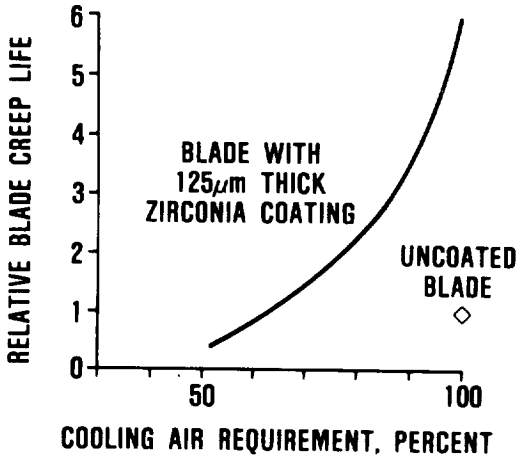

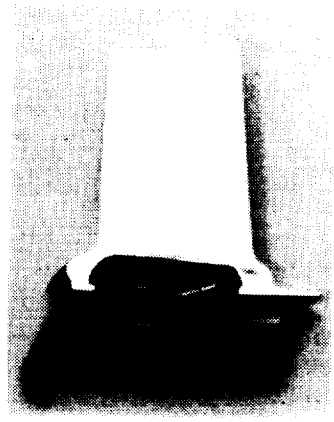

65-195-1

Figure 1. TBCs Improve Creep Life and Reduce Cooling Air Requirements for the GTEC High-Pressure Turbine Blade.

	PLASMA SPRAY	PLASMA SPRAY	ELECTRON BEAM — PHYSICAL VAPOR DEPOSITION
TBC	APS Y_2O_3 (8%) STABILIZED ZrO_2	APS Y_2O_3 (8%) STABILIZED ZrO_2	EB-PVD Y_2O_3 (20%) STABILIZED ZrO_2
BOND COAT	LPPS Ni-31Cr-11Al-0.5Y	ASPS Co-32Ni-21Cr-8Al-0.5Y	EB-PVD Ni-23Co-18Cr-12Al-0.3Y
SUBSTRATE	MAR-M 247 SUPERALLOY	MAR-M 247 SUPERALLOY	MAR-M 247 SUPERALLOY
SUPPLIER	• CHROMALLOY • KLOCK	• UNION CARBIDE	• TEMESCAL

G5-195-2

Figure 2. Life Prediction Models are Being Developed for Plasma-Sprayed and EB-PVD TBC Systems.

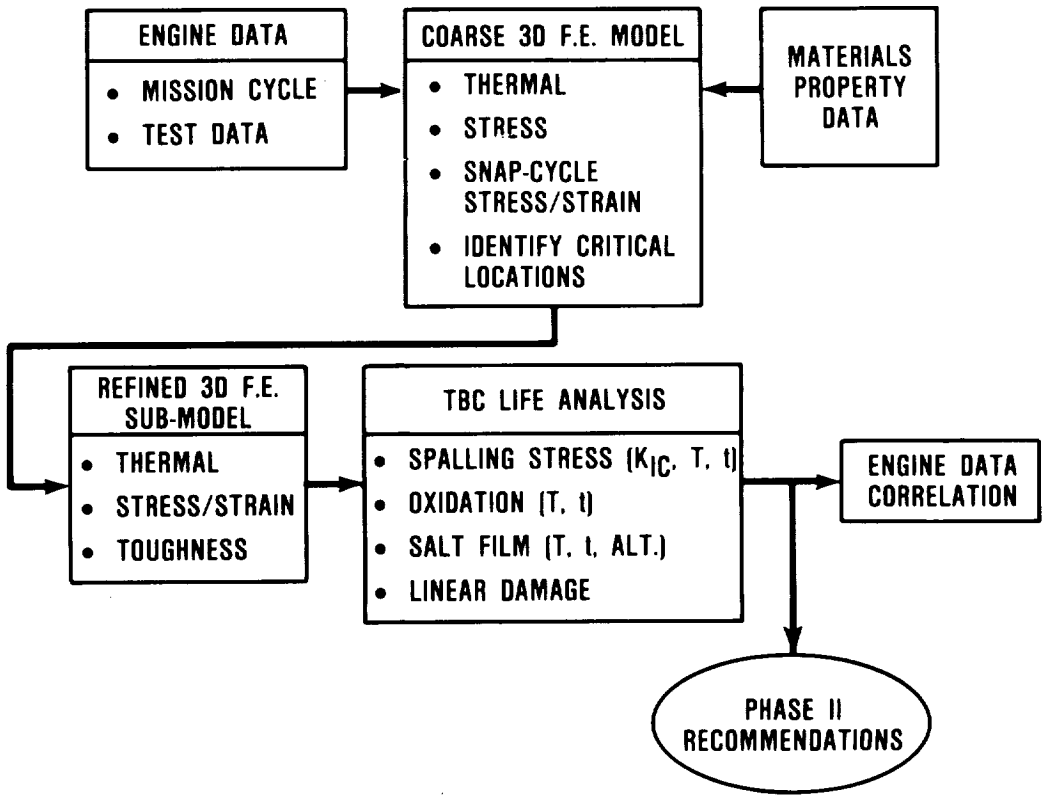

G6-095-45

Figure 3. Three TBC Damage Modes are Evaluated in TFE731 Blade Analysis.

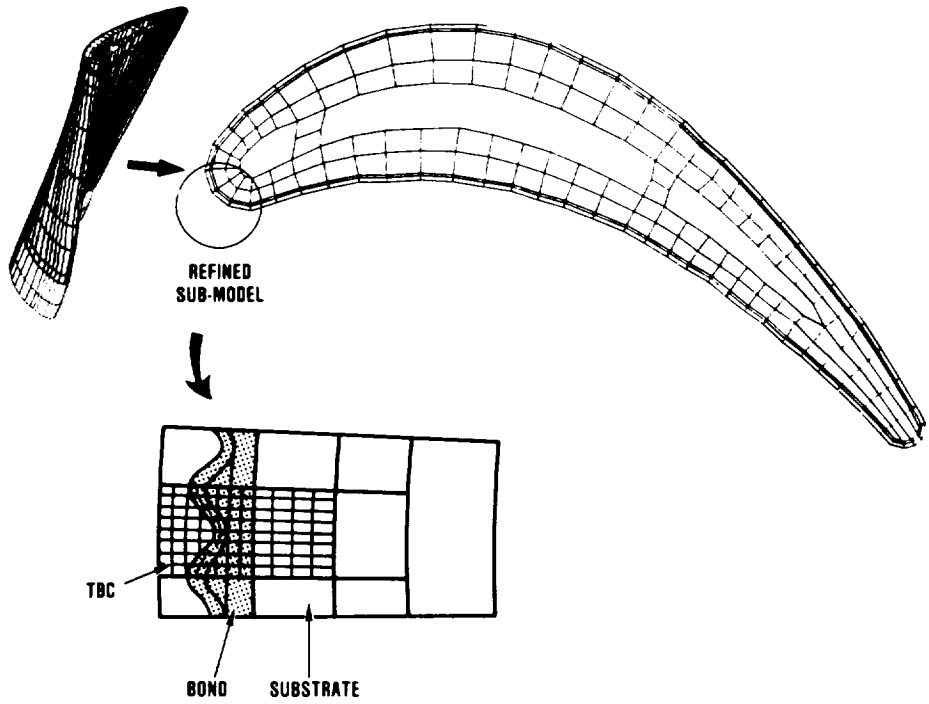

Figure 4. TFE731 HP Turbine Blade F.E. Model Incorporates Bond Coating and Zirconia Layers.

For computational efficiencies, typical preliminary design (PD) finite element models were first constructed to analyze the bulk behavior of the TBC systems on the airfoil component (Figure 4). Critical locations, in terms of temperatures, stresses, and strains or their combinations, can be identified from these PD models. Refined sub-models are then constructed for analysis of critical locations. Detailed thermomechanical and thermochemical behaviors of the TBC systems and the interactions between the individual material regimes and the interfacial conditions are being analyzed via these refined sub-models. Major analysis work in this program is being performed with ANSYS, a commercially available general purpose finite element code.

For preliminary component design analyses (Phase I), TBC lives are being independently calculated for three operative damage modes:

- o Bond coating oxidation
- o Molten salt film damage, and
- o Thermomechanical stress induced spalling

Computation of the oxidation life of a TBC system in the preliminary design model is driven by the component thermal analysis and engine power requirements during a mission cycle.

Molten salt film damage life is calculated using the component thermal analysis, engine power requirements during a mission, and aircraft altitude (salt ingestion).

Zirconia spalling associated with thermomechanical stresses is calculated based on the analysis of the snap-cycle thermal transients as well as the steady-state condition and the rotational loads in a mission cycle. Calculated snap-cycle interfacial tensile stresses and the largest pre-existing flaw diameter (determined by NDE or calculated from bond strength tests) are used to estimate a stress intensity factor that the coating must endure without spalling. As indicated in subsequent paragraphs, the fracture toughness of the zirconia or the bond coating-zirconia interface is dependent upon exposure temperature and time. Time and temperature dependent changes in the zirconia or interfacial toughness are calculated based on the thermal analysis results of the component and a linear cumulative damage model to account for variations in a mission cycle.

Figure 5 is a schematic of the TBC life model that illustrates these three failure modes and the respective temperatures regimes at which these failure modes are likely to occur. Figure 6 illustrates parameters that affect each of these three major failure modes.

The preliminary design TBC life is assessed via a linear damage rule, composed of damages from these three modes during each of the mission cycles, assuming no interactions between these failure modes; that is

$$\text{Life} = [(\text{Life}_{\text{oxid}})^{-1} + (\text{Life}_{\text{salt}})^{-1} + (\text{Life}_{\text{stress}})^{-1}]^{-1}$$

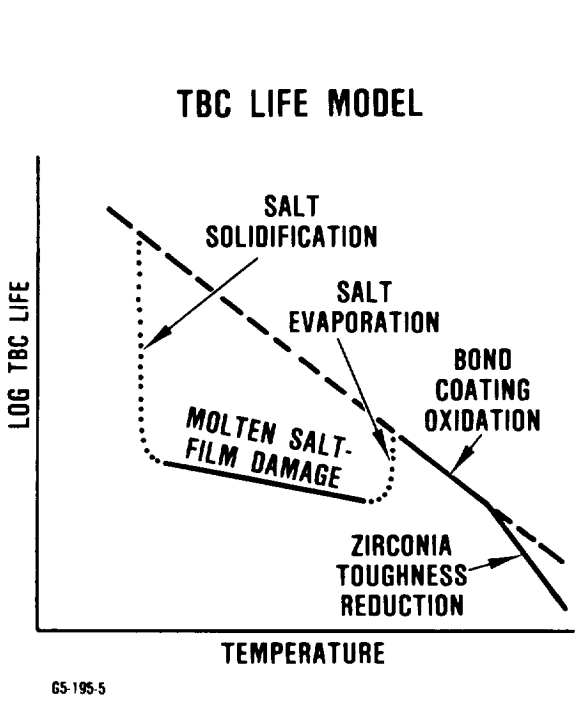

Figure 5. TBC Life Model Has Three Failure Modes.

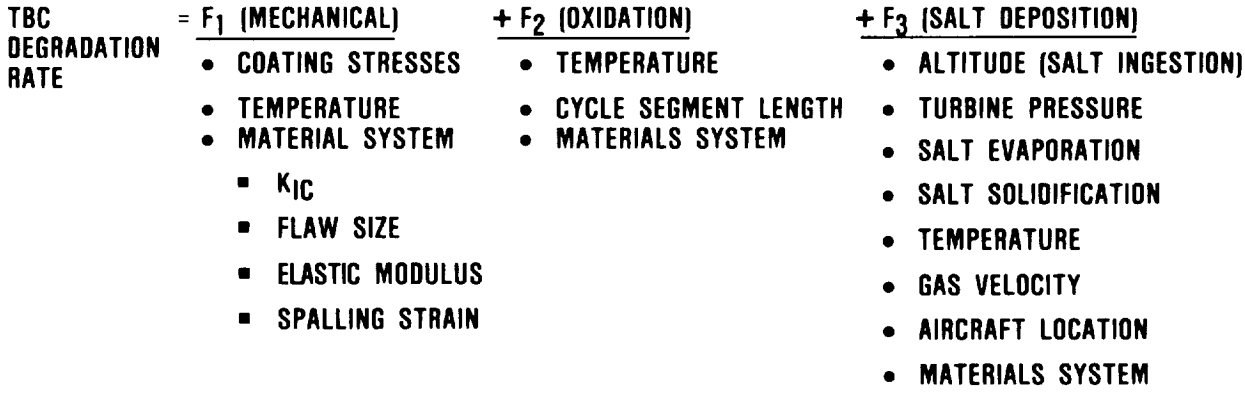

Figure 6. TBC Life is a Function of Engine, Mission, and Materials System Parameters.

However, the refined sub-models are being constructed to be sufficiently flexible and detailed to analyze the interactions between these models. Subsequent improvements in Phase II of the program will incorporate failure mechanism interactions into the life prediction model.

Burner rig and mechanical property data have been obtained to quantify the capabilities of each of the TBC systems for each major mode of degradation. Burner rig test data are illustrated in Figures 7 and 8 for plasma-sprayed and EB-PVD TBC coating systems. These data indicate that bond coating oxidation, high temperature zirconia densificiation (sintering), and molten salt film damage at intermediate temperatures significantly affect TBC life (Figure 7). The length of the heating cycle must also be considered when computing a coating life (Figure 8).

Cohesive and interfacial toughness data have also been measured for plasma-sprayed and EB-PVD TBC systems (Figure 9). It has been observed for both types of coating systems that toughness is reduced by exposure at high temperatures. A step transition in toughness, which is associated with sintering shrinkage, is illustrated for plasma-sprayed TBC systems as a function of exposure time at 1100C in Figure 10. The transition to lower toughness levels correlates well with high temperature burner rig test data, as indicated in Figure 7.

Lives of these TBC systems are being predicted for TFE731 high-pressure turbine blades for factory engine test conditions, as well as business aircraft mission. Thermal analysis of the turbine airfoil (Figure 11) indicates that the bond coating oxidation degradation mode results in minimum predicted lives of approximately 7300 hours with the plasma-sprayed TBC system for the business aircraft missions and 1000 hours for the factory engine test conditions. Lives for other failure modes for the plasma-sprayed as well as the EB-PVD TBC systems are currently being analyzed.

This program is now in the third year of Phase I. The program schedule is provided in Figure 12.

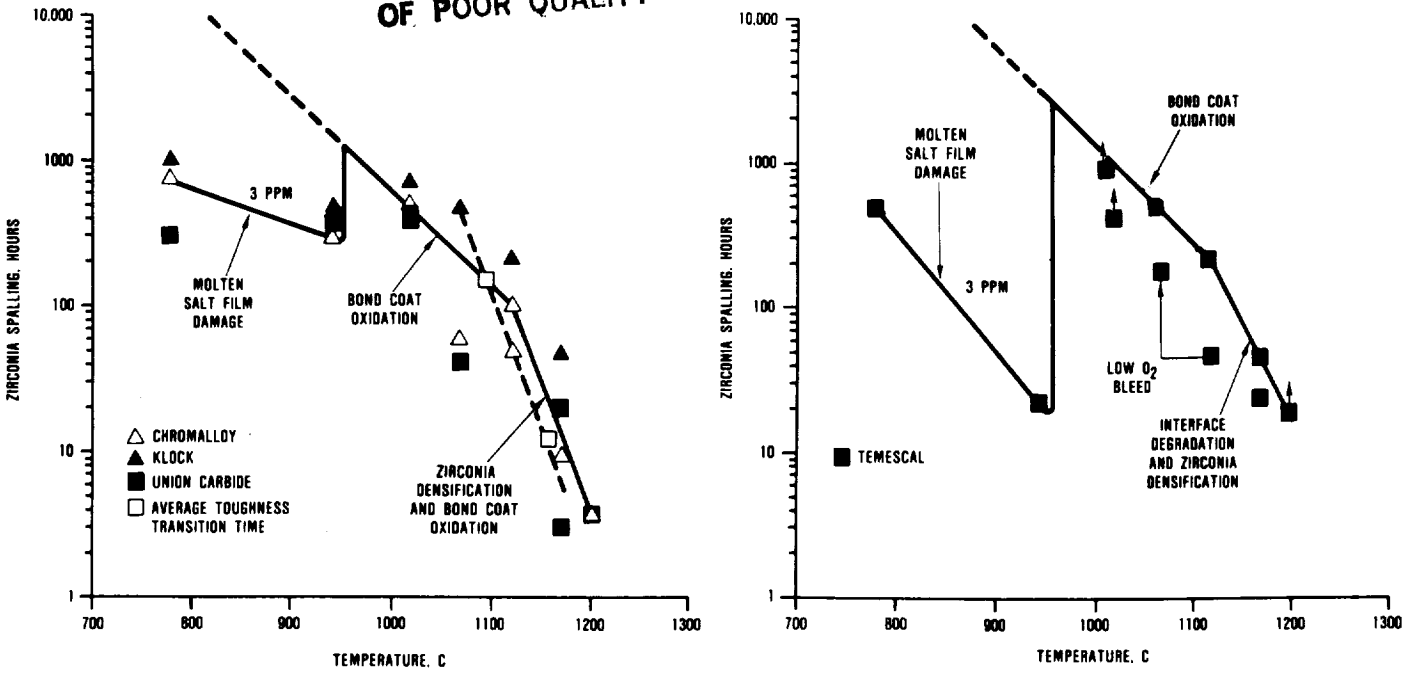

Figure 7. Three Degradation Modes Affect the Durability of Plasma-Sprayed and EB-PVD TBC Systems.

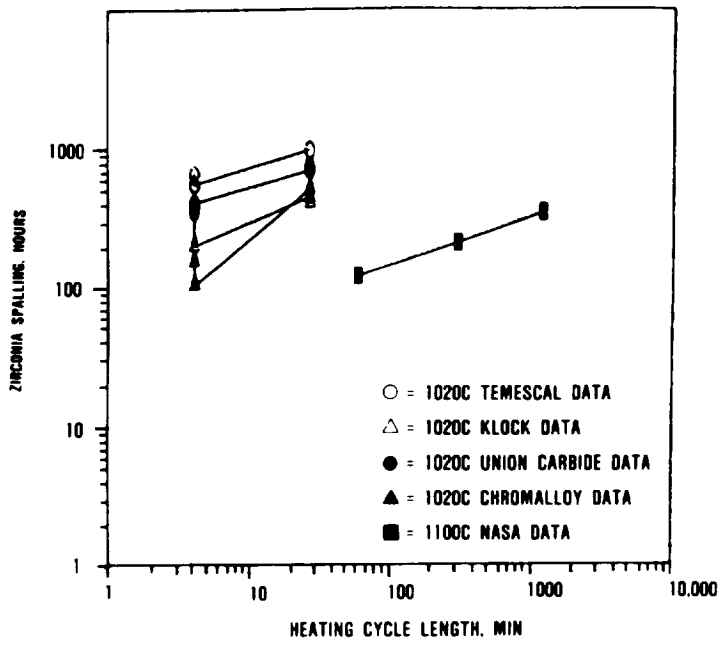

Figure 8. TBC Life Decreases with a Shorter Heating Cycle.

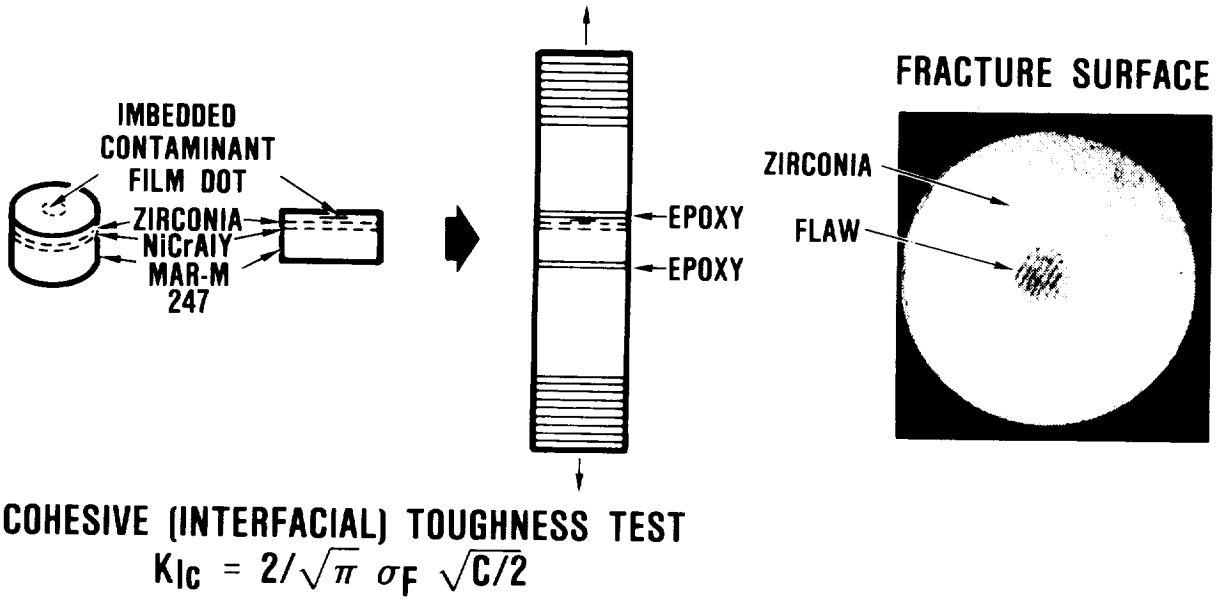

G5-0070-5

FIGURE 38

Figure 9. Cohesive and Interfacial Toughness are Determined with Modified Bond Strength Test.

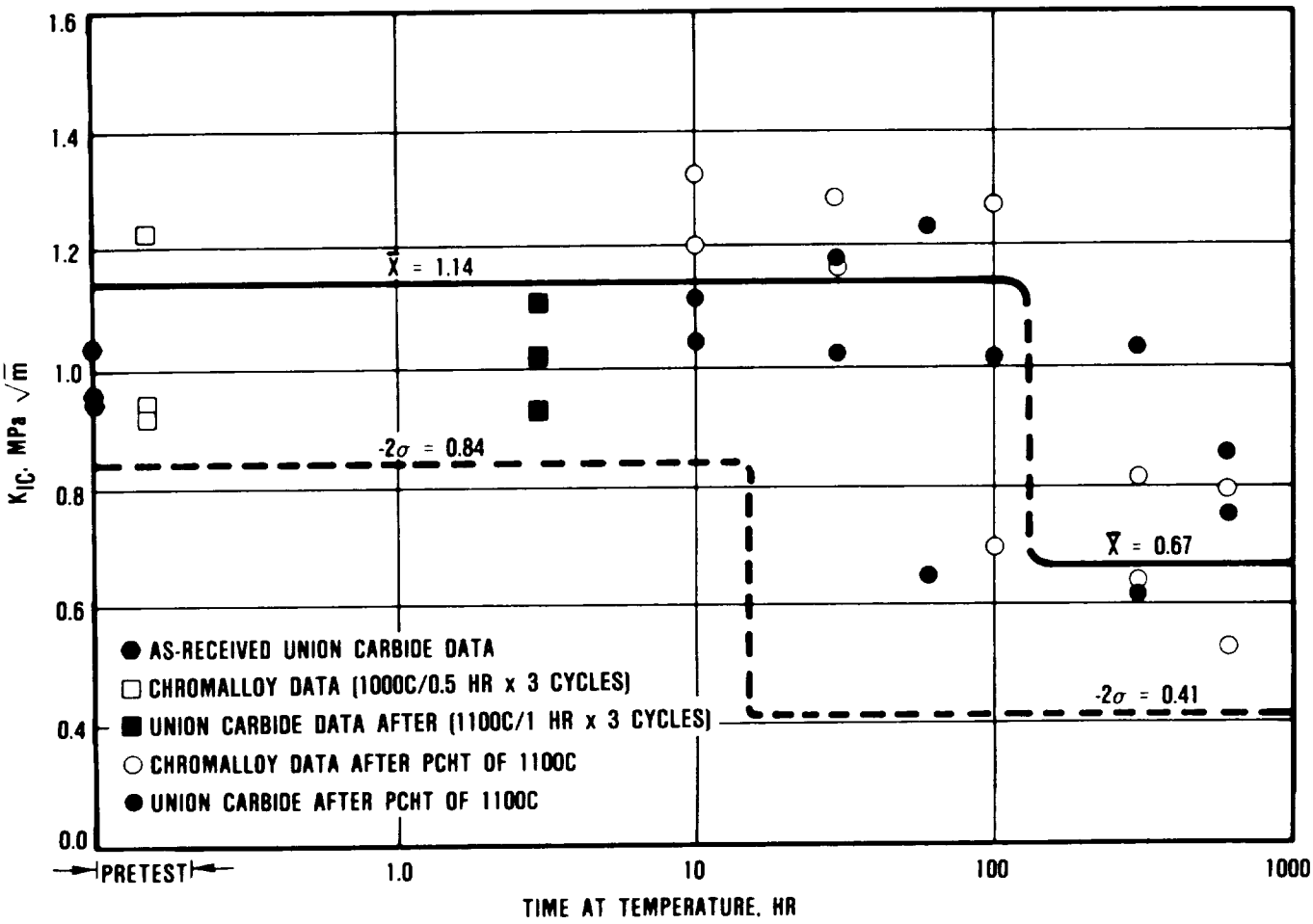

Figure 10. Fracture Toughness of Plasma-Sprayed Yttria (8 percent) Stabilized Zirconia is Reduced After Long Exposures at 1100C.

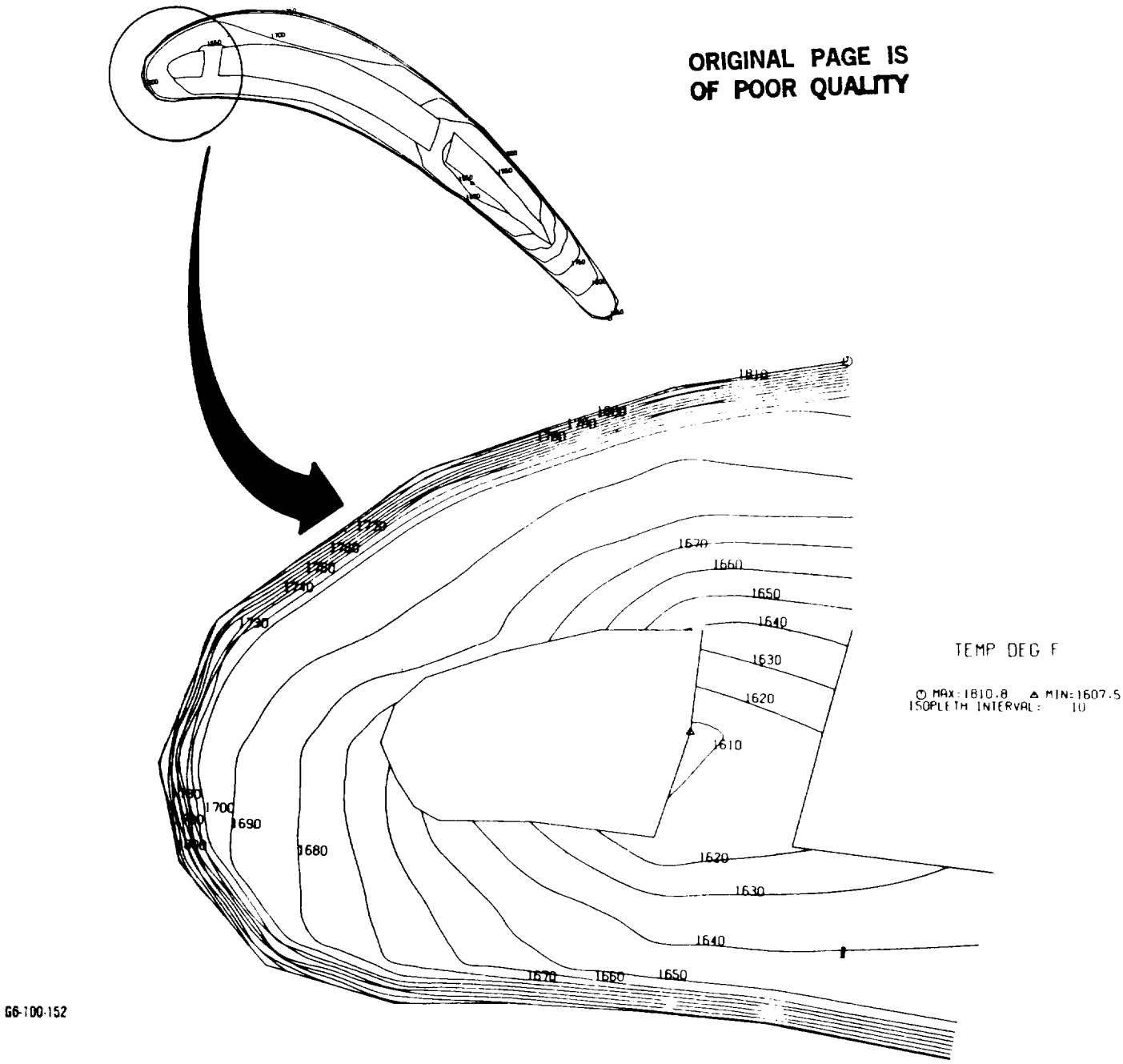

Figure 11. Thermal Analysis of TBC-Coated Blade has been Conducted.

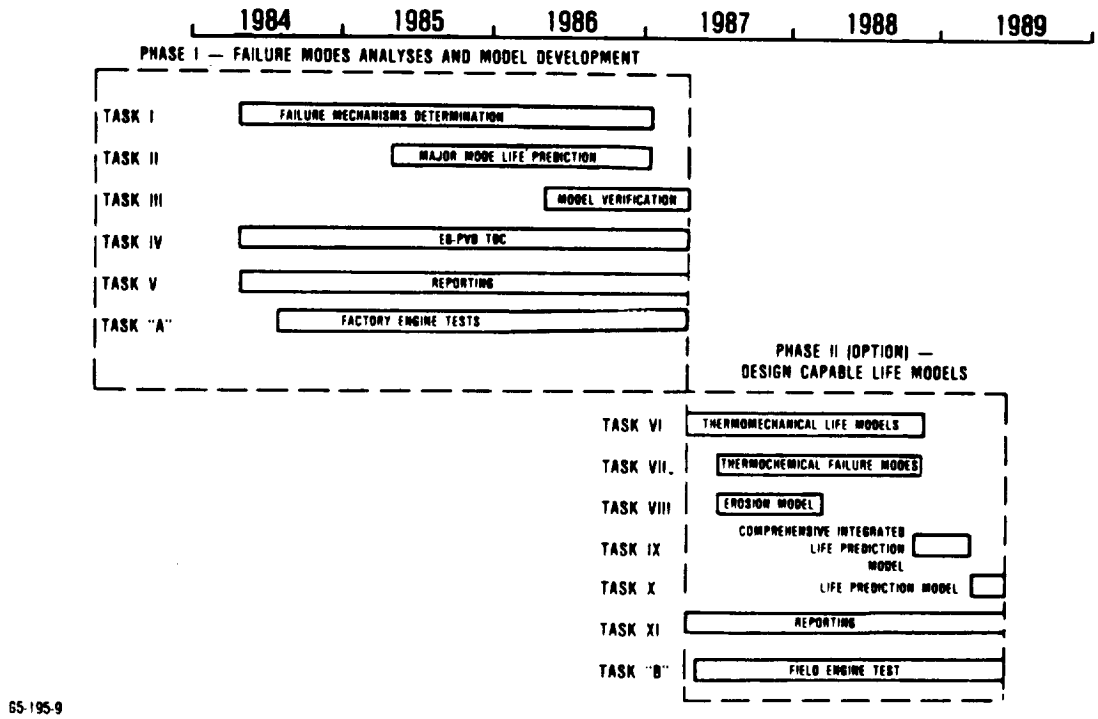

Figure 12. TBC Life Prediction Schedule.

THERMAL BARRIER COATING LIFE PREDICTION MODEL*

B.H. Pilsner, R.V. Hillery, R.L. McKnight, T.S. Cook, K.S. Kim, and E.C. Duderstadt
General Electric
Aircraft Engine Business Group

INTRODUCTION

The objectives of this program are to determine the predominant modes of degradation of a plasma sprayed thermal barrier coating system, and then to develop and verify life prediction models accounting for these degradation modes. The program is divided into two phases, each consisting of several tasks. The work in Phase I is aimed at identifying the relative importance of the various failure modes, and developing and verifying life prediction model(s) for the predominant mode for a thermal barrier coating system. Two possible predominant failure mechanisms being evaluated are bond coat oxidation and bond coat creep. The work in Phase II will develop design-capable, causal, life prediction models for thermomechanical and thermochemical failure modes, and for the exceptional conditions of foreign object damage and erosion.

Currently, work is continuing in Task II of Phase I aimed at developing a preliminary TBC life prediction model. This model will be created by combining the results of the analytical program, the thermomechanical experiments and the results of the failure mechanism examinations of Task I.

TBC SYSTEMS

The primary TBC system consists of a low pressure plasma-sprayed (LPPS) bond coat layer of Ni-22Cr-10Al-0.3Y, an air plasma sprayed yttria partially stabilized zirconia (ZrO_2-8%Y_2O_3) top coat, on a conventionally cast Rene' 80 substrate alloy (Table 1). This bond coat composition has been demonstrated to possess good oxidation resistance and has a large data base as a TBC bond coat. The ZrO_2-8%Y_2O_3 top coat was chosen since numerous studies have shown that zirconia partially stabilized with 6-8 wt.% Y_2O_3 is the best composition for plasma sprayed TBCs (ref. 1). The Rene' 80 substrate was chosen since a large TBC data base exists for this substrate composition.

Four different TBC systems utilizing four different bond coats have been evaluated in the experiment to evaluate the effect of bond coat creep strength on TBC thermal cycle life (Table 2). These four TBC systems also utilize ZrO_2-8%Y_2O_3 top coats and Rene' 80 substrates. TBC system #1 has the same NiCrAlY bond coat utilized in the primary TBC system. TBC systems #2, #3, and #4 have modified NiCoCrAlY bond coats with alloy additions to increase the bond coat creep strength. An aluminide overcoat was used in each of these systems (1-4) to reduce differences in oxidation resistance for the four bond coats. A comparison of the primary TBC system and its counterpart with an aluminide overcoat is shown in Figure 1.

*Work done under NASA Contract NAS3-23943.

THERMAL CYCLE TESTING

Thermal cycle testing is being performed in an automated Rapid Temperature Furnace (Figure 2). The thermal cycles consist of ten minutes heat up, a 45 minute exposure at 1093°C (2000°F), and 15 minutes forced air cooling (Figure 3). This furnace utilizes a lift which automatically cycles the specimens from the upper furnace exposure zone to the lower cooling compartment where a fan provides forced air cooling. Both air and argon pre-exposures have been used to create changes in both bond coat and top coat prior to these thermal cycle tests.

BOND COAT OXIDATION EXPERIMENTS

In the bond coat oxidation experiments, pre-exposures in air or argon were utilized. The goal of pre-exposures in air was to develop oxide scales prior to thermal cycling, while the goal of the pre-exposures in argon was to allow the other thermally activated phenomena present in the air pre-exposures to occur without developing the oxide scale. The intent was to isolate the effect of bond coat oxidation on thermal cycle life.

As reported previously (ref. 2), the specimens pre-exposed in argon failed before the specimens pre-exposed in air (Figure 4). The detrimental effect of argon was believed to be associated with its effect on the type of oxide that forms on the bond coat surface and an in-house program (ref. 3) was performed to help understand this phenomenon. This study indicated that a possible cause of the shortened life was the diffusion of Cr, Ta, W, and other substrate elements to the bond coat/top coat interface during the argon pre-exposure prior to significant bond coat oxidation. The result was a less protective oxide scale.

To further evaluate this phenomenon, an experiment was run in which all specimens (except one set of baselines) received a 10 hour air pre-exposure at 1093°C (2000°F) prior to either air or argon pre-exposures, and thermal cycle testing. In this case, it can be assumed that all specimens developed the same (Al_2O_3) film in the initial air exposure and that the effect of further oxidation of the bond coat would be seen only in those specimens exposed for additional times in air. The results (Figure 5) clearly indicate that continued exposure to air is more detrimental than a prolonged argon exposure (when both are preceded by the air pre-exposure). The larger decrease in thermal cycle life for air exposures is attributed to the continued growth of oxide scales, whereas little or no additional growth occurred in the argon exposures. These results demonstrate the importance of bond coat oxidation to the overall TBC failure mechanism.

Further evidence of the importance of bond coat oxidation is shown by the following observations. Continuous oxide scales of approximately 4 μm were typically observed at the bond coat/top coat interface for the "as-sprayed" and "air pre-exposed" specimens at failure after thermal cycle testing (Figure 6). This observation of a "critical" oxide thickness being necessary to cause failure is consistent with the work of Miller (ref. 4), who noted similar weight changes (oxidation) at failure of specimens with a $CaSiO_4$/MCrAlY TBC, regardless of test temperature.

BOND COAT CREEP EXPERIMENTS

The effect of bond coat creep strength on thermal cycle life was evaluated utilizing four different bond coat alloys (Table II) that had significantly different creep strengths. The modified NiCoCrAlY bond coats include various additions of Mo, Ta, W, Re, Hf, C, B, Si, Zr, and Ti and also received an aluminide (Codep) coating (Figure 1b) as described earlier. All specimens were coated with the same ZrO_2-8%Y_2O_3 ceramic layer. Six specimens of each TBC system were thermal cycle tested. Two were exposed in argon for 100 hours at 1093°C (2000°F), two were exposed in air for the same time and temperature, and two specimens received no pre-exposure. The difference in thermal cycle lives was expected to be a function of bond coat creep strength and pretest conditions.

The results clearly showed that the TBC specimens with the NiCrAlY + aluminide bond coat, which has the lowest creep strength, resulted in the shortest thermal cycle life for all pre-exposure conditions (Figures 7 & 8). However, the thermal cycle life differences for the other TBC systems appears to be minimal. The small differences may indicate that the bond coat creep strength differences (Table II) were not large enough to offset the effect of other failure mechanisms (NiCrAlY is significantly lower in strength than the other three). Interestingly, the 100 hour air pre-exposure did not significantly affect the thermal cycle life of the systems with "high strength" bond coats (Systems 2, 3, and 4). This indicates that, as the thermal cycle life increases (as a result of increasing the bond coat creep strength), the relative contribution of the pre-exposure (oxidation) to the overall failure mechanism is reduced.

In a recent additional study at GE, different bond coat creep strengths were produced by applying various heat treatments to the same bond coat (System #4) to eliminate any differences that might have resulted from aluminide effects on the four bond coats. The results of this study (ref. 5) indicate that TBC thermal cycle life increases with heat treatment temperature (increasing creep strength), again demonstrating that creep strength of the bond coat does indeed influence TBC life.

KEY PROPERTY DETERMINATIONS

Tensile strength, Poisson's ratio, dynamic elastic modulus, and coefficient of thermal expansion for the bond coat were determined from room temperature to approximately 1093°C (2000°F). Standard testing procedures and test specimens were utilized for the NiCrAlY bond coat specimens. The specimens were machined from 5.1 cm (2 inches) by 15.2 cm (6 inches) heat treated LPPS NiCrAlY billets of various heights. The as-sprayed billets received a four hour vacuum heat-treatment at 1093°C (2000°F) to increase the machinability of the billets. The 1093°C heat treatment was chosen since this is the soak temperature utilized in thermal cycle testing. The test results are listed in Table III and IV, and Figures 9 and 10.

Dynamic elastic modulus, dynamic shear modulus, Poisson's ratio, and coefficient of thermal expansion for the top coat were determined from room temperature to approximately 1093°C. In all tests, free-standing air plasma sprayed specimens were utilized and were produced by depositing the ceramic material on stainless steel substrates and inducing a thermal shock to cause spallation of the intact ceramic sheet. Some final machining was required to achieve the desired specimen configurations. These specimens also received a four hour heat treatment in air at 1093°C (2000°F) prior to testing. The test results are listed in Table V and VI,

and Figure 11. Interestingly, the average elastic modulus value determined at room temperature from the bend test (Table V) is a factor of 10 less than the values measured by the resonant frequency method (Table VI). The difference is possibly associated with the presence of cracks, porosity, and splats which would tend to decrease the apparent modulus in the bend test. These factors should play a smaller role in the resonant frequency method.

TBC ANALYTICAL MODELING PROGRAM

Five different analytical tasks, each dealing with a particular aspect of TBC failure, are being investigated using finite element analysis. The first three tasks involve an axisymmetric model (Figures 12 & 13) of a multilayer cylinder, the fourth task examines a disk model, and the fifth task is intended to combine finite element models with simple crack and diffusion models. The specific conditions of each task are discussed below.

Task a. In this evaluation, the same temperature was assumed at the inner and outer surfaces of the specimen (i.e. no gradient across the TBC coated tubular specimen). The GE cyclic temperature rig's cycle (10-minute heat up, 45-minute exposure at 1093°C, 15-minute cooling, Figure 3) was modeled.

Task b. In this task, a temperature distribution generated by a gradient across the TBC cooled tubular specimen is modeled. The work models the effect of the large gradients (100-150°C) developed across the ceramic.

Task c. In this evaluation, cracks will be "placed" along the bond coat/top coat interface, thereby producing a ring crack. One or more cracks perpendicular to the free surface will then be added. The goal is to examine crack tip driving forces to determine any changes resulting from accommodation of displacements by the multiple cracks. Small submodels involving a number of cracks may be studied applying perturbation approaches (localized crack changes). The conditions for this modeling will be based on the results of the first two tasks described above.

Task d. The importance of edge effects in multilayer disk specimens will be evaluated. Since most TBC applications involve edge effects (coating "patches", component edges, cooling holes, etc.), it is important to examine how these edges affect thermal cycle life.

Task e. In this task, the finite element model results from the four preceding tasks, along with some simple elastic crack models, thermal mismatch strains, a diffusion model (e.g., $\ell \propto Dt$), and the effect of hydrostatic pressure to further examine crack tip driving force. Since this is an elastic model only, there are limits on its potential but it is hoped that some significant insight on cracking in ceramics can be gained in this Task.

In the first four tasks of the modeling work, emphasis will be placed on extracting stress and displacement data as a function of time and location under changes in geometry and boundary conditions. In cases where sufficient material

data is available (crack initiation, propagation, or failure data), quantities predicted by the models will be compared to this data for failure information.

The axisymmetric finite element program (Figures 12 & 13) has been applied to the first two analytical tasks. The bond coat stress free temperature was assumed to be 982°C (1800°F), while the top coat stress free temperature was assumed to be 204°C (400°F). These are the temperatures of the substrate during application of these coatings. In the analysis, both elastic and plastic deformation were included, but no plasticity developed for the temperature conditions selected (time at temperature was not included). Analysis of the results for the first two analytical tasks is discussed below.

In Task a, the specimen was assumed to undergo the thermal cycle of 21°C - 1093°C - 21°C in the cycling rig. Since this is a quasistatic test, the entire specimen was assumed to be at a given temperature. Effective, radial, axial, and hoop stresses versus distance in the radial direction are plotted in Figure 14 for four different temperatures [21°C (70°F), 204°C (400°F), 982°C (1800°F), and 1093°C (2000°F)]. As indicated, the stress free temperature for the top coat is 204°C (400°F), therefore, zero stress is found in the top coat at this temperature. However, since the top coat was applied to the bond coat, 982°C (1800°F) is no longer the bond coat stress free temperature. Therefore, small stresses due to the top coat application develop in the bond coat at this temperature.

In the Task b, a temperature distribution across the TBC system was modeled. In this examination, the surface of the ceramic was set at 1093°C (2000°F), the bond coat/top coat interface at 943°C (1730°F), the bond coat/substrate interface at 941°C (1725°F), and the inner wall of the tube at 927°C (1700°F). These results (Figure 15) were plotted and compared with the results present when the system was at 21°C (70°F). Interestingly, the largest effective stress is present in the ceramic near the bond coat/top coat interface which is the typical failure location for thermal barrier coatings. Comparison of the results of deformation behavior for Tasks a and b (Figures 14 and 15) indicate how significantly the presence of thermal gradients can affect the stress state present in TBCs.

THERMOMECHANICAL EXPERIMENTS

Three different thermomechanical experiments have been planned to evaluate the thermomechanical characteristics of TBCs. The primary goal of these examinations is to measure the strains induced during thermal cycling of TBCs, and to relate these strains to the observed failure modes.

In the first experiment, a thermal barrier coated LCF (low cycle fatigue) tube specimen (Figure 16) will be thermally cycled using an induction heating system and a forced air cooling system. The thermomechanical nature of two different thermal cycles will be evaluated. The first thermal cycle will be as close to the GE cyclic temperature rig's cycle (Figure 3) as possible. This experiment is aimed at determining the magnitude of strains induced by thermal cycling of the TBC specimen under essentially zero mechanical load. This experiment will also attempt to determine if any phasing exists between the strains observed for the substrate and the ceramic, or if the ceramic simply follows the displacement of the metal substrate.

In the second experiment, a thermal barrier coated LCF tube specimen will again be thermally cycled using an induction heating system and a forced air cooling system. Tensile, compressive, and zero loading will be applied to three TBC specimens and these specimens will be thermally cycled to failure. The goal is to evaluate the effect of compressive and tensile loading on TBC thermal cycle life.

In the third experiment, the thermal barrier coating will be applied to thin Rene' 80 (substrate) strips which will then be heated and cooled using induction heating and forced air cooling. It is anticipated that the thin Rene' 80 strips and their TBC coatings will bend measurably during thermal transients because of the stresses induced by thermal expansion differences. Values of the curvature changes during coating deposition and during subsequent thermal transients will be compared to predicted curvatures based on natural properties of Rene' 80 and the coating materials. This data, in conjunction with data from the uncoated Rene' 80 strip and free-standing ceramic strip should provided insight into the behavior of coated specimens, and thus contribute to a better understanding of the thermomechanical characteristics of TBCs.

REFERENCES

1. Stecura, S., "Effects of Compositional Changes on the Performance of a Thermal Barrier Coating System," NASA TM 78976, 1979.

2. Hillery, R.V. and Pilsner, B.H., "Thermal Barrier Coating Life Prediction Model - First Annual Report," NASA CR - 175010, 1985.

3. Saegusa, F., "Failure Mechanism Studies on Thermal Barrier Coatings," GE Internal Communication.

4. Miller, R.A., "High Temperature Protective Coatings," S.C. Singhal, Editor, AIME, page 293, 1982.

Table I

BASELINE THERMAL BARRIER COATING SYSTEM (WEIGHT PERCENT)

Substrate (Rene '80): Ni-14Cr-9.5Co-5Ti-4W-4Mo-3Al-0.17C-0.03Zr-0.015B

Bond Coating : Ni-22Cr-10Al-0.3Y (Low Pressure Plasma Spray)

Top Coating : ZrO_2-$8Y_2O_3$ (Air Plasma Spray)

Table II

BOND COAT CREEP EFFECT TBC SYSTEMS

Systems	Substrate	Bond Coating	Over Coating	Top Coating	Bond Coat Creep (Larson/Miller Parameter @ 3 KSI - rupture test)
1	Rene'80	Bond Coating 1'	Aluminide	ZrO_2-Y_2O_3	39.0
2	Rene'80	Bond Coating 2*	Aluminide	ZrO_2-Y_2O_3	45.7
3	Rene'80	Bond Coating 3*	Aluminide	ZrO_2-Y_2O_3	47.0
4	Rene'80	bond Coating 4*	Aluminide	ZrO_2-Y_2O_3	48.4

' Ni-22Cr-10Al-0.3Y

* Modified NiCoCrALY bond coats

Table III

LPPS Ni-22Cr-10Al-0.3Y BOND COAT TENSILE PROPERTIES

TEST TEMPERATURE °C	ULTIMATE STRENGTH MPa	0.2 YIELD MPa	% ELONGATION	% REDUCTION IN AREA
Ambient 25° (77°F)[1]	1320 (191 KSI)	--	--	--
538°C (1000°F)[2]	1240 (179 KSI)	1120 (162 KSI)	5.2	6.2
760°C (1400°F)[2]	450 (65 KSI)	160 (23 KSI)	18.3	19.6
1038°C (1800°F)[3]	16 (2.3 KSI)	13 (1.9 KSI)	149.3	95.6
1093°C (2000°F)[3]	4 (0.6 KSI)	3 (0.4 KSI)	248.3	92.4

[1]No measurable plastic deformation (1 specimen)

[2]Average of three test specimens.

[3]Average of two test specimens.

Table IV

ELASTIC MODULI AND POISSON'S RATIO OF LPPS Ni-22Cr-10Al-0.3Y

Temperature °C	E (Axial) GPa	E (Diametral) GPa	Poisson's Ratio
20 (R.T.)	206 (29.9 MSI)	696 (100.8 MSI)	0.30
538 (1000°F)	180 (26.1 MSI)	602 (87.3 MSI)	0.30
760 (1400°F)	101 (14.7 MSI)	273 (39.6 MSI)	0.37
982 (1800°F)	--	--	--*
1093 (2000°F)	--	--	--*

* No linear portion to stress/strain curves.

Table V

MECHANICAL TESTING OF PLASMA-SPRAYED ZIRCONIA BARS
BEND TEST

Sample I.D.	Width, cm	Thickness, cm	Length, cm	Ultimate Load, Kg (lb)	Ultimate Stress MPa (ksi)	Strain to Failure in/inx10^{-3}	Elastic Modulus GPa (MSI)
1-1	0.648	0.238	5.746	7.03 (15.5)	53.3 (7.73)	2.89	19.9 (2.80)
1-2	0.648	0.235	5.747	6.21 (13.69)	56.8 (8.23)	3.07	20.5 (2.92)
1-3	0.648	0.232	5.746	5.26 (11.59)	49.3 (7.15)	2.59	21.8 (3.15)
				Average Elastic Modulus		20.6 GPa (2.98 MSI)	

Table VI

ELEVATED TEMPERATURE DETERMINATION OF ELASTIC MODULUS, SHEAR MODULUS, AND POISSON'S RATIO OF APS ZrO_2-$8Y_2O_3$

Temp., °C	Resonant Frequency (Hz) Flexural	Torsional	E Elastic Modulus GPa (MSI)	G Shear Modulus GPa (MSI)	Poisson's Ratios
25*	1472	3697	210 (30.5)	91 (13.2)	0.15
25	1466	3672	208 (30.2)	90 (13.1)	0.16
100	1453	3630	205 (29.7)	88 (12.8)	0.16
150	1444	3610	202 (29.3)	87 (12.6)	0.16
200	1436	3573	200 (29.0)	86 (12.4)	0.17
300	1425	3443	197 (28.6)	79 (11.5)	0.24
400	1412	3343	193 (28.0)	75 (10.8)	0.29
450	1411	3325	193 (28.0)	74 (10.7)	0.31
500	1401	3299	190 (27.6)	72 (10.5)	0.31
538	1395	3281	189 (27.4)	72 (10.4)	0.31
600	1387	3265	187 (27.1)	71 (10.3)	0.31
700	1375	3209	184 (26.6)	69 (10.0)	0.33
800	1360	3160	179 (26.0)	67 (9.7)	0.34
900	1342	3135	175 (25.3)	66 (9.5)	0.33
982	1340	3122	175 (25.3)	65 (9.4)	0.34
1000	1362	3147	179 (26.1)	66 (9.6)	0.36
1038	1374	3163	183 (26.5)	67 (9.7)	0.37
1093	1342	3185	175 (25.3)	68 (9.8)	0.29

* Specimen suspended on cotton thread, all others suspended on Pt wire.

"NiCrAlY" Bond Coat TBC

Figure 1a

"NiCrAlY + Codep" Bond Coat TBC

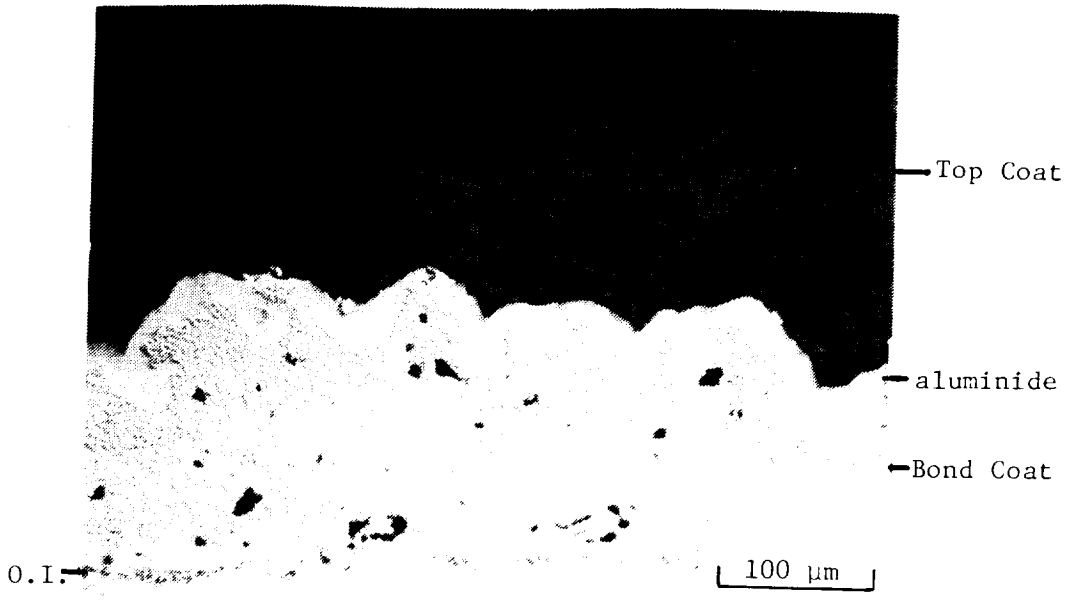

Figure 1b

RAPID TEMP FURNACE

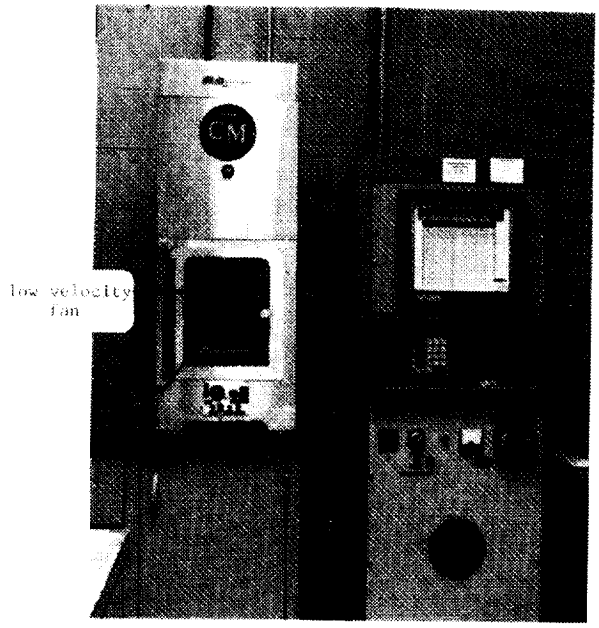

Figure 2

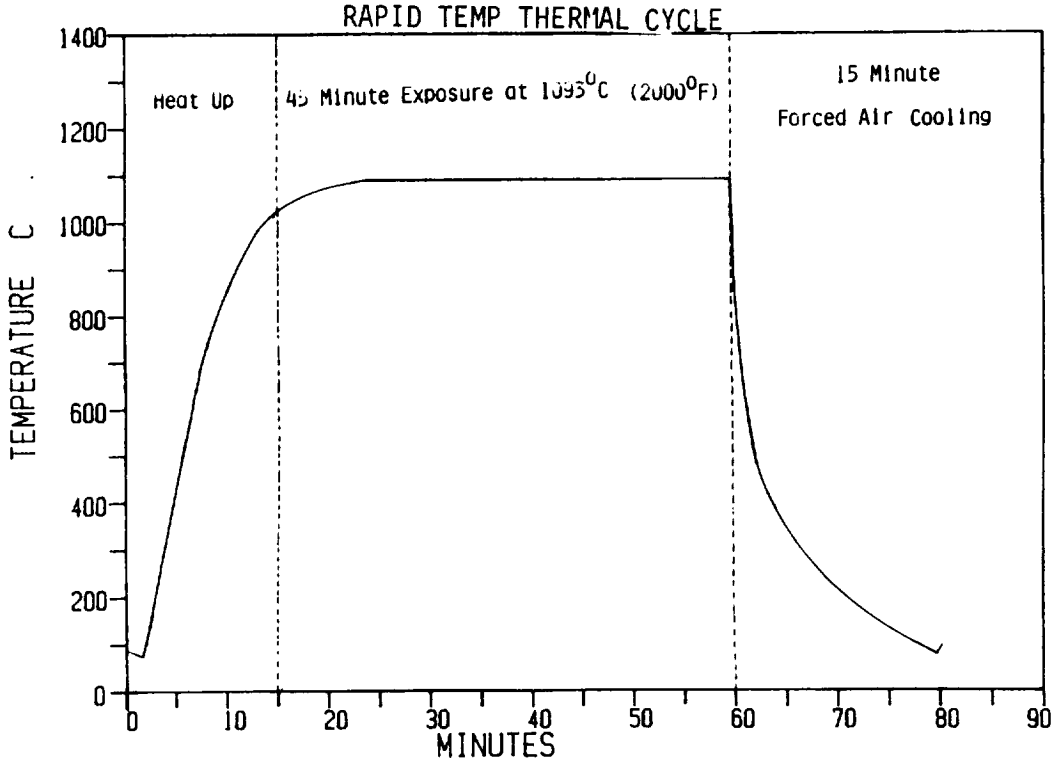

Figure 3

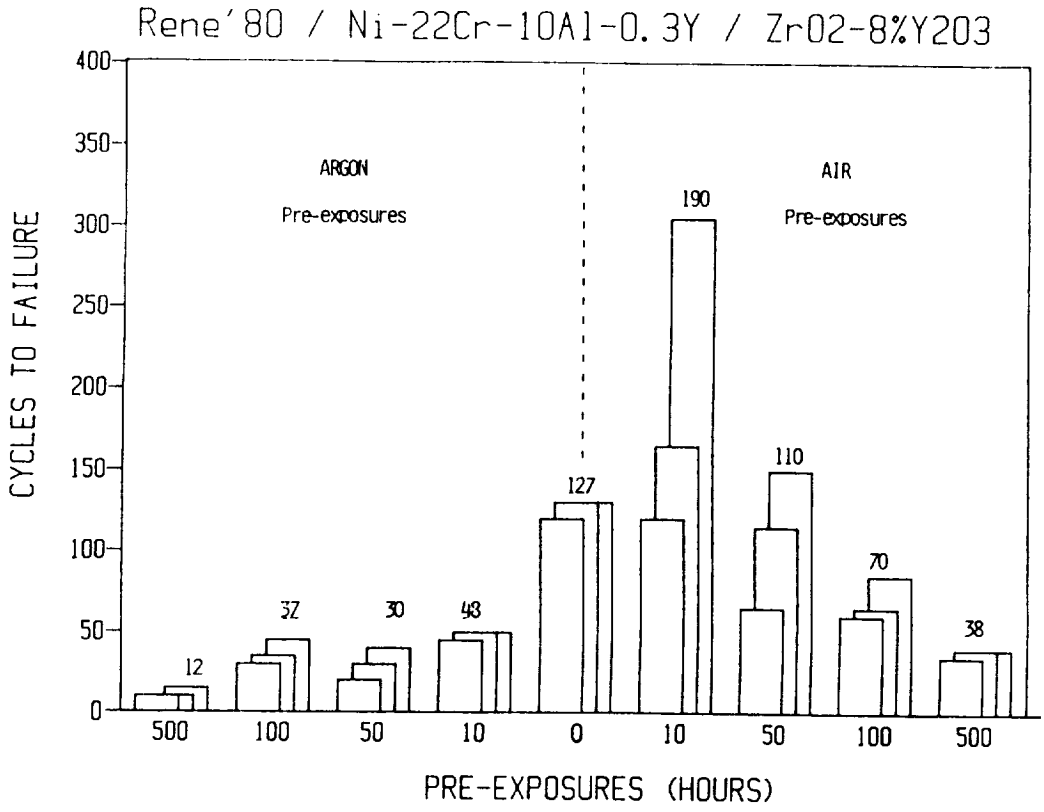

Figure 4

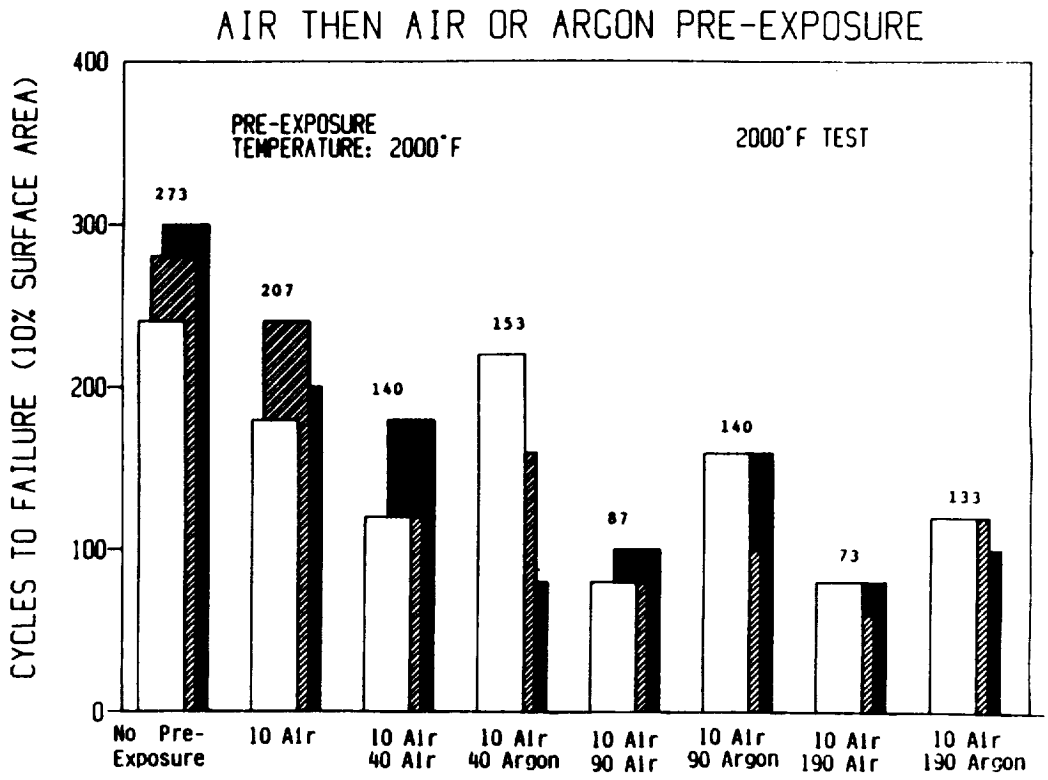

Figure 5

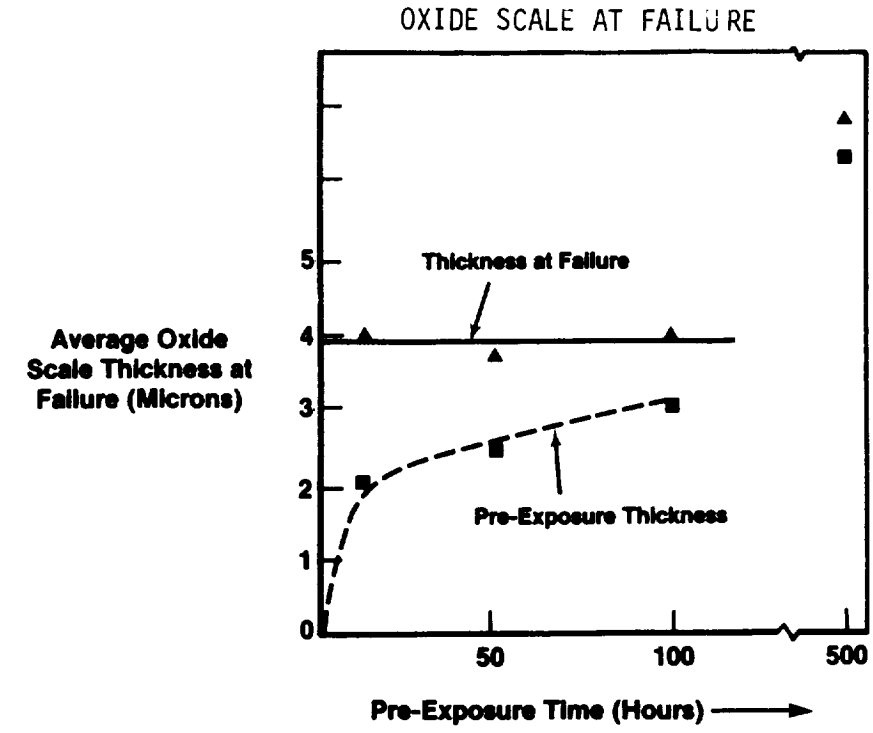

Figure 6

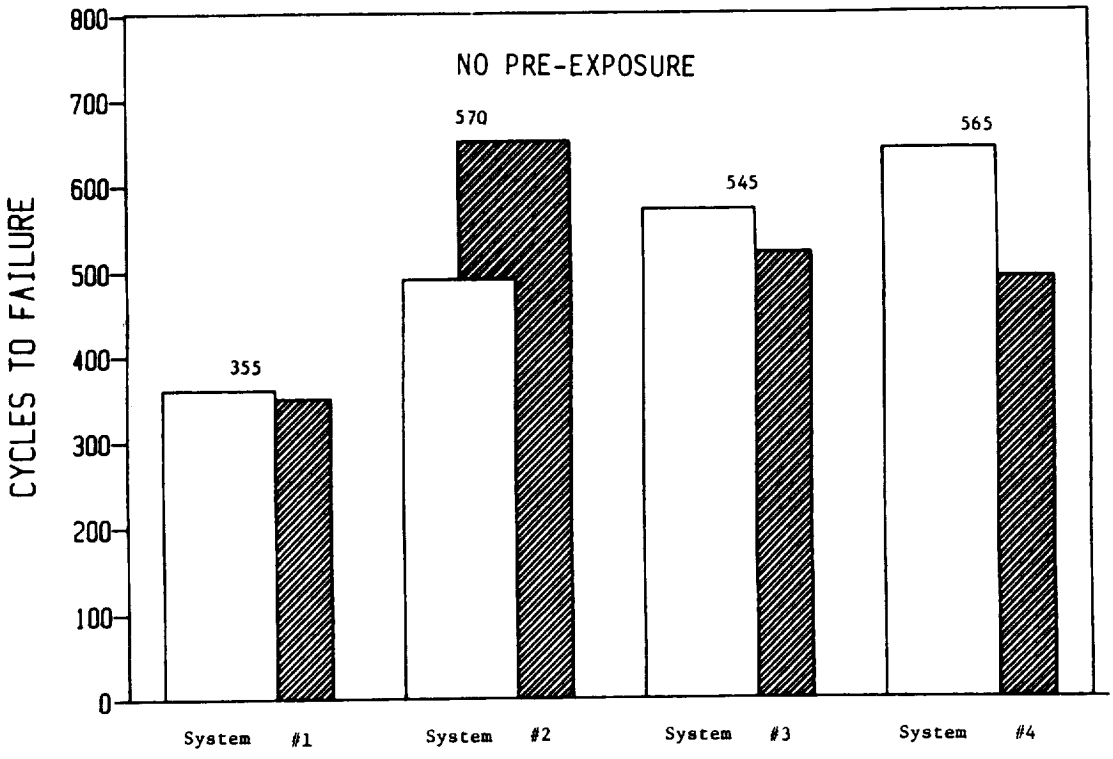

Figure 7

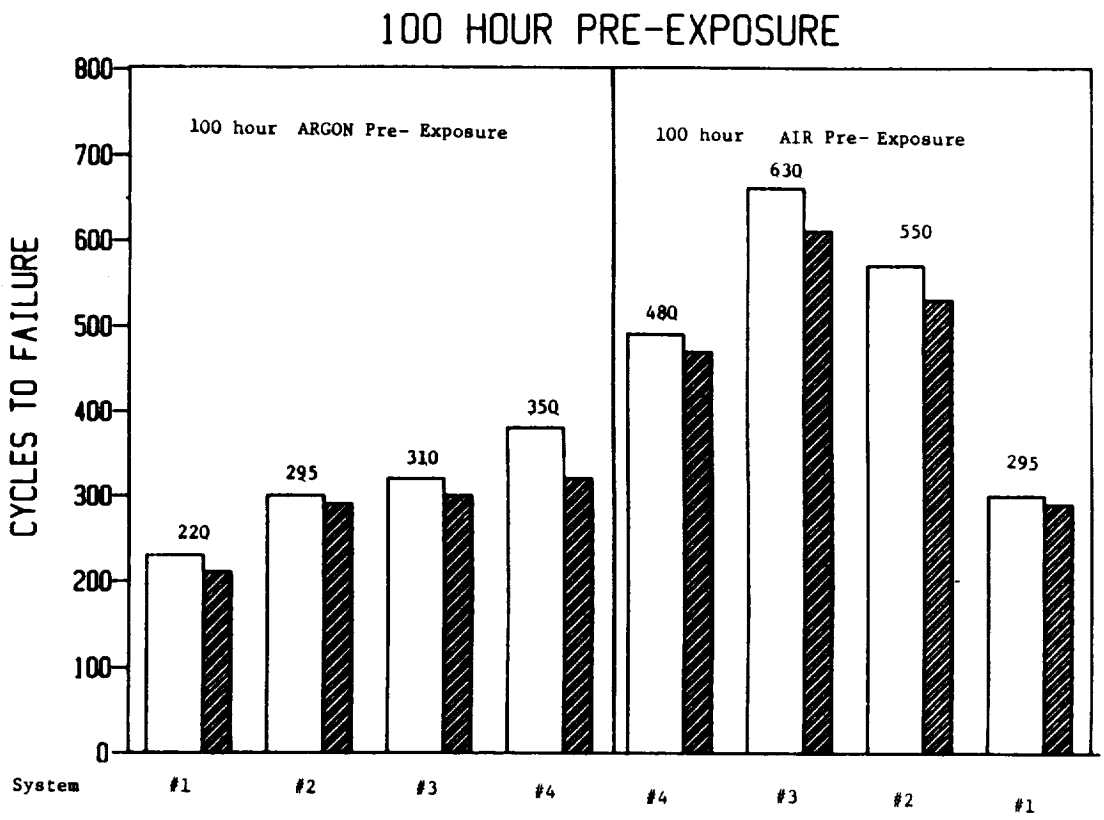

Figure 8

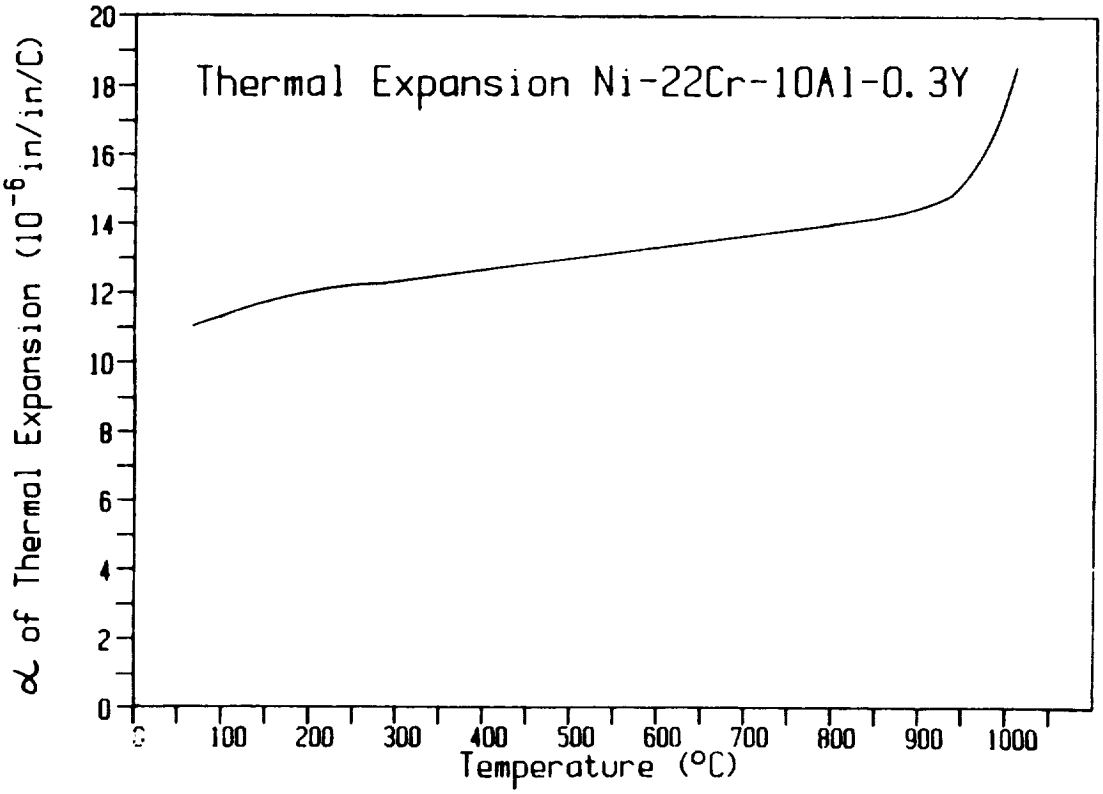

Figure 9

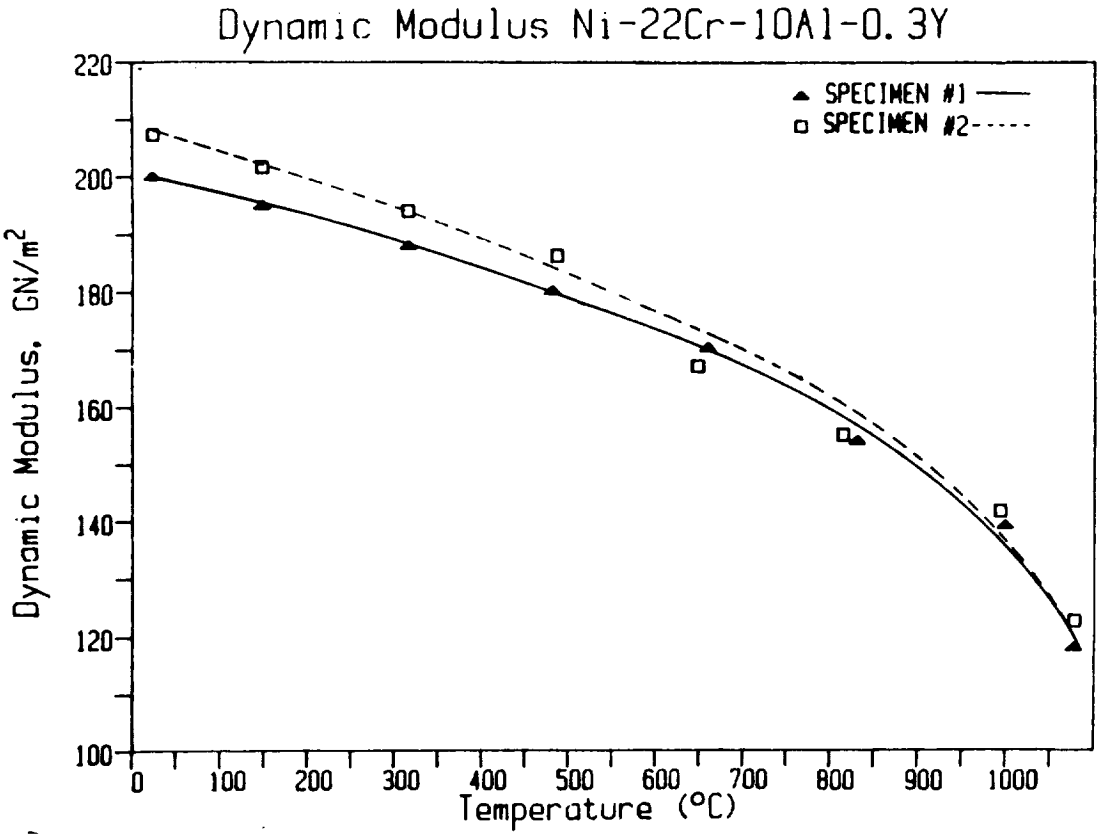

Figure 10

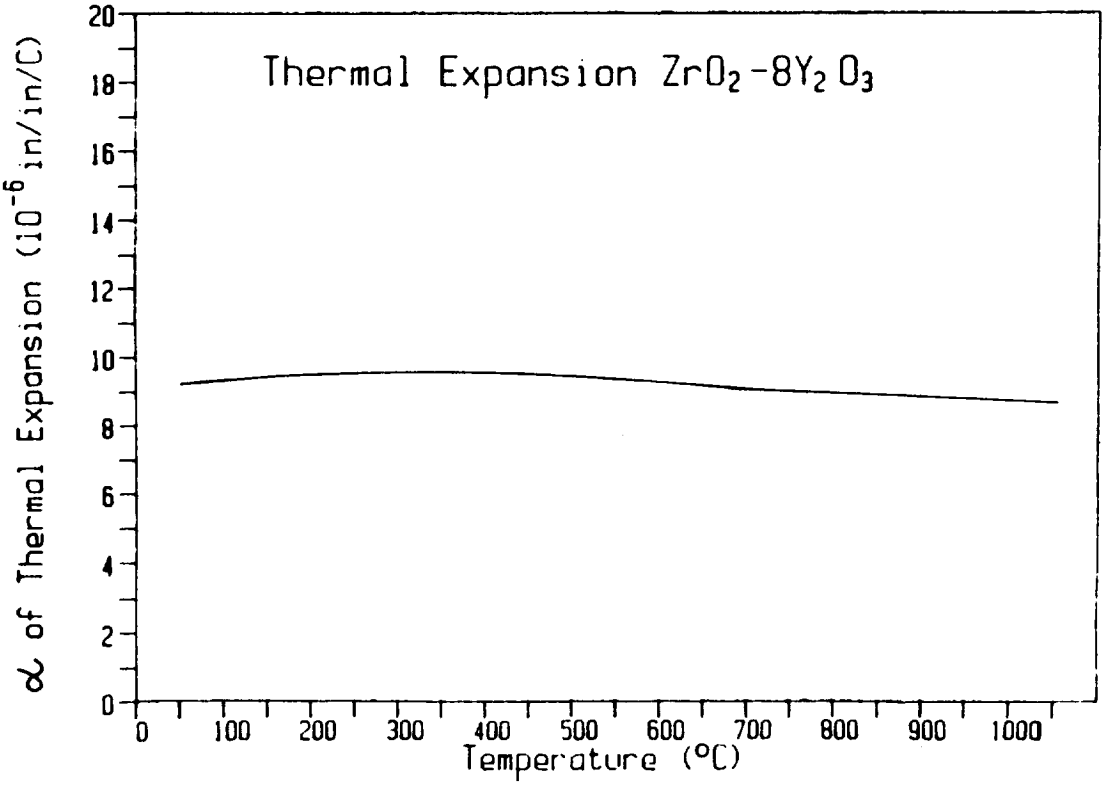

Figure 11

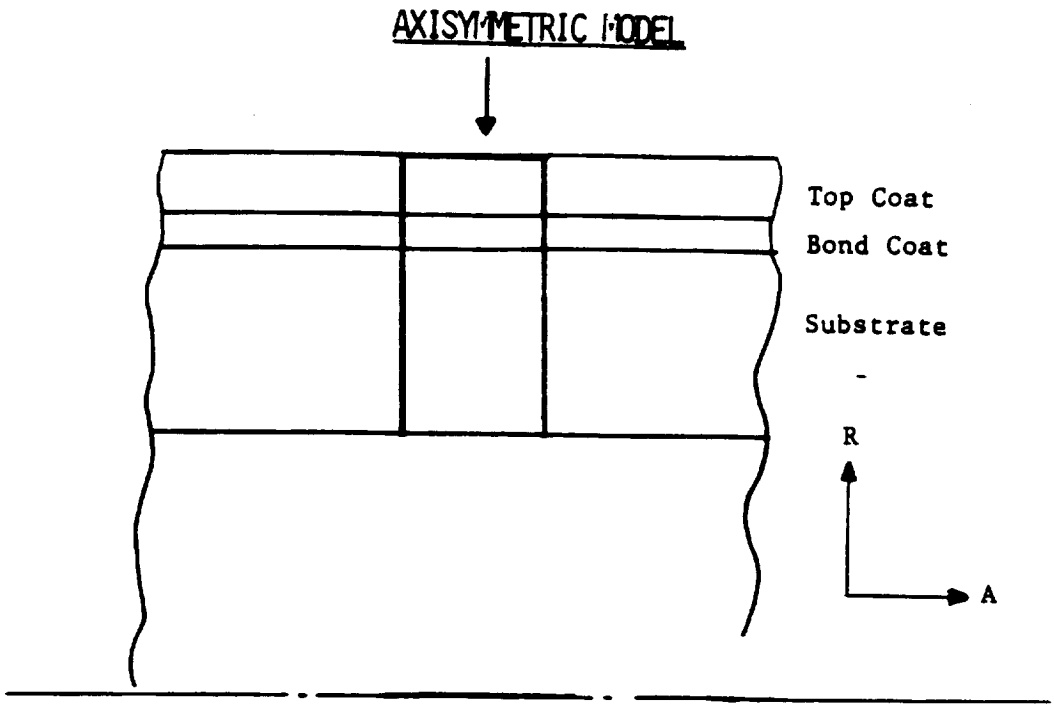

Figure 12

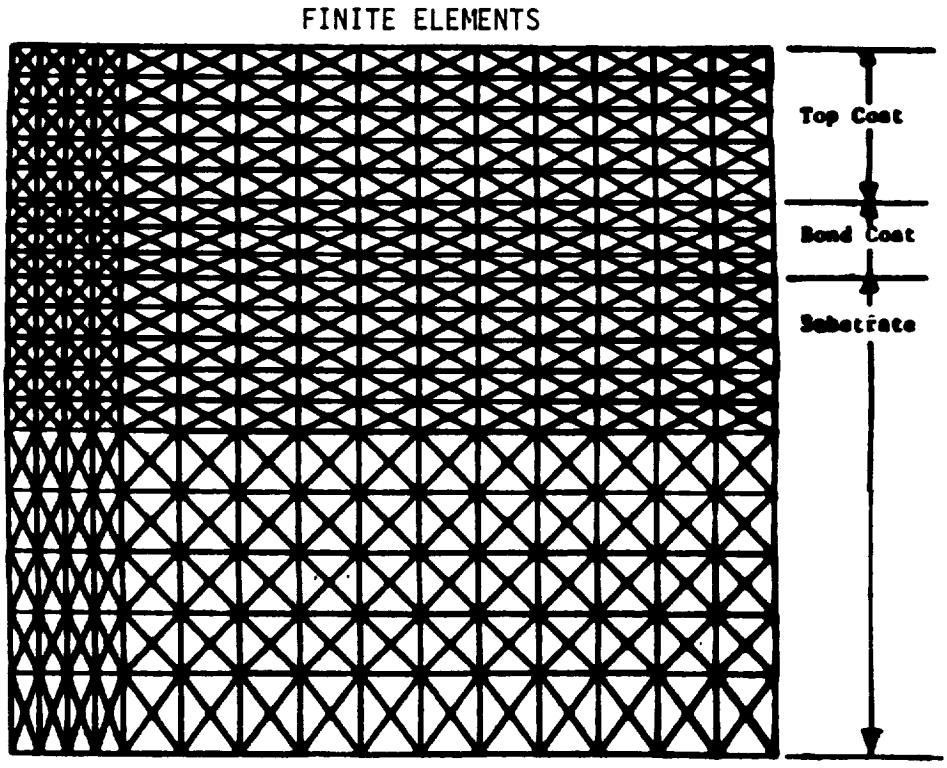

Figure 13

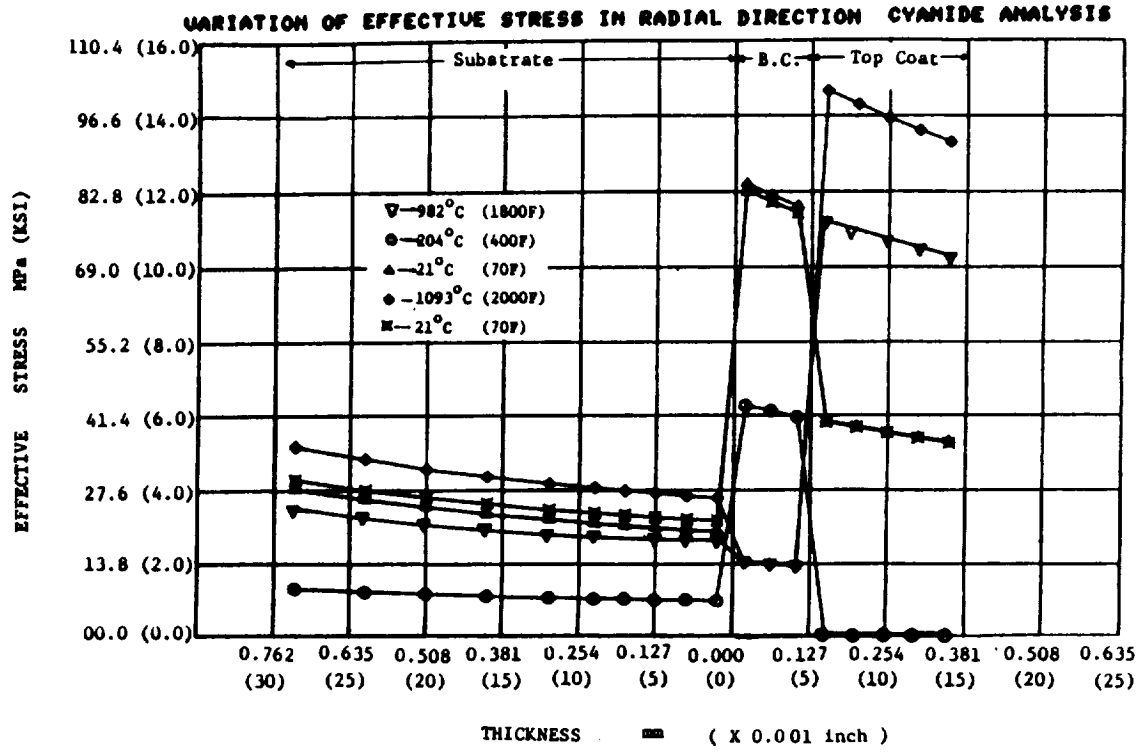

Figure 14a

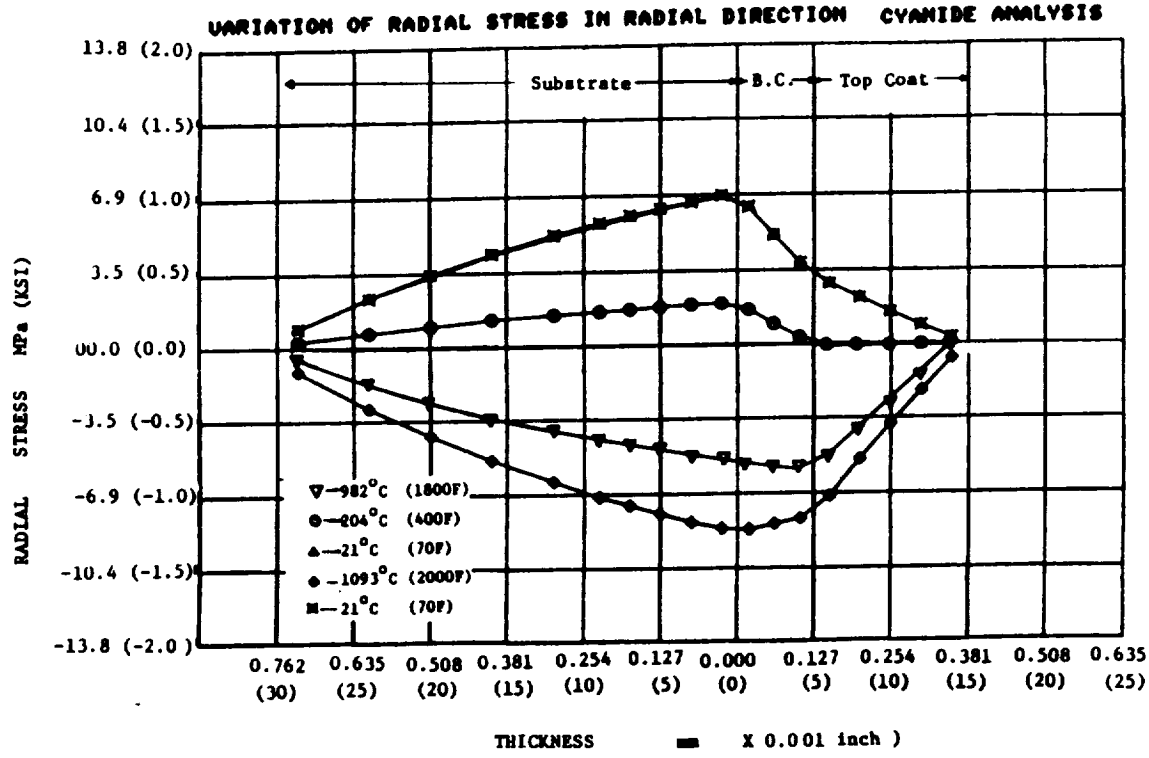

Figure 14b

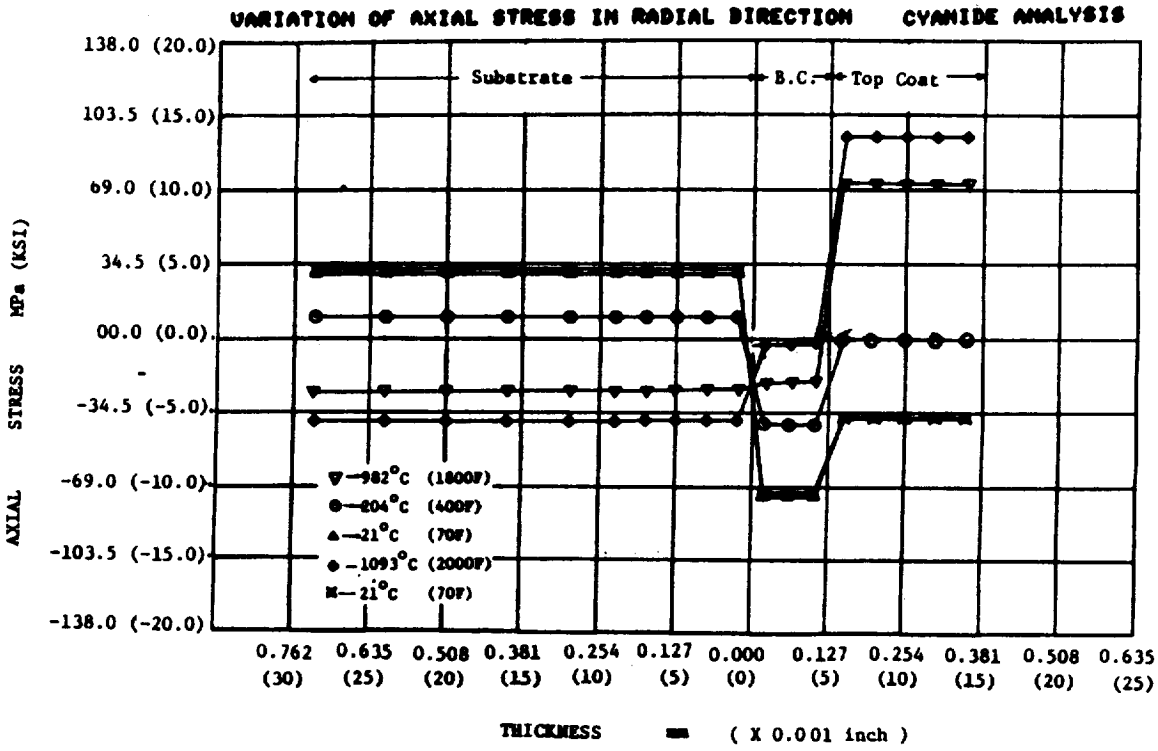

Figure 14c

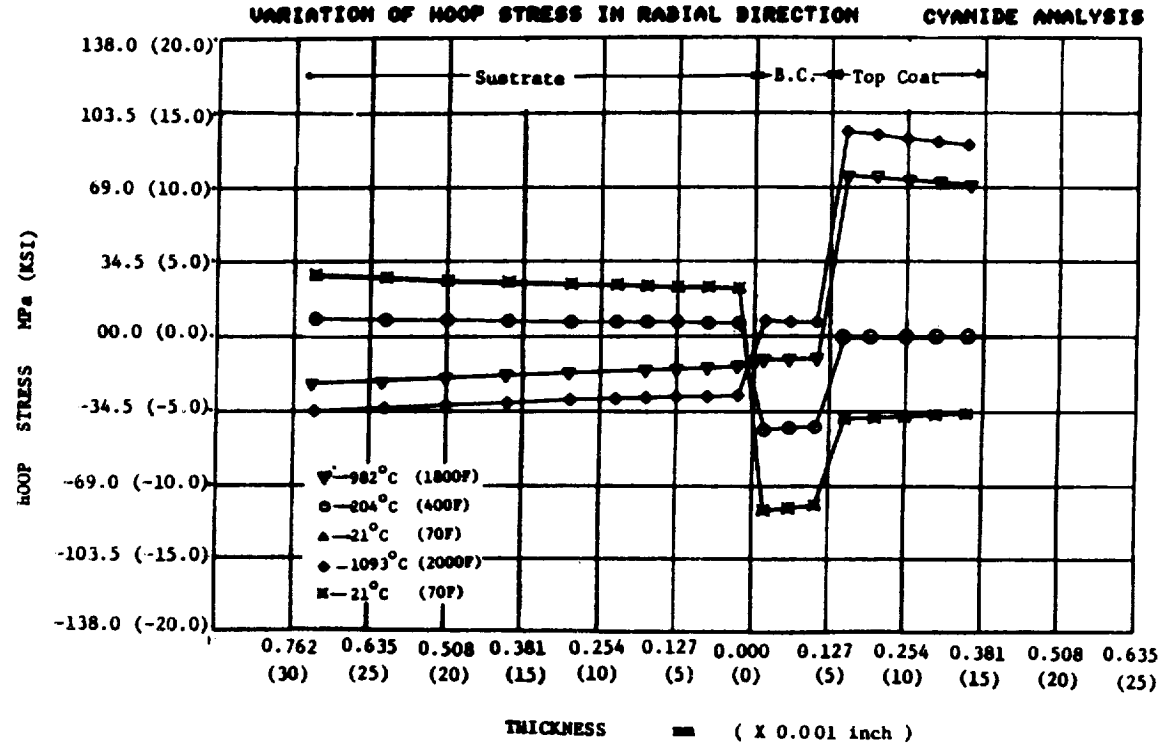

Figure 14d

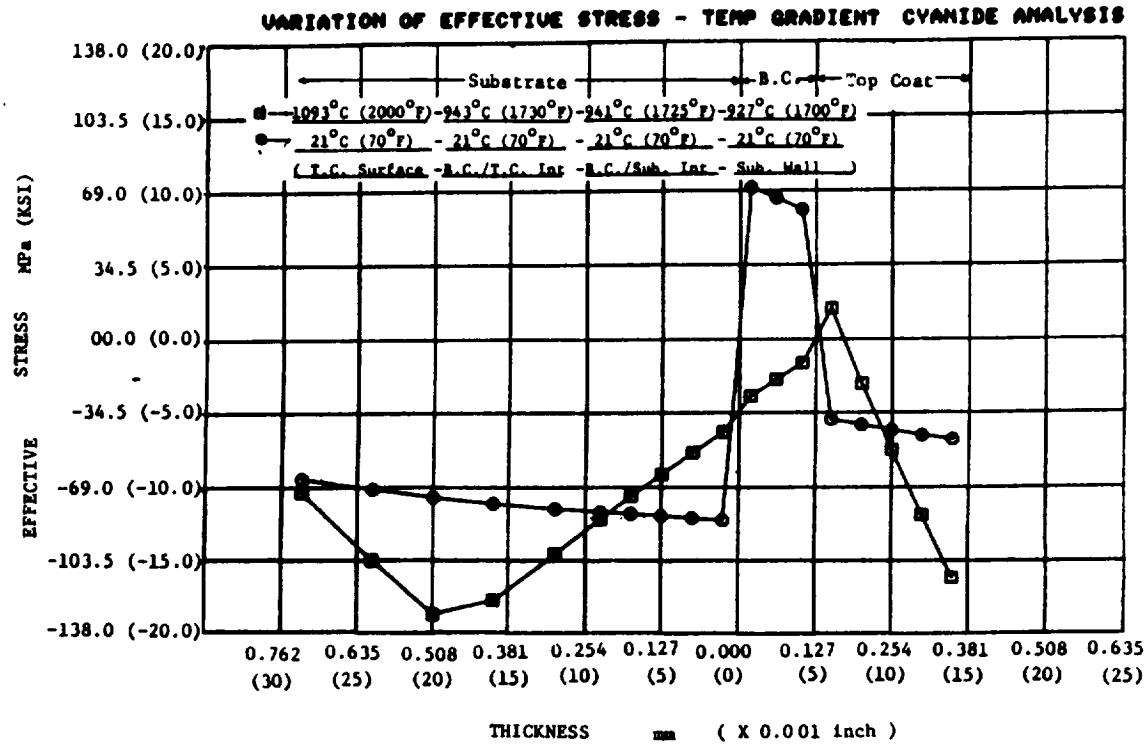

Figure 15a

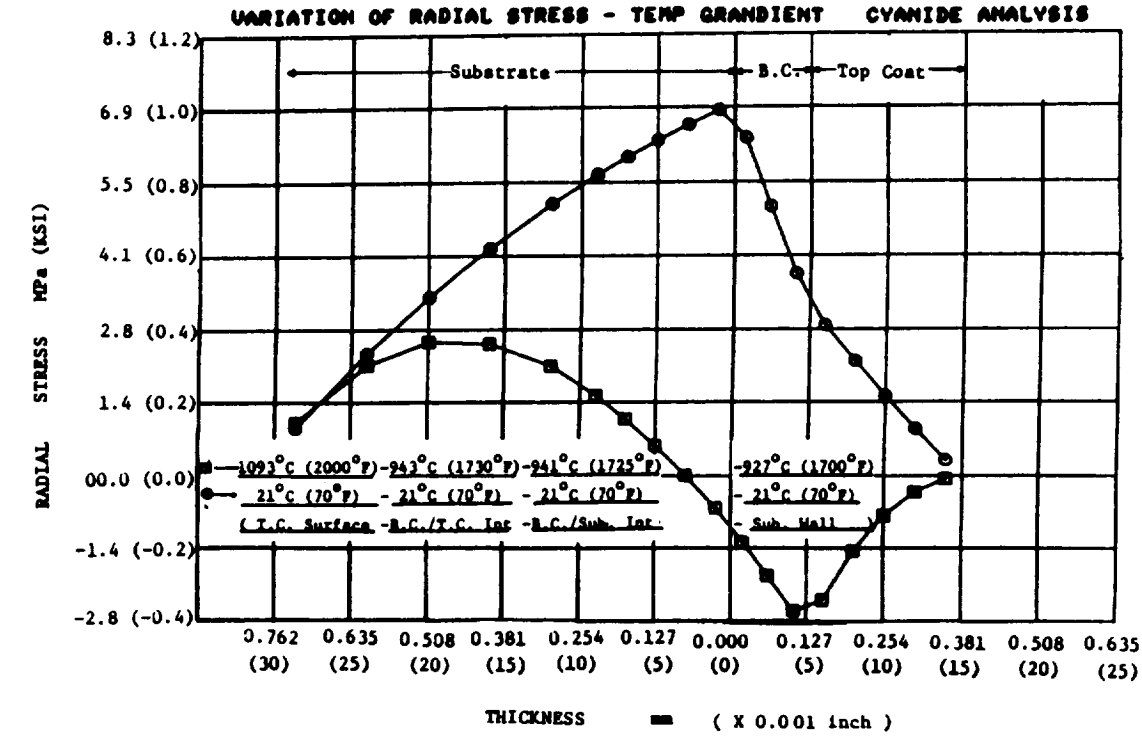

Figure 15b

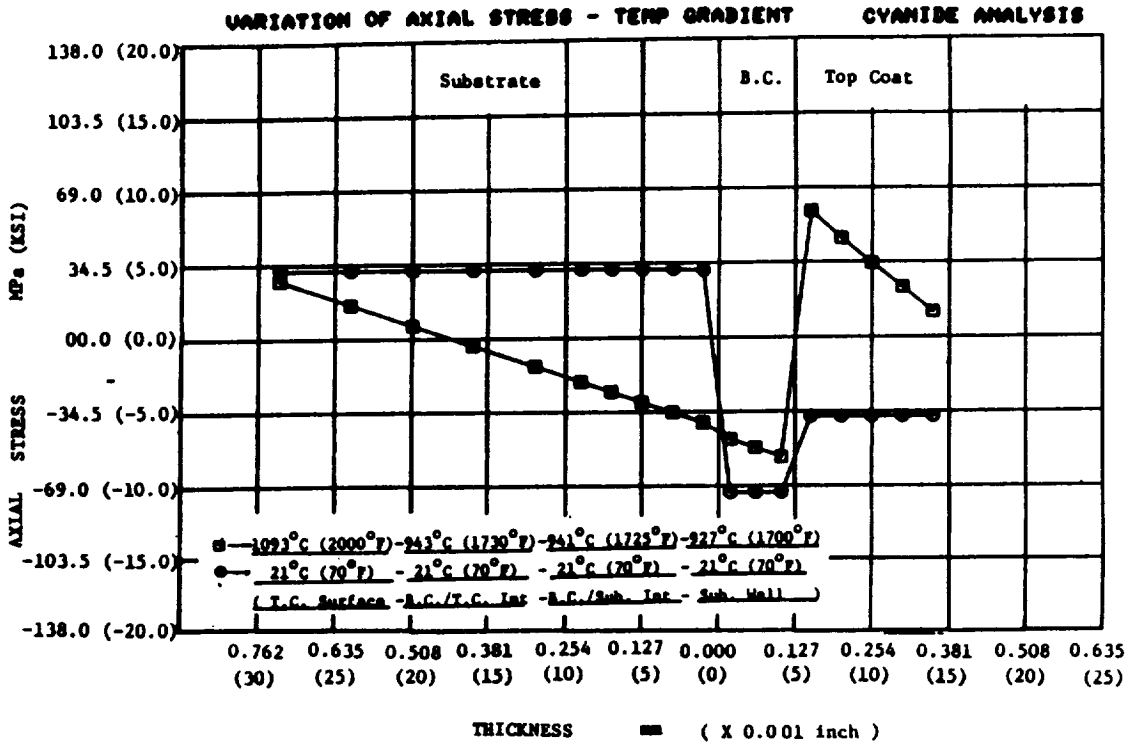

Figure 15c

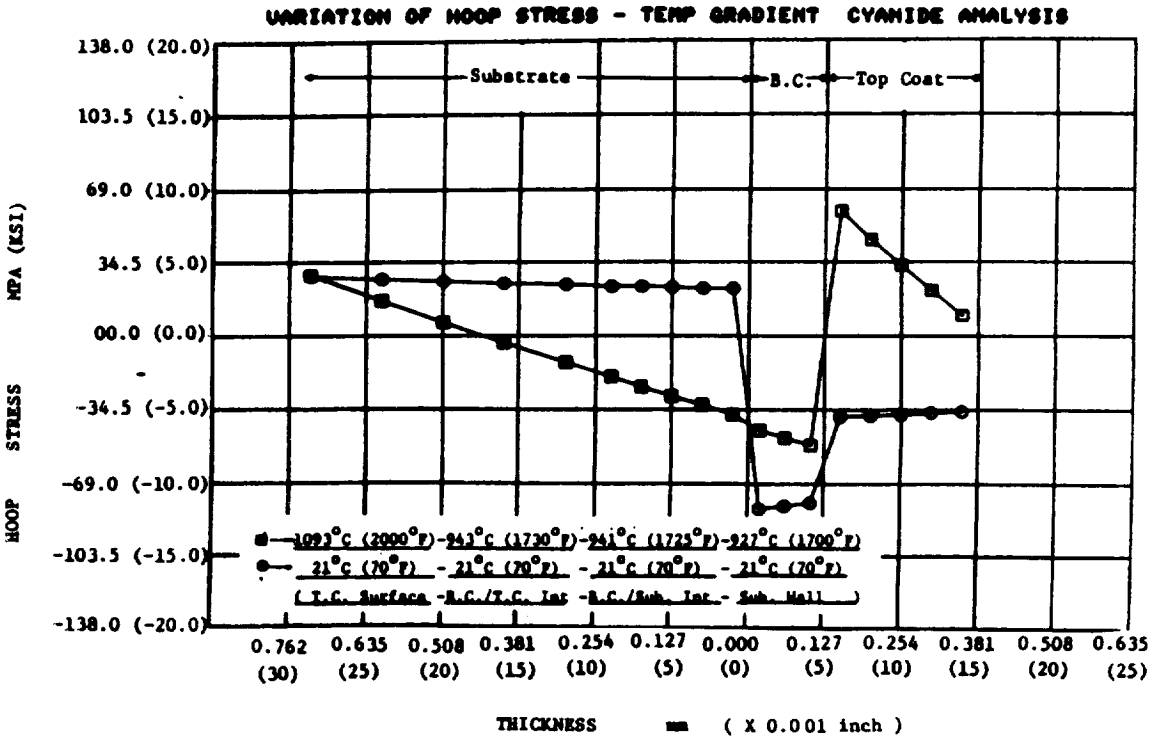

Figure 15d

LCF TUBULAR SPECIMEN

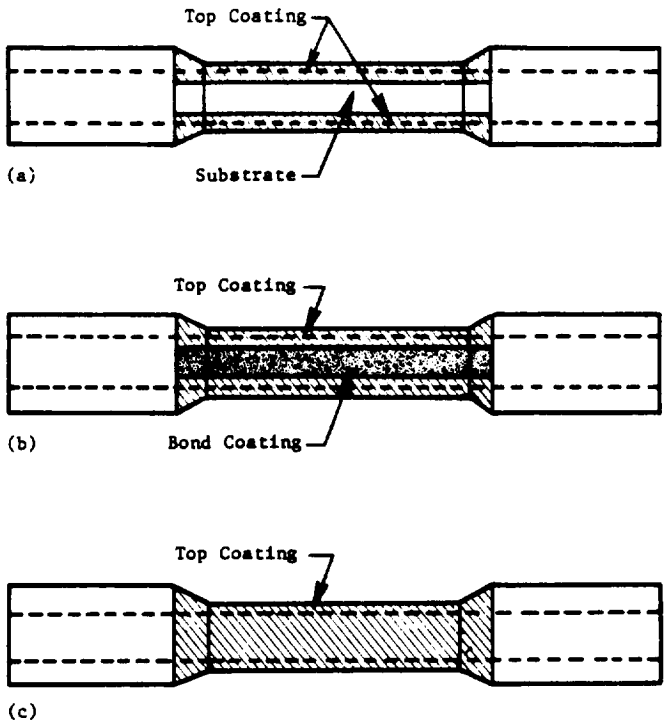

(a) Type 1 - Uncoated Substrate on Gage Section
(b) Type 2 - Uncoated Bond Coat Strip on Gage Section
(c) Type 3 - Fully Coated Gage Section

Figure 16

THERMAL BARRIER COATING LIFE PREDICTION MODEL DEVELOPMENT*

J. T. DeMasi and Dr. K. D. Sheffler
United Technologies Corporation
Pratt & Whitney

The objective of this program is to establish a methodology to predict Thermal Barrier Coating (TBC) life on gas turbine engine components. The approach involves experimental life measurement coupled with analytical modeling of relevant degradation modes. The coating being studied is a flight qualified two layer system, designated PWA 264, consisting of a nominal ten mil layer of seven percent yttria partially stabilized zirconia plasma deposited over a nominal five mil layer of low pressure plasma deposited NiCoCrAlY. Thermal barrier coating degradation modes being investigated include: thermomechanical fatigue, oxidation, erosion, hot corrosion, and foreign object damage.

The program is divided into two phases; the first phase, currently in progress, has identified cyclic mechanical damage to the ceramic and interfacial oxidation as the predominant degradation and failure modes (Task I) and is developing (Task II) and substantiating (Task III) a correlative life prediction model for these predominant modes. Phase II will address mechanistically based modeling for all relevant degradation modes.

PHASE I, TASK I - FAILURE MECHANISM DETERMINATION

The objective of Task I was to identify predominant TBC failure modes and to develop a preliminary correlative life prediction model for these modes. The approach to failure mode identification included an extensive review of experimental and flight service hardware, together with a laboratory test program designed to study the influence of driving forces such as temperature, frequency, transients, environment, coating thickness, etc. on degradation and failure life.

Results of the hardware evaluation indicate the predominant failure mode to be thermomechanical spallation of the ceramic coating layer, resulting from the formation of a dominant ceramic crack parallel and closely adjacent to the metal-ceramic interface as shown in figure 1.

Laboratory burner rig and furnace exposure test results show cyclic coating life to be reduced by increased temperature, increased coating thickness, reduced cycle rate, pre-induced oxidation damage, and artificial sea salt injected into the burner flame. Analysis of these data leads to the conclusion that cyclic mechanical damage to the ceramic and interfacial oxidation of the underlying metal layer are the predominant degradation modes in clean fuel cyclic thermal exposure. Exposure to salt contamination more severe than that normally encountered in commercial flight service can cause premature ceramic failure.

Metallographic examination of specimens removed from the burner rig test at various fractions of expected spallation life shows ceramic cracking as early as 20% of expected life. Examination of crack morphology at successively increasing life

*Work conducted under NASA Contract NAS3-23944

fractions suggests that spallation results from progressive link-up of adjacent subcritical cracks as opposed to subcritical growth of a single dominant crack as presented in figure 2. Direct evidence of interfacial initiated cracking is difficult to find, indicating that the role of oxidation in damage accumulation may be less direct then previously thought. It is interesting to note that examples of scale initiated cracking are easier to find in older specimens, occurring in the same structure together with larger numbers of well developed longer cracks which appear to be isolated from the interface. This observation could suggest that the thicker oxide scale developed at longer exposure times can initiate cracks, but that this is not the "critical" damage mode in the sense that those cracks which propagate to failure are initiated early in life and appear to be isolated from the interface. An example of this is found in figure 3.

To support the Task I preliminary modeling effort, mechanical property tests were conducted on bulk ceramic fabricated by plasma deposition with a structure that closely simulates the strain tolerant ceramic coating. The most significant result of these tests is the observation of highly non-linear tensile stress-strain behavior at all temperatures between ambient and 2200°F. This data is summarized in figure 4. While there is significant variability of initial and overall stiffness, the basic non-linear shape of the stress-strain curve is similar at temperatures up to 2000°F. At 2200°F there is substantially more curvature than at lower temperatures. Both ultimate tensile strength and tensile failure strain are relatively low ($\approx$ 3Ksi and $\approx$ 0.3%) at all temperatures.

Compressive stress-strain behavior, summarized in figure 5, differs significantly from tensile behavior; compressive strengths are much higher than tensile strengths, and there appears to be distinct linear and non-linear segments to the stress-strain curves. The 1000°F and 1600°F compressive stress-strain curves clearly are shaped differently than corresponding tensile stress-strain curves. At 2200°F, compressive deformation begins to resemble tensile deformation. Initial compressive stiffness appears to be essentially independent of temperature in the range studied.

As shown in figures 6 and 7, the strain tolerant ceramic exhibits a significant creep response at 1800°F and 2200°F; no response was observed in a tensile creep test conducted at 1000°F. Based on this observation, it will be important to incorporate a time dependent material response in the advanced modeling effort.

The data plotted in figure 8 shows an apparently real fatigue response in the strain tolerant ceramic, but with a stress dependence substantially different from that observed in metals. Whereas metallic materials typically exhibit slopes ranging from $\approx$ -1.5 with reversed plasticity to $\approx$ -8 in the fully elastic range, the data in figure 8 appears to have a slope on the order of -50. Specific degradation and failure mechanisms responsible for this very stress sensitive fatigue behavior are not presently understood.

Preliminary fracture toughness tests indicate that toughness for cracking perpendicular to the splat structure is on the order of 0.5 Ksi $\sqrt{\text{in}}$; it is expected that toughness for in-plane cracking, where predominant failure cracks are located in the coating, would be even lower.

PHASE I, TASK I PRELIMINARY LIFE PREDICTION MODEL DEVELOPMENT

The preliminary life prediction model focuses on the two major damage modes identified in the laboratory testing described above. The first of these modes in-

volves a mechanical driving force, resulting from cyclic strains and stresses in the ceramic layer caused by thermally induced and externally imposed loads. The second is an environmental driving force which appears, based on the experimental results, to be related to "oxidation damage", due to the in-service growth of a NiCoCrAlY oxide scale at the metal-ceramic interface. Based on the apparently "mechanical" mode of ceramic failure (near interfacial ceramic cracking), and on the difficulty in finding metallographic evidence of a direct physical link between the growing oxide scale and incipient cracking in specimens exposed to a relatively small fraction of expected life, it was elected to follow the approach of Miller (ref. 1) and employ an existing phenomenological fatigue model (Manson - Coffin) as the basis for the TBC life model. In traditional form, this model relates cyclic inelastic strain range to a number of cycles to fatigue failure. To incorporate an environmental effect, the mechanical driver is analytically modified in such a way as to reduce the apparent fatigue strength of the ceramic layer. The use of inelastic strain range as a damage driver for the ceramic coating layer is considered justified in view of the previously mentioned nonlinearity observed in constitutive tests conducted on the strain tolerant ceramic material, including the observation of an open hysteresis loop in preliminary tests with reversed loading.

The mathematical form of the model is: $(\Delta\epsilon_i / \Delta\epsilon_f)^b = N_f$

where $\Delta\epsilon_i$ = Total cyclic inelastic strain range
$\Delta\epsilon_f$ = Failure strain
N_f = Number of cycles to failure
b = Constant

The total cyclic inelastic strain, $\Delta\epsilon_i$, is the sum of the $\Delta(\alpha\Delta T)$ strain plus the heatup and cooldown strains, $\Delta\epsilon_C$ and $\Delta\epsilon_H$ respectively, due to the initial heatup and cooldown transient part of the burner rig thermal cycle:

$$\Delta\epsilon_i = \Delta(\alpha\Delta T) + \Delta\epsilon_C + \Delta\epsilon_H - 2(\sigma \text{ y.s.}/E)$$

The failure strain, $\Delta\epsilon_f$, is a function of the inelastic strain and is reduced by the strain due to the oxide thickness ratio, δ / δ_c, where δc is the critical oxide thickness which will cause ceramic failure in a single thermal cycle:

$$\Delta\epsilon_f = \Delta\epsilon_{fo}(1 - \delta/\delta_c)^c + \Delta\epsilon_i(\delta/\delta_c)^d$$

The static failure strain $\Delta\epsilon_{fo}$, is the strain required to fail the ceramic in the absence of bond coat oxidation; c and d are "adjustable" constants set equal to unity in the preliminary analysis. Results achieved using this model to correlate approximately one hundred individual burner rig test results obtained on Task I are shown in figure 9. Achievement of a correlation coefficient of almost 0.9 is considered quite a good fit for this preliminary attempt.

PHASE I, TASK I - PRELIMINARY MODEL VERIFICATION TESTING

To challenge the preliminary model, three burner rig verification tests were conducted using a single, internally cooled hollow specimen. This specimen permits exposure of the ceramic with a steady state through a thickness gradient to more closely simulate engine exposure of the coating, and also allows more precise instrumentation and control of the thermal environment. The hollow verification test specimen is twice the diameter of the previously utilized specimen, and rotates

about its own axis to assure circumferential temperature uniformity. These substantial changes from the Task IB experimental condition assured that the preliminary model was effectively challenged by the verification testing.

Comparisons between observed and predicted cyclic life, presented in figure 10 indicate the need for significant model refinement in Task II. While the model predicts the uncooled test result quite accurately, the two cooled test results are not well predicted. Refinement of the model to improve prediction capability currently is being performed in Task II, described below.

PHASE I, TASK II - MAJOR MODE LIFE PREDICTION MODEL DEVELOPMENT

The objective of this task is to improve the prediction capability of the preliminary model developed in Task I. The approach involves refinement of the analytical model as well as the generation of additional "design data" for model calibration, using the improved test method first employed for the Task IC verification tests.

Analytical enhancements involve improved modeling of the ceramic constitutive and time dependent behavior, incorporation of an improved oxidation model developed by Dr. Robert A. Miller (which has yet to be published but which has been related to Pratt & Whitney through private communications with NASA), and refinement of the finite element calculation of temperature and stress-strain distribution. In addition to the improved simulation of engine exposure conditions, the experimental program incorporates an expanded parameter envelope to cover a broader range of mechanical and oxidation forcing functions, as depicted in figure 11. A large portion of this test matrix has been completed and the data is being used to correlate a new life prediction model.

More accurate modeling of ceramic behavior, including nonlinear stress-strain characteristics, assymmetric tensile and compressive response, and time dependent inelastic deformation, is being accomplished using a time dependent constitutive model developed by Walker (ref. 2). An example of the application of this model to the 2200°F tension and compression data is shown in figure 12. These results show the tensile behavior to be well modeled by the Walker approach; predictive capability in compression is quite good up to $\approx$ -1% strain; beyond this point the prediction departs significantly from observed behavior. An example of a hysteresis loop calculated for a typical strain emphasis burner rig cycle is shown schematically in figure 12. There are two significant observations concerning the calculated behavior. First, compressive strain remains below the -1% limit, beyond which the prediction capability of the model breaks down. Second, the model predicts a very open loop with a quite large reversed plastic strain range to drive ceramic fatigue damage. Prediction for all of the experimental burner rig cycles currently is being made with this model for incorporation into the improved life prediction system.

Oxidation experiments were conducted using the program's substrate - TBC system, at the NASA Lewis Research Center. Dr. Robert Miller used this data to develop a new more accurate oxidation model for the improved life prediction system. The recommended weight gain expression for the data showed that the oxide growth rate is not parabolic, but approximates $t^{0.29}$. This new oxide growth rate expression in terms of oxide thickness is being incorporated into the advanced life prediction model.

PHASE I - TASK III - MODEL VERIFICATION

The objective of this task is to validate the model developed in Task II through a series of approved benchmark engine mission simulation tests. Experimental approaches to further improve the simulation capability of the test method (i.e., generate higher heat fluxes and larger through thickness gradients), and thus more effectively challenge the model, currently are being explored for incorporation in the Task III verification testing. Based on results of these tests, recommendations for further research or refinement required to arrive at a fully satisfactory engine life prediction methodology shall be made, if necessary.

REFERENCE

1. Miller, R.A.; "Oxidation-Based Model for Thermal Barrier Coating Life". J. Am. Cer. Soc. Vol. 67 No. 8, 1984, pp. 517-521.

2. Walker, K.P.; "Research and Development Program for Nonlinear Structural Modeling with Advanced Time-Temperature Dependent Constitutive Relationships". NASA-CR 165533.

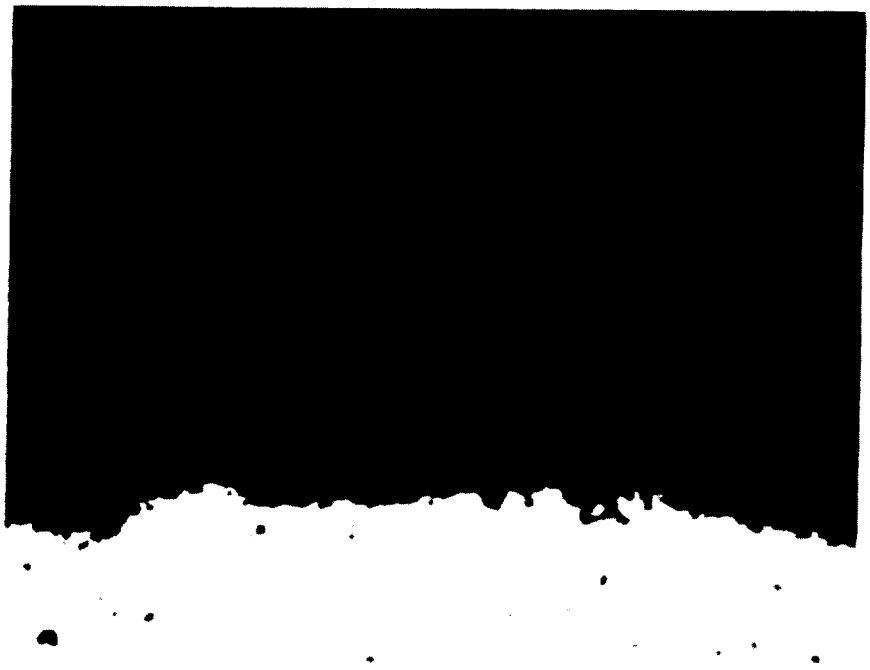

200X

Figure 1 Typical Thermal Barrier Coating Engine Failure Mode

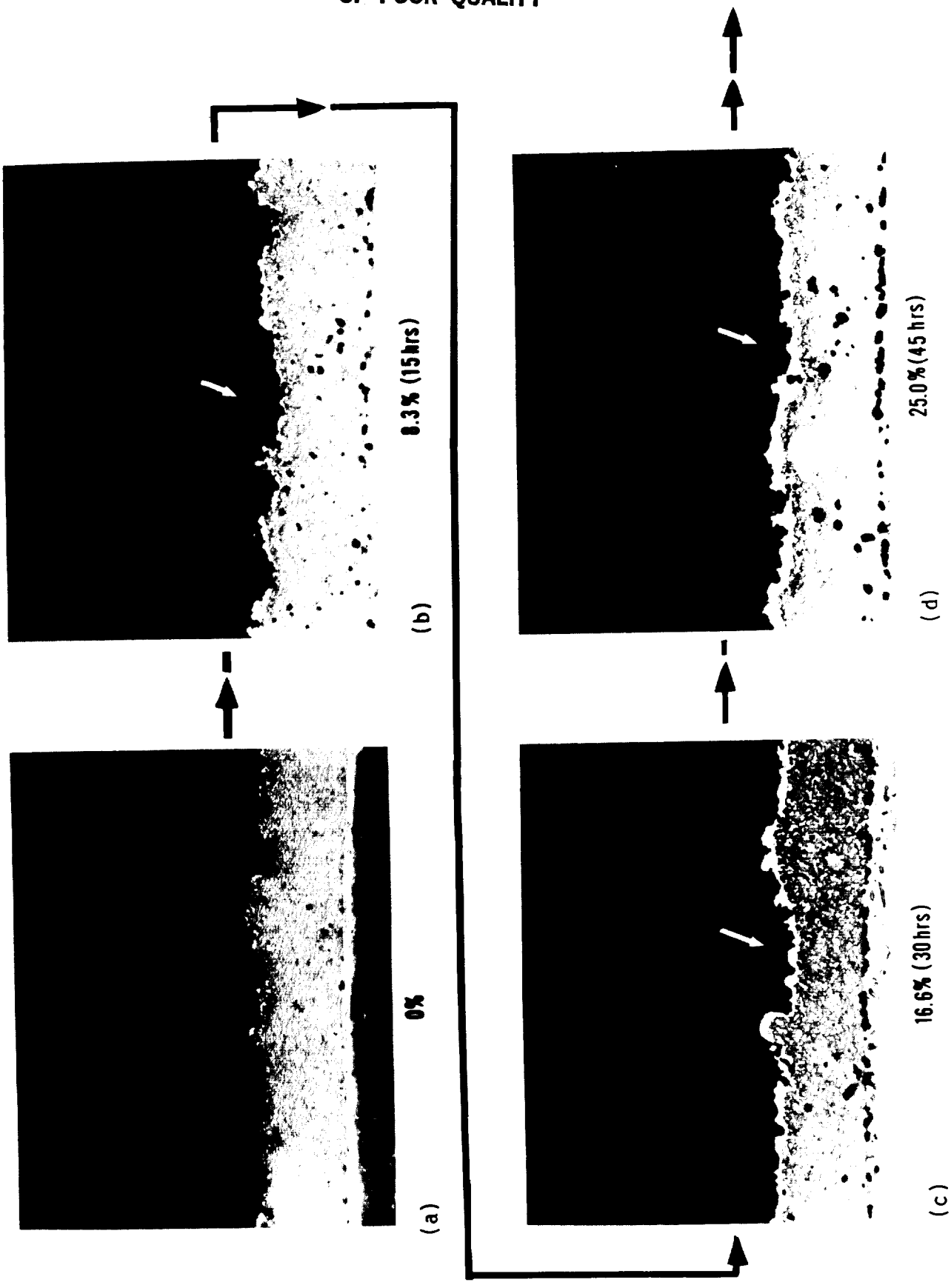

Figure 2 Thermal Barrier Coating Damage Progression

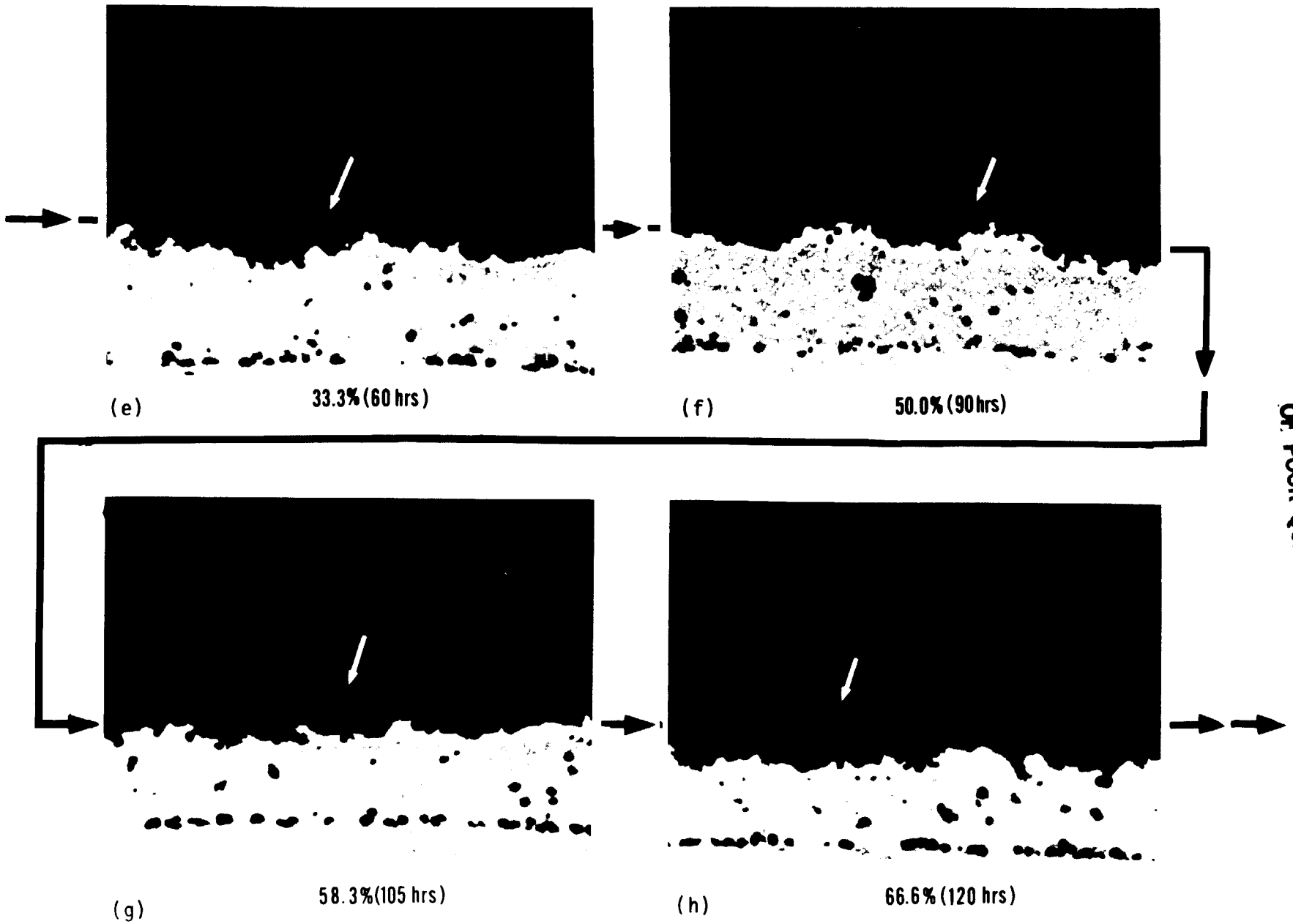

Figure 2 (Continued)

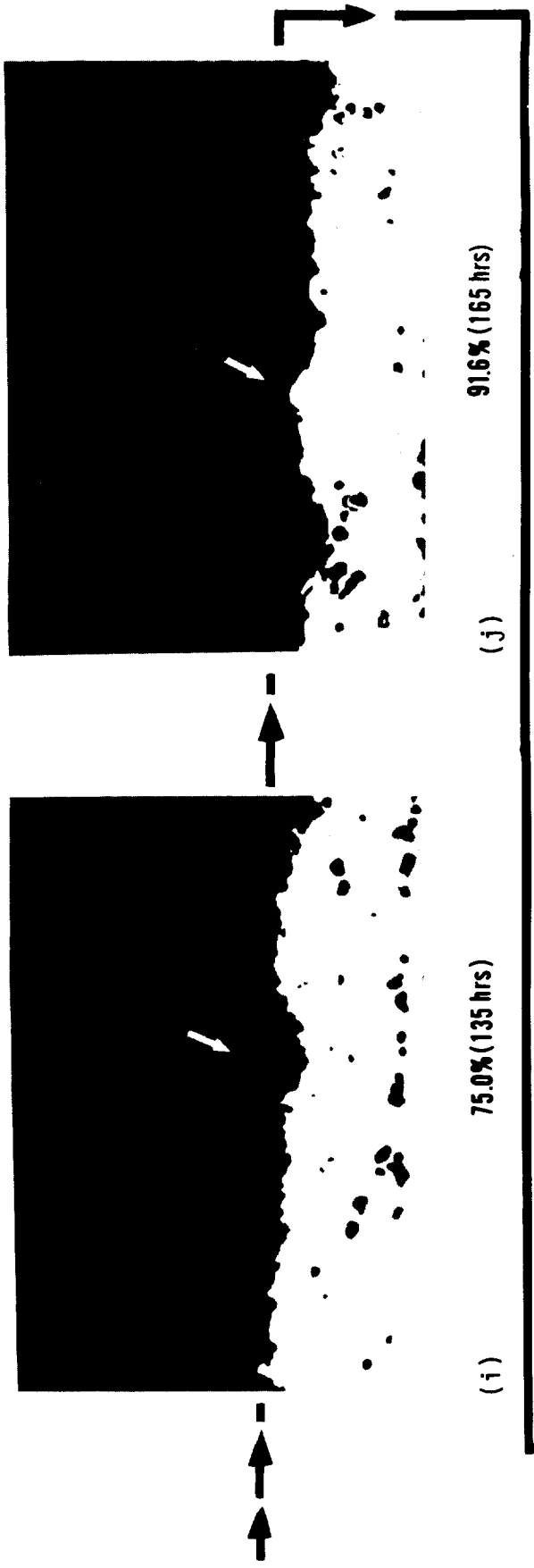

Figure 2 (Continued)

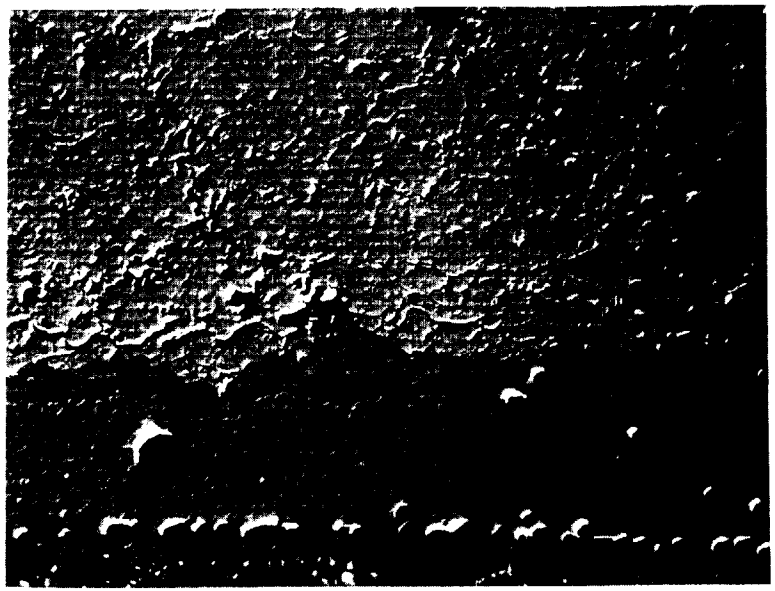

85-197 200X

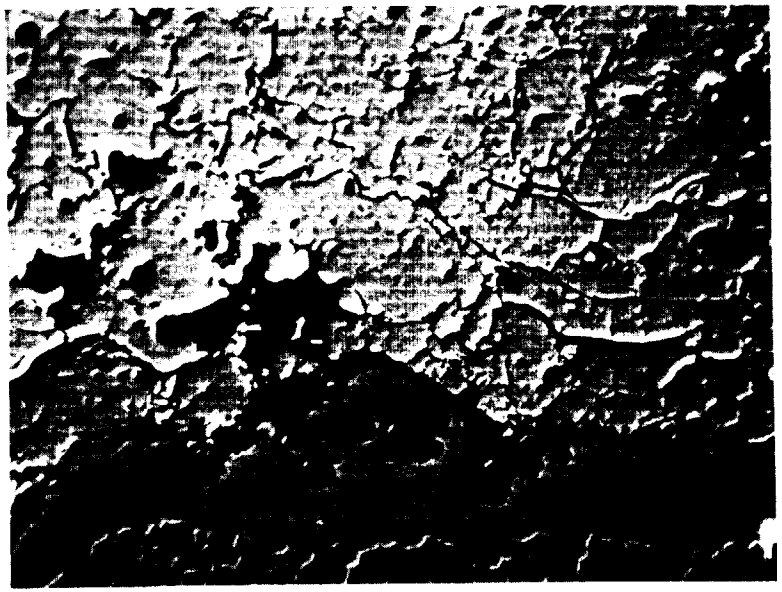

85-197 500X

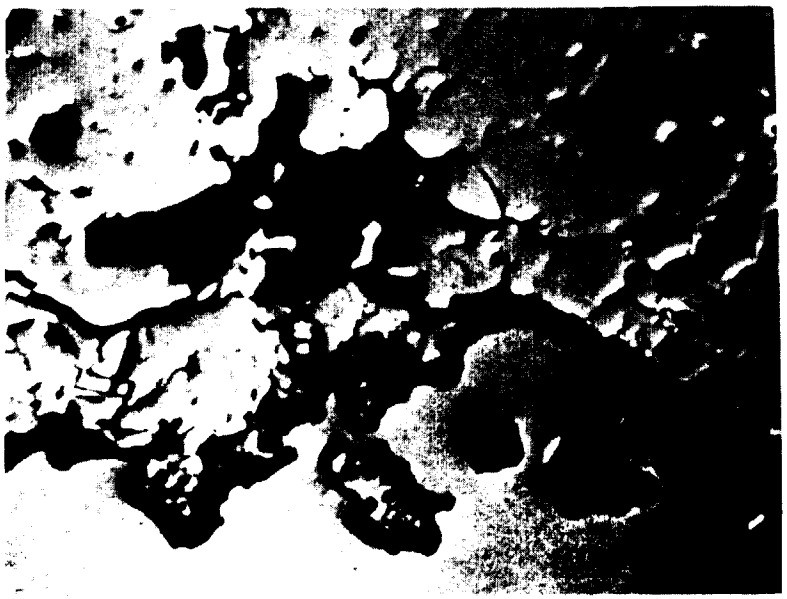

85-197 1000X

85-197 2000X

Figure 3 BSI of TBC After 105 Hours of Burner Rig Test Time at 2100°F/Short Cycle/Fast Heatup

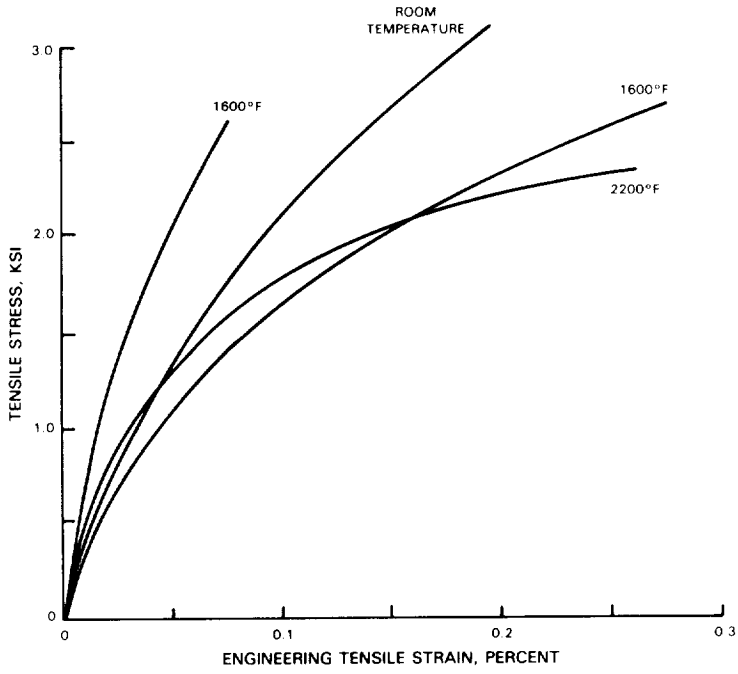

Figure 4 Representative Strain Tolerant Ceramic Tensile Stress Strain Curves at Various Temperatures. Room temperature strain data measured by strain gage; temperature curves obtained from corrected cross head displacement.

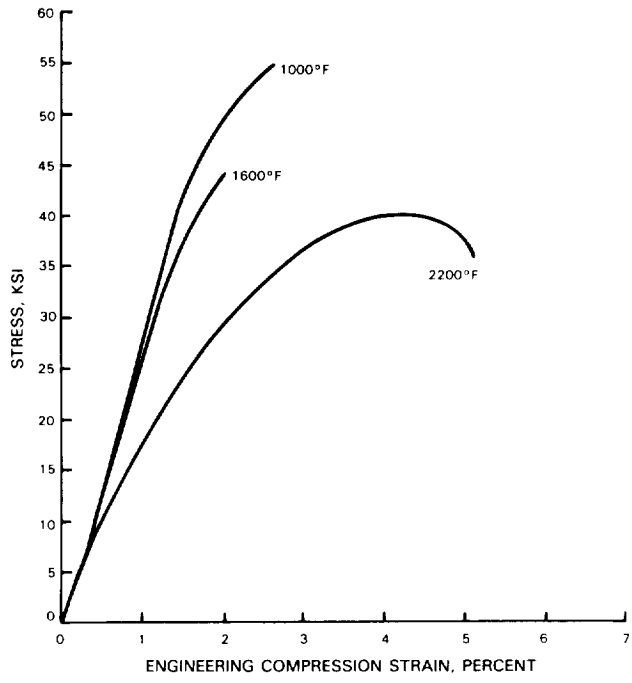

Figure 5 Representative Strain Tolerant Ceramic Compressive Stress-Strain Curves at Various Temperatures. Compressive strains calculated from corrected crosshead displacement.

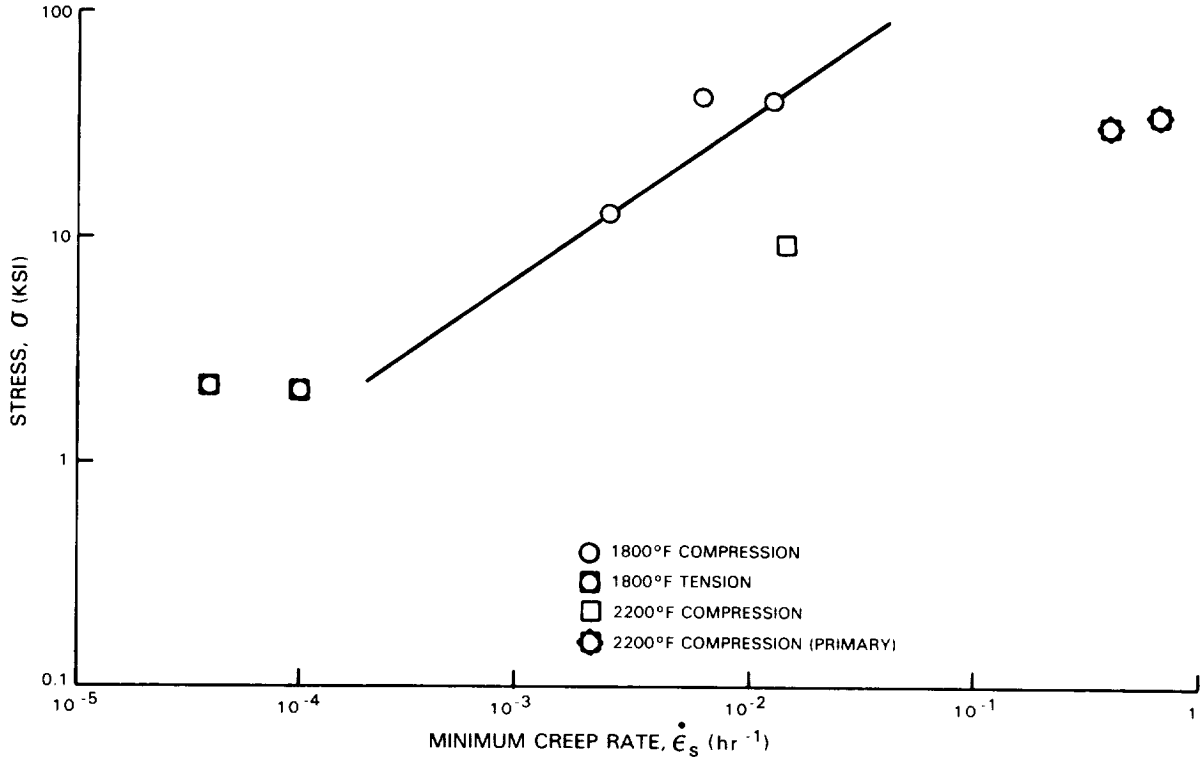

Figure 6 Stress Versus Creep Rate

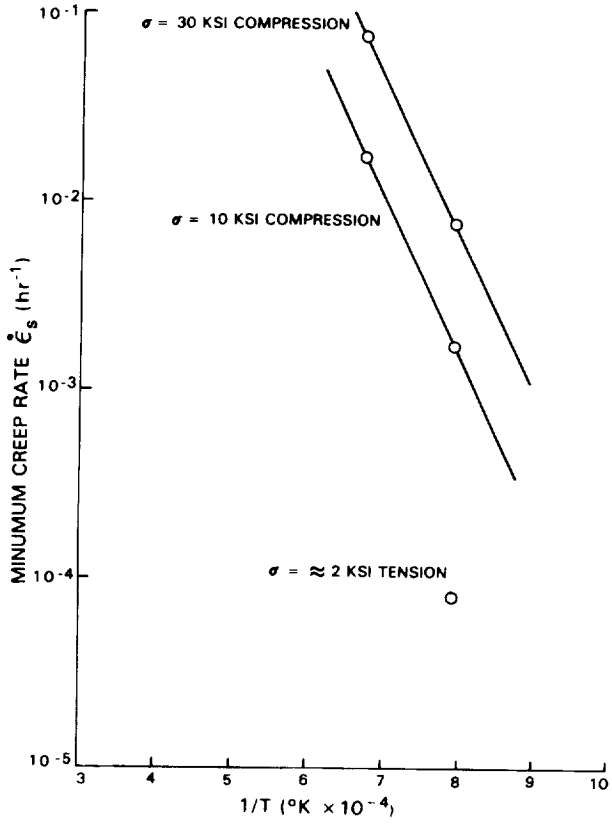

Figure 7 Creep Rate Versus Temperature

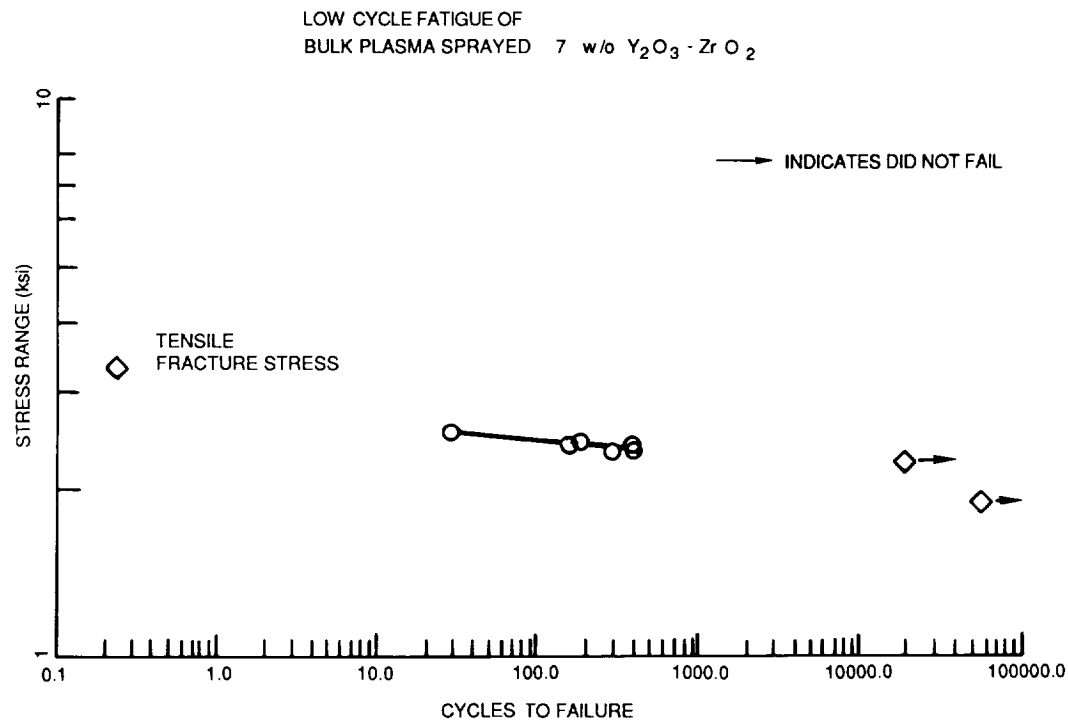

Figure 8 S-N Curve for 7YsZ (1000°F and 1600°F data plotted together)

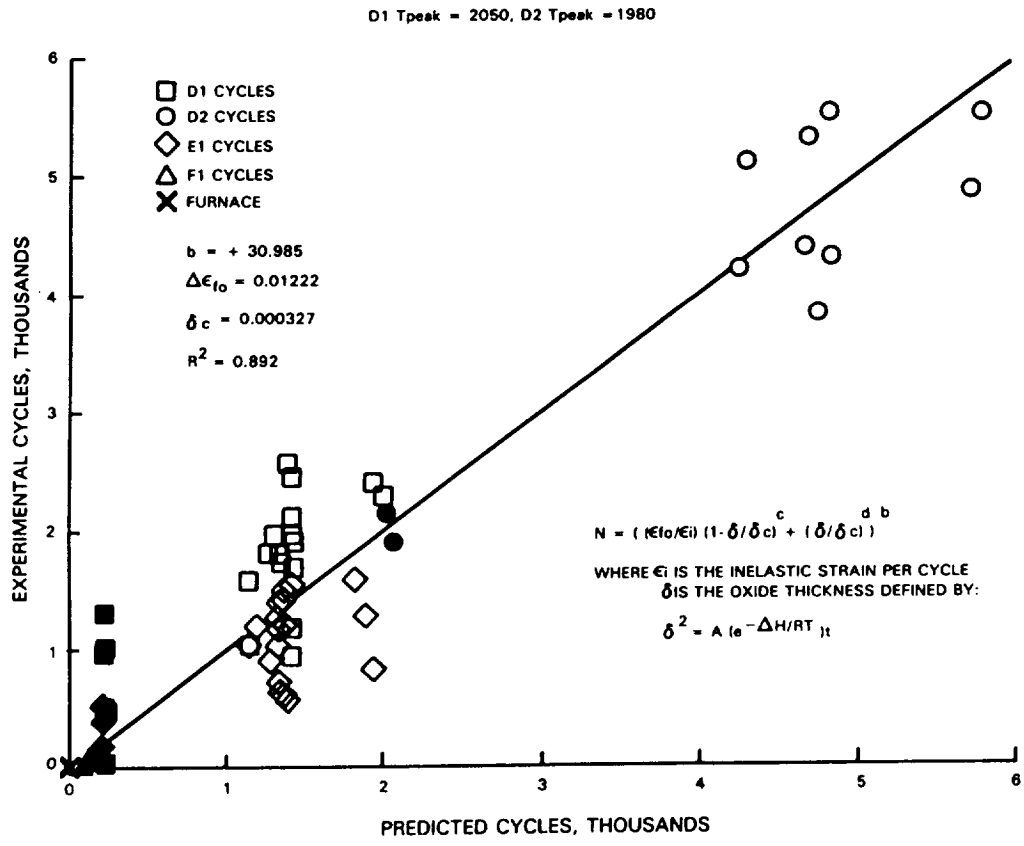

Figure 9 Preliminary Life Model Correlation

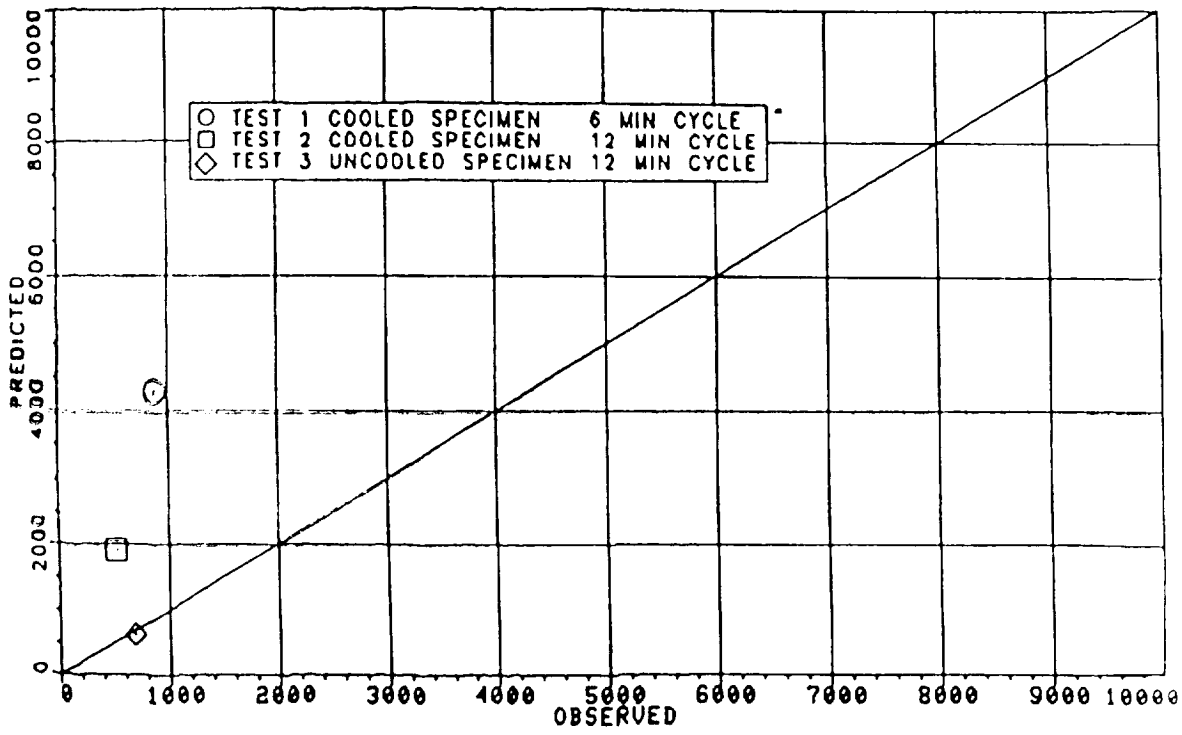

Figure 10 Predicted Cycles Versus Observed Cycles for the Task IC Verification Tests

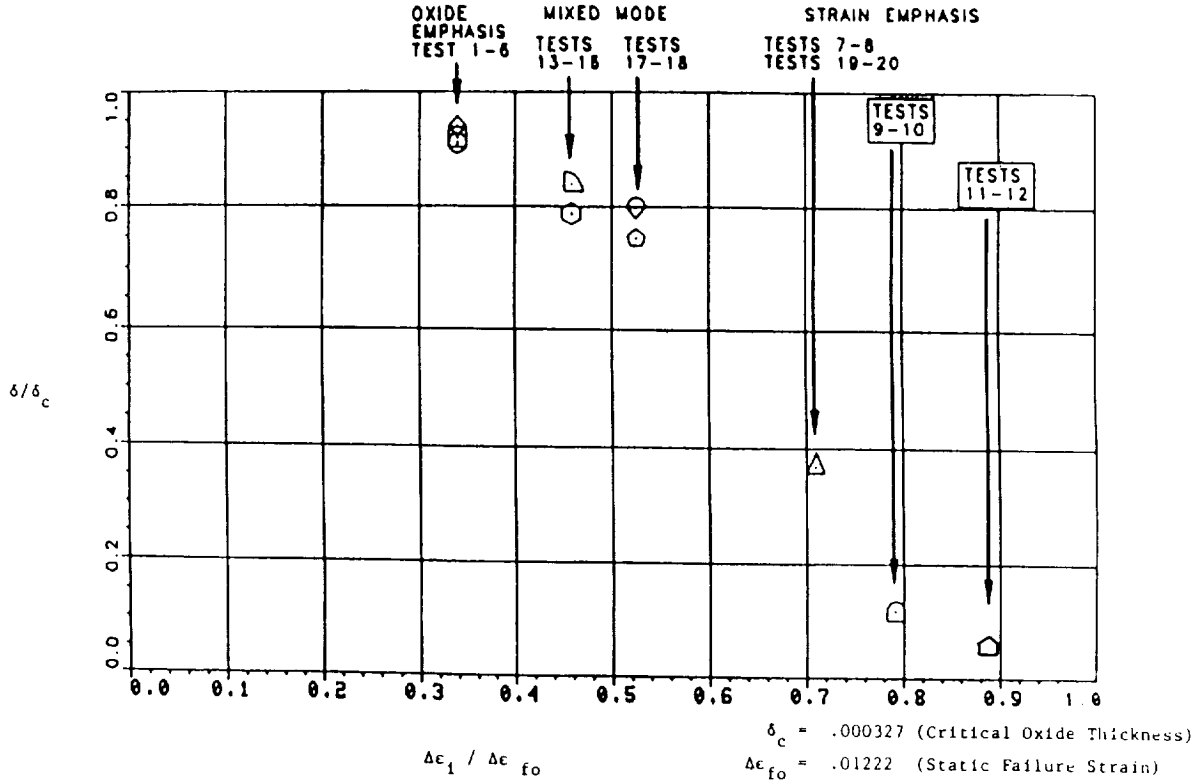

Figure 11 Task II Predictions; Oxide Thickness Ratio Versus Strain Ratio

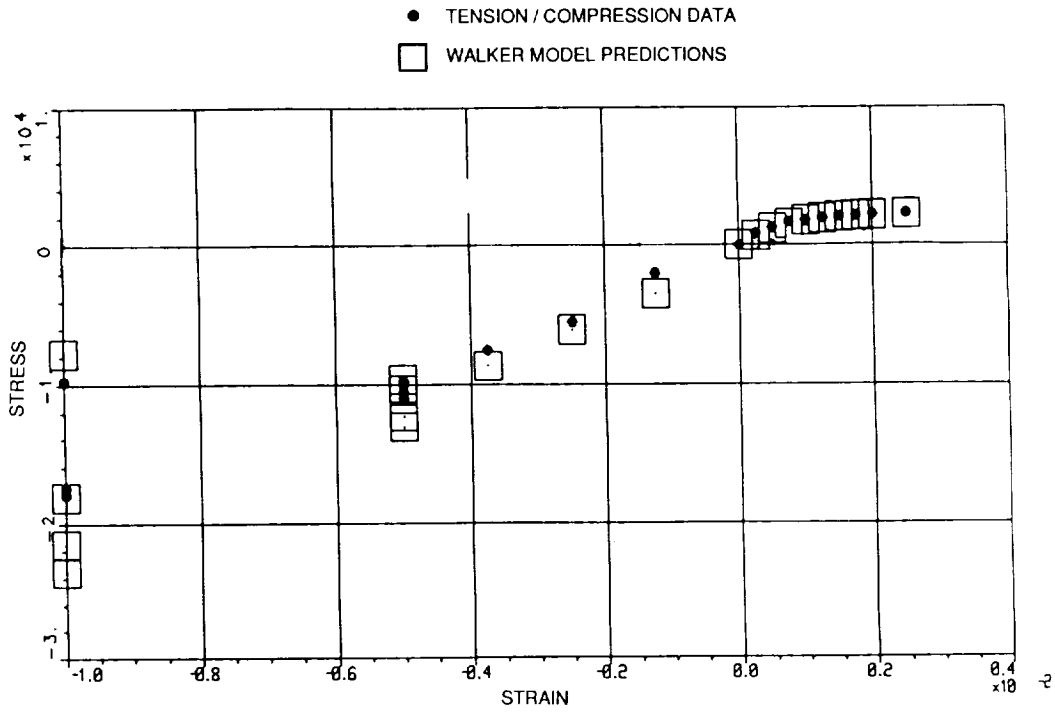

Figure 12 Compression and Tension Data at 2200°F Kevin Walker Model Predictions

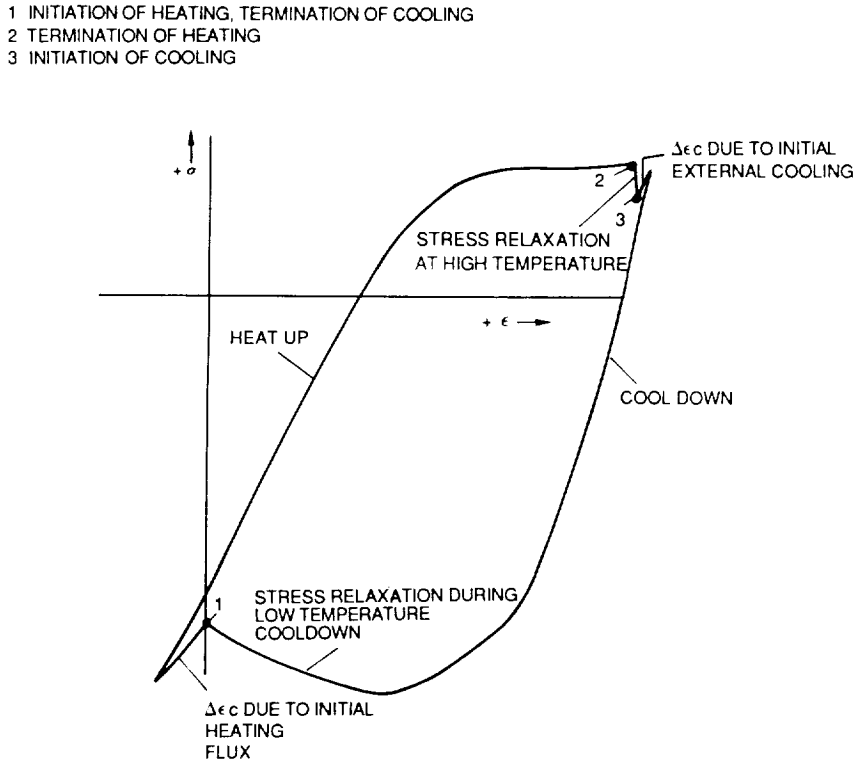

Figure 13 Schematic of Thermally Driven Ceramic Stress Strain Cycle (mature

CONCLUDING REMARKS: FIFTH ANNUAL WORKSHOP FOR THE HOST PROJECT

Daniel E. Sokolowski
NASA Lewis Research Center
Cleveland, Ohio

As reported at this workshop, the HOST Project's technical activities are producing substantial results. Many contractor reports have become available and are listed in a recently prepared bibliography of HOST papers. In addition, workshops such as this will continue on an annual basis. The HOST Sixth Annual Workshop is tentatively scheduled for October 20-21, 1987.

The nature of the problem of durability requires not only that numerous disciplines be involved, as discussed in the opening remarks, but also that the research itself be interdisciplinary. The success of the HOST Project to date is due in large part to unprecedented teamwork at Lewis, at the contractors, and between contractors and universities. In addition, the HOST Project is recognized for the value of focused as well as interdependent research when compared with generic, independent base R&T activities. The problem being addressed, however, has much influence in the advocation and successful implementation of such a project.

To date, $32.0 million has been invested in HOST. In FY 1987 another $5.0 million will be spent. The present plan for FY 1988-89 is for a total of $7.3 million to be spent.

Finally, I want to say "thank you" to the HOST Project Team for a job well done in conducting this workshop. In particular, I want to thank the contractor speakers; the Subproject Managers for being session chairman; and my assistant manager, Bob Ensign, and our Conference Coordinator, Karen Wester, for helping organize and coordinate the multitude of efforts required.

BIBLIOGRAPHY

The following is a compilation of technical reports for activities supported by the HOST Project. The reports are separated into each of the six project disciplines along with a general category. They include contractor, university grantee, NASA Technical Memorandums, and professional society publications. In addition, reports that are considered to be pre-HOST (activities initiated just prior to the HOST Project that support the project's objective) are denoted by an asterick (*).

INSTRUMENTATION

*1. Grant, H. P.; and Przybyszewski, J. S.: Thin Film Temperature Sensor. NASA CR-159782, (Pratt and Whitney, NAS3-20831), February 1980.

*2. Claing, R. G.; Grant, H. P.; and Przybyszewski, J. S.: Turbine Blade Temperature Measurements Using Thin Film Temperature Sensors. NASA CR-165201, (Pratt and Whitney, NAS3-20831), March 1981.

*3. Anderson, W. L.; Claing, R. G.; Grant, H. P.; and Przybyszewski, J. S.: Thin Film Temperature Sensors Phase III. NASA CR-165476, (Pratt and Whitney, NAS3-22002), April 1982.

4. Atkinson, W. H.; and Strange, R. R.: Development of Advanced High-Temperature Heat Flux Sensors. NASA CR-165618, (Pratt and Whitney, NAS3-22133), September 1982.

5. Elmore, D. L.; Robinson, W. W.; and Watkins, W. B.: Dynamic Gas Temperature Measurement System, Final Report, Volume I - Technical Efforts. NASA CR-168267, (PWA/GPD-FR-17145 - Vol. I, Pratt and Whitney, NAS3-23154), May 1983.

6. Elmore, D. L.; Robinson, W. W.; and Watkins, W. B.: Dynamic Gas Temperature Measurement System, Final Report, Volume II - Operation and Program Manual. NASA CR-168267, (PWA/GPD-FR-17145-Vol. II, Pratt and Whitney, NAS3-23154), May 1983.

*7. Stetson, K. A.: Demonstration Test of Burner Liner Strain Measuring System. NASA CR-174743, (United Technologies Research Center, NAS3-23690), June 1984.

8. Oberle, L. G.; Seasholtz, R. G.; and Weikle, D. H.: Optimization of Fringe-Type Laser Anemometers for Turbine Engine Component Testing. AIAA-84-1459, June 1984.

9. Atkinson, W. H.; Cyr, M. A.; and Strange, R. R.: Turbine Blade and Vane Heat Flux Sensor Development, Phase I, Final Report. NASA CR-168297, (Pratt and Whitney, NAS3-23529), August 1984.

PRECEDING PAGE BLANK NOT FILMED

10. Elmore, D. L.; and Watkins, W. B.: Further Development of the Dynamic Gas Temperature Measurement System. FR-18639, Pratt and Whitney, NAS3-24228, September 1984.

11. Morey, W. W.: Hot Section Viewing System. NASA CR-174773, (United Technologies Research Center, NAS3-23156), September 1984.

12. Bailey, R.S.; Hulse, C. O.; and Lemkey, F. D.: High Temperature Static Strain Gage Alloy Development Program. NASA CR-174833, (United Technologies Research Center, NAS3-23169), March 1985.

13. Hobart, H. F.: Evaluation Results of the 700 °C Chinese Strain Gauges. NASA TM-86973, March 1985.

14. Hulse, C. O.; Bailey, R. S.; and Lemkey, F. D.: High Temperature Static Strain Gage Alloy Development Program. NASA CR-174833, (United Technologies Research Center, NAS3-23169), March 1985.

15. Atkinson, W. H.; Cyr, M. H.; and Strange, R. R.: Turbine Blade and Vane Heat Flux Sensor Development, Phase II Final Report. NASA CR-174995, (Pratt and Whitney, NAS3-23529), October 1985.

16. Oberle, L. G.; and Seasholtz, R. G.: Filter Induces Errors in Laser Anemometer Measurements Using Counter Processors. NASA TM-87047, November 1985.

COMBUSTION

1. Sturgess, G. J.: Aerothermal Modeling - Phase I, Task Report, Description of Aerothermal Model and Relation to Design System. PWA-5907-2, Pratt and Whitney, NAS3-23524, August 1982.

2. Sturgess, G. J.: Aerothermal Modeling - Phase I, Task Report, Model Assessement Procedure. PWA-5907-3, Pratt and Whitney, NAS3-23524, August 1982.

3. Holdeman, J. D.: Dilution Zone Mixing. Combustion Fundamentals Research, NASA CP-2268, pp. 65-76, October 1982.

4. Srinivasan, R.; Berenfeld, A.; and Mongia, H. C.: Dilution Jet Mixing Program, Phase I Report. NASA CR-168031, (Garrett-21-4302, Garrett Turbine Engine Company, NAS3-22110), November 1982.

5. Holdeman, J. D. and Srinivasan, R.: Experiments in Dilution Jet Mixing. AIAA 83-1201 presented at the 19th Joint Propulsion Conference, Seattle, Washington, NASA TM-83434, June 1983.

6. Holdeman, J. D.: Perspectives on the Mixing of a Row of Jets with a Confined Crossflow. AIAA 83-1200 presented at the 19th Joint Propulsion Conference, Seattle, Washington, NASA TM-83457, June 1983.

7. Sturgess, G. J.: Aerothermal Modeling Program - Phase I, Final Report, NASA CR-168202, (PWA-5907-19, Pratt and Whitney, NAS3-23524), July 1983.

8. Srinivasan, R.; et al: Executive Summary, Aerothermal Modeling Program - Phase I. NASA CR-174602, (Garrett-21-4766, Garrett Turbine Engine Company, NAS3-23523), August 1983.

9. Srinivasan, R.; et al: Aerothermal Modeling Program - Phase I, Final Report, Volume I, NASA CR-168243-Vol. 1, (Garrett-21-4742-1, Garrett Turbine Engine Company, NAS3-23523), August 1983.

10. Srinivasan, R.; et al: Aerothermal Modeling Program - Phase I, Final Report, Volume II. NASA CR-168243-Vol. 2, (Garrett-21-4742-2, Garrett Turbine Engine Company, NAS3-23523), August 1983.

11. Roback, R.; and Johnson, B. V.: Mass and Momentum Turbulent Transport Experiments with Confined Swirling Coaxial Jets. NASA CR-168252, (United Technology Research Center, NAS3-22771), August 1983.

12. Kenworthy, M. K.; Correa, S. M.; and Burrus, D. L.: Aerothermal Modeling - Phase 1, Final Report, Executive Summary. NASA CR-168330, (General Electric Company, NAS3-23525), November 1983.

13. Kenworthy, M. K.; Correa, S. M.; and Burrus, D. L.: Aerothermal Modeling - Phase I, Final Report, Volume I - Model Assessment. NASA CR-168296-Vol. I, (General Electric Company, NAS3-23525), November 1983.

14. Kenworthy, M. K.; Correa, S. M.; and Burrus, D. L.: Aerothermal Modeling Phase I, Final Report, Volume II - Experimental Data. NASA CR-168296-Vol. II, (General Electric Company, NAS3-23525), November 1983.

15. Kenworthy, M. K.; and Correa, S. M.: Aerothermal Modeling, Final Report. NASA CR-168330, (General Electric Company, NAS3-23525), December 1983.

16. Abujelala, M. T.; Busnaina, A. A.; Ferrell, G. B.; and Lilley, D. G.: Lateral Jet Injection Into Typical Combustor Flowfields. University of Oklahoma, NAG3-549, January 1984.

17. Srinivasan, R.; Coleman, E.; and Johnson, K.: Dilution Jet Mixing Program, Phase II Program. NASA CR-174624, (Garrett Turbine Engine Company, NAS3-22110), June 1984.

18. Holdeman, J. D.; and Srinivasan, R.: Modeling of Dilution Jet Flowfields, Combustion Fundamentals Research, AIAA-84-1379, NASA CP-2309, pp. 175-187, April 1984.

19. Holdeman, J. D.; and Srinivasan, R.: On Modeling Dilution Jet Flowfields. AIAA 84-1379 presented at the 20th Joint Propulsion Conference, Cincinnati, Ohio, NASA TM-83708, June 1984.

20. Holdeman, J. D.; Srinivasan, R.; and Berefeld, A.: Experiments in Dilution Jet Mixing. AIAA Journal, Volume 22, Number 10, pp. 1436-1443, October 1984.

21 Johnson, B. V.; and Roback, R.: Turbulent Transport and Length Scale Measurement Experiments with Conbined Coaxial Jets. NASA CR-174831, (United Technologies Research Center, NAS3-22771), November 1984.

22. Johnson, B. V.; and Roback, R.: Scalar and Momentum Turbulent Transport Experiments with Swirling and Nonswirling Flows. ASME 105th Winter Annual Meeting, December 1984.

23. Lilley, D. G.: Swirling Flows in Typical Combustor Geometries. AIAA 85-0148 presented at the 23rd Aerospace Sciences Meeting, Reno, Nevada, January 1985.

24. Ferrell, G. B.; and Lilley, D. G.: Lateral Jet Injection into Swirling Flowfields. AIAA 85-0059 presented at the 23rd Aerospace Sciences Meeting, Reno, Nevada, January 1985.

25. Ferrell, G. B.; Aoki, K.; and Lilley, D. G.: Flow Visualization of Lateral Jet Injection into Swirling Crossflow. University of Oklahoma, AIAA 85-0059, January 1985.

26. Ferrell G. B.; and Lilley D. G.: Deflected Jet Experiments in a Turbulent Combustor Flowfield. Oklahoma State University, NASA CR-174863, February 1985.

27. Chiappetta, L. M.; Gosman, A. D.; and Syed, S. A.: Error Reduction Program - Final Report. NASA CR-174776, (Pratt and Whitney, NAS3-23686), April 1985.

28. Ferrell, G. B.; and Lilley, D. G.: Turbulence Measurements of Lateral Jet Injection into Confined Turbulent Crossflow. AIAA 85-1102 presented at the 21st Joint Propulsion Conference, Monterey, California, June 1985.

29. Holdeman, J. D.; Srinivasan, R.; Coleman, E. B.; Meyers, G. D.; and White, C. D.: Experiments in Dilution Jet Mixing: Effects of Multiple Rows and Non-circular Orifices. AIAA Paper 85-1104 presented at the 21st Joint Propulsion Conference, Monterey, California, NASA TM-86996, June 1985.

30. Srinivasan, R.; Coleman, E.; Meyers, G. D.; and White C.: Dilution Jet Mixing Program Phase III Report. NASA CR-174884, (Garrett Turbine Engine Company, NAS3-22110), September 1985.

31. Holdeman, J. D.; and Srinivasan, R.: Modeling of Dilution Jet Flowfields. Journal of Propulsion and Power, November/December 1985.

32. Ong, L. H.; and Lilley, D. G.: Measurements of a Single Lateral Jet Injected into Swirling Crossflow. NASA CR-175040. (Oklahoma State University, NAG3-549), January 1986.

33. McMurry, C. B.; and Lilley, D. G.: Experiments on Two Opposed Lateral Jets Injected into Swirling Crossflow. NASA CR-175041. (Oklahoma State University, NAG3-549), January 1986.

34. Srinivasan R.; and White C.: Dilution Jet Mixing Program, Supplementary Report. NASA CR-175043, (GTEC 21-5705, Garrett Turbine Engine Company, NAS3-22110), March 1986.

35. Holdeman J. D.; and Srinivasan, R.: Perspectives on Dilution Jet Mixing. AIAA 86-1611, NASA TM-87294, June 1986.

36. Lilley, D. G.: Lateral Jet Injection Into Typical Combustor Flowfields. NASA CR-3997, (Oklahoma State University, NAG3-549), July 1986.

TURBINE HEAT TRANSFER

1. Florschuetz, L. W.; and Isoda, Y.: Flow Distributions and Discharge Coefficients for Jet Array Impingements with Initial Crossflow. ASME 82-GT-156, April 1982.

2. Florschuetz, L. W.; Metzges, D. E.; Su, C. C.; Isoda, Y.; and Tseng, H. H.: Jet Array Impingement Flow Distributions and Heat Transfer Characteristics - Effects of Initial Crossflow and Nonuniform Array Geometry---Gas Turbine Engine Component Cooling. NASA CR-3630, November 1982.

3. Gladden, H. J.; Hylton, L. D.; Mihelc, M. S.; and Nealy, D. A.: Measurement of Heat Transfer Distribution Over the Surfaces of Highly Loaded Turbine Nozzle Guide Vanes. ASME 83-GT-53, March 1983.

4. Florschuetz, L. W.; Metzger, D. E.; and Su, C. C.: Heat Transfer Characteristics for Jet Array Impingement with Initial Crossflow. ASME 83-GT-28, March 1983.

5. Hylton, L. D.; Mihelc, M. S.; Nealy, D. A.; Turner, E. R.; and York, R. E.: Analytical and Experimental Evaluation of the Heat Transfer Distribution Over the Surfaces of Turbine Vanes. NASA CR-168015, (Allison Gas Turbine Division, NAS3-22761), May 1983.

6. Richards, D. R.; and Florschuetz, L. W.: Forced Convection Heat Transfer to Air/Water Vapor Mixtures. NASA CR-3769, January 1984.

7. Nealy, D. A.; Mihelc, M. S; Hylton, L. D.; and Gladden, H. J.: Measurements of Heat Transfer Distribution Over the Surfaces of Highly Loaded Turbine Nozzle Guide Vanes. Journal of Engineering for Gas Turbines and Power, January 1984, Vol. 106.

8. Florschuetz, L. W.; and Tseng, H. H.: Effect of Nonuniform Geometries on Flow Distributions and Heat Transfer Characteristics for Arrays of Impinging Jets. ASME 84-GT-156, June 1984.

9. Vatsa, V. N.: A Three-Dimensional Boundary Layer Analysis Including Heat-Transfer and Blade-Rotation Effects. United Technologies Research Center, January 1985.

10. Fronek, D. L.; Gladden, H. J.; and Yeh, F. C.: Heat Transfer Results and Operational Characteristics of the NASA Lewis Research Center Hot Section Cascade Test Facility. NASA TM-86890, March 1985.

11. Weinberg, B. C.; Yang, R. J.; McDonald, H.; and Shamroth, S. J.: Calculations of Two- and Three-Dimensional Transonic Cascade Flow Fields Using the Navier-Stokes Equations. ASME 85-GT-66, (Scientific Research Associates, Inc., NAS3-23695), March 1985.

12. Hippensteele, S. A.; Russel, L. M.; and Torres, F. J.: Local Heat-Transfer Measurements on a Large, Scale-Model Turbine Blade Airfoil Using a Composite of a Heater Element and Liquid Crystals. NASA TM-86900, March 1985.

13. Florschuetz L. W.; and Su, C. C.: Recovery Effects on Heat Transfer Characteristics Within an Array of Impinging Jets. Arizona State University, NSG3-075, April 1985.

14. Hylton, L. D.; Kaufman, R. M.; Turner, E. R.; and Wilson, M. D.: Turbir Vane External Heat Transfer, Volume I - Analytical and Experimental Evaluation of Surface Heat Transfer Distributions With Leading Edge Showerhead Film Cooling. NASA CR-174827, (Allison Gas Turbine Division, NAS3-23695), July 1985.

15. McDonald, H.; Shamroth, S. J.; Weinberg, B. C.; and Yang, R. J.: Turbir Vane External Heat Transfer, Volume II - Numerical Solutions of the Navier-Stokes Equations for Two- and Three-Dimensional Turbine Cascades With Heat Transfer. NASA CR-174828, (Allison Gas Turbine Division, NAS3-23695), July 1985.

16. Gladden, H. J.; and Proctor, M. P.: Transient Technique for Measuring Heat Transfer Coefficients on Stator Airfoils in a Jet Engine Environment. NASA TM-87005, July 1985.

17. Anderson, O. L.; and Caplin, B.: User's Manual for Three Dimensional Boundary Layer (BL3-D) Code. NASA CR-174899, (United Technologies Research Center, NAS3-23716), August 1985.

18. Anderson, O. L.: Assessment of a 3-D Boundary Layer Analysis to Predict Heat Transfer and Flow Field in a Turbine Passage. NASA CR-174899, (United Technologies Research Center, NAS3-23716), August 1985.

19. Florschuetz, L. W.; and Su, C. C.: Heat Transfer Characteristics Within an Array of Impinging Jets. NASA CR-3936, (Arizona State University, NSG3-075), October 1985.

20. Anderson, O. L.: Calculation of Three-Dimensional Boundary Layers on Rotational Turbine Blades. United Technologies Research Center, NAS3-23716, November 1985.

21. Florschuetz, L. W.; and Su, C. C.: Heat Transfer Characteristics Within an Array of Impinging Jets- Effects of Crossflow Temperature Relative to Jet Temperature. NASA CR-3936, (Arizona State University, NSG3-075), December 1985.

22. Crawford, R. A.; Peters, C. E.; Steinhoff, J. S.; Hornkohl, J. O.; Nourinejad, J.; and Ramachandran, K.: Mean Velocity and Turbulence Measurements in a 90° Curved Duct With Thin Inlet Boundary Layer. NASA CR-174811, (Tennessee University Space Institute, NAS3-23278), December 1985.

23. Florschuetz, L. W.; and Metzger, D. E.: Effect of Initial Crossflow Temperature on Turbine Cooling With Jet Arrays. Arizona State University, NSG3-075.

24. Kopper, F.: Coolant Side Heat Transfer With Rotation. Pratt and Whitney, NAS3-23691.

25. Dring, R. P.; Blair, M. F.; and Joslyn, H. D.: The Effects of Inlet Turbulence and Rotor/Stator Interactions on the Aerodynamics and Heat Transfer of a Large-Scale Rotating Turbine Model. Vol. I, Final Report, NASA CR-179466, (United Technologies Research Center, NAS3-23717).

26. Dring, R. P.; Blair, M. F.; and Joslyn, H. D.: The Effects of Inlet Turbulence and Heat Transfer of a Large-Scale Rotating Turbine Model. Vol. II, Heat Transfer Data Tabulation. 15% Axial Spacing. NASA CR-179467, (United Technologies Research Center, NAS3-23717), May 1986..

27. Dring, R. P.; Blair, M. F.; and Joslyn, H. D.: The Effects of Inlet Turbulence and Heat Transfer of a Large-Scale Rotating Turbine Model. Vol. III, Heat Transfer Data Tabulation. 65% Axial Spacing. NASA CR-179468, (United Technologies Research Center, NAS3-23717), May 1986.

28. Dring, R. P.; Blair, M. F.; and Joslyn, H. D.: The Effects of Inlet Turbulence and Rotor/Stator Interactions on the Aerodynamics and Heat Transfer of a Large-Scale Rotating Turbine Model. Vol. IV, Aerodynamic Data Tabulation. NASA CR-179469, (United Technologies Research Center, NAS3-23717).

29. Chyn, M. K.; Metzger, D. E.; and Hwan, C. I.: Heat Transfer in Shrouded Rectangular Cavities, 4th AIAA/ASME Thermophysics and Heat Transfer Conference, 1986.

STRUCTURAL ANALYSIS

1. Robinson, D. N.: Constitutive Relationships for Anisotropic High-Temperature Alloys. NASA TM-83437, September 1983.

2. Wilson, R. B.; Bak, M. J.; Nakazawa, S.; and Banerjee, P. K.: 3-D Inelastic Analysis Methods for Hot Section Components (Base Program), Turbine Blades, Turbine Vanes, and Combustor Liners. NASA CR-174700, (PWA-5940-19, Pratt and Whitney, NAS3-23697), February 1984.

3. Lindholm, U. S.; Chan, K. S.;, Bodner, S. R.; Weber, R. M.; Walker, K. P.; and Cassenti, B. N.: Constitutive Modeling for Isotropic Materials (HOST), 1st Annual Report. NASA CR-174718, (Southwest Research Institute, NAS3-23925), May 1984.

4. Maffeo, R. J.: Burner Liner Thermal/Structural Load Modeling. NASA CR-174892, (General Electric Company, NAS3-23272), October 1984.

5. Rasmaswany, V. G.; Van Stone, R. H.; Dame, L. T.; and Laflen, J. H.: Constitutive Modeling for Isotropic Materials, Annual Report. NASA CR-17485, (General Electric Company, NAS3-23927), March 1985.

6. Ellis, J. R.; and Robinson D. N.: Some Advances in Experimentation Supporting Development of Viscoplastic Constitutive Models. NASA CR-174855, (University of Akron, NAG3-379), April 1985.

7. McKnight, R. L.: Component-Specific Modeling, First Annual Status Report, 1983. NASA CR-174765, (General Electric Company, NAS3-23687), May 1985.

8. McKnight, R. L.: Component Specific Modeling, Second Annual Status Report, 1985. NASA CR-174925, (General Electric Company, NAS3-23687), 1985.

9. Robinson, D. N.: On Thermomechanical Testing in Support of Constitutive Equation Development for High-Temperature Alloys. NASA CR-174879, (University of Akron, NAG3-379), May 1985.

10. Nagtegaal, J. C.; S. Nakazawa S.; and Wertheimer T. B.: 3-D Inelastic Analysis Methods for Turbine Engine Hot Section Components, Special Finite Element Models - Users Manual. MARC Corporation, May 1985.

11. Dias, J. B.; Nagtegaal, J. C.; Nakazawa S.; and Wertheimer, T. B.: Users' Manual (Version 2.1). MARC Corporation, May 1985.

12. McKnight, R. L.: Component-Specific Modeling - Annual Status Report 1984, CR-174765, (General Electric Company, NAS3-23687), May 1985.

13. Nonlinear Constitutive Relations for High Temperature Application - 1984, NASA CP-2369, June 1985.

14. Lindholm, U. S.; Chan, K. S.; Bodner, S. R.; Weber, R. M.; Walker, K. P.; and Cassenti, B. N.: Constitutive Modeling for Isotropic Materials, (HOST) Second Annual Report. NASA CR-174980, (Southwest Research Institute, NAS3-23925), July 1985.

15. Hwang, S. Y.; and Kaufman, A.: On Local Total Strain Redistribution Using a Simplified Cyclic Inelastic Analysis Base on an Elastic Solution. NASA TM-86913, July 1985.

16. Kaufman A.; Laflen, J. H.; and Lindholm, V. S.: Unified Constitutive Material Models for Nonlinear Finite-Element Structural Analysis. NASA TM-86985, July 1985.

17. Robinson, D. N.: A Continuous Damage Model Based on Stepwise-Stress Creep Rupture Tests. NASA CR-174941, (University of Akron, NAG3-379), July 1985.

18. Ellis, J. R.: Results of an Interlaboratory Fatigue Test Program Conducted on Alloy 800H at Room and Elevated Temperatures. NASA CR-174940, (University of Akron, NAG3-379), July 1985.

19. Maffeo, R.: Burner Liner Thermal/Structural Load Modeling TRANCITS Program User's Manual. NASA CR-174891, (General Electric Company, NAS3-23272), August 1985.

20. Bartolotta, P. A.: Thermomechanical Cyclic Hardening Behavior of Hastelloy-X. NASA CR-174999, (University of Akron, NAG3-379), November 1985.

21. Banerjee, P. K.; Snow D. W.; and Wilson R. B.: Stress Analysis of Gas Turbine Engine Structures Using the Boundary Element Method. Pratt and Whitney, November 1985.

22. Ellis, J. R.: An Experimental Study of Biaxial Yield in Modified 9Cr-1Mo Steel at Room Temperature. NASA CR-175012, (University of Akron, NAG3-379), November 1985.

23. Nonlinear Constitutive Relations for High Temperature Applications. NASA CP-2271.

24. Dame, L. T.; and Stouffer, D. C.: Anisotropic Constitutive Model for Nickel Base Single Crystal Alloys: Development and Finite Element Implementation. NASA CR-175015, (University of Cincinnati, NAG3-511), March 1986.

25. Ramaswamy, V. G.: A Constitutive Model for the Inelastic Mutliaxial Cyclic Response of a Nickel Base Supperalloy Rene 80. NASA CR-3998, (University of Cincinnati, NAS3-23927), July 1986.

*1. McKnight, R. L.; Laflen, J. H.; and Spamer, G. T.: Turbine Blade Tip Durability Analysis. NASA CR-165268, (General Electric Company, NAS3-22020, GE-R81AEG372), 1981.

*2. Moreno, V.: Combustor Liner Durability Analysis. NASA CR-165250, (P&WA-5684-19, Pratt & Whitney), 1981.

*3. Walker, K. P.: Research & Development for Nonlinear Structural Modeling with Advanced Time-Dependent Constitutive Relationships. NASA CR-165533, (P&WA-5700-50, Pratt & Whitney) 1981.

*4. Meyers, G. J.: Fracture Mechanics Criteria for Turbine Engine Hot Section Components. NASA CR-167896, (PWA-5772-23, Pratt & Whitney), May 1982.

*5. Domas, P. A.; Sharp, W. N.; Ward, M.; and Yau, J.: Benchmark Notch Test for Life Prediction. NASA CR-165571, (General Electric Company, NAS3-22522, GE-R82AEB358), June 1982.

*6. Laflen, J. H.; and Cook, T. S.: Equivalent Damage - A Critical Assessment. NASA CR-167874, (General Electric Company), November 1982.

*7. McKnight, R. L.; Laflen, J. H.; Halford, G. R.; and Kaufman, A.: Turbine Blade Nonlinear Structural & Life Analysis. J. of Aircraft, Vol. 20, No. 5, pp. 475-480, May 1983.

8. Moreno, V.: Creep Fatigue Life Prediction for Engine Hot Section Materials (Isotropic), First Annual Report. NASA CR-168228, (PWA-5894-17 AR-1, Pratt and Whitney, NAS3-23288), August 1983.

*9. Sharpe, W. N.; and Ward, M.: Benchmark Cyclic Plastic Notch Strain Measurements. J. Eng. Matl's & Tech., Vol. 115, October 1983.

*10. Morena, V.: Development of a Simplified Analytical Method for Representing Material Cyclic Response. NASA CR-168100, (Pratt & Whitney, NAS3-22821, P&WA-5843-13), 1983.

*11. Moreno, V.; Meyers, G. J.; Kaufman, A. and Halford, G. R.: Nonlinear Structural & Life Analyses of a Combustor Liner. Computers & Structures, Vol. 16, No. 1-4, pp. 509-515, 1983. (See also NASA TM-82846, 1982.)

12. Liu, H. W.; and Oshida, Y.: Literature Survey on Oxidation and Fatigue Lives at Elevated Temperatures. NASA CR-174639, (Syracuse University, NAG3-348), March 1984.

13. Minzhong, Z.; and Liu, H. W.: Crack Tip Field and Fatigue Crack Growth in General Yielding and Low Cycle Fatigue. NASA CR-174686 (Syracuse University, NAG3-348), April 1984.

14. Halford, G. R.; and Kaufman, A.: Engine Cyclic Durability by Analysis and Material Testing. NASA TM-83577, presented at the 61st Meeting of the Propulsion and Energetics Panel, AGARD, Lisse, Netherlands, May 30 - June 1, 1984.

15. Liu, L. S.; Moreno, V.; and Nissley, D. M.: Creep Fatigue Life Prediction for Engine Hot Section Materials (Isotropic), Second Annual Report. NASA CR-174844, (Pratt and Whitney, NAS3-23288), December 1984.

16. Mauerer, G.; and Liu, H. W.: Morphological Study of Fatigue Crack Growth in the Near Threshold Region. (Syracuse University, NAG3-348), Proceedings, 2nd International Conference on Fatigue and Fatigue Thresholds, University of Birmingham, 1984, pp. 297-306.

17. Kim, K. S.; and Orange, T. W.: A Review of Path-Independent Integrals in Elastic-Plastic Fracture Mechanics. Presented at the 18th National Symposium on Fracture Mechanics, June 24-27, 1985, Boulder, Colorado (to be published by ASTM in a Special Technical Publication).

18. Moreno, V.; Nissley, D. M.; Halford, G. R.; and Saltsman, J. F.: Application of Two Creep Fatigue Life Models for the Prediction of Elevated Temperature Crack Initiation of a Nickel Base Alloy. AIAA Preprint No. 85-1420, July 1985.

19. Kim, K. S.: A Review of Path-Independent Integrals in Elastic-Plastic Fracture Mechanics, Task 4, Interim Report. NASA CR-174956, (General Electric Company, NAS3-23940), September 1985.

20. Malik, S. N.; Vanstone, R. H.; Kim, K. S.; Laflin, J. H.; and Yau J. F.: Elevated Temperature Crack Growth. NASA CR-174957, (General Electric Company, NAS3-23940), September 1985.

21. Kaufman, A.; and Moreno, V.: Two Simplified Procedures for Estimating Cyclic Material Response From a Strain History. NASA CP-2369, 1985.

22. Liu, H. W.: Shear Fatigue Crack Growth: A Literature Survey. Fatigue of Engineering Materials and Structures, Vol. 8, No. 4, 1985.

23. Gayda, J.; Hebsur, M. G.; and Miner, M. V.: Creep-Fatigue Behavior of NiCoCrAlY Coated PWA 1480 Superalloy Crystals. NASA TM-87110, 1985.

24. Liu, H. W.; and Oshida, Y.: Grain Boundary Oxidation and Oxidation Accelerated Fatigue Crack Nucleation and Propagation, NASA CR-175050, (Syracuse University, NAG3-348), January 1986.

25. Minzhong, Z.; and Liu, H. W.: Fatigue Crack Growth Under General Yielding Cyclic-Loading. NASA CR-175049, (Syracuse University, NAG3-348), February 1986.

26. Linask, I.; Swanson, G. A.; Nissley, D. M.; Norris, P. P.; Meyer, T. G. D.; and Walker, K. P.: Life Prediction and Constitutive Models for Engine Hot Section Anisotropic Materials Program. NASA CR-174952, (Pratt and Whitney, NAS3-23939), February 1986.

27. Gayda, J.; Gabb, T. P.; and Miner, R. V.: The Low Cycle Fatigue Behavior of a Plasma-Sprayed Coating Material, to be published in International Journal of Fatigue, September 1986. Also NASA TM-87318.

28. Hebsur, M. G.; and Miner, R. V.: High Temperature Tensile and Creep Behavior of Low Pressure Plasma Sprayed NiCoCrAlY Coating Alloy. Materials Science and Engineering, Vol. 83, No. 2, 1986, pp. 241-53.

29. Liu, H. W.; and Oshida, Y.: Grain Boundary Oxidation and Fatigue Crack Growth at Elevated Temperatures, NASA CR-179529, (Syracuse University, NAG3-348), 1986.

30. Gabb, T. P.; Miner, R. V.; and Gayda, J.: The Tensile and Fatigue Deformation Structures in a Single Crystal Ni-Base Superalloy. Scripta Metallurgica, Vol. 20, 1986, pp. 513-518.

31. Gabb, T. P.; and Welsch, G. E.: The Cyclic Stress-Strain Behavior of a Nickel-Base Superalloy at 650°C. Scripta Metallurgica, Vol. 20, 1986, pp. 1049-1054.

32. Bartallotta, P.; and McGaw, M. A.: An Elevated Temperature Fatigue and Constitutive Behavior Testing Facility. Proposed TM, 1986.

32. Hebsur, M. G.; and Miner, R. V.: Stress Rupture and Creep Behavior of a Low Pressure Plasma Sprayed NiCoCrAlY Coating Alloy in Air and Vacuum, Thin Solid Films, to be published January 1987.

33. Kaufman, A.; Tong, M.; Saltsman, J. F.; and Halford, G. R.: Structural Analysis of Turbine Blades Using Unified Constitutive Models. NASA TM-88807, to be presented at the International Conference on Computers in Engine Technology, Cambridge, March 24-27, 1987.

SURFACE PROTECTION

1. Fernandez de la Mora, J.; and Rosner, D. E.: Small Particle Transport Across Turbulent Non-Isothermal Boundary Layers. ASME Trans.-Journal Engineering for Power, 104, pp. 885-894, 1982.

2. Kohl, F. J.: Airfoil Deposition Model, NASA TM-83022, 1982.

3. Israel, R.; and Rosner, D. E.: Use of a Generalized Stokes Number to Determine the Aerodynamic Capture Efficiency of Non-Stokesian Particles from a Compressible Gas Flow. Aerosol Science of Technology, 2, pp. 45-51, 1983.

4. Gokoglu, S; and Rosner, D. E.: Note on the 'Windward Fraction' for Total Mass/Heat Transport Flow Past a Circular Cylinder. Aerosol Science of Technology, 2, pp. 275-287, 1983.

5. Gunes, D.; Nazih-Anous, N.; and Rosner, D. E.: Aerodynamically-Driven Condensate Layer Thickness Distributions on Isothermal Cylindrical Surfaces. Chemical Engineering Communications, 24, pp. 275-287, 1983.

6. Gokoglu, S.; Israel, R.; and Rosner, D. E.: Rational Engineering Correlations of Diffusional and Inertial Particle Deposition Behavior in Non-Isothermal Forced Convection Environments. Fouling of Heat Exchanger Surfaces, Engineering Foundation, Inc., ed. R. Bryers, pp. 235-256, 1983.

7. Atkins, R. M.; and Rosner, D. E.: Experimental Studies of Salt/Ash Deposition Rates from Combustion Products Using Optical Techniques. Fouling and Slagging Resulting from Impurities in Combustiuon Gases, Engineering Foundation, Inc., ed. R. Bryers, pp. 469-492, 1983.

8. Kohl, F. J.; Rosner, D. E.; and Stearns, C. A.: Combustion System Processes Leading to Corrosive Deposits. NASA TM 81752, 1983.

9. Rosner, D. E.: Turbine Airfoil Deposition Models, NASA CP-2289, 1983.

10. Gokoglu, S. A.: Verification of Airfoil Deposition Model. NASA CP-2289, 1983.

11. Gokoglu, S. A.: Application of Vapor and Particle Deposition Theory to the Interpretation of Burner Rig Experiments, "Oxidation, Deposition and Hot Corrosion in Combustion Turbine Engines". 1983.

12. Gokoglu, S. A.; and Rosner, D. E.: Comparisons of Rational Engineering Correlations of Thermophoretically-Augmented Particle Mass Transfer with STAN5-Predictions for Developing Boundary Layers. NASA CR-168221, (Yale University, NAG3-201), January 1984.

13. Gokoglu, S. A.; and Rosner, D. E.: Computer Program for the Calculation of Multicomponent Conventive Diffusion Deposition Rates from Chemically Frozen Boundary Layer Theory. NASA CR-168329, (Yale University, NAG3-201), January 1984.

14. Gokoglu, S. A.; and Rosner, D. E.: Engineering Correlations of Variable-Property Effects on Laminar Forced Convection Mass Transfer for Dilute Vapor Species and Small Particles in Air. NASA CR-168322, (Yale University, NAG3-201), January 1984.

15. Rosner, D. E.; and Seshadri, K.: Optical Methods and Results of Dew Point and Deposition Rate Measurements in Salt/Ash-Containing Combustion Gases-B_2O_3(l) Deposition Rates by Interference Methods and Comparisons with Theory. American Institute of Chemical Engineering J., 30, 187-196, March 1984.

16. Gokoglu, S. A.; and Rosner, D. E.: Effect of Particulate Thermophoresis in Reducing the Fouling Rate Advantages of Effusion-Cooling. International Journal of Heat and Fluid Flow, Volume 5, Number 1, pp. 37-41, March 1984.

17. Gokoglu, S. A.; and Rosner, D. E.: Correlation of Thermophoretically-Modified Small Particle Diffusional Deposition Rates in Forced Convection Systems with Variable Properties, Transpiration Cooling and/or Viscous Dissipation. International Journal of Heat and Mass Transfer, Volume 27, Number 5, pp. 639-645, May 1984.

18. Gokoglu, S. A.; and Rosner, D. E.: Comparisons of Rational Engineering Correlations of Thermophoretically-Augmented Particle Mass Transfer with STAN5-Predictions for Developing Boundary Layers. ASME 84-GT-158, June 1984.

19. Fryxell, R. E.: Effects of Surface Chemistry on Hot Corrosion Life, First Annual Report. NASA CR-174683, (R84AEB422, General Electric Company, NAS3-23926), June 1984.

*20. Miller, R. A.: Oxidation-Based Model for Thermal Barrier Coating Life. Published in the J. of the American Ceramic Society, Vol. 67, No. 8, pp. 517-521, August 1984.

21. Miller, R. A.; and Berndt, C. C.: The Performance of Thermal Barrier Coatings in High Heat Flux Environments. Published in Thin Solid Films 119, No. 2 (1984). Also NASA TM 83663.

22. Berndt, C. C.; and Miller, R. A.: Mechanical Property Measurements of Plasma-Sprayed Thermal Barrier Coatings Subjected to Oxidation. Published in Ceramic Engineering and Science Proceedings, Vol. 5, 1984.

23. Berndt, C. C.: Acoustic Emission Evaluation of Plasma-Sprayed Thermal Barrier Coatings. Presented at 29th International Gas Turbine Conference and Exhibit, Amsterdam, The Netherlands, June 4-7, 1984. Published in Trans. ASME J. of Engineering for Gas Turbines, Vol. 107, pp. 142-146, 1985.

24. Berndt, C. C.: Behavior of Plasma-Sprayed Coatings. Published in Ultrastructure Processing of Ceramics, Glasses and Composites, pp. 524-534, ed. L. L. Hench and D. R. Ulrich, Publ. J. Wiley and Sons, 1984.

25. Berndt, C. C.: Fracture Toughness Tests on Plasma-Sprayed Coatings. Advances in Fracture Research, Vol. 107, pp. 2545-2552, ed. S. R. Valluri, et al., Pergamon Press, 1984.

26. Berndt, C. C.; and Miller, R. A.: Failure Analysis of Plasma-Sprayed Thermal Barrier Coatings. Published in Thin Solid Films 119, No. 2, pp. 173-184 (1984). Also NASA TM 83777.

27. Gokoglu, S. A.: Experimental Verification of Vapor Deposition Model in Mach 0.3 Burner Rigs. NASA CP-2339, 1984.

28. Fernandez de la Mora, J.; and Rosner, D. E.: Boundary Layer Effects on Particle Impaction and Capture. ASME Trans.-Journal of Fluids Engineering, 107, 1984.

29. Gokoglu, S. A.; Kohl, F. J.; Rosner, D. E.; and Santoro, G. J.: Experimental and Theoretical Deposition Rates from Salt-Seeded Combustion Gases of a Mach 0.3 Burner Rig. NASA TP-2225, 1984.

30. Gokoglu, S. A.; Kohl, F. J.; Rosner, D. E.; Santoro, G. J.; and Stearns, C. A.: Deposition of Na_2SO_4 from Salt-Seeded Combustion Gases of a High Velocity Burner Rig. NASA TM-83751, 1984.

31. Kim, S. S.; and Rosner, D. E.: Optical Experiments on Thermophoretically Augmented Submicron Particle Deposition from "Dusty" High Temperature Gas Flows. Chemical Engineering Journal, 29, 147-157, 1984.

32. Rosner, D. E.: Turbine Airfoil Deposition Models, CP-2339, 1984.

33. Rosner, D. E.: Non-Fickian Mass Transfer Across Combustion Gas Thermal Boundary Layers -- Power Production and Materials Processing Implications. Proceedings NSF Workshop for Interactive Thermal and Materials Sciences in Materials Processing, 1985.

34. Strangman, T. E.: Development of Thermomechanical Life Prediction Models for Thermal Barrier Coatings in Thermal Barrier Coatings Workshop Abstracts and Figures. Lewis Research Center, May 1985.

35. Fryxell, R. E.: Effects of Surface Chemistry on Hot Corrosion Life, NASA CR-174915, (General Electric Company, NAS3-23926), June 1985.

36. Nuemann J.; and Strangman T. E.: Thermal Barrier Coating Life Prediction Model Development. NASA CR-175002, (Garrett Turbine Engine Company, NAS3-23945), September 1985.

37. Gokoglu, S. A.; and Santoro, G. J.: Experimental Verification of Vapor Deposition Rate Theory in High Velocity Burner Rigs. NASA CP-2405, 1985.

38. Gokoglu, S. A.; and Santoro, G. J.: Determination of Convective Diffusion Heat/Mass Transfer Rates to Burner Rig Test Targets Comparable in Size to Cross-Stream Jet Diameter. NASA TM-87176, 1985. (Also ASME 86-GT-68.)

39. Gokoglu, S. A.; and Rosner, D. E.: Viscous Dissipation Effects on Thermophoretically-Augmented Particle Transport Across Laminar Boundary Layers. International Journal of Heat and Fluid Flow, 6, 293-297, 1985.

40. Nagarajan, R.; and Rosner, D. E.: Transport-Induced Shifts in Condensate Dew-Point and Composition in High Temperature Multicomponent Systems with Chemical Reaction. Chemical Engineering Science, 40, 177-186, 1985.

41. Gokoglu, S. A.; and Rosner, D. E.: Thermophoretically Enhanced Mass Transport Rates to Solid and Transpiration-Cooled Walls Across Turbulent (Law-of-the-Wall) Boundary Layers. I/EC Fundamentals, 24, 208-214, 1985.

42. Rosner, D. E.; and Nagarajan, R.: Turbine Airfoil Deposition Models and Their Hot Corrosion Implications, NASA CP-2405, 1985.

43. Strangman, T. E. and Nuemann, J.: NASA CR-175002, (Garrett Turbine Engine Company), 1985.

44. DeMasi, J. T.; and Sheffler, K. D., NASA CR-175087,(Pratt & Whitney Aircraft), 1985.

45. Hillery, R. . and Pilsner, B. H., NASA CR-175010, (General Electric Company), 1985.

46. Gokoglu, S. A.; and Rosner, D. E.: Thermophoretically-Augmented Mass Transfer Rates to Solid Walls Across Laminar Boundary Layers. AIAA Journal, 24, 172-179, 1986.

47. Gokoglu, S. A.; and Santoro, G. J.: Comparison of Theoretical and Experimental Sodium Sulfate Deposition Rates from Combustion Gases in a High Velocity Burner Rig, NASA TM-87287, 1986.

48. Rosner, D. E.; and Liang, Baishen: Laboratory Studies of the Deposition of Alkali Sulfate Vapors from Combustion Gases Using a Flash-Evaporation Technique. Chemical Engineering Communications, 42, 171-196, 1986.

49. Liang, Baishen; and Rosner, D. E.: Laboratory Studies of the Deposition of Binary Alkali Sulfate Vapors from Salt-Seeded Combustion Gases Using a Flash-Evaporation Technique. AICHE Fall Meeting, Miami, Florida, 1986.

50. Liang, Baishen and Rosner, D. E.: Simplification of Multi-Salt Dew Point Predictions Allowing for Salt/Combustion Product Chemical Reactions and Solution Non-Ideality. J. Electrochemical Society, 1986.

51. Rosner, D. E.; and Nagarajan, R.: Vapor Deposition and Condensate Flow on Combustion Turbine Blades: Theoretical Model to Predict/Understand Some Corrosion Rate Consequences of Molten Alkali Sulfate Deposition in the Field Laboratory. Int. J. Turbo of Jet Engines, 1986.

52. Santoro, G. T.; and Gokoglu, S. A.: Experiments for the Determination of Convective Diffusion Heat/Mass Transfer Rates to Burner Rig Test Targets Comparable in Size to Jet Stream Diameter, NASA TM-87196, 1986.

53. Gokoglu, S. A.; and Rosner, D. E.: Prediction and Rational Correlation of Thermophoretically Reduced Particle Mass Transfer to Hot Surfaces Across Laminar or Turbulent Forced-Convection Gas Boundary Layers. Chemical Engineering Communications, 44, 107-119, 1986.

54. Gokoglu, S. A.: Discussion of the Effect of Wall Suction and thermophoresis on Aerosol Particle Deposition from a Laminar Boundary Layer on a Flat Plate. Int. J. of Heat and Mass Transfer, 1986.

55. DeMasi, J. T.; and Sheffler, K. D.: Mechanisms of Thermal Barrier Coating Degradation and Failure. IBID.

56. Miller, R. A.: The Effect of Oxidation on the High Heat Flux Behavior of a Thermal Barrier Coating. IBID.

57. Duderstadt, E. C.; and Pilsner, B. H.: Effect of Bond Coat Creep and Oxidation. IBID.

58. Chang, G. C. and Phucharoen, W.: Finite Element Analysis of Thermal Barrier Coatings. IBID.

GENERAL

*1. Cruse, T. A.; and Dennis, A. J.: Cost Benefits from Improved Hot Section Life Prediction Technology. AIAA 79-1154, Pratt and Whitney, June 1979.

2. Aircraft Engine Diagnostics. NASA CP-2190, May 1981.

3. Turbine Engine Hot Section Technology (HOST). NASA TM-83022, October 1982.

4. Turbine Engine Hot Section Technology 1983. NASA CP-2289, October 1983.

5. Turbine Engine Hot Section Technology 1984. NASA CP-2339, October 1984.

6. Turbine Engine Hot Section Technology 1985. NACA CR-2405, September 1985.

7. Sokolowski, D. E.; and Ensign, C. R.: Toward Improved Durability in Advanced Combustors and Turbines -- Progress in the Prediction of Thermomechanical Loads. Presented at the International Gas Turbine Conference and Exhibit, Dusseldorf, West Germany, June 8-12, 1986. ASME 86-GT-172.

1. Report No.	2. Government Accession No.	3. Recipient's Catalog No.
NASA CP-2444		

4. Title and Subtitle	5. Report Date
Turbine Engine Hot Section Technology 1986	October 1986
	6. Performing Organization Code: 533-04-11
7. Author(s)	8. Performing Organization Report No.: E-3205
	10. Work Unit No.
9. Performing Organization Name and Address: National Aeronautics and Space Administration, Lewis Research Center, Cleveland, Ohio 44135	11. Contract or Grant No.
	13. Type of Report and Period Covered: Conference Publication
12. Sponsoring Agency Name and Address: National Aeronautics and Space Administration, Washington, D.C. 20546	14. Sponsoring Agency Code

15. Supplementary Notes

16. Abstract

On October 21 and 22, 1986, the Turbine Engine Hot Section Technology (HOST) Project of the NASA Lewis Research Center sponsored a workshop to discuss current research pertinent to turbine engine durability problems. Presentations were made concerning the hot-section environment and the behavior of combustion liners, turbine blades, and turbine vanes. The presentations were divided into six sessions: Instrumentation, Combustion, Turbine Heat Transfer, Structural Analysis, Fatigue and Fracture, and Surface Protection. The principal objective of each session was to disseminate research results to date. Topics discussed included modeling of thermal and fluid-flow phenomena, structural analysis, fatigue and fracture, surface protective coatings, constitutive behavior of materials, stress-strain response, and life-prediction methods. Researchers from industry, academia, and government presented results of their work sponsored by the HOST Project. This publication contains extended abstracts and visual material presented during the workshop.

17. Key Words (Suggested by Author(s))	18. Distribution Statement
Turbine Engine Hot Section Technology (HOST); Life prediction; Combustor liners; Turbine airfoils; Material behavior; Aircraft engines; Durability analysis methods	STAR Category 39

19. Security Classif. (of this report)	20. Security Classif. (of this page)	21. No. of pages	22. Price*
Unclassified	Unclassified		